



Trehalose mediated stabilisation of cellobiase aggregates from the filamentous fungus *Penicillium chrysogenum*

Ahana Das^a, Pijush Basak^b, Arnab Pramanick^b, Rajib Majumder^c, Debadrita Pal^d, Avishek Ghosh^a, Manas Guria^e, Maitree Bhattacharyya^{b,*}, Samudra Prosad Banik^{a,*}

^a Department of Microbiology, Maulana Azad College, 8 Rafi Ahmed Kidwai Road, Kolkata 700013, West Bengal, India

^b Jagadis Bose National Science Talent Search, 1300, Rajdanga Main Road, Sector C, East Kolkata Township, Kolkata 700107, West Bengal, India

^c School of Life Science and Biotechnology, Department of Biotechnology, Adamas University, Kolkata 700126, West Bengal, India

^d Department of Biology, New Mexico State University, PO Box 30001, MSC 3AF, Las Cruces, NM 88003, United States of America

^e Department of Biochemistry, University of Calcutta, 35, Ballygunge Circular Road, Kolkata 700019, West Bengal, India

ARTICLE INFO

Article history:

Received 25 August 2018

Received in revised form 12 January 2019

Accepted 14 January 2019

Available online 15 January 2019

Keywords:

Fungal cellobiase

Protein aggregation

Trehalose

Glycated protein

ABSTRACT

Extracellular fungal cellobiases develop large stable aggregates by reversible concentration driven interaction. *In-vitro* addition of trehalose resulted in bigger cellobiase assemblies with increased stability against heat and dilution induced dissociation. In presence of 0.1 M trehalose, the size of aggregates increased from 344 nm to 494 nm. The increase in size was also observed in zymography of cellobiase. Activation energy of the trehalose stabilised enzyme ($E_a = 220.9$ kJ/mol) as compared to control ($E_a = 257.734$ kJ/mol), suggested enhanced thermostability and also showed increased resistance to chaotropes. Purified cellobiase was found to contain 196.27 μ g of sugar/ μ g of protein. It was proposed that presence of glycan on protein's surface impedes and delays trehalose docking. Consequently, self-association of cellobiase preceded coating by trehalose leading to stabilisation of bigger cellobiase aggregates. In unison with the hypothesis, ribosylated BSA failed to get compacted by trehalose and developed into bigger aggregates with average size increasing from 210 nm to 328 nm. Wheat Germ Lectin, in presence of trehalose, showed higher molecular weight assemblies in DLS, native-PAGE and fluorescence anisotropy. This is the first report of cross-linking independent stabilisation of purified fungal glycosidases providing important insights towards understanding the aggregation and stability of glycated proteins.

© 2019 Published by Elsevier B.V.

1. Introduction

Industrially exploited enzymes from fungal origin are more stable than their bacterial counterparts owing to their natural tendency to develop into big assemblies [1], both through reversible concentration driven association [2,3], as well as inter-subunit disulphide bond formation [4]. The phenomenon has been extensively studied with extracellular cellobiase (3.2.1.21) from filamentous fungi [5,6], a typical β -glucosidase catalysing the final rate limiting step of cellulose hydrolysis that is conversion of cellobiose to glucose [7,8]. Therefore most of the current technological advancements involved in boosting production of the Biofuel industry are aimed towards manipulation of this step to increase glucose productivity. The enzyme is secreted by filamentous fungus in the form of big cellulolytic multienzyme complex [9]. During subsequent purification steps, it loses both stability as well as catalytic efficiency due to decrease in size affected by sheer dilution [2], as well as loss of contact with the other enzymes in the aggregate [10]. When

reconcentrated during final stages of purification, the globular subunits again coalesce together replenishing partially the lost activity and stability [2]. This points to the fact that the intersubunit association or aggregation of extracellular cellobiase is intrinsic to its structural make-up as is observed for some other globular proteins [11]. However, these native enzyme agglomerates are fundamentally different from the misfolded aggregates [12] as well as reversible aggregates of globular proteins [11], where there is a simultaneous departure from native state as indicated by loss of functionality and altered secondary structure. Although technologies such as use of cross-linked enzyme aggregates [13], organic solvents [14], and other physical adsorption or entrapment based immobilisation [15] procedures have been carried out to stabilise and improve the activity of these enzymes, none of the studies thus far have been able to prevent the dilution induced dissociation of cellobiase and other related fungal enzymes.

Trehalose, an otherwise inert non reducing disaccharide serves as an excellent cellular osmolyte in a wide range of prokaryotes as well as the lower rung of the eukaryotic kingdom [16]. Besides serving as a storage sugar, it is implicated in many dynamic cellular functions [17], from acting as a signalling molecule to regulate various metabolic pathways [18], to serving as an autophagic inducer [19]. However, probably the

* Corresponding authors.

E-mail addresses: bmaitree@gmail.com (M. Bhattacharyya), samudrapb@gmail.com (S.P. Banik).

most exciting area in trehalose research owes to its role in stabilisation of native protein structures from misfolding and aggregation [20]. Under conditions of intracellular stress, trehalose binds to partially unfolded protein intermediates and prevents them from developing into misfolded protein aggregates [21]. However, it is enzymatically degraded immediately after stress subsides since post stress presence of trehalose interferes with the functioning of cellular chaperones [22]. Many theories have been proposed thus far to explain the mechanism of trehalose action amongst which the vitrification theory, the water replacement theory and the preferential exclusion theory have been the most popular ones [21]. *In vitro* elucidation of the mechanism of trehalose action has suggested that the disaccharide stabilizes protein's native structure by either replacing water from its solvent accessible surface (the water replacement theory) [23, 24] or sequestering water molecules away from the protein (Preferential exclusion theory) [25] thereby bringing about its structural rigidity and compaction. This water replacement of the protein prevents its interaction with other subunits and inhibits development of big protein aggregates [23]. However, trehalose mediated increase in stability of the protein comes at a cost of reduced functionality chiefly due to high viscosity of the glassy microenvironment around the protein imparted by trehalose [23]. Although many studies have been carried out on the trehalose mediated stabilisation of protein's native structure and subsequent prevention of aggregation [26–28], few have been directed so far to specifically understand its effect on aggregation prone globular proteins like the serum albumins [23]. It has been demonstrated earlier in our lab that trehalose effectively sequesters BSA monomers from self-association by inducing surface compaction and subsequent coating [23]. Therefore it was also worthwhile to investigate how trehalose would modulate the concentration driven aggregation of fungal glycosidases most of which are globular, highly glycosylated, and intrinsically prone to aggregation. In the present studies, the effect of trehalose on the activity, stability and aggregation of purified extracellular cellobiase from *Penicillium chrysogenum* was investigated keeping in mind these hitherto unexplored domains of the mechanism of trehalose action. Unlike cellobiase, BSA does not have any surface attached glycans. Therefore in order to better simulate the effects of trehalose on globular aggregation prone cellobiase, we generated an *in vitro* ribosylated BSA. Parallely, we also wanted to investigate whether trehalose can mediate aggregation of sugar binding lectins [29], many of which being also able to bind trehalose with high specificity [30,31]. In the present study, Wheat Germ Agglutinin was used since it spontaneously associates to form a dimer at neutral pH [32] and does not have a specific binding affinity for trehalose ensuring a loose nonspecific docking of trehalose on WGA monomer/dimer.

2. Materials and methods

2.1. Chemicals and reagents

Bovine Serum Albumin (highest available purity), Guanidium hydrochloride (GdHCl), Urea, glutaraldehyde, Sephacryl S-200 and Diethyl-aminoethyl (DEAE)-Cellulose, *para*-Nitrophenyl β -D-glucopyranoside (pNPG), Dialysis bag (3 kDa), sucrose and maltose were purchased from Sigma Chemicals. Trehalose was purchased from Calbiochem. Media components were purchased from HiMedia and other chemicals and salts from SRL. SDS-PAGE molecular weight standard was from Fermentas (Cat No. SM0671).

2.2. Strain and culture conditions

Penicillium chrysogenum BF02 (GenBank Accession No. KC469896) was used in the present studies as the producer organism of extracellular cellobiase (E.C. 3.2.1.21). The organism was grown in batches of 50 ml shake flask cultures in 1% cellobiose medium supplemented

with salt solution for three days as described earlier [7], and terminated by separating the mycelia from the culture filtrate.

2.3. Purification of extracellular cellobiase

The enzyme was purified from culture media using ultrafiltration, gel filtration and ion exchange chromatography as described earlier [8]. Briefly, the culture medium was freed from suspended mycelia and/or spores by centrifugation at 4300g for 10 min and subsequent filtration of the supernatant with a 0.22 μ m membrane (Millipore) and was dialysed in a 3 kDa dialysis bag (Sigma) against 0.1 M acetate buffer (pH 5). The retentate was concentrated by lyophilisation and loaded on a Sephacryl S-200 gel permeation column (20 cm \times 1.8 cm) in batches of 0.5 ml. Protein fractions, eluted at the rate of 8.0 ml/h, were monitored for protein (A280) and cellobiase activities, and pooled as pool I (fractions 9–11) and pool II (fractions 13–15). It was desalted against 0.01 M of the same buffer by dialysis and concentrated by lyophilisation. Subsequently, the pooled protein was loaded in a DEAE-Cellulose (3.2 \times 18 cm) anion exchange chromatography column pre-equilibrated with 10 mM acetate buffer pH 5.0 at a flow rate of 18 ml/h. The proteins were then eluted with a linear gradient of sodium chloride from 0 to 1 M NaCl in the same buffer. The eluted fractions were assayed for cellobiase activity, pooled, and dialysed for final use as purified extracellular cellobiase. The purity of the preparation was assessed by 10% SDS PAGE.

2.4. Enzyme and protein assay

Cellobiase (EC 3.2.1.21) assay was carried out spectrophotometrically by using pNPG (Sigma) as substrate [33]. The reaction mixture (1 ml) contained 4 mM of pNPG in 0.1 M sodium acetate buffer, pH 5.0 and an appropriate amount of the enzyme. Incubation was carried out at 60 °C for 10 min. Reaction was terminated by the addition of 0.25 ml of Na₂CO₃ (0.5 M). Intensity of the yellow colour developed by liberation of *para*-nitro phenyl phosphate (pNP) was measured at 400 nm. One unit (U) of enzyme activity was expressed by the enzyme that produced 1 μ mol of pNP per min under the assay conditions. Protein content in the crude culture filtrate and intracellular extract was ascertained using Bradford reagent after extensive dialysis to remove the interfering sugars [34].

2.5. Thermal inactivation studies

Thermal inactivation of extracellular cellobiase preparations was determined by incubating the enzyme solutions in 100 mM sodium acetate, pH 5 buffer at a particular temperature. Aliquots were withdrawn at different times, cooled on ice for 3 h [35], and assayed for cellobiase activity at 60 °C, as described before. This procedure was repeated at four different temperatures ranging from 60 °C to 67 °C. The values of k_d were obtained as the slopes of thermal inactivation at the respective temperatures. The values of ΔG^* were calculated from the relationship $\Delta G^* = -RT \ln (k_d h / K_B T)$, h being the Planck constant, R the gas constant and K_B the Boltzmann constant. The data were subsequently used for calculation of activation energies of denaturation. Arrhenius plots were drawn with the first order rate constants for denaturation (k_d) of cellobiase and activation energy of denaturation (E_a) was calculated in each case from the slope of the plots. The thermodynamic data were calculated by rearrangement of the absolute rate equations:

$$K_d = K_B(T/h) e^{(-\Delta H^*/RT)} e^{(\Delta S^*/R)} \quad (1)$$

where, h (Planck constant) and K_B (Boltzman constant).

$$[R/N] = 1.38 \times 10^{-23} \text{ J/K} \quad (2)$$

where, N (Avogadro's no.) = $6.023 \times 10^{-23}/\text{mol}$

$$\Delta H^* \text{ (enthalpy of activation)} = E_a - RT \quad (3)$$

where, R (gas constant) = 8.314 J/Kmol

$$\Delta G^* \text{ (free energy of activation)} = -RT \ln [k_d(h)/K_B T] \quad (4)$$

$$\Delta S^* \text{ (entropy of activation)} = (\Delta H^* - \Delta G^*)/T \quad (5)$$

2.6. Chaotrope denaturation study

Guanidium hydrochloride (GdHCl) and urea are known as chaotropic agents that denature the protein structure. In order to assess the extent of protection offered by trehalose towards the enzyme, it was subjected to denaturation by increasing concentrations of GdHCl and Urea, in presence and absence of 0.5 M trehalose following which the enzyme assay were performed as described before.

2.7. SDS-PAGE, gradient PAGE and native zymography

SDS-polyacrylamide gel electrophoresis under reducing condition was carried out according to the methods described earlier [36,37]. Thereafter, it was immediately subjected to silver staining using ProteoSilverTM silver stain kit (Sigma) according to the manufacturer's instructions. Finally, the molecular weights of the partially purified protein bands were determined. Zymography or activity staining for in gel detection of cellobiase activity was performed as reported in Kwon et al. [38]. Briefly, after electrophoresis (5% Native PAGE), the gel was soaked in a 100 mM sodium citrate buffer (pH 5.0) containing esculin ferric chloride for 5 min. It was then incubated at 50°C for several minutes until a black band appeared.

2.8. Glycation of BSA

Bovine Serum Albumin (10 mg/ml) was incubated with 0.5 M ribose in 0.05M sodium phosphate buffer, pH 7.4 at 37°C . Reaction mixtures were kept in this condition for 10 days. To prevent bacterial contamination, it was kept into sterile glass tubes in presence of 3 mM sodium azide. Aliquots were taken under sterile conditions at desired times and frozen at -20°C until further assayed. In order to reduce the glycated protein, samples were then diluted five times with 0.2 M sodium acetate buffer, pH 5 and incubated at 37°C for 2 h to release glycosylamine adducts. This treated protein was then dialyzed overnight against 0.1 M sodium phosphate buffer, pH 7.4, at 4°C to remove free ribose. The dialyzed protein was reduced by adding a 50-fold molar excess of sodium borohydride in presence of 0.1 M sodium hydroxide. The solution was then kept at room temperature for 4 h after which the reaction was terminated by the adding 1 N HCl slowly to eliminate excess sodium borohydride. Finally, the samples were dialyzed overnight at 4°C against double distilled water [39].

2.9. Dynamic light scattering

Dynamic light scattering measurements were carried out as reported previously [23], in a Nano zeta-sizer (Malvern Instruments) at a fixed 90° scattering angle using a Nd-doped solid state laser of 632.5 nm with 100 s of integration time. Different concentrations of purified cellobiase, ribosylated BSA and lectin with and without 0.5 M trehalose were taken to perform the measurements. The concentration range was obtained depending on the response and sensitivity of the instrument. The intensity correlation function was obtained by acquiring data between 5 and 1000 ms, in 200 channels.

2.10. Transmission electron microscopy

TEM was carried out as reported earlier [2], with little modifications. In brief, twenty five square mesh copper grids with continuous carbon film (Electron Microscopy Sciences) were taken to incubate the samples. 10 μl of each purified cellobiase and the enzyme in presence of 0.05 M trehalose were applied onto the grids and allowed to dry in air before analysis. TEM images were acquired using JEOL-JEM 2100 (Japan) electron microscope operated at 200 kV and size of the proteins was determined using the associated software.

2.11. FITC- BSA conjugation

BSA and ribosylated BSA were labeled with fluorescein isothiocyanate (Sigma) in 0.1 M carbonate buffer, pH 9. The samples were kept at room temperature and in the dark for 4 h. The labelling ratio (F:P) for BSA and ribosylated BSA were 1:1 and 0.5:1, respectively. The solutions were then dialysed four times for 1 day against 0.01 M phosphate buffered saline (PBS), pH 7.4. All these dialyses were performed in the dark at 4°C to remove any unbound FITC. The F:P ratio range was selected according to the sensitivity and photophysics of the dye conjugated to the protein [40].

2.12. Circular dichroism

Circular dichroic (CD) spectra measurements were performed as described earlier [23,41], on a JASCO J-720 spectropolarimeter (calibrated with *d*-10-camphor-sulfonic acid). BSA and ribosylated BSA (0.1 mg/ml) were taken in a cylindrical quartz cuvette of path length 0.2 cm to measure the respective CD spectra in the far-UV wavelength range (190–250 nm) at 25°C . Each spectrum had an average of four consecutive scans. All the spectra were corrected by deducting blank runs on appropriate protein-free buffer (10 mM-phosphate buffer, pH 7.0). Alpha helix content was determined using the following formula:

$$\% \text{ of } \alpha\text{-helix} = \{(\text{MRE}_{222} \text{ nm} - 2340)/30,300\} \times 100$$

where, Mean Residual Ellipticity (MRE) = $\text{MRE}_{222} = \theta_{\text{obs}}(\text{mdeg}) / (10 * n * c * l)$, n = number of peptide bonds, c = concentration of the sample in M, l = path length = 0.2 cm.

2.13. Fluorescence anisotropy

Fluorescence anisotropy decays of FITC conjugated BSA and lectin (in presence and absence of 0.1 M trehalose) were recorded in a Varian-Cary-UV Eclipse spectrofluorimeter at 25°C according to [42]. Polarized decays were collected at the vertical (I_{VV}) and horizontal (I_{VH}) positions of the emission polarizer. The samples were excited at 490 nm and the bandwidth used for excitation and emission monochromator was 5 nm. The emission intensities were measured at 522 nm. Fluorescence spectra were corrected for the emission of the control solution containing buffer (with specific concentration of trehalose). Both decays were collected in the same conditions and for the same amount of time. A high number of counts were necessary to increase the signal-to-noise ratio for anisotropy decays. G corresponds to a correction factor for the sensitivity of the optics to light with different polarizations. The G factor was recovered using the instruments software for the samples in the absence of protein, for which the rotational correlation time was short and the anisotropy decayed to zero within the time scale for the measurement. This procedure is essential since small changes in the G factor can bring about changes in the baseline for the anisotropy of the samples. The G factor determined in the absence of protein was then used for anisotropy decays in the presence of the proteins.

2.14. MALDI–mass spectroscopy analysis

Mass spectra of BSA and ribosylated BSA were obtained from Bruker spectrophotometer (model: Ultra Fiex Treme) [43]. Samples were prepared in microcrystalline matrix surfaces that were made on the probe tips of the mass spectrometer. Protein samples were spotted by mixing the protein samples in a 50% aqueous acetonitrile solution (0.6 μ l) saturated with sinapinic acid and containing 0.05% TFA. Analyses of samples were done in linear TOF mode with 550 ns delay. Further data processing and calibrations were carried out using the computer program attached to the spectrophotometer [44]. The number (N) of ribose residues conjugated with BSA molecule was calculated as follows:

$$N = (MW_{BSA-Ribose} - MW_{BSA}) / MW_{Ribose}$$

2.15. Orcinol assay for quantification of total protein glycation

Orcinol reagent was prepared according to the method of Brückner et al. [45]. Purified cellobiase was TCA precipitated in order to remove

any free sugar and resolubilised. Subsequently orcinol reagent was added to 2 μ g of the resolubilised protein and kept in boiling water bath for 5 min. After that, the tubes were allowed to cool down in room temperature. Absorption of the samples was recorded at 540 nm and interpreted in terms of total sugar from the standard curve obtained from different known glucose concentrations.

2.16. Statistical analysis

Analysis of anisotropy data were carried out using Minitab (ver 16.1) from eight independent set of measurements. Results were expressed as mean \pm standard deviation. A two sample *t*-test for equal means was carried out for each set of proteins (in presence and absence of trehalose) to determine the significance at 95% level of confidence. A value of $P < 0.01$ was interpreted as statistically significant. All cellobiase activity assay based results were performed in five replicates and mean values were plotted. The standard deviation was represented in plots and mentioned in tables as and where applicable.

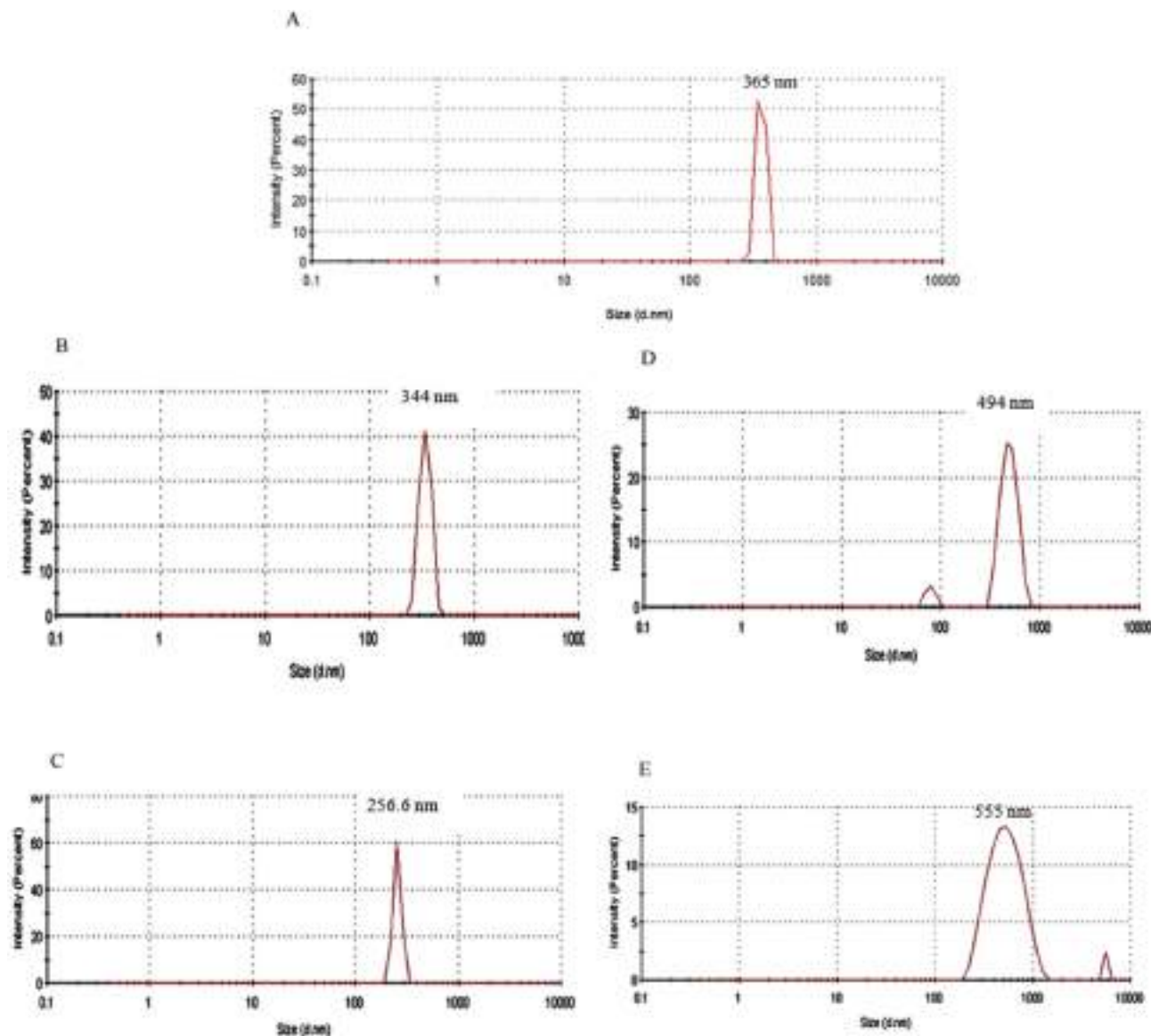


Fig. 1. Hydrodynamic radii of cellobiase ascertained by DLS: A) cellobiase at 0.01 mg/ml B) cellobiase concentrated to 0.1 mg/ml C) cellobiase diluted to 0.05 mg/ml D) cellobiase concentrated to 0.1 mg/ml cellobiase with 0.1 M trehalose the enzyme in presence of 0.1 M trehalose and E) cellobiase with trehalose after half dilution.

Table 1

Hydrodynamic radii analyses of cellobiase, glycosylated BSA and lectin in presence and absence of trehalose through DLS.

Sample	Hydrodynamic radius (d·nm)	Polydispersity index (P·I)
Cellobiase (before lyophilisation)	365 ± 28.8	1
Cellobiase	344.1 ± 43.12	0.848
Cellobiase + Tre 0.1 M	494.3 ± 92.93	0.858
	78.75 ± 8.36	
Glycosylated BSA	396.9 ± 15.19	1
Glycosylated BSA + Tre 0.1 M	915.2 ± 161.1	0.737
	1.002 ± 0.114	
Lectin	164.2 ± 1.907 × 10 ⁻⁶	1
Lectin + Tre 0.1 M	249.1 ± 24.87	1
	1.283 ± 0.087	

Standard deviation was calculated using instrument associated software. Polydispersity of less than equal to 1 indicated homogeneity of the protein preparations.

3. Results and discussions

Extracellular cellobiase was purified from the third day culture medium of *Penicillium chrysogenum* (Supplementary Table 1) as described earlier under Methodology section. Gel filtration chromatography yielded two active cellobiase peaks corresponding to a higher molecular weight and a lower molecular weight enzyme which probably corresponded to different oligomeric forms of the same enzyme as has been observed earlier [46]. Although the first peak had a lower specific activity (92.2 U/mg) as compared to the higher MW form (22.41 U/mg), the latter was further purified with the idea of obtaining the least aggregated purified cellobiase. The final step of anion exchange chromatography led to a 4 fold purification of the enzyme. Purity was checked through SDS PAGE of 5 µg of desalted protein which gave a single 29 kDa band on silver staining (Supplementary Fig. 1).

Trehalose is known to prevent self aggregation of globular proteins by vitrification mediated compaction [23]. Extracellular cellobiase also happens to be a globular protein which develops into multitude of aggregated assemblies through spontaneous concentration driven interaction [2,9]. We wanted to investigate whether trehalose can equally result in compaction of cellobiase resulting in the prevention of their self aggregation as has been observed for other globular proteins like BSA.

In order to find out the effect of trehalose on cellobiase, purified cellobiase at a concentration of 0.01 mg/ml was mixed with 0.01 M trehalose and concentrated ten times through lyophilisation.

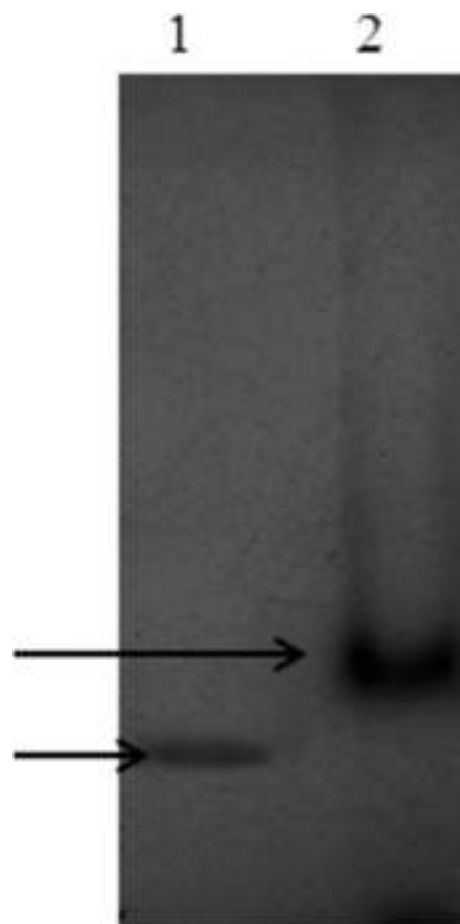


Fig. 3. Zymography of cellobiase after native PAGE gel electrophoresis lane 1: cellobiase, lane 2: cellobiase in presence of 0.1 M trehalose. 8 µg of purified protein were loaded in each lane.

Subsequently, the molecular sizes were estimated through DLS, TEM and native PAGE zymography. Just before lyophilisation, cellobiase in presence or absence of trehalose showed a single species at 365 nm (Fig. 1A). At a concentration of 0.1 mg/ml cell, it showed a single species of hydrodynamic radius 344 nm (Fig. 1B) whereas when half diluted, the size decreased to 256.6 nm

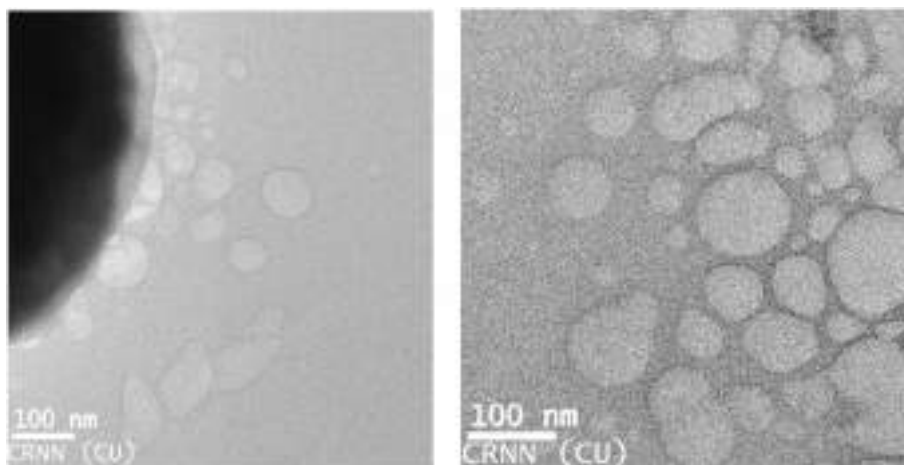


Fig. 2. Transmission electron microscopic images of globular cellobiase aggregation A) cellobiase in presence of trehalose and B) cellobiase. Bar indicates 100 nm in both images. Mean sizes and standard deviation were computed by surveying at-least 25 protein globules from three different fields using the associated software.

(Fig. 1C). This was characteristic of the dilution mediated dissociation shown by extracellular cellobiase aggregates from filamentous fungi [2,9] (Table 1). In presence of trehalose, the size of the concentrated cellobiase increased to 494 nm and there was an additional species at 78.75 nm (Fig. 1D). The spontaneous aggregation and dissociation of cellobiase subunits is a dynamic process and therefore at a given time, we can see only an average of many differently aggregated species. The lower molecular weight probably represented the smallest cellobiase entity which was coated by trehalose before being associated with its counterparts. At a concentration of 0.05 mg/ml, a dominant 555 nm species was observed. Additionally, one huge 5560 nm species was observed albeit of much lower intensity (Fig. 1E). This proved that in presence of trehalose, the cellobiase aggregates didn't disintegrate through dilution and trehalose by virtue of its known vitrification effect was able to stabilise the aggregates. Significant size increase in presence of 0.05 M trehalose was also noted in TEM (Fig. 2) from 55.28 (± 9.98) nm (Control Fig. 2A) to 87.50 (± 6.53) nm (Trehalose Fig. 2B). However, trehalose concentration couldn't be elevated further for sample preparation in TEM because of the high viscosity of the sugar preventing optimal drying of the carbon coated grids.

In order to further confirm our observation regarding stabilisation of cellobiase aggregates by trehalose, a native PAGE zymography of cellobiase in presence and absence of trehalose was also carried out (Fig. 3). Cellobiase showed a single activity band which came at a zone of higher molecular weight in presence of trehalose (lane 2) as compared to the control (lane 1). The corresponding Coomassie stained native PAGE showed higher molecular weight assemblies in presence of

Table 2

Thermodynamics of thermal denaturation of cellobiase in presence of 0.1 M trehalose.

Sample	Temp (K)	ΔG^* (kJ/mol)	ΔH^* (kJ/mol)	ΔS^* (J/mol/K)
Cellobiase	333	91.76	-2.51	-283.09
	336	89.93	-2.53	-275.21
	338	89.38	-2.55	-272.01
	340	87.84	-2.57	-265.92
Cellobiase + 0.1 M Tre	333	92.69	-2.55	-285.99
	336	91.16	-2.57	-279.02
	338	91.55	-2.59	-278.51
	340	89.47	-2.61	-270.82

trehalose that were testimonial to stabilisation of bigger aggregates of cellobiase by the disaccharide even under migration through an electric field (data not shown). It has been shown by earlier studies that although many differently aggregated forms of purified cellobiase occur in solution, all of them are not catalytically active [46]. Therefore, inspite of multiple bands in the native gel, only one activity band corresponding to zymography was noted. As expected, no shift in migration pattern was visible in SDS-PAGE since SDS disrupts all the non covalent inter-subunit associations (data not shown).

It has been seen earlier that bigger cellobiase aggregates have higher resistance to heat induced denaturation [2]. Accordingly, thermal stability of purified cellobiase was investigated in presence and absence of 0.1 M trehalose. Purified cellobiase was found to retain >25% higher residual enzyme activity in presence of trehalose as compared to the control enzyme in the temperature range of 55 to 65 °C (Fig. 4A). In order to

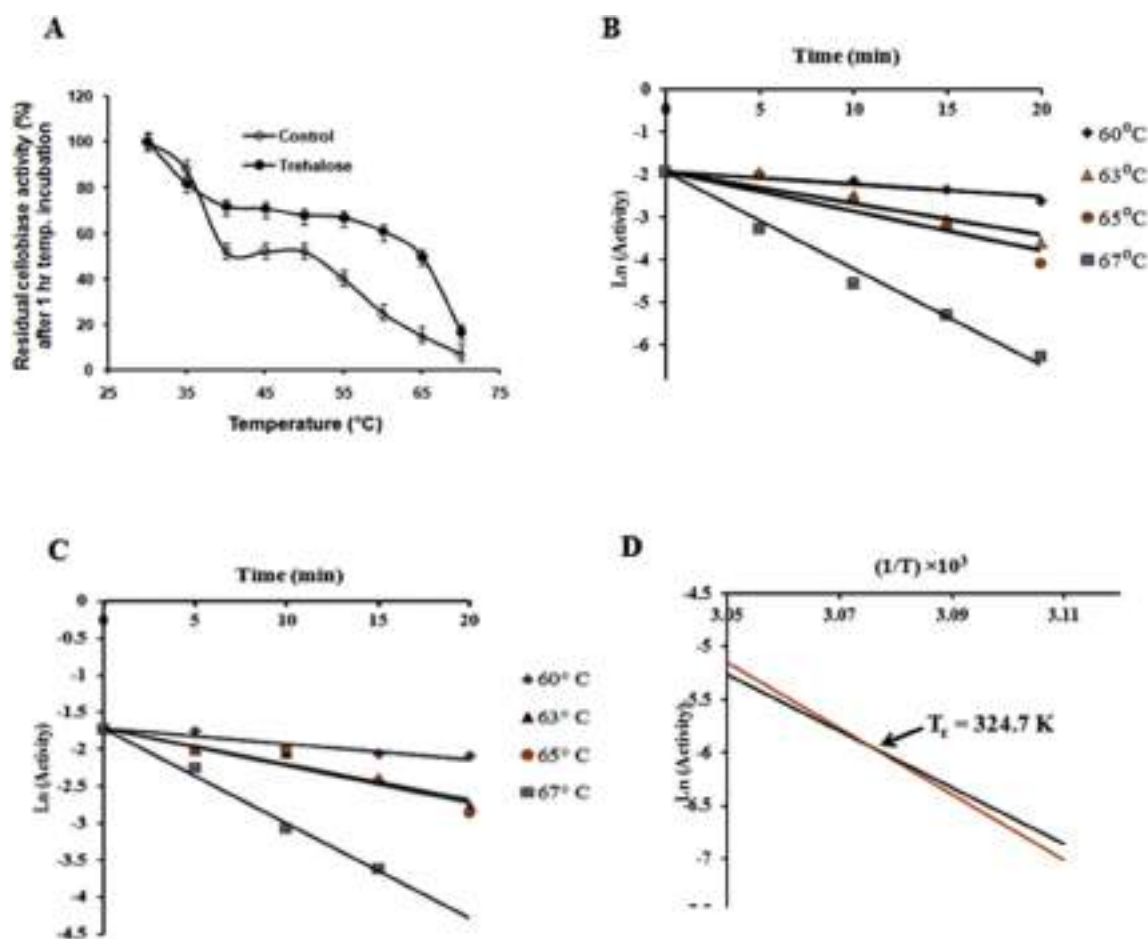


Fig. 4. Thermal stability and denaturation profile of the extracellular enzyme, A) Thermal stability of cellobiase in presence and absence of trehalose B) Thermal denaturation profile of cellobiase C) Same in presence of 0.1 M trehalose D) Arrhenius plot of the enzyme (black and red indicate $\ln(k_d)$ values of the enzyme in presence and absence of trehalose respectively). Data were plotted from five replicate experiments.

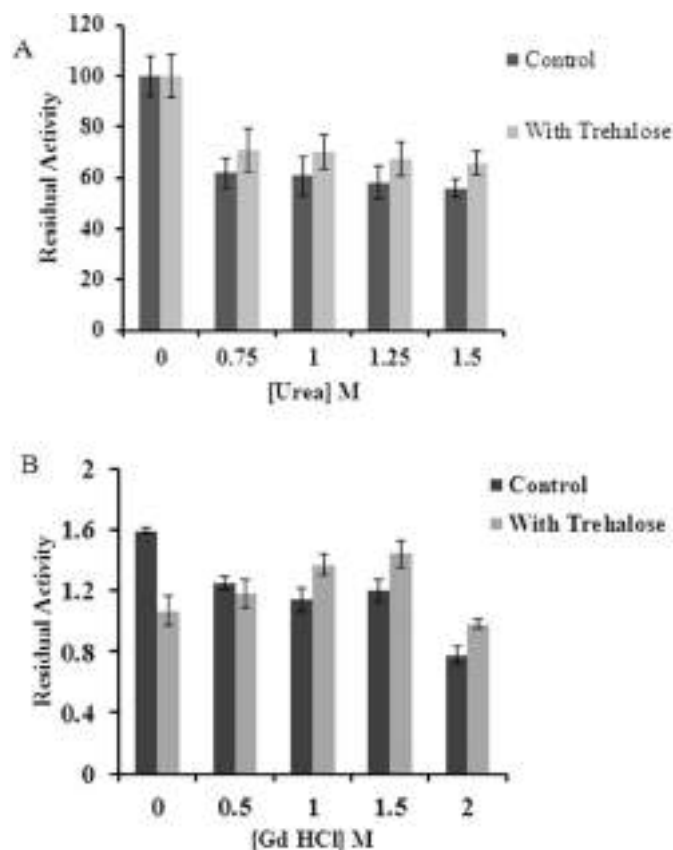


Fig. 5. Effect of trehalose on chaotrope induced cellobiase denaturation A) Urea (0–1.5 M) and B) Guanidium hydrochloride (0–2 M). Error bars were computed from five replicate experiments.

gain more insight into this increased thermostability, thermodynamic parameters were calculated from enzyme activity data (Supplementary Table 2) at various temperatures of incubation as stated in methodology

section and the corresponding Arrhenius plots were examined. Both enzyme forms showed first-order inactivation kinetics characteristic of monomolecular denaturation mechanism (Fig. 4B – Control and Fig. 4C – with trehalose). Free energies of both the forms were found to decrease with increasing temperature as is expected for gradual thermal denaturation (Table 2) which involves disruption of non-covalent linkages, including hydrophobic interactions, with a consequent increase in the enthalpy of activation (ΔH^*) [47,48]. In addition, the increase in entropy change (ΔS^*) also indicated the gradual loss of enzyme structure [49–51]. Arrhenius plot (Fig. 4D) confirmed that cellobiase in presence of 0.1 M trehalose had a better thermostability as compared to the control enzyme as indicated by a higher enthalpy of activation of denaturation [52]. Simultaneously, its activation energy for substrate hydrolysis ($E_a = 220.9$ kJ/mol) was also lower than that of the control enzyme ($E_a = 257.73$ kJ/mol) [53,54]. This was attributable to the trehalose mediated stabilisation of the larger cellobiase aggregates which didn't disintegrate spontaneously on elevation of temperature. The isokinetic temperature of both enzyme forms was found to be 324.7 K. As a consequence of this trehalose mediated stabilisation, specific activity of cellobiase also increased from 1.35 U/mg to 1.8 U/mg. This was attributable to the higher V_{max} of the larger cellobiase agglomerates formed and stabilised in presence of trehalose [2]. Next, we investigated the effect of trehalose over chaotrope induced denaturation of cellobiase (Fig. 5). A marginal protection was conferred by trehalose as there was a 10% increase in residual activity in presence of 1.5 M urea (Fig. 5A). At higher concentrations of GdHCl (1.5 M and 2 M), the protective action of trehalose was better visible as >15% retention of cellobiase activity occurred (Fig. 5B).

The observations were in stark contrast to what is known about the effect of trehalose on structural modulation of globular aggregation prone proteins [23]. Instead of mediating their compaction and subsequent prevention of aggregation, trehalose stabilised the big cellobiase aggregates against heat and dilution induced dissociation. The most popular theory about mechanism of trehalose based protein stabilisation suggests that trehalose replaces water from the vicinity of protein's accessible interface by itself forming hydrogen bonds with the protein [24]. Almost all of the fungal extracellular glycosidases bear substantial amount of glycosylation [55,56] which are high

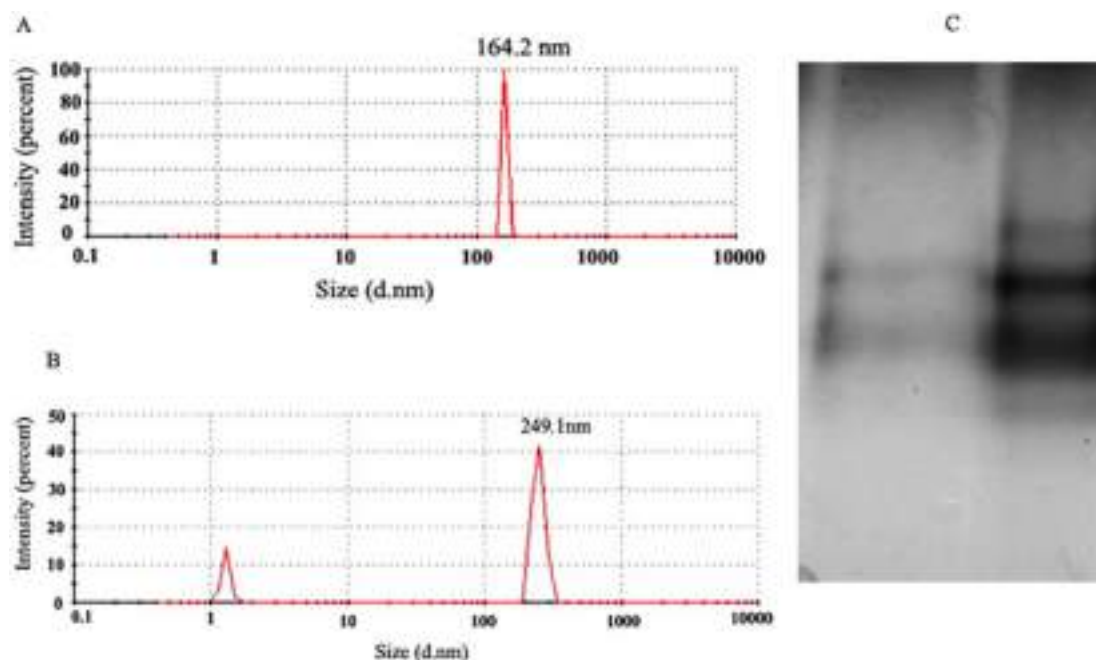


Fig. 6. Size analysis of Wheat Germ Lectin by DLS and PAGE: A) Lectin B) Lectin in presence of 0.1 M trehalose; C) Native PAGE electrophoresis (10%) of Lectin (lane 1) and lectin with 0.1 M trehalose (lane 2). 3 µg of protein was loaded in each lane.

mannose type and unique to filamentous fungi [57]. Glycan content of the purified cellobiase employed in the current studies was determined to be 196.27 μg of sugar/ μg of protein. We reasoned that for a protein surface coated with sugars like that of cellobiase, the effective approach and formation of hydrogen bonds by trehalose is delayed and/or impaired. As a result, the intrinsically aggregation prone cellobiase subunits associate with each other before they can be coated with trehalose. Eventually, trehalose can replace water from the interface of the large aggregates and stabilise them. In order to test our hypothesis, we carried out similar experiments with two model proteins; one with

attached sugar residues (*In vitro* glycated BSA carrying about 60 ribose residues) and another with a known pedigree of binding sugars (wheat germ lectin) [58,59]. The extent of glycation of BSA was confirmed through MALDI-TOF MW analysis of the glycated protein (Supplementary Fig. 2A and Fig. 2B). About 62 molecules of ribose were found to be conjugated per molecule of BSA. Structural analysis of the glycated BSA indicated that there was a partial loss in the secondary structure as alpha helicity decreased from 49.67% to 34.49% (Supplementary Fig. 2C). However, the protein retained its functionality as revealed by its ability to bind efficiently to two of its physiological

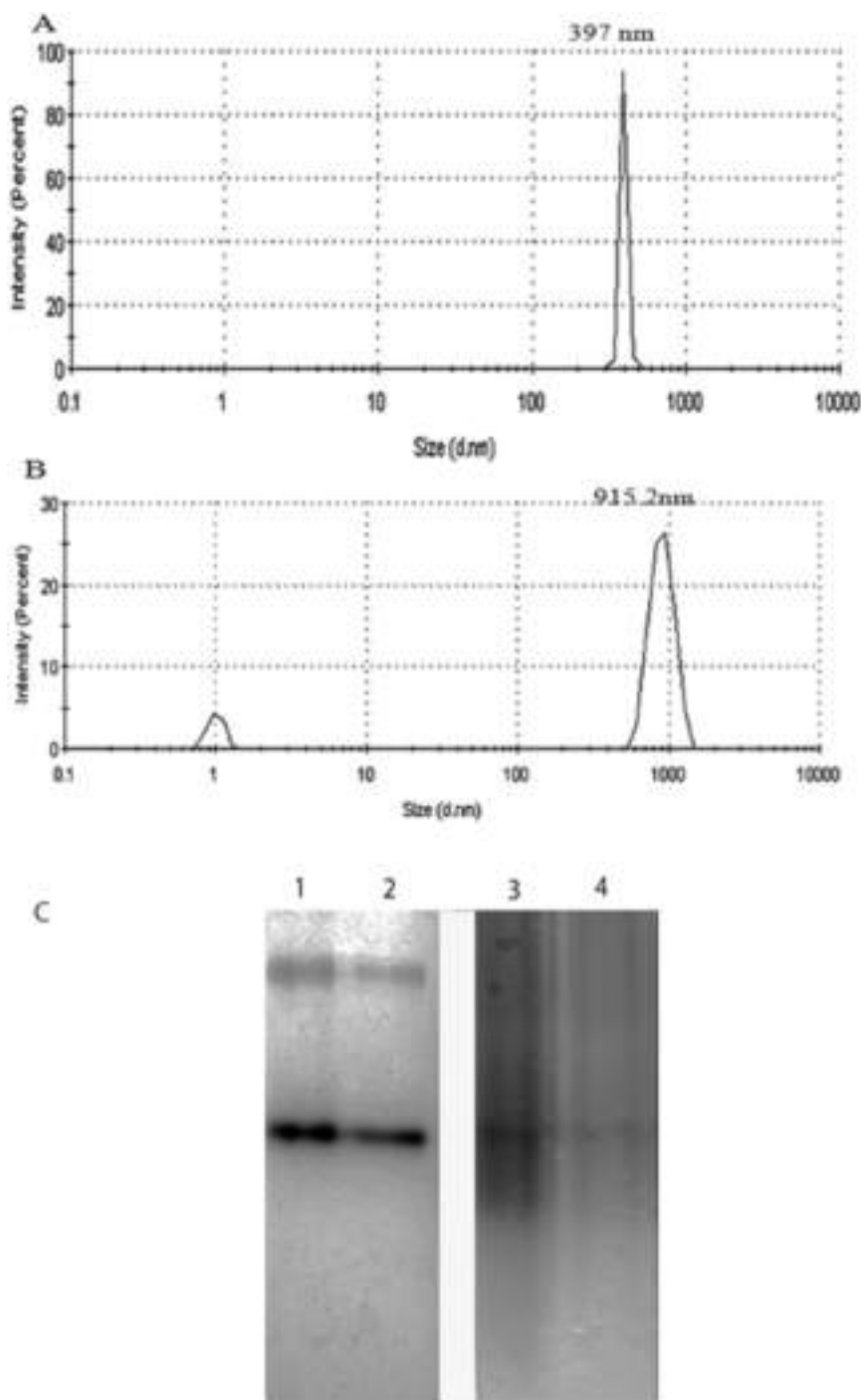


Fig. 7. Hydrodynamic radii distribution of a) glycated BSA and b) glycated BSA in presence of 0.1 M trehalose; C) Native PAGE electrophoresis (10%) of BSA (lane 1), BSA with trehalose (lane 2), glycated BSA (lane 3), glycated BSA with trehalose (lane 4). 5 μg of each protein was loaded in the gel.

substrates resveratrol and curcumin (data not shown here). Both the samples were concentrated five fold in presence of 0.02 M trehalose (0.1 M effective) before analysis to induce concentration dependent aggregation. DLS showed increase in size of lectin from 164 nm (Fig. 6A) to 249 nm in presence of trehalose (Fig. 6B). In the latter case, the 1.28 nm peak probably corresponded to monomeric lectin with a molecular weight of 17 kDa [60]. Wheat germ lectin exists as a monomer of about 17 kDa at pH 2.0 which dimerises subsequently at pH values higher than 5.0 [61]. DLS data indicated stabilisation of higher oligomeric forms of lectin mediated by trehalose as well as the monomeric form before it could have dimerised and developed further into higher oligomeric forms. This observation was similar to that of cellobiase, where a lower molecular weight cellobiase assembly at 78 nm was visible in presence of trehalose and probably appeared since in a trehalose coated form it failed to aggregate or associate with its counterpart subunits. Native PAGE (Fig. 6C) also exhibited the same trend where a higher molecular band was seen additionally (lane 2) to that of the control lectin (lane 1) indicating trehalose mediated lectin aggregation.

Trehalose mediated vitrification results in compaction of BSA thus preventing its self association [23]. However in case of ribosylated BSA, this was not seen since diameter of the glycosylated protein increased from 397 nm (Fig. 7A) to 915 nm (Fig. 7B) indicating trehalose mediated stabilisation of higher molar mass entities of BSA which are not noticeable otherwise due to rapid formation and dissociation of the reversible self aggregates of the protein. The diameter of glycosylated BSA observed was much larger than the known minimum hydrated diameter of BSA of around 10 nm [23]. This can be attributable to the fact that glycosylated BSA is more aggregation prone [62], than its non-glycosylated counterpart and therefore at the concentration studied (0.1 mg/ml), the least diameter species was not visible. This was reconfirmed by studying the glycosylated BSA at a tenfold lesser concentration where a diameter of $24.54 \text{ nm} \pm 3.58 \text{ nm}$ was observed (DLS figure not shown). The observations were further corroborated through electrophoretic migration patterns of the proteins in Native PAGE (Fig. 7C). The lower molecular weight bands corresponding to glycosylated BSA in absence and presence of trehalose (lanes 3 and 4 respectively) in native PAGE were slightly retarded as compared to control BSA in (lanes 1 and 2 in absence and presence of trehalose respectively) due to increased molecular weight *via* glycosylation. The bands corresponding to the glycosylated BSA (lanes 3 and 4) were also rendered smeary probably due to enhanced aggregation of the ribosylated BSA. Surprisingly, no further change was effected by trehalose for the glycosylated sample. We reasoned that unlike lectin and cellobiase, the trehalose coated higher oligomeric assembly of ribosylated BSA was not stable and dissociated into smaller units by sheer dilution during gel electrophoresis. Therefore, the trehalose mediated higher molecular weight aggregated entities of BSA were detectable in DLS but dissociated subsequently under migration in an electric field.

Fluorescence polarisation or anisotropy is a powerful tool to investigate the rotational dynamics of a macromolecule with a fluorophore tagged to it [63]. Although generally known to be concentration independent, it can be used to assess the aggregation of proteins since higher the size of the protein through aggregation, higher will be the anisotropy value [64,65]. In order to gain further evidence about the aggregation prone nature of the test glycoproteins, we determined the anisotropy values of FITC conjugated wheat germ lectin and ribosylated BSA. According to our expectations, the anisotropy of lectin in presence of 0.1 M trehalose increased from 0.174 ± 0.00205 to 0.189 ± 0.0026 suggesting an increase in size of the lectin aggregate mediated by trehalose with a corresponding *P* value of 0.000 in the two sample *t*-test. The *R* value of BSA-FITC (0.210 ± 0.002) didn't change significantly in presence of 0.1 M trehalose (0.209 ± 0.002). In case of glycosylated BSA, a slight increase in anisotropy was observed (0.163 ± 0.001 to 0.170 ± 0.002) in presence of 0.1 M trehalose with a *P* value of 0.000. However, this increase in size was not stable as on diluting the protein to half of its original concentration, the anisotropy decreased again to 0.166 ± 0.003 ; in

contrast the anisotropy of the control half diluted glycosylated BSA increased to 0.179 ± 0.003 (*P* value 0.000) reflecting the increased self aggregating nature of the glycosylated BSA. The observations from native PAGE and Anisotropy experiments indicated that the trehalose mediated aggregation of glycosylated BSA was not as stable as cellobiase and lectin and was susceptible to dilution induced dissociation. This might be attributable to many reasons; the sugar residues spanning the surface of lectin and cellobiase are fundamentally different in being much more complex than ribose attached to BSA. Additionally, they have been enzymatically attached to strategic locations of the respective proteins encompassing both side chain amino and hydroxyl groups in order to increase inter-subunit aggregation without sacrificing the native structure. Therefore, subsequent docking by trehalose only helps to further stabilise the strength and rigidity of these aggregates making them more resistant to dilution induced dissociation. On the contrary, ribose molecules were randomly attached to mostly surface exposed lysine groups of BSA through amino group mediated Amadori adducts. However, in the process the native structure of the BSA was somewhat sacrificed. Therefore it is imperative that docking of trehalose on a glycosylated BSA will not be as strong as that on glycosylated proteins.

4. Conclusion

The molecular basis of trehalose mediated stabilisation of proteins has been extensively studied and now it is almost an accomplished fact that trehalose results in vitrification of the protein's native structure by replacing water molecules from the solvent accessible interface itself making up for the lost hydrogen bonds in the process. This unique property of the present studies are believed to add a new dimension to trehalose research by reporting for the first time the role of trehalose on stabilisation of aggregation prone glycoproteins. The studies are believed to provide important insights for management of protein glycation related ailments frequently occurring in diabetic individuals. Present studies also report a cross-linking free method to stabilise β -glucosidase aggregates for enhanced resistance to demanding production parameters frequently encountered in biofuel industries.

Supplementary data to this article can be found online at <https://doi.org/10.1016/j.ijbiomac.2019.01.062>.

Acknowledgement

The studies were funded by University Grants Commission, Government of India, Major Research Project, Sanction No. F No. – 43-69/2014 (SR) dated 23rd July 2015 and by STAR College scheme support, Department of Biotechnology, Government of India. Instrumental facility was provided by World Bank-ICZMP (54-ICZMP/3P), and DBT-IPLS, Government of India in the Department of Biochemistry, Calcutta University. Sincere thanks are also due to Dr. Partha Pal, Dr. Arijit Kundu, Dr. Arpan Das and Mrs. Bipasha Roy, Faculty members, Maulana Azad College and also to Principal, Maulana Azad College for lending all helps possible to execute the works within limited infrastructural resources.

Conflict of interest

The authors declare no conflict of interest.

Author contribution

AD performed all the experiments except DLS, MALDI and HPLC and Arrhenius plots of cellobiase and wrote the manuscript along with SPB. PB carried out MALDI, AP interpreted the anisotropy experiments, RM carried out HPLC of cellobiase and prepared the references of the manuscript, DP carried out the Arrhenius plots, AG helped AD in preparing the ribosylated BSA and prepared the graphical abstract and figures. MG carried out the DLS analyses. SPB and MB conceived and designed the entire study and wrote the manuscript.

References

- [1] P.J. Punt, N. van Biezen, A. Conesa, A. Albers, J. Mangnus, C. van den Hondel, Filamentous fungi as cell factories for heterologous protein production, *Trends Biotechnol.* 20 (5) (2002) 200–206.
- [2] S.P. Banik, S. Pal, S. Ghorai, S. Chowdhury, R. Majumder, S. Mukherjee, S. Khowala, In situ reversible aggregation of extracellular cellulase in the filamentous fungus *Termitomyces clypeatus*, *Bioprocess Biosyst. Eng.* 17 (5) (2012) 925–936.
- [3] R. Pavišić, I. Dodig, A. Horvatić, L. Mijić, M. Sedić, M.R. Linarić, I.G. Sovulj, T. Prečanin, M.B. Krajačić, M. Cindrić, Differences between reversible (self-association) and irreversible aggregation of rHuG-CSF in carbohydrate and polyol formulations, *Eur. J. Pharm. Biopharm.* 76 (3) (2010) 357–365.
- [4] N. Sarkar, M. Kumar, V.K. Dubey, Effect of sodium tetrathionate on amyloid fibril: insight into the role of disulfide bond in amyloid progression, *Biochimie* 93 (5) (2011) 962–968.
- [5] S.P. Banik, S. Mukherjee, S. Pal, S. Ghorai, R. Majumder, S. Khowala, Enhancement of extracellular cellulase activity by reducing agents in the filamentous fungus *Termitomyces clypeatus*, *Biotechnol. Lett.* 37 (1) (2015) 175–181.
- [6] S.P. Banik, S. Pal, S. Ghorai, R. Majumder, S. Mukherjee, S. Chowdhury, S. Khowala, Comparative elucidation of properties of sucrase-cellobiase co-aggregate produced in media containing sucrose by *Termitomyces clypeatus*, *Indian J. Biotechnol.* 10 (2011) 468–479.
- [7] S.P. Banik, S. Bhattacharyya, S. Ghorai, Isolation of a new *Penicillium chrysogenum* strain bf02 from agricultural soil of rural India producing a thermostable low km cellobiase, *J. Microbiol. Biotechnol. Food Sci.* 3 (4) (2014) 322.
- [8] S. Ghorai, S. Chowdhury, S. Pal, S.P. Banik, S. Mukherjee, S. Khowala, Enhanced activity and stability of cellobiase (β -glucosidase: EC 3.2.1.21) produced in the presence of 2-deoxy-D-glucose from the fungus *Termitomyces clypeatus*, *Carbohydr. Res.* 345 (8) (2010) 1015–1022.
- [9] R. Saha, S.B. Roy, S. Sengupta, Stabilization and improvement of catalytic activity of a low molar mass cellobiase by cellobiase-sucrase aggregation in the culture filtrate of *Termitomyces clypeatus*, *Biotechnol. Prog.* 18 (6) (2002) 1240–1248.
- [10] S. Mukherjee, S. Khowala, Secretion of cellobiase is mediated via vacuoles in *Termitomyces clypeatus*, *Biotechnol. Prog.* 18 (6) (2002) 1195–1200.
- [11] A. Bhattacharya, R. Prajapati, S. Chatterjee, T.K. Mukherjee, Concentration-dependent reversible self-oligomerization of serum albumins through intermolecular β -sheet formation, *Langmuir* 30 (49) (2014) 14894–14904.
- [12] S.K. Chaturvedi, M.K. Siddiqi, P. Alam, R.H. Khan, Protein misfolding and aggregation: mechanism, factors and detection, *Process Biochem.* 51 (9) (2016) 1183–1192.
- [13] G.H. Podrepšek, M. Primožič, Ž. Knez, M. Habulin, Immobilization of cellulase for industrial production, *Chem. Eng. Trans.* 27 (2012) 235–240.
- [14] V. Stepankova, S. Bidmanova, T. Koudelakova, Z. Prokop, R. Chaloupkova, J. Damborsky, Strategies for stabilization of enzymes in organic solvents, *ACS Catal.* 3 (12) (2013) 2823–2836.
- [15] N.R. Mohamad, N.H.C. Marzuki, N.A. Buang, F. Huyop, R.A. Wahab, An overview of technologies for immobilization of enzymes and surface analysis techniques for immobilized enzymes, *Biotechnol. Biotechnol. Equip.* 29 (2) (2015) 205–220.
- [16] M.A. Singer, S. Lindquist, Multiple effects of trehalose on protein folding in vitro and in vivo, *Mol. Cell* 1 (5) (1998) 639–648.
- [17] A.D. Elbein, Y. Pan, I. Pastuszak, D. Carroll, New insights on trehalose: a multifunctional molecule, *Glycobiology* 13 (4) (2003) 17R–27R.
- [18] G. Iturriaga, R. Suárez, B. Nova-Franco, Trehalose metabolism: from osmoprotection to signaling, *Int. J. Mol. Sci.* 10 (9) (2009) 3793–3810.
- [19] S. Sarkar, J.E. Davies, Z. Huang, A. Tunnacliffe, D.C. Rubinsztajn, Trehalose, a novel mTOR-independent autophagy enhancer, accelerates the clearance of mutant huntingtin and α -synuclein, *J. Biol. Chem.* 282 (8) (2007) 5641–5652.
- [20] J.K. Kaushik, R. Bhat, Why is trehalose an exceptional protein stabilizer?: an analysis of the thermal stability of proteins in the presence of compatible osmolyte trehalose, *J. Biol. Chem.* 278 (2003) 26458–26465.
- [21] N.K. Jain, I. Roy, Effect of trehalose on protein structure, *Protein Sci.* 18 (1) (2009) 24–36.
- [22] P.V. Attfield, Trehalose accumulates in *Saccharomyces cerevisiae* during exposure to agents that induce heat shock response, *FEBS Lett.* 225 (1–2) (1987) 259–263.
- [23] A. Das, P. Basak, R. Pattanayak, T. Kar, R. Majumder, D. Pal, A. Bhattacharya, M. Bhattacharyya, S.P. Banik, Trehalose induced structural modulation of bovine serum albumin at ambient temperature, *Int. J. Biol. Macromol.* 105 (2017) 645–655.
- [24] S. Paul, S. Paul, Investigating the counteracting effect of trehalose on urea-induced protein denaturation using molecular dynamics simulation, *J. Phys. Chem. B* 119 (34) (2015) 10975–10988.
- [25] M.V. Fedorov, J.M. Goodman, D. Nerukh, S. Schumm, Self-assembly of trehalose molecules on a lysozyme surface: the broken glass hypothesis, *Phys. Chem. Chem. Phys.* 13 (6) (2011) 2294–2299.
- [26] C. Olsson, H.N. Jansson, J. Swenson, The role of trehalose for the stabilization of proteins, *J. Phys. Chem. B* 120 (20) (2016) 4723–4731.
- [27] S. Siddhanta, I. Barman, C. Narayana, Revealing the trehalose mediated inhibition of protein aggregation through lysozyme-silver nanoparticle interaction, *Soft Matter* 11 (37) (2015) 7241–7249.
- [28] M. Siri, M. Grasselli, S.D.V. Alonso, Albumin-based nanoparticle trehalose lyophilisation stress-down to preserve structure/function and enhanced binding, *J. Pharm. Biomed. Anal.* 126 (2016) 66–74.
- [29] S. André, H. Kaltner, J.C. Manning, P.V. Murphy, H.-J. Gabius, Lectins: getting familiar with translators of the sugar code, *Molecules* 20 (2) (2015) 1788–1823.
- [30] C.D. Braganza, T. Teunissen, M.S. Timmer, B.L. Stocker, Identification and biological activity of synthetic macrophage inducible C-type lectin ligands, *Front. Immunol.* 8 (2018) 1940.
- [31] S. Shanmugavel, V. Velayutham, T. Kamalanathan, M. Periasamy, A. Munusamy, J. Sundaram, Isolation and analysis of mannose/trehalose/maltose specific lectin from jack bean with antibacterial activity, *Int. J. Biol. Macromol.* 91 (2016) 1–14.
- [32] R. Afrin, A. Ikai, Subunit unbinding mechanics of dimeric wheat germ agglutinin (WGA) studied by atomic force microscopy, *FEBS Lett.* 588 (23) (2014) 4472–4477.
- [33] S. Mukherjee, S. Chowdhury, S. Ghorai, S. Pal, S. Khowala, Cellobiase from *Termitomyces clypeatus*: activity and secretion in presence of glycosylation inhibitors, *Biotechnol. Lett.* 28 (21) (2006) 1773–1778.
- [34] S.P. Banik, S. Pal, S. Ghorai, S. Chowdhury, S. Khowala, Interference of sugars in the Coomassie blue G dye binding assay of proteins, *Anal. Biochem.* 386 (1) (2009) 113–115.
- [35] M. Rashid, K. Siddiqui, Thermodynamic and kinetic study of stability of the native and chemically modified β -glucosidases from *Aspergillus niger*, *Process Biochem.* 33 (2) (1998) 109–115.
- [36] U.K. Laemmli, Cleavage of structural proteins during the assembly of the head of bacteriophage T4, *Nature* 227 (5259) (1970) 680.
- [37] R. Majumder, S.P. Banik, S. Khowala, AkP from mushroom *Termitomyces clypeatus* is a proteoglycan specific protease with apoptotic effect on HepG2, *Int. J. Biol. Macromol.* 91 (2016) 198–207.
- [38] K.-S. Kwon, J. Lee, H.G. Kang, Y.C. Hah, Detection of β -glucosidase activity in polyacrylamide gels with esculin as substrate, *Appl. Environ. Microbiol.* 60 (12) (1994) 4584–4586.
- [39] N.G. Watkins, S.R. Thorpe, J.W. Baynes, Glycation of amino groups in protein. Studies on the specificity of modification of RNase by glucose, *J. Biol. Chem.* 260 (19) (1985) 10629–10636.
- [40] G. Hungerford, J. Benesch, J.F. Mano, R.L. Reis, Effect of the labelling ratio on the photophysics of fluorescein isothiocyanate (FITC) conjugated to bovine serum albumin, *Photochem. Photobiol. Sci.* 6 (2) (2007) 152–158.
- [41] R. Majumder, S.P. Banik, S. Khowala, Purification and characterisation of κ -casein specific milk-clotting metalloprotease from *Termitomyces clypeatus* MTCC 5091, *Food Chem.* 173 (2015) 441–448.
- [42] N. Jain, S. Mukhopadhyay, Applications of fluorescence anisotropy in understanding protein conformational disorder and aggregation, *Appl. Spectrosc. Sci. Nanomater.* (2015) 41–57, https://doi.org/10.1007/978-981-287-242-5_3 Springer.
- [43] R. Théberge, S. Dikler, C. Heckendorf, D.H. Chui, C.E. Costello, M.E. McComb, MALDI-MS mass spectrometry analysis of hemoglobin variants: a top-down approach to the characterization of hemoglobinopathies, *J. Am. Soc. Mass Spectrom.* 26 (8) (2015) 1299–1310.
- [44] W. Liu, M.A. Cohenford, L. Frost, C. Seneviratne, J.A. Dain, Inhibitory effect of gold nanoparticles on the D-ribose glycation of bovine serum albumin, *Int. J. Nanomedicine* 9 (2014) 5461.
- [45] J. Brückner, Estimation of monosaccharides by the orcinol-sulphuric acid reaction, *Biochem. J.* 60 (2) (1955) 200.
- [46] S. Pal, S.P. Banik, S. Ghorai, S. Chowdhury, S. Khowala, Purification and characterization of a thermostable intra-cellular β -glucosidase with transglycosylation properties from filamentous fungus *Termitomyces clypeatus*, *Bioresour. Technol.* 101 (7) (2010) 2412–2420.
- [47] A.N. Shirke, A. Su, J.A. Jones, G.L. Butterfoss, M.A. Koffas, J.R. Kim, R.A. Gross, Comparative thermal inactivation analysis of *Aspergillus oryzae* and *Thielavia terrestris* cutinase: role of glycosylation, *Biotechnol. Bioeng.* 114 (1) (2017) 63–73.
- [48] I.W. Sizer, Effects of temperature on enzyme kinetics, *Adv. Enzymol. Relat. Areas Mol. Biol.* 3 (1943) 35–62.
- [49] S. Dagan, T. Hagai, Y. Gavrilov, R. Kapon, Y. Levy, Z. Reich, Stabilization of a protein conferred by an increase in folded state entropy, *Proc. Natl. Acad. Sci. U. S. A.* 110 (26) (2013) 10628–10633.
- [50] P.V. Iyer, L. Ananthanarayan, Enzyme stability and stabilization—aqueous and non-aqueous environment, *Process Biochem.* 43 (10) (2008) 1019–1032.
- [51] C. Vieille, J.G. Zeikus, Thermozymes: identifying molecular determinants of protein structural and functional stability, *Trends Biotechnol.* 14 (6) (1996) 183–190.
- [52] A.A. Saqib, M. Hassan, N.F. Khan, S. Baig, Thermostability of crude endoglucanase from *Aspergillus fumigatus* grown under solid state fermentation (SSF) and submerged fermentation (SmF), *Process Biochem.* 45 (5) (2010) 641–646.
- [53] I. Ahmad, S.M.A. Basra, A. Wahid, Exogenous application of ascorbic acid, salicylic acid and hydrogen peroxide improves the productivity of hybrid maize at low temperature stress, *Int. J. Agric. Biol.* 16 (4) (2014) 825–830.
- [54] M. Rajoka, I. Durrani, A. Khalid, Kinetics of improved production and thermostability of an intracellular β -glucosidase from a mutant-derivative of *Cellulomonas biazotea*, *Biotechnol. Lett.* 26 (4) (2004) 281–285.
- [55] C.S. Evans, Properties of the β -D-glucosidase (cellobiase) from the wood-rotting fungus, *Coriolus versicolor*, *Appl. Microbiol. Biotechnol.* 22 (2) (1985) 128–131.
- [56] A. Yoneda, H.-W.D. Kuo, M. Ishihara, P. Azadi, S.-M. Yu, T.-h.D. Ho, Glycosylation variants of a β -glucosidase secreted by a Taiwanese fungus, *Chaetomella raphigera*, exhibit variant-specific catalytic and biochemical properties, *PLoS One* 9 (9) (2014), e106306.
- [57] N. Deshpande, M.R. Wilkins, N. Packer, H. Nevalainen, Protein glycosylation pathways in filamentous fungi, *Glycobiology* 18 (8) (2008) 626–637.
- [58] N. Urtasun, M.F. Baieli, O. Cascone, F.J. Wolman, M.V. Miranda, High-level expression and purification of recombinant wheat germ agglutinin in *Rachiplusia nu larvae*, *Process Biochem.* 50 (1) (2015) 40–47.
- [59] H. Wang, Isolation and purification of wheat germ agglutinin and analysis of its properties, *IOP Conference Series: Earth Environ. Sci.* IOP Publishing 2017, p. 012021.
- [60] E.A. Chavelas, A.P. Beltrán, G. Pérez-Hernández, E. García-Hernández, Spectroscopic characterization of the thermal unfolding of wheat germ agglutinin, *Rev. Soc. Quím. Mex.* 48 (4) (2004) 279–282.

- [61] M. del Carmen Portillo-Téllez, M. Bello, G. Salcedo, G. Gutiérrez, V. Gómez-Vidales, E. García-Hernández, Folding and homodimerization of wheat germ agglutinin, *Biophys. J* 101 (6) (2011) 1423–1431.
- [62] Y. Wei, L. Chen, J. Chen, L. Ge, R.Q. He, Rapid glycation with D-ribose induces globular amyloid-like aggregations of BSA with high cytotoxicity to SH-SY5Y cells, *BMC Cell Biol.* 10 (1) (2009) 10.
- [63] S. Inoué, O. Shimomura, M. Goda, M. Shribak, P. Tran, Fluorescence polarization of green fluorescent protein (GFP), *Proc. Natl. Acad. Sci. U. S. A.* 99 (2002) 4272–4277.
- [64] D. Allsop, L. Swanson, S. Moore, Y. Davies, A. York, O.M. El-Agnaf, I. Soutar, Fluorescence anisotropy: a method for early detection of Alzheimer β -peptide ($A\beta$) aggregation, *Biochem. Biophys. Res. Commun.* 285 (1) (2001) 58–63.
- [65] S. Arya, A. Kumari, V. Dalal, M. Bhattacharya, S. Mukhopadhyay, Appearance of annular ring-like intermediates during amyloid fibril formation from human serum albumin, *Phys. Chem. Chem. Phys.* 17 (35) (2015) 22862–22871.

Cytocompatible, thermostable hydrogel with utility to release drug over skin

**Biva Ghosh, Debalina Bhattacharya,
Atanu Kotal, Arindam Kuila & Mainak
Mukhopadhyay**

**Journal of Sol-Gel Science and
Technology**

ISSN 0928-0707

Volume 94

Number 3

J Sol-Gel Sci Technol (2020) 94:616-627

DOI 10.1007/s10971-019-05187-w

Your article is protected by copyright and all rights are held exclusively by Springer Science+Business Media, LLC, part of Springer Nature. This e-offprint is for personal use only and shall not be self-archived in electronic repositories. If you wish to self-archive your article, please use the accepted manuscript version for posting on your own website. You may further deposit the accepted manuscript version in any repository, provided it is only made publicly available 12 months after official publication or later and provided acknowledgement is given to the original source of publication and a link is inserted to the published article on Springer's website. The link must be accompanied by the following text: "The final publication is available at link.springer.com".



Cytocompatible, thermostable hydrogel with utility to release drug over skin

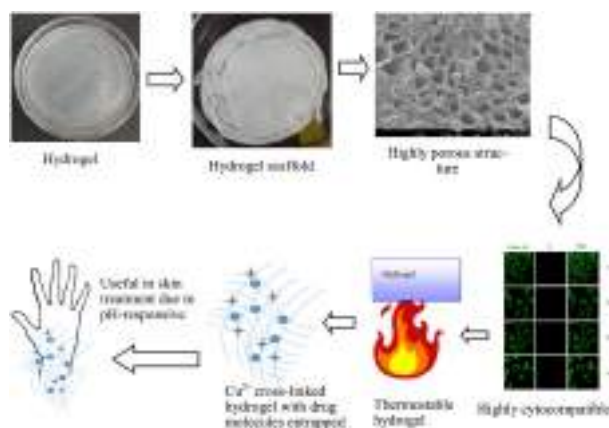
Biva Ghosh¹ · Debalina Bhattacharya² · Atanu Kotal¹ · Arindam Kuila³ · Mainak Mukhopadhyay¹

Received: 9 August 2019 / Accepted: 8 November 2019 / Published online: 25 November 2019
 © Springer Science+Business Media, LLC, part of Springer Nature 2019

Abstract

Hydrogel has wide applicability in biomedical applications and other industrial applications due to its strong biocompatibility. A natural polymer is eco-friendly, nontoxic, and biocompatible. There are vast varieties of natural polymers whose combination can form excellent hydrogels. Pectin and carboxymethyl cellulose (CMC) are some such kinds of polymers. Plasticizer has wide applicability to enhance properties of polymers mix. Glycerol has been widely used as a plasticizer in many hydrogels but it does not render thermostability whereas, PEG is known to render thermostability. Thermostable hydrogel provides easy sterilization by using heat and pressure such as an autoclave. Small molecular size plasticizer is known to provide more space among the polymer mix and affect the porosity and water uptake capability. PEG 400 has wide applications in pharmaceutical industries and it is one of the small molecular size plasticizers. Other than this, copper ions are known to render skin regenerative property with biocidal property help in the wound healing treatment. Thus, a hydrogel was fabricated using pectin and CMC with PEG 400 as the plasticizer and copper ion as cross-linker (PCPEG2). The resulted hydrogel not only showed high thermal stability but also has high porosity, a high degree of swelling, pH sensitivity and good cytocompatibility and good drug release efficiency. The hydrogel was characterized by using FTIR, XRD, DSC, TGA/DTG/DTA, and XPS which showed good fabrication of hydrogel with high thermal stability. Thus, a novel hydrogel of pectin/CMC with PEG 400 was fabricated with enhancing properties applicable in biomedical applications and other industrial applications.

Graphical Abstract



Supplementary information The online version of this article (<https://doi.org/10.1007/s10971-019-05187-w>) contains supplementary material, which is available to authorized users.

✉ Mainak Mukhopadhyay
 mainak.mukhopadhyay12@gmail.com

¹ Department of Biotechnology, JIS University, 81, Nilgunj Road, Agarpara, Kolkata, West Bengal 700109, India

² Department of Microbiology, Moulana Azad College, 8 Rafi Ahmed Kidwai Road, Kolkata, West Bengal 700013, India

³ Department of Bioscience and Biotechnology, Banasthali University, Niwai—Jodhpuriya Road, Vanasthali, Rajasthan 304022, India

Highlights

- Fabrication of pH responsive thermostable PEG 400 based hydrogel.
- The hydrogel has high porosity (21.72 μm), which favors high cell viability (Live/Dead cell staining).
- Cu^{2+} is used for ionic cross-linking among the polymers, which is explained via XPS analysis.
- Capability of having high industrial value especially as skin dressing agent.

Keywords Carboxymethyl cellulose · Copper ions · Hydrogel · Pectin · PEG 400

1 Introduction

The hydrogel is a macromolecular polymer gel consisting of polymer chains, cross-linked among each other with a hydrophilic nature. Hydrogel has multiple advantages in industry, environmental areas [1, 2], and medical science [3]. Due to its high entrapment capability, it has wide application in wastewater treatment [4–6], tissue culture [7–11], pharmaceuticals [12–14], and other industrial and nonindustrial applications. Natural polysaccharides are widely used for hydrogel formation due to their low toxicity, low cost, high biocompatibility [15, 16]. Lyophilized hydrogel forms a scaffold-like structure which is highly porous [17–24]. This porosity can be used for entrapment of useful molecules which play vital roles in drug entrapment and control drug release [25–28], cell proliferation [29–32], entrapment of toxins, and waste molecules in wastewater treatment [33].

Pectin has high applicability but poor mechanical strength which can be improved by blending with other biopolymers [34]. Pectin consists of complex polymers which are homogalacturonan (HG), rhamnogalacturonan I (RG I) and rhamnogalacturonan II (RG II) covalently linked to each other. Pectin is mainly found from the cell wall of plants. Pectin plays vital roles in plant growth and development, wall porosity, cell–cell adhesion, morphogenesis, signaling, fruit development, and many more. HG consist of α -1, 4-linked galacturonic acid monomers which are negatively charged and partially methyl-esterified at the C–O–6 carboxyl [17]. The degree of methyl esterification (DE) decides the pectin gelation by multivalent cations. Pectin with low methoxy can form the network in the presence of divalent cations. High methoxy pectin also forms the network in the presence of divalent cations but their gel strength is low [17]. In the case of the plant's cell wall, pectin contributes to the mechanical property but in combination with the cellulose network. Thus pectin in combination with sodium carboxymethyl cellulose (CMC) can provide similar kind of strength due to poroelastic effect [17]. Since cellulose is insoluble in water, thus, another form of it i.e. sodium CMC is a water-soluble derivative of cellulose with β -(1→4) glucopyranose residues [17]. Besides this CMC is having excellent bioadhesive, biocompatible, biodegradable properties

which makes it an excellent polymer for casting hydrogel. It is also a polyelectrolyte which provides pH sensitivity and ionic strength variation. The OH groups of CMC are highly reactive for polymer chain formation. Other than this the carboxyl group present in it helps in the cross-linking of polymer chains in the presence of multivalent ions. CMC hydrogels have wide applicability in food industries, cosmetics pharmaceuticals, and agricultural industries, etc [35]. Since ancient times copper has been used for wound healing and biocidal properties [36]. Copper is known to have numerous positive effects on human tissues, especially on the skin. It helps in the synthesis and stabilization of the extracellular matrix of skin proteins and helps in angiogenesis. Thus, copper has wide applications in wound healing, improvement of skin elasticity, curing an infection, etc [36]. Copper sulfate (CuSO_4) is a salt with divalent Cu^{2+} ion which helps in the cross-linking of pectin and CMC hydrogel. The addition of plasticizers in the polymer blend helps the polymer to align properly and thus increases its flexibility [37–39]. PEG 400 has wide applicability in medical applications such as stability of protein during encapsulation [40], cosmetics, ointments, toothpaste, capsule coatings, tissue engineering, etc [41]. According to past studies, PEG can avoid nonspecific binding of protein or cells [42, 43]. The high structure flexibility, biocompatibility, amphiphilicity, lacking any steric hindrances, and high hydration capacity are some of the eminent features of PEG which earns high significance at industries [41, 44]. PEG > 1000 molecular weight is liquid at room temperature, whereas < 1000 molecular weight is solid at room temperature. The molecular weight of PEG is directly proportional to its melting point. PEG 400 is widely used in the cream, ointment base, lotion, etc. Moreover, PEG 400 is liquid at room temperature and easily mixable with solvents at room temperature [41]. These properties of PEG 400 make it an ideal plasticizer for the fabrication of hydrogel with other polymers.

As thermostable hydrogels are easy to sterilize by heat and pressure such as using an autoclave, therefore, with the above consideration in mind, this work signifies to fabricate a thermostable hydrogel using pectin and CMC as polymers. The significance of pectin, CMC, PEG 400, and copper ions are already discussed above which states its

importance in the industrial fields such as biomedical applications. The hydrogel fabricated is characterized by using Fourier transform infrared spectra (FTIR), X-ray diffraction (XRD), differential scanning calorimetry (DSC), TGA/DTG/DTA, and XPS which showed good fabrication of hydrogel with high thermal stability. The other experiment such as SEM analysis, the study of swelling properties, MTT assay, drug release study showed high porosity, the degree of swelling (DOS), cytocompatibility, efficient drug release of the fabricated hydrogel as discussed further.

2 Materials and methods

2.1 Materials

CMC and apple pectin (50–75% degree of methyl esterification) and citrus pectin (65–74% degree of methyl esterification) were brought from Hi-media. Glycerol (99% purity) and PEG 400 (polyethylene glycol 400) were brought from Merck. Copper sulfate pentahydrate ($\text{CuSO}_4 \cdot 5\text{H}_2\text{O}$) (98%), tris-buffer, hydrochloric acid, and absolute ethanol were brought from Sisco Research Laboratories. Double distilled water was prepared in the laboratory.

2.2 Preparation of hydrogel

A stock solution of all polymers 4% (w/v) (pectin (apple + citrus pectin; 1:1), 1.6% (w/v)) CMC were prepared using double distilled water. All the polymers were mixed in different ratios for 1 h at 700 rpm on a magnetic stirrer. The addition of PEG 400/glycerol as the plasticizer to the above-mixed solution in different ratios of wt% (v/v) was done and left to stir for another 1 h. Details of the formation of hydrogels in different parameters such as the difference in polymer composition ratio, plasticizers, cross-linker are mentioned in Supplementary data 1. After the above step, a glass Petri dish was cleaned and by using ethanol it was made grease-free. The above solution of polymers was poured into the Petri dish. The polymer solutions with glycerol as a plasticizer was named as PCGY and the polymer solutions with PEG 400 as a plasticizer was named as PCPEG and the polymer solutions without plasticizer were named as PC. A solution of 2% CuSO_4 was prepared and sprayed over the polymer solutions present in the Petri dish. The CuSO_4 helps in cross-linking the polymer solutions immediately to form the hydrogel. Wash the hydrogel with double distilled water to remove excess CuSO_4 solution. The hydrogel was kept at -20°C for a minimum of 4 h for proper solidification. The hydrogel was lyophilized (Creatrust – CTED - 1P) at room temperature to form the scaffold. Among all the polymers mixtures which are

mentioned in Supplementary data 1, only those were selected which formed proper hydrogels which are PC, PCPGY1, PCGY2, PCPEG1, and PCPEG2.

2.3 Characterization

The field emission scanning electron microscope (FE-SEM) is used to study the structural morphology of the hydrogel scaffolds. FTIR spectra of the hydrogel scaffolds were recorded by FTIR spectroscopy: Agilent, Cary 630, USA and the frequency range scanned was $400\text{--}4000\text{ cm}^{-1}$. XRD patterns of the hydrogel scaffolds were obtained by using Bruker AXS, D2 Phaser. A thin section of $1 \times 1\text{ cm}$ hydrogel scaffolds was used for the study of the XRD pattern. The $\text{CuK}\alpha$ radiation was fixed at a wavelength of 1.5418 \AA . The diffraction spectra of the hydrogel scaffolds were verified over a 2θ range with the scanning rate of 0.2° s^{-1} at room temperature. Thermogravimetric (TGA) and differential thermal analysis (DTA) of thin sections of hydrogel scaffolds were carried out by using Perkin Elmer Pyris Diamond TG-DTA with a scanning rate of $10^\circ\text{C min}^{-1}$ under a nitrogen atmosphere in a room temperature ranging from 20 to 1000°C . DSC of the hydrogel scaffolds was performed using Perkin Elmer Pyris Diamond DSC. Samples were heated from 10°C – 100°C at a heating rate of $10^\circ\text{C min}^{-1}$ in the nitrogen atmosphere.

2.4 Water uptake studies

The water uptake capability of the hydrogel scaffolds can be measured as the DOS. A small piece of dried scaffolds with equal weight (W_i) was immersed in double distilled water or buffer of different pH at room temperature. The wet weight (W_f) of the sample was determined after 6 days by gently blotting the sample over the filter paper. The degree of swelling (Eq. 1) was measured according to the following equation [45]:

$$\text{Degree of swelling} = \frac{W_f - W_i}{W_i} \quad (1)$$

2.5 Cell viability studies

Cell viability of hydrogel scaffolds was evaluated by using MTT assay which is a colorimetric assay that measures the reduction of yellow color MTT 3-(4, 5-dimethylthiazol-2-yl)-2, 5-diphenyl tetrazolium bromide (MTT) by mitochondrial succinate dehydrogenase. The MTT enters the cells and gets reduced in mitochondria into insoluble formazan product which is dark in color. The cells are then dissolved in organic solvents and measured spectrophotometrically [46]. MTT is only reduced when the cells are metabolically active, thus, it demonstrates the viability of the cell. WI-38 cells

(lung fibroblast cell line) were cultured in RPMI media with 10% fetal bovine serum, 100 U/ml penicillin and 100 U/ml streptomycin as antibiotics at 37 °C in 5% CO₂ and humid atmosphere. In 96 well plate, WI-38 cells were seeded at a density of 1×10^5 . An equal weight of hydrogel scaffolds was incubated in different well plates and exposed to the cells for different hours (24, 48, and 72 h). Also, an equal weight of samples PCGY1 and PCPEG2 were incubated separately for 24, 48, and 72 h. After incubation 1X phosphate buffer saline (PBS) was used to wash cells twice. After that 0.5 mg/ml MTT solution was added to the well and incubated for 3 to 4 h at 37 °C until a purple color develops. The resulting product obtained was dissolved in DMSO (Dimethyl sulfoxide) and spectrophotometrically measured at 570 nm using a microplate reader (Biorad). The survival percentage was calculated considering the untreated cells having 100% viability.

2.5.1 Live/dead cell staining

The viability of cells cultured with PCPEG2 was assessed using live/dead cells staining procedure. WI-38 cells were cultured in coverslip in 35 mm plate and incubated with PCPEG2 for 3, 5, 7 days respectively along with control. Working solutions of calcein-AM (2 μ M) and propidium iodide (PI) (4 μ M) were prepared from stock solutions. After washing the cells with 1X PBS three times, an equimolar mixture of dyes was added at 500 μ l/well. After incubation at 37 °C for 30 min, the samples were observed by fluorescence microscopy (Leica) using an excitation wavelength of 490 nm and the green emission at 515 nm to observe the live cells, while an excitation wavelength of 535 nm and the red emission at 615 nm were used to observe the dead cells. Images were taken at $\times 40$ magnification.

2.6 Drug release study

To study the drug release rate of hydrogel scaffolds, bovine serum albumin (BSA) was used as a model drug. A stock solution of 1 mg/ml of BSA was prepared using distilled water. The hydrogel scaffolds were cut into small pieces and dipped in BSA solution. After 6 days the respective hydrogel was removed from the solution and was blotted slightly to remove excess solution and dipped it again in 10 ml of distilled water. The solution was kept in slightly shaking condition using SPINIX – Orbital shaker. After every equivalent interval, 1 ml of solution was removed from the beaker and 1 ml of distilled water was added to the beaker, respectively [47]. Bradford protein assay was used to estimate the concentration of protein in the solution against the standard curve. The spectrophotometrical

reading was taken at 595 nm. The above process was used to estimate protein release from hydrogels in pH 4, 5, 6. The drug release rate was estimated as Eq. 2, where x is the maximum drug release at time T .

$$\text{Drug release rate} = (\text{Amount of drug release } (x) \text{ in } T \text{ time})/T \text{ time.} \quad (2)$$

3 Results and discussions

3.1 Structural analysis using FE-SEM

The structural analysis of the hydrogel scaffolds was done by FE-SEM analysis. Figure 1 depicts the FE-SEM image of PC (pectin: CMC), PCGY1(pectin: CMC: 4% (v/v) glycerol), PCGY2 (pectin: CMC: 6% (v/v) glycerol), PCPEG1 (pectin: CMC: 4% (v/v) PEG 400), and PCPEG2 (pectin: CMC: 6% (v/v) PEG 400). The difference in plasticizers and their percentage has greatly affected the porosity of the hydrogel. When no plasticizers were added to the polymer mixture then the resulted hydrogel (PC) formed has no porosity as shown in Fig. 1a whereas, when glycerol was used as plasticizer then at 4% (v/v) of glycerol in solution resulted in higher porosity of hydrogel (PCGY1) than 6% (v/v) of glycerol in solution (PCGY2) as shown in Fig. 1b, c, respectively. Whereas, 6%(v/v) of PEG 400 in solution resulted in higher porosity of hydrogel (PCPEG1) than 4% (v/v) of PEG 400 in solution (PCPEG2) as shown in Fig. 1d, e, respectively. Even when drawn center of attention towards Fig. 1 it can be concluded that PCGY1 and PCPEG2 are more porous then other hydrogels but PCPEG2 has higher uniformity and deep pores than PCGY1. The mean pore size of PCGY1 and PCPEG2 are 36.41 (Fig. 1b) and 21.72 μ m (Fig. 1e), respectively. Therefore, it can be concluded that though PCPEG2 has a slightly small pore size than PCGY1 the pores of PCPEG2 are more uniform and deeper than PCGY1 which can be helpful in drug entrapment and cell viability. The images of hydrogels at different magnifications are mentioned in Supplementary data 2 for a better understanding of porosity.

3.2 Study of interaction among polymers using FTIR spectroscopy

The FTIR spectra of PCGY1 (Fig. 2) show a clear absorption peak at 2994–3741 cm^{-1} which are due to –OH stretch vibration peaks. The peak at 2899 and 2946 cm^{-1} is due to C–H stretching due to alkane. The peak at 1741 cm^{-1} is due to strong C=O stretching due to the presence of the carboxymethyl group (–COOCH₃). The peak at 1641 cm^{-1} is due to C=C stretching due to the presence of conjugated alkene. The peaks at 1461 and 1243 cm^{-1} represent CH₂ and –OH

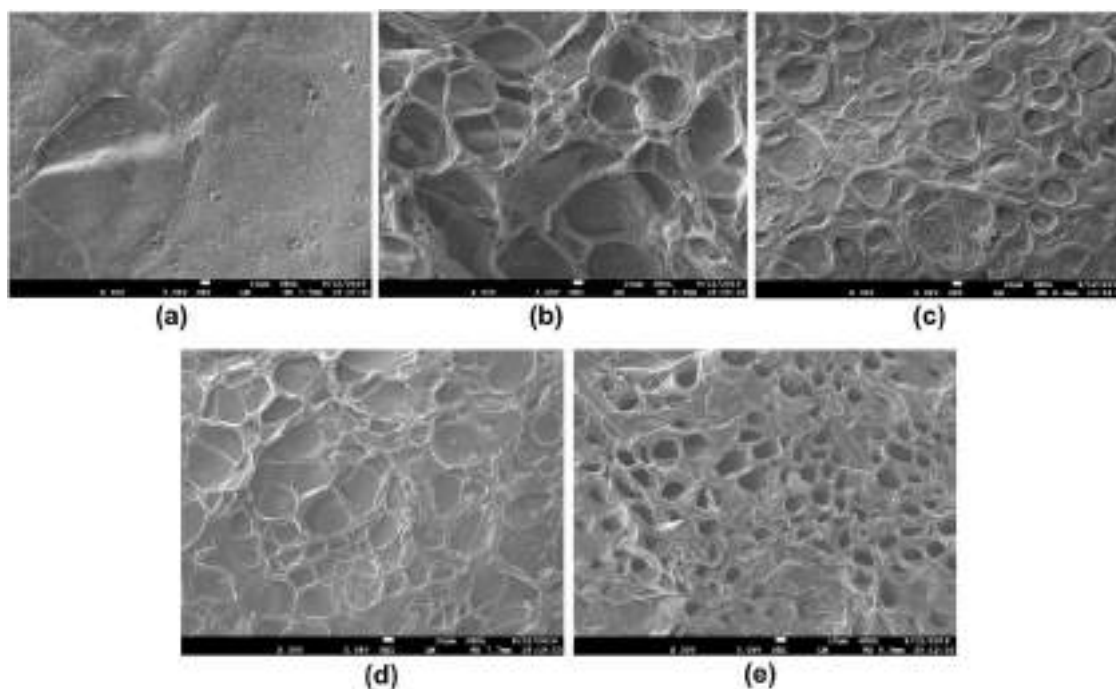


Fig. 1 FE-SEM image of (a) PC, (b) PCGY1, (c) PCGY2, (d) PCPEG1 and (e) PCPEG2

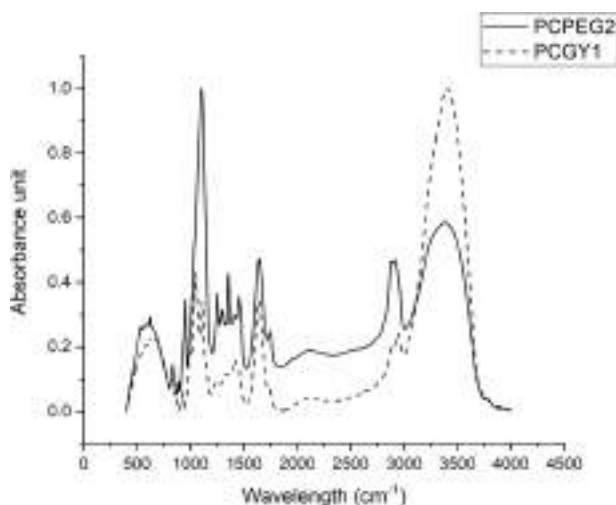


Fig. 2 The graphical representation of FTIR peaks of PCGY1 and PCPEG2

bending vibration peaks, respectively. The peaks $1045\text{--}1116\text{ cm}^{-1}$ represent the C–O stretching vibration peak in the hydrogel [48]. The shift of peaks is due to interaction among the polymer compounds and cross-linking by Cu^{2+} ions in hydrogel [17, 47, 49, 50].

The FTIR spectra of PCPEG2 (Fig. 2) show a clear absorption peak at $3230\text{--}3490\text{ cm}^{-1}$ which is due to –OH stretch and 2889 and 2923 cm^{-1} is due to –CH stretching vibration peaks. The peak at 1641 cm^{-1} is due to C=C stretching due to the presence of conjugated alkene. The peak at 1750 cm^{-1} represents the carboxymethyl group ($-\text{COOCH}_3$)

due to C=O stretching. The peaks at $1414\text{--}1452\text{ cm}^{-1}$ and $1253\text{--}1357\text{ cm}^{-1}$ represent CH_2 and –OH bending vibration peaks respectively. The peaks $955\text{--}1101\text{ cm}^{-1}$ represent the C–O stretching vibration peak in the hydrogel [48]. The peak at $624\text{--}842\text{ cm}^{-1}$ represents the C–H bending. The cross-linking by Cu^{2+} ions and interaction of polymers in hydrogel leads to shifting in peaks in FTIR analysis.

The increase in the intensity of peaks signifies more of that particular type of bond. PCGY1 and PCPEG2 have peaks position at the same wavelength range but the peak intensity differs which signifies that the number of bond formation is more at that peak intensity [51, 52]. According to Munajad et al. [51], there is a linear correlation between the intensity of the peak absorbance of the functional groups or bonds with the average number of functional group formation or bond formation [52]. Thus, it implies that the intensity of the peak absorbance signifies the formation of new bonds due to cross-linking by Cu^{2+} ions. The FTIR peaks represented in the graph (Fig. 2) proves the favorable interactions between pectin and CMC with glycerol and PEG 400 which lead to successful hydrogel scaffold formation [17, 47, 49, 50].

3.3 Study of crystallization using XRD

The XRD pattern of PCGY1 and PCPEG2 state the crystallization of both the hydrogels (Fig. 3). The broad peak at 21.23° shows the amorphous nature of the PCGY1 and PCPEG2 hydrogel (Fig. 3). The peak at 27.97° represents a

low crystallinity of the polymer blend in the case of PCPEG2 (Fig. 3) [53]. PCGY1 and PCPEG2 have different plasticizers which are glycerol and PEG 400, respectively, which affect the crystallinity nature of the polymer blend. As plasticizers provide mobility between the polymer molecules layer thus, they affect the crystalline nature of the polymer blend [54]. The above discussion confirms the amorphous nature of both the hydrogel (PCGY and PCPEG) [47].

3.4 Thermogravimetric analysis (TGA)/derivative thermogravimetric analysis (DTG) and differential thermal analysis (DTA)

Figure 4 represents the TGA profile of hydrogel PCGY1 and PCPEG2. The TGA graph plot represents thermal

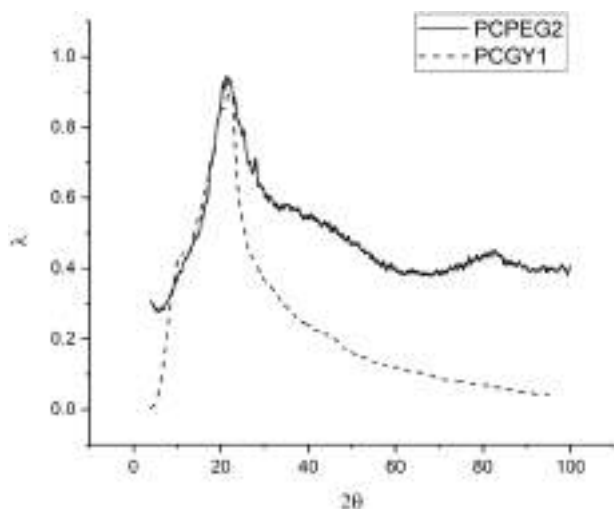


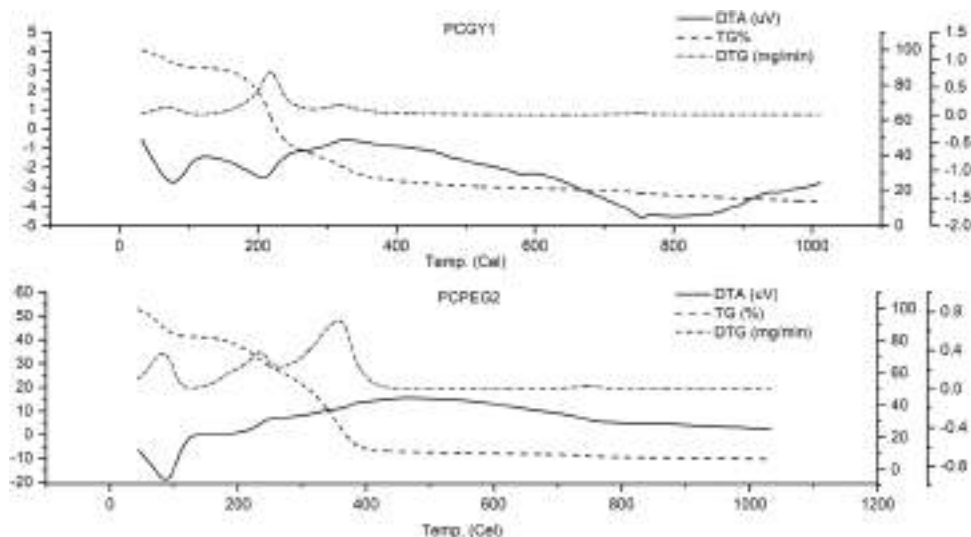
Fig. 3 The graphical representation of XRD peaks of PCGY1 and PCPEG2

stability with a change in temperature. At 170 °C the initial degradation of PCGY1 starts and degradation continues till 351 °C. The weight loss percentage of PCGY1 is 60%. The DTA graph plot represents the endothermic degradation of PCGY1. The first degradation occurs at 70 °C which is degraded due to the evaporation of water molecules strongly bound to the PCGY1 sample [55]. At 210 °C major degradation of the polymer occurs which is an endothermic reaction. The DTG graph plot confirms the degradation of the sample and represents the exact temperature at which the degradation starts and ends. The degradation due to loss of water starts at 10 °C and ends at 110 °C. The major degradation of polymer starts at 170 °C and ends at 280 °C, whereas a small peak from 290 to 351 °C represents the final degradation of the polymer. The height or depth of the peaks defines reactivity intensity in the case of DTA and DTG graph [56].

At 190 °C the initial degradation of the PCPEG2 starts and degradation continues till 410 °C. The initial weight loss percentage of PCPEG2 is 72%. The DTA graph plot represents the endothermic degradation of PCPEG2. The first degradation of PCPEG2 occurs at 80 °C which is degradation due to the evaporation of water molecules strongly bound to the sample which is an endothermic reaction [55]. The DTG graph plot confirms the degradation of the sample and represents the exact temperature at which the degradation starts and ends [55]. The degradation due to loss of water starts at 10 °C and ends at 120 °C. Similarly, the major degradation of the polymer occurs at 200–270 °C and 270–450 °C [56].

So, according to the above discussion, the conclusion reflects that PCPEG2 has more thermal stability than PCGY1. PCPEG2 approximately degrades at 450 °C whereas PCGY1 degrades at 351 °C, thus, PCPEG2 has high thermal stability which has great use in industries.

Fig. 4 The graphical representation of TGA/DTA analysis **a** PCGY1 and **b** PCPEG2



3.5 Thermal analysis using differential scanning calorimetry

The T_g value of PCGY1 is 57.4 °C, whereas the T_g value of PCPEG2 is 54.75 °C which is nearly similar (Fig. 5). As the T_g value is at low temperature represents high molecular mobility. The T_g value of PCGY1 and PCPEG2 shows that the materials are amorphous in nature. When the plasticizer is added to the polymer, the plasticizer molecules help in spacing the polymer chains apart from each other and increases the free volume. Therefore the plasticizer molecules help in smooth movement of the polymer chain over each other at low temperature subsequent in the decrease of T_g of the polymer [57]. According to Jadhav et. al. 2014, some such plasticizers are PEG, propylene glycol, nitrobenzene, glycerin, etc. which deliver such properties as described in the above text [57]. This discussion, when correlated with the above discussed XRD analysis, confirms the amorphous nature of the polymer blend of hydrogel (PCGY1 and PCPEG2).

3.6 X-ray photoelectron spectroscopy

As discussed above in FE-SEM that the pores of PCPEG2 are more uniform and deeper than PCGY1, therefore PCPEG2 was considered for XPS analysis. Figure 6 describes the XPS of PCPEG2, where Fig. 6a–d represents the presence of carbon, copper, oxygen, sulfur compound, respectively. The intensity of the peaks is directly proportional to the amount of those particular compounds. From Fig. 6 it can be easily predicted that the hydrogel has a high amount of carbon and oxygen-related compounds than copper- and sulfur-related compounds due to the presence of polysaccharides such as pectin and CMC along with PEG

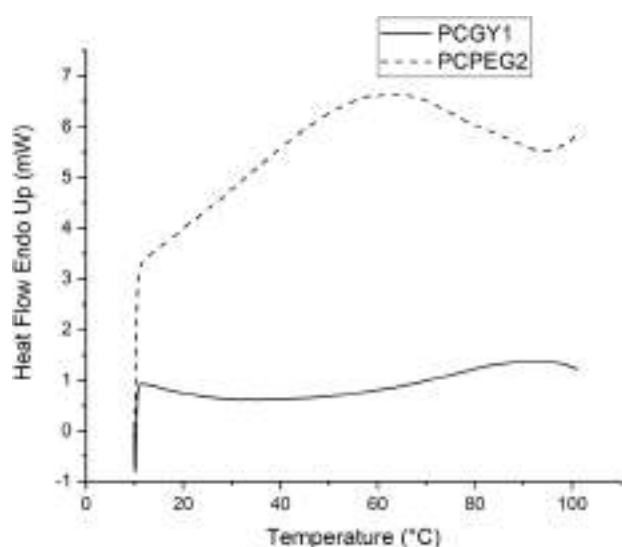
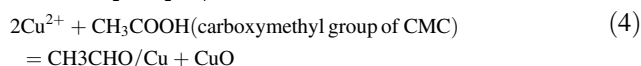
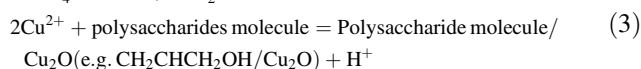
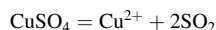


Fig. 5 The graphical representation of DSC analysis **a** PCGY1 and **b** PCPEG2

400. This XPS analysis intends to evaluate the possible cross-linking reaction of polysaccharides due to CuSO_4 . Therefore, compounds expected to involve in this cross-linking reaction are more emphasized.

In Fig. 6a two peaks are observed at 284.90 and 286.10 which represent the presence of polysaccharides compounds along with carbon and other hydrocarbons. Among these compounds $\text{CH}_3\text{CHO}/\text{Cu}$, $\text{CH}_2\text{CHCH}_2\text{OH}/\text{Cu}_2\text{O}$, $\text{CH}_2\text{CHCH}_2\text{OH}/\text{Cu}_2\text{O}$, $\text{CH}_2\text{CHCHO}/\text{Cu}_2\text{O}$, $\text{CH}_3\text{CH}_2\text{CHO}/\text{Cu}_2\text{O}$, $\text{CH}_3\text{CH}_2\text{CH}_2\text{OH}/\text{Cu}_2\text{O}$, $\text{CH}_3\text{CH}_2\text{CH}_2\text{OH}/\text{Cu}_2\text{O}$, $\text{CH}_3\text{CH}_2\text{CH}_2\text{OH}/\text{Cu}_2\text{O}$, $\text{CH}_2\text{CHCH}_2\text{OH}/\text{Cu}_2\text{O}$, $\text{CH}_3\text{CH}_2\text{CH}_2\text{OH}/\text{Cu}_2\text{O}$ are the compounds formed due to reaction of CuSO_4 with polysaccharides as mentioned in the proposed Eqs. 3 and 4).



In Fig. 6c peak at 532.50 represents the presence of oxygen rich compound such as H_2SO_4 , $\text{S}(\text{CH}_2\text{COOH})_2$, $(-\text{CH}_2\text{CH}(\text{OH})-)_n$, $(-\text{CH}_2\text{CH}(\text{C}(\text{O})\text{OH})-)_n$, $(-\text{CH}_2)_4\text{O}-)_n$, $(-(\text{C}_6\text{H}_7\text{O}_2)(\text{OCH}_2\text{CH}_3)_x(\text{OH})_{3-x}-)_n$, $(-\text{CH}(\text{CH}_3)\text{CH}_2\text{O}-)_n$, $(-\text{OCH}_2\text{C}(\text{O})-)_n$, $(-\text{C}_6\text{H}_4-\text{C}(\text{CH}_3)_2-\text{C}_6\text{H}_4-\text{O}-\text{C}(\text{O})\text{O}-)_n$ among which H_2SO_4 is formed due to the cross-linking reaction of polysaccharides with CuSO_4 as mentioned in proposed Eq. 3.

In Fig. 6b peak at 932.70 represents the presence of copper-rich compounds such as Cu/O_2 , $\text{Cu}(\text{OH})_2$, Cu_2O , Cu_2S , CuO , Cu , among which the possibilities of CuO and Cu are high during the cross-linking reaction.

Figure 6d peak at 168.10 represents the presence of SO_2 due to the cross-linking reaction mentioned in the proposed Eqs. 3 and 4.

Therefore from the above discussion, it can be concluded that when CuSO_4 solution was added to the polymer mixtures CuSO_4 breaks down into Cu^{2+} and SO_2 . Cu^{2+} further reacts with the polysaccharide molecules to eliminate H^+ ion and formation of polysaccharide/ Cu_2O (e.g. $\text{CH}_2\text{CHCH}_2\text{OH}/\text{Cu}_2\text{O}$). The eliminated H^+ ion reacts with SO_2 to the formation of H_2SO_4 . When Cu^{2+} reacts with the carboxymethyl (CH_3COOH) group of cellulose leads to the formation of $\text{CH}_3\text{CHO}/\text{Cu}$ and CuO . In this way, CuSO_4 leads to ionic reaction for cross-linking among the polysaccharides and the formation of a hydrogel.

3.7 Swelling properties

Table 1 describes the analysis of the DOS of PCGY1 and PCPEG2 in water and different pH. DOS in the water of

PCPEG2 is 12.96 which is greater than DOS in the water of PCGY1 which is 5.17. With increasing pH, the DOS value increases to pH 5.5 and decreases from pH 6 in the case of PCGY1, whereas in case of PCPEG2 DOS value increases till pH 6 and decreases at higher pH which discloses the pH-sensitive nature of hydrogel. PCPEG2 has the highest DOS value of 14.54 at pH 6, whereas PCGY1 has the highest DOS value of 18.77 at pH 5. The highest DOS value of PCGY1 (18.77) is greater than the highest DOS value of PCPEG2 (14.54) which reflects the fact that glycerol-based hydrogel is more hydrophilic than PEG 400 based hydrogel. The porosity of the hydrogels PCPEG2 and PCGY1 affects the swelling property of hydrogels. More porous the hydrogels, the higher is the DOS value. From Table 1 it can also be

concluded that PCPEG2 has consistently high DOS value in water and pH 4.5–6. The high swelling properties of PCPEG2 is an effective drug delivery system over skin-based problems as the skin has an average pH from pH 5 to pH 5.5 [58].

3.8 Cell compatibility studies

The MTT assay was performed to measure the change in the viability of WI-38 cells after incubation with PCGY1 and PCPEG2 for different time intervals. Figure 7 represents the survival percentage at different time points. The survival percentage of PCPEG2 was higher than PCGY1. PCPEG2 showed an increase in cell viability from 48 to 72 h. Though there was a slight decrease in cell viability at

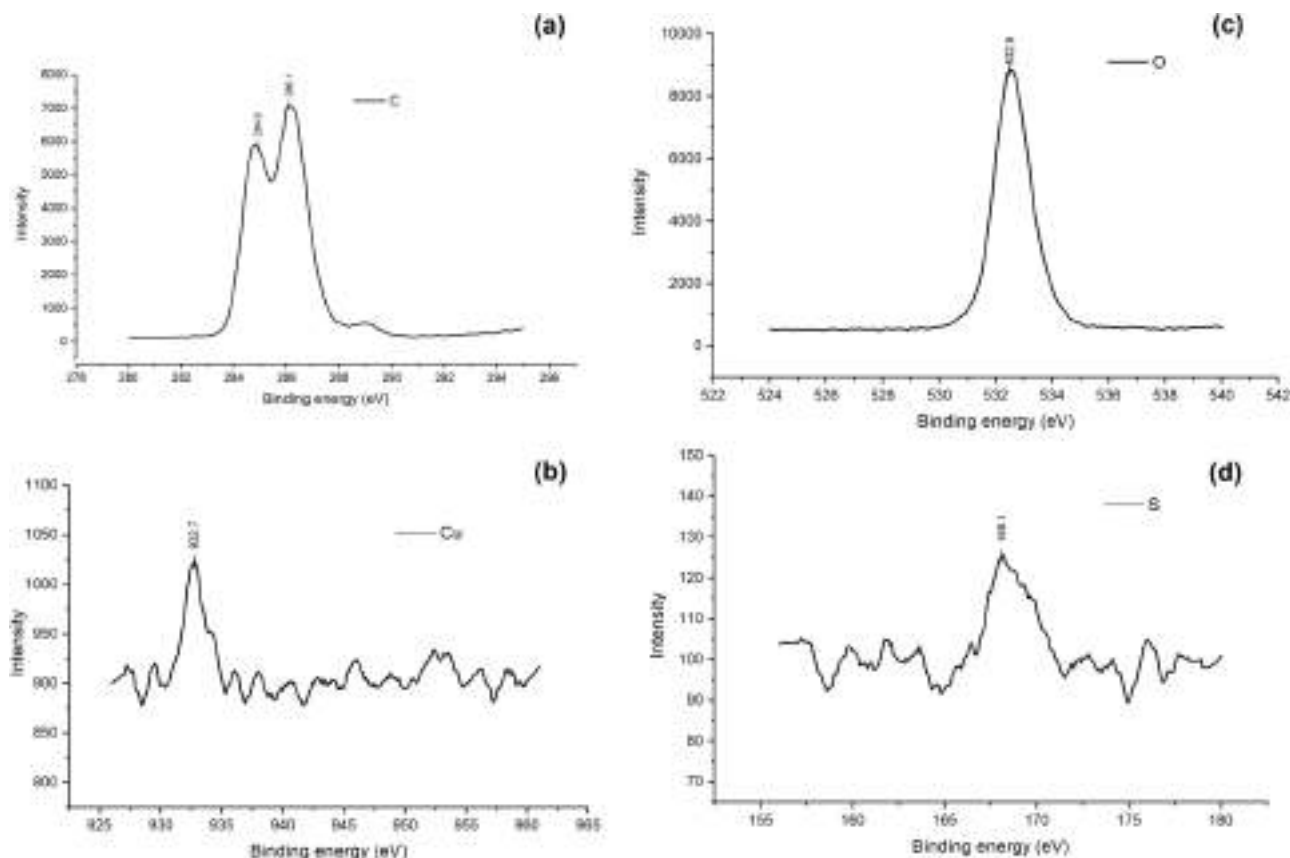


Fig. 6 The graphical representation of XPS analysis **a** Carbon compounds, **b** Copper compounds, **c** Oxygen compounds, and **d** Sulfur compounds

Table 1 Degree of swelling (DOS) in water and different pH of PCGY1 and PCPEG2

Sample	DOS in water	DOS in pH 4.5	DOS in pH 5	DOS in pH 5.5	DOS in pH 6	DOS in pH 6.5	DOS in pH 7	DOS in pH 7.5
PCGY1	5.17 ± 0.12	6.52 ± 0.22	18.77 ± 0.07	16.13 ± 0.27	13.9 ± 0.63	Dissolved	Dissolved	Dissolved
PCPEG2	12.96 ± 0.25	12.93 ± 0.24	12.97 ± 0.23	13.37 ± 0.23	14.54 ± 0.07	Dissolved	Dissolved	Dissolved

Symbol “±” denotes standard deviation with $n = 4$

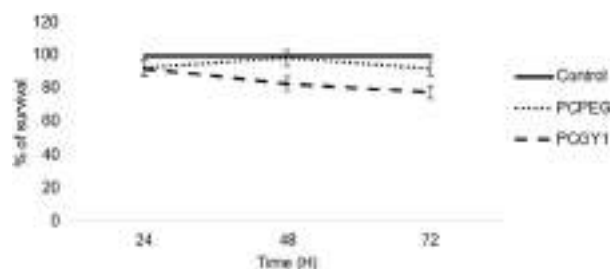


Fig. 7 The graphical representation of the survival percentage of PCGY1 and PCPEG2 with respect to time

72 h concerning 48 h in the case of PCPEG2 still has higher cell viability than PCGY1. The decrease in the cell survival rate by 72 h was probably due to the percolation of Cu^{2+} from slowly degrading hydrogels with time due to the basic pH of the media [59]. In Fig. 7 it was observed that PCPEG2 is highly nontoxic among the two samples in all time points. Therefore the live–dead cell count was performed for PCPEG2 in WI-38 cells for 3, 5, and 7 days. The above discussion reveals good cytocompatibility of PEG 400-based pectin/CMC hydrogel i.e. PCPEG2. Thus, it shows no significant cytotoxicity to time.

3.8.1 Live/dead cell staining

To evaluate cell activity, the Live/Dead assay was used to monitor the growth and proliferation of WI-38 cells with PCPEG2. Fluorescence images for WI-38 cells with specific live–dead staining after 3, 5, and 7 days respectively are provided in Fig. 8. The live cells were stained with calcein-AM (green), while the dead cells were stained with PI (red). It can be seen that the cells incubated with the PCPEG2 were highly active, with dead cells hardly visible up to 5 days, respectively. But after 7 days of incubation with PCPEG2, few cells were dies as seen by red nuclei. These results indicate that PCPEG2 can support cell survival and proliferation.

3.9 Drug release study

Based on the above discussion PCPEG2 has high porosity, high DOS value, and high cytocompatibility, due to which PCPEG2 is considered for drug release study. The drug release study was done using 1000 $\mu\text{g}/\text{ml}$ of BSA as a stock solution. Figure 9 represents the BSA release rate in water, pH 4, pH 5, pH 6 of PCPEG2. In the case of water, the BSA release increased stiffly from 0 to 10 min and then consistently increased further. In the case of pH 4, the BSA release was averagely consistent throughout the time, whereas in the case of pH 5 the BSA release increased from 0 to 45 min and then stayed consistent. In the case of pH 6,

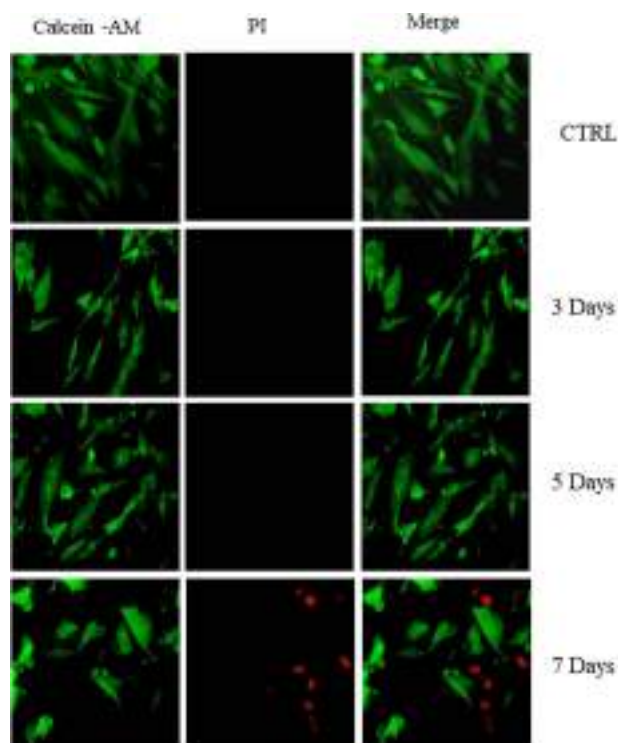


Fig. 8 The live and dead cell study of PCPEG2

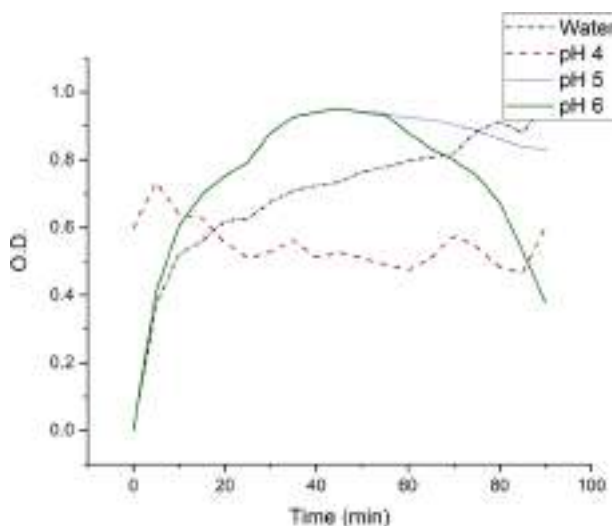


Fig. 9 Release of BSA from PCPEG2 with respect to time in the water, pH 4, pH 5, and pH 6

the BSA release stiffly increased from 0 to 25 min and then stayed constant till 60 min and decreased rapidly further. The BSA release rate in water, pH 4, pH 5, and pH 6 are 0.00026, 0.00007, 0.00040, 0.00048 $\mu\text{g}/\text{min}$. respectively. From Fig. 9 it can also be concluded that with the increase of pH, the DOS value also increases and resulting in a rapid influx of the buffer which results in increased release of BSA. Therefore PCPEG2 has good drug release efficiency.

4 Conclusion

The above results describe the successful fabrication of the hydrogel scaffold (PCPEG2). PCPEG2 has high porosity, high thermal stability, high cytocompatibility, and high DOS value with efficient drug release as described in FE-SEM, TGA/DTA, cytocompatibility and cell viability study and swelling property study. XRD and DSC results confirmed the amorphous nature in PCPEG2, as well as FTIR, confirmed the successful fabrication of PCPEG2. The XPS result interpreted the possible cross-linking reaction of polysaccharide molecules due to CuSO_4 . Therefore based on the results and discussions, it can be concluded that PCPEG2 can be considered as a valuable industrial product such as a drug delivery system over the skin.

Acknowledgements The authors of this paper are thankful to the Department of Metallurgy, IIT Kharagpur for providing research facility regarding XRD, TGA/DTG/DTA, and DSC, Department of Central Scientific Service, Indian Association for the Cultivation of Science, Kolkata for providing research facility regarding FE-SEM, FTIR, XRD, and XPS.

Compliance with ethical standards

Conflict of interest The authors declare that they have no conflict of interest.

Publisher's note Springer Nature remains neutral with regard to jurisdictional claims in published maps and institutional affiliations.

References

- Guilherme MR, Aouada FA, Fajardo AR, Martins AF, Paulino AT, Davi MFT, Rubira AF, Muniz EC (2015) Superabsorbent hydrogels based on polysaccharides for application in agriculture as soil conditioner and nutrient carrier: a review. *Eur Polym J* 72:365–385. <https://doi.org/10.1016/j.eurpolymj.2015.04.017>
- Rudzinski WE, Dave AM, Vaishnav UH, Kumbhar SG, Kulkarni AR, Aminabhavi TM (2002) Hydrogels as controlled release devices in agriculture. *Des Monomers Polym* 5(1):39–65. <https://doi.org/10.1163/156855502760151580>
- Hoffman AS (2012) Hydrogels for biomedical applications. *Adv Drug Deliv Rev* 64:18–23. <https://doi.org/10.1016/j.addr.2012.09.010>
- Gad YH (2008) Preparation and characterization of poly(2-acrylamido-2-methylpropane-sulfonic acid)/Chitosan hydrogel using gamma irradiation and its application in wastewater treatment. *Radiat Phys Chem* 77(9):1101–1107. <https://doi.org/10.1016/j.radphyschem.2008.05.002>
- Crini G (2005) Recent developments in polysaccharide-based materials used as adsorbents in wastewater treatment. *Prog Polym Sci* 30(1):38–70. <https://doi.org/10.1016/j.progpolymsci.2004.11.002>
- Lutchmiah K, Verliefe ARD, Roest K, Rietveld LC, Cornelissen ER (2014) Forward osmosis for application in wastewater treatment: a review. *Water Res* 58:179–197. <https://doi.org/10.1016/j.watres.2014.03.045>
- Souza GR, Molina JR, Raphael RM, Ozawa MG, Stark DJ, Levin CS, Bronk LF, Ananta JS, Mandelin J, Georgescu M-M, Bankson JA, Gelovani JG, Killian TC, Arap W, Pasqualini R (2010) Three-dimensional tissue culture based on magnetic cell levitation. *Nat Nanotech* 5:291. <https://doi.org/10.1038/nnano.2010.23>
- Landers R, Hübner U, Schmelzeisen R, Mülhaupt R (2002) Rapid prototyping of scaffolds derived from thermoreversible hydrogels and tailored for applications in tissue engineering. *Biomaterials* 23(23):4437–4447. [https://doi.org/10.1016/S0142-9612\(02\)00139-4](https://doi.org/10.1016/S0142-9612(02)00139-4)
- Seliktar D (2012) Designing cell-compatible hydrogels for biomedical applications. *Science* 336(6085):1124–1128. [10.1126/science.1214804](https://doi.org/10.1126/science.1214804) %J Science
- Drury JL, Mooney DJ (2003) Hydrogels for tissue engineering: scaffold design variables and applications. *Biomaterials* 24(24):4337–4351. [https://doi.org/10.1016/S0142-9612\(03\)00340-5](https://doi.org/10.1016/S0142-9612(03)00340-5)
- Lee KY, Mooney DJ (2001) Hydrogels for tissue engineering. *Chem Rev* 101(7):1869–1880. <https://doi.org/10.1021/cr000108x>
- Peppas NA, Bures P, Leobandung W, Ichikawa H (2000) Hydrogels in pharmaceutical formulations. *Eur J Pharm Biopharm* 50(1):27–46. [https://doi.org/10.1016/S0939-6411\(00\)00090-4](https://doi.org/10.1016/S0939-6411(00)00090-4)
- Van Tomme SR, Storm G, Hennink WE (2008) In situ gelling hydrogels for pharmaceutical and biomedical applications. *Int J Pharm* 355(1):1–18. <https://doi.org/10.1016/j.ijpharm.2008.01.057>
- Gupta P, Vermani K, Garg S (2002) Hydrogels: from controlled release to pH-responsive drug delivery. *Drug Discov Today* 7(10):569–579. [https://doi.org/10.1016/S1359-6446\(02\)02255-9](https://doi.org/10.1016/S1359-6446(02)02255-9)
- Malafaya PB, Silva GA, Reis RL (2007) Natural-origin polymers as carriers and scaffolds for biomolecules and cell delivery in tissue engineering applications. *Adv Drug Deliv Rev* 59(4):207–233. <https://doi.org/10.1016/j.addr.2007.03.012>
- Vieira MGA, da Silva MA, dos Santos LO, Beppu MM (2011) Natural-based plasticizers and biopolymer films: a review. *Eur Polym J* 47(3):254–263. <https://doi.org/10.1016/j.eurpolymj.2010.12.011>
- Ninan N, Muthiah M, Park I-K, Elain A, Thomas S, Grohens Y (2013) Pectin/carboxymethyl cellulose/microfibrillated cellulose composite scaffolds for tissue engineering. *Carbohydr Polym* 98(1):877–885. <https://doi.org/10.1016/j.carbpol.2013.06.067>
- Nazarov R, Jin H-J, Kaplan DL (2004) Porous 3-D scaffolds from regenerated silk fibroin. *Biomacromolecules* 5(3):718–726. <https://doi.org/10.1021/bm034327e>
- Chung TW, Yang J, Akaike T, Cho KY, Nah JW, Kim SI, Cho CS (2002) Preparation of alginate/galactosylated chitosan scaffold for hepatocyte attachment. *Biomaterials* 23(14):2827–2834. [https://doi.org/10.1016/S0142-9612\(01\)00399-4](https://doi.org/10.1016/S0142-9612(01)00399-4)
- Sheridan MH, Shea LD, Peters MC, Mooney DJ (2000) Bioabsorbable polymer scaffolds for tissue engineering capable of sustained growth factor delivery. *J Control Release* 64(1):91–102. [https://doi.org/10.1016/S0168-3659\(99\)00138-8](https://doi.org/10.1016/S0168-3659(99)00138-8)
- Luu YK, Kim K, Hsiao BS, Chu B, Hadjiargyrou M (2003) Development of a nanostructured DNA delivery scaffold via electrospinning of PLGA and PLA-PEG block copolymers. *J Control Release* 89(2):341–353. [https://doi.org/10.1016/S0168-3659\(03\)00097-X](https://doi.org/10.1016/S0168-3659(03)00097-X)
- Agrawal CM, Ray RB (2001) Biodegradable polymeric scaffolds for musculoskeletal tissue engineering. *J Biomed Mater Res* 55(2):141–150. [https://doi.org/10.1002/1097-4636\(200105\)55:2<141::AID-JBM1000>3.0.CO;2-J](https://doi.org/10.1002/1097-4636(200105)55:2<141::AID-JBM1000>3.0.CO;2-J)
- Mao JS, Zhao LG, Yin YJ, Yao KD (2003) Structure and properties of bilayer chitosan–gelatin scaffolds. *Biomaterials* 24(6):1067–1074. [https://doi.org/10.1016/S0142-9612\(02\)00442-8](https://doi.org/10.1016/S0142-9612(02)00442-8)
- Xiao W, He J, Nichol JW, Wang L, Hutson CB, Wang B, Du Y, Fan H, Khademhosseini A (2011) Synthesis and characterization

- of photocrosslinkable gelatin and silk fibroin interpenetrating polymer network hydrogels. *Acta Biomater* 7(6):2384–2393. <https://doi.org/10.1016/j.actbio.2011.01.016>
25. Chen M-C, Tsai H-W, Liu C-T, Peng S-F, Lai W-Y, Chen S-J, Chang Y, Sung H-W (2009) A nanoscale drug-entrapment strategy for hydrogel-based systems for the delivery of poorly soluble drugs. *Biomaterials* 30(11):2102–2111. <https://doi.org/10.1016/j.biomaterials.2008.12.047>
26. Bhattarai N, Gunn J, Zhang M (2010) Chitosan-based hydrogels for controlled, localized drug delivery. *Adv Drug Deliv Rev* 62(1):83–99. <https://doi.org/10.1016/j.addr.2009.07.019>
27. He H, Cao X, Lee LJ (2004) Design of a novel hydrogel-based intelligent system for controlled drug release. *J Control Release* 95(3):391–402. <https://doi.org/10.1016/j.jconrel.2003.12.004>
28. Soppimath KS, Kulkarni AR, Aminabhavi TM (2000) Controlled release of antihypertensive drug from the interpenetrating network poly(vinyl alcohol)–guar gum hydrogel microspheres. *J Biomater Sci Polym Ed* 11(1):27–43. <https://doi.org/10.1163/156856200743472>
29. Williams CG, Malik AN, Kim TK, Manson PN, Elisseeff JH (2005) Variable cytocompatibility of six cell lines with photo-initiators used for polymerizing hydrogels and cell encapsulation. *Biomaterials* 26(11):1211–1218. <https://doi.org/10.1016/j.biomaterials.2004.04.024>
30. Mann BK, Gobin AS, Tsai AT, Schmedlen RH, West JL (2001) Smooth muscle cell growth in photopolymerized hydrogels with cell adhesive and proteolytically degradable domains: synthetic ECM analogs for tissue engineering. *Biomaterials* 22(22):3045–3051. [https://doi.org/10.1016/S0142-9612\(01\)00051-5](https://doi.org/10.1016/S0142-9612(01)00051-5)
31. Kobayashi H, Ikacia Y (1991) Corneal cell adhesion and proliferation on hydrogel sheets bound with cell-adhesive proteins. *Curr Eye Res* 10(10):899–908. <https://doi.org/10.3109/02713689109020325>
32. Banerjee A, Arha M, Choudhary S, Ashton RS, Bhatia SR, Schaffer DV, Kane RS (2009) The influence of hydrogel modulus on the proliferation and differentiation of encapsulated neural stem cells. *Biomaterials* 30(27):4695–4699. <https://doi.org/10.1016/j.biomaterials.2009.05.050>
33. Basak S, Nandi N, Paul S, Hamley IW, Banerjee A (2017) A tripeptide-based self-shrinking hydrogel for waste-water treatment: removal of toxic organic dyes and lead (Pb²⁺) ions. *Chem Commun* 53(43):5910–5913. <https://doi.org/10.1039/C7CC01774J>
34. Ninan N, Muthiah M, Park I-K, Kalarikkal N, Elain A, Wui Wong T, Thomas S, Grohens Y (2014) Wound healing analysis of pectin/carboxymethyl cellulose/microfibrillated cellulose based composite scaffolds. *Mater Lett* 132:34–37. <https://doi.org/10.1016/j.matlet.2014.06.056>
35. Akalin GO, Pulat M (2018) Preparation and characterization of nanoporous sodium carboxymethyl cellulose hydrogel beads. *J Nanomater* 2018:12. <https://doi.org/10.1155/2018/9676949>
36. Borkow G (2014) Using copper to improve the well-being of the skin. *Curr Chem Biol* 8(2):89–102. <https://doi.org/10.2174/2212796809666150227223857>
37. Sothornvit R, Krochta JM (2001) Plasticizer effect on mechanical properties of β -lactoglobulin films. *J Food Eng* 50(3):149–155. [https://doi.org/10.1016/S0260-8774\(00\)00237-5](https://doi.org/10.1016/S0260-8774(00)00237-5)
38. Baiardo M, Frisoni G, Scandola M, Rimelen M, Lips D, Ruffieux K, Wintermantel E (2003) Thermal and mechanical properties of plasticized poly(L-lactic acid). *J Appl Polym Sci* 90(7):1731–1738. <https://doi.org/10.1002/app.12549>
39. Srinivasa PC, MNR, Tharanathan RN (2007) Effect of plasticizers and fatty acids on mechanical and permeability characteristics of chitosan films. *Food Hydrocoll* 21(7):1113–1122. <https://doi.org/10.1016/j.foodhyd.2006.08.005>
40. Péan J-M, Boury F, Venier-Julienne M-C, Menei P, Proust J-E, Benoit J-PJP (1999) Why does PEG 400 co-encapsulation improve NGF stability and release from PLGA biodegradable microspheres? *Pharm Res* 16(8):1294–1299. <https://doi.org/10.1023/a:1014818118224>
41. D'souza AA, Shegokar R (2016) Polyethylene glycol (PEG): a versatile polymer for pharmaceutical applications. *Expert Opin Drug Deliv* 13(9):1257–1275. <https://doi.org/10.1080/17425247.2016.1182485>
42. Charles PT, Stubbs VR, Soto CM, Martin BD, White BJ, Taitt CR (2009) Reduction of non-specific protein adsorption using poly(ethylene) glycol (PEG) modified polyacrylate hydrogels in immunoassays for *Staphylococcal* enterotoxin B detection. *Sensors* 9(1):645–655. <https://doi.org/10.3390/s90100645>
43. Chiu YC, Larson JC, Isom Jr. A, Brey EM (2010) Generation of porous poly(ethylene glycol) hydrogels by salt leaching. *Tissue Eng Part C Methods* 16(5):905–912. <https://doi.org/10.1089/ten.TEC.2009.0646>
44. Strzelczyk AK, Wang H, Lindhorst A, Waschke J, Pompe T, Kropf C, Luneau B, Schmidt S (2017) Hydrogel microparticles as sensors for specific adhesion: case studies on antibody detection and soil release polymers. *Gels* 3(3):31
45. Sadeghi MJABAS (2011) Synthesis and investigation of swelling behavior natural based superabsorbent composites with high thermal resistance. *Aust J Basic Appl Sci* 5:887–895
46. Liu Y, Peterson DA, Kimura H, Schubert D (1997) Mechanism of cellular 3-(4,5-dimethylthiazol-2-yl)-2,5-diphenyltetrazolium bromide (MTT) reduction. *J Neurochem* 69(2):581–593. <https://doi.org/10.1046/j.1471-4159.1997.69020581.x>
47. Mishra RK, Datt M, Banthia AK (2008) Synthesis and characterization of pectin/PVP hydrogel membranes for drug delivery system. *AAPS Pharm Sci Tech* 9(2):395–403. <https://doi.org/10.1208/s12249-008-9048-6>
48. COLDEA TE, SOCACIU C, FETEA F, RANGA Fa, POP RM, FLOREA M (2013) Rapid quantitative analysis of ethanol and prediction of methanol content in traditional fruit brandies from romania, using FTIR spectroscopy and chemometrics NOT BOT HORTI AGROBO 41(1):7. <https://doi.org/10.15835/nbha4119000>
49. Yang J, Duan J, Zhang L, Lindman B, Edlund H, Norgren MJC (2016) Spherical nanocomposite particles prepared from mixed cellulose–chitosan solutions. *Cellulose* 23(5):3105–3115. <https://doi.org/10.1007/s10570-016-1029-4>
50. Luna-Martínez JF, Hernández-Uresti DB, Reyes-Melo ME, Guerrero-Salazar CA, González-González VA, Sepúlveda-Guzmán S (2011) Synthesis and optical characterization of ZnS–sodium carboxymethyl cellulose nanocomposite films. *Carbohydr Polym* 84(1):566–570. <https://doi.org/10.1016/j.carbpol.2010.12.021>
51. Munajad A, Subroto C, Suwarno SJE (2018) Fourier transform infrared (FTIR) spectroscopy analysis of transformer paper in mineral oil-paper composite insulation under accelerated thermal aging. *Energies* 11(2):364
52. Bandara K, Ekanayake C, Saha TK, Annamalai PKJIToD, Insulation E (2016) Understanding the ageing aspects of natural ester based insulation liquid in power transformer. *IEEE T Dielect El In* 23(1):246–257
53. Bhattacharya R, Phaniraj TN, Shailaja D (2003) Polysulfone and polyvinyl pyrrolidone blend membranes with reverse phase morphology as controlled release systems: experimental and theoretical studies. *J Memb Sci* 227(1):23–37. <https://doi.org/10.1016/j.memsci.2003.07.014>
54. Saravana S, Bheemaneni G, Kandaswamy R (2018) Effect of polyethylene glycol on mechanical, thermal, and morphological properties of talc reinforced polylactic acid composites. *Mater Today Proc* 5(1):1591–1598. <https://doi.org/10.1016/j.matpr.2017.11.251>
55. Malik NS, Ahmad M, Minhas MU (2017) Cross-linked betacyclodextrin and carboxymethyl cellulose hydrogels for controlled drug delivery of acyclovir. *PloS one* 12(2):e0172727. <https://doi.org/10.1371/journal.pone.0172727>

56. Namdeo R Jadhav, VLG, Karthik J Nair, Hanmantrao M Kadam (2009) Glass transition temperature: basics and application in pharmaceutical sector. *Asian J Pharm* 3(2)
57. Palermo PJ (2001) 6 Solid Dosage-Form Analysis. In: Ahuja S, Scypinski S (eds.) *Separation science and technology*, vol 3. Academic Press, pp 235–267. [https://doi.org/10.1016/S0149-6395\(01\)80008-8](https://doi.org/10.1016/S0149-6395(01)80008-8)
58. Sadeghi M (2011) Synthesis, and investigation of swelling behavior natural based superabsorbent composites with high thermal resistance *Aust J Basic Appl Sci* 5(11):887–895
59. Lang F, Hoffmann EK (2012) Role of ion transport in control of apoptotic cell death. *Compr Physiol* 2(3):2037–2061. <https://doi.org/10.1002/cphy.c110046>



Research article

Ribosylation induced structural changes in Bovine Serum Albumin: understanding high dietary sugar induced protein aggregation and amyloid formation



Ahana Das^a, Pijush Basak^b, Arnab Pramanik^b, Rajib Majumder^c, Avishek Ghosh^a, Saugata Hazra^d, Manas Guria^e, Maitree Bhattacharyya^{b,*,**}, Samudra Prosad Banik^{a,*}

^a Department of Microbiology, Maulana Azad College, 8 Rafi Ahmed Kidwai Road, Kolkata 700013, West Bengal, India

^b Jagadis Bose National Science Talent Search, 1300, Rajdanga Main Road, Sector C, East Kolkata Township, Kolkata 700107, West Bengal, India

^c Department of Biotechnology, School of Life Science and Biotechnology, Adamas University, Kolkata 700126, West Bengal, India

^d Department of Biotechnology, Centre for Nanotechnology, Indian Institute of Technology Roorkee (IITR), Roorkee, Uttarakhand, India

^e Department of Biochemistry, University of Calcutta, 35, Ballygunge Circular Road, Kolkata 700019, West Bengal, India

ARTICLE INFO

Keywords:

Chemistry
Biochemistry
Ribosylated BSA
Globular amyloid
Thermostability of glycated protein
Glycation driven vs. heat induced protein aggregation
Dietary sugar induced amyloid formation

ABSTRACT

Non-enzymatic glycation of proteins is believed to be the root cause of high dietary sugar associated pathophysiological maladies. We investigated the structural changes in protein during progression of glycation using ribosylated Bovine Serum Albumin (BSA). Non enzymatic attachment of about 45 ribose molecules to BSA resulted in gradual reduction of hydrophobicity and aggregation as indicated by red-shifted tryptophan fluorescence, reduced ANS binding and lower anisotropy of FITC-conjugated protein. Parallely, there was a significant decrease of alpha helicity as revealed by Circular Dichroism (CD) and Fourier transformed-Infra Red (FT-IR) spectra. The glycated proteins assumed compact globular structures with enhanced Thioflavin-T binding resembling amyloids. The gross structural transition affected by ribosylation led to enhanced thermostability as indicated by melting temperature and Transmission Electron Microscopy. At a later stage of glycation, the glycated proteins developed non-specific aggregates with increase in size and loss of amyloidogenic behaviour. A parallel non-glycated control incubated under similar conditions indicated that amyloid formation and associated changes were specific for ribosylation and not driven by thermal denaturation due to incubation at 37 °C. Functionality of the glycated protein was significantly altered as probed by Isothermal Titration Calorimetry using polyphenols as substrates. The studies demonstrated that glycation driven globular amyloids form and persist as transient intermediates during formation of misfolded glycated adducts. To the best of our knowledge, the present study is the first systematic attempt to understand glycation associated changes in a protein and provides important insights towards designing therapeutics for arresting dietary sugar induced amyloid formation.

1. Introduction

Dietary sugars are an inevitable part of the metabolic load of our body since carbohydrates constitute the primary source of energy. However, the detrimental effects associated with dietary sugars are have been complicated in modern urban lifestyle due to consumption of high calorie overcooked or junked food. One of the major cellular complications arising out of consistent persistence of reducing sugars is posed by non-enzymatic glycation of proteins leading to their subsequent aggregation. Protein aggregation is implicated in many detrimental conditions

ranging from neurodegenerative diseases to degeneration of therapeutically important proteins [1, 2]. Despite protein folding and protein aggregation being distinct processes, both intrinsic and extrinsic factors govern whether a folding pathway will lead to a native structure or to misfolded aggregate [3]. In recent years, many unnatural post-translational modifications have been discovered which can significantly alter the native structure and function of proteins [4]. One of these is the non-enzymatic glycation or attachment of reducing sugars to the lysine and arginine residues and free thiols of cysteine side chains via Schiff base formation [5]. Glycation of proteins eventualize in a complex

* Corresponding author.

** Corresponding author.

E-mail addresses: bmaitree@gmail.com (M. Bhattacharyya), samudrapb@gmail.com (S.P. Banik).

<https://doi.org/10.1016/j.heliyon.2020.e05053>

Received 6 July 2020; Received in revised form 28 August 2020; Accepted 21 September 2020

2405-8440/© 2020 The Author(s). Published by Elsevier Ltd. This is an open access article under the CC BY-NC-ND license (<http://creativecommons.org/licenses/by-nc-nd/4.0/>).

series of reactions known as Maillard reactions [5] which terminate in the form of stable irreversibly misfolded adducts - the Advanced Glycation End (AGE) products [6]. Glycation has been associated with severely altered structure and functionality of native proteins [7] including formation of covalent cross-links with nearby proteins [8]. AGE formation and accumulation has a diverse spectrum of diseases encompassing several physiological maladies such as arteriosclerosis, renal failure, diabetic complications and Alzheimer disease [9]. Cellular effects of AGEs are exerted by binding to specific receptors termed RAGE (Receptor for AGE) with subsequent initiation of downstream signaling cascade leading ROS generation, oxidative stress and NF- κ B activation [8, 10]. More significantly, glycated proteins have been found to resemble the behaviour of other misfolded proteins associated with amyloid deposits such as beta-amyloid, tau, prions etc. [11, 12, 13]. Glycation has the potential to induce unfolding and refolding of globular proteins into cross- β structure thus automatically making it eligible as a candidate amyloidogenic protein [14, 15]. However, contrasting reports have been obtained thus far regarding the role of glycation in creation of amyloidogenic aggregates. While many reports suggest that glycation selectively makes the protein amyloidogenic [16, 17, 18], few others indicate that glycation of amyloidogenic precursor protein inhibits fibril formation [19, 20]. Additionally, the glycated proteins have also been reported to be more thermostable than their native counterparts [21, 22]. *In vitro* glycation of whey proteins is a well-known practice to improve its thermostability for industrial applications [23].

Bovine Serum albumin (BSA), the most abundant serum protein with versatile applications both *in vivo* and *in vitro*, has been a particularly popular model for understanding the effects of glycation [18, 24, 25, 26, 27]. However, the majority of reports in this regard have only concentrated on the structural characterization of the final glycated form instead of probing the changes that occur progressively throughout the entire period of glycation starting from initial formation of sugar-protein adduct to generation of the terminally misfolded Advanced Glycated End Product. Additionally, the methodology used universally to glycate proteins involves incubation of the protein with the respective sugars at 37 °C. Sustained incubation at such elevated temperatures is known to cause structural alterations in the protein [2, 26] including formation of aggregates. However, most of the studies have not systematically accounted for the changes which occur in the control non glycated protein incubated under similar conditions. The present studies report the formation of a globular amyloid like aggregate as an intermediate in the generation of terminally misfolded protein aggregate resulting from *in vitro* ribosylation of BSA and characterizes its physico-chemical attributes in terms of thermostability and substrate binding efficiency. The structural and functional changes entailed by the protein due to glycation are also compared with a parallel non glycated control maintained under similar conditions.

2. Material and methodology

2.1. Chemicals

Bovine Serum Albumin (highest available purity), ANS (8-anilino-1-naphthalenesulfonic acid), NPN (N-Phenyl-1-naphthylamine), Thioflavin-T, FITC (fluorescein isothiocyanate) were purchased from Sigma Chemicals. Other chemicals and reagents needed of Analytical grade were purchased locally from SRL.

2.2. Glycation of BSA

Bovine Serum Albumin (0.15 mM) was incubated separately with 0.5 M of different sugars (glucose, galactose, fructose, ribose and mannose) in presence of 0.05 M sodium phosphate buffer, pH 7.4 at 37 °C. Reaction mixtures were kept in this condition for 10 days. It was kept into sterile glass tubes in presence of 3 mM sodium azide to prevent bacterial contamination. Aliquots were taken under sterile conditions at desired

times and frozen at -20 °C until further assayed. The samples were then diluted five times with 0.2 M sodium acetate buffer, pH 5 to reduce the glycated protein and incubated at 37 °C for 2 h to release glycosylamine adducts. In order to remove free ribose molecules, this treated protein was then dialyzed overnight against 0.1 M sodium phosphate buffer, pH 7.4, at 4 °C. After that the dialyzed protein was reduced by adding a 50-fold molar excess of sodium borohydride in presence of 0.1 M sodium hydroxide. The solution was then kept at room temperature for 4 h after which the reaction was terminated by the adding 1 N HCl slowly to eliminate excess sodium borohydride. Finally, the samples were dialyzed overnight at 4 °C against double distilled water [28]. Parallely, the control incubated samples (without ribosylation) were also treated in a similar manner and protein concentrations were measured by Bradford assay.

2.3. Fluorescence spectroscopy

2.3.1. AGE fluorescence

The formation of Advanced Glycated End products (AGE) was monitored by measuring the emitted fluorescence spectra of 1.5 μ M glycated BSA with excitation at 370 nm. The emission spectra were obtained in the range of 390–500 nm with both excitation and emission bandwidths at 5 nm [29]. All these measurements were performed on Perkin-Elmer LS55 spectrofluorimeter.

2.3.2. Intrinsic tryptophan fluorescence

Steady state fluorescence was recorded with 3 μ M protein dissolved in 50 mM phosphate buffer on a Perkin-Elmer LS55 spectrofluorimeter. Intrinsic tryptophan fluorescence spectra were carried out by exciting the samples at 295 nm with excitation and emission slit widths set at 5 nm. The emission spectra were recorded between 315 to 500 nm. Baseline corrections were performed with buffer in all cases [30, 31].

2.3.3. ANS fluorescence

Steady-state fluorescence of ANS was measured on the same Perkin-Elmer LS55 spectrofluorimeter as of intrinsic tryptophan fluorescence measurements. ANS concentration was 0.1 mM and bandwidth for excitation and emission monochromators were 5 nm. Fluorescence of ANS was measured by excitation at 360 nm with protein concentration of 0.2 μ M in a 50 mM sodium phosphate buffer (pH 7.2). The emission spectra for the samples were recorded in the range of 380 and 600 nm [32].

2.3.4. NPN fluorescence

NPN fluorescence of BSA samples was carried out on the Perkin-Elmer LS55 spectrofluorimeter using 60 μ M aqueous solution of NPN fluorophore [33]. Fluorescence spectra were recorded with 1.5 μ M of protein samples in the range of 370–600 nm. The emission spectra were measured by exciting the samples at 350 nm and bandwidths of both excitation and emission spectra at 5 nm.

2.4. MALDI – mass spectroscopy analysis

Extents of glycation in BSA samples were obtained by Mass spectroscopy analysis of the samples from Bruker spectrophotometer (model: Ultra FieXTreme). Samples were prepared in microcrystalline matrix surfaces that were made on the probe tips of the mass spectrometer. Protein samples were spotted by mixing the samples in a 50% aqueous acetonitrile solution (0.6 μ L) saturated with sinapinic acid and containing 0.05% TFA. Sample analysis was carried out in linear TOF mode with 550 ns delay. Further data processing and calibrations were done using the computer program attached to the spectrophotometer [34]. The number (N) of ribose residues conjugated with BSA molecule was calculated from the following formula:

$$N = (\text{MW}_{\text{BSA-ribose}} - \text{MW}_{\text{BSA}}) / \text{MW}_{\text{Ribose}}$$

2.5. DTNB assay

The free thiol contents in BSA, incubated and glycated BSA samples were determined using Ellman's assay [35]. 0.1mM DTNB (5,5'-dithiobis-2-nitrobenzoic acid) or Ellman's reagent in presence of 0.1mMTris buffer (pH 8) were mixed with different concentrations of cysteine (10 μ M–100 μ M) to obtain a standard curve. The samples were then incubated at room temperature for 5 min and the absorbance was measured at 412 nm in Jasco V-630 spectrophotometer. The assay was carried out with the protein samples as well and from the standard curve of cysteine, the free thiol contents of the proteins were obtained.

2.6. FITC- BSA conjugation

BSA samples were labeled with fluorescein isothiocyanate (Sigma) in 0.1 M carbonate buffer, pH 9. The samples were kept at room temperature and in the dark for 4 h. The labelling ratio (F:P) for control and incubated BSA were 1:1 and for ribosylated BSA it was 0.5:1. Then the solutions were dialyzed four times in dark at 4 °C against 0.01 M phosphate buffered saline (PBS), pH 7.4 in order to remove any unbound FITC. The F:P ratio range was selected depending on the sensitivity and photophysics of the dye conjugated to the protein [36].

2.7. Fluorescence anisotropy

Fluorescence anisotropy decays of FITC conjugated BSA samples were recorded in a Varian-Cary-UV Eclipse spectrofluorimeter at 25 °C [37]. Polarized decays were collected at the vertical (I_{VV}) and horizontal (I_{VH}) positions of the emission polarizer. The samples were excited at 490 nm and the bandwidth for excitation and emission monochromator were set at 5 nm. The emission intensities were measured at 522 nm. Fluorescence spectra were corrected for the emission of the control solution containing buffer. Both decays were collected in the same conditions and for the same amount of time. A high number of counts were essential to increase the signal-to-noise ratio for anisotropy decays. G represents a correction factor for the sensitivity of the optics to light with different polarizations. The G factor was determined using the instruments software for the samples in the absence of protein, for which the rotational correlation time was short and the anisotropy decayed to zero within the time scale for the measurement. This procedure is necessary since small changes in the G factor can bring about changes in the baseline for the anisotropy of the samples. Then the G factor determined in the absence of protein was used for anisotropy decays in the presence of the proteins.

2.8. DLS

Dynamic light scattering measurements were performed with BSA in the concentration of 0.1 mg/ml [38]. The concentration range was selected according to the response and sensitivity of the instrument. Data were obtained in a Nano zeta-sizer (Malvern Instruments) and a Beckman Coulter DLS instrument at a fixed 90° scattering angle using Nd-doped solid state laser of 632.5 nm with 100 s of integration time; the intensity correlation function was obtained by acquiring data between 5 and 1,000 ms, in 200 channels.

2.9. Native gel electrophoresis

Native-polyacrylamide gel electrophoresis (7%) under reducing condition was carried out according to the methods described earlier [39, 40]. The protein samples (10 μ g) were incubated at different temperatures between 25 °C and 85 °C for 1 h and subsequently were dissolved in the sample buffer. The gel was run at 20 mA till the tracking dye reached its lower edge. Thereafter, it was immediately subjected to silver staining using ProteoSilverTM silver stain kit (Sigma) according to the manufacturer's instructions.

2.10. Circular Dichroism

Circular dichroic (CD) spectra of different preparations of BSA (1.5 μ M) in the far-UV wavelength range (190–250 nm) were recorded at 25 °C on a JASCO J-720 spectropolarimeter (calibrated with d-10-camphorsulfonic acid) using a cylindrical quartz cuvette of path length 1 mm. The following scan parameters were used: 1 nm bandwidth, 2 s response time, 0.1 nm step resolution and 20 nm/min scan speed [40, 41, 42]. Each spectrum had an average of four continuous scans. The final spectra were acquired by subtracting blank runs on appropriate protein-free buffer (10 mM-phosphate buffer, pH 7.0) and subjected to a moderate degree of noise-reduction analysis. Alpha helix content was obtained using the formula:

$$\% \alpha\text{-helix} = ((\text{MRE}_{222\text{nm}} - 2340) / 30300) \times 100$$

Where, Mean Residual Ellipticity (MRE) = $\text{MRE}_{222} = \theta_{\text{obs}}(\text{mdeg}) / (10 \times n \times c \times l)$, n = number of peptide bonds, c = concentration of the sample in M, l = pathlength = 0.1 cm.

2.11. FT-IR analysis

Fourier Transform-Infra Red (FT-IR) spectra of BSA samples were recorded on a Perkin-Elmer FTIR instrument. The samples were prepared by grinding 1 mg of the protein sample with 100 mg of KBr together previously kept in dessicator [43, 44, 45]. After mixing properly pellets were made by pressing the samples at 10 tons for 1 min. The spectral data were obtained within the range of 4000 cm^{-1} - 450 cm^{-1} with a spectral resolution of 1 cm^{-1} . The spectrum of the background was recorded initially and it was further subtracted from the spectra of samples.

2.12. Melting point analysis from spectral studies

Melting points of glycated and incubated BSA were acquired from absorption measurements of the samples [46]. In brief, absorbance (280 nm) of BSA samples (7.5 μ M aliquots) were taken corresponding to the temperature range of 25–90 °C in a Jasco V-630 spectrophotometer fitted with a peltier. Baseline corrections for each sample were performed with buffer in absence of the protein.

2.13. Thioflavin T binding

A ThT stock solution was prepared by dissolving 2.5 mM Thioflavin T (Sigma) in phosphate buffer (10 mM phosphate, 150 mM NaCl, pH 7.0) and then filtering it through a 0.2 μ m syringe filter [47]. The working solution was generated by diluting the stock solution 50 fold in the phosphate buffer on the day of analysis. BSA samples at concentration of 1.5 μ M were mixed with the working solution and were allowed to bind the ThT for 1min. The fluorescence intensities of the samples were measured on Perkin-Elmer LS55 spectrofluorimeter by excitation at 440 nm (slit width 5 nm) and emission 482 nm (slit width 10 nm) at medium speed.

2.14. Transmission Electron Microscopy (TEM)

TEM was carried out as reported earlier [48], with few modifications. Briefly, twenty five square mesh copper grids with continuous carbon film (Electron Microscopy Sciences) were taken to incubate the samples. 10 μ L of each BSA samples (control BSA, non-glycated and glycated BSA) were applied onto the grids and allowed to dry in air before analysis. Glycated and non-glycated BSA samples were kept at 60 °C for 1hour before applying onto the grids. TEM images were collected using JEOL-JEM 2100 (Japan) electron microscope operated at 200 kV and size of the proteins were acquired using the associated software.

2.15. Isothermal titration calorimetric measurements (ITC)

The isothermal titration calorimetric experiments were performed on a VP-ITC titration microcalorimeter (MicroCal Inc., Northampton, MA). Protein and ligand concentrations were adjusted at 12 μ M and 250 μ M, respectively, to maintain a high ligand:protein ratio. After that multiple injections of 60 μ l each from curcumin and resveratrol (250 μ M) were made into the sample cell maintaining the temperature of the system at 25 °C. The principle method of ITC necessitates presence of 30–40 times ligand concentration from that of protein [49]. To correct the heat effect due to mixing and dilution, control experiments were performed in which ligands were injected into the buffer solution without BSA.

2.16. Statistical analyses

Standard deviations in all fluorescence measurements and DLS were performed with instrument associated software. Statistical analyses of ITC data was carried out in Origin ver 9.0.

3. Results and discussion

3.1. Monitoring the formation of AGE through characteristic fluorescence emission

In order to generate a working model of glycated protein, *in vitro* glycation of Bovine Serum Albumin was carried out individually with the monosaccharides, ribose, glucose and fructose, galactose and mannose. The reaction was monitored by the characteristic fluorescence emission of Advanced Glycation End product at around 440 nm. AGE fluorescence was highest with ribose followed by fructose whereas no significant increase in fluorescence was noted for BSA glycated with the other sugars (Figure 1A). It may be mentioned here that although glucose is the most commonly encountered sugar in the intracellular milieu, it needs a significantly long time to glycate serum albumins [50, 51]. Since the secondary structure of the protein was abolished almost completely beyond twelve days of sustained incubation at 37 °C (as elaborated later), ribose was selected for generation of a glycated BSA model. Advancement of glycation was followed by observing daywise fluorescence of the samples. Fluorescence intensity was highest on the 8th day of incubation (Figure 1B). It decreased subsequently with a significant red shift in emission indicating that the AGE fluorescence was shifted to a more polar environment due to a gross structural transition of the protein (Figure 1C). This was investigated at a later part of the studies.

3.2. BSA gets optimally ribosylated within 10 days of glycation reaction

Extent of glycation of the 10th day ribosylated sample was measured quantitatively using MALDI-MS (Figure 2) after a round of purification through HPGPLC to separate any glycated peptide from the commercial protein preparation (data not shown). Number of ribose residues

attached was ascertained at different time intervals during the course of glycation. Molecular weight of 4th day sample was found to be 67.45 kD corresponding to attachment of about 5 sugar residues (Figure 2B). Maximum number of ribose residues was attached within 10 days as the molecular weight of the protein increased to 75.08 kD indicating attachment of as many as 56 sugar molecules (Figure 2C). During the later stages of glycation, molecular weight of BSA was found to be about 73.373 kD corresponding to about 45 molecules of ribose (Figure 2D). This can be attributable to partial degradation of the protein or loss of attached sugar or both occurring simultaneously under prolonged thermal incubation. The 10th day glycated protein model was used for some of the subsequent studies such as morphology investigation by TEM, temperature dependence of amyloid formation, FT-IR spectroscopy and evaluation of substrate binding capability by ITC. Since the *in vitro* glycation was performed by incubating the protein at 37 °C, a parallel control without the sugar was maintained in every case to account for the temperature induced structural changes which might have occurred in the protein.

3.3. Glycation delays thermal aggregation of BSA

Bovine Serum Albumin is a naturally aggregation prone protein [52, 53] where intermolecular disulphide bonds are generally held responsible for mediating the aggregation [54]. Although BSA is not naturally amyloidogenic, intermolecular aggregation of BSA is implicated in formation of irreversible amyloid fibrils in the protein [55, 56]. Free thiol content in purified 8th day glycated protein decreased to more than 50% from 18.96 mM to 8.96 mM. However, the same was also noted in a parallel control where the protein was incubated at 37 °C without the sugar. Therefore it was evident that the decrease in number of free thiols (indicating disulphide mediated cross-linking of protein sub-units) was attributable to prolonged incubation at higher temperature and not due to glycation.

Apart from involvement of disulfide bonds, natural aggregation also occurs due to exposed hydrophobic interfaces [57, 58]. This is of commonplace occurrence for non-aggregation prone proteins due to solution induced deviation from native structure [59]. ANS is an extrinsic fluorophore known to bind to hydrophobic surfaces of proteins [60], where binding is mostly mediated by cationic groups in protein side chains [61]. Therefore, it is widely used for probing the extent of accessible hydrophobic surface of a protein during its thermal unfolding. ANS binding at different stages of glycation was monitored and the resultant effect on aggregation was studied using a combination of Dynamic Light Scattering and Fluorescence Anisotropy. ANS fluorescence was reduced significantly in glycated samples on the 5th day of incubation and remained more or less constant thereafter till the 12th day (Figures 3A and 3B). Thereafter, it increased steeply again indicating conversion into a molten globule and hydrophobicity driven aggregation. In contrast, fluorescence from the incubated (control) protein samples was strikingly higher throughout the entire period indicating thermal

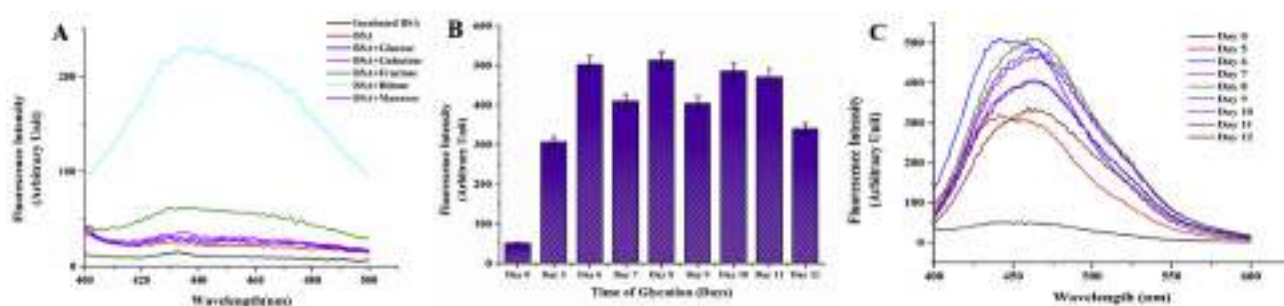


Figure 1. Fluorescence spectrum of Advanced Glycated End Product A) AGE formation with different sugar-protein adducts on 10th day B) Progression of AGE formation in ribosylated BSA. Error bars represent the deviations observed in triplicate data sets C) Corresponding fluorescence spectra of B acquired with 0.15 mM BSA (with 0.5 M ribose) in 0.05 M sodium phosphate buffer, pH 7.4 at 37 °C.

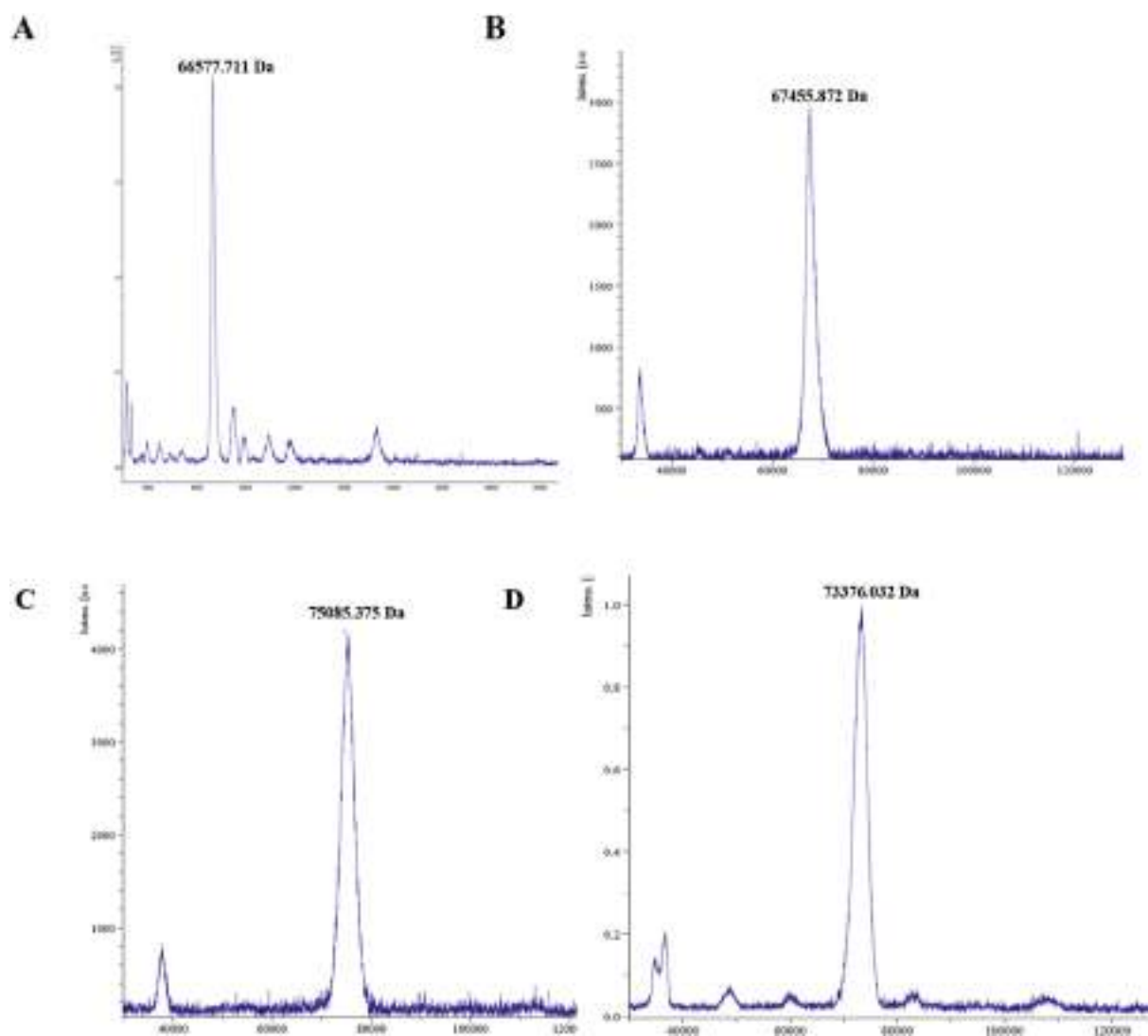


Figure 2. MALDI Spectra of glycated protein A) Control Non-glycated BSA B) BSA glycated with ribose for 4 days C) BSA glycated with ribose for 10 days D) BSA glycated with ribose for 15 days.

denaturation of BSA due to prolonged incubation at 37 °C. Since glycation reaction consumes most of the free amino groups of protein side chains [62], ANS binding was also possibly reduced due to non-availability of free lysine and arginine groups.

1-N-Phenylmethylpyrrolidine (NPN) is another fluorescent dye known to bind to hydrophobic patches in proteins [63]. Binding of NPN to glycated BSA was also significantly lesser than the control protein (Figure 4A and 4B). Therefore, it was plausible that glycation imparted thermostability

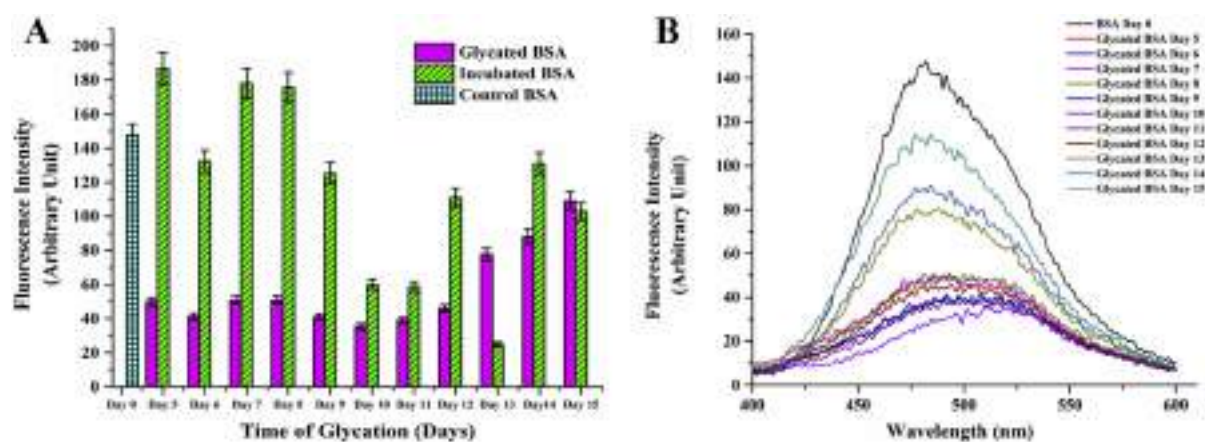


Figure 3. A) ANS binding profile of ribosylated and incubated proteins during progression of glycation. Error bars represent the deviations observed in triplicate data sets B) Corresponding fluorescence spectra of A; the trend reveals reduced ANS binding between the period of 5–12 days.

to the protein during sustained incubation above ambient temperature. Increase or decrease in hydrophobicity has a direct bearing on the aggregation status of the protein [64]. BSA being an intrinsically self-association prone protein, it was imperative to investigate the effect on glycation on aggregation of the protein. Dynamic light scattering data (Table 1, Figure 5) of the control non-incubated protein gave three different peaks of the native protein at around 258 nm, 76 nm and 12 nm justifying its spontaneous aggregation. The glycated protein showed initial increase in hydrodynamic radius from 11.6 nm to 14.6 nm which was probably attributable to the increased solvent hydration shell around the protein. Accordingly, the diameters of the other two species were also increased to 90 nm and 370 nm respectively. However, the corresponding incubated protein revealed only two peaks. This can be probably attributable to the fact that the protein due to sustained incubation at an elevated temperature somewhat lost its natural ability to associate into a plethora of multimeric entities. In case of the glycated protein, three peaks were visible till the sixth day of incubation and thereafter the structural changes inflicted resulted in only one discernible peak on the 12th day. However, the average size of the entities in glycated proteins became significantly smaller than the incubated proteins after 6 days of incubation. This was at the same time indicative of formation of structured entity in the glycated sample and also was in unison to our assumption that prolonged incubation at elevated temperature brought about thermal aggregation of non-resulting into bigger entities. The aggregation propensity was further verified using anisotropy of FITC conjugated BSA and native PAGE. Through the entire period of incubation, the ribosylated BSA-FITC conjugates had significantly lower anisotropy values as compared to their non glycated counterparts incubated under same conditions (Table 2). This was again testimonial to the fact that ribosylation offered protection to the protein from thermal denaturation and resultant aggregation. The proteins were subsequently subjected to progressively higher temperatures (25 °C–85 °C) for 1 h and their migration patterns were analyzed by Native PAGE (Figure 6). The unincubated control protein was seen to form higher MW aggregates at higher temperatures (Figure 6A). In contrast, the positions of the bands for the glycated samples were more or less constant (Figure 6B). The incubated protein did not present any conclusive picture since most of the bands were rendered smeary due to thermal denaturation (Figure 6C). This was again an added testimonial to the integrity of the glycated protein in spite of being kept at elevated temperature (37 °C) for more than a week.

There have been contrasting reports regarding the effect of glycation on aggregation of the protein. While several studies have shown that glycation leads to aggregation of the protein [65, 66], it was found to inhibit/slow down aggregation and resultant plaque formation in most of the amyloidogenic proteins [19]. In the present studies, it was clearly

shown that prolonged incubation at 37 °C brought about thermal aggregation of BSA mediated by increased contact of hydrophobic interfaces. Glycation delayed this thermal aggregation but promoted formation of globular amyloid aggregates (as studied later). Therefore, it was apparent that aggregation caused by thermal denaturation and glycation were mechanistically different from each other. Probably, it is safer to state that glycation induced aggregation is specific and dependent on both the nature of the protein molecules as well as the sugar attached.

3.4. Glycation causes gross structural alteration of BSA

Since there was a marked change in aggregation propensity of the native protein after ribosylation, a corresponding structural change was also imperative. BSA has two tryptophan residues at positions 134 and 212 respectively [67]. Trp-134 is fully solvent accessible being localized in the second helix of the first domain whereas Trp-212 is localized in a hydrophobic pocket of domain II. Therefore, BSA is an ideal model for probing structural transition due to polarity changes [30, 68, 69]. Especially, Trp-134 fluorescence is widely used to gain preliminary idea about the helix integrity of the protein [70]. There was a drastic decrease in fluorescence of ribosylated proteins together with a red shift of about 55 nm (Figure 7). However, for the control incubated protein samples, a higher fluorescence was observed without any significant change in emission maxima. The observations were in unison with our hypothesis that following ribosylation there was a gross increase in polarity around the tryptophan microenvironment due to partial denaturation of the glycated protein which accounted for the red shift. In case of the incubated proteins, there was only a slight red shift which was indicative of a perturbation in structural integrity of the protein. Additionally, there was a marked decrease in fluorescence intensity of the ribosylated protein from 8th to 11th day of incubation and it again increased on the 12th day. This could be accounted for by the fact that due to formation of a compact aggregate of ribosylated BSA, tryptophan fluorescence was quenched due to close proximity with peptide bonds [71].

Since there was a gross indication in disruption of the helical structure of the protein from intrinsic tryptophan fluorescence, the structural changes following glycation were further investigated with CD and FT-IR spectroscopy (Figure 8A and Figure 8B). Alpha helicity decreased gradually in ribosylated sample by more than 7% on the 8th day of incubation (Table 3). However, the loss in helical structure was more drastic till the 10th day of incubation for the control incubated sample without glycation. This was again consistent with our observation that glycation provided resistance against thermal denaturation of the protein. However at later stages (beyond 12 days), the structure of the glycated protein

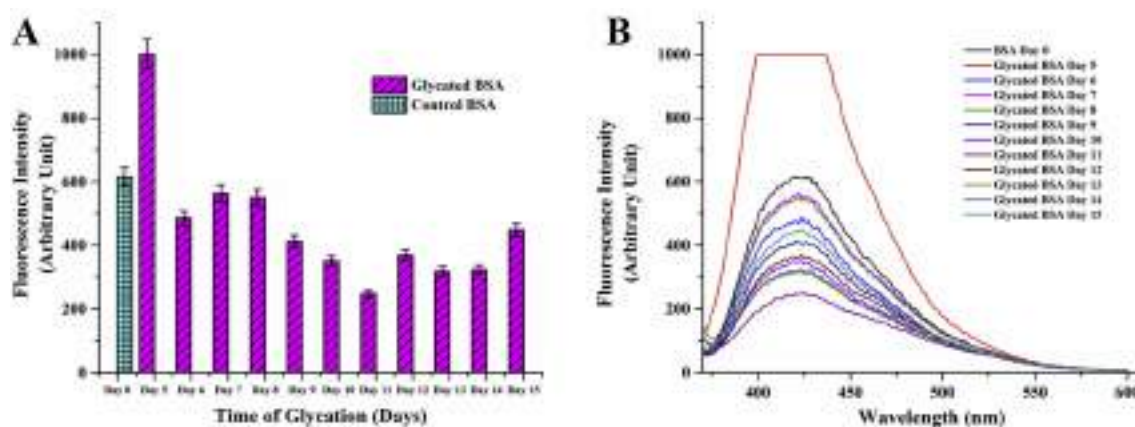


Figure 4. A) NPN Binding spectra of ribosylated and incubated proteins during progression of glycation. Error bars represent the deviations observed in triplicate data sets B) Corresponding fluorescence spectra of A; the trend shows reduced NPN binding indicating suppression of hydrophobicity between 8 to 12 days period.

Table 1. Size distribution of ribosylated and incubated proteins during different times of glycation.

Sample		Hydrodynamic radius (d.nm)	Polydispersity index (P.I)
BSA		258.6 ± 27.88 11.63 ± 0.9924 76.09 ± 7.286	1
Incubated	Day4	72.99 ± 5.361 4.157 ± 0.1266	1
	Day6	264.1 ± 26.81 9.373 ± 0.6883	0.986
	Day8	915.2 ± 161.1 1.002 ± 0.114	1
	Day10	271.6 ± 19.83 8.966 ± 0.5268	1
	Day12	385.1 ± 43.02 89.85 ± 7.137	1
Glycated	Day4	360.7 ± 59.3 14.67 ± 1.186	0.726
	Day6	376.3 ± 52.06 89.95 ± 9.508 13.86 ± 1.037	1
	Day8	393.3 ± 66.93 117.2 ± 15.18	0.858
	Day10	218.7 ± 29.19 21.4 ± 1.037	0.870
	Day12	135 ± 9.236	1

Protein samples at a concentration of 0.1 mg/ml in 0.05 M phosphate buffer with 0.05 M Nacl were used for the studies.

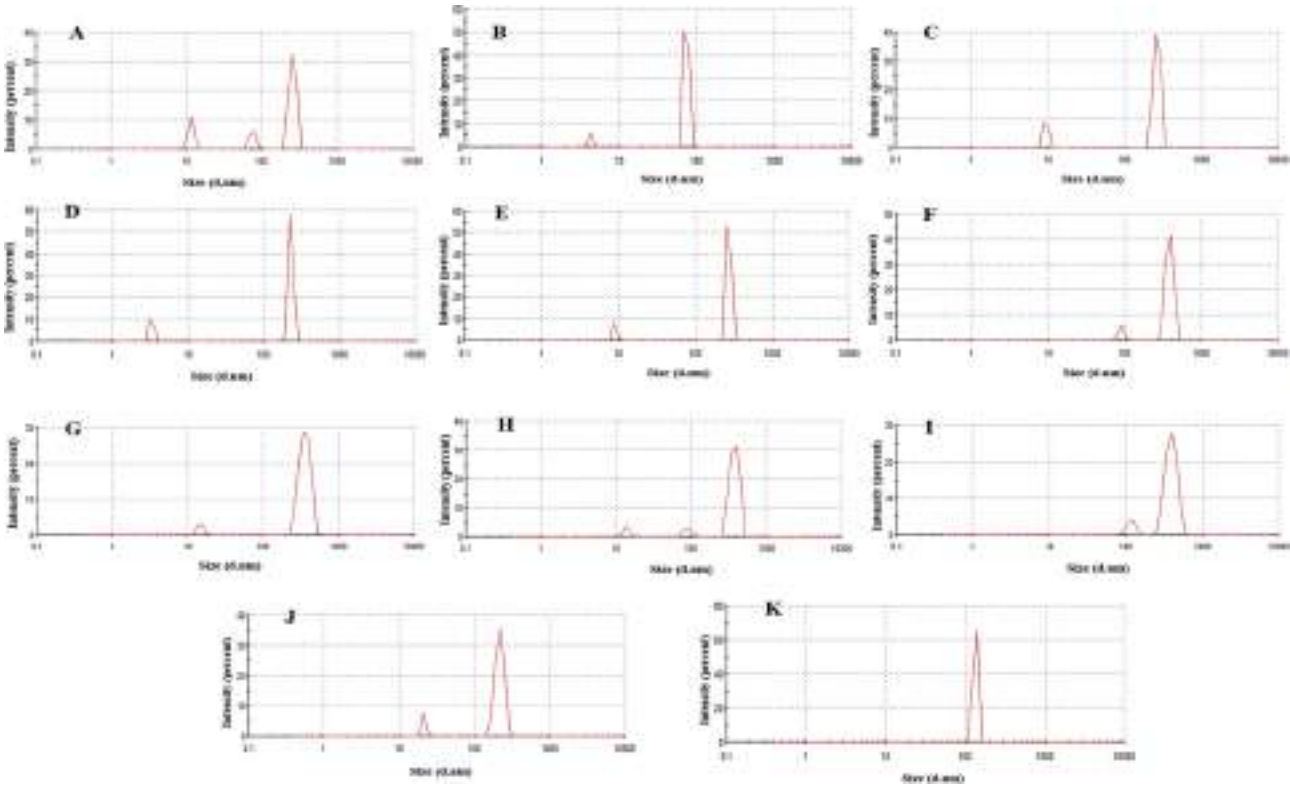


Figure 5. Size distribution of glycated (G–K) and incubated (B–F) BSA (0.1 mg/ml) A) BSA B) 4th day incubated BSA C) 6th day incubated BSA D)8th day incubated BSA E) 10th day incubated BSA F) 12th day incubated BSA G)4th day glycated BSA H) 6th day glycated BSA I) 8th day glycated BSA J)10th day glycated BSA G) 12th day glycated BSA.

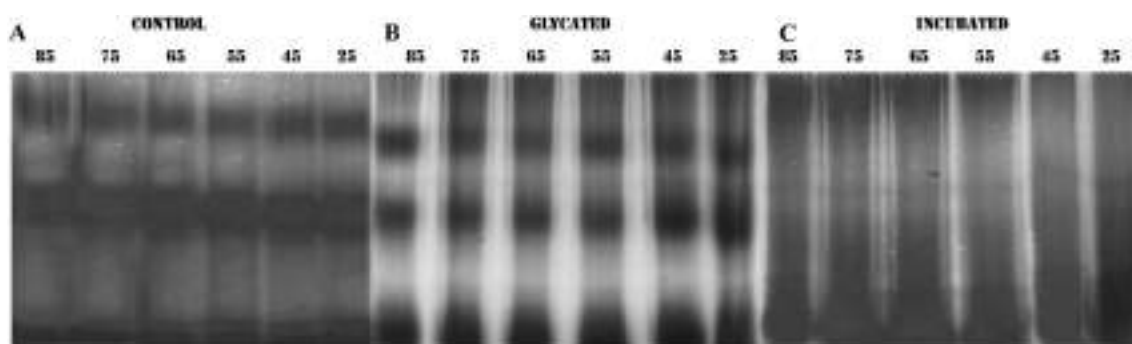
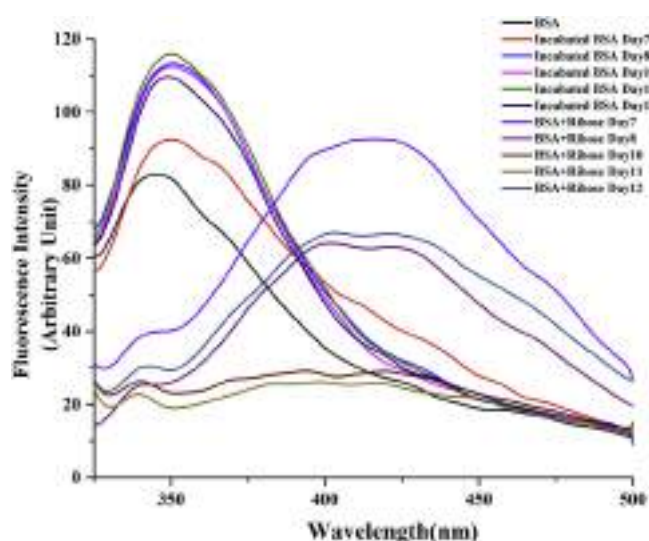
collapsed completely. In order to further warrant the observations, FT-IR spectra of lyophilized protein samples (10th day) were obtained. Alongside CD, FT-IR is also a powerful tool to investigate the changes in secondary structure of proteins by through the study of amide bands [72]. The Amide I band (between 1600 and 1700 cm⁻¹) is mainly associated

with the peptide backbone C=O stretching vibration. The Amide II (between 1510 and 1580 cm⁻¹) region is more complex arising out of in-plane N–H bending and C–N and C–C stretching vibrations (1700–1600 cm⁻¹). Second derivative spectra of the protein revealed that the 1547 cm⁻¹ amide II band was almost non-existent in the glycated

Table 2. Anisotropy values of glycated BSA incubated for different days along with their respective incubated BSA.

Sample		R - value	G - factor
BSA		0.126 ± 0.008	1
Incubated	Day4	0.132 ± 0.007	1
	Day6	0.124 ± 0.01	1
	Day8	0.108 ± 0.009	1
	Day10	0.062 ± 0.007	1
	Day12	0.093 ± 0.007	1
Glycated	Day4	0.062 ± 0.005	1
	Day6	0.064 ± 0.005	1
	Day8	0.059 ± 0.006	1
	Day10	0.065 ± 0.0048	1
	Day12	0.062 ± 0.0053	1

Experiments were performed thrice and mean R values have been reported.

**Figure 6.** Native PAGE analysis of A) control, B) glycated and C) incubated proteins (10 μ g each) after incubation at increasing temperatures. In each case lanes have been labelled with the respective temperature of incubation.**Figure 7.** Intrinsic tryptophan fluorescence of glycated proteins in comparison to incubated protein samples during the period of progression of glycation.

sample which was indicative of substantial loss of alpha helicity of protein.

3.5. Ribosylation imparts thermal stability

It was predicted from structural analysis that the glycated protein was more thermostable than its native counterpart. Melting points of the glycated and incubated protein samples were calculated from

temperature dependent UV absorbance data at three different phases a) initial stage (4th–6th day), intermediate stage (8–12th day) and late stage (13th to 15th day) (Figure 9) to evaluate the thermal stability during the progression of glycation. T_m of incubated and glycated proteins from the 6th day sample (representative of the initial stage) were the same (72.5 °C) and similar to that of the control unincubated protein. However, in case of the 10th day sample (representative of the intermediate stage), it was raised by about 5 °C indicating enhanced thermostability of the glycated protein. At the same time point, T_m of the incubated protein was grossly unaltered. Thermostability of both glycated and incubated samples decreased drastically during the final stages of glycation as assessed from the 14th day sample. The data was in accordance with those acquired from assessment of hydrophobicity and CD spectrum and indicated that thermostability of the protein was visible only during the intermediate stage (day 8–12) and was lost subsequently during subsequent advanced stages of glycation.

The effect of thermal denaturation on the glycated protein was also examined by TEM imaging after incubation at 60 °C for one hour (Figure 10). Globular morphology of glycated protein was found to be preserved in spite of the severe heat treatment (Figure 10B), however, it was significantly more aggregated as compared the control non-incubated protein (Figure 10A). The non-glycated protein treated under similar conditions was grossly denatured and converted into a structureless entity (Figure 10C).

3.6. Globular amyloid formation in BSA occurs due to glycation and does not owe to thermal aggregation

There has been several reports of Advanced Glycated End Products developing into amyloid like aggregates [16, 73] suggesting a direct link between type 2 diabetes and neurodegenerative disorders [74].

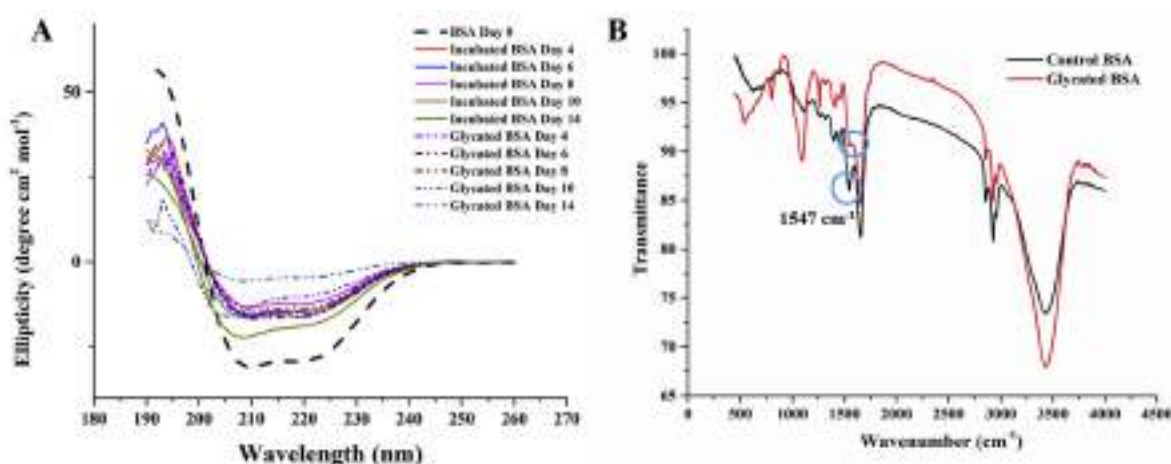


Figure 8. A) CD spectra of ribosylated and incubated sample showing substantial loss of alpha helicity (retention of alpha helicity greater in ribosylated protein as compared to incubated protein) B) FT-IR spectra (of lyophilized protein samples) showing loss of alpha helicity as indicated by reduced 1547 cm⁻¹ amide II band.

Table 3. Alpha helix contents of glycated and incubated BSA samples during progression of glycation.

Period of glycation (in day)	Glycated BSA	Incubated BSA
4	53.39	52.77
6	51.95	49.61
8	46.69	42.59
10	36.308	34.49
14	20.43	28.41
Control BSA	49.67	

Alpha helicity was determined from the average of mean residual ellipticity values from three independent experiment sets.

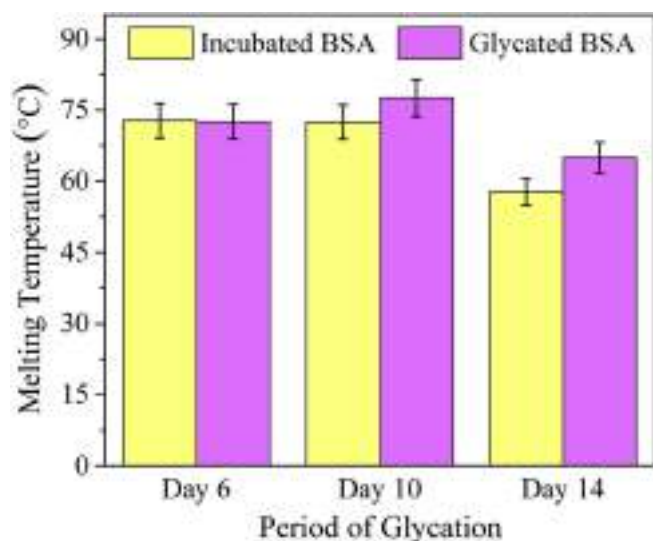


Figure 9. Absorbance based melting temperatures of different protein samples during initial (6 days), intermediate (10 days) and late stages (14 days) of glycation. Error bar represent the deviation from five individual data sets.

However, understanding the structural basis of this correlation has not been simple. Glycation has been found to both promote [17] and inhibit [19] amyloid fibril formation. Moreover, the amyloid like aggregates generated from non-amyloidogenic proteins like serum albumin have been either shown to be transformed into β -fibrils hallmark of classical amyloid plaques [11, 75] or retain their globular structure showing amyloid specific histochemistry [18] depending upon the nature of the attached sugar. In addition, thermal aggregation of serum albumin had

also been shown to induce amyloid formation [76]. We subjected the ribosylated proteins obtained at different times of glycation to Thioflavin T binding analyses. Thio-T fluorescence was found to increase significantly from 9th day of incubation and was highest on the 12th day of glycation (Figure 11A and 11B). Subsequently, the fluorescence decreased gradually. This was testimonial to the fact that amyloid like behaviour of the protein was present only during the intermediate stages of glycation and wasn't necessarily a hallmark of the Advanced Glycation End Product arising out of the protein-ribose adduct. Heat induced fibrillation, as observed for the control non-glycated sample was also present during the initial stages of glycation (till 6th day) which then decreased to a basal level. This indicated that Thio-T binding property of the protein occurred distinctly for a) thermal aggregation, and b) for glycation. In order to further confirm the fact that ribosylation induced amyloidogenic property of the protein was independent of thermal fibrillation, an additional temperature dependent binding profile of Thio-T was carried out (Figure 12) with the 10th day ribosylated protein. Fluorescence intensity was highest at 35 °C and decreased gradually for higher temperatures. The incubated and unincubated controls subjected to similar conditions gave no noticeable Thioflavin T binding. This confirmed our hypothesis that Thio-T binding was specific for ribosylation and amyloidogenic transition of the protein simply could not be induced instantaneously by subjecting the protein to higher temperatures. Thermal aggregation can only be accounted for such structural transitions if the protein is subjected to elevated temperatures for much longer time periods. The glycated protein aggregates, inspite of showing Thio-T binding didn't reveal formation of classical fibrillar structure in TEM and retained their globular structures. Accordingly, they also didn't respond to the Congo red birefringence assay, another hallmark of the amyloid fibrils. Therefore, the amyloids arising out of glycation were non-classical globular in nature as has also been observed earlier for ribosylated proteins [18]. Deposition of non-canonical globular amyloid

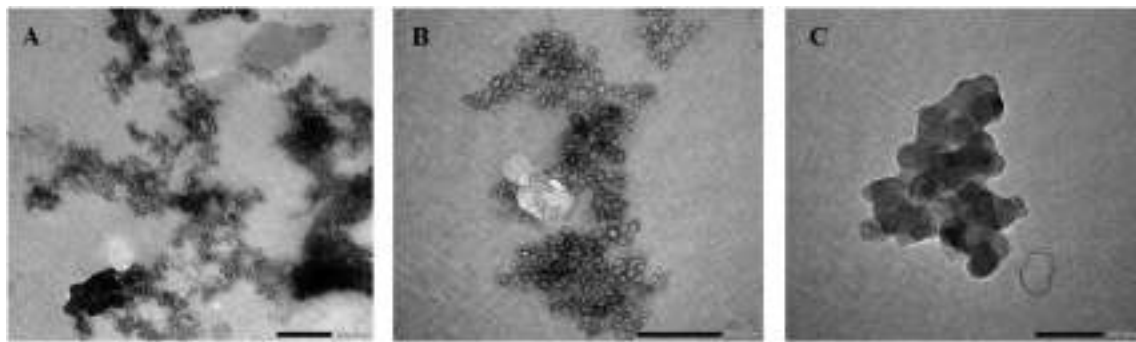


Figure 10. TEM imaging of glycated and incubated BSA (10th day) acquired after subjecting to thermal incubation at 60 °C for one hour. A) Control non-incubated protein B) Glycated protein C) Non-glycated but incubated protein. Scale bar represents 200 nm in figures 9A and 9B and 100 nm in 9C.

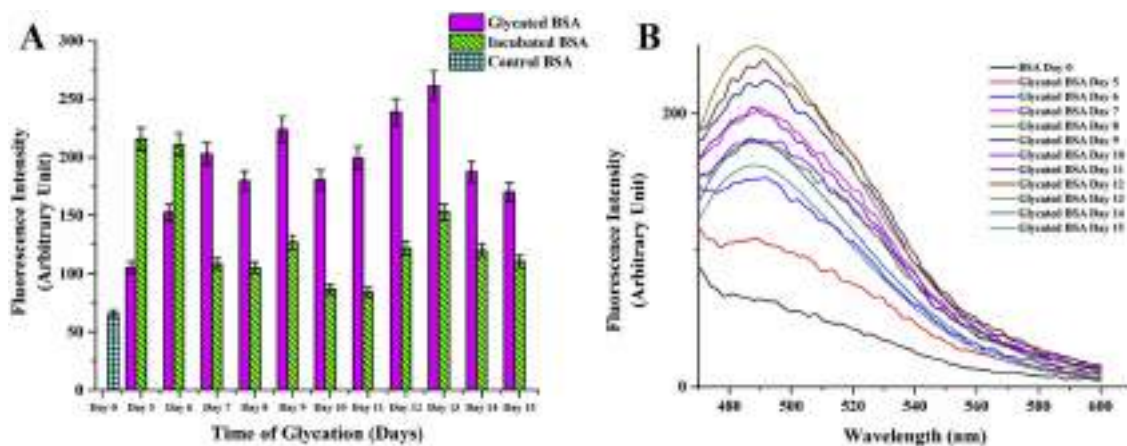


Figure 11. A) Thioflavin T binding profiles of glycated vs incubated proteins during the entire period of glycation. Error bars represent the deviations observed in triplicate data sets B) Corresponding fluorescence spectra of A; the data shows amyloid like formation between 9th and 12th days.

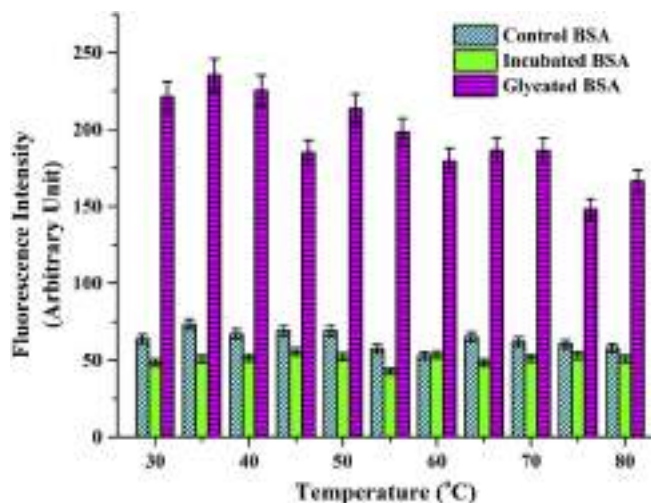


Figure 12. Thioflavin T binding to 10th day ribosylated BSA at different temperatures indicates that amyloid like formation is specific for the glycated protein and is not thermally induced.

aggregates showing classical histochemistry like Thioflavin-T binding or Congo red birefringence have also been reported for other pathophysiological conditions [77, 78]. Therefore, amyloid formation is often more ubiquitous and versatile than is believed and drawing a structural consequence arising out of glycation is evidence based and cannot be generalized.

3.7. Glycation causes significant change in affinity of BSA towards various substrates

Residual substrate binding ability of BSA after ribosylation was checked with two standard polyphenols which are physiological substrates of the protein, curcumin and resveratrol. BSA has got a single binding site for curcumin [79] and two sites for resveratrol [80]. The observed titration curve (Figure 13 A-F) with a single binding site of curcumin indicated an enthalpy driven moderately strong binding of the substrate largely mediated by non-covalent interactions [81]. The Wiseman parameter “c” of 1.836 was a testimonial of this strong binding [82] (Table 4). However, the substrate binding was completely abolished for the 10th day glycated sample with an almost 100 fold decrease in binding constant. Consequently, the Wiseman parameter was decreased drastically to 0.027. It seemed that this drastic fall in activity of the native protein owed more to thermal denaturation since the non-glycated control protein subjected to incubation under similar conditions underwent even more drastic effects with binding constant being decreased more than 10⁵ fold. Binding of resveratrol was also found to be exothermic and enthalpy driven in nature. However, completely dissimilar trends were noted, however, for the other substrate resveratrol having two known binding sites in BSA. For the first site, binding constant increased from 1.11×10^5 to $1.56 \times 10^5 \text{ mol}^{-1}$. However, for the second site, resveratrol bound with greater affinity to control BSA than the glycated counterpart as binding constant declined from 9.28×10^3 to $2.78 \times 10^5 \text{ mol}^{-1}$. The fate of the incubated protein without glycation was an intermediate one as its binding affinity with respect to the first site was not improved as significantly as for the glycated protein but it suffered a lesser decline in affinity with its substrate as compared to the first site. In all cases, where

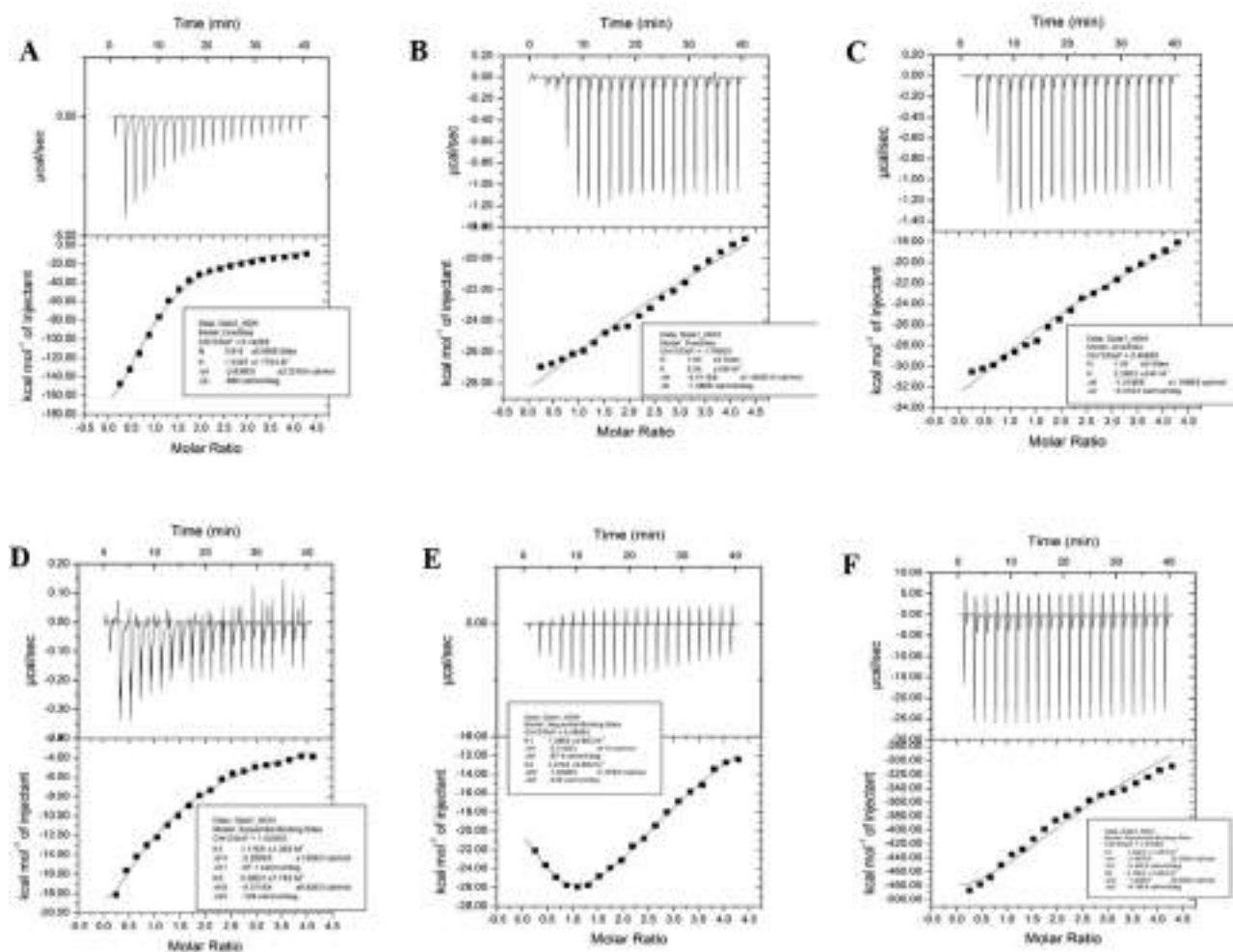


Figure 13. Assessment of residual substrate binding capability of control (A,D), incubated (B,E) and glycated (C,F) BSA against curcumin (A,B,C) and resveratrol (D,E,F) by Isothermal Titration Calorimetry.

Table 4. Evaluation of residual ligand binding capability of glycated BSA against resveratrol and curcumin.

Ligand	Sample	Number of binding sites (n)	Binding constant (K_d) (mol^{-1})	Wiseman parameter(c) (binding constant x receptor concentration)	Free energy change (ΔG) (KJmol^{-1})	Entropy change (ΔS) (Kcal/mol/deg)	Enthalpy change (ΔH) (Kcal/mol)
Curcumin	BSA	1	$1.53 \times 10^5 \pm 1.77 \times 10^4$	1.836	-6.72	-0.86	$-2.64 \times 10^2 \pm 22.21$
	Incubated BSA	1	5.33 ± 180	0.639×10^{-4}	—	—	—
	Glycated BSA	1	$2.28 \times 103 \pm 245$	0.027	—	—	—
Resveratrol	BSA	2	$1.11 \times 10^5 \pm 1.2 \times 10^4$	1.332	-6.874	-0.087	-32.8 ± 1.65
			$9.28 \times 10^3 \pm 7.7 \times 10^2$	0.11136	-5.556	-0.128	-43.7 ± 6.82
	Incubated BSA	2	$1.36 \times 105 \pm 3.8 \times 103$	1.632	-7.055	-0.0874	-33.1 ± 0.414
			$2.91 \times 104 \pm 5.8 \times 102$	0.349	-6.198	-0.449	$-1.4 \times 10^2 \pm 1.67$
	Glycated BSA	2	$1.56 \times 105 \pm 1.2 \times 104$	1.872	-58.88	-2.44	$-7.86 \times 102 \pm 22.5$
			$2.78 \times 103 \pm 1.8 \times 102$	0.033	—	—	—

the Wiseman parameter was evaluated to be much lesser than 1, the corresponding thermodynamic parameters of binding were not evaluated since those cases represented very poor ligand-protein interaction. It was evident that the gross structural transition entailed due to glycation brought about significant loss in functionality of the protein. In fact, this also explains the widespread toxicity caused by glycation induced changes in cellular proteome [83]. In addition to inducing structural perturbation, glycation can also interfere directly by denying physical access of the ligands to their respective binding pockets in the protein. However, this cannot be warranted without actual knowledge of the

location of lysine and arginine residues which have been modified by glycation.

4. Conclusion

Glycation of proteins and other macromolecules occurs as inevitable consequence of carbohydrate based regimen of our diet. Slow accumulation and attachment of sugar residues to proteins gradually bring about a structural transition in them which eventualize into terminally misfolded aggregates termed as Advanced Glycation End Products. The role

of glycation in amyloid formation is well documented and many studies have reported thus far that glycation may accelerate or inhibit formation of amyloid plaques. Based upon the reports obtained thus far, glycation has been mostly associated with non-canonical amyloidogenic aggregates from non amyloidogenic proteins without the formation of classical cross β fibrillar structure. We have shown in this study that dietary sugar induced glycation and amyloid formation is not a generic property of the ribosylated BSA; rather it occurs transiently during a specific phase of progression of glycation, which finally eventualize into irreversibly misfolded aggregate termed as Advanced Glycation End Product. We have also shown that these globular amyloids possess enhanced thermostability, have minimal solvent accessible hydrophobic interface and therefore not prone to hydrophobic aggregation. In addition, we have been able to dissect the amyloidogenic behavior arising out of glycation from that caused by sheer thermal aggregation of proteins. The observation of enhanced thermostability of amyloids although doesn't come as a surprise because of stubborn recalcitrant nature of amyloid plaques or fibrils formed intracellularly. However, these globular amyloids do raise an important issue, are these clearable by the RAGE axis eventually? AGE molecules are recognized chiefly by their ability to bind to specific receptors on the surfaces of predatory immune cells such as macrophages and initiate a plethora of cellular defense mechanisms such as release of inflammatory cytokines and elicitation of oxidative stress response [8, 10]. Probably, the AGE-RAGE pathway has evolved as a defense mechanism to sequester these toxic protein aggregates from the cellular microenvironment, because presence of these aggregates can mediate aggregation and malfunctioning of other cellular proteins. However, whether the intermediates of glycation pathway can also bind to RAGE and initiate downstream signaling is yet to be deciphered. Under the circumstances, the present studies are believed to provide significant insights to predict glycation associated malfunctioning of cellular and extracellular proteins and design therapeutics to arrest the transformation of the Schiff base adducts to obnoxious amyloids and AGE molecules.

Declarations

Author contribution statement

S. Banik: Conceived and designed the experiments; Performed the experiments; Contributed reagents, materials, analysis tools or data; Wrote the paper.

M. Bhattacharyya: Conceived and designed the experiments; Contributed reagents, materials, analysis tools or data.

A. Das: Performed the experiments; Wrote the paper.

A. Ghosh and M. Guria: Performed the experiments.

P. Basak: Performed the experiments; Analyzed and interpreted the data; Contributed reagents, materials, analysis tools or data.

A. Pramanik and R. Majumder: Performed the experiments; Contributed reagents, materials, analysis tools or data.

S. Hazra: Analyzed and interpreted the data.

Funding statement

This work was supported by STAR College Scheme, Department of Biotechnology, Govt. of India. A. Das was supported by a Fellowship provided by University Grants Commission, Govt. of India.

Competing interest statement

The authors declare no conflict of interest.

Additional information

No additional information is available for this paper.

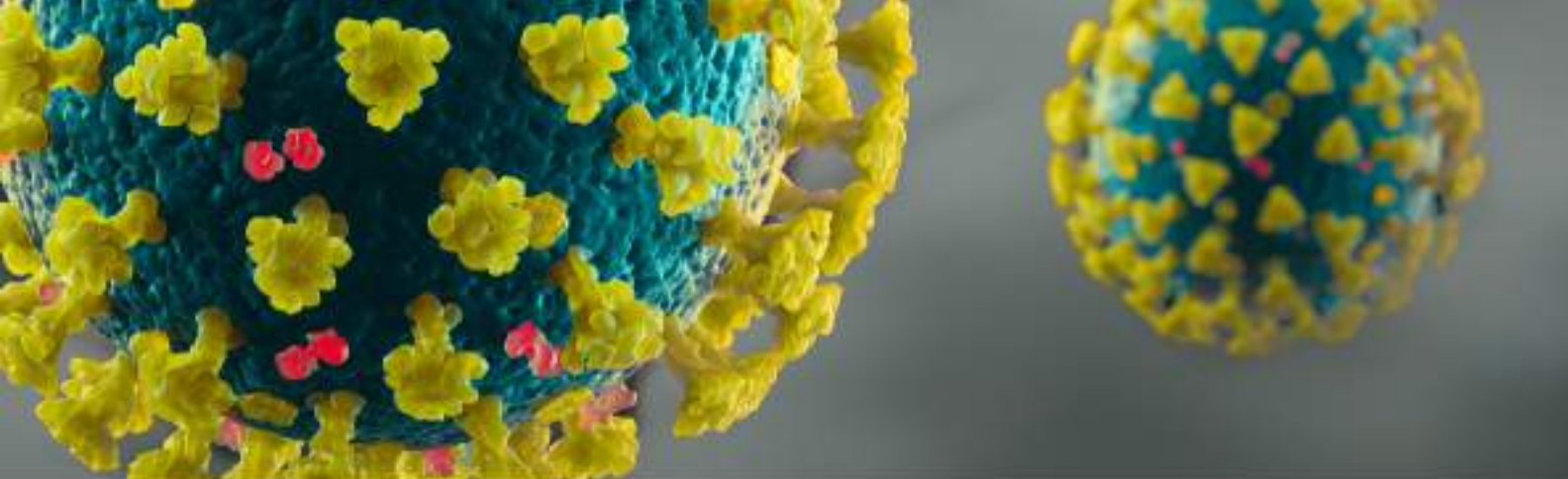
Acknowledgements

TEM images were acquired from the facility at University Science Instrumentation Centre, University of Burdwan with technical supervision from Dr. Subhajit Karmakar and Mr. Debanjan Mukherjee.

References

- [1] V. Kumar, N. Sami, T. Kashav, A. Islam, F. Ahmad, M.I. Hassan, Protein aggregation and neurodegenerative diseases: from theory to therapy, *Eur. J. Med. Chem.* 124 (2016) 1105–1120.
- [2] M. Verdugo, J.R. Encinar, J.M. Costa-Fernández, M. Menendez-Miranda, D. Bouzas-Ramos, M. Bravo, W. Quiroz, Study of conformational changes and protein aggregation of bovine serum albumin in presence of Sb (III) and Sb (V), *PLoS One* 12 (2) (2017).
- [3] M. Stefani, Protein misfolding and aggregation: new examples in medicine and biology of the dark side of the protein world, *Biochim. Biophys. Acta (BBA) - Mol. Basis Dis.* 1739 (1) (2004) 5–25.
- [4] F. del Monte, G. Agnetti, Protein post-translational modifications and misfolding: new concepts in heart failure, *Proteomics-Clin. Appl.* 8 (7–8) (2014) 534–542.
- [5] Q. Zhang, J.M. Ames, R.D. Smith, J.W. Baynes, T.O. Metz, A perspective on the Maillard reaction and the analysis of protein glycation by mass spectrometry: probing the pathogenesis of chronic disease, *J. Proteome Res.* 8 (2) (2009) 754–769.
- [6] P. Gkogkolou, M. Böhm, Advanced glycation end products: key players in skin aging? *Derm. Endocrinol.* 4 (3) (2012) 259–270.
- [7] M. Luthra, D. Balasubramanian, Nonenzymatic glycation alters protein structure and stability. A study of two eye lens crystallins, *J. Biol. Chem.* 268 (24) (1993) 18119–18127.
- [8] C. Ott, K. Jacobs, E. Haucke, A.N. Santos, T. Grune, A. Simm, Role of advanced glycation end products in cellular signaling, *Redox Biol.* 2 (2014) 411–429.
- [9] P. Salahuddin, M.T. Fatima, A.S. Abdelhameed, S. Nusrat, R.H. Khan, Structure of amyloid oligomers and their mechanisms of toxicities: targeting amyloid oligomers using novel therapeutic approaches, *Eur. J. Med. Chem.* 114 (2016) 41–58.
- [10] R. Ramasamy, S.F. Yan, A.M. Schmidt, Receptor for AGE (RAGE): signaling mechanisms in the pathogenesis of diabetes and its complications, *Ann. N. Y. Acad. Sci.* 1243 (2011) 88.
- [11] B. Bouma, L.M. Kroon-Batenburg, Y.-P. Wu, B. Brünjes, G. Posthuma, O. Kranenburg, P.G. de Groot, E.E. Voest, M.F. Gebbink, Glycation induces formation of amyloid cross- β structure in albumin, *J. Biol. Chem.* 278 (43) (2003) 41810–41819.
- [12] S.-Y. Ko, H.-A. Ko, K.-H. Chu, T.-M. Shieh, T.-C. Chi, H.-I. Chen, W.-C. Chang, S.-S. Chang, The possible mechanism of advanced glycation end products (AGEs) for Alzheimer's disease, *PLoS One* 10 (11) (2015).
- [13] S.M. Khan, N. Rabbani, S. Tabrez, B. Ul Islam, A. Malik, A. Ahmed, M. AAlsenaity, A. M. Alsenaity, Glycation induced generation of amyloid fibril structures by glucose metabolites, *Protein Pept. Lett.* 23 (10) (2016) 892–897.
- [14] C. Iannuzzi, G. Irace, I. Sirangelo, Differential effects of glycation on protein aggregation and amyloid formation, *Front. Mol. Biosci.* 1 (2014) 9.
- [15] C. Iannuzzi, R. Maritato, G. Irace, I. Sirangelo, Glycation accelerates fibrillization of the amyloidogenic W7FW14F apomyoglobin, *PLoS One* 8 (12) (2013), e80768.
- [16] A. Arasteh, S. Farahi, M. Habibi-Rezaei, A.A. Moosavi-Movahedi, Glycated albumin: an overview of the in vitro models of an in vivo potential disease marker, *J. Diabetes Metab. Disord.* 13 (1) (2014) 49.
- [17] M.E. Obrenovich, V.M. Monnier, Glycation stimulates amyloid formation, *Sci. Aging Knowl. Environ.* 2 (2004) 3.
- [18] Y. Wei, L. Chen, J. Chen, L. Ge, R.Q. He, Rapid glycation with D-ribose induces globular amyloid-like aggregations of BSA with high cytotoxicity to SH-SY5Y cells, *BMC Cell Biol.* 10 (1) (2009) 1–15.
- [19] A. Emendato, G. Milordini, E. Zacco, A. Sicorello, F. Dal Piaz, R. Guerrini, R. Thorogate, D. Picone, A. Pastore, Glycation affects fibril formation of A β peptides, *J. Biol. Chem.* 293 (34) (2018) 13100–13111.
- [20] I. Moreno-Gonzalez, C. Soto, Misfolded protein aggregates: mechanisms, structures and potential for disease transmission, in: *Semin. Cell Dev. Biol.*, Elsevier, 2011, pp. 482–487.
- [21] G. Liu, Q. Zhong, Glycation of whey protein to provide steric hindrance against thermal aggregation, *J. Agric. Food Chem.* 60 (38) (2012) 9754–9762.
- [22] H. Trębacz, A. Szczesna, M. Arczewska, Thermal stability of collagen in naturally ageing and in vitro glycated rabbit tissues, *J. Therm. Anal. Calorim.* 134 (3) (2018) 1903–1911.
- [23] G. Liu, Q. Zhong, High temperature-short time glycation to improve heat stability of whey protein and reduce color formation, *Food Hydrocolloids* 44 (2015) 453–460.
- [24] P.J. Coussons, J. Jacoby, A. McKay, S.M. Kelly, N.C. Price, J.V. Hunt, Glucose modification of human serum albumin: a structural study, *Free Radic. Biol. Med.* 22 (7) (1997) 1217–1227.
- [25] D.L. Mendez, R.A. Jensen, L.A. McElroy, J.M. Pena, R.M. Esquerre, The effect of non-enzymatic glycation on the unfolding of human serum albumin, *Arch. Biochem. Biophys.* 444 (2) (2005) 92–99.
- [26] P. Rondeau, S. Armenta, H. Caillens, S. Chesne, E. Bourdon, Assessment of temperature effects on β -aggregation of native and glycated albumin by FTIR spectroscopy and PAGE: relations between structural changes and antioxidant properties, *Arch. Biochem. Biophys.* 460 (1) (2007) 141–150.

- [27] P. Rondeau, G. Navarra, F. Cacciabauda, M. Leone, E. Bourdon, V. Militello, Thermal aggregation of glycosylated bovine serum albumin, *Biochim. Biophys. Acta Protein Proteomics* 1804 (4) (2010) 789–798.
- [28] N.G. Watkins, S.R. Thorpe, J.W. Baynes, Glycation of amino groups in protein. Studies on the specificity of modification of RNase by glucose, *J. Biol. Chem.* 260 (19) (1985) 10629–10636.
- [29] E. Sharifi, N. Sattarahmady, M. Habibi-Rezaei, M. Farhadi, N. Sheibani, F. Ahmad, A.A. Moosavi-Movahedi, Inhibitory effects of β -cyclodextrin and trehalose on nanofibril and AGE formation during glycation of human serum albumin, *Protein Pept. Lett.* 16 (6) (2009) 653–659.
- [30] A. Das, P. Basak, R. Pattanayak, T. Kar, R. Majumder, D. Pal, A. Bhattacharya, M. Bhattacharyya, S.P. Banik, Trehalose induced structural modulation of Bovine Serum Albumin at ambient temperature, *Int. J. Biol. Macromol.* 105 (2017) 645–655.
- [31] A. Das, P. Basak, A. Pramanick, R. Majumder, D. Pal, A. Ghosh, M. Guria, M. Bhattacharyya, S.P. Banik, Trehalose mediated stabilisation of cellobiose aggregates from the filamentous fungus *Penicillium chrysogenum*, *Int. J. Biol. Macromol.* 127 (2019) 365–375.
- [32] E. Schönbrunn, S. Eschenburg, K. Luger, W. Kabsch, N. Amrhein, Structural basis for the interaction of the fluorescence probe 8-anilino-1-naphthalene sulfonate (ANS) with the antibiotic target MurA, *Proc. Natl. Acad. Sci. U.S.A.* 97 (12) (2000) 6345–6349.
- [33] H.-L. Li, L.-Y. Zhang, S.-L. Zhuang, C.-X. Ni, H.-W. Shang, Fluorescence investigation on the interaction of a prevalent competitive fluorescent probe with entomoc odorant binding protein, *Spectrosc. Lett.* 46 (7) (2013) 527–534.
- [34] W. Liu, M.A. Cohenford, L. Frost, C. Seneviratne, J.A. Dain, Inhibitory effect of gold nanoparticles on the D-ribose glycation of bovine serum albumin, *Int. J. Nanomed.* 9 (2014) 5461.
- [35] G. Bulaj, T. Kortemme, D.P. Goldenberg, Ionization– reactivity relationships for cysteine thiols in polypeptides, *Biochemistry* 37 (25) (1998) 8965–8972.
- [36] G. Hungerford, J. Benesch, J.F. Mano, R.L. Reis, Effect of the labelling ratio on the photophysics of fluorescein isothiocyanate (FITC) conjugated to bovine serum albumin, *Photochem. Photobiol. Sci.* 6 (2) (2007) 152–158.
- [37] N. Jain, S. Mukhopadhyay, Applications of fluorescence anisotropy in understanding protein conformational disorder and aggregation, in: *Appl. Spectrosc. Sci. Nanomater*, Springer, 2015, pp. 41–57.
- [38] S. Li, D. Xing, J. Li, Dynamic light scattering application to study protein interactions in electrolyte solutions, *J. Biol. Phys.* 30 (4) (2004) 313–324.
- [39] U.K. Laemmli, Cleavage of structural proteins during the assembly of the head of bacteriophage T4, *Nature* 227 (5259) (1970) 680–685.
- [40] R. Majumder, S.P. Banik, S. Khowala, AkP from mushroom *Termitomyces clypeatus* is a proteoglycan specific protease with apoptotic effect on HepG2, *Int. J. Biol. Macromol.* 91 (2016) 198–207.
- [41] R. Majumder, S.P. Banik, S. Khowala, Purification and characterisation of κ -casein specific milk-clotting metalloprotease from *Termitomyces clypeatus* MTCC 5091, *Food Chem.* 173 (2015) 441–448.
- [42] C.J. Wilson, D. Apiyo, P. Wittung-Stafshede, Role of cofactors in metalloprotein folding, *Q. Rev. Biophys.* 37 (3–4) (2004) 285–314.
- [43] R. Majumder, L. Sheikh, A. Naskar, M. Mukherjee, S. Tripathy, Depletion of Cr (VI) from aqueous solution by heat dried biomass of a newly isolated fungus *Arthrinium malaysianum*: a mechanistic approach, *Sci. Rep.* 7 (1) (2017) 1–15.
- [44] A. Naskar, R. Majumder, M. Goswami, Bioaccumulation of Ni (II) on growing cells of *Bacillus* sp.: response surface modeling and mechanistic insight, *Environ. Technol. Innov.* (2020) 101057.
- [45] A. Naskar, R. Majumder, M. Goswami, S. Mazumder, S. Maiti, L. Ray, Implication of greener biocomposite bead for decontamination of nickel (II): column dynamics study, *J. Polym. Environ.* 28 (7) (2020) 1985–1997.
- [46] A.N. Schechter, C.J. Epstein, Spectral studies on the denaturation of myoglobin, *J. Mol. Biol.* 35 (3) (1968) 567–589.
- [47] S.G. Bolder, L.M. Sagis, P. Venema, E. van der Linden, Thioflavin T and birefringence assays to determine the conversion of proteins into fibrils, *Langmuir* 23 (8) (2007) 4144–4147.
- [48] S.P. Banik, S. Pal, S. Ghorai, S. Chowdhury, R. Majumder, S. Mukherjee, S. Khowala, In situ reversible aggregation of extracellular cellobiose in the filamentous fungus *Termitomyces clypeatus*, *Biotechnol. Bioeng.* 17 (5) (2012) 925–936.
- [49] N. Zaidi, E. Ahmad, M. Rehan, G. Rabbani, M.R. Ajmal, Y. Zaidi, N. Subbarao, R.H. Khan, Biophysical insight into furosemide binding to human serum albumin: a study to unveil its impaired albumin binding in uremia, *J. Phys. Chem. B* 117 (9) (2013) 2595–2604.
- [50] A. Raghav, J. Ahmad, K. Alam, Nonenzymatic glycosylation of human serum albumin and its effect on antibodies profile in patients with diabetes mellitus, *PLoS One* 12 (5) (2017), e0176970.
- [51] M.E. Rubio-Ruiz, E. Díaz-Díaz, M. Cárdenas-León, R. Argüelles-Medina, P. Sánchez-Canales, F. Larrea-Gallo, E. Soria-Castro, V. Guarnier-Lans, Glycation does not modify bovine serum albumin (BSA)-induced reduction of rat aortic relaxation: the response to glycated and nonglycated BSA is lost in metabolic syndrome, *Glycobiology* 18 (7) (2008) 517–525.
- [52] K. Dubey, B.G. Anand, D.S. Shekhawat, K. Kar, Eugenol prevents amyloid formation of proteins and inhibits amyloid-induced hemolysis, *Sci. Rep.* 7 (2017) 40744.
- [53] A. Polyanchiko, N. Mikhailov, N. Romanov, Y.G. Baranova, E. Chikhirzhina, Intermolecular interactions in solutions of serum albumin, *Cell Tissue Biol.* 11 (1) (2017) 9–15.
- [54] T. Maruyama, S. Katoh, M. Nakajima, H. Nabetani, Mechanism of bovine serum albumin aggregation during ultrafiltration, *Biotechnol. Bioeng.* 75 (2) (2001) 233–238.
- [55] M. Bhattacharya, N. Jain, S. Mukhopadhyay, Insights into the mechanism of aggregation and fibril formation from bovine serum albumin, *J. Phys. Chem. B* 115 (14) (2011) 4195–4205.
- [56] M. Dasgupta, N. Kishore, Selective inhibition of aggregation/fibrillation of bovine serum albumin by osmolytes: mechanistic and energetics insights, *PLoS One* 12 (2) (2017).
- [57] J.-E. Lee, J.C. Sang, M. Rodrigues, A.R. Carr, M.H. Horrocks, S. De, M.N. Bongiovanni, P. Flagmeier, C.M. Dobson, D.J. Wales, Mapping surface hydrophobicity of α -synuclein oligomers at the nanoscale, *Nano Lett.* 18 (12) (2018) 7494–7501.
- [58] Z. Wang, Y. Li, L. Jiang, B. Qi, L. Zhou, Relationship between secondary structure and surface hydrophobicity of soybean protein isolate subjected to heat treatment, *J. Chem.* 2014 (2014).
- [59] H.S. Tarar, B.C. Roughton, K.V. Camarda, Designing optimum protein-excipient interactions using molecular docking simulations, in: *Comput. Aided Chem. Eng.* 34, Elsevier, 2014, pp. 441–446.
- [60] M. Cardamone, N. Puri, Spectrofluorimetric assessment of the surface hydrophobicity of proteins, *Biochem. J.* 282 (2) (1992) 589–593.
- [61] O.K. Gasymov, B.J. Glasgow, ANS fluorescence: potential to augment the identification of the external binding sites of proteins, *Biochim. Biophys. Acta Protein Proteomics* 1774 (3) (2007) 403–411.
- [62] P. Stefanowicz, M. Kijewska, A. Kluczyk, S. Szewczuk, Detection of glycation sites in proteins by high-resolution mass spectrometry combined with isotopic labeling, *Anal. Biochem.* 400 (2) (2010) 237–243.
- [63] B. Loh, C. Grant, R. Hancock, Use of the fluorescent probe 1-N-phenyl-naphthylamine to study the interactions of aminoglycoside antibiotics with the outer membrane of *Pseudomonas aeruginosa*, *Antimicrob. Agents Chemother.* 26 (4) (1984) 546–551.
- [64] A.J. Weids, S. Ibbstedt, M.J. Tamás, C.M. Grant, Distinct stress conditions result in aggregation of proteins with similar properties, *Sci. Rep.* 6 (2016) 24554.
- [65] A. Iram, T. Alam, J.M. Khan, T.A. Khan, R.H. Khan, A. Naem, Molten globule of hemoglobin proceeds into aggregates and advanced glycosylated end products, *PLoS One* 8 (8) (2013).
- [66] M. Linetsky, E. Shipova, R. Cheng, B.J. Ortwerth, Glycation by ascorbic acid oxidation products leads to the aggregation of lens proteins, *Biochim. Biophys. Acta (BBA) - Mol. Basis Dis.* 1782 (1) (2008) 22–34.
- [67] D. Sarkar, Probing the interaction of a globular protein with a small fluorescent probe in the presence of silver nanoparticles: spectroscopic characterization of its domain specific association and dissociation, *RSC Adv.* 3 (46) (2013) 24389–24399.
- [68] A.B. Ghisaidoobe, S.J. Chung, Intrinsic tryptophan fluorescence in the detection and analysis of proteins: a focus on Förster resonance energy transfer techniques, *Int. J. Mol. Sci.* 15 (12) (2014) 22518–22538.
- [69] F.M. Ursache, I. Aprodu, O.V. Nistor, M. Bratu, E. Botez, N. Stănciuc, Probing the heat-induced structural changes in bovine serum albumin by fluorescence spectroscopy and molecular modelling, *Int. J. Dairy Technol.* 70 (3) (2017) 424–431.
- [70] M.F. Ali, A. Kaushik, D. Gupta, S. Ansari, M.A. Jairajpuri, Changes in strand 6B and helix B during neuroserpin inhibition: implication in severity of clinical phenotype, *Biochim. Biophys. Acta Protein Proteomics* (2020) 140363.
- [71] Y. Chen, B. Liu, H.-T. Yu, M.D. Barkley, The peptide bond quenches indole fluorescence, *J. Am. Chem. Soc.* 118 (39) (1996) 9271–9278.
- [72] J. Kong, S. Yu, Fourier transform infrared spectroscopic analysis of protein secondary structures, *Acta Biochim. Biophys. Sin.* 39 (8) (2007) 549–559.
- [73] Y.-H. Hsu, Y.-W. Chen, M.-H. Wu, L.-H. Tu, Protein glycation by glyoxal promotes amyloid formation by islet amyloid polypeptide, *Biophys. J.* 116 (12) (2019) 2304–2313.
- [74] M.P. Vitek, K. Bhattacharya, J.M. Glendening, E. Stopa, H. Vlassara, R. Bucala, K. Manogue, A. Cerami, Advanced glycation end products contribute to amyloidosis in Alzheimer disease, *Proc. Natl. Acad. Sci. U.S.A.* 91 (11) (1994) 4766–4770.
- [75] F. Chiti, C.M. Dobson, Amyloid formation by globular proteins under native conditions, *Nat. Chem. Biol.* 5 (1) (2009) 15.
- [76] N.K. Holm, S.K. Jespersen, L.V. Thomassen, T.Y. Wolff, P. Sehgal, L.A. Thomsen, G. Christiansen, C.B. Andersen, A.D. Knudsen, D.E. Otzen, Aggregation and fibrillation of bovine serum albumin, *Biochim. Biophys. Acta Protein Proteomics* 1774 (9) (2007) 1128–1138.
- [77] B. Demirhan, B. Bilezikçi, H. Kiyici, S. Boyacioglu, Globular amyloid deposits in the wall of the gastrointestinal tract: report of six cases, *Amyloid* 9 (1) (2002) 42–46.
- [78] H.R. Makhlof, Z.D. Goodman, Globular hepatic amyloid: an early stage in the pathway of amyloid formation: a study of 20 new cases, *Am. J. Surg. Pathol.* 31 (10) (2007) 1615–1621.
- [79] P. Bourassa, C. Kanakis, P. Tarantilis, M. Pollissiou, H. Tajmir-Riahi, Resveratrol, genistein, and curcumin bind bovine serum albumin, *J. Phys. Chem. B* 114 (9) (2010) 3348–3354.
- [80] N. Latruffe, M. Menzel, D. Delmas, R. Buchet, A. Lançon, Compared binding properties between resveratrol and other polyphenols to plasmatic albumin: consequences for the health protecting effect of dietary plant microcomponents, *Molecules* 19 (11) (2014) 17066–17077.
- [81] X. Du, Y. Li, Y.-L. Xia, S.-M. Ai, J. Liang, P. Sang, X.-L. Ji, S.-Q. Liu, Insights into protein–ligand interactions: mechanisms, models, and methods, *Int. J. Mol. Sci.* 17 (2) (2016) 144.
- [82] W.B. Turnbull, A.H. Daranas, On the value of c: can low affinity systems be studied by isothermal titration calorimetry? *J. Am. Chem. Soc.* 125 (48) (2003) 14859–14866.
- [83] M. Fournet, F. Bonté, A. Desmoulière, Glycation damage: a possible hub for major pathophysiological disorders and aging, *Aging Dis.* 9 (5) (2018) 880.



Vaccine Discovery and Development: Lessons from COVID-19

Free eBook

Emerging infectious diseases (EIDs) can evolve into a global healthcare crisis or pandemic. Scientists have previously required years to develop vaccines or therapeutics. The use of high throughput technology can greatly broaden the insights collected during discovery, augment efficiency and safety of handling EIDs, and shorten timelines.

Download this publication for an overview of many lessons learned in virology, immunology, and vaccine research during COVID-19 vaccine development.

[Download here](#)

RESEARCH ARTICLE

Mutations in membrane-fusion subunit of spike glycoprotein play crucial role in the recent outbreak of COVID-19

Soumita Podder¹  | Avishek Ghosh² | Tapash Ghosh^{1,3}

¹Department of Microbiology, Raiganj University, Uttar Dinajpur, West Bengal, India

²Department of Microbiology, Maulana Azad College, Kolkata, West Bengal, India

³Department of Bioinformatics, Bose Institute, Kolkata, West Bengal, India

Correspondence

Soumita Podder, Department of Microbiology, Raiganj University, Uttar Dinajpur-733134, W.B, India.

Email: s.podder@raiganjuniversity.ac.in and piu2007.soumita@gmail.com

Abstract

Coronavirus disease-2019 (COVID-19), the ongoing pandemic caused by severe acute respiratory syndrome coronavirus 2 (SARS-CoV-2) is a major threat to the entire human race. It is reported that SARS-CoV-2 seems to have relatively low pathogenicity and higher transmissibility than previously outbreak SARS-CoV. To explore the reason of the increased transmissibility of SARS-CoV-2 compared with SARS-CoV, we have performed a comparative analysis on the structural proteins (spike, envelope, membrane, and nucleoprotein) of two viruses. Our analysis revealed that extensive substitutions of hydrophobic to polar and charged amino acids in spike glycoproteins of SARS-CoV2 creates an intrinsically disordered region (IDR) at the beginning of membrane-fusion subunit and intrinsically disordered residues in fusion peptide. IDR provides a potential site for proteolysis by furin and enriched disordered residues facilitate prompt fusion of the SARS-CoV2 with host membrane by recruiting molecular recognition features. Here, we have hypothesized that mutation-driven accumulation of intrinsically disordered residues in spike glycoproteins play dual role in enhancing viral transmissibility than previous SARS-coronavirus. These analyses may help in epidemic surveillance and preventive measures against COVID-19.

KEYWORDS

intrinsically disordered region, molecular recognition feature, SARS-CoV2, spike glycoprotein

1 | INTRODUCTION

Novel coronavirus (2019-nCoV or SARS-CoV-2) has caused ongoing global epidemics with high morbidity and mortality. Coronaviruses (order Nidovirales, family Coronaviridae, and subfamily Coronavirinae) are primarily known to cause enzootic infections in birds and mammals; however, in the last few decades; they have crossed the animal-human species barrier.^{1,2} The outbreak of severe acute respiratory syndrome (SARS) in 2002–2003 and, more recently, Middle-East respiratory syndrome (MERS) in 2012 has confirmed the lethality of CoVs when they crossed the species barrier and started to infect humans. The consequent outbreak of SARS in 2003, 8096 cases and 774 deaths reported worldwide, resulting in a fatality rate of 9.6%.³ Whereas the outbreak of MERS in April 2012 up until

October 2018, 2229 cases, and 791 associated deaths have been confirmed globally, resulting in a case-fatality rate of 35.5%.⁴ The novel coronavirus has reported to share about 79% sequence similarity with the SARS-coronavirus, about 50% with the MERS-coronavirus.⁵ SARS-CoV-2 is associated with an ongoing outbreak of atypical pneumonia (coronavirus disease-2019 [COVID-2019]) that has affected 4,425,485 people and killed 302,059 of those affected in more than 60 countries as on May 16, 2020.⁶ On January 30, 2020, the World Health Organization declared the SARS-CoV-2 as a pandemic.

Coronaviruses are enveloped viruses with a positive sense, single-stranded RNA genome. The viral genome encodes four major structural proteins: the spike (S) protein, nucleocapsid (N) protein, membrane (M) protein, and the envelope (E) protein, all of which are

crucial to produce a structurally complete viral particle.⁷ Coronavirus enter into host cells by using transmembrane spike (S) glycoprotein that forms homotrimers extended from the viral envelope.⁸ S encompasses two functional subunits-S1, responsible for binding to the host cell receptor and S2, involved in fusion of the viral envelope and host cellular membranes. For many CoVs, S protein is cleaved at the boundary between the S1 and S2 subunits, which remain as a single polypeptide in the prefusion conformation.⁹ The distal S1 subunit comprises the receptor-binding domain (RBD) and facilitates the stabilization of the prefusion state of the membrane-anchored S2 subunit containing the fusion machinery.¹⁰ The cleavage at S1/S2 boundary has been anticipated to stimulate the protein by irreversible conformational changes for membrane fusion.¹¹ The host proteases for S protein cleavage differ among different coronaviruses, which play crucial roles in determining the epidemiological and pathological features of virus, including host range, tissue tropism, transmissibility, and mortality. For example, a variety of human proteases, such as trypsin, tryptase Clara, human airway trypsin-like protease, and transmembrane protease serine 2 are reported to cleave and activate the S protein of SARS-CoV.^{12,13} Depending on the viral species, coronaviruses recognize a variety of entry receptors to infect the host. SARS-CoV and several SARS-related coronaviruses (SARSr-CoV) interact directly with angiotensin-converting enzyme 2 via S protein to enter into the target cells.¹⁴ Recently, it is reported that mutation in the RBD in SARS-CoV-2 renders more efficient human-human transmission.¹⁵ Scientists have found that SARS-CoV-2 S glycoprotein possesses a furin cleavage site at the boundary between the S₁/S₂ subunits which helps in activating the fusion machinery of the virus.^{16,17} These two distinctive features in SARS-CoV2 could partially explain the efficient transmission of SARS-CoV-2 in humans.

A recent study by Zhao et al.¹⁸ has estimated basic reproduction number (R_0) for 2019-nCoV in the early phase of the outbreak and revealed that mean R_0 for SARS-CoV2 is ranging from 3.3 to 5.5 which is higher than those of SARS-CoV (R_0 : 2–5). The higher transmissibility of this virus turns the outbreak into a pandemic. Thus, it is of the prime interests of the researchers to untangle all the uniqueness of this newly emerged coronavirus by comparing with the previous human infecting SARS-CoV for designing protective measures against it.

We have studied an in depth mutational spectra and evolutionary dynamics of these four structural proteins by comparing SARS-CoV2 and human infecting SARS-CoV. Analyzing the impact of a mutation in proteins we have found that an intrinsically disordered region is acquired at the beginning of fusion protein (S2) which offers furin cleavage site in SARS-CoV2. Moreover, higher predisposition of intrinsically disordered residues in S2 observed to contain three molecular recognition features (MoRFs). We here hypothesized a unique fusion mechanism favored by the MoRFs present in the fusion peptide of the novel coronavirus. Thus, our study provides new insight into the genomic feature responsible for the rapid transmission of SARS-CoV2 as well as it could help in designing preventives against COVID-19.

2 | MATERIALS AND METHODS

2.1 | Sequence retrieval

Up to date, 1590 genome sequences of SARS-CoV2 are deposited in ViPR database (<https://www.viprbrc.org>).¹⁹ Complete genome is available for 1017 isolates from different geographical regions. We have retrieved 1017 coding sequences of SARS-CoV2 structural proteins (S, E, M, and N) and human infecting SARS-CoV three isolates from China, Germany, and USA. Genome accession numbers for all genome studied here are provided in Table S1.

2.2 | Calculation of evolutionary rate

Coding sequences of S, E, M, and N of SARS-CoV and SARS-CoV2 were aligned by CLUSTAL W, then Pairwise synonymous (ds) and nonsynonymous (dn) distances between the orthologous genes were calculated using the Phylogenetic Analysis Using Maximum Likelihood²⁰ package (PAML, yn00) to identify regions and sites under evolutionary selection.²¹

Pairwise amino acid residues of all proteins between SARS-CoV and SARS-CoV2 and within different strains of SARS-CoV2 were aligned by CLUSTAL omega and amino acid substitution were calculated by house-build Perl program.

Mutation analysis was done by PROVEAN (<http://provean.jcvi.org/index.php>) and SIFT (<https://sift.bii.a-star.edu.sg/>). PROVEAN is very much useful for filtering sequence variants to identify non-synonymous or indel variants that are predicted to be functionally important²² and in SIFT algorithm for sorting Intolerant from Tolerant could efficiently predict whether an amino acid substitution affects protein function or not.²³

2.2.1 | Prediction of IDR and MoRF

Coordinates of S1 and S2 subunits of S proteins in SARS-CoV and SARS-CoV-2 were retrieved from Pfam (<https://pfam.xfam.org/>).

Intrinsically disordered region (IDRs) of all four proteins of SARS-CoV and CoV2 were predicted by PONDR® VLXT (<http://www.pondr.com/>), predictors of natural disorder region. PONDR® VLXT applies three different feedforward neural networks (VL1, XN, and XC). XN and XC [22] for N- terminal and C-terminal region, respectively and VL1²⁴ for the internal region of the sequence. This method is frequently used for disorder calculation in virus.^{25–27}

MoRF was predicted by MoRFchibi (<https://morf.msl.ubc.ca/index.xhtml>). This tool is used for its high accuracy predictions and it provides more than double the precision of other predictors.²⁸

2.3 | Statistical test

All the statistical tests were performed using the SPSS package.

3 | RESULTS

3.1 | Mutational spectrum in the structural protein-coding genes in SARS-CoV2 arisen during evolution

Bayesian evolutionary rate and divergence date estimates were shown that nonsynonymous-to-synonymous substitution rate ratio is decreasing from SARS (1.41) to MERS (0.35) and MERS to HCoV-OC43 (0.133).²⁹ Here, we have measured evolutionary distance between 1017 strain of SARS-CoV2 spreading throughout the world with human infecting SARS-CoV predominantly had spread in three different geographical regions (USA, China, and Germany) in 2003–2004. For this, we have calculated nonsynonymous substitution per nonsynonymous site (dn) and synonymous substitution per synonymous site (ds) among the four structural protein-coding sequences (S, M, E, and N) of orthologous genes present in SARS-CoV and SARS-CoV-2. We have noticed significantly ($p = .001$) higher nonsynonymous substitution rates and synonymous substitution rates in S protein compared with the other three proteins (Table 1). A similar observation is also documented in the recent study of Tang et al.³⁰ Pairwise alignment by Needleman–Wunsch algorithm between the four structural proteins of SARS-CoV and SARS-CoV2, have shown that average percentages of amino acid substitutions occurred in S, M, N, and E proteins are 21.9, 9.5, 8.76, and 4, respectively. These results imply that significantly ($p = .001$) higher amino acid substitutions have occurred in S proteins than the other three proteins during evolution which is reflected in the higher dN value of S proteins. Analyzing the effects of amino acids substitution in proteins by PROVEAN and SIFT, we revealed five deleterious mutations, that is, the mutations may cause protein structural destabilization (C19T, L54S, L286T, P335A, and Y1070H) have occurred in S protein whereas no such deleterious mutations were observed in other three proteins. S protein is very much crucial for virus entry since it interacts with receptor and fuse with host membrane. It was evident from different studies that genes which crucial for the survival of the organisms are remained conserved (low dN/dS) over the evolutionary time scale.³⁰ Thus, according to the neutral theory of evolution³¹ higher nonsynonymous substitution rate compelled S proteins to experience significantly ($p = .001$) higher synonymous substitution rates than other proteins to retain overall conservation of the S proteins (Table 1).

Though, it was well evidenced that RNA viruses accumulate more mutation rates than DNA viruses due to lack of proofreading

TABLE 1 Comparison on average nonsynonymous (dN) and synonymous (dS) substitution rates of four structural proteins in SARS-CoV-2

Protein name	Average dN (n = 1017)	Average dS (n = 1017)
S	0.156	1.262
M	0.067	0.551
N	0.057	0.368
E	0.031	0.136

Abbreviations: E, envelope; M, membrane; N, nucleocapsid; S, spike, SARS-CoV-2, severe acute respiratory syndrome coronavirus 2.

activity in RNA polymerase they have encoded.³² However, it would be interesting to investigate whether the accumulation of non-synonymous mutation preferentially in S proteins than others offer any benefits to the virus for enhancing their potency of infectivity.

3.2 | Effects of mutations on the protein structural features in SARS-CoV2

We have analyzed the properties of substituted amino acids in the four structural proteins during evolution from SARS-CoV to SARS-CoV2 to investigate whether the amino acids substituted with a similar group of amino acids or not. We have detected extensive hydrophobic (Hy) to polar (P) and charged (C) amino acids exchange in S proteins than other three structural proteins (S: Hy-P/C = [51/91] = 56.1% and P/C-Hy = [40/91] = 43.9% [p -value = .02]; M: Hy-P/C = [4/7] = 57.2%, P/C-Hy = [3/7] = 42.8% [p -value = .59]; N: Hy-P/C = [7/15] = 46.6%, P/C-Hy = [8/15] = 53.3% [p -value = .71]). In E proteins, no substitution of amino acid with the different groups has found. The details of amino acid mutations of S, M, and N proteins which took place during evolution from SARS-CoV to SARS-CoV2 have delineated in Table 2. Several high throughput studies on protein structure have evidenced that regions in a protein-enriched with polar and charged amino acids have a tendency to conform IDR.³³ Moreover, IDRs in virus endure several structural features associated with viral pathogenicity.³⁴ Thus, we have predicted IDR in all structural proteins in SARS-CoV2 by PONDR-VLXT and compared the predisposition of IDR with the corresponding proteins present in SARS-CoV. Here, we have found that M and E proteins of both SARS-CoV and SARS-CoV2 do not contain any IDR (consecutive disordered residues > 30 amino acids) in their proteins (Table 3). N proteins contain three IDRs and percentages of intrinsically disordered residues in their proteins are remarkably high. However, the enrichment of IDR in N proteins is similar for both viruses (Table 3). Interestingly, we have revealed an IDR (671–708) in S proteins of SARS-CoV-2 but no IDR is found in their previous orthologous SARS-CoV (Figure 1A, Table 3). Moreover, percentages of disordered residues (PID) are significantly ($p = .035$) increased in S proteins of SARS-CoV2 compared with SARS-CoV which implies more disorder residues become enriched in S proteins after evolution (Table 3). Genomic analysis of S genes deduced that out of 1017 genome of SARS-CoV2, 491 viral strains are 100% similar and 526 strains have differed from each other. Multiple alignments of Spike protein sequences from 526 different isolates with one of the similar isolates have revealed a total of 31 Single Amino Acid Polymorphisms (SAPs) but none of them has occurred in the predicted IDR (671–708) which indicates the region is conserved among all of them (Figure 2A). We also noticed D614G mutation is predominant in 504 isolates (Figure 2A; Table S1). Next, comparing the IDR between SARS-CoV/CoV2, we have traced an insertion mutation which allows to incorporate three new disorder promoting amino acids serine, proline, and arginine in S proteins of SARS-CoV2 (Figure 2A). Along with this, the substitution of order promoting to disorder promoting amino

TABLE 2 Position wise amino acid substitution between S, M, and N proteins of SARS-CoV and SARS-CoV2

Protein	Position of hydrophobic to polar/charged amino acids substitution	Position of polar/charged to hydrophobic amino acids substitution
S	L16C; F22R; M37T; L54S; G77D; A91S; A126K; P143K; M144S; M151R; F153Y; F157N; F193Y; G199K; F232Q; A233T; A237Y; I244S; G246T; F253Y; A284S; L286T; V308Q; G311E; F360S; V404K; M417T; A430S; G446S; V458E; F460Y; P461Q; G464S; P470E; L515K; P540E; F558T; A590T; A618T; V663Q; L665N; A714T; A732S; L792S; A854Q; A857S; A866S; A1037S; F1079S; F1092Y; A1229C	T9P; T11V; D17V; C19L; N29A; S36F; T51V; Y63F; T71A; H74G; S120A; T146M; T150F; E174G; K190I; T215A; T247A; S248G; S279A; Q280L; T359A; S432V; T433G; K439L; Y442L; D463G; T485P; Q546L; S556A; S607P; T608V; T669V; S670A; T775P; N827A; S861A; Q904L; S914G; S924A; S1052A
M	A29T; M32C; A210S; G211S	C27F; S39A; T188G
N	G32E; P38S; G80S; G193N; G214N; A380T; P391Q	D26G; S121G; N153A; T158I; S213G; T218A; Q268A; T377A

Abbreviations: M, membrane; N, nucleocapsid; S, spike, SARS-CoV-2, severe acute respiratory syndrome coronavirus 2.

TABLE 3 Comparison on the intrinsic disorder content of four proteins between SARS-CoV and SARS-CoV-2

Disorder features	SARS-CoV-S	SARS-CoV2-S
Total disorder residues	65	98
No of disorder region (>30a.a)	NIL	1
PID	5.18	7.70
	SARS-CoV-M	SARS-CoV2-M
Total disorder residues	14	13
No of disorder region (>30a.a)	NIL	NIL
PID	6.28	5.86
	SARS-CoV-E	SARS-CoV2-E
Total disorder residues	10	9
No of disorder region (>30a.a)	NIL	NIL
PID		
	SARS-CoV-N	SARS-CoV2-N
Total disorder residues	212	208
No of disorder region (>30a.a)	3	3
PID	50.74	49.6

Note: PID indicates the proportion of disorder residues to the total length of amino acids predicted by PONDR-VLXT.

Abbreviations: E, envelope; M, membrane; N, nucleocapsid; PID, percentages of disordered residues; S, spike, SARS-CoV-2, severe acute respiratory syndrome coronavirus 2.

acids in five positions (H661Q, V663Q, L665N, L666A, and D684E) help to create the new IDR in SARS-CoV2 (Figure 2B). These results imply that the novel coronavirus acquired a new intrinsically disordered region in their spike glycoprotein which is crucial for entry into the host. Thus, it is imperative to explore the connection between IDR and elevated transmissibility in SARS-CoV2.

3.3 | Role of IDR in S protein in the rapid transmission of SARS-CoV-2

S proteins contain two subunits-S1 and S2. Pfam prediction on S proteins of two viruses depicted two domains: (i) Receptor binding domain (321–556 in SARS-CoV and 330–583 in SARS-CoV-2); (ii) S2 domain (635–1240 in SARS-CoV and 671–1270 in SARS-CoV-2). Thus, it is clearly observed that the IDR (671–708) has enriched in membrane fusion domain (S2) of spike glycoproteins in SARS-CoV-2 (Figure 1A). Recently, two research groups have reported that fusion protein acquired a new furin cleavage site (682–685) at the upstream of fusion peptide (S2').^{16,17} We have found that this cleavage site actually resides in the IDR. Since, intrinsically disordered proteins (IDPs)/IDPRs lack stable well-folded three-dimensional structures, the structural instability renders exceptional sensitivity to proteolysis.³⁵ Thus, the new IDR offers the cleavage site of furin protease as well as assists in efficient proteolytic cleavage of S proteins to activate the fusion peptide in SARS-CoV-2.

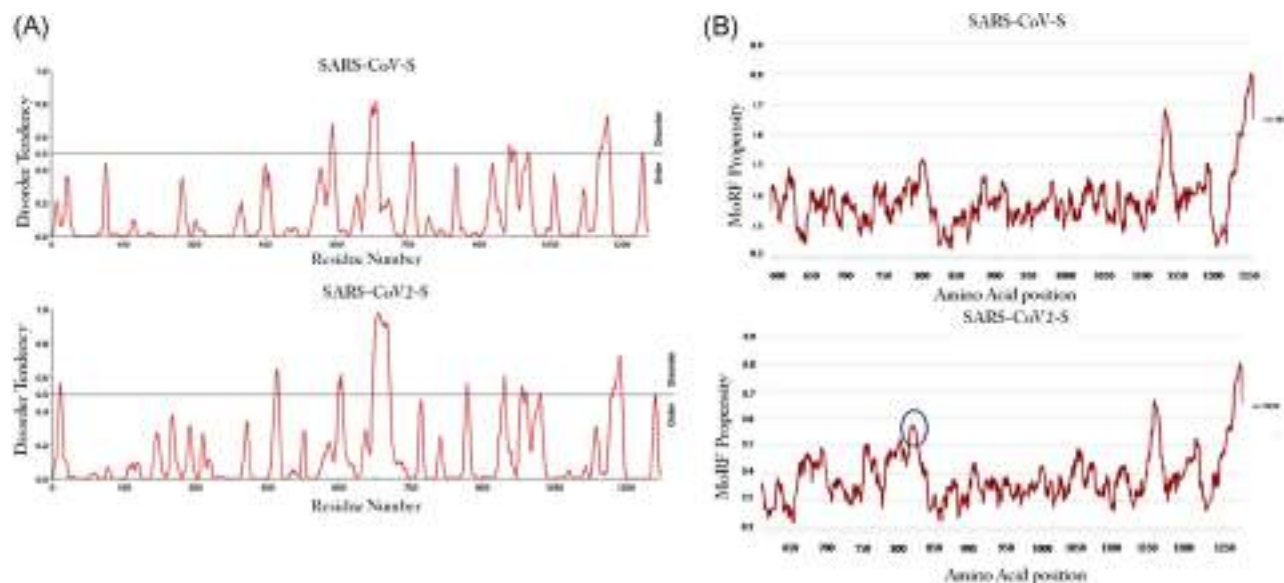


FIGURE 1 Comparison on IDR and MoRF between SARS-CoV and SARS-CoV2. (A) Comparison on the intrinsic disorder tendency of the amino acid residues in spike glycoproteins of SARS-CoV and SARS-CoV2. Disorder score above 0.5 is considered as cut-off value. (B) Comparison between MoRF content in SARS-CoV and SARS-CoV2. MoRF propensity score 0.5 was considered as cutoff. Circle shows the enrichment of additional MoRF in SARS-CoV2. IDR, intrinsically disordered region; MoRF, molecular recognition feature; SARS-CoV-2, severe acute respiratory syndrome coronavirus 2

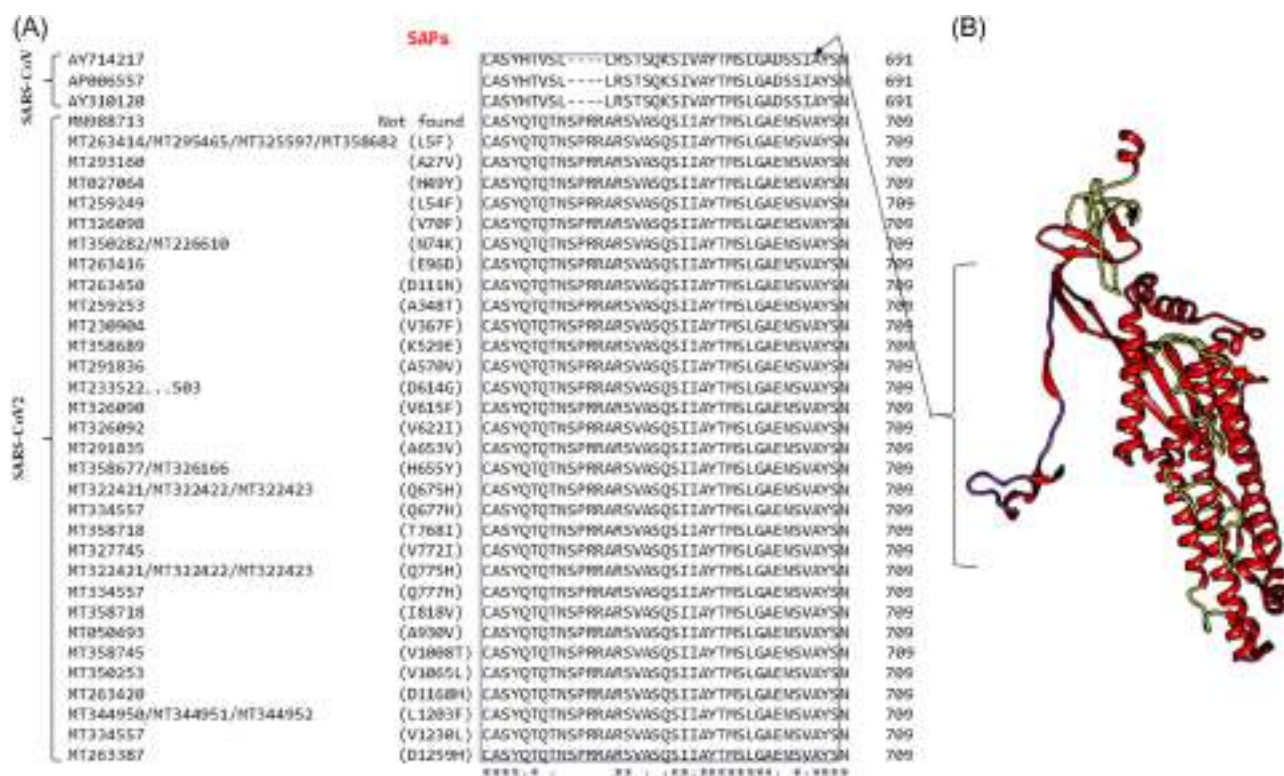


FIGURE 2 Conservation of IDR in all isolates of SARS-CoV2. (A) Pairwise alignment of IDR of S proteins in three strains of SARS-CoV and different strains of SARS-CoV-2 having change in amino acid level shows the amino acid substitutions between the two viruses as well as the conservation of this region (indicated by black box) in all SARS-CoV-2 isolates. (B) IDR in S2 subunits of spike glycoprotein in SARS-CoV-2 (PDB Id: 6VSB) represents in purple color and other disorder residues in green color. IDR, intrinsically disordered region; SARS-CoV-2, severe acute respiratory syndrome coronavirus 2

Moreover, analyzing the PID separately in S2 domains of SARS-CoV and SARS-CoV-2, we have found that PID of S2 is significantly ($p = .025$) higher in SARS-CoV-2 (13.83) than SARS-CoV (8.75). Earlier it was reported that the enormous flexibility of intrinsically disordered regions in the membrane proteins imposes the potentiality to involve in the membrane remodeling process.^{36,37} The membrane remodeling is essential for efficient fusion of the enveloped virus with host cellular membrane. Subsequently, it was also described that IDRs mediated remodeling of the membrane depends on the presence of MoRFs and posttranslational protein modifications.³⁸ The MoRF is a short peptide (10–70 residues) present in the disordered region and the flexibility of this facilitates membrane curvature. MoRF prediction by MoRFchibi has revealed the three MoRFs (804–823, 1147–1159, and 1249–1272) in the fusion peptide of SARS-CoV-2, whereas in SARS-CoV it was two (1129–1142 and 1232–1255; Figure 1B). In an earlier study,³⁸ it was elucidated that the membrane curvature increases with two factors: the size of the inserted MoRF and surface density of the disordered protein. Thus, the acquisition of one additional MoRF in SARS-CoV-2 escalated MoRF and disorder residue density on the viral protein which could be able to trigger more rapid fusion with host membrane than the SARS-CoV. Together these results have deduced that preponderance of intrinsically disordered residues in S2 domain offers protease-sensitive region for prompt activation of fusion peptide and enrichment of MoRFs for efficient fusion with host membrane. So, it could be treated as a novel feature observed exclusively in 2019-nCoV distinguishing this virus from SARS-CoV.

4 | DISCUSSION

The protein expressed on the surface of a pathogen is supposed to be more accessible to surveillance by the immune system than one within the interior of a pathogen.³⁹ Thus, more genetic variations in surface proteins are the signatures of host-pathogen coevolution. In this study, we have found that amongst the four structural proteins, an extensive higher rate of nonsynonymous substitution is occurred in spike glycoproteins of SARS-CoV-2 when compared with the human infecting SARS-CoV strain. Along with the amino acid substitution having neutral effects on virus fitness, S proteins also experienced five deleterious mutations that may cause destabilization of viral structure. The neutral theory of molecular evolution suggested that the mutations decreasing the carrier's fitness tend to disappear from populations through the process of negative or purifying selection ($dN/dS < 1$).⁴⁰ Thus, S protein has also experienced higher synonymous substitution rate to balance overall selection pressure on it. Now, it was also depicted that slightly deleterious and slightly advantageous mutations are engulfed by neutral mutations. Thus, the ratio of dN and dS is frequently used to study positive Darwinian selection operating at highly variable genetic loci, but it could not able to detect adaptively important codons offering benefits to the organism for adaptation.⁴¹ Thus, we have extensively studied amino acid changes in all the structural proteins of

SARS-CoV-2 occurred during evolution from SARS-CoV to search out the mutation posing advantages to the novel virus for their systematic infection in the human body.

We have revealed that mutations in the four structural proteins of SARS-CoV-2 prompt a significant hydrophobic to polar and charged amino acids exchange in S proteins compared with E, M, and N proteins (Table 2). This trend of amino acid exchange in S proteins is observed to generate an intrinsically disordered region (38 residues) at the upstream of fusion peptide in S2 domain which is embedded inside the envelope of SARS-CoV-2. However, amino acid substitution in M, E, and N proteins did not show any enrichment of new IDR in SARS-CoV-2 compared with SARS-CoV. Though, it was earlier reported that N proteins of SARS-CoV extensively enriched with intrinsically disordered residues.⁴² We found that the propensity of disordered residues in N proteins of SARS-CoV-2 (49.6%) is nearly similar with SARS-CoV (50.7%). The enrichment of disordered residues in N proteins has suggested as a crucial phenomenon for their transmission in respiratory routes.⁴² Whereas, lower content of disordered residues in shell proteins (E and M) of SARS-CoV as well as SARS-CoV-2 eliminate the chances of transmission via oral–fecal routes.⁴² Since, the intrinsic disorder content in E, M, and N proteins already reported to regulate the behavior of viral transmission, it is a prerequisite to illustrate the impact of IDR in S proteins. Viral entry is mediated by S proteins containing RBD and fusion domain (S2). The IDR which is exclusively found in SARS-CoV-2 is located in S2 domain. The IDR in this domain offers the furin cleavage site (682–685). Furin protease is ubiquitously expressed in a wide range of organs and tissues, including the brain, lung, gastrointestinal tract, liver, pancreas, and reproductive tissues. The structural flexibility of IDR stimulates this region sensitive to proteolysis.^{35,43} Similar kind of observation was also reported in Zika virus where the prefusion protein prM contains IDR with a protease cleavage site.⁴⁴ Thus, the acquisition of a disordered region imposes efficient proteolytic cleavage of S2 which in turn activates fusion peptide to fuse with the host membrane. Moreover, in comparison with the structured proteins, disordered proteins of similar length have large volumes and flexibility, so that they are able to furnish different coupled binding-folding reactions.⁴⁵ The highly flexible nature of IDR is frequently exploited by eukaryotic cells including viruses for modulating membrane properties during membrane trafficking.³⁷ Viral envelopes are made up of lipid bilayer where a number of spike proteins with considerable disordered regions are observed to be anchored. They are free to diffuse in the lipid leaflets. According to the hypothesis described in Fakhree et al.,³⁹ we could explicate our observation in a way that the free movement of intrinsically disordered residues containing in the fusion peptide will result in collisions with other membrane-anchored macromolecules. The collisions generate a lateral pressure on the membrane. The presence of a large fraction of charged and polar amino acids in disordered proteins makes them more efficient in generating lateral pressure. This pressure is consequently used to incite membrane curvature. It has been seen that many IDRs induce membrane curvature by recruiting MoRFs.⁴⁶ MoRFs are relatively short (10–70 residues) and typically possessing higher numbers of hydrophilic amino acids and prolines.^{47,48} Thus they could play a vital role in protein–protein interactions, metal binding, and

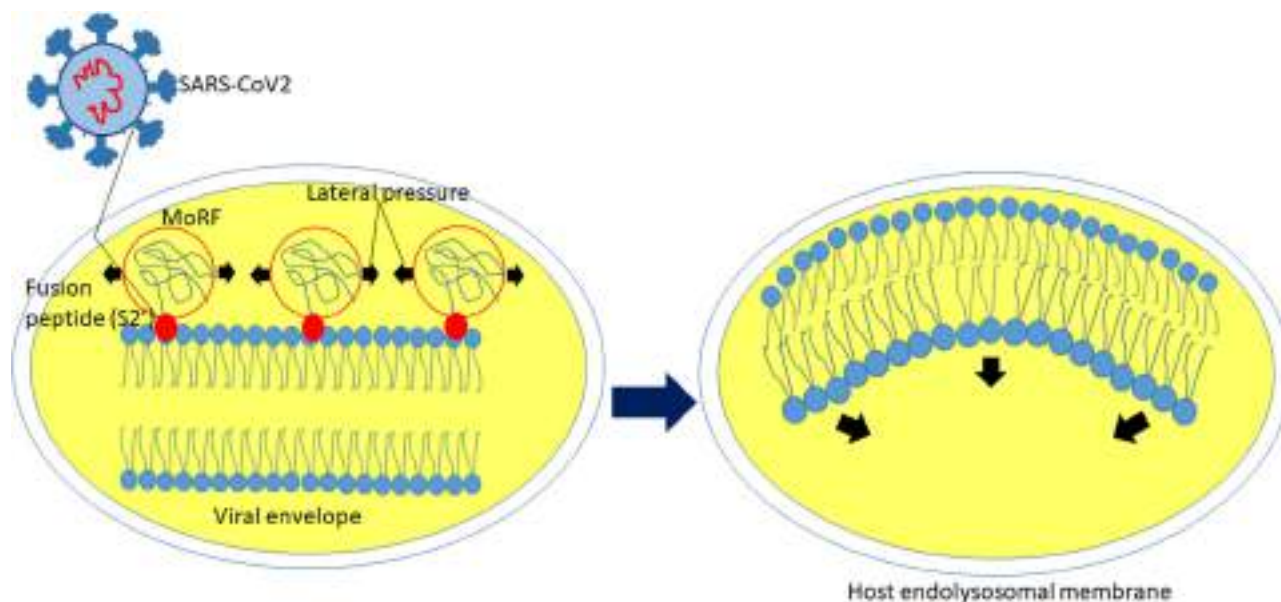


FIGURE 3 Mechanism of viral lipid bilayer curvature by MoRF which helps prompt fusion of SARS-CoV-2 with host endolysosomal membrane. MoRF, molecular recognition feature; SARS-CoV-2, severe acute respiratory syndrome coronavirus 2

cellular communications.⁴⁹ Several roles of MoRFs are also documented in Chikungunya virus.⁵⁰ We have noticed that an abundance of disordered residues in SARS-CoV-2 generates three MoRFs in the fusion peptide. It was explained in an earlier review³⁸ that the presence of MoRF result in a unilateral increase in the surface area of the membrane. This changes the ratio between the outer and inner surface area of the membrane and subsequently to adopt topography with this new ratio, the membrane remodels by increasing its curvature.^{38,51} Thus, it could be interpreted that MoRFs help for curving the lipid bilayer of the virus and initiate efficient fusion with the host cell membrane (Figure 3). Such ability of intrinsically disordered domains to create steric pressure on membrane surfaces to drive its curvature was depicted in endocytic adapter proteins, Epsin1 and AP180 by a combination of in vitro biophysical studies and quantitative experiments in live cells.⁵² Another couple of examples of membrane curvature by the MoRF motif of was established in an IDP ArfGAP1 (ADP-ribosylation factor GTPase-activating protein 1)⁵³ and α -synuclein, by site-directed mutagenesis, limited proteolysis, circular dichroism experiments,⁵⁴ and FRET microscopy study in live cell,⁵⁵ respectively. Hence, we have hypothesized that the acquisition of disordered residues in SARS-CoV-2 makes them highly competent for systematic infection in human. Nowadays, IDPs are becoming attractive candidates for therapeutic intervention by small drug-like molecules. Thus, this study will help in epidemic surveillance and designing drug targets to battle COVID-19.

In summary, these analyses provide insights into the mutational effects in originating intrinsically disordered residues in the S2 subunits of spike glycoprotein present in SARS-CoV-2. We have also hypothesized a unique fusion mechanism of the viral envelope and host membrane by MoRF. However, these propositions are mainly based on our sequence studies and experimental evidence in other

organisms, thus further experimental validations are required to confirm this mechanism in coronavirus.

ACKNOWLEDGMENTS

We are thankful to Mr. Sanjib Kumar Gupta, Senior technical assistant, Bioinformatics Center, Bose institute for his kind help. We are also thankful to two anonymous referees for their valuable suggestions.

CONFLICT OF INTERESTS

All the authors declare that there are no conflict of interests.

AUTHOR CONTRIBUTIONS

Soumita Podder designed, executed experiments, and wrote the manuscript. Avishek Ghosh performed some parts of the experiment. Tapash Ghosh helped in manuscript preparation.

DATA AVAILABILITY STATEMENT

All data will be available in the Supplementary Table.

ORCID

Soumita Podder  <http://orcid.org/0000-0002-8140-508X>

REFERENCES

- Chan JFW, To KKW, Tse H, Jin DY, Yuen KY. Interspecies transmission and emergence of novel viruses: Lessons from bats and birds. *Trends Microbiol.* 2013;21(10):544–555. <https://doi.org/10.1016/j.tim.2013.05.005>
- Lu G, Wang Q, Gao GF. Bat-to-human: spike features determining 'host jump' of coronaviruses SARS-CoV, MERS-CoV, and beyond. *Trends Microbiol.* 2015;23(8):468–478. <https://doi.org/10.1016/j.tim.2015.06.003>

3. World Health Organization WHO. Summary of probable SARS cases with onset of illness from 1 November 2002 to 31 July 2003. http://www.who.int/csr/sars/country/table2004_04_21/en/index.html Accessed August 9, 2020.
4. World Health Organization. WHO MERS-CoV Global Summary and Assessment of Risk, August 2018 (WHO/MERS/RA/August18) 2018. http://www.who.int/csr/disease/coronavirus_infections/riskassessment-august-2018.pdf Accessed June 6, 2019.
5. Lu R, Zhao X, Li J, et al. Genomic characterisation and epidemiology of 2019 novel coronavirus: implications for virus origins and receptor binding. *Lancet*. 2020;395(10224):565–574. [https://doi.org/10.1016/S0140-6736\(20\)30251-8](https://doi.org/10.1016/S0140-6736(20)30251-8)
6. World Health Organization (2020) Coronavirus disease (COVID-19) outbreak. Situation report – 117, 16th May 2020. <https://www.who.int>. Accessed May 17, 2020.
7. Masters PS. The molecular biology of coronaviruses. *Adv Virus Res*. 2006;66:193–292. [https://doi.org/10.1016/S0065-3527\(06\)66005-3](https://doi.org/10.1016/S0065-3527(06)66005-3)
8. Tortorici MA, Veasler D. Structural insights into coronavirus entry. *Adv Virus Res*. 2019;105:93–116. <https://doi.org/10.1016/bs.aivir.2019.08.0028>
9. Belouzard S, Chu VC, Whittaker GR. Activation of the SARS coronavirus spike protein via sequential proteolytic cleavage at two distinct sites. *Proc Natl Acad Sci USA*. 2009;106:5871–5876. <https://doi.org/10.1073/pnas.0809524106>
10. Gui M, Song W, Zhou H, et al. Cryo-electron microscopy structures of the SARS-CoV spike glycoprotein reveal a prerequisite conformational state for receptor binding. *Cell Res*. 2017;27:119–129. <https://doi.org/10.1038/cr.2016.152>
11. Millet JK, Whittaker GR. Host cell proteases: critical determinants of coronavirus tropism and pathogenesis. *Virus Res*. 2015;202:120–134. <https://doi.org/10.1016/j.virusres.2014.11.021>
12. Bosch BJ, Bartelink W, Rottier PJ. Cathepsin L functionally cleaves the severe acute respiratory syndrome coronavirus class I fusion protein upstream of rather than adjacent to the fusion peptide. *J Virol*. 2008;82:8887–8890. <https://doi.org/10.1128/JVI.00415-08>
13. Bertram S, Glowacka I, Muller MA, et al. Cleavage and activation of the severe acute respiratory syndrome coronavirus spike protein by human airway trypsin-like protease. *J Virol*. 2011;85:13363–13372. <https://doi.org/10.1128/JVI.05300-11>
14. Kirchdoerfer RN, Wang N, Pallesen J, et al. Ward Stabilized coronavirus spikes are resistant to conformational changes induced by receptor recognition or proteolysis. *Sci Rep*. 2018;8:15701. <https://doi.org/10.1038/s41598-018-34171-7>
15. Wan Y, Shang J, Graham R, Baric RS, Li R. Receptor recognition by the novel coronavirus from Wuhan: an analysis based on decade-long structural studies of SARS coronavirus. *J Virol*. 2020;94(7):1–9. <https://doi.org/10.1128/JVI.00127-20>
16. Wang Q, Qiu Y, Li JY, Zhou ZH, Liao CH, Ge XY. A unique protease cleavage site predicted in the spike protein of the novel pneumonia coronavirus (2019-nCoV) potentially related to viral transmissibility. *Virologica Sinica*. 2020;35:337–339. <https://doi.org/10.1007/s12250-020-00212-7>
17. Walls AC, Park YJ, Tortorici MA, Wall A, McGuire AT, Veasler D. Structure, function, and antigenicity of the SARS-CoV-2 spike glycoprotein. *Cell*. 2020;180:1–12. <https://doi.org/10.1016/j.cell.2020.02.058>
18. Zhao S, Lin Q, Ran J, et al. Preliminary estimation of the basic reproduction number of novel coronavirus (2019-nCoV) in China, from 2019 to 2020: a data-driven analysis in the early phase of the outbreak. *Int J Infect Dis*. 2020;92:214–217. <https://doi.org/10.1016/j.ijid.2020.01.050>
19. Pickett BE, Sadat EL, Zhang Y, et al. ViPR: an open bioinformatics database and analysis resource for virology research. *Nucleic Acids Res*. 2012;40:D593–D598. <https://doi.org/10.1093/nar/gkr859>
20. Yang Z. PAML 4: Phylogenetic Analysis by Maximum Likelihood. *Mol Biol Evol*. 2007;24(8):1586–1591. <https://doi.org/10.1093/molbev/msm088>
21. Nei M, Gojobori T. Simple methods for estimating the number of synonymous and nonsynonymous nucleotide substitutions. *Mol Biol Evol*. 1986;3:418–426. <https://doi.org/10.1093/oxfordjournals.molbev.a040410>
22. Choi Y, Chan AP. PROVEAN web server: a tool to predict the functional effect of amino acid substitutions and indels. *Bioinformatics*. 2015;31(16):2745–2747. <https://doi.org/10.1093/bioinformatics/btv195>
23. Kumar P, Henikoff S, Ng PC. Predicting the effects of coding non-synonymous variants on protein function using the SIFT algorithm. *Nat Protoc*. 2009;4(7):1073–1081. <https://doi.org/10.1038/nprot.2009.86>
24. Li X, Romero P, Rani M, Dunker AK, Obradovic Z. Predicting protein disorder for N-, C-, and internal regions. *Genome Inform Ser Workshop Genome Inform*. 1999;10:30–40.
25. Romero P, Obradovic Z, Li X, Garner EC, Brown CJ, Dunker AK. Sequence complexity of disordered protein. *Proteins*. 2001;42:38–48. <https://doi.org/10.1002/1097-0134>
26. Charon J, Barra A, Walter J, et al. First experimental assessment of protein intrinsic disorder involvement in an RNA virus natural adaptive. *Process Mol. Biol. and Evol*. 2018;35(1):38–49. <https://doi.org/10.1093/molbev/msx249>
27. Singh A, Kumar A, Yadav R, Uversky VN, Giri R. Deciphering the dark proteome of Chikungunya virus. *Sci Rep*. 2018;8:5822. <https://doi.org/10.1038/s41598-018-23969-0>
28. Redwan EM, AlJaddawi AA, Uversky VN. Structural disorder in the proteome and interactome of Alkhurma virus (ALKV). *Cell Mol Life Sci*. 2019;76:577–608. <https://doi.org/10.1007/s00018-018-2968-8>
29. Malhis N, Jacobson M, Gsponer J. MoRFchibi SYSTEM: software tools for the identification of MoRFs in protein sequences. *Nucleic Acids Res*. 2016;44:W488–W493. <https://doi.org/10.1093/nar/gkw409>
30. Tang X, Wu C, Li X, et al. On the origin and continuing evolution of SARS-CoV-2 [published online ahead of print March 03, 2020]. *Microbiology*. 2020. <https://doi.org/10.1093/nsr/nwaa036>
31. Podder S, Ghosh TC. Exploring the differences in evolutionary rates between monogenic and polygenic disease genes in human. *Mol Biol Evol*. 2010;27:934–941. <https://doi.org/10.1093/molbev/msp297>
32. Kimura M. Evolutionary rate at the molecular level. *Nature*. 1968;217(5129):624–626. <https://doi.org/10.1038/217624a0>
33. Peck KM, Lauring AS. Complexities of viral mutation rates. *J Virol*. 2018;92(14):e01031–17. <https://doi.org/10.1128/JVI.01031-17>
34. Uversky VN, Gillespie JR, Fink AL. Why are “natively unfolded” proteins unstructured under physiologic conditions? *Proteins: Struct Funct Genet*. 2000;41:415–427. <https://doi.org/10.1002/1097-0134>
35. Saha D, Podder S, Ghosh TC. Overlapping regions in HIV-1 genome act as potential sites for host–virus interaction. *Front Microbiol*. 2016;7:1735.
36. Uversky VN. Intrinsically disordered proteins and their “mysterious” meta physics. *Front Phys*. 2019;7(10). <https://doi.org/10.3389/fphy.2019.00010>
37. Snead WT, Hayden CC, Gadok AK, Zhao C, Lafer EM, Rangamani P. Membrane fission by protein crowding. *Proc Natl Acad Sci USA*. 2017;114:E3258–E3267. <https://doi.org/10.1073/pnas.1616199114>
38. Snead D, Eliezer D. Intrinsically disordered proteins in synaptic vesicle trafficking and release. *J Biol Chem*. 2019;294(10):3325–3342. <https://doi.org/10.1074/jbc.REV118.006493>
39. Fakhree MAA, Blum C, Claessens MMAE. Shaping membranes with disordered proteins. *Arch Biochem Biophys*. 2019;677:108163. <https://doi.org/10.1016/j.abb.2019.108163>
40. Davies MN, Flower DR. Harnessing bioinformatics to discover new vaccines. *Drug Discov Today*. 2007;12:389–395. <https://doi.org/10.1016/j.drudis.2007.03.010>
41. Duret L. Neutral theory: the null hypothesis of molecular evolution. *Nature Education*. 2008;1(1):218.
42. Nei M. Selectionism and neutralism in molecular evolution. *Mol Biol Evol*. 2005;22(12):2318–2342. <https://doi.org/10.1093/molbev/msi242>
43. Goh GKM, Dunker AK, Uversky VN. Understanding viral transmission behavior via protein intrinsic disorder prediction: coronaviruses. *J Pathol*. 2012;1–13. <https://doi.org/10.1155/2012/738590>

44. Johnson DE, Xue B, Sickmeier MD, Meng J, Cortese MS, Oldfield CJ. High-throughput characterization of intrinsic disorder in proteins from the protein structure initiative. *J Struct Biol*. 2012;180:201–215. <https://doi.org/10.1016/j.jsb.2012.05.013>
45. Giri R, Kumar D, Sharma N, Uversky VN. Intrinsically disordered side of the zika virus proteome. *Front Cell Infect Microbiol*. 2016;6(144): 1–12. <https://doi.org/10.3389/fcimb.2016.00144>
46. Miller M. The importance of being flexible: the case of basic region leucine zipper transcriptional regulators. *Curr Protein Pept Sci*. 2009; 10(3):244–269. <https://doi.org/10.2174/138920309788452164>
47. Cheng Y, Oldfield CJ, Meng J, Romero P, Uversky VN, Dunker AK. Mining α -helix-forming molecular recognition features with cross species sequence alignments. *Biochemistry*. 2007;46(47):13468–13477. <https://doi.org/10.1021/bi7012273>
48. Vacic V, Oldfield CJ, Mohan A, et al. Characterization of molecular recognition features, MoRFs, and their binding partners. *J Proteome Res*. 2007;6(6):2351–2366. <https://doi.org/10.1021/pr0701411>
49. Katuwawala P, Zhenling Y, Lukasz JK. Computational prediction of MoRFs, short disorder-to-order transitioning protein binding regions. *Comput Struct Biotechnol J*. 2019;17:454–462. <https://doi.org/10.1016/j.csbj.2019.03.013>
50. Kotta-Loizou TGN, Hamodrakas SJ. Analysis of molecular recognition features (MoRFs) in membrane proteins. *Biochim Biophys Acta*. 2013; 1834(4):798–807. <https://doi.org/10.1016/j.bbapap.2013.01.006>
51. Singh AK, Uversky VN, Giri R. Understanding the interactability of chikungunya virus proteins via molecular recognition feature analysis. *RSC Adv*. 2018;8:27293–27303. <https://doi.org/10.1039/C8RA04760J>
52. Braun AR, Sevcsik E, Chin P, Rhoades E, Tristram-Nagle S, Sachs JN. Alphasynuclein induces both positive mean curvature and negative Gaussian curvature in membranes. *J Am Chem Soc*. 2012;134: 2613–2620. <https://doi.org/10.1021/ja208316h>
53. Bigay J, Casella JF, Drin G, Mesmin B, Antonny B. ArfGAP1 responds to membrane curvature through the folding of a lipid packing sensor motif. *EMBO J*. 2005;24:2244–2253. <https://doi.org/10.1038/sj.emboj.7600714>
54. Busch DJ, Houser JR, Hayden CC, Sherman MB, Lafer EM, Stachowiak JC. Intrinsically disordered proteins drive membrane curvature. *Nat Commun*. 2015;6:7875. <https://doi.org/10.1038/ncomms8875>
55. Fakhree MAA, Zijlstra N, Raiss CC, et al. The number of α -synuclein proteins per vesicle gives insights into its physiological function. *Sci Rep*. 2016;6:30658. <https://doi.org/10.1038/srep30658>

SUPPORTING INFORMATION

Additional supporting information may be found online in the Supporting Information section.

How to cite this article: Podder S, Ghosh A, Ghosh T.

Mutations in membrane-fusion subunit of spike glycoprotein play crucial role in the recent outbreak of COVID-19. *J Med Virol*. 2021;93:2790–2798. <https://doi.org/10.1002/jmv.26598>

RESEARCH ARTICLE

The protective role of metformin in autophagic status in peripheral blood mononuclear cells of type 2 diabetic patients

Debalina Bhattacharya¹ | Moumita Dutta² | Mainak Mukhopadhyay³ |
Maitree Bhattacharyya⁴ | Subhankar Chowdhury⁵ | Parimal Karmakar⁶

¹Department of Microbiology, Maulana Azad College, Kolkata, West Bengal, India

²Division of Electron Microscopy, ICMR-NICED, Kolkata, West Bengal, India

³Department of Biotechnology, JIS University, Agarpara, Kolkata, West Bengal, India

⁴Department of Biochemistry, University of Calcutta, Kolkata, West Bengal, India

⁵Department of Endocrinology & Metabolism, Institute of Postgraduate Medical Education and Research, Kolkata, West Bengal, India

⁶Department of Life Science and Biotechnology, Jadavpur University, Kolkata, West Bengal, India

Correspondence

Parimal Karmakar, Department of Life Science and Biotechnology, Jadavpur University, Kolkata-700032, West Bengal, India.
Email: pkarmakar_28@yahoo.co.in

Funding information

University Grants Commission,
Grant/Award Number: BL/14-15/0033

Abstract

Autophagy plays an important role in the pathophysiology of type 2 diabetes (T2D). Metformin is the most common antidiabetic drug. The main objective of this study was to explore the molecular mechanism of metformin in starvation-induced autophagy in peripheral blood mononuclear cells (PBMCs) of type 2 diabetic patients. PBMCs were isolated from 10 diabetic patients and 7 non-diabetic healthy volunteers. The autophagic puncta and markers were measured with the help of monodansylcadaverine staining and western blot. Additionally, transmission electron microscopy was also performed. No significant changes were observed in the initial autophagy marker protein levels in PBMCs of T2D after metformin treatment though diabetic PBMCs showed a high level of phospho-mammalian target of rapamycin, p62 and reduced expression of phospho-AMP-activated protein kinase and lysosomal membrane-associated protein 2, indicating a defect in autophagy. Also, induction of autophagy by tunicamycin resulted in apoptosis in diabetic PBMCs as observed by caspase-3 cleavage and reduced expression of Bcl2. Inhibition of autophagy by bafilomycin rendered consistent expression of p62 indicating a defect in the final process of autophagy. Further, electron microscopic studies also confirmed massive vacuole overload and a sign of apoptotic cell death in PBMCs of diabetic patients, whereas metformin treatment reduced the number of autophagic vacuoles perhaps by lysosomal fusion. Thus, our results indicate that defective autophagy in T2D is associated with the fusion process of lysosomes which could be overcome by metformin.

KEYWORDS

autophagy, lysosomal fusion, starvation, transmission electron microscopy, tunicamycin

1 | INTRODUCTION

Autophagy is a well-described evolutionarily conserved physiological process of elimination of cellular organelles and damaged proteins

in a regulated manner (Klionsky & Emr, 2000). It begins with the formation of double-membrane autophagic vacuoles with or without the portion of cytosols. After maturation, these structures fuse with the lysosome to form autolysosome which delivers the

Abbreviations: AMPK, AMP-activated protein kinase; BSA, bovine serum albumin; EBSS, Earle's balanced salt solution; EDTA, ethylenediaminetetraacetic acid; EGTA, ethylene glycol tetraacetic acid; ER, endoplasmic reticular; FBS, fetal bovine serum; HRP, horseradish peroxidase; MDC, monodansylcadaverine; MTT, 3-(4,5-dimethylthiazoyl-2-yl)-2,5-diphenyltetrazolium bromide; ND, non-diabetic; OsO₄, osmium tetroxide; PBMCs, peripheral blood mononuclear cells; PBS, phosphate-buffered saline; PMSF, phenylmethylsulfonyl fluoride; PVDF, polyvinylidene difluoride; SDS-PAGE, sodium dodecyl sulfate-polyacrylamide gel electrophoresis; T2D, type 2 diabetes.

hydrolytic enzymes responsible for the degradation of the engulfed material (Klionsky & Emr, 2000; Mehrpour, Esclatine, Beau, & Codogno, 2010). Normally, autophagy is a survival process, since it regulates aged protein turnover, eliminates damaged organelles, damaged proteins, and protects cells during starvation by recycling amino acids (Dalby, Tekedereli, Lopez-Berestein, & Ozpolat, 2010; Edinger & Thompson, 2004; Klionsky & Emr, 2000). Degradation and recycling of building blocks of the organelles or proteins are also important for the maintenance of cellular homeostasis, and other essential cellular processes such as programmed cell death (e.g., apoptosis), inflammation, adaptive immune mechanisms, etc. (Rubinsztein, Mariño, & Kroemer, 2011). It is well reported that autophagy regulates the inflammatory reactions in macrophages (Saitoh et al., 2008), keratinocytes (Lee et al., 2011), hypothalamus (Meng & Cai, 2011), adipocytes (Zhang, Zeng, & Jin, 2012), and peripheral blood mononuclear cells (PBMCs). However, cell death can also be triggered in a non-apoptotic manner through conspicuous autophagy. Failure of autophagy leads to the accumulation of damaged proteins inside the cells, which becomes the causal agent for the development of different types of disorders (Martinez-Vicente & Cuervo, 2007), autoimmunity (Choi, Ryter, & Levine, 2013), cancer (Yun & Lee, 2018), and cellular aging (Mizushima, Levine, Cuervo, & Klionsky, 2008), etc. Recent studies have revealed that autophagy may also play an important role in the development of type 2 diabetes (T2D; Las & Shirihi, 2010).

Global emergence of T2D and its association with obesity, dyslipidemia, hypertension and other metabolic disorders have become a major health challenge in this millennium. T2D is described as the abnormal regulation of nutrients and their metabolites that develop as a consequence of the combined insulin resistance and relative insulin deficiency (Islam et al., 2017). **T2D is also widely associated with oxidative stress, endoplasmic reticulum (ER) stress (Rovira-Llopis, Banuls, Apostolova, Morillas, & Hernandez-Mijares, 2014), inflammation and mitochondrial dysfunction that induces initiation of autophagy as a protective mechanism to maintain the cellular homeostasis and pancreatic beta-cell mass, but excessive and dysregulated autophagy may also play a role in the pathogenesis of T2D** (Nisbet, Sturtevant, & Prins, 2004). Available treatments for T2D mostly include different types of oral antidiabetic drugs. Among them, metformin (dimethylbiguanide) is the most commonly used drug, prescribed to almost 120 million people for the treatment of T2D (Pernicova & Korbonits, 2014). It acts by lowering the plasma insulin concentration through increasing the peripheral uptake of glucose and decreasing hepatic glucose production. Although, many studies have revealed that metformin acts by inhibiting the mitochondrial complex I and activating AMP-activated protein kinase (AMPK) along with improving insulin sensitivity (Galdieri, Gatla, Vancurova, & Vancura, 2016; Diaz-Morales et al., 2017; He, Zhu, Li, Zou, & Zhonglin, 2013; Samuel et al., 2017), the exact molecular mechanism of metformin-induced autophagy have not yet been fully explained. Another report has claimed that the activation of AMPK by metformin has stimulated the JNK1-Bcl2 signaling pathway and

disrupted the Beclin-1-Bcl2 complex, which, in turn, has induced autophagy in addition to attenuating high glucose-induced apoptosis in cultured human H9c2 cells (Uchizono, Alarcon, Wicksteed, Marsh, & Rhodes, 2007). However, the exact relationship between autophagy and T2D has been scarcely studied due to the lack of proper animal models (Rovira-Llopis, Diaz-Morales, Banuls, Blas-Garcia, & Polo, 2015). In this aspect, PBMCs offers a unique opportunity to perform these studies. Research has also implicated both oxidative and ER stress signaling pathways in the induction of autophagy as observed in the leukocytes of T2D patients. It has also been observed that autophagic markers Beclin-1, atg7, and LC3II/I increase in non-metformin-treated T2D, whereas metformin treatment reduces the mitochondrial superoxide concentration and increases the glutathione levels (Diaz-Morales et al., 2017). On the other hand, the association of inflammation with reduced levels of autophagy in PBMCs of T2D patients has also been detected (Alidazeh et al., 2018).

Consequently, the objective of this study was to explore the relationship between autophagy and the pathogenesis of T2D in PBMCs and also to analyze the molecular mechanism of autophagy induction by metformin in T2D. Therefore, an investigation was carried out by inducing autophagy either by Earle's balanced salt solution (EBSS) starvation or by metformin treatment in PBMCs isolated from type 2 diabetic patients and healthy non-diabetic (ND) controls. The outcome as observed through western blotting and transmission electron microscopy (TEM) identified certain defects in the later phases of autophagy after it was initiated in T2D PBMCs in the media. Also, T2D PBMCs are unable to overcome stress by themselves under prolong starvation and mostly dies by apoptosis, which can be readily prevented by metformin treatment that induces autophagy under cellular stress.

2 | MATERIALS AND METHODS

2.1 | Materials

EBSS, L-glutamine, Heparin and RPMI-1640 were purchased from Himedia. 3-(4,5-Dimethylthiazoyl-2-yl)-2,5-diphenyltetrazolium bromide (MTT) and bovine serum albumin (BSA) were purchased from SRL (India). Fetal bovine serum (FBS), penicillin-streptomycin were obtained from Life Technologies, USA. Ficol-Histopaque 1077, bafilomycin, tunicamycin, metformin hydrochloride, monodansylcadaverine (MDC), and OsO₄, Fura 2/AM, poly-L-lysine were obtained from Sigma-Aldrich (USA).

2.2 | Clinical subjects

A laboratory investigation was performed with 17 adults of both sexes, 55–65 years of age. Among them, 10 were type 2 diabetic patients whereas 7 were carefully matched as ND control. Healthy

controls in good health were defined as one who does not have any family history of chronic diseases such as diabetes, hypertension, or hypercholesterolemia, and were not taking any prescribed drugs, neither hypertensive nor lipid-lowering therapy or anti-platelet drugs. T2D was diagnosed according to the American Diabetes Association (ADA) criteria (Alberti & Zimmet, 1998). The exclusion criteria for T2D patients were based on the documented history of cardiovascular disease (stroke, ischemic heart disease, peripheral vascular disease, etc.), autoimmune, infectious, chronic inflammatory diseases, hematological, or malignant diseases. Moreover, none of the patients received insulin therapy, anti-inflammatory drugs (e.g., aspirin), antioxidant and micronutrient supplements, vitamins, and immunosuppressive drugs. The research has been carried out in accordance with the Declaration of Helsinki (2008) of the World Medical Association, that the ethical committee of the University of Calcutta and Institute of Post Graduate Medical Education and Research and Seth Sukhlal Karnani Memorial Hospital (IPGMER and SSKM) Kolkata, India, in which the work was performed has approved it, and that the subjects have given written informed consent to the work. The clinical and metabolic characteristics are given in Table 1.

2.3 | Isolation of PBMCs from venous blood

In all, 7–10 ml venous blood samples were collected from both ND healthy volunteers and T2D patient subjects in a heparinized vial. PBMCs were isolated by Ficol-Histopaque (1.077 g/ml) density gradient centrifugation (Bhattacharya, Santra, Ghosh, & Karmakar, 2014). After isolating PBMCs, 1×10^6 cells/ml were

cultured in RPMI-1640 medium (Himedia, India) supplemented with 10% fetal bovine serum $1 \times$ non-essential amino acids, $1 \times$ L-glutamine and 100 U/ml penicillin–100 μ g/ml streptomycin and incubated at 37°C with loose lids in a humidified atmosphere containing 5% CO₂ for 24 hr.

2.4 | MDC staining

PBMCs were attached in poly-L-lysine coated coverslip in a 35 mm plate for 2 hr at 37°C in a CO₂ incubator. Both the control and T2D PBMCs were either kept starved with EBSS or treated with 5 mM metformin in the media for 24 hr, respectively. The cells were then washed with $1 \times$ phosphate-buffered saline (PBS) thrice and incubated with 50 mmol/L MDC for 10 min at 37°C. After which the cells were mounted with DAPI on glass slides and viewed under a fluorescence microscope (Leica DM 2500).

2.5 | MTT assay

To study the cytotoxic effects of ER stress inducer tunicamycin and autophagy inhibitor bafilomycin A1 in a dose-dependent manner, healthy PBMCs were cultured at a density of 1×10^5 cells/ml in RPMI-1640. Tunicamycin and bafilomycin were suspended separately in a supplemented medium in different concentrations and incubated for 4 hr and 24 hr (tunicamycin) and 16 hr (bafilomycin) in 5% CO₂ incubator at 37°C. After incubation, cells were washed with $1 \times$ PBS twice and MTT assay was performed according to the standard protocol.

TABLE 1 Clinical and metabolic characteristics of the study subjects

n (female/male)	Healthy control 7 (3/4)	Type 2 diabetic 10 (4/6)
Age (years)	57.5 \pm 5.09	59 \pm 4.45
BMI (kg/m ²)	28 \pm 1.8	32.9 \pm 2
Duration of type 2 diabetes (years)	–	5–10
HbA1C (%)	5.5 \pm 1.2	7.47 \pm 0.35
Fasting plasma glucose (mmol/L)	5.7 \pm 0.18	9.2 \pm 0.8
Plasma triacylglycerols (mmol/L)	0.83 \pm 1.2	1.72 \pm 0.23
Hypertension (SBP \geq 140 mm Hg, DBP \geq 90 mm Hg)	–	4
Are diabetic patients taking metformin medicine during study	–	8 patients out of 10 ^a
Anti-hypertensive drug	–	4

Data are means \pm SD.

Abbreviations: BMI, body mass index; DBP, diastolic blood pressure; HbA1C, hemoglobin A1c; n, number of male and female donors; SBP, systolic blood pressure.

^aIn all, 8 patients out of 10 were taking metformin previously but remaining 2 of them were not taking metformin medicine from last 3–6 months. PBMCs obtained from the patients had been exposed to “metformin” for a long time.

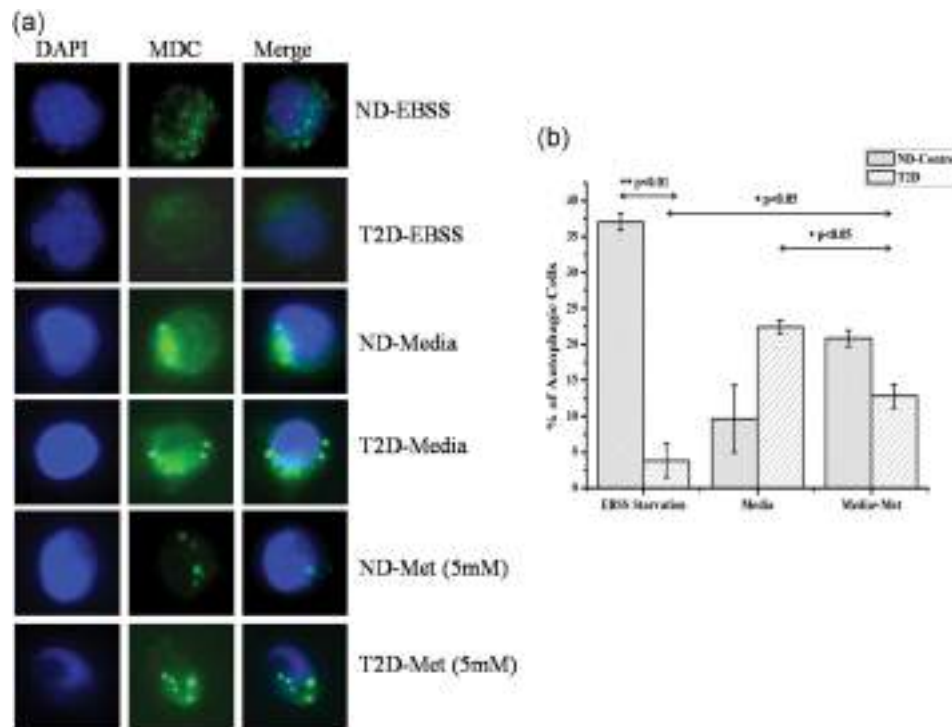


FIGURE 1 Measurement of autophagic puncta in PBMCs of T2D patients and ND control: PBMCs of ND control and T2D were starved with or without EBSS or treated with metformin (5 mM) along with the complete medium for 24 hr. (a) After MDC staining the autophagic (LC3) puncta was observed under fluorescence microscopy in $\times 100$ magnification. (b) Graphical representation of MDC staining at 24 hr of all the experimental set. More than 300 cells were analyzed for each condition. Data are shown as mean \pm SEM. Data shown are representative of three ND control and three T2D patient samples from three independent experiments * $p < .05$ statistical analysis was performed using one-way ANOVA followed by the Sidak test when a subset of conditions (ND control EBSS and T2D EBSS as experimental subset 1 and ND control metformin and T2D metformin as subset 2) was selected for pairwise comparisons; and Tukey test when all possible combinations were tested. ANOVA, analysis of variance; EBSS, Earle's balanced salt solution; MDC, monodansylcadaverine; ND, non-diabetic; PBMCs, peripheral blood mononuclear cells; SEM, standard error of the mean; T2D, type 2 diabetes

2.6 | Western blotting

After treatment, PBMCs were lysed in lysis buffer containing 1% Triton X-100, 50 mM sodium chloride, 50 mM sodium fluoride, 20 mM Tris (pH 7.4), 1 mM ethylenediaminetetraacetic acid (EDTA), 1 mM ethylene glycol tetraacetic acid (EGTA), 1 mM sodium vanadate, 0.2 mM phenylmethylsulfonyl fluoride (PMSF; Sigma), 0.5% NP-40 and protease inhibitor cocktail (Sigma) for 30 min. Protein concentration was measured by the Bradford method (Bradford, 1976). Cell lysate containing equal quantities of protein (75 μ g) were solubilized in Laemmli buffer, boiled for 5 min, and electrophoresed on a 10–12% sodium dodecyl sulfate (SDS) polyacrylamide gel and transferred to polyvinylidene difluoride (PVDF) membrane. Nonspecific binding was blocked with 5% nonfat dry milk in 1 \times Tris-Cl, pH 7.6, with 0.1% Tween 20 (1 \times TBS-T) followed by incubation with the appropriate primary antibodies for overnight. Membranes were washed with 1 \times TBS-T, and blots were incubated with anti-rabbit or anti-mouse secondary antibodies conjugated to horseradish peroxidase (HRP) (Santa Cruz) at RT. Bound antibodies were detected by the ECL (enhanced chemiluminescent) immunoblotting detection reagent (Santa Cruz).

2.7 | TEM

PBMCs were kept in cell media or treated with 5 mM metformin for 24 hr. Cells were then collected and prefixed with 3% glutaraldehyde in 0.1 M sodium cacodylate buffer (pH 7.4). These cells were then postfixed with 1% osmium tetroxide, followed by dehydration with ascending grades of acetone and finally embedded in Agar 100 resin and polymerization at 60°C. The ultrathin sections of the cells were obtained using a Leica Ultracut UCT ultramicrotome, picked up on nickel grids and dual-stained with 2% aqueous uranyl acetate and 0.2% lead citrate. The sections were visualized under an FEI Tecnai 12 Bio-twin transmission electron microscope at an accelerating voltage of 100 kV.

2.8 | Statistical analysis

Statistical analysis was performed using R statistical software version 3.5.1 (R: A language and environment for statistical computing; R Foundation for Statistical Computing, Vienna, Austria). The data were expressed as mean value \pm standard error of the mean (SEM).

Comparisons between the control groups and T2D groups for parametric data were made with one-way analysis of variance (ANOVA) followed by the Sidak test when a subset of conditions was selected for pairwise comparisons; and Tukey test when all possible combinations were tested. $p < .05$ was considered as significant, coded by asterisks: $<.05$ (*).

3 | RESULT

3.1 | Autophagic activity in PBMCs of diabetic patients and healthy individuals

Starvation induced autophagy was measured in PBMCs of diabetic patients (T2D) and ND healthy control by MDC staining. In Figure 1a, ND control PBMCs starved with EBSS showed many MDC-stained green puncta (** $p < .01$) whereas T2D PBMCs starved with EBSS, loses its morphology and membrane integrity. Interestingly T2D PBMCs kept in media showed some MDC-stained green puncta (* $p < .05$) which is reduced in metformin-treated T2D PBMCs. Figure 1b shows the percentage of autophagic punctuated cells in graphical representation. We also confirmed our observation with the immune blotting of total cellular extract for autophagy marker

proteins from PBMCs of T2D patients treated with or without metformin, along with ND control PBMCs (Figure 2). As seen in Figure 2a the band intensity of LC3B-II is almost equal in T2D PBMCs with or without metformin treatment (compares L3 with L5). In both the cases, PBMCs were cultured in a complete medium. A faint band of LC3B-II was observed in T2D PBMCs starved with EBSS (L2) that correlates with the data found in the intensity diagram as shown in Figure 2b.

The initiator protein of autophagy Beclin-1 and Atg5 were significantly reduced (** $p < .01$) in T2D PBMCs starved with EBSS as seen in Figure 2a (L2). But the expression was almost the same with or without the metformin treatment (L3 and L5) whereas ND control PBMCs starved with EBSS show an increased expression of Beclin-1 (L1 of Figure 2a and 2c) and ATG5 (L1 of Figure 2a and 2d).

In Figure 2a the bands of p62 were increased in both T2D PBMCs starved with EBSS and without metformin treatment, respectively (L2 and L3). But T2D PBMCs treated with metformin as well as ND control PBMCs either with EBSS or metformin showed much-reduced expression of p62. Statistical analysis of the same has been shown in Figure 2e.

In Figure 3a, T2D PBMCs either starved with EBSS or kept in media showed increased phosphorylation of mammalian target of rapamycin (mTOR; L2 and L3). But the total mTOR status remains the

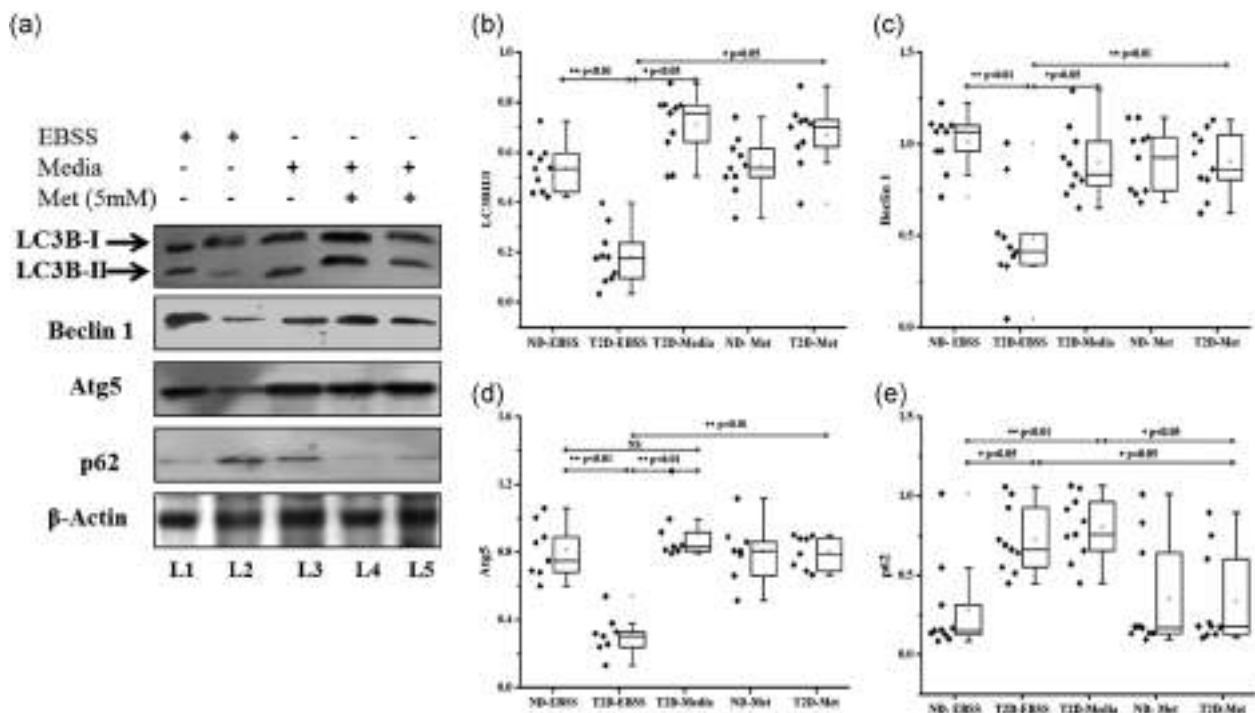


FIGURE 2 Expression of autophagic markers in PBMCs of T2D patients and ND controls: PBMCs of ND control and T2D PBMCs were starved with or without EBSS or treated with metformin (5 mM) along with complete medium for 24 hr. (a) Total cell lysate was immunoblotted with anti-LC3B, anti-Beclin-1, anti-Atg5, and anti-p62 antibodies. Here β-actin was used as a loading control. (b–e) Bands intensity was measured and box plot represents the ratio of LC3B-II/LC3B-I, Beclin-1/β-actin, Atg5/β-actin, and p62/β-actin for 10 T2D and 7 ND control, respectively ($n = 10$). * $p < .05$ statistical analysis was performed using one-way ANOVA followed by Tukey test for all possible combinations. L1 = ND EBSS, L2 = T2D EBSS, L3 = T2D Media, L4 = ND Met, L5 = T2D Met. ANOVA, analysis of variance; EBSS, Earle's balanced salt solution; ND, non-diabetic; PBMCs, peripheral blood mononuclear cells; T2D, type 2 diabetes

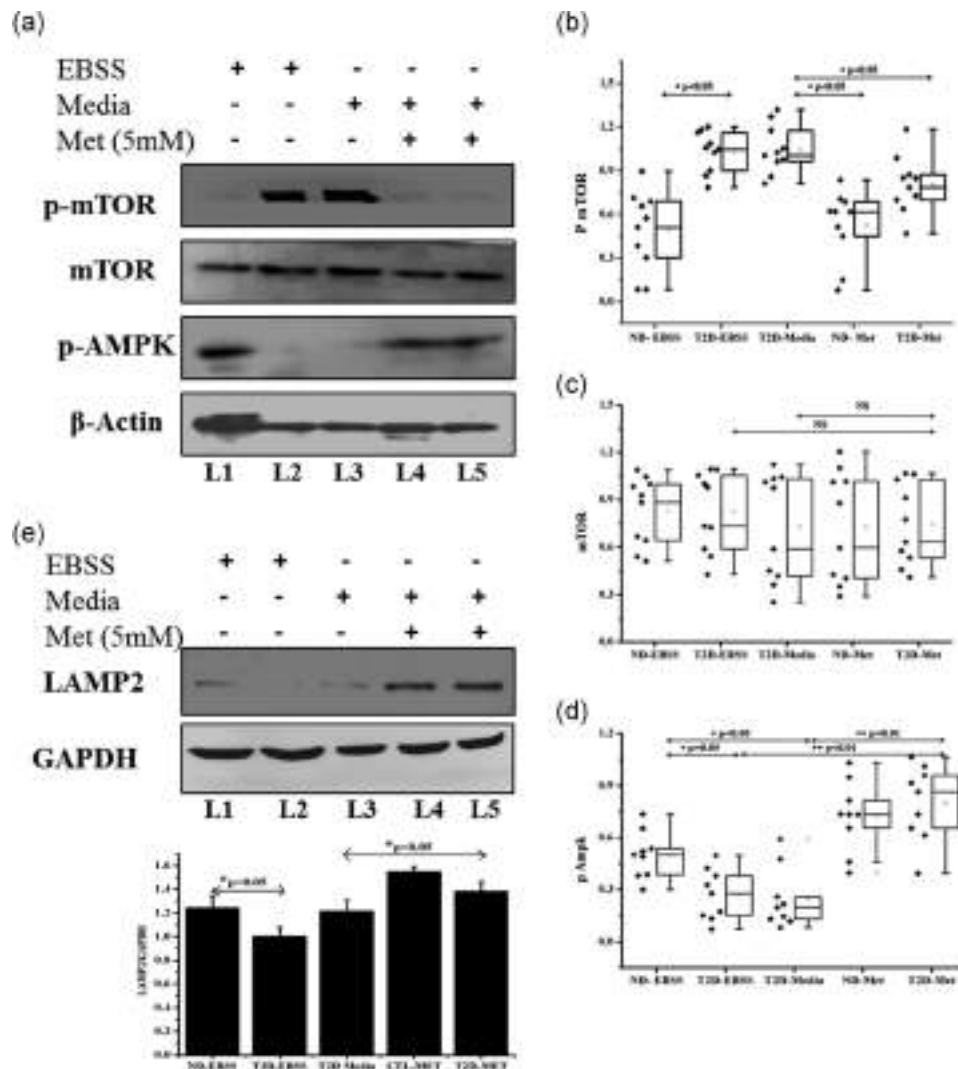


FIGURE 3 Expression of autophagic regulator in PBMCs from T2D patients and ND controls: PBMCs of ND control and T2D were starved with or without EBSS or treated with metformin (5 mM) along with complete medium for 24 hr. (a) Total cell lysate was immunoblotted with anti-p-mTOR, anti-mTOR, and anti-p-AMPK antibodies. Here β-actin was used as a loading control. (b–d) Band intensity was measured and box plot represents the ratio of p-mTOR/β-actin, mTOR/β-actin, and p-AMPK/β-actin for 10 T2D and 7 ND control, respectively (n = 10). (e) Total cell lysate was immunoblotted with anti-LAMP2 antibody. Here GAPDH was used as a loading control. Graphical representation of ratio LAMP2/GAPDH of three T2D and three ND control was used. *p < .05 statistical analysis was performed using one-way ANOVA followed by Tukey test for all possible combinations. L1 = ND EBSS, L2 = T2D EBSS, L3 = T2D Media, L4 = ND Met, L5 = T2D Met. ANOVA, analysis of variance; EBSS, Earle's balanced salt solution; GAPDH, glyceraldehyde 3-phosphate dehydrogenase; LAMP2, lysosomal membrane-associated protein 2; ND, non-diabetic; p-AMPK, phospho-AMP-activated protein kinase; p-mTOR, phospho-mammalian target of rapamycin; PBMCs, peripheral blood mononuclear cells; T2D, type 2 diabetes

same, which is uniform with the intensity diagram of phospho-mTOR (p-mTOR), as shown in Figure 3b. Simultaneously, the phosphorylation of AMPK of T2D PBMCs was hardly visible in the above-mentioned condition, but the band was readily observed in ND control PBMCs either with EBSS (L1), or metformin (L4) and T2D PBMCs (L5) treated with metformin, respectively. The band intensity diagram of phospho-AMP-activated protein kinase (p-AMPK) is shown in Figure 3d. In Figure 3e as can be observed lysosomal membrane-associated protein 2 (LAMP2) expression is visible in ND control PBMCs starved with EBSS or with metformin treatment. But the band intensity gets significantly reduced in T2D PBMCs starved

with EBSS (L2) or kept only in media (L3) whereas metformin treatment increases the band intensity (L5).

3.2 | The ER stress induced by tunicamycin in T2D PBMCs reduces autophagy and induces apoptosis

To investigate the autophagic status in T2D, another autophagy inducer tunicamycin was applied in T2D PBMCs instead of metformin. The dose of tunicamycin was determined by cytotoxicity assay in PBMCs of healthy donors with different concentrations as seen in

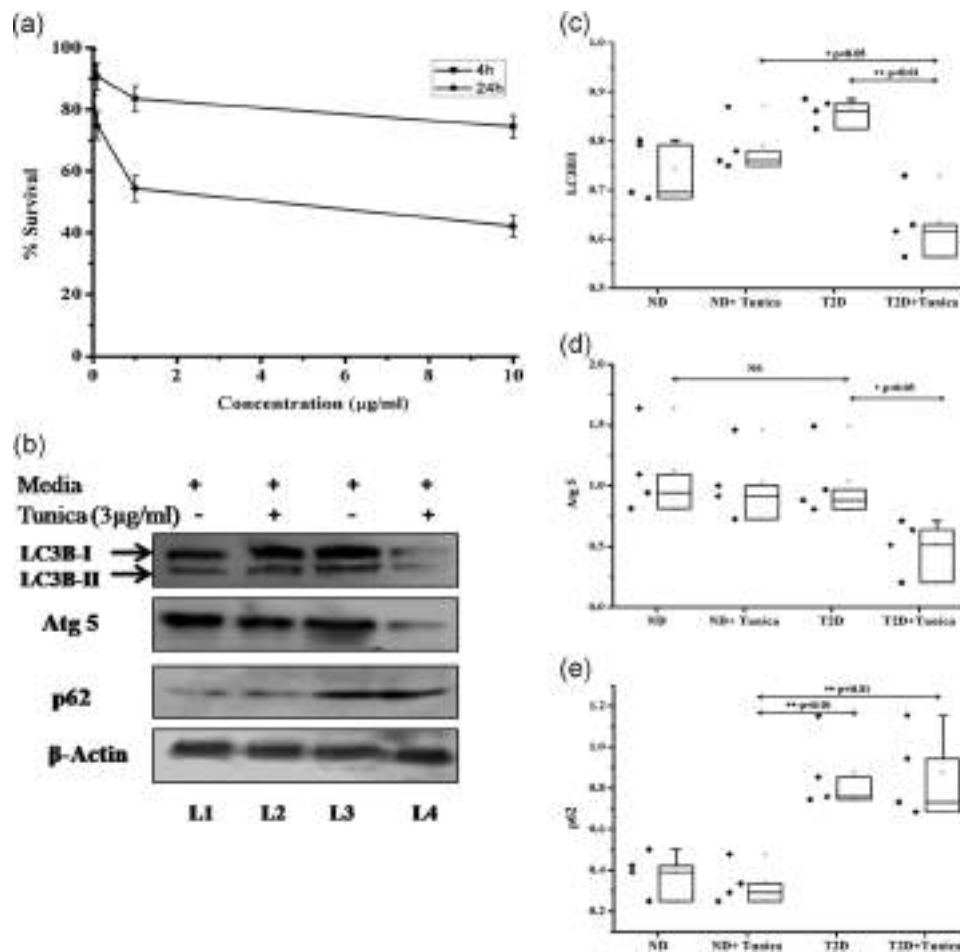


FIGURE 4 Effect of tunicamycin in induction of autophagy in PBMCs of T2D patients and ND control: (a) % of survival of PBMCs of ND control with tunicamycin from 0 to 10 µg/ml at 4 and 24 hr. (b) PBMCs of ND control and T2D were treated with 3 µg/ml tunicamycin along with a complete medium for 24 hr. Total cell lysate was immunoblotted with anti-LC3B-I, anti-Atg5, and anti-p62 antibodies. Here β-actin was used as a loading control. (c–e) Band intensity was measured and the box plot represents the ratio of LC3B-II/LC3B-I, Atg5/β-actin, and p62/β-actin for four T2D and four ND control, respectively ($n = 4$). $*p < .05$ statistical analysis was performed using one-way ANOVA followed by Sidak test when a subset of conditions (ND control media and T2D media as subset 1 and ND control Tunica and T2D Tunica as subset 2) was selected for pairwise comparisons; and Tukey test when all possible combinations were tested. L1 = ND, L2 = ND Tunica, L3 = T2D, L4 = T2D Tunica. ANOVA, analysis of variance; ND, non-diabetic; PBMCs, peripheral blood mononuclear cells; T2D, type 2 diabetes

Figure 4a. Next, we investigated the role of tunicamycin in autophagy in T2D PBMCs compared to ND control PBMCs. As seen in Figure 4b the band corresponding to LC3B-II was significantly reduced ($**p < .01$) in T2D PBMCs treated with tunicamycin. The ratio of LC3B-II/LC3B-I was shown in the intensity diagram of Figure 4c. Similarly, Atg5 expression was reduced only in T2D PBMCs (L4) treated with tunicamycin as shown in Figure 4b and in the intensity diagram of Figure 4d. In Figure 4e, we found that the band intensity of p62 was significantly ($**p < .01$) increased in both T2D PBMCs with (L4) or without tunicamycin treatment (L3).

Next, the apoptotic status of T2D PBMCs was examined that were treated with or without tunicamycin. In Figure 5a the cleavage of caspase-3 was shown in T2D PBMCs treated with tunicamycin (L4). Similarly, Bcl2 was significantly ($*p < .05$) reduced in the above case (L4). The cleavage of caspase-3 and Bcl2 compared to β-actin were plotted in Figure 5b and 5c, respectively.

3.3 | Inhibition of autophagosome fusion with lysosome by bafilomycin A1

To investigate the autophagic flux, we blocked LC3 degradation with the inhibitor of acidification inside the lysosome by using bafilomycin A1, in T2D PBMCs. In Figure 6a the dose of bafilomycin A1 was determined in ND control PBMCs by cytotoxicity assay with different concentrations of bafilomycin A1. In Figure 6b, the band of LC3B-II was only visible in ND control PBMCs at 50 nM of bafilomycin A1 (L3). Interestingly, in the presence of bafilomycin A1 the conversion of cytosolic LC3B-I into autophagosome bound LC3B-II was stimulated in T2D PBMCs (L4–L6) but there was no significant change ($p > .05$) in the band ratio of LC3B-II/I in T2D PBMCs as shown in Figure 6c.

Another method for detecting the autophagic flux is the measurement of p62 (SQSTM1/sequestosome 1), a selective substrate

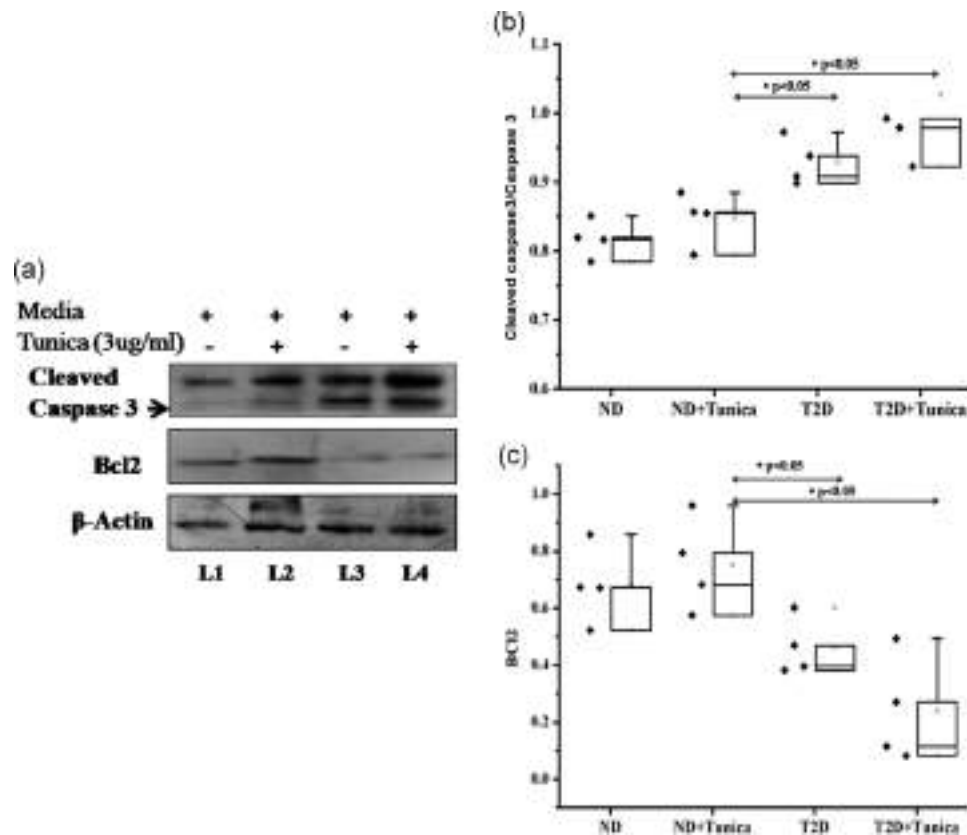


FIGURE 5 Effect of tunicamycin in apoptosis in PBMCs of T2D patients and ND controls: (a) PBMCs of ND control and T2D were treated with 3 μ g/ml tunicamycin along with complete medium for 24 hr. Total cell lysate was immunoblotted with anti-caspase-3, anti-Bcl2 antibodies. Here β -actin was used as a loading control. (b,c) Band intensity was measured and the box plot represents the ratio of caspase-3/ β -actin and Bcl2/ β -actin for four T2D and four ND control, respectively ($n = 4$). * $p < .05$ statistical analysis was performed using one-way ANOVA followed by the Sidak test when a subset of conditions (ND control media and T2D media as subset 1 and ND control Tunica and T2D Tunica as subset 2) was selected for pairwise comparisons; and Tukey test when all possible combinations were tested. L1 = ND, L2 = ND Tunica, L3 = T2D, L4 = T2D Tunica. ANOVA, analysis of variance; ND, non-diabetic; PBMCs, peripheral blood mononuclear cells; T2D, type 2 diabetes

of autophagy degradation. The band intensity of p62 was significantly (* $p < .05$) increased with the increasing dose of bafilomycin A1 from 10 to 50 nM in T2D PBMCs compared to ND control PBMCs as seen in Figure 6b as well as in the intensity diagram of Figure 6d.

3.4 | Altered autophagy in T2D PBMCs with and without metformin treatment by electron microscopic study

Electron microscopy was used to directly visualize autophagic vacuoles in T2D PBMCs with or without metformin treatment compared to ND control PBMCs (Figure 7). As observed in Figure 7b, T2D PBMCs in media exhibits multiple vesicle formation together with polymorphonuclear structure and chromatin clumping (massive vacuole overload and sign of apoptotic cell death) as compared to normal healthy PBMCs (Figure 7a), whereas T2D PBMCs in media with 5 mM metformin (Figure 7c) reveals double-membrane structure of autophagic vacuoles with cytoplasmic material fused with black dense autolysosome.

4 | DISCUSSION

Recent studies have concluded that reduced autophagy is a characteristic feature of T2D PBMCs (Bhansali, Bhansali, Walia, Saikia, & Dhawan, 2017) but the exact mechanisms underlying the dysfunction of autophagy in PBMCs of diabetic patients still remain unknown. Efforts have been made to understand the defective autophagic pathway in PBMCs of diabetic patients and the role of metformin in the modulation of such pathways. Diaz-Morales et al. (2018) have reported that diabetic PBMCs have higher ER stress than ND control that are greatly reduced when treated with metformin. In the present work, it was observed that T2D PBMCs undergo autophagy in normal cell culture media to overcome these ER stress and give more MDC-stained puncta as shown in Figure 1 whereas treatment with metformin reduces the puncta significantly. The probable cause may be attributed to the fact that the formation of puncta mostly occurs in the early phase of autophagy whereas metformin treatment causes the cells to enter the later phase of autophagy, which subsequently leads to the fusion of autophagosomes with the lysosome and giving rise to reduced puncta. In addition to this, no significant difference

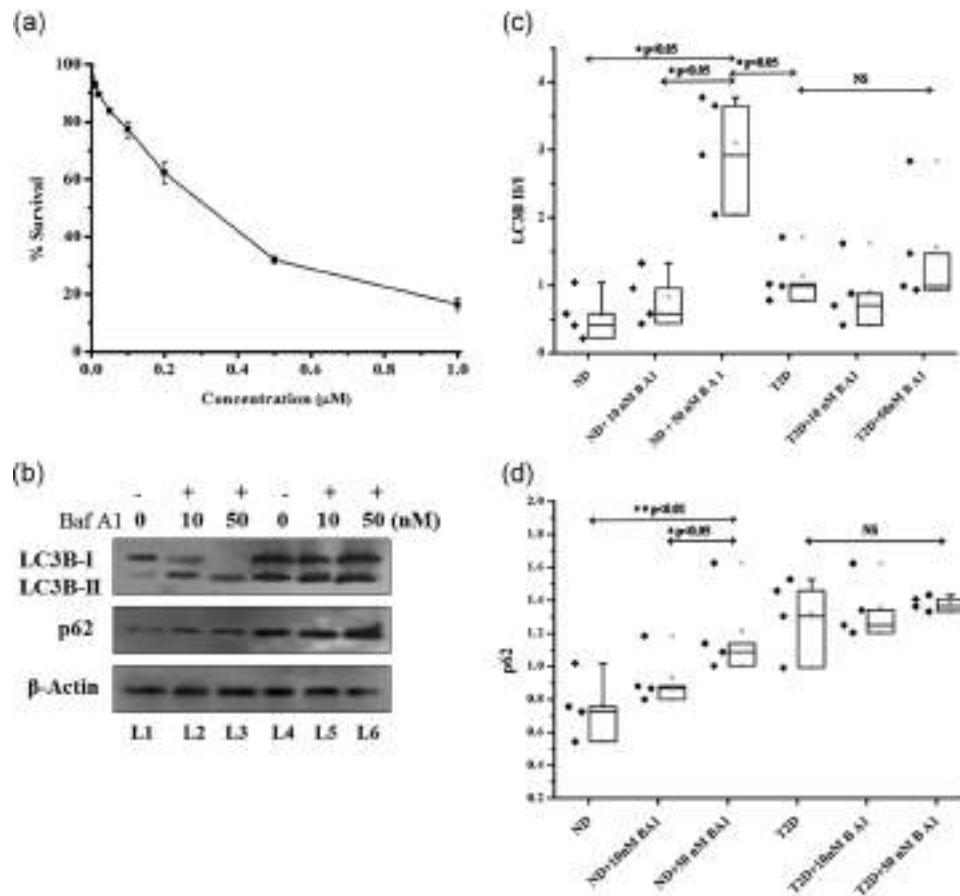


FIGURE 6 Effect of bafilomycin A1 in inhibition of autophagosome fusion in PBMCs of T2D patients and ND controls: (a) % of survival of PBMCs of ND control with bafilomycin A1 from 0 to 1 μM for 16 hr. (b) PBMCs of ND control and T2D were treated with 0, 10, and 50 nM for 6 hr. Total cell lysate was immunoblotted with anti-LC3B and anti-p62 antibodies. Here β-actin was used as a loading control. (c,d) Band intensity was measured and the box plot represents the ratio LC3B-II/LC3B-I and p62/β-actin for four T2D and four ND control, respectively ($n = 4$). * $p < .05$ statistical analysis was performed using one-way ANOVA followed by the Sidak test when a subset of conditions (ND control media and T2D media as experimental subset 1 and ND control B A1 10 nM and T2D B A1 10 nM as subset 2 and so on) was selected for pairwise comparisons; and Tukey test when all possible combinations were tested. L1 = ND, L2 = ND + 10 nM BA1, L3 = ND + 50 nM BA1, L4 = T2D, L5 = T2D + 10 nM BA1, L6 = T2D + 50 nM BA1. ANOVA, analysis of variance; ND, non-diabetic; PBMCs, peripheral blood mononuclear cells; T2D, type 2 diabetes

was detected in the protein expression of LC3B, Beclin-1, and Atg5 (two proteins involved in the initiation and elongation process of autophagy) of T2D PBMCs with or without metformin treatment. It is due to the fact that the three proteins are absolutely required before autophagosomal fusion to take place, so their levels are maintained both in the presence or absence of metformin (Figure 2a, compare L3 and L5). Therefore, our data strongly support the previous study (Alexandraki et al., 2008) where it was reported that metformin has little or no role in the initiation of autophagy in diabetic PBMCs. Moreover, starvation also gives added value to the pre-existing stress for T2D PBMCs where the lack of autophagy enforces the cells to die. Thus, further experiments need to be carried out in order to study the cellular conditions of diabetic PBMCs under nutrient-deficiency.

Though reports available regarding the expression of different autophagy-related genes in T2D is confusing, but investigation carried out in leukocytes from T2D patients display activation

of autophagy, expressed by higher LC3B, Beclin-1 than those seen in healthy volunteers, whereas metformin also helps in the modulation of autophagy-related genes and proteins (Diaz-Morales et al., 2017, 2018). Other studies show that the level of autophagy-related genes and proteins, MAP1LC3B, Atg5, Atg12, and Atg7, are normal in muscle and adipose tissues in T2D patients (Kruse, Vind, Petersson, Kristensen, & Hojlund, 2015). Information regarding altered autophagy in β cells of T2D patients where gene expression of Beclin-1 and ATG1 remains unaltered has also been confirmed (Masini, Bugliani, Lupi, Del Guerra, & Boggi, 2009; Ost et al., 2010). These findings along with our observation indicate that the changes in the autophagic activity do not necessarily require alteration of the expression of all autophagy-related genes but autophagy pathway regulation may be the key factor.

Autophagic flux is a more reliable indicator of autophagic activity than measurements of autophagosome numbers (Loos, Toit, & Hofmeyr, 2014). Accumulation of the p62/SQSTM1 protein could be

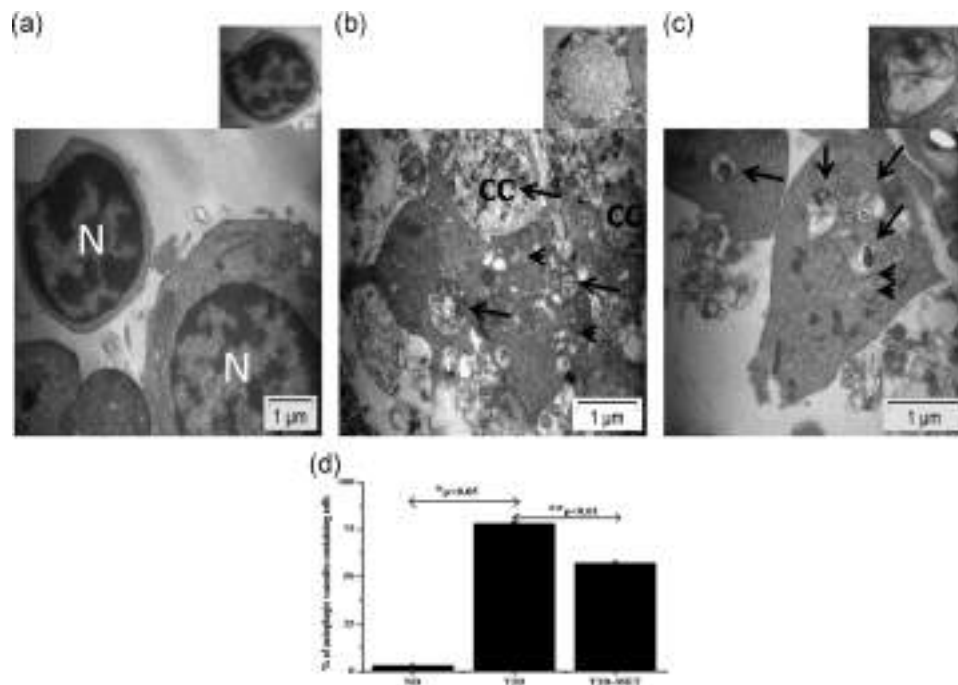


FIGURE 7 Autophagic vacuole formations in T2D PBMCs with or without metformin treatment by TEM: transmission electron micrographs of (a) ND control PBMCs in media (b) T2D PBMCs in media showing multiple vesicle formation and polymorphonuclear structure (c) T2D PBMCs in media with 5 mM metformin showing autophagic vacuoles. Arrows indicate autophagic vacuoles and arrowheads indicate multiple vesicle formation in type 2 diabetes. Inset picture of image (c) shows a double-membrane structure of autophagosome with cytoplasmic material fused with black dense autolysosome which is indicated in the original image (double arrowheads); $\times 10,000$ magnification. CC, chromatin clumping; N, nucleus; ND, non-diabetic; PBMCs, peripheral blood mononuclear cells; T2D, type 2 diabetes; TEM, transmission electron microscopy

an important marker of the consequences of altered autophagic flux, especially when down stream autophagy pathway is suppressed (Mizushima and Yoshimori, 2007). Our data shows that PBMCs of diabetic patients have a higher p62/SQSTM1 protein level both in the starved condition as well as in the media compared to ND control (compare L2 and L3, Figure 2a). These suggest that the defect in the removal of autophagosome leads to the accumulation of autophagic cargo in diabetic PBMCs both in prolong starvation as well as in media.

Several studies have reported that reduced expression of LAMP2 and cathepsin B and D alter the later phases of autophagy (autophagosome maturation and lysosomal events) in diabetic β cells (Marchetti et al., 2007; Kaniuk et al., 2007; Masini et al., 2009). Similar findings have also been observed in our case, where LAMP2 expression was significantly reduced in T2D PBMCs when the cells were kept in media (L3) or in starved condition (L2) in addition to metformin treatment which increases the expression of LAMP2 in T2D PBMCs (L5, Figure 3e).

Several studies have stated that metformin potentiates AMPK activity (Galdieri et al., 2016; Eriksson and Nyström, 2014; Kobayashi, Xu, Chen, & Liang, 2012). In our study, metformin induces phosphorylation of AMPK in ND control and T2D PBMCs (L4 and L5, Figure 3a). This data was further supported by the previous findings where it was reported that insulin reduces the phosphorylation of AMPK and

inhibits its activity in L6 myotubes (Deng et al., 2015). AMPK is an important energy-sensing enzyme involved in the maintenance of cellular energy homeostasis. Besides several other actions, AMPK can also inhibit the mTOR activity thereby promoting autophagy (Masini et al., 2009). Our results clearly establish the fact that mTOR gets activated in T2D PBMCs when kept in cell media and gets deactivated mostly after metformin treatment (Figure 3a). Reports into the main causal agent which leads to the accumulation of autophagic materials identifies mTOR which acts by inhibiting autophagy initiation and nucleation by further inhibiting the ULK1 complex and Vps34 complex (Dossou & Basu, 2019; Loos et al., 2014), and metformin that promotes the elimination of this autophagic vacuoles by reducing the activation of mTOR in autophagy. It is also reported that metformin can inhibit mTORC1 in an AMPK-independent manner (Kalendar et al., 2010). These findings suggest that a defect in autophagy in T2D is associated with the deregulation of p-AMPK and p-mTOR activity which can be corrected by metformin (Figure 3).

Tunicamycin, an ER stress inducer stimulates an autophagic response in normal cells. In our study, it was found that in presence of tunicamycin the autophagic response was significantly reduced ($**p < .01$) in diabetic PBMCs in terms of LC3B and Atg5 as compared to ND controls (L4, Figure 4b). But p62/SQSTM1 protein level gets significantly increased in T2D PBMCs with or without tunicamycin indicating that there may be some dispute in the clearance of

autophagic vacuoles in diabetic condition as an accumulation of p62 indicates blockade of autophagic flux (compare L3 and L4, Figure 4b). Additionally, under excessive ER stress conditions, autophagic vacuoles accumulate and lead to apoptotic features as observed by caspase-3 cleavage and low expression of anti-apoptotic protein Bcl2 in T2D PBMCs treated with tunicamycin (Figure 5).

In addition, our results also showed the LC3B-II/I ratio in the presence of bafilomycin remains unaltered in PBMCs of T2D patients in comparison to ND control (Figure 6b). But the increased expression of p62 in PBMCs of T2D suggests that T2D PBMCs are able to enter the early phases of autophagy but the later phases of autophagy are likely to be defective. Consistently with this data, we also found an increased number of autophagic vacuoles and chromatin clumping in T2D PBMCs that were kept only in cell media, and which disappears after metformin treatment indicating the positive role of metformin in the clearance of autophagy vacuoles, that is the fusion of the autophagosome with the lysosome (Figure 7).

5 | CONCLUSION

In conclusion, type 2 diabetic PBMCs, after nutrient deprivation or tunicamycin treatment can initiate an autophagic response but due to lack of fusion with the lysosome, it helps in the accumulation of autophagic vacuoles and cells eventually die by apoptosis. Thus, in type 2 diabetic PBMCs there might be no prevailing hindrance in the initial phase of autophagy but the later phase of autophagy may have some dispute in fusion with lysosome which can be completely reversed by metformin treatment.

ACKNOWLEDGEMENT

This work was fully funded by UGC-Dr. D.S. Kothari postdoctoral fellowship, India (File No. BL/14-15/0033).

CONFLICT OF INTERESTS

The authors declare that there are no conflict of interests.

REFERENCES

- Alberti, K. G., & Zimmet, P. Z. (1998). Definition, diagnosis and classification of diabetes mellitus and its complications. Part 1: Diagnosis and classification of diabetes mellitus provisional report of a WHO consultation. *Diabetic Medicine*, 15(7), 539–553. [https://doi.org/10.1002/\(sici\)1096-9136\(199807\)15:7<539::aid-dia668>3.0.co;2-s](https://doi.org/10.1002/(sici)1096-9136(199807)15:7<539::aid-dia668>3.0.co;2-s)
- Alexandraki, K. I., Piperi, C., Ziakas, P. D., Apostolopoulos, N. V., Makrilakis, K., ... Kalofoutis, A. (2008). Cytokine secretion in long-standing diabetes mellitus type 1 and 2: Associations with low-grade systemic inflammation. *Journal of Clinical Immunology*, 28(4), 314–321. <https://doi.org/10.1007/s10875-007-9164-1>
- Alidazeh, S., Mazloom, H., Sadeghi, A., Emamgholipour, S., Golestani, A., ... Meshkani, R. (2018). Evidence for the link between defective autophagy and inflammation in peripheral blood mononuclear cells of type 2 diabetic patients. *Journal of Physiology and Biochemistry*, 74(3), 369–379. <https://doi.org/10.1007/s13105-018-0624-2>
- Bhansali, S., Bhansali, A., Walia, R., Saikia, U. N., & Dhawan, V. (2017). Alterations in mitochondrial oxidative stress and mitophagy in subjects with prediabetes and type 2 diabetes mellitus. *Front Endocrinol (Lausanne)*, 8, 347. <https://doi.org/10.3389/fendo.2017.00347>
- Bhattacharya, D., Santra, C. R., Ghosh, A. N., & Karmakar, P. (2014). Differential toxicity of rod and spherical zinc oxide nanoparticles on human peripheral blood mononuclear cells. *Journal of Biomedical Nanotechnology*, 10(4), 707–716. <https://doi.org/10.1166/jbn.2014.1744>
- Bradford, M. M. (1976). A rapid and sensitive method for the quantitation of microgram quantities of protein utilizing the principle of protein-dye binding. *Analytical Biochemistry*, 72(1-2), 248–254. [https://doi.org/10.1016/0003-2697\(76\)90527-3](https://doi.org/10.1016/0003-2697(76)90527-3)
- Choi, A. M., Ryter, S. W., & Levine, B. (2013). Autophagy in human health and disease. *The New England Journal of Medicine*, 368, 651–662. <https://doi.org/10.1056/NEJMr1205406>
- Dalby, K. N., Tekedereli, I., Lopez-Berestein, G., & Ozpolat, B. (2010). Targeting the prodeath and prosurvival functions of autophagy as novel therapeutic strategies in cancer. *Autophagy*, 6(3), 322–329. <https://doi.org/10.4161/auto.6.3.11625>
- Deng, H. P., Chai, J. K., Shen, C. A., Zhang, X. B., Ma, L., Sun, T. J., ... Dong, N. (2015). Insulin down-regulates the expression of ubiquitin E3 ligases partially by inhibiting the activity and expression of AMP-activated protein kinase in L6 myotubes. *Bioscience Reports*, 35, e00242. <https://doi.org/10.1042/BSR20150017>
- Diaz-Morales, N., Iannantuoni, F., Escribano-Lopez, I., Bañuls, C., Rovira-Llopis, S., ... Victor, V. M. (2018). Does metformin modulate endoplasmic reticulum stress and autophagy in type 2 diabetic PBMCs? *Antioxidants and Redox Signaling*, 28(17), 1562–1569. <https://doi.org/10.1089/ars.2017.7409>
- Diaz-Morales, N., Rovira-Llopis, S., Banuls, C., Lopez-Domenech, S., Escribano-Lopez, I., ... Victor, V. M. (2017). Does metformin protect diabetic patients from oxidative stress and leukocyte-endothelium interactions? *Antioxidants and Redox Signaling*, 27(17), 1439–1445. <https://doi.org/10.1089/ars.2017.7122>
- Dossou, A. S., & Basu, A. (2019). The emerging roles of mTORC1 in macromanaging autophagy. *Cancers*, 11(10), 1422–1439. <https://doi.org/10.3390/cancers11101422>
- Edinger, A. L., & Thompson, C. B. (2004). Death by design: Apoptosis, necrosis and autophagy. *Current Opinion in Cell Biology*, 16(6), 663–669. <https://doi.org/10.1016/j.ceb.2004.09.011>
- Eriksson, L., & Nyström, T. (2014). Activation of AMP-activated protein kinase by metformin protects human coronary artery endothelial cells against diabetic lipooptosis. *Cardiovascular Diabetology*, 13, 152–160. <https://doi.org/10.1186/PREACCEPT-9581518081340209>
- Galdieri, L., Gatla, H., Vancurova, I., & Vancura, A. (2016). Activation of AMP-activated protein kinase by metformin induces protein acetylation in prostate and ovarian cancer cells. *Journal of Biological Chemistry*, 25, 25154–25166. <https://doi.org/10.1074/jbc.M116.742247>
- He, C., Zhu, H., Li, H., Zou, M. H., & Zhonglin, X. (2013). Dissociation of Bcl-2–Beclin1 complex by activated AMPK enhances cardiac autophagy and protects against cardiomyocyte apoptosis in diabetes. *Diabetes*, 62(4), 1270–1281. <https://doi.org/10.2337/db12-0533>
- Islam, M. T., Uddin, M. S., Lucky, K. N., Islam, M. M., Islam, S. M. S., ... Amran, S. (2017). Autophagic dysfunction in type 2 diabetes mellitus: Pathophysiology and therapeutic implications. *Journal of Diabetes and Metabolism*, 8(5), 742–749. <https://doi.org/10.4172/2155-6156.1000742>
- Kalender, A., Selvaraj, A., Kim, S. Y., Gulati, P., Brule, S., ... Thomas, G. (2010). Metformin, independent of AMPK, inhibits mTORC1 in a rag GTPase-dependent manner. *Cell Metabolism*, 11(5), 390–401. <https://doi.org/10.1016/j.cmet.2010.03.014>
- Kaniuk, N. A., Kiraly, M., Bates, H., Vranic, M., Volchuk, A., & Brumell, J. H. (2007). Ubiquitinated-protein aggregates form in pancreatic beta-cells during diabetes-induced oxidative stress and are regulated by autophagy. *Diabetes*, 56(4), 930–939. <https://doi.org/10.2337/db06-1160>

- Klionsky, D. J., & Emr, S. D. (2000). Autophagy as a regulated pathway of cellular degradation. *Science*, 290(5497), 1717–1721. <https://doi.org/10.1126/science.290.5497.1717>
- Kobayashi, S., Xu, X., Chen, K., & Liang, Q. (2012). Suppression of autophagy is protective in high glucose-induced cardiomyocyte injury. *Autophagy*, 8(4), 577–592. <https://doi.org/10.4161/auto.18980>
- Kruse, R., Vind, B. F., Petersson, S. J., Kristensen, J. M., & Hojlund, K. (2015). Markers of autophagy are adapted to hyperglycaemia in skeletal muscle in type 2 diabetes. *Diabetologia*, 58(9), 2087–2095. <https://doi.org/10.1007/s00125-015-3654-0>
- Las, G., & Shiriha, O. S. (2010). The role of autophagy in β -cell lipotoxicity and type 2 diabetes. *Diabetes, Obesity and Metabolism*, 12(02), 15–19. <https://doi.org/10.1111/j.1463-1326.2010.01268.x>
- Lee, H. M., Shin, D. M., Yuk, J. M., Shi, G., Choi, D. K., ... Jo, E. K. (2011). Autophagy negatively regulates keratinocyte inflammatory responses via scaffolding protein p62/SQSTM1. *Journal of Immunology*, 186(2), 1248–1258. <https://doi.org/10.4049/jimmunol.1001954>
- Loos, B., Toit, A., & Hofmeyr, J. H. S. (2014). Defining and measuring autophagosome flux-concept and reality. *Autophagy*, 10(11), 2087–2096. <https://doi.org/10.4161/15548627.2014.973338>
- Marchetti, P., Bugliani, M., Lupi, R., Marselli, L., Masini, M., ... Cnop, M. (2007). The endoplasmic reticulum in pancreatic beta cells of type 2 diabetes patients. *Diabetologia*, 50(12), 2486–2494. <https://doi.org/10.1007/s00125-007-0816-8>
- Martinez-Vicente, M., & Cuervo, A. M. (2007). Autophagy and neurodegeneration: When the cleaning crew goes on strike. *The Lancet Neurology*, 6(4), 352–361. [https://doi.org/10.1016/S1474-4422\(07\)70076-5](https://doi.org/10.1016/S1474-4422(07)70076-5)
- Masini, M., Bugliani, M., Lupi, R., Del Guerra, S., & Boggi, U. (2009). Autophagy in human type 2 diabetes pancreatic beta cells. *Diabetologia*, 52(6), 1083–1086. <https://doi.org/10.1007/s00125-009-1347-2>
- Mehrpour, M., Esclatine, A., Beau, I., & Codogno, P. (2010). Overview of macroautophagy regulation in mammalian cells. *Cell Research*, 20(7), 748–762. <https://doi.org/10.1038/cr.2010.82>
- Meng, Q., & Cai, D. (2011). Defective hypothalamic autophagy directs the central pathogenesis of obesity via the I κ B kinase beta (IKK β)/NF- κ B pathway. *Journal of Biological Chemistry*, 286(37), 32324–32332. <https://doi.org/10.1074/jbc.M111.254417>
- Mizushima, N., Levine, B., Cuervo, A. M., & Klionsky, D. J. (2008). Autophagy fights disease through cellular self-digestion. *Nature*, 451(7182), 1069–1075. <https://doi.org/10.1038/nature06639>
- Mizushima, N., & Yoshimori, T. (2007). How to interpret LC3 immunoblotting. *Autophagy*, 3(6), 542–545. <https://doi.org/10.4161/auto.4600>
- Nisbet, J. C., Sturtevant, J. M., & Prins, J. B. (2004). Metformin and serious adverse effects. *Medical Journal of Australia*, 180(2), 53–54. <https://doi.org/10.5694/j.1326-5377.2004.tb05796.x>
- Ost, A., Svensson, K., Ruishalme, I., Brannmark, C., Franck, N., Krook, H., ... Stralfors, P. (2010). Attenuated mTOR signaling and enhanced autophagy in adipocytes from obese patients with type 2 diabetes. *Molecular Medicine*, 16(7-8), 235–246. <https://doi.org/10.2119/molmed.2010.00023>
- Pernicova, I., & Korbonits, M. (2014). Metformin—Mode of action and clinical implications for diabetes and cancer. *Nature Review Endocrinology*, 10(3), 143–156. <https://doi.org/10.1038/nrendo.2013.256>
- Rovira-Llopis, S., Banuls, C., Apostolova, N., Morillas, C., & Hernandez-Mijares, A. (2014). Is glycemic control modulating endoplasmic reticulum stress in leukocytes of type 2 diabetic patients? *Antioxidants & Redox Signaling*, 21(12), 1759–1765. <https://doi.org/10.1089/ars.2014.6030>
- Rovira-Llopis, S., Diaz-Morales, N., Banuls, C., Blas-Garcia, A., & Polo, M. (2015). Is autophagy altered in the leukocytes of type 2 diabetic patients? *Antioxidants & Redox Signaling*, 23, 1050–1056. <https://doi.org/10.1089/ars.2015.6447>
- Rubinsztein, D. C., Mariño, G., & Kroemer, G. (2011). Autophagy and aging. *Cell*, 146(5), 682–695. <https://doi.org/10.1016/j.cell.2011.07.030>
- Saitoh, T., Fujita, N., Jang, M. H., Uematsu, S., Yang, B. G., ... Akira, S. (2008). Loss of the autophagy protein Atg16L1 enhances endotoxin-induced IL-1 β production. *Nature*, 456(7219), 264–268. <https://doi.org/10.1038/nature07383>
- Samuel, S. M., Ghosh, S., Majeed, Y., Arunachalam, G., Emara, M. M., Ding, H., & Triggle, C. R. (2017). Metformin represses glucose starvation induced autophagic response in microvascular endothelial cells and promotes cell death. *Biochemical Pharmacology*, 132, 118–132. <https://doi.org/10.1016/j.bcp.2017.03.001>
- Uchizono, Y., Alarcon, C., Wicksteed, B. L., Marsh, B. J., & Rhodes, C. J. (2007). The balance between proinsulin biosynthesis and insulin secretion: Where can imbalance lead? *Diabetes, Obesity and Metabolism*, 9(S2), 56–66. <https://doi.org/10.1111/j.1463-1326.2007.00774.x>
- Yun, C. W., & Lee, S. H. (2018). The role of autophagy in cancer. *International Journal of Molecular Sciences*, 19(11), 3466–3484. <https://doi.org/10.3390/ijms19113466>
- Zhang, Y., Zeng, X., & Jin, S. (2012). Autophagy in adipose tissue biology. *Pharmacological Research*, 66(6), 505–512. <https://doi.org/10.1016/j.phrs.2012.09>

How to cite this article: Bhattacharya D, Dutta M, Mukhopadhyay M, Bhattacharyya M, Chowdhury S, Karmakar P. The protective role of metformin in autophagic status in peripheral blood mononuclear cells of type 2 diabetic patients. *Cell Biol Int*. 2020;1–12. <https://doi.org/10.1002/cbin.11355>



ADVANCES IN CELLULOSIC ENZYME TECHNOLOGIES FOR ENHANCED STABILITY AND CATALYSIS

Souvik Roy¹, Shakuntala Ghorai², Lopamudra Choudhury³, Ahana Das⁴,
Rituparna Banik Ghosh⁵, Samudra Prosad Banik^{*4}

¹St. Xavier's College (Autonomous), Post-Graduate Department of Biotechnology, 30, Mother Teresa Sarani, Kolkata, West Bengal, India

²Raidighi College, Department of Microbiology, West Bengal, India

³Sarsuna College, Department of Microbiology, 4/HB/A, Ho-Chi-Minh Sarani, Sarsuna Upanagari, Kolkata, West Bengal, India

⁴Maulana Azad College, Department of Microbiology, 8, Rafi Ahmed Kidwai Road, Taltala, Kolkata, West Bengal, India

⁵Bhairab Ganguly College, Department of Physiology, 2, Feeder Road, Belgoria, Kolkata, West Bengal, India

*Corresponding author: samudrapb@gmail.com, samudraprosad.banik@maulanaazadcollegekolkata.ac.in

ABSTRACT

Cellulosic ethanol has been the most promising second-generation biofuel in terms of raw material availability. The production process mandates efficient removal of lignin followed by a three-step sequential enzymatic conversion of cellulose to glucose. Cellobiase (E.C. 3.2.1.21), a β -glucosidase (BGL), obtained preferably from filamentous fungi catalyzes the final rate limiting step of this reaction, namely, the hydrolysis of cellobiose to glucose. It is therefore the most sought after model for cellulosic enzyme research. Efficient conversion of cellulosic biomass to glucose requires enhanced stability and superior catalysis. This in turn mandates strong producer organism able to secrete a high titer of the enzyme into the extracellular medium, optimized media formulation and improvised technologies for catalysis. Particularly, stabilization of the big cellobiose aggregates remains a significant technological bottleneck in this regard. Large aggregates of cellulosic enzymes are indispensable for industrial scale catalysis; however, these enzymes are prone to spontaneous dissociation by sheer dilution. Conventional immobilization and cross-linking approaches involving glutaraldehyde or entrapment in alginate beads have either proven cost-ineffective or have resulted in retention of poor specific activity for efficient catalysis. Over the last decade, new generation enzyme technologies such as synthetic multi-enzyme cellulosome complex, use of protein stabilizing osmolytes and reducing agents to maximize substrate exposure has opened up new avenues for cross-linker free stabilization and enhanced catalysis. The review is a fresh update of the producer strains, media optimizations and enzyme technologies to boost the production of cellulosic ethanol.

Keywords: Lignocellulosic bioethanol, Extracellular cellobiase, Filamentous fungi, Enzyme stabilization, Cellobiase aggregates.

1. INTRODUCTION

Sustainability is the most vital aspect of natural resource management of Mother Earth. This involves achieving operational efficiency and minimization of toxic impact on the environment, keeping in mind socio-economic considerations, all of which are mutually inter-dependent. However, a prolonged dependence on traditional fossil fuel energy resources is grossly unsustainable, owing to its super-swift-depletion worldwide following decades of overuse and misuse [1]. An acute energy crisis is thus looming large on the face of the globe due to the unprecedented increase in the consumption of fossil fuels, and it has been estimated that the projected depletion time of crude oil reserves at the current rate of

consumption is only a meager forty years [2]. Associated with this is the uncontrolled, but steady emission of harmful greenhouse gases (GHGs) from the usage of fossil fuels, resulting in acute global warming [1], thus jeopardizing the environmentalists' dream of a self-sustainable, greener and technologically-sound Mother Earth.

Consequently, a collective quest for the discovery of carbon neutral solid, liquid and gaseous fuels as alternative, renewable energy resources for potential use for transportation purposes of vehicles has been kindled over the past few decades [1, 2]. One of the most promising and scientifically-sound developments in this regard has been the discovery of 'biofuels' or fuels

derived from geologically recent carbon fixation [3]. Production of such biofuels from pre-existing biomass is one of the safer and greener alternatives to reduce consumption of crude oils, much needed for the abatement of environmental pollution.

2. BIOFUEL: SCOPES AND TYPES

In order to be considered a biofuel, a fuel must contain over eighty percent renewable materials. The scope of this term encompasses a wide range of alternative fuel

sources, and has evolved from the first generation (1G) bioethanol produced from sugar, starch or vegetable oil to the more advanced, energy efficient and economic third generation (3G) biodiesels derived from algae (fig.1). Bioethanol can be produced from three categories of agro-based raw materials-simple sugars, complex starch and the inedible, intricate plant biomass called lignocelluloses [3]. As the price of these raw materials usually varies largely, it can, in turn, significantly affect the cost of the large-scale production of bioethanol [3].

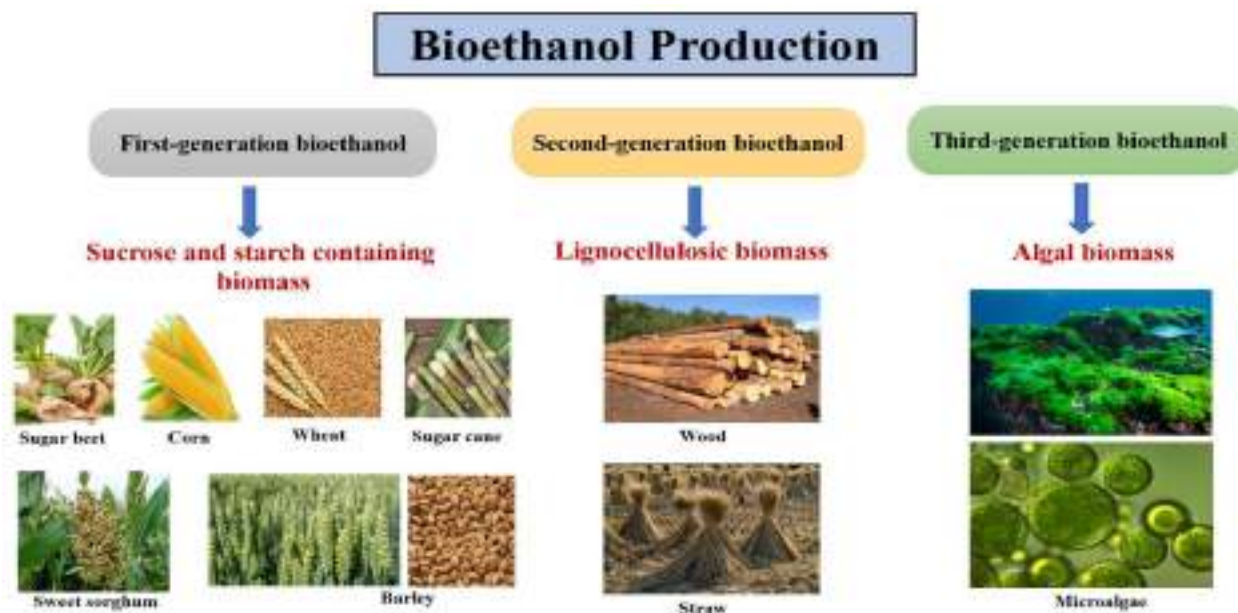


Fig 1: First generation, second generation and third generation biofuels as classified according to nature of raw materials used

Use of simple sugars and starch, akin to 1st generation bioethanol directly interferes with water conservation strategies, occupies a substantial area of agriculturally productive lands for the production of the fuel, consumes a significant part of world's forest reserves and puts a tremendous pressure on world food markets [1, 2]. For example, production of starch-based bioethanol from corn was much popular for quite a while due to the efficiency of the technology, but soon met with some inevitable socio-economic objections. The cultivation of corn encroached upon the farmlands dedicated for growing higher food crops, and thus threatened to breach the UN food security norms. *Jatropha* spp., another potential biofuel crop also met with the same fate. Under such circumstances, an improved thought for probing into an alternative source of bioethanol production was much needed. This set the ideal platform for the development of the most

promising 2G biofuel-cellulosic (lignocellulosic) ethanol. As cellulose (lignocellulose) is the most abundant biomolecule on the earth, therefore the idea of its utilization for the production of cellulosic bioethanol is a sustainable, eco-friendly option for the biofuel industry. Also, such 2G bioethanol derived from lignocellulosic agriculture and forest residues, and from non-food crop feedstocks resolves some of the major conflicts raised by 1G bioethanol production [1, 2]. It releases significantly lesser amounts of GHGs as compared to corn-bioethanol. Additionally, the raw material required for its industrial production is present in surplus even in agro-wastes which are not considered as fodders, and therefore no additional farmland is required. So, the production of bio-based products and bioenergy from cheap, renewable sources like lignocelluloses is beneficial not only to the environment, but also to local economy and national energy security across the globe

[4]. Cellulose is derived mostly from plant sources acting as the largest contributor of the total cellulose pool of the biosphere [5]. Cellulose is a structural homopolysaccharide, present as an essential cell wall constituent of a vast niche of the Plant kingdom, ranging from the red algae to conifers. It is a linear homopolymer of β -D-anhydroglucopyranoside residues, linked by β -(1,4)-glycosidic bonds, connecting several hundred to many thousands of glucose units. Although plant biomass is mostly cellulose (35-48%), it is occluded by hemicelluloses (22-30%) and lignin (15-27%), together constituting a complex intricate network of a biomolecule, known as lignocellulose [6, 2]. Being a low-cost energy resource based on its energy content (\$3-4/GJ), cellulose (lignocellulose) has multifarious commercial applications, starting from the production of nanomaterials on one hand to applications in biofuel production, textile polishing and finishing, pulp and paper industry, and lifestyle agriculture on the other [4, 5, 7].

3. BOTTLENECKS IN INDUSTRIAL PRODUCTION OF CELLULOSIC BIOETHANOL

3.1. Efficient removal of lignin

In spite of being the most promising feedstock for its easy availability and low cost, there has been a few technological constraints in the large-scale commercial production of bioethanol from lignocellulosic materials [3]. In fact, enzyme-catalyzed conversion of lignocellulosic plant biomass to simple sugars for the production of biofuels is highly inefficient a process, and is still considered as one of the key steps, limiting industrial biofuel production at a cheap cost [6]. One of the significant reasons hindering efficient bioconversion is the structural rigidity of the recalcitrant lignocelluloses which hugely restrict the physical access of soluble microbial lignocellulases for depolymerizing the cellulose in order to release glucose for the production of bioethanol [8, 9]. As lignin is recalcitrant to microbial degradation, a pre-treatment process to loosen up the lignin is often mandatory for altering or removing structural and compositional impediments of lignocelluloses by hydrolysis in order to improve the rate of enzymatic action and increase the yields of fermentable sugars [9]. Pre-treatment processing conditions must be tailor-made in accordance to the specific chemical and structural composition of the different sources of lignocellulosic biomass. Even if the toughest lignin is efficiently removed, the hemicellulose encapsulation reduces optimal enzyme exposure and hinders the

breakdown of cellulose. An efficient method of removing this hemicellulose is the ammonia freeze explosion pre-treatment, which simultaneously reduces both lignin and hemicelluloses, as well as decrystallizes cellulose for an optimum hydrolysis [9]. Therefore, hydrolysis of complex lignocellulose into simpler fermentable sugars, sugar acids and phenolics has become a mandatory pre-requisite for a faster downstream conversion into glucose [4, 9-11].

3.2. Enzymatic conversion of lignocellulose to glucose

It was in 1819 that the French chemist Henri Braconnot first discovered that cellulose could be hydrolyzed into sugars by treatment with sulfuric acid [3]. However, it was found subsequently that acidic hydrolysis suffered from a number of intrinsic disadvantages including denaturation of enzymes in the subsequent downstream fermentation process since the residual acid cannot be neutralized effectively [3]. With the rapid development of enzyme technologies over the past few decades, acid hydrolysis process of lignocellulose has gradually been replaced by enzymatic hydrolysis [3, 12]. Biocatalysts exert lesser corrosive effects to industrial processing equipments, and due to their extreme substrate specificity, they generally produce lesser toxic wastes to ensure better environmental sustainability [13].

Enzymatic hydrolysis of lignocellulosic material into fermentable sugars is carried out by a complex mixture of lignocellulolytic enzymes. Lignocellulolytic enzymes constitute mostly extracellular enzymes, including ligninolytic ones (peroxidases and oxidases) and hydrolytic ones (cellulases, hemicellulases, amylases, pectinases, chitinases, esterases, proteases and mannanases) [11, 14]. Most of these enzymes find indispensable applications in diverse areas and are excellent study models for the research fraternity [15]. The various sectors routinely employing lignocellulolytic enzyme preparations include breweries, textile, animal feed, food, pulp and paper industries, and laundry, besides they being used as additive in detergents and for improving the digestibility of animal feeds [4, 13, 16]. The lignocellulosic wastes generated are converted by cellulases to commercially-important products like glucose, soluble sugars, enzymes, alcohol, and single cell proteins (SCPs) [17]. In the natural environmental niche, synergistic associations among different cellulolytic microbes play a significant role in the hydrolysis of lignocellulosic polymers [7]. The complex structure of lignocellulose is biologically

simplified into its monomeric building blocks, the β -D-glucosyl unit, which is subsequently fermented to different products such as ethanol (biofuel), acetic acid, lactic acid, antibiotics and others [5]. So, after efficient removal of lignin and hemicelluloses, the core cellulosic biomass is subjected to saccharification involving sequential and synergistic actions of three cellulolytic enzymes [8]; (1) endo-glucanases (EGs, E.C. 3.2.1.4), which cleave the cellulose chains internally at random sites, acting mainly on the amorphous parts of the cellulose fiber to generate oligosaccharides and new chain ends; (2) exoglucanases, including cellodextrinases (E.C. 3.2.1.74) and cello-biohydrolases (CBHs; E.C. 3.2.1.91 for the cellobiohydrolases acting on the non-reducing end, and E.C. 3.2.1.176 for the cellobiohydrolases acting on the reducing end), producing glucose, cellobiose and higher celooligosaccharides; and (3) β -glucosidases (BGLs, E.C. 3.2.1.21, cellobiase) which catalyze the last rate limiting step to hydrolyze inhibitory cellobiose and short and soluble cello-oligosaccharides into additional glucose units [6, 16, 18, 19]. This process is collectively referred to as 'enzymatic saccharification' of cellulose. The final end product glucose is then converted to ethanol via yeast-mediated alcoholic fermentation.

A hallmark of this cellulase-enzyme system is synergy that ensures an efficient hydrolysis. This means that the catalytic activity of the entire enzyme-system is higher than the sum total of the respective activities of individual enzymes in the system [19]. The last step of the saccharification represents the technically most challenging step, and hence it constitutes the bottleneck for efficient saccharification. Therefore isolation and maintenance of a good producer strain of cellobiase is as critical as any other of the other processes during the actual fermentation.

4. PRODUCER MICROORGANISMS OF CELLULOSIC ENZYMES

The key elements in the saccharification process of lignocellulosics are the cellulolytic microorganisms [17]. To efficiently hydrolyze and degrade the insoluble biopolymer of cellulose, the microorganisms must secrete the cellulases, possibly excepting the BGLs, that are either extracellular or bound to the producer cell-surface [4]. Cellulolytic activity is hugely common among many genera in the Domain Bacteria, and within the fungal, protozoal, plant and a few animal groups in the Domain Eukarya [5, 19]. No cellulolytic genus has yet been identified in the Domain Archaea [19].

4.1. Fungal producers

Among all the lignocellulolytic microorganisms thrown a light upon, the fungi have been the subject of most extensive experimentation and research, due to their rich diversity and secretion of copious amounts of lingo-cellulolytic enzymes extracellularly [11, 20]. They are beneficial microbes that help in the recovery of energy from degraded ecosystems [21]. With a sound understanding of the enzyme production capabilities of these fungi, their industrial applications can be mapped easily [21]. Everyday large amounts of recalcitrant lingo-cellulosic wastes are dumped into the environment by mostly agricultural and industrial sources, leading to environmental pollution. Solid state fermentation (SSF) using these agro-industrial wastes as substrates for fungal growth is an efficient method to degrade such lignocellulosic masses by the cellulolytic fungi, in the process producing enzymes at low cost [22]. Such cellulolytic fungi can be easily isolated from natural resources like cattle dung and cattle dung-contaminated soil samples [23]. Scientists have found that these natural fungal isolates, once grown by SSF technique on non-pretreated saw dust, could produce copious cellulases to be suitably applied for bioethanol production [23]. The use of fungi like *Penicillium* and wine yeast would help biotechnologists to identify genes that could improve the production yield and nitrogen efficiency. Adaptive evolution over the years is also producing high-yielding strain (HYS) that have the potential to be directly applied in breweries at large. Among the fungal divisions, the widely-diverse subdivisions of Ascomycetes, Basidiomycetes (polypores), and Deuteromycetes harbor most of the cellulolytic species. More than hundred cellulolytic fungi have been reported till date, and this number is still increasing. Among the most well-studied aerobic fungi, belongs the yeasts and the mold genera *Trichoderma*, *Penicillium*, *Aspergillus*, *Termitomyces*, *Poria*, *Humicola*, *Acremonium*, *Chaetomium*, *Coriolus*, *Phanerochaete*, *Schizo-phyllum*, *Serpula*, *Fusarium*, *Geotrichum* and *Paecilomyces*, whereas the best studied anaerobic fungal cellulase producers are species of the genera *Piromyces* and *Neocallimastix* [19].

Sixty aerobic, non-*Saccharomyces* yeast strains have been isolated from grape musts in Uruguayan vineyards, including *Metschnikowiapulcherrima*, the best source of thermo stable (temperature optimum at 50°C) and acid-stable (pH optimum at 4.5) BGL [24]. Among the aerobic filamentous fungi, the soft-rot fungi *Trichoderma reesei* (teleomorph: *Hypocrea jecorina*), *Penicillium* spp. (like *P. purpurogenum*, *P. pinophilum*, *P. brasilinum*, *P.*

citrinum, *P. occitanis*, *P. decumbens* and *P. echinulatum*), *Aspergillus* spp. (like *A. niger*, *A. nidulans* and *A. oryzae*) and *Termito-mycesclypeatus* deserve special mention [6, 18, 25, 26].

Trichoderma reesei is the best-studied cellulolytic fungus, and are the most efficient producers of cellulases and hemicellulases [27, 28]. In more than one way, the extracellular cellulase enzyme-system of *T. reesei* has been instrumental for detailed studies on different cellulase systems from different sources [19]. The cellulase enzymatic system of *T. reesei* has five EGs and two CBHs, as well as some additional cellulolytic enzymes, such as the low-catalytic swollenin, vital for applications in the pulp and paper industries [19]. *T. reesei* secretes large amounts of all three types of cellulases - EGs, exoglucanases and BGLs, required for the degradation of crystalline cellulose [28].

Aerobic fungal cellulose degraders produce large amounts of extracellular enzymes [19]. Many *Penicillium* species can produce extracellular lignocellulases. The fungus *Penicillium purpurogenum* produces intracellular BGL, with maximum enzyme activity observed when sucrose is used as the substrate [29]. Various cultural parameters are thereby optimized for the cultivation of *P. purpurogenum* to enhance the production of BGL, which resulted in a maximum extracellular release of the enzyme after 96 h of cultivation at 30°C by the addition of amino acids like histidine and cysteine [29]. BGL of *P. purpurogenum* shows acid-stability (pH optimum at 2), thus being widely applied for debittering in breweries [25; 29]. *P. pinophilum* shows an extensive array of cellulase enzymes, containing eight EG components. An enzyme-preparation of particular lingo-cellulolytic importance is the 1:1 (v/v) blended enzyme extract of *Chrysosporthe cubensis*: *P. pinophilum* [29]. A similar repertoire of extracellular cellulases is secreted by *P. brasilinum*, from whose culture medium, three different EGs and two CBHs were purified [29]. While *P. citrinum* MTCC 6489 strain produces high amounts of xylanase and cellulases, extracellular endo- β -1, 4-xylanase was obtained from *P. occitanis* Pol6, grown on oat-based xylan medium [29]. Although both the *Penicillium* species strains CR-316 and CR-313 secrete high levels of cellulases, *Penicillium* CR-316 produces thermostable cellulases, making the strain industrially viable [29]. Comparative genomics analysis of *P. chrysogenum* and *P. decumbens* (*P. oxalicum*) showed that *P. decumbens* has more genes for cellulases. Besides, it was also found that *P. decumbens* has more diverse components of the lignocellulolytic enzyme-system

and hemicellulases, and their productions are induced in the medium when cellulose is the carbon source in wheat bran rather than glucose, in comparison to the much popular *T. reesei* [29].

4.2. Bacterial producers

Cellulases are produced in abundance by bacteria, particularly by the members of the Order Actinomycetales, of the anaerobic Order Clostridiales and of several aerobic Orders [19]. The cellulolytic machineries however differ between the aerobic and anaerobic bacteria [19]. For the first time, in the early 1980s, the scientists observed the multi-enzyme complex present in the thermophilic, anaerobic bacterium *Clostridium thermocellum*, which is meant for the degradation of lignocellulosic biomass, and termed it 'cellulosome' [19, 30]. Since then, cellulosome-producing bacteria have been isolated from a large variety of environments, indicative of their wide presence [30]. Like, apart from Clostridia, the cellulosome has been reportedly found in other anaerobic bacteria, including members of the *Ruminococcus* species, which are symbionts present in ruminant animals, with cellulosomes attached onto their surface [2, 19]. Cellulosomes are the bacterial nanomachines required for dismantling of complex plant polysaccharides like lignocelluloses [30]. Not only that in a given species the cellulosomes exhibit intrinsic heterogeneity, but also between different species, there exist huge differences in the structure and composition of these cellulosomes [30]. Generally, a cellulosome comprise of a complex of 'scaffoldin' along with various enzymatic subunits. It is the structural subunit containing a huge diversity of secreted cellulases and other plant cell-wall digesting enzymes bound to a common protein scaffold [30, 31]. These scaffold proteins have 'cohesin' modules that bind conserved 'dockerin' modules on the enzymes [31]. Co-localization of these modules on the scaffold allows them to function synergistically [31]. The inter-subunit interactions in these multi-enzyme complexes are mediated by these cohesin and dockerin modules [30, 31]. The cellulosome is catalytically more efficient than the free enzyme system, because it has the unique property of properly orienting the whole enzymatic machinery onto the substrate surface to promote an effective interaction [19]. Most of the cellulosome systems studied so far have been shown to harbor cellulases from many glycosyl hydrolase (GH) families [19]. Because of their highly efficient structural

organization and associated hydrolytic activities, cellulosomes have much promising application in the degradation of lignocellulosic biomass, leading to its conversion to valuable products, like biofuels [30]. Genetic engineering techniques can also be used to improve the biodegradative action of cellulosomes by reconstituting cellulosomes with potent enzymes from different microbial sources [2].

5. FUNGAL CELLOBIASES: COMPLEX AGGREGATES OF GLYCOSIDASES WITH HIGHER STABILITY

Cellobiases from filamentous fungi are preferred over their bacterial counterparts owing to the high titre, specific activity, low K_m and high thermo stability of the former [8, 32]. The enzyme is secreted into the culture medium as big aggregates which form spontaneously [33]. However, catalysis and thermal stability of the enzyme are highly dependent on its intrinsic self-association [33] and this factor highly limits the enzyme efficiency. Additionally product inhibition by glucose represents another aspect to address during enzymatic conversion of cellulosic substrates [34]. In anaerobic bacteria and some fungi, cellobiase is an integral part of the cellulolytic enzyme complex structured in the form of a scaffold known as 'cellulosome', where upto eleven different enzymes are tethered in a definite array [35]. The arrangement of different proteins in this scaffold represents another layer of structural complexity in terms of optimizing its stability and performance. Therefore, a significant amount of biofuel research in recent times has been concentrated towards technological advancements for better understanding the functioning of these complex enzyme aggregates.

6. BOTTLENECKS AND PROMISES IN CELLULOSIC ENZYME TECHNOLOGIES

Understanding the cellulosic enzymes at the molecular level may help in unraveling some of the integral features that equip them with their catalytic prowess [21]. Cellulases have non-catalytic carbohydrate-binding modules (CBMs) and/or other functionally known or cryptic modules at the N- or C-terminal ends of the catalytic module [4]. It is the combined action of three major enzymes of the cellulase enzyme-system which determines the overall efficiency of cellulose degradation [7]. However, cellobiase (BGL) has the highest biotechnological value of all, since it regulates the final turnover of glucose, and at the same time reduces the inhibitory effect of cellobiose on EGs and CBHs [18]. Also, as BGL's substrate is soluble, the

hydrolysis reaction is performed in the liquid phase, rather than on the surface of the insoluble cellulose particles, as in the case of EGs and CBHs [18]. To ensure improved industrial yields, individual cellulases are improved by either rational designing or by directed evolution [4]. As BGL activity has often been found to be rate-limiting during enzymatic hydrolysis of cellulose, the commercial cellulase enzyme preparations are often supplemented with BGL-activity [18]. Cellulolytic enzymes often suffer from low substrate affinity, thermolability and end product (glucose) inhibition. A higher temperature is needed during the enzymatic saccharification process to enhance the reaction rate, and minimize chances of microbial contamination. Therefore, finding an efficient cellulolytic enzyme preparation still eludes the biofuel industry.

6.1. Enzyme conjugation to nanoparticles

Over the last few decades, advancement in technology and newer scientific interventions has been able to provide some valuable insights about facilitating these enzymatic bioconversions. In order to minimise the recalcitrance of crystalline cellulose to enzymatic degradation, advanced technologies like conjugation of cellulases to synthetic nanoparticles (NPs) have been developed so as to increase the substrate accessibility as well as the catalytic efficiency of the enzyme [8]. Scientists have conjugated cellulase from the mold *Trichoderma viride* to polystyrene NPs, and tested the efficiency of the hydrolytic activity of this NP-conjugated complex on cellulosic substrates from purified and natural sources [8]. They found that the complexed enzyme displayed a higher efficiency in its action on microcrystalline cellulose [8]. Similarly, the NP-conjugated complex was observed to be more efficient in degrading natural cellulose structures in the thickened walls of cultured wood cells, both the results keeping hopes ablaze about the potential applications of cellulose-NP complexes in biofuel production from physically-intractable materials [8].

6.2. Stabilization of cellobiase assemblies for enhanced stability and catalysis

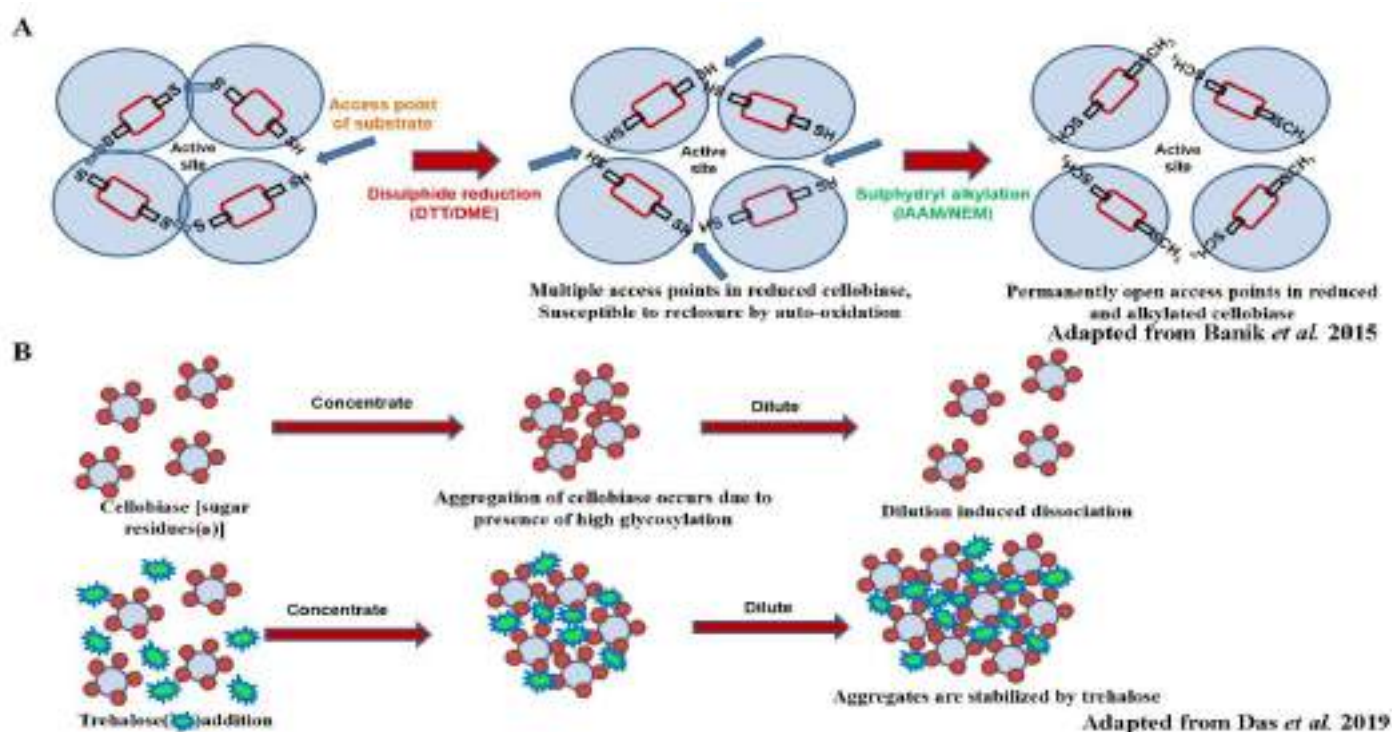
As stated earlier, fungal cellobiase is released extracellularly into the culture medium in co-aggregation with other enzymes, and the big aggregates subsequently associate again through reversible concentration driven protein-protein interaction. Both homoaggregation as well as heteroaggregation is vital for stability and catalysis of the protein [33, 36]. Therefore,

during the subsequent purification steps, activity and stability of the enzyme is severely hampered, mostly due to dissociation of the aggregates caused by sheer dilution. Therefore, stabilization of these unique natively aggregated fungal enzyme assemblies has been a major area of research for biotechnologists. Over the

last few decades, quite a few cross-linking and immobilization based stabilization strategies have been reported (table 1) alongside a few immobilization independent approaches to increase enzyme catalysis (fig. 2A) and stability (fig 2B).

Table 1: Cross-linking/immobilization/other technologies used to stabilize cellulolytic enzyme aggregates

Brief description of technology used	Enzyme targeted	Reference
Cross-Linked Enzyme Aggregates (CLEAs)	Cellulase, Xylanase	[37]
Peptide chain extensions	Cellulase	[38]
Alteration of surface electrostatics	Cellulase	[39]
NPG (Nanoporous gold) immobilization of enzyme by physisorption	Xylanase	[40]
Cellulase nanoparticles	Cellulase	[41]
Immobilization of enzyme in an inorganic-organic hybrid support (TiO ₂ -lignin)	Cellulase	[42]
Immobilization of cross-linked enzyme aggregates (CLEA) on the amine-functionalized Fe ₃ O ₄ @silica core-shell magnetic nanoparticles (MNP)	Cellulase	[43]
Immobilization of enzyme on magnetic nanoparticles encapsulated in polymeric nanospheres	Cellulase	[44]
Immobilization of enzyme on modified PVA (Polyvinyl alcohol) coated chitosan beads	Cellulase	[45]
Artificial multifunctional chimeras	Cellulase, Xylanase	[46]
Salt bridge design	Cellulase	[47]



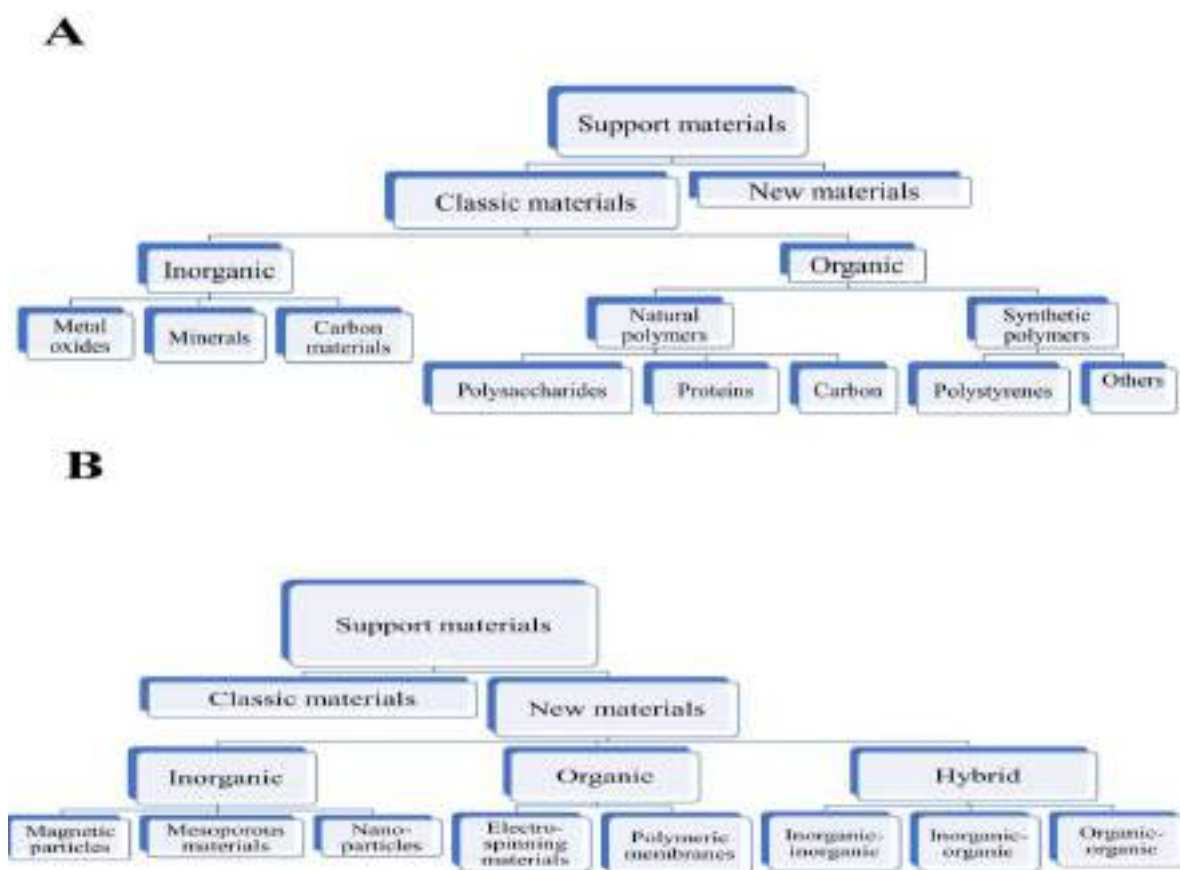
A) Addition of reducing agents decrease K_m of cellobiose [48] B) Trehalose stabilizes big aggregates of cellobiases against spontaneous dilution induced dissociation (49)

Fig 2: Newer technologies for *in situ* enhancement of cellobiose activity

6.3. Immobilisation/Cross-linking of cellobiase

With growing need in numerous application areas like food, pharmaceuticals, textile, chemical etc, industrial enzyme market expanded rapidly throughout the last few decades. In view of this, the process of immobilization was in demand as it rendered the biocatalyst several advantages over the free one. First and foremost, the cost of operation is reduced significantly as the immobilized enzymes can be used repeatedly or recycled. In some cases, stability of the enzyme is also increased. Immobilization also imparts more control and usability of the enzyme as in downstream processing, immobilized enzymes are more easily separated. [50-52]. In addition to these, some enzymes had shown higher efficiency and regio/stereo-specificity or selectivity through immobilization [53]. Although the

process of immobilization of enzymes dates back to 1940s, immobilized whole cells were in use long before, around 1815. Initially, single enzymes were immobilized, but later on from 1985, multiple enzymes were immobilized simultaneously for the ease of production and processing. Over the time, various methods were applied for immobilization and numerous support matrix were exploited for different catalytic processes. Support matrix plays very important role in providing suitable physical and chemical properties to the enzymes like hydrophilicity, compressibility, derivatization and compatibility etc. [53-57]. They can be broadly categorized into two classes-organic and inorganic [58]. Several natural as well as synthetic varieties are available for both of them (fig. 3).



A) Classic materials B) New materials [42, 58]

Fig 3: Support materials for enzyme immobilization

Porous matrices are preferred over non porous one as the enzyme loading is higher and immobilized enzymes are more protected from the environment. Considering the performance of the enzyme in hydrophilic environment, organic matrices are exploited in industries to a

greater extent compare to inorganic matrices although the latter is more stable physically and chemically [59]. Interaction between the support matrix and the enzyme can be irreversible or reversible [60]. Covalent coupling, entrapment and crosslinking are irreversible

in nature whereas adsorption and disulfide linkages are reversible. The process of immobilization and support matrix vary depending on the type of the enzyme, the nature and conditions of the catalysis reaction. The interactions between the support matrix and the enzyme are also dependent on the method of immobilization [42]. This is especially important in case of covalent binding.

Betaglucosidase has been immobilized on several surfaces such as sponge [61], chitosan beads [62], clay minerals or mineral-organic substances, adsorbed via covalent binding to solid supports, agarose gels, nylon polymers, alginate gels, silica gel, Eupergit C, carbon nanotubes, SiO₂ nanoparticles [63], polyacrylamide gel, hybrid nanomaterials of magnetic iron oxide nanoparticle with graphene oxide [64] etc. Recently wrinkled and mesoporous silica nanoparticles [65] and super-paramagnetic nanoparticles [66] were also explored for their effectivity. Polyacrylamide has been in use as matrix since long because of its low cost, chemical stability, uniform physical state and porosity. One thermo stable betaglucosidase from *Bacillus subtilis* was investigated after immobilization in polyacrylamide gel for extraction of phenolics from sugarcane juice. Results showed concentration of reducing sugar was more in case of free enzyme (9.438mg/l) compared to the immobilized one (8.134mg/l). Reduced activity of the immobilized enzyme may be due to several reasons like denaturation and leakage of the enzyme from gels because of use and diffusion effects [67]. In polyacrylamide gels, enzyme is exposed to a strong electrostatic field due to highly electronegatively charged acryl acid groups created in the macro-environment. This also affects the enzyme activity. Moreover, immobilization may change the structure and steric interactions of the enzyme in three-dimensional network [68]. When betaglucosidase from Novozyme's cellulosic ethanol enzyme kit was immobilized on 29 nm mesoporous silica particles both via physical adsorption and covalent binding, it resulted in increase in the activity and substrate affinity of the enzyme compared to the adsorbed enzyme. Physical absorption was done with 50mM citrate buffer at pH 4.7 and covalent linking was performed via glutaraldehyde. NaCl helped in adsorption whereas Triton X-100 decreased the adsorption. This explained the electrostatic attractive forces between the enzyme and the support surface. Whereas Triton-X 100 might weaken van der Waals interaction and impose additional physical hinderance via formation of small aggregates [69]. Super

paramagnetic iron oxide nanoparticles are small synthetic particles of core size less than 10nm. They are well dispersed in liquid and can easily be removed applying magnetic field. Olive betaglucosidase immobilized on super paramagnetic iron oxide nanoparticles showed higher thermal stability compared to the free enzyme [70]. Alginate, a polysaccharide of glucuronic and mannuronic acids, is a popular support matrix for immobilization due to its compatibility and processivity. Immobilized betaglucosidase showed high activity at 50°C and 80°C but substrate affinity and reaction velocity were lower compared to the free enzyme. The active sites might be less accessible to the substrate molecules and decreased affinity of the enzyme towards the substrate at higher temperatures may also be attributed to the internal diffusion of the immobilized enzyme.

Immobilisation of the enzyme has also been tested on macro porous carrier *Amberlite IRA 900 Cl* via adsorption with subsequent crosslinking by glutaraldehyde. Although reaction velocity was increased, there was a significant increase in K_m as compared to the native enzyme. This may be attributable to the immobilization of the enzyme molecules at sites or positions with decreased substrate accessibility. On the other hand, ionic and covalent bonds and diffusive effects created by immobilization increased the stability of the enzyme against heat inactivation [71]. The enzyme also retained high cellulolytic activity at acidic pH. In other studies, crude culture filtrate of *Aspergillus niger* was immobilized on various carriers via adsorption, covalent bonding, ionic bonding and entrapment [61]. When properties of immobilized betaglucosidase were compared with free enzyme, covalently linked immobilized enzyme showed higher thermal stability but lower substrate affinity and reaction velocity. In addition, the immobilized enzyme was also found to be more resistant to the inhibitory effect of different chemicals. However, enzyme activity recovery was not much in case of several matrices like chitosan, sol-gel beads, sodium alginates, Eupergit C and S-layer [62]. Betaglucosidase immobilized on magnetite again showed low activity recovery and poor accessibility towards substrate. Contrary to the usual trend of immobilized enzymes, enzymes immobilized on super paramagnetic particles showed lower K_m value or higher substrate affinity compared to the free enzyme. It also rendered the immobilized enzyme reusable with enhanced thermostability and higher shelf life. Similar observations were obtained when betaglucosidase was immobilized on non-porous magnetic

particles activated with cyanuric chloride and polyglutaraldehyde. Immobilized enzyme showed greater thermostability and better performance in hydrolysing lignocellulosic material.

Traditional approaches of stabilization of enzyme aggregates through the use of cross-linking agents such as glutaraldehyde were initially in vogue [72, 73]. However, use of glutaraldehyde was a non-ecofriendly costlier option, and had to be abandoned soon. A cellobiase preparation covalently coupled to cyanogen bromide was reported to have enhanced thermostability with a lowering of K_m [74]. Immobilization of cellobiase in Concanavalin A-sepharose beads followed by entrapment in polypropylene glycol-alginate beads stabilized the aggregates for about four consecutive days [75]. In a more recent study, bubbling immobilisation of cellobiase in sodium alginate with chitosan as carrier achieved a significant reduction in K_m with enhanced catalysis at higher temperature [76]. Optimized immobilization was subsequently achieved through Response Surface Methodology tool [77]. A new and promising cross-linking independent approach of stabilizing the cellobiase aggregates has been reported employing trehalose, a small molecule osmolyte [49]. Trehalose is thought to act by docking onto cellobiase aggregates through replacement of hydrogen bonded water from solvent accessible surface area. In this way, the big enzyme aggregates are shielded by a viscous trehalose matrix which prevents their subsequent dissociation on dilution.

7. GENETICALLY ENGINEERED CELLULOSIC ENZYMES

A thrust area to improve performance of cellulolytic enzymes over the last decade has been the use of genetic engineering tools to design cellulolytic enzymes with improved catalysis and high thermostability, the two indispensable attributes for successful, revenue-earning commercialization of lignocellulose-biorefineries [4]. These thermostable and alkali-tolerant lignocellulolytic enzymes are gaining much attention as biocatalysts due to their robust activities at both high temperature and alkaline pH [13]. The development and optimization of suitable fermentation processes for the production of such thermo-alkali-stable lignocellulolytic enzymes, including thorough research on producer microorganisms (i.e. strain screening and strain improvement via mutation and other recombinant techniques) and their performances, optimization of bioreactors, culture media (i.e. fixing concentrations of particularly C and

N) and other fermentation parameters like temperature, pH, inoculum size, speed of agitation, rate of aeration, and dissolved oxygen tension (DOT), along with different modes of operation (i.e. submerged fermentation, SmF and solid state fermentation, SSF) are nowadays dealt with in much details for a successful, eco-friendly and low-cost industrial application [13]. Therefore future prospects in lignocellulolytic enzyme research are directed towards bio-prospecting of robust and new fungal enzymes to overcome the challenges in the degradation of recalcitrant, stubborn wastes and complex physiological regulations of enzymes, use of multiple high-yielding fungal strains or a mixture of purified enzymes from such different sources, use of unique and novel inducers to maximize enzyme production, gene cloning to screen for new generation of enzymes, and application of various other genetic engineering techniques to widen the horizon of applicability of these enzymes [14]. With the development of modern tools such as genomics and proteomics, the entire protein content of the cellulosomes and their respective expression levels can now be studied and appropriately controlled. Over the past two decades, integrated genomics have been used to find new cellulosomal genes, providing information that has led to a better understanding of the structure-function relationships of the cellulosome systems [19]. An 18-subunit protein complex called a 'rosettasome' was found by scientists to be amenable for genetic engineering, so that they can bind to dockerin-containing enzymes in order to function like an 'artificial' cellulosome [31]. Rosettasomes are thermo stable, Group II chaperonins isolated from the hyperthermo-acidophilic archaeon *Sulfolobus shibatae* [31]. By artificially fusing a cohesin module from *Clostridium thermocellum* to a circular permutant of a rosettasome subunit, it was demonstrated that the cohesin-rosettasomes (these engineered multi-enzyme structures are termed 'rosettazymes') bind dockerin-containing exo- and endo-gluconases. These bound enzymes were reported to show increased cellulolytic activity compared to free state in solution, and that this increased activity depends on the number and ratio of the bound glucanases [31]. On the other hand, the lactic acid bacterium (LAB) *Leuconostoc mesenteroides* produce an intracellular thermostable (temperature optimum at 50°C), acid-stable (pH optimum at 5.5-6.0) and low K_m (0.07 mM for p-nitrophenyl- β -D-glucopyranoside or pNPG, high substrate affinity) BGL when grown on an arbutin-containing medium [78].

8. USE OF ENGINEERED STRAINS FOR CELLULOLYTIC ENZYME PRODUCTION

As the cellulase enzymes are produced in very small quantities by the wild-type (WT) organisms, strain improvement in industries are extensively carried out by extensive application of mutation and selection processes [17] (table 2). Such improved HYS can cut down the cost of the production processes by the virtue of an increased yield, alongside providing some specialized characteristics to the products.

Table 2: Recombinant strains used for increased cellulolytic enzyme production

Recombinant strain	Gene altered	Reference
<i>Trichoderma reesei</i>	Cel7A	[80]
<i>Saccharomyces cerevisiae</i>	CBH1	[81]
<i>Trichoderma reesei</i>	cel3A	[82]
<i>Aspergillus oryzae</i>	eg1	[83]
<i>Pichia pastoris</i>	CBH3	[84]
<i>Saccharomyces cerevisiae</i>	CBH2	[85]
<i>Pichia pastoris</i>	bgl1	[86]
<i>Trichoderma reesei</i>	xyn2	[87]
<i>Pichia pastoris</i>	XylA	[88]
<i>Pichia pastoris</i>	BCC7197	[89]
<i>E. coli</i>	Xynsig	[90]
<i>Hansenula polymorpha</i>	xyn2	[91]
<i>Hansenula polymorpha</i>	xlnD	[91]
<i>Pichia pastoris</i>	PcXylB	[92]
<i>E. coli</i>	xynB	[93]

Genetically-engineered strains derived from *A. niger* are now finding much applications in industrial processes [6, 19]. Cellulolytic enzymes are abundantly expressed in many different *Aspergillus* species, like endoglucanases A (*eglA*), B (*eglB*), and C (*eglC*), which are members of GH families 12, 5, and 74, respectively; cellobiohydrolases A (*cbhA*) and B (*cbhB*), both of which are members of GH family 7; and a GH3 BGL (*bglA*) in the industrially important *A. niger*. Numerous genes for lytic polysaccharide monooxygenase (LPMO) enzymes from the GH61 family are also traced in *A. niger*, *A. nidulans* and *A. oryzae* [18]. A study has reported an increase in enzymatic efficiency by co-culturing two different fungal strains [79]. This study indicated that the cellulases obtained from a compatible mixed culture obtained after simultaneous mixing of both *A. niger* and *P. chrysogenum* have more lignocellulolytic activity as compared to their respective pure cultures when grown on the solid wastes of sugar and paper industries including baggase, paper waste and cotton waste by SSF

technique [79]. It was revealed that newspaper, an industrial carbon waste, at pH 5.0 and 40°C temperature was the best source of carbon for the enhanced production of cellulase in the compatible mixed culture after 8 days of incubation, at the same time reducing much of the environmental pollution [79].

Genomic analysis reveals that orthologs of multiple components like Cre1, ACEI and LaeA have been found to control cellulase production in *T. reesei* [29]. Nowadays, much of the research in this field has been focused on mutation and selection of better *T. reesei* strains for the commercialization of cellulase enzymes, and both WT and genetically-engineered strains derived from *T. reesei* are being used in industrial processes [6,19]. To date, 17 cellulase-encoding genes have been discovered and cloned from *T. reesei*, of which only four cellulases (Cel5A, Cel6A, Cel7A and Cel7B) are secreted in large quantities (90-95% of the total secreted cellulases) into the culture medium [28]. CBHs constitute about 80% of the total cellulolytic proteins in the secretome of *T. reesei* [19]. A cre1⁻ *T. reesei* mutant created was found to over-expresses Cel61A (encoding an EG) twice as much as the WT under cellulose-inducing conditions [29]. The use of DNA microarray technology for the identification of new *T. reesei* genes involved in cellulosic biomass conversion via high throughput analysis of expression of cDNA libraries generated by suppression subtractive hybridization (SSH) is also already underway [27]. Presently, the hyper-secreting mutant Rut C-30 strain of *T. reesei* is generated by three steps of random mutagenesis (successive treatments with UV light, *N*-nitroguanidine, and again UV light), which is a highly efficient extracellular enzyme protein producer (around 19 g L⁻¹) [28]. Although another mutant strain, CL847, was found to yield higher amounts of extracellular protein (about 40 g L⁻¹), the proteins secreted from Rut-C30 has been reported to have a higher percentage of cellulase [28]. Up to seven BGL genes have been found in the *T. reesei* genome. Their expression is regulated by a unique system different from that of other cellulases. It was found that, BglR, a specific regulator of BGLs, is an activator for efficient BGL expression in *T. reesei* [29]. However, as they are mostly intracellular proteins, the action of a lesser percentage of extracellular BGLs is insufficient to completely degrade the cellobiose to glucose [28]. As a result, cellobiose accumulates in the media to cause feedback inhibition of the endo-and exoglucanases [6, 28]. So, to overcome this problem,

commercial cellulases are often composed of multi-component enzyme mixtures produced by different fungal strains. Complete hydrolysis of cellulose by purified *T. reesei* BGL is made possible only after its supplementation with a commercial BGL preparation from *A. niger* (Novozymes SP188) [6, 28]. Studies on possible differences between wild-type *T. reesei* BGL1 and supplemented SP188 BGLs shows that SP188 BGLs (K_m for cellobiose = 0.57 mM, low substrate affinity) has a lower specific activity than *T. reesei* BGL1 (K_m for cellobiose = 0.38 mM, around 1.5-fold high substrate affinity), and is also more sensitive to glucose inhibition [6]. Presently, several *T. reesei* cellulose cocktails with improved BGL activities have been commercialized by MNCs like Novozymes (C-Tec cocktail) and Genencor International Inc. (Accellerase cocktail) [28]. However, use of such cellulase mixtures turned out problematic in their applications in pulp and paper industries, because of their non-specificity and hyper-degradative power, much detrimental to the strength properties of the fibers being processed [19]. Hence, recent advancements in modern biotechnological tools have resulted in commercial mono-component cellulase preparations targeted for specific process applications, like EGs meant for textile processing finding their use in pulp and paper processing as well [19].

Orthologs of Cre1, ACEI and LaeA also control the cellulase production in *P. decumbens*, just like *T. reesei* [29]. Interestingly, CreA and its orthologs majorly repress cellulolytic gene expression in *P. decumbens*, making their deletions important for constructing industrially-important cellulose hyper-producing strains [29]. On the other hand, species or genus-specific regulators like ACEII, ENVOY, Xpp1, and GRD1 are diminished in *P. decumbens*. While lactose induces the expression of lignocellulolytic genes in *P. decumbens* at lower concentration, sophorose, the transglycosylation product of BGL, cannot induce the expression of cellulolytic genes in the same fungi [29]. Experiments involving mutagenesis are also widely carried out nowadays in order to alter the expression of regulatory genes of *P. decumbens* for maximizing cellulase production. Although random mutagenesis is often applied, it is not only cumbersome and time-consuming, but most of the times, also screens out for undesired phenotypes. However, in this regard, the HYS JU-A10-T of *P. decumbens* is industrially well-acclaimed [29]. An over-expression of cellulose regulator B (ClrB) activator was associated with a drastic increase in cellulase production in *P. decumbens*. As functional redundancy was seen to be

exhibited by cellodextrin transporters (Cdt) in *P. decumbens*, the deletion of any one among CdtC, CdtD, and CdtG cellodextrin transporter proteins does not affect cellulase expression in it. Similarly, strain carrying carbon catabolite repressor, removal of *creA/creI* was partially unrepressed in both *P. decumbens* and *T. reesei*, thus improving FPA activity by 1.5-fold under induction condition in *P. decumbens*. Further, deletion of *creA* and over-expression of the activator ClrB in the same fungus was found necessary to avoid the dependence on inducer for maximum cellulose production. Other double-gene mutations including overexpression of *clrB* with *bgl2* deletion and alternating, the double deletion of both *creA* and *bgl2* were found able to induce the expression and over-secretion of cellulase enzyme. A triple-mutant strain of *P. decumbens*, RE-10, created by three-step genetic engineering for the purpose of induction of cellulolytic gene expression in comparison to the WT *P. decumbens*, is the best genetically-engineered strain till date. However, the activity of extracellular BGL of this RE-10 mutant is undetectable in comparison to WT strain, a phenomenon observed only in presence of cellulose, but not wheat bran, and no homolog of *bglR* exists in its genome. The EG Cel61A with a CBM oxidatively degrade cellulose using redox-active cofactor, which could only be found secreted by this high-cellulase producing RE-10 mutant. Four GH61 family protein-encoding genes have been identified in the genome of *P. decumbens*, two of which were detected in the RE-10 strain as well, which are candidate-genes for studies on probing into the alternative lignocellulose-degrading mechanism in molds, and also on how to supplement industrial cellulases with improved hydrolytic activity. Moreover, several hemicellulases are also elaborated by RE-10, including α -l-arabinofuranosidase, endo- β -1,4-xylanase, β -xylosidase, and β -1,3-glucanosyltransglycosylase [29]. Mutants of *P. echinulatum* can produce large amounts of cellulases and its thermostable enzyme-complex (temperature optimum at 50°C). This enzymatic complex of *P. echinulatum* is capable of exhibiting higher glucose-dase activities as demonstrated by filter paper activity (FPA, representing overall cellulose activity) assays in comparison to the enzymatic complex of *T. reesei*. Further studies with the *P. echinulatum* 9A02S1 mutant strain have shown that presence of lactose and cellulose both induces their production of cellulases, but when lactose was used as the sole C-source, cellulase secretion was not found,

quite in contrary to the results observed for *T. reesei* [29].

9. OPTIMIZATION OF PRODUCTION MEDIA

Optimization of carbon and nitrogen sources is a critical aspect in obtaining an industrial titre of cellobiase. Experiments using residues from cheap agro-wastes like mustard stalk and straw (MSS) with a low lignin percentage and high cellulose and hemicellulose contents indicated that these raw materials could be utilized for a huge yield of glucose by the action of lignocellulolytic enzymes by *Termitomyces* in submerged culture [10]. Enzyme productions increased by 2-10 times through addition of commonly available cheap agro-residues such as wheat bran and rice straw (MWR) in 1:1:1 ratio and by using alkali-treated MSS (TMSS) into the fermentation media. The enzymes obtained from the MWR and TMSS media were found to saccharify 10% (w/v) wheat bran up to 53% and 58% in 24 h, results indicating that MSS from India has a huge potential as a cheap and renewable raw material for production of bioethanol. In a few Basidiomycota like *Termitomyces*

clypeatus, extracellular release of cellobiase and other glycosidases is found to increase significantly under secreting conditions induced by addition of sodium succinate in the medium [94]. The titre of extracellular cellobiase was further boosted through inclusion of glycosylation inhibitors like 2-Deoxy-glucose in the culture medium [36; 26]. This under-glycosylated cellobiase was also found to be resistant towards proteolytic as well as endoglycosidase-H digestion and showed higher stability and specific activity than its native counterpart [26]. Analyses of metabolic enzymes, together with molecular analyses through proteomic profiling and transcriptomics data revealed that 2-Deoxy-glucose exerted its effect through catabolite repression [69], and subsequent induction of metabolic stress in the fungus [95]. Concomitant with the reformulation of production media, a few studies have also reported that *in situ* inclusion of small molecule additives like salts, detergents, amino acid and vitamins can also substantially boost activity and catalytic efficiency of extracellular cellobiase activity (table 3).

Table 3: Additives used in the production media for increased enzyme titer

Additives used	Carbon source	Nitrogen source	Enzyme produced	Reference
Lichenan	Lichenan	Peptone	Bacterial cellulase	[97]
β -glucan	β -glucan	Peptone	Bacterial cellulase	[97]
Cotton seed	CMC	NaNO ₃ and cotton seed	Endoglucanase, glucoamylase, and xylanase	[98]
L-cystine	CMC	NaNO ₃	Endoglucanase, filter paperase and β -glucosidase	[98]
Valine	CMC	NaNO ₃	Endoglucanase and glucoamylase	[98]
Thiamine	CMC	NaNO ₃	Endoglucanase and glucoamylase	[98]
Riboflavin	CMC	NaNO ₃	Endoglucanase and glucoamylase	[98]
CoCl ₂	CMC	NaNO ₃	Endoglucanase and glucoamylase	[98]
MnCl ₂	CMC	NaNO ₃	Endoglucanase and glucoamylase	[98]
Lactose	Lactose	Peptone	Fungal cellulase	[99]
CaCl ₂	CMC	3,5-Dinitrosalicylic acid	Endoglucanase and β -glucosidase	[100]
MgCl ₂	CMC	3,5-Dinitrosalicylic acid	Endoglucanase and β -glucosidase	[100]
KCl	CMC	Peptone	Endoglucanase	[101]

Most of them are either thought to act by loosening up the aggregates for better substrate availability or increase production of enzymes by supplementing nutrient resource [96]. In one such study, the activity of the enzyme from *T. clypeatus* was found to increase in the presence of common reducing agents like dithiothreitol (DTT) and β -mercaptoethanol (ME), with a resultant decrease in K_m (thereby signifying an increase in substrate affinity) from 0.4 mM to 0.3 mM in case of DTT, and from 0.4 mM to 0.35 mM in case of ME [48].

Thus it was postulated that the reduction of disulphide bonds allowed for a better cellobiase-substrate interaction. Catalysis was further observed to be enhanced if the reduced enzyme was pre-alkylated in accordance with the hypothesis that reduced thiols can be aerially oxidized to reform the di-sulphides, thus hindering active site accessibility of the substrate.

However, despite all technological advancements, the huge cost of purified cellulases required for the hydrolysis of pre-treated lignocellulosic materials poses

the biggest obstacle for the successful commercialization of biomass biorefineries, because a large amount of this enzyme is consumed for biomass saccharification [4]. So, for a successful decrease in cellulase usage, increase in volumetric productivity and reduction in capital investment, consolidated bioprocessing (CBP) is nowadays practiced through successful integration of cellulase production, cellulose hydrolysis and ethanol fermentation in only a single step [4]. Also, over the last few years, the traditional way of cellulose degradation has been remarkably re-framed by the discovery of a novel class of enzymes, particularly abundant in the saprophytic fungi known as lytic polysaccharide monooxygenases (LPMO)[18]. Together with cellobiose dehydrogenase (CDH, E.C. 1.1.99.18), LPMO forms an oxidative enzymatic system that speeds up the enzymatic hydrolysis of lignocellulose [18]. These enzymes require copper for their activity, and cleave cellulose oxidatively using electrons from CDH or even ascorbate [18]. Often LPMO genes might even outnumber cellulase genes, although the exact mode of action of these encoded enzymes still remains obscure. The discovery of LPMO thus shatters the age-old notion that only hydrolytic enzymes are the main pioneers in the degradation of recalcitrant cellulose and hemicelluloses to simpler fermentable sugars.

10. CONCLUSION

Ethanol-from-cellulose (EFC) holds a great potential due to the widespread availability and relatively low cost of cellulosic materials. However, although several EFC processes are technically feasible, cost-effective processes are often difficult to achieve. Therefore, we are yet to go a long way to ensure stable and cheap supply of raw material from cellulosic substrates. Based on the present scientific and technical knowledge, third generation biofuels derived from microalgae are considered to be a technically viable and efficient alternative energy resource. The current limitations in conversion of cellulose to ethanol are believed to be alleviated in near future with development of modern tools and cutting-edge research. This will facilitate the production and use of various new generation cellulosic ethanol and the latest algal biomass-based third generation biofuels. Therefore, with the technology in hand, the need of the hour is an increased collaboration between public and private sectors for economical production, implementation of fair Government policies and promotion of mass awareness. Then, we may not be

far from gifting our future generation a cleaner, greener and sustainable Mother Earth.

11. ACKNOWLEDGEMENT

The authors express their sincere thanks to Dr. Suman Khowala, Ex-Principal Scientist, CSIR-Indian Institute of Chemical Biology (IICB), Kolkata in whose laboratory many of the studies reported in this review have been conducted. The authors also like to acknowledge University Grants Commission (UGC), Government of India and Department of Biotechnology (DBT), Government of India, who have funded most of the studies carried out in the authors' laboratories. The authors are also deeply indebted to Rev. Dr. Dominic Savio, S.J., Principal and Rector, St. Xavier's College (Autonomous), Kolkata and Dr. Subhankar Tripathi, Principal, Sarsuna College, Kolkata.

Conflict of interest

All authors have seen and agreed upon the final version of the manuscript. There is no conflict of interest with any authority.

12. REFERENCES

- Brennan L, Owende P. *Renewable and Sustainable Energy Reviews*, 2010; **14**(2):557-577.
- Maheshwari R. *Current Science*, 2008; **95**(5):594-602.
- Balat M. *Energy conversion and Management*, 2011; **52**(2):858-875.
- Zhang X-Z, Zhang Y-Hp. 1st Ed., John Wiley & Sons, Inc. USA, 2013; pp. 131-146.
- Ahmed A, Bibi A. *LIFE:International Journal of Health and Life Sciences*, 2018; **4**(1):19-36.
- Chauve M, Mathis H, Huc D, Casanave D, Monot F, Ferreira N. *Biotechnology for Biofuels*, 2010; **3**:3
- Jayasekara S, Ratnayake R. *Intech Open Limited, London, UK*. 2019; pp.1-21.
- Blanchette C, Lacayo C, Fischer N, Hwang M, Thelen M. *PLoS ONE*, 2012; **7**(8):e42116.
- Mosier N, Wyman C, Dale B, Elander R, Lee Yy, Holtzapple M, Ladisch M. *Bioresource Technology*, 2005; **96**(6):673-686.
- Pal S, Banik SP, Khowala S. *Industrial Crops and Products*, 2013; **41**(1):283-288.
- Sajith S, Priji P, Sreedevi S, Benjamin S. *Journal of Nutrition & Food Science*, 2016; **6**:1.
- Janusz G, Pawlik A, Sulej J, Swiderska-Burek U, Jarosz-Wilkolazka A, Paszczynski A. *FEMS microbiology reviews*, 2017; **41**(6):941-962.

13. Lajis A. *Journal of Biochemical Engineering & Bioprocess Technology*, 2017; **1**:1.
14. Mtui G. *Scientific Research and Essays*, 2012; **7(15)**:1544-1555.
15. Kuhad R, Gupta R, Singh A. *Enzyme Research*, 2011; ID 280696:1-10.
16. Bhat MK. *Biotechnology Advances*. 2000; **18**:355-383.
17. Odelade K, Oladeji O, Aremu S, Adisa M. *MAYFEB Journal of Environmental Science*, 2016; **1**:30-43.
18. Dimarogona M, Topakas E. *New and Future Developments in Microbial Biotechnology and Bioengineering*, Chapter 12, 1st Ed., Science Direct, Elsevier Scientific Publ. Co., NY, US, 2016; pp 171-187.
19. Viikari L, Suurnäkki A, Grönqvist S, Raaska L, Ragauskas A. *Encyclopedia of Microbiology*, 2009; pp. 80-94.
20. Kantharaj P, Boobalan B, Sooriamuthu S, Mani R. *International Journal of Current Research and Review*, 2017; **9(21)**:1-12.
21. Anita B, Thatheyus A, Vidhya R. *Science International*, 2013; **1**:92-97.
22. Nguyen K, Wikee S, Lumyong S. *Mycosphere*, 2018; **9(6)**:1073-1088.
23. Patel PS, Desai RG. *International Journal for Research in Applied Science & Engineering Technology (IJRASET)*, 2019; **7(3)**:2277-2285.
24. González-Pombo P, Pérez G, Carrau F, Guisán Jm, Batista-Viera F, Brena Bm. *Biotechnology Letters*, 2008; **30(8)**:1469-1475.
25. Dhake A, Patil M. *Brazilian Journal of Microbiology*, 2005; **36(2)**:170-176.
26. Ghorai S, Chowdhury S, Pal S, Banik SP, Mukherjee S, Khowala S. *Carbohydrate Research*, 2010; **345(8)**:1015-1022.
27. Bashkirova E, Rey M, Berka R. *Applied Mycology and Biotechnology*, 2005; **5**:275-299.
28. Chulalaksananukul W. *Biotechnology and Biology of Trichoderma*, Chapter 19, Ed., Science Direct, Elsevier Scientific Publ. Co., NY, US. 2014; pp. 281-290.
29. Nigam D, Asthana M, Kumar A. *New and Future Developments in Microbial Biotechnology and Bioengineering*. 2018; Chapter 10, 1st Ed., Science Direct, Elsevier Scientific Publ. Co., NY, US, pp 187-200.
30. Artzi L, Bayer Ea, Morais S. *Nature Reviews Microbiology*, 2016; **15**:83-95.
31. Mitsuzawa S, Kagawa H, Li Y, Chan SL, Paavola CD, Trent JD. *Journal of Biotechnology*, 2009; **143(2)**:139-144.
32. Alessandra M, Luisa M, Elena I, Francesco C, Maurizio R. *Cellulase: types and action, mechanism, and uses. Chapter: 1. Nova Science Publisher*, 2011; pp.1-79.
33. Banik SP, Pal S, Ghorai S, Chowdhury S, Majumder R, Mukherjee S, Khowala S. *Biotechnology and Bioprocess Engineering*. 2012; **17**:925-936.
34. Chia-Wen C, Cannella HD, ørgensen H, Felby C, Thygesen LG. *Journal of Agricultural and Food Chemistry*. 2014; **62(17)**:3800-3805.
35. Schwarz W. *Applied Microbiology and Biotechnology*, 2001; **56**:634-649.
36. Mukherjee S, Chowdhury S, Ghorai S, Pal S, Khowala S. *Biotechnolgy Letters*, 2006; **28**:1773-1778.
37. Dalal S, Sharma A, Gupta MN. *Chemistry Central Journal*, 2007; **1**:16.
38. Liuu JH, Tsai FF, Liu JW, Cheng KJ, Cheng CL. *Enzyme Microbial Technology*, 2001; **28**:582-589.
39. Nordwald E, Brunecky R, Himmel M, Beckham G, Kaar J. *Biotechnology and Bioengineering*, 2014; **111**:1541-1549.
40. Yan X, Wang X, Zhao P, Zhang Y, Xu P, Dingy. *Microporous and Mesoporous Materials*, 2012; **161**:1-6.
41. Hegedüs I, Hancsók J, Nagy E. *Applied Biochemistry and Biotechnology*, 2012; **168**:1372-1383.
42. Zdarta J, Meyer AS, Jesionowski T, Pinelo M. *Catalysts*, 2018; **8**:92.
43. Khorshidi KJ, Lenjannezhadian H, Jamalan M, Zeinali M. *Journal of Chemical Technology and Biotechnology*, 2016; **91**:539-546.
44. Lima JS, Araujo PHH, Sayer C, Souza AAU, Viegas AC, Oliveira DD. *Bioprocess and Biosystems Engineering*. 2017; **40**:511-518.
45. Dincer A, Telefoncu A. *Journal of Molecular Catalysis B: Enzymatic*, 2007; **45**:10-14.
46. Elleuche S. *Applied Microbiology and Biotechnology*, 2015; **99**:1545-1556.
47. Lee CW, Wang HJ, Hwang JK, Tseng CP. *PLoS One*, 2014; **9(11)**.
48. Banik SP, Mukherjee S, Pal S, Ghorai S, Majumder R, Khowala S. *Biotechnology Letters*, 2015; **37**:175-181.
49. Das A, Basak P, Pramanick A, Majumder R, Pal D, Ghosh A, Guria M, Bhattacharyya, Banik SP. *International Journal of Biological Macromolecules*, 2019; **127**:365-375.

50. Tanash EL, Sherief AB, Nour A. *Brazilian Journal of Chemical Engineering*, 2011; **28(03)**:381-391.
51. Alkhatib MF, Alam MZ, Mohammed R. *Australian Journal of Basic and Applied Sciences*, 2012; **6(1)**:30-38.
52. Mazzuca S, Giorno L, Spadafora A, Mazzei R, Drioli E. *Journal of Membrane Science*, 2006; **285**:152-158.
53. Lye GJ, Pavlou OP, Rosjidi M, Stuckey DC. *Biotechnology and Bioengineering*, 1996; **51(1)**: 69-78.
54. Trevan M. Wiley, Chichester, New York, 1980; pp 1-9.
55. Brodelius P, Mosbach K. In: Mosbach K (ed) *Methods in enzymology*, vol 135. Academic, London, 1987; pp 173-454.
56. Khan A, Alzohairy A. *Research Journal of Biological Sciences*, 2010; **5(8)**:565-575.
57. Buchholz K, Klein J. In: Mosbach K (ed) *Methods in enzymology*, vol 135. Academic, London, 1987; pp 3-30.
58. Cabral JMS, Kennedy JF. In: Taylor RF (ed) *Protein immobilization. Fundamentals and applications*, Marcel Dekker, New York, NY, 1991; pp 73-138.
59. Gemeiner P In: Gemeiner P (ed) *Enzyme engineering*, Ellis Horwood, New York, NY. 1992; pp 13-119.
60. Gupta M, Mattiasson B. In: Suelter CH (ed) *Methods of biochemical analysis*, 1992; vol 36. Wiley, New York, NY, pp 1-34.
61. Ahmed SA, El-Shayeb NMA, Hashem AM, Saleh SA, Abdel-Fattah AF. *Brazilian Journal of Chemical Engineering*, 2013; **30(04)**:747 - 758.
62. Zhou Y, Pan S, Wei X, Wang L, Liu Y. *BioResources*, 2013; **8(2)**:2605-2619.
63. Verma AK, Gupta A, Keerti, Dubey A. *International Food Research Journal*, 2018; **25(2)**: 655-660.
64. Orfanakis G, Patila M, Catzikonstantinou AV, Lyra KM, Kouloumpis A, Spyrou K, Katapodis P, Paipetis A, Rudolf P, Gournis D, Stamatis H. *Frontiers in Materials*, 2018; **5**:25.
65. Sannino F, Costantini A, Ruffo F, Aronne A, Venezia V, Califano V. *Nanomaterials*, 2020; **10**:108.
66. Savas E, Kaya MY, Karaagac O, Onat S, Kockar H, Yavas H, Kockar F. *CyTA - Journal of Food*, 2018; **16(1)**:840-847.
67. Yan J, Pan G, Li L, Quan G, Ding C, Luo A. *Journal of Colloid and Interface Science*, 2010; **348**:565-570.
68. Gonzalez-Saiz JM, Pizarro C. *European polymer Journal*. 2001; **37**:435-444.
69. Darjana ŽI, Vladimir VS, Mirjana GA. *Journal of Serbian Chemical Society*, 2014; **79(5)**: 533-543.
70. Onat S, Savaş E. *Italian Journal of Food Sciences*, 2019; **31**:749-763.
71. Radva D. *Theses of the doctoral dissertation Corvinus University of Budapest Department of Applied Chemistry Budapest*, 2013.
72. Kennedy F, Kalogerakis B, Cabral JMS. *Enzyme and Microbial Technology*, 1984; **6(3)**:127-131.
73. Woodward J, Capps KM. *Applied Biochemistry and Biotechnology*, 1992; **34**:341.
74. Abdel-Naby, M. *Microbiological research*, 1999; **154**.
75. Woodward J, Clarke KM. *Applied Biochemistry and Biotechnology*. 1991; **28**:277-283.
76. Wang F, Su RX, Qi W, Zhang MJ, He ZM. *Preparative Biochemistry and Biotechnology*, 2010; **40(1)**:57-64.
77. Zhou Y, Pan S, Wu T, Tang X, Wang L. *Electronic Journal of Biotechnology*, 2013; **16(6)**:6-6.
78. Gueguen Y, Chemardin P, Labrot P, Arnaud A, Galzy P. *Journal of Applied Microbiology*, 2003; **82**:469-476.
79. Jayant M, Rashmi J, Shailendra M, Deepesh Y. *Journal of Yeast and Fungal Research*, 2011; **2**:24-27.
80. Voutilainen SP, Puranen T, Siika-Aho M, Lappalainen M, Alapuranen M, Kallio J, Hooman S, Viikri L, Vehmaanpera J, Koivula A. *Biotechnology and Bioengineering*, 2008; **101(3)**:515-528.
81. Hong J, Tamaki H, Yamamoto K, Kumagai H. *Applied Microbiology and Biotechnology*, 2003; **63(1)**:42-50.
82. Murray P, Aro N, Collins C, Grassick A, Penttila M, Saloheimo M, Tuohy M. *Protein Expression and Purification*, 2004; **38(2)**:248-257.
83. Takashima S, Nakamura A, Hidaka M, Masaki H, Uozumi T, J. *Biotechnology*, 1996; **50(3)**:137-147.
84. Li YL, Li H, Li AN, Li DC. *Journal of Applied Microbiology*, 2009; **106(6)**:1867-1875.
85. Heinzelman P, Snow CD, Smith MA. *Journal of Biological Chemistry*. 2009; **284(39)**: 26229-26233.
86. Hong J, Tamaki H, Kumagai H. *Applied Microbiology and Biotechnology*, 2007; **73(6)**:1331-1339.
87. De Faria FP, Te'o VSJ, Bergquist PL, Azevedo MO, Nevalainen KMH. *Letters in Applied Microbiology*, 2002; **34**:119-123.
88. Kirikyali N, Wood J, Connerton IF. *AMB Express*, 2014; **4(68)**:1-7.
89. Boonyapakron K, Pootanakit K, Chantasingh D, Kirtikara K, Eurwilaichitr L. *DNA Sequence*, 2005; **16(5)**:372-378.
90. Khucharoenphaisan, K, Sinma K. *Biotechnology*, 2011; **10**:209-214.

91. Voronovsky AY, Rohulya OV, Abbas CA, Sibirny AA. *Metabolic Engineering*, 2009; **11**:234-242.
92. Huy ND, Park SM. *Vietnam Journal of Biotechnology*, 2012; **10(4A)**:785-791.
93. Aftab MN, Zafar A, Awan AR. *Bioengineered*, 2017; **8(5)**:665-669.
94. Pal S, Banik SP, Ghorai S, Chowdhury S, Khowala S. *Carbohydrate Research*, 2011; **346(15)**:2426-2431.
95. Mukherjee S, Chandrababunaidu M, Panda A, Khowala S, Tripathy S. *Frontiers in microbiology*, 2016; **7**:596.
96. Obeng E, Budiman C, Ongkudon C. *Biocatalysis and Agricultural Biotechnology*, 2017; **11**:67-74.
97. Deka D, Bhargavi P, Sharma A, Goyal D, Jawed M, Goyal A. *Enzyme Research*, 2011; **2011**: ID 151656.
98. Kshirsagar S, Waghmare P, Saratale G, Saratale R, Kurade M, Jeon BH, Govindwar S. *Applied Biochemistry and Biotechnology*, 2020; **191**:1695-1710.
99. Aro N, Pakula T, Penttilä M. *FEMS Microbiology Reviews*, 2005; **29(4)**:719-739.
100. Obeng E, Budiman C, Ongkudon C. *Biocatalysis and Agricultural Biotechnology*, 2017; **11**:67-74.
101. Seo JK, Park TS, Kwoni H, Piao MY, Lee CH, Jong KH. *Asian-Australasian Journal of Animal Sciences*, 2013; **26**:50-58.

Utilization of Guanidine-Based Ancillary Ligands in Arene–Ruthenium Complexes for Selective Cytotoxicity

Jit Karmakar, Promita Nandy, Saurabh Das, Debalina Bhattacharya, Parimal Karmakar, and Samaresh Bhattacharya*



Cite This: <https://doi.org/10.1021/acsomega.0c06265>



Read Online

ACCESS |



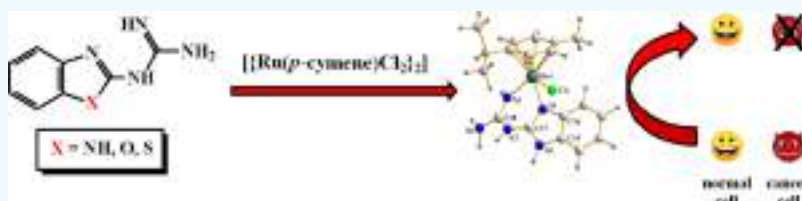
Metrics & More



Article Recommendations



Supporting Information



ABSTRACT: A family of three water-soluble half-sandwich arene–ruthenium complexes, depicted as C_1 – C_3 , having the general formula $[Ru(p\text{-cymene})(L)Cl]Cl$ has been synthesized, where L represents (1*H*-benzo[*d*]imidazol-2-yl)guanidine (L_1) or (benzo[*d*]oxazol-2-yl)guanidine (L_2) or (benzo[*d*]thiazol-2-yl)guanidine (L_3). The crystal structure of complex C_3 has been determined. The complexes show several absorption bands in the visible and ultraviolet regions, and they also show prominent emission in the visible region while excited near 400 nm. Studies on the interaction of ligands L_1 – L_3 and complexes C_1 – C_3 with calf thymus DNA reveal that the complexes are better DNA binders than the ligands, which is attributable to the imposed planarity of the ruthenium-bound guanidine-based ligand, enabling it to serve as a better intercalator. Molecular docking studies show that the complexes effectively bind with DNA through electrostatic and H-bonding interactions and partial intercalation of the guanidine-based ligands. Cytotoxicity studies carried out on two carcinoma cell lines (PC3 and A549) and on two non-cancer cell lines (BPH1 and WI-38) show a marked improvement in antitumor activity owing to complex formation, which is attributed to improvement in cellular uptake on complex formation. The C_1 complex is found to exhibit the most prominent activity against the PC3 cell line. Inclusion of the guanidine-based ligands in the half-sandwich ruthenium–arene complexes is found to be effective for displaying selective cytotoxicity to cancer cells and also for convenient tracing of the complexes in cells due to their prominent emissive nature.

1. INTRODUCTION

Development of a new series of therapeutic agents and modification of any existing series are an essential and challenging aspect of research related to the treatment of cancer. Platinum metal-based species, especially coordination and organometallic complexes, are widely employed as chemotherapeutics in combating this dreadful disease.¹ However, relatively low selectivity and adverse side effects of majority of these species have led to new initiatives toward development of better chemotherapeutic agents, particularly of new platinum metal-based anticancer complexes with minimal side effects and high selectivity and cytotoxicity toward cancer cells.

Among the platinum metal-based species, ruthenium compounds have found a very special position owing to their prominent anticancer activities.² Ruthenium-based molecular species are found to be promising candidates for the development of novel anticancer agents, primarily as they can bind DNA in several possible modes, a property usually not found in platinum-based species. Hence, the ruthenium-based species also have the potential to treat platinum-resistant cancers. Among the different oxidation states of ruthenium, the

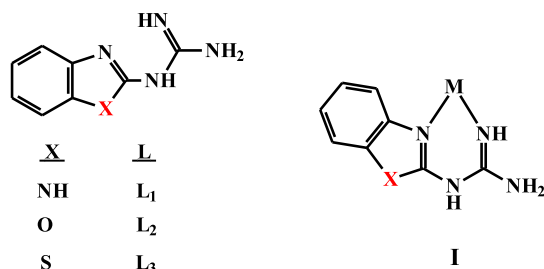
+2 state is most preferred for antitumor activity due to stability of the ruthenium(II) complexes in vitro. Proper choice of a ligand scaffold is crucial for inducing the desired DNA binding and antitumor activity in the ruthenium(II) complexes. In this context, half-sandwich ruthenium–arene complexes are particularly noteworthy.^{3,4} The presence of the planar arene moiety primarily blocks one face of the complex and thus directs most of the reactivity toward the other side. Besides, *para*-cymene, a heavily used arene moiety, is known to cause distortion in DNA conformation that eventually leads to DNA damage.⁵ In half-sandwich ruthenium–arene complexes, there is ample scope of varying the ligand/ligand combination to occupy the remaining three coordination sites on the metal center. In the present work, where our main objective was to develop a new family of half-sandwich ruthenium–arene

Received: December 24, 2020

Accepted: March 11, 2021

complexes for efficient DNA binding and anticancer activity, a group of three guanidine-based compounds was selected (Chart 1) as ancillary ligands. These ligands have several

Chart 1



important features, which are favorable for developing efficient DNA binding and anticancer agents. They have multiple N–H bonds, which are expected to favor solubility in water and binding with pyrimidine or purine bases via H-bonding and thus mislead the transcription process, resulting in DNA damage. In addition, the near-planar geometry of these ligands may enable them to function as intercalating moieties in the derived ruthenium complexes.^{3c,h,6} The skeleton of the selected ligands has close resemblance with that of 4',6-diamidino-2-phenylindole (DAPI), a conjugated system that is known to efficiently stain DNA present in a cell,⁷ which further encouraged us to use this group of ligands, with the hope that the mixed-ligand half-sandwich complexes derived from them may exhibit luminescence property and thus, they will be useful for measuring the capacity for cellular uptake and track a molecule within a cell. Among the three chosen ligands, synthesis of L₁ and L₂ and complexes of L₁ with few metals are known in the literature,^{8,9} while L₃ is, to the best of our knowledge, new and coordination chemistry of L₂ and L₃ appears to remain unexplored. The L₁ ligand is known to coordinate metal centers as a bidentate N,N-donor, forming a stable six-membered chelate ring (I, X = NH),⁹ and the L₂ and L₃ ligands are likely to display a similar mode of binding (I, X = O and S). As a source of ruthenium(II) and the arene moiety the dimeric [$\{\text{Ru}(p\text{-cymene})\text{Cl}_2\}_2$] compound was utilized. Reaction of the selected guanidine-based ligands (L₁–L₃) with [$\{\text{Ru}(p\text{-cymene})\text{Cl}_2\}_2$] indeed afforded half-sandwich ruthenium–arene complexes containing the ligands L₁–L₃. Herein, we describe the formation and characterization of these complexes, their DNA binding properties, and their cytotoxicity toward selected cancer cell lines.

2. EXPERIMENTAL SECTION

2.1. Materials. Ruthenium trichloride was purchased from Arora Matthey, Kolkata, India. α -Phellandrene, [$\text{Ru}(\text{bpy})_3$](ClO_4)₂, and dicyandiamide were purchased from Sigma-Aldrich, USA. *o*-Phenylenediamine, 2-aminophenol, and 2-aminothiophenol were procured from Spectrochem, India. The guanidine-based ligands (L₁–L₃) were synthesized by reaction between *o*-phenylenediamine (or 2-aminophenol or 2-aminothiophenol) and dicyandiamide following a reported protocol.⁸ [$\{\text{Ru}(p\text{-cymene})\text{Cl}_2\}_2$] was synthesized by following a published procedure.¹⁰ All other chemicals and solvents were reagent-grade commercial materials and were used as received.

2.2. Physical Measurements. Microanalyses (C, H, and N) were performed on a Heraeus Carlo Erba 1108 elemental analyzer. Magnetic susceptibilities were measured using a

Sherwood MK-1 balance. NMR spectra were recorded in CDCl_3 solution on Bruker Avance DPX 300 and 400 NMR spectrometers. IR spectra were obtained on a PerkinElmer Spectrum Two spectrometer with samples prepared as KBr pellets. Mass spectra were recorded with a Micromass LCT electrospray (Qtof Micro YA263) mass spectrometer. Electronic spectra were recorded on a PerkinElmer LAMBDA 25 spectrophotometer. Steady-state emission spectra were collected on a PerkinElmer LS 55 fluorescence spectrometer, and the quantum yields were determined by a relative method using [$\text{Ru}(\text{bpy})_3$]²⁺ as the standard. Solution electrical conductivities were measured using an Elico CM 180 conductivity meter with a solute concentration of ca. 10^{-3} M. Geometry optimization by the density functional theory (DFT) method and electronic spectral analysis by TDDFT calculation were performed using the Gaussian 09 (B3LYP/SDD-6-31G) package.¹¹

2.3. X-ray Crystallography. Single crystals of [$\text{Ru}(p\text{-cymene})(\text{L}_3)\text{Cl}]\text{Cl}$ (C₃) were grown by diffusion of diethyl ether vapor into a solution of the complex in acetonitrile. Selected crystal data and data collection parameters are given in Table 1. Data were collected on a Bruker SMART CCD

Table 1. Crystal Data and Details of the Structure Determination for Complex C₃

empirical formula	C ₁₈ H ₂₄ Cl ₂ N ₄ ORuS
formula mass	516.45
crystal system	orthorhombic
space group	<i>P</i> 2 ₁ 2 ₁ 2 ₁
<i>a</i> (Å)	7.5864(4)
<i>b</i> (Å)	12.9878(7)
<i>c</i> (Å)	21.6163(12)
<i>V</i> (Å ³)	2129.9(2)
<i>Z</i>	4
<i>D</i> _{calcd} (g/cm ³)	1.611
<i>F</i> (000)	1048
crystal size (mm)	0.16 × 0.18 × 0.24
<i>T</i> (K)	296
μ (mm ^{−1})	1.101
<i>R</i> ₁ ^a	0.0452
<i>wR</i> ₂ ^b	0.1175
GOF ^c	1.03

^a $R_1 = \sum |F_o| - |F_c| / \sum |F_o|$. ^b $wR_2 = [\sum [w(F_o^2 - F_c^2)^2] / \sum [w(F_o^2)^2]]^{1/2}$. ^cGOF = $[\sum [w(F_o^2 - F_c^2)^2] / (M - N)]^{1/2}$, where *M* is the number of reflections and *N* is the number of parameters refined.

diffractometer using graphite monochromated Mo $K\alpha$ radiation ($\lambda = 0.71073$ Å) at 296 K. X-ray structure solution and refinement were done using the SHELX-97 package.¹² H atoms were added at calculated positions.

2.4. Synthesis of Complexes. The [$\text{Ru}(p\text{-cymene})(\text{L})\text{Cl}]\text{Cl}$ complexes (C₁–C₃) were synthesized by following a general procedure as described below.

The guanidine-based ligand (L₁–L₃) (0.2 mmol) was dissolved in hot methanol (50 mL). To it was added a solution of [$\{\text{Ru}(p\text{-cymene})\text{Cl}_2\}_2$] (50 mg, 0.08 mmol) in dichloromethane (10 mL). The resulting solution was heated at reflux for 4 h to generate a yellowish-orange solution. The solvent was evaporated to almost one-fourth of its initial volume, diethyl ether (50 mL) was added to it, and the mixture was kept in a freezer for 12 h. Orange crystalline solid was

separated, which was collected by filtration, washed with dichloromethane followed with diethyl ether, and dried in air.

2.4.1. [Ru(*p*-cymene)(L₁)Cl]Cl (C₁). Yield: 79%. Anal. Calcd for C₁₈H₂₃N₅Cl₂Ru: C, 44.90; H, 4.78; N, 14.55. Found: C, 45.02; H, 4.68; N, 14.42%. MS-ES⁺ in CH₃OH (*m/z*): 410.1216 [M – HCl – Cl]⁺. IR data/cm^{−1}: 3367, 2969, 1673, 1611, 1581, 1462, 1268. ¹H NMR (DMSO-*d*₆, 500 MHz): δ (ppm) 7.43 (br s, 1H, NH), 7.28 (m, 2H, ArH), 7.09 (m, 2H, ArH), 6.03 (d, 2H, ArH, ³J_{HH} = 5.6 Hz), 5.87 (d, 2H, ArH, ³J_{HH} = 5.5 Hz), 3.43 (m, 1H, CH), 2.49 (s, 3H, CH₃), 1.01 (m, 6H, 2CH₃). ¹³C NMR (DMSO-*d*₆, 400 MHz): δ (ppm) 158.6, 152.3, 129.2, 126.4, 122.0, 112.4, 111.5, 30.5, 24.3. Molar conductivity in methanol at 298 K [Λ_M/S m² M^{−1}]: 83.

2.4.2. [Ru(*p*-cymene)(L₂)Cl]Cl (C₂). Yield: 74%. Anal. Calcd for C₁₈H₂₂N₄O₁Cl₂Ru: C, 44.81; H, 4.56; N, 11.61. Found: C, 44.50; H, 4.41; N, 11.91%. MS-ES⁺ in CH₃OH (*m/z*): 411.1928 [M – HCl – Cl]⁺. IR data/cm^{−1}: 3392, 1690, 1620, 1562, 1457, 1324, 1243. ¹H NMR (DMSO-*d*₆, 500 MHz): δ (ppm) 7.91 (br s, NH), 7.50 (d, 1H, ArH, ³J_{HH} = 8.0 Hz), 7.48 (d, 1H, ArH, ³J_{HH} = 8.0 Hz), 7.27 (m, 1H, ArH), 7.21 (m, 1H, ArH), 5.77 (d, 1H, ArH, ³J_{HH} = 6.0 Hz), 5.72 (d, 1H, ArH, ³J_{HH} = 5.5 Hz), 2.80 (m, 1H, CH), 2.50 (s, 3H, CH₃), 1.17 (m, 6H, 2CH₃). ¹³C NMR (DMSO-*d*₆, 400 MHz): δ (ppm) 158.1, 154.5, 135.5, 122.2, 116.0, 110.2, 106.3, 43.4, 35.6. Molar conductivity in methanol at 298 K [Λ_M/S m² M^{−1}]: 81.

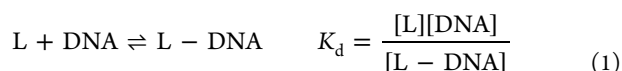
2.4.3. [Ru(*p*-cymene)(L₃)Cl]Cl (C₃). Yield: 81%. Anal. Calcd for C₁₈H₂₂N₄S₁Cl₂Ru: C, 43.37; H, 4.41; N, 11.24. Found: C, 43.20; H, 4.43; N, 11.40%. MS-ES⁺ in CH₃OH (*m/z*): 427.0103 [M – HCl – Cl]⁺. IR data/cm^{−1}: 3408, 3246, 2964, 2817, 1680, 1613, 1598, 1520, 1445, 1390, 1284, 1254, 1230. ¹H NMR (DMSO-*d*₆, 400 MHz): δ (ppm) 7.25 (s, NH), 6.96 (d, 2H, ArH, ³J_{HH} = 8.5 Hz), 6.73 (d, 2H, ArH, ³J_{HH} = 8.5 Hz), 5.20 (br m, 2H, ArH), 4.96 (br m, 2H, ArH), 2.99 (m, 1H, CH), 1.59 (s, 3H, CH₃), 1.40 (m, 6H, 2CH₃). ¹³C NMR (DMSO-*d*₆, 500 MHz): δ (ppm) 160.1, 157.5, 152.0, 125.6, 120.0, 102.5, 30.7, 22.6. Molar conductivity in methanol at 298 K [Λ_M/S m² M^{−1}]: 85.

2.5. Biological Studies. 2.5.1. Interaction with CT-DNA.

Phosphate buffer was prepared using NaH₂PO₄ and Na₂HPO₄ using triple-distilled water. Sodium nitrate (AR) was used to maintain the ionic strength of the medium. Calf thymus DNA, purchased from Sisco Research Laboratories, India, was dissolved in triple-distilled water containing 120 mM NaCl, 35 mM KCl, and 5 mM CaCl₂. Absorbance was recorded at 260 and 280 nm; A₂₆₀/A₂₈₀ was determined. The ratio being between 1.8 and 1.9 suggests that the DNA was sufficiently free from protein. It was characterized by measuring its CD spectrum at 260 nm using a CD spectropolarimeter (J815, JASCO). Concentration was determined in terms of nucleotide, considering the molar extinction coefficient at 260 nm to be 6600 M^{−1} cm^{−1}.

50 μM L₁ (ligand) and 50 μM C₁ (complex) were titrated separately with calf thymus DNA at constant pH and ionic strength of the medium. For the interaction of L₁ followed by fluorescence spectroscopy, excitation was done at 295 nm and emission was recorded at 331 nm. For the complex, the excitation was done at 425 nm and emission was recorded at 496 nm. Ionic strength was maintained using NaCl and NaNO₃. The interaction of the compounds with DNA during titration led to a decrease in fluorescence in the case of the ligand and to an increase in fluorescence for the complex at the respective wavelengths where they were followed. The

interaction of compounds with DNA could be realized with eq 1.^{13–18}



L represents compounds and K_d is the dissociation constant for the interaction whose reciprocal provides the apparent binding constant (K_{app}). Equation 2 is obtained from eq 1 where the reciprocal of the change in absorbance was plotted against the reciprocal of (C_D – C₀).^{13–18} C_D refers to concentration of calf thymus DNA and C₀ refers to concentration of compounds. Using eq 2, ΔF_{max} could be determined along with K_{app} (1/K_d) from the intercept and slope.^{13–18}

$$\frac{1}{\Delta F} = \frac{1}{\Delta F_{\max}} + \frac{K_d}{\Delta F_{\max}(C_D - C_L)} \quad (2)$$

ΔF represents the change in fluorescence of the compounds interacting with the calf thymus DNA during titration, while ΔF_{max} indicates the maximum possible change in fluorescence.

$$K_d = \frac{\left[C_L - \left(\frac{\Delta F}{\Delta F_{\max}} \right) C_L \right] \left[C_D - \left(\frac{\Delta F}{\Delta F_{\max}} \right) C_L \right]}{\left(\frac{\Delta F}{\Delta F_{\max}} \right) C_L} \quad (3)$$

$$C_L \left(\frac{\Delta F}{\Delta F_{\max}} \right)^2 - (C_L + C_D + K_d) \left(\frac{\Delta F}{\Delta F_{\max}} \right) + C_D = 0 \quad (4)$$

ΔF/ΔF_{max} was plotted against C_D. Equations 3 and 4 were used to fit the data to a non-linear square fit that provides another set of values for the apparent binding constant.^{13–18} Titrations were also analyzed using a modified form of the Scatchard equation [eq 5].¹⁹ The overall binding constant (K') and site size (n) were determined.

$$\frac{r}{C_f} = K'(n - r) \quad (5)$$

r denotes the ratio of the concentration of the compound bound to DNA to the total concentration of DNA present in the reaction mixture at any point of the titration (C_b/C_D); C_b is the concentration of the bound compound, while C_f is that of the free compound. “n” provides binding stoichiometry in terms of the bound compound per nucleotide, while “n_b” being the reciprocal of “n” denotes binding site size in terms of the number of nucleotides bound to a compound. “n_b” was obtained by plotting ΔF/ΔF_{max} against C_D/[compound]. K' may also be obtained by multiplying K_{app} with “n_b” and is compared with values obtained from a modified form of the Scatchard equation.

2.5.2. Molecular Docking Studies. Molecular docking studies on complexes C1–C₃ were performed using HEX 6.3 software to identify possible binding sites in biomolecules. The three guanidine-based ligands (L₁–L₃) were also docked using AutoDockTools 1.5.6 software. The coordinates of each ruthenium complex were taken from its optimized structure as a .mol file and converted to a .pdb format using PyMOL 2.4 software. The crystal structure of B-DNA (PDB ID: 1BNA) was retrieved from the Protein Data Bank (<http://www.rcsb.org/pdb>). Visualization of the docked systems was performed using BIOVIA Discovery Studio Visualizer (DSV) 2020 software. Default parameters were used for docking calculations with the correlation type shape only, FFT mode at the

3D level, and grid dimension of 0.6 with receptor range 180 and ligand range 180 with twist range 360 and distance range 40.

2.5.3. Cell Culture. PC3, BPH1, A549, and WI-38 lung fibroblast cells were cultured in RPMI or DMEM medium (GIBCO, Invitrogen, Carlsbad, CA, US) supplemented with 10% fetal bovine serum (GIBCO), 100 IU/mL penicillin, and 100 $\mu\text{g/mL}$ streptomycin at 37 °C in a humidified atmosphere containing 5% CO_2 (Heraeus, Thermo Scientific, MA, USA). All cell lines were procured from the National Centre for Cell Science in Pune, India. Cells were seeded in 96 well plates for 24 h prior to treatment with compounds.

2.5.4. MTT Assay. The antiproliferative effect of three complexes and the guanidine-based ligands on four cell lines, PC3, BPH1, A549, and WI-38 was determined by the MTT assay. Cells were seeded at a density of 1×10^4 cells per well in a 24-well plate. Next, the cells were exposed to the complex and its ligand at different concentrations for another 24 h. After incubation, cells were washed with $1\times$ PBS twice. Thereafter, they were treated with 0.5 mg mL^{-1} MTT solution (SRL) and incubated for 3–4 h at 37 °C until an insoluble purple-colored formazan product developed. The resulting product was dissolved in MTT extraction buffer and the OD was measured at 570 nm using a microplate reader (Epoch). The percentage survival was calculated considering the untreated cells as 100%.

2.5.5. Single-Cell Gel Electrophoresis/Comet Assay. A comet assay was performed after treating the cells (PC3 and BPH1) with complex C_1 for 24 h at the lower (20 μM) and higher (80 μM) concentrations of the IC_{50} dose of 39.5 μM for PC3. Briefly, 1×10^5 cells mL^{-1} were mixed with 0.7% LMPA and embedded onto frosted slides. The slides were then dipped in a lysis solution [2.5 M NaCl, 100 mM EDTA, 10 mM Tris–HCl (pH 10)] that contains freshly added 1% Triton-X 100 and 10% DMSO and incubated for 1 h at 4 °C and placed into a horizontal electrophoresis tank filled with freshly prepared buffer (1 mM EDTA, 300 mM NaOH). Next, electrophoresis was performed for 20 min at a fixed voltage of 25 V and 300 mA. After that, slides were washed with a neutralization buffer (0.4 M Tris–HCl, pH 7.5) followed by staining with 20 mg mL^{-1} ethidium bromide (SRL, India) for 15 min. The slides were then washed three times with $1\times$ PBS and observed under a fluorescence microscope (model: Leica, Germany). Around 50 comets per slide were counted for both the cell lines. An extension of each comet was analyzed using a computerized image analysis system (Kometsoftware 5.5) that gave % of tail DNA.²⁰

2.5.6. DAPI Staining. After exposure with complex C_1 at lower and higher concentrations of the IC_{50} dose of PC3 (39.5 μM) for 24 h, both the cells (PC3 and BPH1) were washed several times with $1\times$ PBS and stained with 0.2 mg mL^{-1} DAPI in Vecta shield (Vector Laboratories Inc.). The percentage of cells with ruptured and decondensed nuclei was counted under a fluorescence microscope (Leica) and photographs were taken at $40\times$ magnification.

2.5.7. Measurement of Intracellular Reactive Oxygen Species. The production of intracellular reactive oxygen species (ROS) was estimated using a fluorescent dye, DCFDA. Approximately, 3×10^5 cells per well were seeded in 35 mm plates, and after 24 h of seeding, cells were incubated with 20 μM DCFDA (Sigma) dye for 1 h at 37 °C under dark conditions followed by the treatment of complex C_1 for 24 h, at the lower (20 μM) and higher (80 μM) concentrations of

the IC_{50} doses of PC3 (39.5 μM). Cells without the complex were used as control. Fluorescence intensity was measured in a fluorescence spectrophotometer (model Hitachi, USA) at excitation and emission wavelengths of 504 and 529 nm, respectively. To nullify the autofluorescence of the complex which may interfere with the DCFDA dye, a set of experiments without cells were performed simultaneously.

2.5.8. Cellular Imaging Study. Both the cell lines PC3 and BPH1 were seeded in a cover slip for overnight. Next day, cells were incubated with 3 mM complex C_1 for 1 h in 37 °C in a CO_2 incubator. After incubation, cells were washed several times with $1\times$ PBS under dark conditions. Cells were then stained with DAPI in Vecta shield and observed under a fluorescence microscope.

3. RESULTS AND DISCUSSION

3.1. Synthesis and Characterization. As delineated in the Introduction, the first task of the present study was to synthesize a group of arene–ruthenium complexes using the chosen guanidine-based ancillary ligands (L_1 – L_3). Accordingly, reactions of these ligands (L_1 – L_3) with $[\{\text{Ru}(p\text{-cymene})\text{Cl}_2\}_2]$ were carried out in 5:1 methanol/dichloromethane, which furnished the desired complexes of type $[\text{Ru}(p\text{-cymene})(\text{L})\text{Cl}]\text{Cl}$ in decent yields. The three complexes obtained with ligands L_1 , L_2 , and L_3 are depicted, respectively, as C_1 , C_2 , and C_3 . Preliminary characterization (microanalysis, mass, IR, and NMR) data of these complexes agreed well with their compositions. In order to ascertain the coordination mode of the guanidine-based ligands in these complexes, the crystal structure of C_3 was determined by X-ray crystallography.²¹ The structure is presented in Figure 1, and

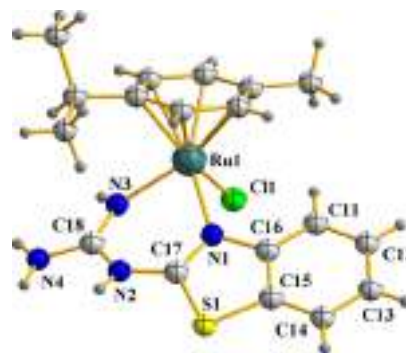


Figure 1. Crystal structure of the $[\text{Ru}(p\text{-cymene})(\text{L}_3)\text{Cl}]^+$ complex.

some selected bond distances and angles are provided in Table 2. The structure reveals that the guanidine-based ligand (L_3) is

Table 2. Selected Bond Distances and Bond Angles of Complex C_3

Bond Distances (Å)			
Ru1–Cl1	2.4309(16)	N2–C18	1.377(8)
Ru1–N1	2.106(4)	N3–C18	1.308(8)
Ru1–N3	2.074(5)	N4–C18	1.340(9)
N1–C16	1.406(8)	S1–C15	1.734(7)
N1–C17	1.316(7)	S1–C17	1.739(6)
N2–C17	1.356(8)		
Bond Angles (deg)			
N1–Ru1–N3	82.83(19)	Cl1–Ru1–N1	86.13(16)
		Cl1–Ru1–N3	88.50(17)

coordinated to ruthenium as a neutral N,N-donor, forming a six-membered chelate ring (I, X = S and M = Ru) with a bite angle of $\sim 83^\circ$. The Ru(L₃) fragment of the complex is found to be nearly planar, as envisaged. The *p*-cymene moiety is bound to ruthenium in the usual π -fashion, and a chloride ion has taken up the sixth coordination site on the metal center. Another isolated chloride ion was located outside the coordination sphere. The bond parameters around ruthenium and within the coordinated organic ligands are all found to be quite usual.^{3,9} Based on the similarity of the synthetic method and properties (vide infra), the other two complexes (C₁ and C₂) are assumed to have similar structures as C₃.

3.2. Spectral Studies. Magnetic susceptibility measurements show that the C₁–C₃ complexes are diamagnetic, which is consistent with the +2 oxidation state of ruthenium (low-spin d^6 $S = 0$) in them. In the ¹H NMR spectra of the complexes, signals from both the coordinated *p*-cymene and guanidine-based ligand were expected, majority of which could be identified. For example, all the signals for the *p*-cymene ligand could be distinctly observed in all three complexes. Three signals from the alkyl groups are observed within 1.1–3.5 ppm and two signals from the aromatic fragment are observed within 5.2–5.8 ppm. From the guanidine-based ligands, the NH and NH₂ signals appeared within 6.5–8.2 ppm, while signals from the aromatic protons are observed around 7.5 ppm. In complex C₁, a broad signal is observed at 10.50 ppm, which is absent in the spectra of the other two complexes, and hence, it is attributable to the benzimidazole-NH in metal-bound L₁. ¹³C NMR spectra of the complexes are also found to be consistent with their compositions. For the *p*-cymene ligand, three signals from the alkyl carbons are found below 40 ppm and four from the aromatic carbons appear within 70–90 ppm. For the guanidine-based ligands, two signals are observed above 150 ppm and signals from the phenyl ring are found within 110–130 ppm.

The mass spectra of complexes C₁–C₃, recorded in the positive ion mode, provide proof of coordination of the guanidine-based ligands. Each complex shows a peak at a m/z value that corresponds to the [Ru(*p*-cymene)(L-H)]⁺ fragment, which is generated via loss of HCl from the cationic [Ru(*p*-cymene)(L)Cl]⁺ unit. Associated with loss of the coordinated chloride ion, loss of proton is believed to take place from the central –NH– moiety of the guanidine-based ligand. This particular proton in such ligands is known to undergo facile dissociation.²² Elimination of one equivalent HCl from compositionally similar arene–ruthenium complexes is precedent.²² A similar mass spectral behavior of complexes C₁–C₃ supports their similar composition and structure.

Infrared spectra of complexes C₁–C₃, recorded in the 450–4000 cm^{−1} region, exhibit several bands. Upon comparison of the spectrum of each complex with that of the starting [Ru(*p*-cymene)Cl₂]₂ complex reveals the presence of several new bands (near 3400, 3180, 1680, 1615, 1256, and 752 cm^{−1}) in the spectra of the complexes, which are attributable to the coordinated guanidine-based ligand. Among these bands, the two near 3400 and 3180 cm^{−1} are attributable to the –NH– and –NH₂ fragments, respectively. The NMR and IR data are therefore in good agreement with the composition of the complexes.

The C₁–C₃ complexes are soluble in polar solvents, such as water, methanol, ethanol, dimethylformamide, and dimethylsulfoxide, producing yellow solutions. Electronic spectra of the complexes were recorded in methanol solutions. Spectral data

are presented in Table 3. Each complex shows four absorptions spanning the visible and ultraviolet regions. To have an insight

Table 3. Electronic Absorption and Emission Spectral Data of the Complexes

complex	absorption spectral data ^a		emission spectral data ^a	
	λ_{max} , nm (ϵ , M ^{−1} cm ^{−1})	λ_{F} , nm [$\Phi_{\text{F}} \times 10^{-3}$] ^c	life time (τ)	
C ₁	451 (400), 294 (5940), 237 ^b , 211 (21,970)	518 [8.6]	$\tau_1 = 0.26$ ns, $\tau_2 = 4.10$ ns	
C ₂	449 (530), 282 (9190), 239 ^b , 209 (22,770)	558 [6.5]	$\tau_1 = 1.75$ ns	
C ₃	429 (490), 289 (7780), 255 ^b , 220 (28,780)	486 [17.3]	$\tau_1 = 0.36$ ns, $\tau_2 = 5.02$ ns	

^aIn methanol. ^bShoulder. ^cQuantum yield was calculated with reference to [Ru(bpy)₃]²⁺ ($\Phi_{\text{F}} = 0.09$).

into the nature of these absorptions, TDDFT calculations have been performed on the C₁–C₃ complexes, using the Gaussian 09 package,¹¹ and the results are found to be similar for all the complexes. The DFT-optimized structures of the complexes are shown in Figure S1 (Supporting Information) and some computed bond parameters are listed in Table S1 (Supporting Information). The computed bond parameters in the DFT-optimized structure of C₃ are comparable with those found in its crystal structure. The main calculated transitions for the C₁–C₃ complexes and compositions of the molecular orbitals associated with the transitions are presented in Tables S2–S7 (Supporting Information), and contour plots of selected molecular orbitals are shown in Figure S2 (Supporting Information). As the computed optical transitions and compositions of the participating orbitals are similar for all three complexes, the case of C₁ is described here as representative. Plots of experimental and theoretical spectra for C₁ are deposited in Figure S3 (Supporting Information). The close match between each set of experimental and theoretical spectra testifies validity of the optimized structures of the complexes, particularly of complexes C₁ and C₂, for which crystal structures remained elusive. The lowest energy absorption at 451 nm is attributable primarily to a HOMO – 1 → LUMO transition, with much less HOMO – 3 → LUMO, HOMO – 2 → LUMO and HOMO → LUMO character. Additionally, based on the nature of the participating orbitals, the electronic excitation is best described as a MMCT transition mixed with some MLCT, LMCT, and LLCT character. The next absorption at 294 nm is mostly due to a HOMO – 1 → LUMO + 2 transition and assignable primarily to a MLCT transition with much less LLCT and ILCT character. The third absorption at 237 nm is largely due to a HOMO – 3 → LUMO + 2 transition and has a dominant MLCT character. The fourth absorption at 211 nm has a dominant HOMO – 3 → LUMO + 4 character and is assignable to a MLCT transition with some LLCT character.

Luminescence property of the complexes was examined in methanol solution. All three complexes were found to show prominent emission when excited near 400 nm (Table 3). It is interesting to note that the complexes absorb and emit in the visible region, a property much sought after in an antitumor agent for its easy identification in a biological matrix.

3.3. DNA Binding Studies. The interaction of the calf thymus DNA with complex C₁, a representative of this family of complexes, was studied in detail to assess its potential as an antitumor agent. Initially, titration of the uncoordinated

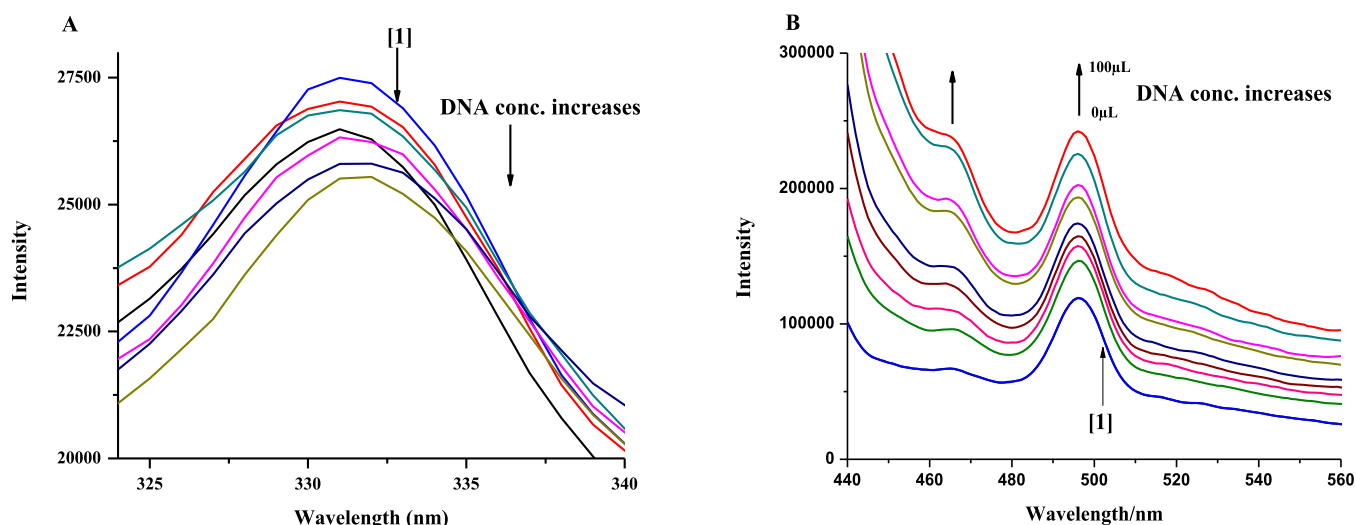


Figure 2. Fluorescence emission spectra of (A) 50 μM L_1 and (B) 50 μM C_1 in aqueous solution in the presence of 0.12 M NaCl and 30 mM Tris buffer (pH 7.4) in the absence (1) and presence of different concentrations of calf thymus DNA; temperature = 300 K.

Table 4. Binding Constant Values Obtained for the Interaction of Ligand L_1 and Complex C_1 with the Calf Thymus DNA that was Followed by Fluorescence Spectroscopy

compound	expt	K_{app}				site size n_b	$K^* = K_{\text{app}} \times n_b$				n_b from Scatchard as $n_b = (n^{-1})$
		from double-reciprocal plot (a)	from non-linear plot (b)	from double-reciprocal plot with y -intercept = 1 (c)			from double-reciprocal plot (a)	from non-linear plot (b)	from double-reciprocal plot with y -intercept = 1 (c)	K^* from Scatchard	
L_1	1	2.80×10^3	3.30×10^3	1.60×10^3	8		2.20×10^4	2.60×10^4	1.28×10^4	1.86×10^4	8
	2	2.20×10^3	2.80×10^3	2.20×10^3	9		1.98×10^4	2.50×10^4	1.98×10^4	3.60×10^4	7
C_1	1	0.94×10^4	0.80×10^4	0.70×10^4	13		1.20×10^4	1.04×10^4	0.91×10^4	1.53×10^4	15
	2	1.60×10^3	1.04×10^3	0.78×10^3	14		2.20×10^4	1.40×10^4	1.09×10^4	2.15×10^4	14

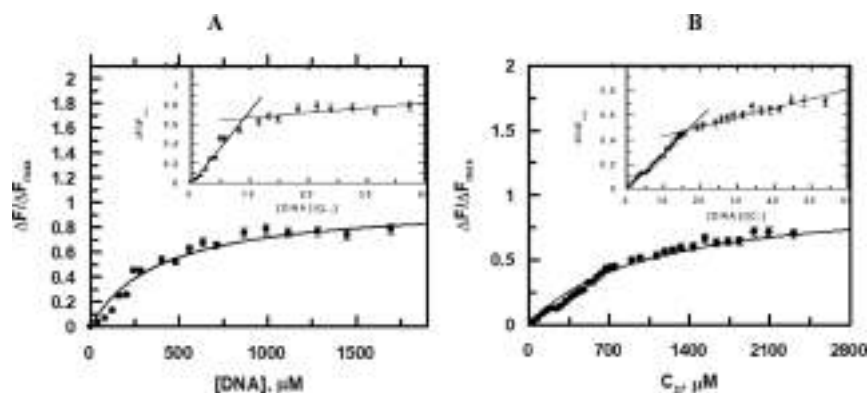


Figure 3. Binding isotherms for (A) ligand L_1 and (B) complex C_1 binding to the calf thymus DNA at pH ~ 7.4 and an ionic strength of 0.12 M. Corresponding non-linear fits are shown for these titrations that evaluate K_{app} . Inset: plot of the normalized increase in fluorescence as a function of the ratio of the calf thymus DNA to (A) ligand L_1 and (B) complex C_1 . $[\text{L}_1] = [\text{C}_1] = 50 \mu\text{M}$, pH = 7.40, $T = 300 \text{ K}$.

guanidine-based ligand L_1 was carried out with the calf thymus DNA. Figure 2A shows a typical plot of this titration at the ionic strength and pH mentioned. Figure 2B is a similar plot for a titration performed with complex C_1 . The plots show that saturation is achieved in the binding of the compounds with DNA. Representative plots based on eq 2 are shown in Figure S4 (Supporting Information), from which the apparent binding constant (K_{app}) was evaluated (Table 4).^{13–18} Plots in Figure 3A,B were fitted by the non-linear square fit analysis that also helps to evaluate K_{app} . Different binding parameters are shown in Table 4. The inset of Figure 3A,B provides n_b , the number of nucleotides bound to each compound (Table 4).^{13–18} It is

worth mentioning that the value for n_b obtained in the case of the complex binding to the calf thymus DNA was approximately 1.5 times greater than that obtained when the guanidine-based ligand L_1 binds to the same DNA, suggesting that the complex engages more nucleic acid bases when it interacts with DNA, thus being able to bring about more distortion in DNA, an outcome of enforced planarity of the guanidine portion of the ligand following chelation to ruthenium (Table 4).^{15,16,18}

Utilizing K_{app} and n_b from Table 4 and the relation $K_{\text{app}} \times n_b = K'$, the overall binding constants could be evaluated for the uncoordinated guanidine-based ligand L_1 and complex

C_1 .^{13–18} Overall binding constants were also obtained from a modified version of the original Scatchard equation (eq 5),¹⁹ and plots obeying this equation are shown in Figure S5 (Supporting Information). The overall binding constant values from the Scatchard equation were strikingly similar to those evaluated by multiplying K_{app} with n_b (eqs 2 and 4).

An interesting aspect regarding titration of the complex with the calf thymus DNA, followed by fluorescence spectroscopy, was that with an increase in the concentration of DNA (Figure 4), there was a gradual increase in fluorescence similar to that

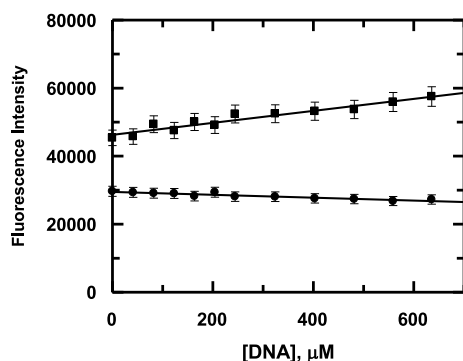


Figure 4. Gradual variation in fluorescence observed for the compounds as the calf thymus DNA was added during titration; (■) complex C_1 , (●) ligand L_1 . Ionic strength of medium = 0.12 M; pH \sim 7.4; $[L_1] = [C_1] = 50 \mu\text{M}$; temperature = 300 K.

observed for compounds including ethidium bromide that are known to intercalate DNA.^{23–26} Hence, a logical conclusion is that the complex too is able to intercalate DNA, registering an increase in fluorescence. Such an increase in fluorescence upon interactions is an important attribute of the complex that may be utilized in a number of biological experiments to realize possible interactions of the compound with a biological target.

3.4. Molecular Docking with DNA. To elucidate the mode of interaction and binding affinity, docking studies were performed on B-DNA (PDB ID: 1BNA) in the presence of all the three complexes. The results show that the complexes interact with DNA quite similarly via the electrostatic mode. This is illustrated in Figure 5 for complex C_1 and in Figures S6 and S7 (Supporting Information) for complexes C_2 and C_3 , respectively. In each case, the guanidine-based ligand is observed to form H-bonds with oxygen atoms of the phosphate backbone and also with the N3 atom of adenine of a single DNA strand. Additional H-bonding is observed in

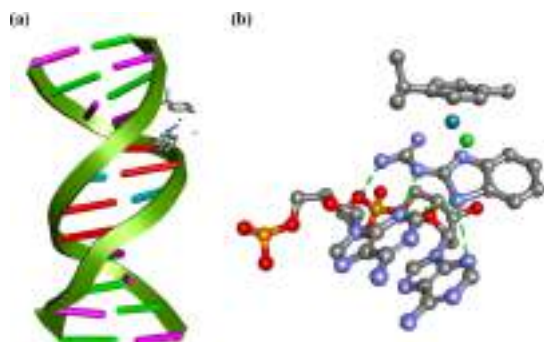


Figure 5. (a) Complex C_1 interacted with the DNA strand and (b) core view of the interaction (ball and stick model).

complex C_1 due to the presence of an NH fragment in L_1 that is absent in L_2 or L_3 . The coordination-induced planarity of the guanidine-based ligands is found to favor strong H-bonding interactions, with better match of the complexes inside DNA strands allowing partial intercalation. Due to the combined effect of the van der Waals and H-bonding interactions, the complexes fit comfortably into the minor groove of the targeted DNA near the A–T rich regions.

Docking of the individual guanidine-based ligands with DNA has also been looked into. From the docked structures (Figure S8; Supporting Information), it is observed that the L_1 ligand shows the highest binding affinity to DNA, which is attributable to additional H-bonding possible due to the presence of an NH fragment in L_1 , instead of oxygen (in L_2) or sulfur (in L_3). The same trend is observed in the complexes, which is also manifested in the biological studies. It is interesting to note that while all the uncoordinated guanidine-based ligands preferred to approach the G–C base pairs, upon binding to the metal center, the A–T base pairs have become their preferred binding location. Planarity of the guanidine-based ligands in the complexes and the presence of the Ru-coordinated *p*-cymene probably have caused this observed variation in their binding preference.

3.5. Cytotoxicity Studies. Cisplatin shows a remarkable efficacy in treating prostate cancer and has been quite successfully and extensively used in the last few decades.^{27–29}

However, as delineated in the Introduction, ruthenium-based molecular species, particularly the half-sandwich ruthenium–arene complexes, are also attracting attention owing to their demonstrated anticancer activities with minimal side effects. Encouraged by the prominent DNA binding properties of our three complexes (C_1 , C_2 , and C_3), we also determined the potency of these three complexes and cisplatin on the human prostate cancer cell line PC3 and the human benign prostate tumor cell line BPH1. Similarly, we have evaluated the toxic effect of these three complexes and cisplatin on the lung cancer cell line A549 and the normal lung fibroblast cell line WI-38. Cells were treated with three complexes (C_1 , C_2 , and C_3) in the concentration range of 0–100 μM for 24 h, followed by MTT assay. The results are displayed in Figure 6. Complex C_1 was found to be the most cytotoxic to PC3 cells ($IC_{50} = 39.5 \pm 1.57 \mu\text{M}$) among the three complexes (Figure 6A). Complex C_1 was found to be non-toxic to the human prostate benign tumor cell line BPH1 even after 24 h of treatment, which suggests no side effects of it on non-carcinoma cells in our body. In this context, it is worth mentioning that cisplatin shows comparable cytotoxicity toward both PC3 and BPH1 cell lines. In A549 and WI-38 cell lines, C_1 shows moderate (IC_{50} values 69.4 ± 1.2 and 69.6 ± 3.45) and almost comparable cytotoxicity like cisplatin (IC_{50} values 60.1 ± 2.43 and 66.5 ± 2.12). Guanidine-based ligands (L_1 , L_2 , and L_3) have no cytotoxicity toward any type of cell lines, which signifies the effect of their coordination to ruthenium in antiproliferative activity. Figure 6B shows the % cell survival comparison between BPH1 and PC3 with C_1 complex for 24 h. The IC_{50} doses for all the complexes and cisplatin are summarized in Table 5. Interestingly, it was observed that the complexes could not exert significant toxicity toward A549 and WI-38. Among the different cells we have tested, only PC3 is PTEN-negative. Thus, it is reasonable to state that cytotoxicity generated through the compounds is presumably governed by nonfunctional PTEN. Similar results are also found in the case

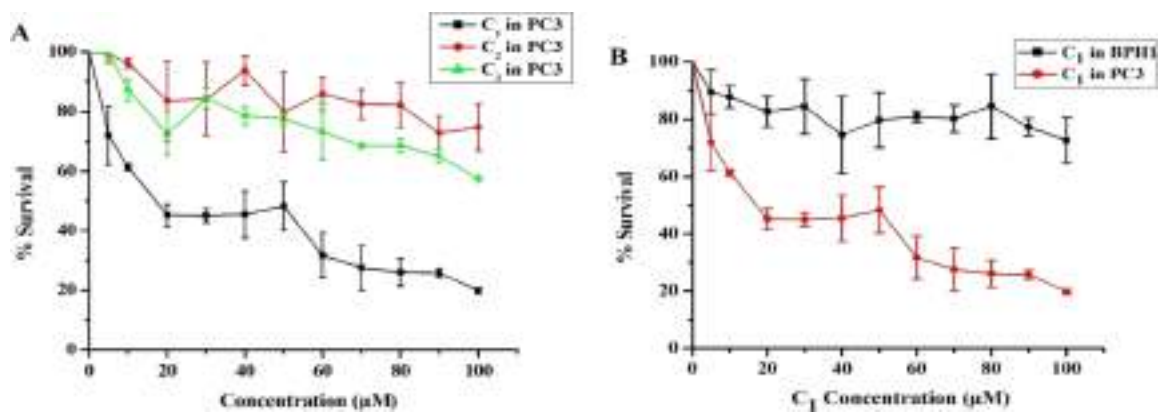


Figure 6. (A) MTT assay on the PC3 cell line after 24 h of treatment with three separate complexes C₁–C₃. (B) MTT assay on PC3 and BPH1 cell lines after 24 h of treatment with the C₁ complex. Data are presented as % survival relative to the untreated control. They are the mean ± SD of three independent experiments.

Table 5. IC₅₀ Values of Ligands (L) and Complexes toward Different Cell Lines^a

complex	PC3	BPH1	A549	WI-38	R ₁ ^b	R ₂ ^c
L ₁	121.0 ± 1.57	>500 ± 4.5	>200 ± 2.2	>500 ± 4.67	nd	nd
L ₂	168.8 ± 1.9	>500 ± 4.09	167.4 ± 1.77	>500 ± 5.03	nd	nd
L ₃	446.4 ± 1.05	>500 ± 2.32	>200 ± 1.86	>500 ± 4.41	nd	nd
C ₁	39.5 ± 1.57	263.0 ± 1.87	69.4 ± 1.2	69.6 ± 3.45	6.6	1.0
C ₂	267.3 ± 2.01	443.9 ± 1.04	168.6 ± 1.5	135.9 ± 3.21	1.6	0.8
C ₃	125.0 ± 1.43	175.2 ± 1.88	112.2 ± 1.9	135.7 ± 4.89	1.4	1.2
cisplatin	5.4 ± 1.93	8.0 ± 1.03	60.1 ± 2.43	66.5 ± 2.12	1.4	1.1

^aThe drug treatment period was 24 h. ^bR₁ = IC₅₀ ratio of BPH1 cells to PC3 cells. ^cR₂ = IC₅₀ ratio of WI-38 cells to A549 cells.

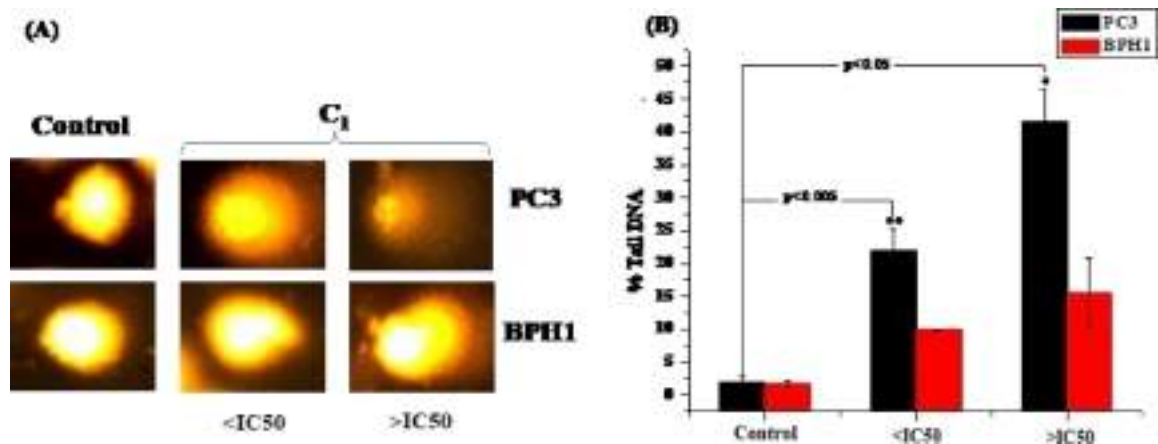


Figure 7. (A) Representative images of the comet assay of PC3 and BPH1 cell lines treated with the C₁ complex with respect to the untreated control. (B) Histogram shows % of comet tail DNA for PC3 and BPH1 cells treated with the C₁ complex for 24 h with respect to their untreated control at two different doses (<IC₅₀ and >IC₅₀ doses of PC3). Values are the mean ± SD of three independent experiments. *($p < 0.005$) and **($p < 0.005$) denote the statistically significant difference compared to the untreated control.

of curcumin.³⁰ All the other biological studies were done on two cell lines, PC3 and BPH1, taking C₁ as a model complex. The cytotoxic effect of the C₁ complex is most likely linked to the DNA-damaging effects of the compound, and hence, we performed comet assay, a very useful and sensitive experiment for elucidating single- or double-strand DNA damage caused by any exogenous or endogenous species.³¹ A small amount of nuclides/cells is required to perform this experiment and the tail length is considered to represent the level of DNA damage.³² As shown in Figure 7A, the C₁ complex caused significantly ($p < 0.05$) more DNA damage at a concentration <IC₅₀ or >IC₅₀ dose in the case of PC3. However, at the same

concentrations, no significant ($p > 0.05$) DNA damage was observed when BPH1 is used. Consistent with these data, the percentage of tail DNA increased significantly ($p < 0.05$) for C₁ complex-treated PC3 cells after 24 h of treatment (Figure 7B). Nuclear morphology and the nature of cell death were studied by DAPI staining. The fluorescence micrographs of DAPI-stained PC3 and BPH1 cell lines are shown in Figure 8A, and the percentage of apoptotic cells is presented graphically in Figure 8B. When PC3 cells were treated with the C₁ complex at a concentration >IC₅₀ dose for 24 h, we

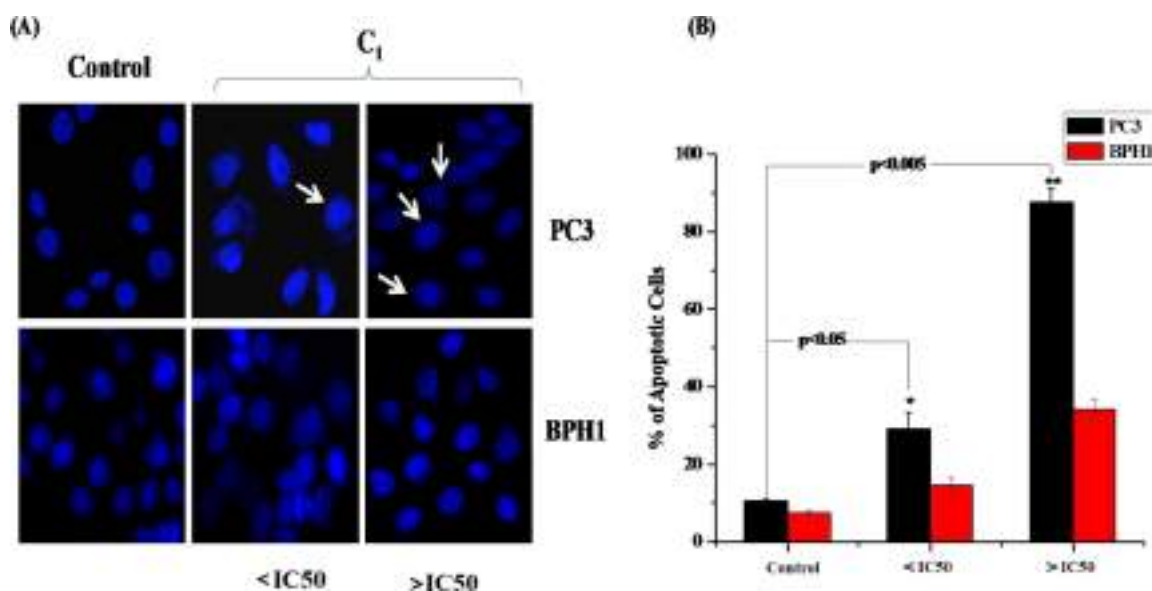


Figure 8. (A) Fluorescence micrographs of DAPI-stained PC3 and BPH1 cell lines under 40 \times magnification. Both the cells are treated with the C₁ complex for 24 h at two different doses (<IC₅₀ and >IC₅₀ doses of PC3). The arrow represents the decondensed nucleus of the apoptotic cells. (B) % of apoptotic cells as determined by DAPI staining followed by fluorescence microscopic observations. Each value represents the mean \pm S.D. of three independent experiments. *($p < 0.05$) and **($p < 0.005$) denote the statistically significant difference compared to the untreated control.

found that 80–85% cells were apoptotic in nature, whereas for BPH1, the amount of apoptotic cells reduced to only 30–35%.

Ru(II)–arene complexes are well known to bring about cell damage via production of ROS within the cells.³³ It is interesting to note that among the other metals (such as Pt, Pd, and Au) used as therapeutics, only Ru shows higher antitumor activity mediated by an enhanced ROS production.³⁴ Apoptotic cell death and DNA damage are connected with ROS production, and we also estimated ROS production induced by the C₁ complex in PC3 and BPH1, where we have used a fluorescent dye, DCFDA (2',7'-dichlorofluorescein diacetate), for indicating oxidative stress and hydroxyl and peroxyl radical generation.³⁵ The ROS generation in PC3 and BPH1 cell lines after treating with the C₁ complex for 24 h is shown in Figure 9. It was observed that PC3 cells exposed to

the C₁ complex produced a significantly high amount ($p < 0.005$) of ROS, compared to BPH1 cells. The intracellular imaging behavior of the C₁ complex was studied in both PC3 and BPH1 cell lines using fluorescence microscopy, and the results obtained are illustrated in Figure 10. After incubation with the C₁ complex, BPH1 cells display no intracellular fluorescence. However, PC3 shows green fluorescence both in the cytoplasm and nuclei, suggesting that the C₁ complex was distributed both in the cytosol and nucleus in the proliferating cancer cell line.

4. CONCLUSIONS

The present study shows that the guanidine-based ligands (L) undergo facile reaction with [$\text{Ru}(\text{p-cymene})\text{Cl}_2$]₂ to furnish cationic half-sandwich complexes of type $[\text{Ru}(\text{p-cymene})(\text{L})\text{-Cl}]^+$. This study also reveals that the complexes are better DNA binders than the corresponding uncoordinated guanidine-based ligands, and the observed enhancement in DNA binding is attributable to the imposed planarity of the guanidine-based ligand upon coordination to ruthenium that enabled it to serve as a better intercalator. Cytotoxicity studies also show a similar trend, the complexes being more cytotoxic than the uncoordinated guanidine-based ligands, presumably because complex formation leads to an improvement in cellular uptake that permits more molecules to enter cells, showing greater cytotoxicity. The other important aspect is that compared to cancer cells, the complexes were found to be significantly less toxic to normal cells, and this is most prominent in the C₁ complex. This is probably due to the increased uptake of the complex molecules in cancer cells than normal cells, as the membrane transport system of cancer cells is more active than that of the normal cells or benign cells. Additionally, more uptake of complex molecules generates more reactive oxygen species that lead to more oxidative DNA damage as observed by the comet assay.³⁶ This study also demonstrates that inclusion of the guanidine-based ligands in the half-sandwich ruthenium–arene complexes, particularly in the C₁ complex, has been useful for exhibition of remarkable

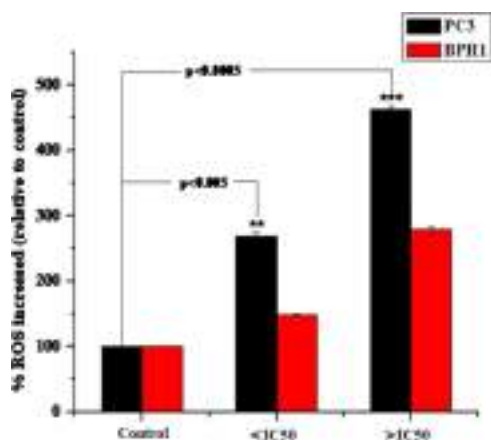


Figure 9. Intracellular ROS generation of PC3 and BPH1 cell lines treated with the C₁ complex for 24 h at two different doses (<IC₅₀ and >IC₅₀ doses of PC3). Data are presented as % increase in ROS relative to untreated controls. Values are the mean \pm SD of three independent experiments. ***($p < 0.0005$) and **($p < 0.005$) denote the statistically significant difference compared to untreated controls.

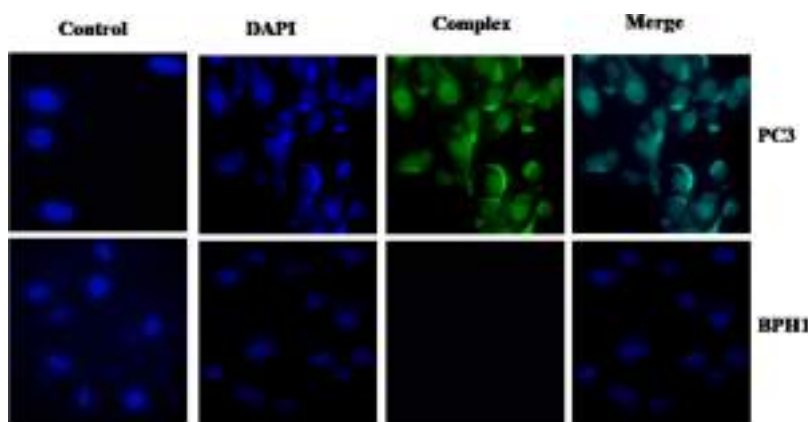


Figure 10. Cellular imaging of the C_1 complex in both PC3 and BPH1 cell lines under a fluorescence microscope. DAPI and the C_1 complex are visible as blue and green fluorescence, respectively. BPH1 cells display no intracellular fluorescence but PC3 shows green fluorescence both in the cytoplasm and nuclei.

antiproliferative activity against cancer cells with high selectivity and also for convenient tracing of the complexes in cells due to their prominent emissive nature. It is worth highlighting that such studies involving ligand modification at a single point (NH vs O vs S) are rare in the literature.³⁷

■ ASSOCIATED CONTENT

SI Supporting Information

The Supporting Information is available free of charge at <https://pubs.acs.org/doi/10.1021/acsomega.0c06265>.

DFT-optimized structures and computed bond parameters; data and figures related to TDDFT calculations; and figures and tables related to biological studies (PDF)

Crystallographic data (CIF)

Accession Codes

CCDC 1955587 contains the supplementary crystallographic data for this paper.

■ AUTHOR INFORMATION

Corresponding Author

Samaresh Bhattacharya – Department of Chemistry, Inorganic Chemistry Section, Jadavpur University, Kolkata 700 032, India; orcid.org/0000-0002-6245-9752; Email: samaresh_b@hotmail.com

Authors

Jit Karmakar – Department of Chemistry, Inorganic Chemistry Section, Jadavpur University, Kolkata 700 032, India

Promita Nandy – Department of Chemistry, Inorganic Chemistry Section, Jadavpur University, Kolkata 700 032, India

Saurabh Das – Department of Chemistry, Inorganic Chemistry Section, Jadavpur University, Kolkata 700 032, India; orcid.org/0000-0002-0455-8760

Debalina Bhattacharya – Department of Life Science and Biotechnology, Jadavpur University, Kolkata 700 032, India; Department of Microbiology, Maulana Azad College, Kolkata 700 013, India

Parimal Karmakar – Department of Life Science and Biotechnology, Jadavpur University, Kolkata 700 032, India

Complete contact information is available at:

<https://pubs.acs.org/10.1021/acsomega.0c06265>

Notes

The authors declare no competing financial interest.

■ ACKNOWLEDGMENTS

Financial assistance received from the JU-RUSA 2.0 program (ref. no.: R-11/438/19 (S.D.); R-11/76/19 (P.K.); R-11/96/19 (S.B.)) is gratefully acknowledged. The UGC-CAS, DST-FIST, and DST-PURSE programs of the Department of Chemistry, Jadavpur University, are also gratefully acknowledged for providing financial and infrastructural supports. P.K. acknowledges financial support from DST-SERB (EMR/2016/001151), Government of India. J.K. thanks CSIR, New Delhi, for his fellowship (grant no.: 09/096(0842)/2015-EMR-I). D.B. thanks the National Postdoctoral Fellowship Program of DST, Government of India, for her fellowship (grant no.: PDF/2017/001334).

■ REFERENCES

- (1) (a) Soldevila-Barreda, J. J.; Metzler-Nolte, N. Intracellular Catalysis with Selected Metal Complexes and Metallic Nanoparticles: Advances toward the Development of Catalytic Metallotherapeutics. *Chem. Rev.* **2019**, *119*, 829–869. (b) Kenny, R. G.; Marmion, C. J. Toward Multi-Targeted Platinum and Ruthenium Drugs – A New Paradigm in Cancer Drug Treatment Regimens? *Chem. Rev.* **2019**, *119*, 1058–1137. (c) Thota, S.; Rodrigues, D. A.; Crans, D. C.; Barreiro, E. J. Ru(II) Compounds: Next-Generation Anticancer Metallotherapeutics? *J. Med. Chem.* **2018**, *61*, 5805–5821. (d) Meier-Menches, S. M.; Gerner, C.; Berger, W.; Hartinger, C. G.; Keppler, B. K. Structure-activity relationships for ruthenium and osmium anticancer agents – towards clinical development. *Chem. Soc. Rev.* **2018**, *47*, 909–928. (e) Zeng, L.; Gupta, P.; Chen, Y.; Wang, E.; Ji, L.; Chao, H.; Chen, Z.-S. The development of anticancer ruthenium(II) complexes: from single molecule compounds to nanomaterials. *Chem. Soc. Rev.* **2017**, *46*, 5771–5804. (f) Murray, B. S.; Babak, M. V.; Hartinger, C. G.; Dyson, P. J. The development of RAPTA compounds for the treatment of tumors. *Coord. Chem. Rev.* **2016**, *306*, 86–114. (g) Medici, S.; Peana, M.; Nurchi, V. M.; Lachowicz, J. I.; Crisponi, G.; Zoroddu, M. A. Noble metals in medicine: Latest advances. *Coord. Chem. Rev.* **2015**, *284*, 329–350. (h) Singh, A. K.; Pandey, D. S.; Xu, Q.; Braunstein, P. Recent advances in supramolecular and biological aspects of arene ruthenium(II) complexes. *Coord. Chem. Rev.* **2014**, *270*–271, 31–56. (i) Hartinger, C. G.; Metzler-Nolte, N.; Dyson, P. J. Challenges and Opportunities in the Development of Organometallic Anticancer Drugs. *Organometallics* **2012**, *31*, 5677–5685. (j) Gasser, G.; Ott, I.; Metzler-Nolte, N. Organometallic Anticancer Compounds. *J. Med. Chem.* **2011**, *54*, 3–25.

- (2) (a) Li, H.; Xie, C.; Lan, R.; Zha, S.; Chan, C.-F.; Wong, W.-Y.; Ho, K.-L.; Chan, B. D.; Luo, Y.; Zhang, J.-X.; Law, G.-L.; Tai, W. C. S.; Bünzli, J.-C. G.; Wong, K.-L. A Smart Europium-Ruthenium Complex as Anticancer Prodrug: Controllable Drug Release and Real-Time Monitoring under Different Light Excitations. *J. Med. Chem.* **2017**, *60*, 8923–8932. (b) Martínez, M. Á.; Carranza, M. P.; Massaguer, A.; Santos, L.; Organero, J. A.; Aliende, C.; de Llorens, R.; Ng-Choi, I.; Feliu, L.; Planas, M.; Rodríguez, A. M.; Manzano, B. R.; Espino, G.; Jalón, F. A. Synthesis and Biological Evaluation of Ru(II) and Pt(II) Complexes Bearing Carboxyl Groups as Potential Anticancer Targeted Drugs. *Inorg. Chem.* **2017**, *56*, 13679–13696. (c) Qu, F.; Park, S.; Martinez, K.; Gray, J. L.; Thowfeik, F. S.; Lundeen, J. A.; Kuhn, A. E.; Charboneau, D. J.; Gerlach, D. L.; Lockart, M. M.; Law, J. A.; Jernigan, K. L.; Chambers, N.; Zeller, M.; Piro, N. A.; Kassel, W. S.; Schmehl, R. H.; Paul, J. J.; Merino, E. J.; Kim, Y.; Papish, E. T. Ruthenium Complexes are pH-Activated Metallo Prodrugs (pHAMPs) with Light-Triggered Selective Toxicity Toward Cancer Cells. *Inorg. Chem.* **2017**, *56*, 7519–7532. (d) Lenis-Rojas, O. A.; Roma-Rodrigues, C.; Fernandes, A. R.; Marques, F.; Pérez-Fernández, D.; Guerra-Varela, J.; Sánchez, L.; Vázquez-García, D.; López-Torres, M.; Fernández, A.; Fernández, J. J. Dinuclear Ru(II)(bipy)₂ Derivatives: Structural, Biological, and in vivo Zebrafish Toxicity Evaluation. *Inorg. Chem.* **2017**, *56*, 7127–7144. (e) Shen, J.; Kim, H.-C.; Wolfram, J.; Mu, C.; Zhang, W.; Liu, H.; Xie, Y.; Mai, J.; Zhang, H.; Li, Z.; Guevara, M.; Mao, Z.-W.; Shen, H. A Liposome Encapsulated Ruthenium Polypyridine Complex as a Theranostic Platform for Triple-Negative Breast Cancer. *Nano Lett.* **2017**, *17*, 2913–2920. (f) Heinemann, F.; Karges, J.; Gasser, G. Critical Overview of the Use of Ru(II) Polypyridyl Complexes as Photosensitizers in One-Photon and Two-Photon Photodynamic Therapy. *Acc. Chem. Res.* **2017**, *50*, 2727–2736.
- (3) (a) Jeyalakshmi, K.; Haribabu, J.; Balachandran, C.; Swaminathan, S.; Bhuvanesh, N. S. P.; Karvembu, R. Coordination Behavior of N,N',N''-Trisubstituted Guanidine Ligands in Their Ru-Arene Complexes: Synthetic, DNA/Protein Binding, and Cytotoxic Studies. *Organometallics* **2019**, *38*, 753–770. (b) Muralisankar, M.; Dheepika, R.; Haribabu, J.; Balachandran, C.; Aoki, S.; Bhuvanesh, N. S. P.; Nagarajan, S. Design, Synthesis, DNA/HSA Binding, and Cytotoxic Activity of Half-Sandwich Ru(II)-Arene Complexes Containing Triarylamine-Thiosemicarbazone Hybrids. *ACS Omega* **2019**, *4*, 11712–11723. (c) Sarkar, B.; Mondal, A.; Madaan, Y.; Roy, N.; Moorthy, A.; Kuo, Y.-C.; Paira, P. Luminescent anticancer ruthenium(II)-p-cymene complexes of extended imidazophenanthroline ligands: synthesis, structure, reactivity, biomolecular interactions and live cell imaging. *Dalton Trans.* **2019**, *48*, 12257–12271. (d) Yousuf, I.; Arjmand, F.; Tabassum, S.; Ahmad, M. Design and synthesis of a DNA intercalative half-sandwich organoruthenium(II)-chromone complex: cytotoxicity evaluation and topoisomerase α inhibition assay. *New J. Chem.* **2019**, *43*, 5475–5487. (e) Lari, M.; Martínez-Alonso, M.; Busto, N.; Manzano, B. R.; Rodríguez, A. M.; Acuña, M. I.; Domínguez, F.; Albasanz, J. L.; Leal, J. M.; Espino, G.; García, B. Strong Influence of Ancillary Ligands Containing Benzothiazole or Benzimidazole Rings on Cytotoxicity and Photoactivation of Ru(II) Arene Complexes. *Inorg. Chem.* **2018**, *57*, 14322–14336. (f) Lenis-Rojas, O. A.; Robalo, M. P.; Tomaz, A. I.; Carvalho, A.; Fernandes, A. R.; Marques, F.; Folgueira, M.; Yáñez, J.; Vázquez-García, D.; López Torres, M.; Fernández, A.; Fernández, J. J. Ru(II)(p-cymene) Compounds as Effective and Selective Anticancer Candidates with No Toxicity in Vivo. *Inorg. Chem.* **2018**, *57*, 13150–13166. (g) Li, J.; Tian, M.; Tian, Z.; Zhang, S.; Yan, C.; Shao, C.; Liu, Z. Half-Sandwich Iridium(III) and Ruthenium(II) Complexes Containing PP-Chelating Ligands: A New Class of Potent Anticancer Agents with Unusual Redox Features. *Inorg. Chem.* **2018**, *57*, 1705–1716. (h) Paitandi, R. P.; Sharma, V.; Singh, V. D.; Dwivedi, B. K.; Mobin, S. M.; Pandey, D. S. Pyrazole appended quinoline-BODIPY based arene ruthenium complexes: their anticancer activity and potential applications in cellular imaging. *Dalton Trans.* **2018**, *47*, 17500–17514. (i) Mandal, P.; Kundu, B. K.; Vyas, K.; Sabu, V.; Helen, A.; Dhankhar, S. S.; Nagaraja, C. M.; Bhattacharjee, D.; Bhabak, K. P.; Mukhopadhyay, S. Ruthenium(II) arene NSAID complexes: inhibition of cyclooxygenase and antiproliferative activity against cancer cell lines. *Dalton Trans.* **2018**, *47*, 517–527. (j) Gopalakrishnan, D.; Ganeshpandian, M.; Loganathan, R.; Bhuvanesh, N. S. P.; Sabina, X. J.; Karthikeyan, J. Water soluble Ru(II)-arene complexes of the antidiabetic drug metformin: DNA and protein binding, molecular docking, cytotoxicity and apoptosis-inducing activity. *RSC Adv.* **2017**, *7*, 37706–37719. (k) Jeyalakshmi, K.; Haribabu, J.; Balachandran, C.; Bhuvanesh, N. S. P.; Emi, N.; Karvembu, R. Synthesis of Ru(II)-benzene complexes containing aroylthiourea ligands, and their binding with biomolecules and in vitro cytotoxicity through apoptosis. *New J. Chem.* **2017**, *41*, 2672–2686. (l) Barragán, F.; López-Senín, P.; Salassa, L.; Betanzos-Lara, S.; Habtemariam, A.; Moreno, V.; Sadler, P. J.; Marchán, V. Photo-controlled DNA Binding of a Receptor-Targeted Organometallic Ruthenium(II) Complex. *J. Am. Chem. Soc.* **2011**, *133*, 14098.
- (4) (a) Ashraf, A.; Aman, F.; Movassaghi, S.; Zafar, A.; Kubanik, M.; Siddiqui, W. A.; Reynisson, J.; Söhnle, T.; Jamieson, S. M. F.; Hanif, M.; Hartinger, C. G. Structural Modifications of the Antiinflammatory Oxicam Scaffold and Preparation of Anticancer Organometallic Compounds. *Organometallics* **2019**, *38*, 361–374. (b) Swaminathan, S.; Haribabu, J.; Kalagatur, N. K.; Konakanchi, R.; Balakrishnan, N.; Bhuvanesh, N.; Karvembu, R. Synthesis and Anticancer Activity of [RuCl₂(η^6 -arene)(aroylthiourea)] Complexes – High Activity against the Human Neuroblastoma (IMR-32) Cancer Cell Line. *ACS Omega* **2019**, *4*, 6245–6256. (c) Hager, L. A.; Mokesch, S.; Kieler, C.; Alonso-de Castro, S.; Baier, D.; Roller, A.; Kandlioller, W.; Keppler, B. K.; Berger, W.; Salassa, L.; Terenzi, A. Ruthenium-arene complexes bearing naphthyl-substituted 1,3-dioxindan-2-carboxamides ligands for G-quadruplex DNA recognition. *Dalton Trans.* **2019**, *48*, 12040–12049. (d) Sarkar, A.; Acharya, S.; Khushvant, K.; Purkait, K.; Mukherjee, A. Cytotoxic Ru^{II}-p-cymene complexes of an anthraimidazoleione: halide dependent solution stability, reactivity and resistance to hypoxia deactivation. *Dalton Trans.* **2019**, *48*, 7187–7197. (e) Laurent, Q.; Batchelor, L. K.; Dyson, P. J. Applying a Trojan Horse Strategy to Ruthenium Complexes in the Pursuit of Novel Antibacterial Agents. *Organometallics* **2018**, *37*, 915–923. (f) Gatti, A.; Habtemariam, A.; Romero-Cañelón, I.; Song, J.-I.; Heer, B.; Clarkson, G. J.; Rogolino, D.; Sadler, P. J.; Carcelli, M. Half-Sandwich Arene Ruthenium(II) and Osmium(II) Thiosemicarbazone Complexes: Solution Behavior and Antiproliferative Activity. *Organometallics* **2018**, *37*, 891–899. (g) Zhao, J.; Zhang, D.; Hua, W.; Li, W.; Xu, G.; Gou, S. Anticancer Activity of Bifunctional Organometallic Ru(II) Arene Complexes Containing a 7-Hydroxycoumarin Group. *Organometallics* **2018**, *37*, 441–447. (h) Mu, C.; Prosser, K. E.; Harrypersad, S.; MacNeil, G. A.; Panchmatia, R.; Thompson, J. R.; Sinha, S.; Warren, J. J.; Walsby, C. J. Activation by Oxidation: Ferrocene-Functionalized Ru(II)-Arene Complexes with Anticancer, Antibacterial, and Antioxidant Properties. *Inorg. Chem.* **2018**, *57*, 15247–15261. (i) Lenis-Rojas, O. A.; Robalo, M. P.; Tomaz, A. I.; Carvalho, A.; Fernandes, A. R.; Marques, F.; Folgueira, M.; Yáñez, J.; Vázquez-García, D.; López Torres, M.; Fernández, A.; Fernández, J. J. Ru(II)(p-cymene) Compounds as Effective and Selective Anticancer Candidates with No Toxicity in vivo. *Inorg. Chem.* **2018**, *57*, 13150–13166. (j) Ma, L.; Lin, X.; Li, C.; Xu, Z.; Chan, C.-Y.; Tse, M.-K.; Shi, P.; Zhu, G. A Cancer Cell-Selective and Low-Toxic Bifunctional Heterodinuclear Pt(IV)-Ru(II) Anticancer Prodrug. *Inorg. Chem.* **2018**, *57*, 2917–2924. (k) Shanmugaraju, S.; la Cour Poulsen, B.; Arisa, T.; Umadevi, D.; Dalton, H. L.; Hawes, C. S.; Estalayo-Adrián, S.; Savvasachi, A. J.; Watson, G. W.; Williams, D. C.; Gunnlaugsson, T. Synthesis, structural characterization and antiproliferative activity of a new fluorescent 4-amino-1,8-naphthalimide Tröger's base-Ru(II)-curcumin organometallic conjugate. *Chem. Commun.* **2018**, *54*, 4120–4123. (l) Batchelor, L. K.; Păunescu, E.; Soudani, M.; Scopelliti, R.; Dyson, P. J. Influence of the Linker Length on the Cytotoxicity of Homodinuclear Ruthenium(II) and Gold(I) Complexes. *Inorg. Chem.* **2017**, *56*, 9617–9633. (m) Guerriero, A.; Oberhauser, W.; Riedel, T.; Peruzzini, M.; Dyson, P. J.; Gonsalvi, L. New Class of Half-Sandwich Ruthenium(II) Arene Complexes Bearing the Water-Soluble CAP

- Ligand as an in vitro Anticancer Agent. *Inorg. Chem.* **2017**, *56*, 5514–5518. (n) Mitra, R.; Samuelson, A. G. Mitigating UVA light induced reactivity of 6-thioguanine through formation of a Ru(II) half-sandwich complex. *RSC Adv.* **2014**, *4*, 24304–24306. Romero-Canelón, I.; Salassa, L.; Sadler, P. J. The Contrasting Activity of Iodido versus Chlorido Ruthenium and Osmium Arene Azo- and Imino-pyridine Anticancer Complexes: Control of Cell Selectivity, Cross-Resistance, p53 Dependence, and Apoptosis Pathway. *J. Med. Chem.* **2013**, *56*, 1291–1300. (p) Das, S.; Sinha, S.; Britto, R.; Somasundaram, K.; Samuelson, A. G. Cytotoxicity of half sandwich ruthenium(II) complexes with strong hydrogen bond acceptor ligands and their mechanism of action. *J. Inorg. Biochem.* **2010**, *104*, 93–104.
- (5) Novakova, O.; Chen, H.; Vrana, O.; Rodger, A.; Sadler, P. J.; Brabec, V. DNA Interactions of Monofunctional Organometallic Ruthenium(II) Antitumor Complexes in Cell-free Media. *Biochemistry* **2003**, *42*, 11544–11554.
- (6) (a) Arkin, M. R.; Jenkins, Y.; Murphy, C. J.; Turro, N. J.; Barton, J. K. Metallointercalators as Probes of the DNA π -way. *Mechanistic Bioinorganic Chemistry*; American Chemical Society, 1996; Chapter 17, pp 449–469. (b) Elmes, R. B. P.; Ryan, G. J.; Erby, M. L.; Frimannsson, D. O.; Kitchen, J. A.; Lawler, M.; Williams, D. C.; Quinn, S. J.; Gunnlaugsson, T. Synthesis, Characterization, and Biological Profiling of Ruthenium(II)-Based 4-Nitro- and 4-Amino-1,8-naphthalimide Conjugates. *Inorg. Chem.* **2020**, *59*, 10874–10893. (c) Zhang, S.-Q.; Meng, T.-T.; Li, J.; Hong, F.; Liu, J.; Wang, Y.; Gao, L.-H.; Zhao, H.; Wang, K.-Z. Near-IR/Visible-Emitting Thiophenyl-Based Ru(II) Complexes: Efficient Photodynamic Therapy, Cellular Uptake, and DNA Binding. *Inorg. Chem.* **2019**, *58*, 14244–14259. (d) Abreu, F. D.; Paulo, T. d. F.; Gehlen, M. H.; Ando, R. A.; Lopes, L. G. F.; Gondim, A. C. S.; Vasconcelos, M. A.; Teixeira, E. H.; Sousa, E. H. S.; de Carvalho, I. M. M. Aryl-Substituted Ruthenium(II) Complexes: A Strategy for Enhanced Photocleavage and Efficient DNA Binding. *Inorg. Chem.* **2017**, *56*, 9084–9096.
- (7) (a) Banerjee, D.; Pal, S. K. Excited-State Solvation and Proton Transfer Dynamics of DAPI in Biomimetics and Genomic DNA. *J. Phys. Chem. A* **2008**, *112*, 7314–7320. (b) Bourzac, K. M.; LaVine, L. J.; Rice, M. S. Analysis of DAPI and SYBR Green I as Alternatives to Ethidium Bromide for Nucleic Acid Staining in agarose Gel Electrophoresis. *J. Chem. Educ.* **2003**, *80*, 1292–1296. (c) Reha, D.; Kabelác, M.; Ryjáček, F.; Sponer, J.; Sponer, J. E.; Elstner, M.; Suhai, S.; Hobza, P. Intercalators. 1. Nature of Stacking Interactions between Intercalators (Ethidium, Daunomycin, Ellipticine, and 4',6-Diaminide-2-phenylindole) and DNA Base Pairs. Ab Initio Quantum Chemical, Density Functional Theory, and Empirical Potential Study. *J. Am. Chem. Soc.* **2002**, *124*, 3366. (d) Lan, T.; McLaughlin, L. W. The Energetic Contribution of a Bifurcated Hydrogen Bond to the Binding of DAPI to dA-dT Rich Sequences of DNA. *J. Am. Chem. Soc.* **2001**, *123*, 2064–2065. (e) Vlieghe, D.; Sponer, J.; Meervelt, L. V. Crystal Structure of d(GGCCAATTGG) Complexed with DAPI Reveals Novel Binding Mode. *Biochemistry* **1999**, *38*, 16443–16451. (f) Albert, F. G.; Eckdahl, T. T.; Fitzgerald, D. J.; Anderson, J. N. Heterogeneity in the Actions of Drugs That Bind in the DNA Minor Groove. *Biochemistry* **1999**, *38*, 10135–10146.
- (8) (a) Mohamed, S. K.; Soliman, A. M.; El-Remaly, M. A. A.; Abdel-Ghany, H. Eco Friendly Synthesis of Pyrimidine and Dihydropyrimidinone Derivatives under Solvent Free Condition and their Anti-microbial Activity. *Chem. Sci. J.* **2013**, *2013*, 1. (b) King, F. E.; Acheson, R. M.; Spensley, P. C. 275. Benzimidazole analogues of paludrine. *J. Chem. Soc.* **1948**, *17*, 1366–1371.
- (9) (a) Mukherjee, T.; Ganzmann, C.; Bhuvanesh, N.; Gladysz, J. A. Syntheses of Enantiopure Bifunctional 2-Guanidinobenzimidazole Cyclopentadienyl Ruthenium Complexes: Highly Enantioselective Organometallic Hydrogen Bond Donor Catalysts for Carbon-Carbon Bond Forming Reactions. *Organometallics* **2014**, *33*, 6723–6737. (b) Scherer, A.; Mukherjee, T.; Hampel, F.; Gladysz, J. A. Metal-Templated Hydrogen Bond Donors as “Organocatalysts” for Carbon-Carbon Bond Forming Reactions: Syntheses, Structures, and Reactivities of 2-Guanidinobenzimidazole Cyclopentadienyl Ruthenium Complexes. *Organometallics* **2014**, *33*, 6709–6722. (c) Sánchez-Guadarrama, O.; López-Sandoval, H.; Sánchez-Bartéz, F.; Gracia-Mora, I.; Höpfl, H.; Barba-Behrens, N. Cytotoxic activity, X-ray crystal structures and spectroscopic characterization of cobalt(II), copper(II) and zinc(II) coordination compounds with 2-substituted benzimidazoles. *J. Inorg. Biochem.* **2009**, *103*, 1204–1213. (d) Albada, G. A. v.; Turpeinen, U.; Reedijk, J. Two different isomers of tetrahedrally distorted square-planar Cu(II) triflate compounds with 2-guanidinobenzimidazole; synthesis, X-ray and spectroscopic characterisation. *J. Mol. Struct.* **2006**, *789*, 182–186. (e) Zheng, L.; Zhang, J.; Yu, M.-M.; Ni, Z.-H.; Kou, H.-Z. Bis(2 guanidinobenzimidazole- K^2 N, N')copper(II) bis(dicyanamide). *Acta Crystallogr., Sect. E: Struct. Rep. Online* **2006**, *62*, m2470–m2472. (f) Arablo, N.; Torabi, S. A. A.; Morsali, A.; Skelton, B. W.; White, A. H. Cation Structures in Bis(2-Guanidino-benzimidazole)metal(II) Complexes: Crystal and Molecular Structure of the Copper(II) Perchlorate Adduct. *Aust. J. Chem.* **2003**, *56*, 945–947. (g) Cenicer-Gómez, A. E.; Barba-Behrens, N.; Quiroz-Castro, M. E.; Bernès, S.; Nöth, H.; Castillo-Blum, S. E. Synthesis, X-ray and spectroscopic characterisation of chromium(III) coordination compounds with benzimidazolic ligands. *Polyhedron* **2000**, *19*, 1821–1827. (h) Cenicer-Gómez, A. E.; Barba-Behrens, N.; Bernès, S.; Nöth, H.; Castillo-Blum, S. E. Synthesis, X-ray and NMR characterisation of cobalt(III) coordination compounds with 2-guanidinobenzimidazole. *Inorg. Chim. Acta* **2000**, *304*, 230–236. (i) Barba-Behrens, N.; Vázquez-Olmos, A.; Castillo-Blum, S. E.; Höjer, G.; Meza-Höjer, S.; Hernández, R. M.; de Jesús Rosales-Hoz, M.; Vicente, R.; Escuer, A. Coordination behaviour of 2-guanidinobenzimidazole towards cobalt(II), nickel(II), copper(II) and zinc(II). An experimental and theoretical study. *Transition Met. Chem.* **1996**, *21*, 31–37.
- (10) Bennett, M. A.; Huang, T. N.; Matheson, T. W.; Smith, A. K. *Inorg. Synth.* **1982**, *1*, 75.
- (11) Frisch, M. J.; Trucks, G. W.; Schlegel, H. B.; Scuseria, G. E.; Robb, M. A.; Cheeseman, J. R.; Scalmani, G.; Barone, V.; Mennucci, B.; Petersson, G. A.; Nakatsuji, H.; Caricato, M.; Li, X.; Hratchian, H. P.; Izmaylov, A. F.; Bloino, J.; Zheng, G.; Sonnenberg, J. L.; Hada, M.; Ehara, M.; Toyota, K.; Fukuda, R.; Hasegawa, J.; Ishida, M.; Nakajima, T.; Honda, Y.; Kitao, O.; Nakai, H.; Vreven, T.; Montgomery, J. A., Jr.; Peralta, J. E.; Ogliaro, F.; Bearpark, M.; Heyd, J. J.; Brothers, E.; Kudin, K. N.; Staroverov, V. N.; Kobayashi, R.; Normand, J.; Raghavachari, K.; Rendell, A.; Burant, J. C.; Iyengar, S. S.; Tomasi, J.; Cossi, M.; Rega, N.; Millam, J. M.; Klene, M.; Knox, J. E.; Cross, J. B.; Bakken, V.; Adamo, C.; Jaramillo, J.; Gomperts, R.; Stratmann, R. E.; Yazyev, O.; Austin, A. J.; Cammi, R.; Pomelli, C.; Ochterski, J. W.; Martin, R. L.; Morokuma, K.; Zakrzewski, V. G.; Voth, G. A.; Salvador, P.; Dannenberg, J. J.; Dapprich, S.; Daniels, A. D.; Farkas, Ö.; Foresman, J. B.; Ortiz, J. V.; Cioslowski, J.; Fox, D. J. *Gaussian 9; Gaussian, Inc.: Wallingford CT*, 2009.
- (12) Sheldrick, G. M. *SHELXS-97 and SHELXL-97, Fortran programs for crystal structure solution and refinement*; University of Göttingen: Göttingen, Germany, 1997. (b) Sheldrick, G. M. A short history of SHELX. *Acta Crystallogr., Sect. A: Found. Crystallogr.* **2008**, *64*, 112–122.
- (13) Das, S.; Dasgupta, D. Binding of (MTR)₂Zn²⁺ complex to chromatin: A comparison with (MTR)₂Mg²⁺ complex. *J. Inorg. Biochem.* **2005**, *99*, 707–715.
- (14) Roy, S.; Banerjee, R.; Sarkar, M. Direct binding of Cu(II)-complexes of oxicam NSAIDs with DNA backbone. *J. Inorg. Biochem.* **2006**, *100*, 1320–1331.
- (15) Guin, P. S.; Das, S.; Mandal, P. C. Studies on the formation of a complex of Cu(II) with sodium 1,4-dihydroxy-9,10-anthraquinone-2-sulphonate – An analogue of the core unit of anthracycline anticancer drugs and its interaction with calf thymus DNA. *J. Inorg. Biochem.* **2009**, *103*, 1702–1710.
- (16) Das, P.; Jain, C. K.; Dey, S. K.; Saha, R.; Chowdhury, A. D.; Roychoudhury, S.; Kumar, S.; Majumder, H. K.; Das, S. Synthesis, crystal structure, DNA interaction and *in vitro* anticancer activity of a Cu(II) complex of purpurin: dual poison for human DNA topoisomerase I and II. *RSC Adv.* **2014**, *4*, 59344–59357.

- (17) Das, P.; Jain, C. K.; Roychoudhury, S.; Majumder, H. K.; Das, S. Design, synthesis and *in vitro* anticancer activity of a Cu(II) complex of carminic acid: A novel small molecule inhibitor of human DNA topoisomerase I and topoisomerase II. *ChemistrySelect* **2016**, *1*, 6623–6631.
- (18) Mukherjee Chatterjee, S.; Jain, C. K.; Singha, S.; Das, P.; Roychoudhury, S.; Majumder, H. K.; Das, S. Activity of Co^{II}–Quinalizarin: A novel analogue of anthracycline-based anticancer agents targets human DNA topoisomerase, whereas quinalizarin itself acts via formation of semiquinone on acute lymphoblastic leukemia MOLT-4 and HCT 116 cells. *ACS Omega* **2018**, *3*, 10255–10266.
- (19) Scatchard, G. The attractions of proteins for small molecules and ions. *Ann. N.Y. Acad. Sci.* **1949**, *51*, 660–672.
- (20) Singh, N. P.; McCoy, M. T.; Tice, R. R.; Schneider, E. L. A simple technique for quantitation of low levels of DNA damage in individual cells. *Exp. Cell Res.* **1988**, *175*, 184–191.
- (21) Attempts to grow single crystals of complexes C₁ and C₂ remained unsuccessful.
- (22) Nikolić, S.; Opsenica, D. M.; Filipović, V.; Dojčinović, B.; Arandelović, S.; Radulović, S.; Grgurić-Šipka, S. Strong *in Vitro* Cytotoxic Potential of New Ruthenium-Cymene Complexes. *Organometallics* **2015**, *34*, 3464–3473.
- (23) Morgan, A. R.; Pulleyblank, D. E. Native and denatured DNA, cross-linked and palindromic and circular covalently-closed DNA analyzed by a sensitive fluorimetric procedure. *Biochem. Biophys. Res. Commun.* **1974**, *61*, 396–403.
- (24) Birnboim, H. C.; Jevcak, J. J. Fluorometric method for rapid detection of DNA strand breaks in human white blood cells produced by low doses of radiation. *Cancer Res.* **1981**, *41*, 1889.
- (25) Das, S.; Saha, A.; Mandal, P. C. Radiation-induced double strand modification in calf thymus DNA in the presence of 1,2 dihydroxy-9,10 anthraquinone and its Cu(II) complex. *Environ. Health Perspect.* **1997**, *105*, 1459–1462.
- (26) Das, S.; Mandal, P. C. Anthracyclines as radiosensitizers: a Cu(II) complex of a simpler analogue modifies DNA in Chinese Hamster V79 cells under low-dose γ radiation. *J. Radioanal. Nucl. Chem.* **2014**, *299*, 1665–1670.
- (27) Tripathi, R.; Samadder, T.; Gupta, S.; Surolia, A.; Shaha, C. Anticancer activity of a combination of cisplatin and fisetin in embryonal carcinoma cells and xenograft tumors. *Mol. Cancer Ther.* **2011**, *10*, 255–268.
- (28) Dasari, S.; Bernard Tchounwou, P. Cisplatin in cancer therapy: molecular mechanisms of action. *Eur. J. Pharmacol.* **2014**, *740*, 364–378.
- (29) Gryparis, E. C.; Hatzia Apostolou, M.; Papadimitriou, E.; Avgoustakis, K. Anticancer activity of cisplatin-loaded PLGA-mPEG nanoparticles on LNCaP prostate cancer cells. *Eur. J. Pharm. Biopharm.* **2007**, *67*, 1–8.
- (30) Chen, L.; Li, W.; Wang, H.; Zhao, H.; Tang, J.; Wu, C.; Lu, L.; Liao, W.; Lu, X. Curcumin cytotoxicity is enhanced by PTEN disruption in colorectal cancer cells. *World J. Gastroenterol.* **2013**, *19*, 6814–6824.
- (31) Rodriguez, E.; Azevedo, R.; Fernandes, P.; Santos, C. a. Cr(VI) Induces DNA Damage, Cell Cycle Arrest and Polyploidization: A Flow Cytometric and Comet Assay Study in *Pisum sativum*. *Chem. Res. Toxicol.* **2011**, *24*, 1040–1047.
- (32) Stang, A.; Witte, I. Performance of the comet assay in a high-throughput version. *Mutat. Res., Genet. Toxicol. Environ. Mutagen.* **2009**, *675*, 5–10.
- (33) Dougan, S. J.; Habtemariam, A.; McHale, S. E.; Parsons, S.; Sadler, P. J. Catalytic organometallic anticancer complexes. *Proc. Natl. Acad. Sci. U.S.A.* **2008**, *105*, 11628–11633.
- (34) Molter, A.; Kathrein, S.; Kircher, B.; Mohr, F. Anti-tumour active gold(I), palladium(II) and ruthenium(III) complexes with thio- and selenoureato ligands: a comparative study. *Dalton Trans.* **2018**, *47*, 5055–5064.
- (35) Seršen, S.; Kljun, J.; Kryeziu, K.; Panchuk, R.; Alte, B.; Körner, W.; Heffeter, P.; Berger, W.; Turel, I. Structure-Related Mode-of-Action Differences of Anticancer Organoruthenium Complexes with β -Diketones. *J. Med. Chem.* **2015**, *58*, 3984.
- (36) Tian, Z.; Li, J.; Zhang, S.; Xu, Z.; Yang, Y.; Kong, D.; Zhang, H.; Ge, X.; Zhang, J.; Liu, Z. Lysosome-Targeted Chemotherapeutics: Half-Sandwich Ruthenium(II) Complexes That Are Selectively Toxic to Cancer Cells. *Inorg. Chem.* **2018**, *57*, 10498–10502.
- (37) Ginzinger, W.; Mühlgassner, G.; Arion, V. B.; Jakupec, M. A.; Roller, A.; Galanski, M.; Reithofer, M.; Berger, W.; Keppler, B. K. A SAR Study of Novel Antiproliferative Ruthenium and Osmium Complexes with Quinoxalinone Ligands in Human Cancer Cell Lines. *J. Med. Chem.* **2012**, *55*, 3398–3413.

PAPER • OPEN ACCESS

Fabrication of natural polysaccharide based hydrogel with utility to entrap pollutants

To cite this article: B Ghosh *et al* 2021 *J. Phys.: Conf. Ser.* **1797** 012060

View the [article online](#) for updates and enhancements.



ECS **240th ECS Meeting**
Oct 10-14, 2021, Orlando, Florida

**Register early and save
up to 20% on registration costs**

Early registration deadline Sep 13

REGISTER NOW

The banner features a group of diverse professionals in business attire, smiling and engaged in conversation, set against a blurred background of a modern office or conference space. A diagonal white line cuts across the image from the bottom left towards the top right.

Fabrication of natural polysaccharide based hydrogel with utility to entrap pollutants

B Ghosh¹, D Bhattacharya² and M Mukhopadhyay^{1,3}

¹ Department of Biotechnology, JIS University, 81, Nilgunj Road, Agarpara, Kolkata-700109, West Bengal, India

² Department of Microbiology, Maulana Azad College, 8, Rafi Ahmed Kidwai Rd, Taltala, Kolkata, West Bengal 700013

E-mail- biva.ghosh0@gmail.com, debalina_biotech@yahoo.co.in, mainak.mukhopadhyay12@gmail.com,

³Corresponding author's email address: mainak.mukhopadhyay12@gmail.com

Abstract. In the recent years of innovations hydrogels plays important role in various industrial applications. Hydrogels with combination of natural polymers are widely used for its biocompatibility and ecofriendly nature such as pectin and carboxymethyl cellulose (CMC). Plasticizers are utilized to enrich the physicochemical characteristics of hydrogels based on natural polymers. Polyethylene glycol 400 (PEG 400) is known to render thermostability. Whereas copper ions has wound healing properties and acts as biocide. These hydrogels due to its high porosity can have various utility to entrap small particles such as dust, pathogens and other pollutants and can act as very good face mask. Therefore the fabricated hydrogel is not only thermostable but also have high cytocompatibility, pH sensitivity, porosity and degree of swelling.

Keywords – Divalent cations, Hydrogel, Natural polymers,

1. Introduction

Hydrogel is a combination of polymeric networks cross-linked among each other which can entrap large amount of water inside it. This cross-linked polymeric networks of hydrogels form porous structure which has high entrapment capability and has wide application in multiple industrial applications such as wastewater treatment [1-3], medical applications [4-8], pharmaceuticals [9-11] and other industrial and non-industrial applications. The biocompatibility, abundance and eco-friendly nature of natural polysaccharides makes it ideal for hydrogel formation [12, 13]. Freeze-dried hydrogel develops a scaffold-like anatomy which has high porosity [14-21] helpful for trapping valuable molecules which plays important function in drug trapping and regulated drug release [22-25]. Other than this porosity of hydrogel also allows high cell proliferation [26-29], capturing of waste molecules and contaminants in wastewater management [30].



Pectin is a plant derived natural polysaccharide with great applications but it has low mechanical robustness which can be amended by mixing with other natural or ecofriendly polymers [31]. Pectin comprises of arrangement of rhamnogalacturonan I (RG I), homogalacturonan (HG) and rhamnogalacturonan II (RG II) which are connected to one another by covalent linkage. HG comprise of negatively charged α -1, 4-linked galacturonic acid (GalA) monomers which are methyl-esterified to some extent at the C-O-6 carboxyl [14]. The degree of methyl esterification (DE) helps to determine the effect of pectin jellification by multivalent cations such as poor methyl esterification of pectin easily forms crosslinking among the polymer networks due to divalent cation with respect to high methoxy pectin [14]. The mechanical strength of plants are contributed by the combination of pectin and cellulose due the poroelastic effect [14]. Sodium carboxymethyl cellulose (CMC) is form of cellulose a water soluble which comprise of β -(1 \rightarrow 4) glucopyranose residues [14]. Apart from this CMC being derivative of cellulose is non-toxic and eco-friendly along with has excellent bioadhesive and polyelectrolytic properties which provides pH sensitivity to hydrogels [32]. Since the ancient times, copper is recognized to have plentiful optimistic outcomes over tissues of human beings, chiefly on skin. It aids in production and balance of the skin proteins of the extracellular matrix and supports angiogenesis which benefits in improvement of skin elasticity and curing infections resulting in wound healing [33]. Divalent ionic salts such as copper sulfate (CuSO_4) with Cu^{2+} ion which comes to the aid of cross-linking of CMC and pectin to fabricate hydrogel. Plasticizers helps in increasing the flexibility of the polymer composite by aligning them properly [34-36]. PEG 400 has extensive utilization in the biomedical sectors like encapsulation of the protein and its stabilization [37], ointments, body caring products, capsule coats, tissue engineering etc. [38, 39, 40]. PEG earns immense importance in industrial application due to its eminent features such as the great structural flexibility, biologically compatible, amphiphilicity, absent of any steric hindrances, and high hydration capability [38, 41]. The wide application of PEG 400 in the cosmetics such as lotions, ointment base, cream, etc. makes it an industrially valuable chemical [38]. Additionally, the fluidic nature of PEG 400 at room temperature provides it easy mix-ability in solvents at room temperature. The above mentioned characteristics of PEG 400 makes it a perfect plasticizer for creation of hydrogel along with different polymers.

Since hydrogels with thermostability has various application in industries, therefore formation of hydrogel with pectin, CMC and PEG 400 was accompanished. CMC, Pectin, Copper ions and PEG 400 has numerous significance and applications which are already discussed above among which biocidal property is the most studied one. The hydrogel constructed is experimentally analyzed by utilization of XRD, FTIR, TGA/DTG/DTA, and DSC which indicated favorable assembly of polymer to form hydrogel with elevated thermostability. Other than this, experiments for example SEM analysis, swelling properties studies, and MTT assay revealed good porosity, elevated degree of swelling, high cytocompatibility of the constructed hydrogel which is discussed further.

2. Materials and methods

2.1. Materials

Pectin and sodium carboxymethyl cellulose (CMC) were bought from Hi-media. Glycerol and polyethylene glycol 400 (PEG 400) were purchased from Merck. Copper sulfate pentahydrate ($\text{CuSO}_4 \cdot 5\text{H}_2\text{O}$), hydrochloric acid (HCL), tris-buffer and 98% ethanol were purchased from SRL. MTT reagents and WI-38 cells were supplied by the Department of Life science and Biotechnology, Jadavpur University, India.

2.2. Preparation of Hydrogel

The stock solutions of pectin (3% (w/v) and CMC 1% (w/v)) were formulated by means of double distilled water. Altogether the polymers were blended into diverse ratio for 1 hour over a magnetic stirrer. Different ratio of PEG 400 or glycerol were added to the prior blended solution and was left to

stir for another 1 hour. The obtained polymer mixture was evacuated into the cast. The polymer solution which contain glycerol was named as HGY which is considered as standard and the polymer solution with PEG 400 was named as HPEG which is our interest of study. A solution of 1 % copper sulfate (CuSO_4) was made and poured over the polymers mixture contained into the cast. Hydrogel was formed due to crosslinking done by the CuSO_4 . Double distilled water was utilized to wash the hydrogel formed to eliminate leftover CuSO_4 solution and retained at -20°C for overnight for accurate hardening. The hydrogel scaffold was obtained by lyophilizing the hydrogel at room temperature. The different ratio of polymer mix are as pectin : CMC (1:0.5; 1:1; 0.5:1) with PEG 400 and glycerol variation as 1%, 3%, 5%. Lower the plasticizer brittle the hydrogel and higher the plasticizer, the polymer mix did not crosslink properly. Therefore among these polymer mixture the mix which produced proper hydrogels are pectin : CMC (1:1) with 3% PEG 400 or 3% glycerol entitled as HPEG and HGY respectively (figure 1).



Figure 1. The image of hydrogel along with the hydrogel scaffold

2.3. Characterization

The SEM (analysis scanning electron microscope) is utilised to learn regarding the structural anatomy of the casted scaffolds of hydrogels. Fourier transform infrared spectra (FTIR) of the hydrogel scaffolds were achieved at the frequency range of $400 - 4000\text{ cm}^{-1}$. The study of XRD pattern (X-ray diffraction) of hydrogel was done by using a skinny segment of $1 \times 1\text{ cm}$ scaffolds of hydrogel under $\text{CuK}\alpha$ radiation secure at 1.5418 \AA wavelength with 2θ range of 0.2° s^{-1} at room temperature. A thin segments of hydrogel scaffolds were utilized for the thermogravimetric (TGA) and differential thermal analysis (DTA) analysis to be carried out at the scanning rate of $10^\circ\text{C min}^{-1}$ followed by the atmospheric condition of having nitrogen in a temperature ranging from $20^\circ\text{C} - 1000^\circ\text{C}$. Differential scanning calorimetry (DSC) of the hydrogel scaffolds were achieved by heating 15 mg of samples from $10^\circ\text{C} - 100^\circ\text{C}$ with a speed of $10^\circ\text{C min}^{-1}$ under the nitrogen atmosphere.

2.4. Swelling properties studies

The swelling property of the scaffolds of hydrogels can be calculated as the degree of swelling (DOS). A minor portion of dehydrated scaffolds with equivalent weight (w_i) was submerged in double

distilled water or buffers of diverse pH at room temperature. The final wet weight (w_f) of the hydrogel was obtained after seven days by softly blotting the hydrogel over the blotting paper. The DOS equation (1) was recorded corresponding to the subsequent equations [42].

$$\text{Degree of swelling} = \frac{w_f - w_i}{w_i} \quad (1)$$

2.5. Cytocompatibility studies

Cytocompatibility of HGY and HPEG was estimated by means of MTT assay which is a spectroscopic assay that analyse the reduction of yellow color MTT 3-(4, 5-dimethylthiazol-2-yl)-2, 5-diphenyl tetrazolium bromide (MTT) through mitochondrial succinate dehydrogenase. The MTT penetrate the cells and gets reduced in mitochondria into not soluble formazan product which is dark in color. The cells are then dissolved in organic solvents and analysed spectrophotometrically [43]. The reduction of MTT only occurs in live cell due to it metabolic activity, thus it proves that the cells are living. WI-38 cells were cultured in RPMI media with 100 U/ml streptomycin, 100 U/ml penicillin and 10% fetal bovine serum (FBS) as antibiotics at 37°C in 5% CO₂ and moist atmosphere. In 96 well plate, WI-38 cells were dispersed at a density of 1 X 10⁶. An equivalent weight of HGY and HPEG were incubated in diverse well plates and allowed the cells for diverse hours (24h, 48h, and 72h). After incubation the cells were washed using 1X phosphate buffer saline (PBS) twice. Subsequently 0.5 mg/ml MTT solution was put into the well of the plate and incubated for 4 hours at 37°C until the color changes to a purple. Further the obtained product was solubilized into DMSO (Dimethyl sulfoxide) and measured spectrophotometrically at 570nm by means of a microplate reader (Biorad). The calculation of survival percentage was done bearing in mind the untreated cells having 100% viability.

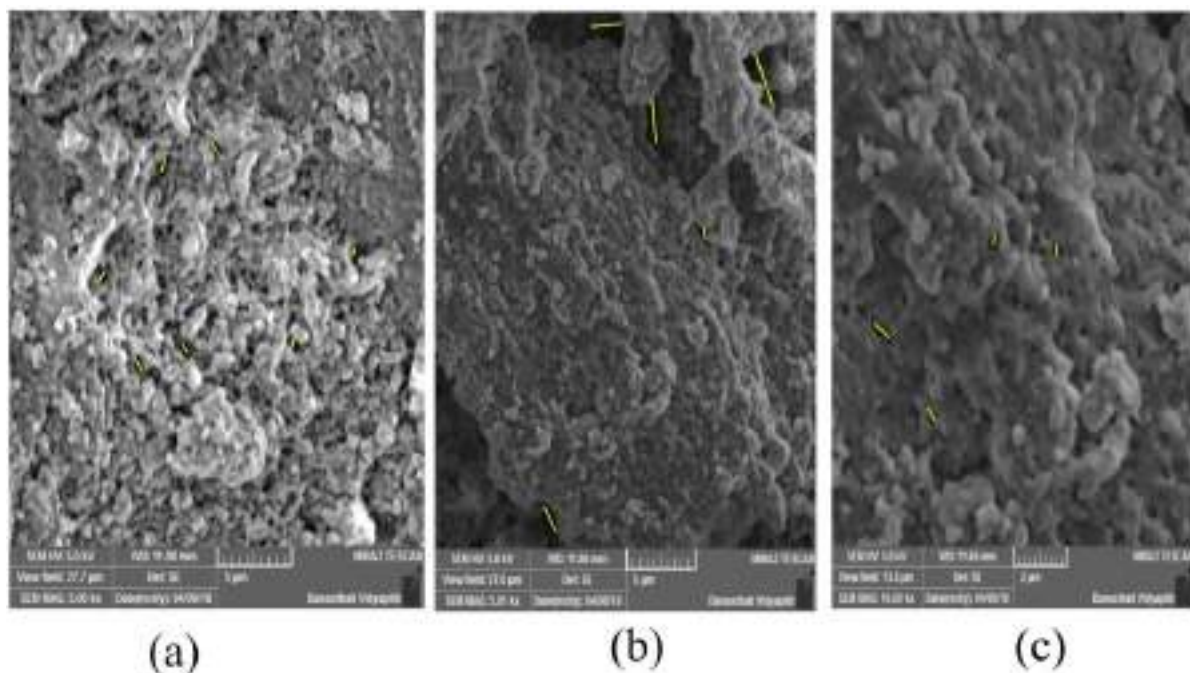


Figure 2. (a) SEM image of HGY, (b) and (c) SEM image of HPEG

3. Results and discussions

3.1. Morphological analysis using SEM

The morphological analysis and porosity determination of the scaffolds of hydrogels (HGY and HPEG) was done by SEM analysis. The SEM image of HG Y and HPEG shows the vastly porous structure of this scaffold with an mean pore size of 41.38 μm (figure 2 (a)) and 6 – 98 μm (figure 2 (b) and (c)) respectively. The porosity of HG Y and HPEG varies greatly due to the use of glycerol and PEG 400 as plasticizer respectively. On the basis of the past studies, it has been found that the pure PEG hydrogels consist of many interconnected pores with a porosity ranging from $6 \pm 15 \mu\text{m}$ to $6 \pm 82 \mu\text{m}$ [40]. HPEG also reflect a similar type of porosity and simultaneously allows cell viability as discussed further in this paper. Therefore, the above discussion reflects that HPEG has higher and variable porosity than HG Y.

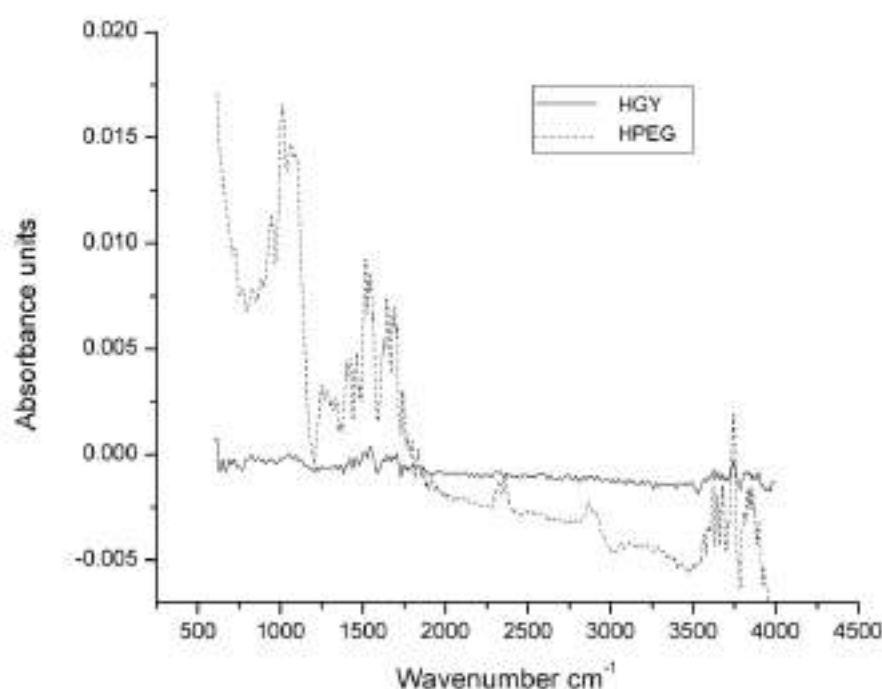


Figure 3. The graphical depiction of FTIR peaks of HG Y and HPEG

3.2. Study of interaction among polymers using FTIR spectroscopy

According to Mishra et al. 2008 [44] the FTIR spectrum of pectin due to $-\text{OH}$ stretching vibration is 3366 cm^{-1} to 3402 cm^{-1} and 2931 cm^{-1} due to $-\text{CH}$ stretching vibration. The 1734 cm^{-1} is assigned due to $\text{C}=\text{O}$ which is an esterified carboxyl group. 1220 cm^{-1} represent to ether ($\text{R}-\text{O}-\text{R}$) and 1008 cm^{-1} represent $\text{C}-\text{C}$ bond which is the part of the ring structure of pectin molecules. $800 - 1000 \text{ cm}^{-1}$ correspond to weak symmetric carbonyl stretching vibration [44].

According to Ninan et al. 2013 [14] the FTIR spectrum of CMC represent $-\text{OH}$ stretching vibration at 3367 cm^{-1} . 1587 cm^{-1} and 1416 cm^{-1} symbolize symmetric and asymmetric modes of stretching vibration or carboxylic groups. $1020 - 1080 \text{ cm}^{-1}$ corresponds to asymmetric stretching vibration [14, 45].

As compared to the above discussing [14, 44, 45] the FTIR spectra of HGY (figure 3) display clear absorption peak at 3424 cm^{-1} to 3491 cm^{-1} which are owing to --OH stretch vibration peaks. The peaks at 1454 cm^{-1} and 1365 cm^{-1} represents CH_2 and --OH bending vibration peaks respectively. The peaks between 1706 cm^{-1} to 1770 cm^{-1} represents carboxymethyl group (--COOCH_3). The peaks 1047 cm^{-1} represents the C--O stretching vibration peak in the hydrogel [46]. The peak 1706 cm^{-1} to 1770 cm^{-1} represent C=O in the hydrogel. The alteration of peaks is due to strong crosslinking by Cu^{2+} ions in hydrogel [47]. The peaks of the carboxylic group have shifted to higher range i.e. 1625 cm^{-1} to 1706 cm^{-1} due to strong crosslinking by Cu^{2+} ions. The FTIR peaks symbolized in the graph (figure 2) verifies the satisfactory interactions among pectin and CMC which inspire to efficacious hydrogel scaffold formation [14, 44, 45, 47].

The FTIR spectra of HPEG (figure 3) display clear absorption peak at 3422 cm^{-1} to 3809 cm^{-1} which is owing to --OH stretch and 2865 cm^{-1} is owing to --CH stretching vibration peaks. The peak 2323 cm^{-1} to 2363 cm^{-1} represents --COO stretch. The peaks at 1424 cm^{-1} to 1478 cm^{-1} and 1339 cm^{-1} – 1396 cm^{-1} represents CH_2 and --OH bending vibration peaks respectively. The peaks between 1705 cm^{-1} to 1770 cm^{-1} signifies the carboxymethyl group (--COOCH_3). The peaks 1011 cm^{-1} to 1063 cm^{-1} represents the C--O stretching vibration peak in the hydrogel [46]. The peaks 1626 cm^{-1} to 1693 cm^{-1} represents --COOH group and the peaks 1705 cm^{-1} to 1798 cm^{-1} represents C=O in the hydrogel. The strong crosslinking by Cu^{2+} ions in hydrogel inspire to shifting in peaks in FTIR analysis. Owing to strong cross-linking by Cu^{2+} ions, the peaks of the carboxylic group have shifted to higher range i.e. 1515 cm^{-1} to 1646 cm^{-1} [47]. The FTIR peaks symbolized in the graph (figure 2) verifies the promising interactions among the pectin and CMC which inspire to efficacious hydrogel scaffold formation [14, 44, 45, 47].

As the intensity increases the number of that particular bonds also increases. The HGY and HPEG have peaks locus at the identical wavelength range however the peak intensity has increased significantly in case of HPEG. This suggests that, at these peak locus where the intensity is high, the bond formation number is more [48, 49]. Therefore, it infers that the intensity of the peaks absorbance implies the creation of fresh bonds owing to crosslinking by Cu^{2+} ions. As PEG 400 ($\text{C}_{2n}\text{H}_{2n+2}\text{O}_{n+1}$; $n=8.2$ to 9.1) has a long polymer chain than glycerol ($\text{C}_3\text{H}_8\text{O}_3$) thus, the --OH group of PEG 400 are more likely available for bond formation with other functional groups present in CMC and pectin during crosslinking. Therefore, hydrogel with PEG 400 (HPEG) has more intense peak absorbance than hydrogel with glycerol (HGY). Other than this, two bonds of --CH and --COO are more prominently detected in FTIR spectra of HPEG at 2865 cm^{-1} and 2323 cm^{-1} wavelength respectively which are not observed in HGY. This further confirms the ionic bond formation in HPEG during crosslinking whereas in case of HGY the bonds formation is mainly hydrogen bond formation.

3.3. Crystallization studies using XRD

The study of crystallization of both the hydrogels are done by XRD pattern analysis. The XRD graph (figure 4) of HGY and HPEG shows both the amorphous nature and crystalline nature of the hydrogel. The broad peak at 9.8° to 12.5° and 19° to 22.5° indicated the amorphous nature of the pectin/CMC hydrogel (figure 4). The peak at 26.5° signifies a low crystallinity of the polymer composite (figure 4) [50]. The crystalline nature of the hydrogel is affected by the plasticizer because plasticizers delivered mobility amid the polymer molecules layer [51]. Irrespective of the difference in plasticizer HGY and HPEG have similar nature of crystallization that is amorphous in nature. Thus, the XRD pattern of PCGY and PCPEG are similar. The above conversation approves the amorphous nature of the two hydrogels (HGY and HPEG) [44].

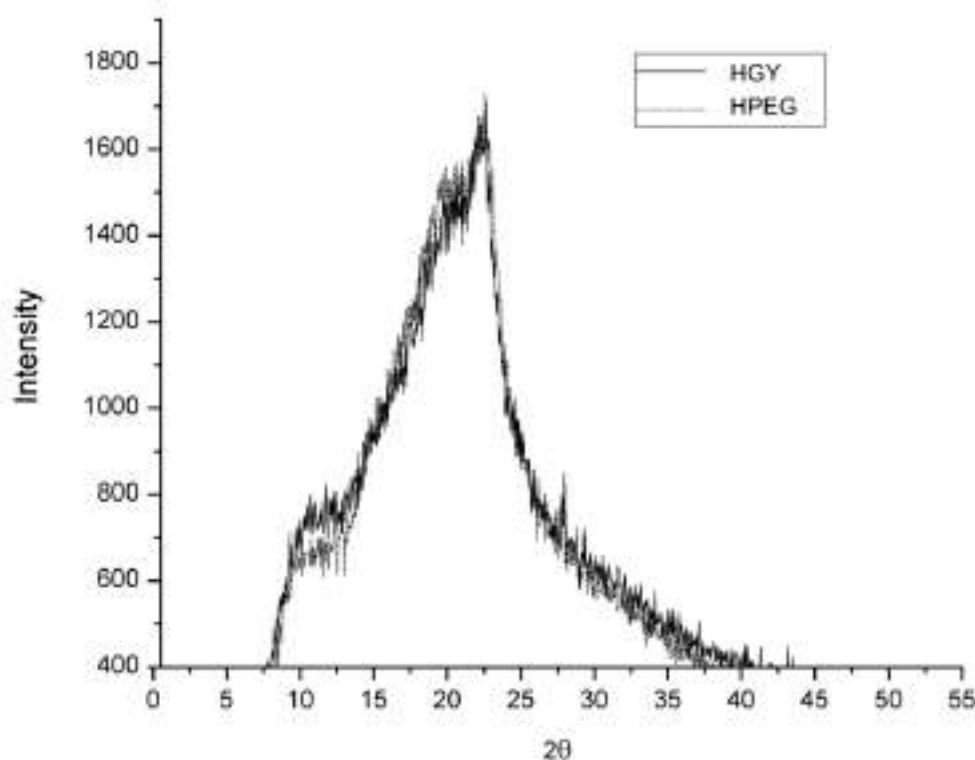


Figure 4. The graphical depiction of XRD peaks of HGY and HPEG

3.4. Thermogravimetric analysis (TGA) / Derivative thermogravimetric analysis (DTG) and Differential thermal analysis (DTA)

The TGA profile of hydrogel HGY and HPEG is represented by figure 5 (a) and (b) respectively. The thermal stability with respect to change of temperature is represented by TGA plot. In figure 5(a), at 160 °C the initial degradation of HGY starts and degradation end at 390 °C. The weight loss percentage of HGY is obtained as 62%. The DTA graph plot denotes the endothermic degradation of HGY. The first degradation happened at 79 °C which is owing to evaporation of water molecules intensely bound to the HGY sample [52]. An endothermic reaction occurred at 200 °C lead to major degradation of the polymer. The further degradation of polymer occurred at 300 °C due to endothermic degradation reaction. On additional heating, an endothermic dehydration reaction of the polymer follows at 750 °C. The DTG graph plot approves the breakdown of the sample and signifies the precise temperature at which the breakdown starts and ends. The deterioration because of loss of water starts at 20 °C and ends at 100 °C. At 180 °C the major breakdown of polymer starts and ends at 300 °C, whereas the final degradation of the polymer is represented by a small peak from 280 °C to 350 °C. On additional heating, a dehydration reaction occurs between 720 °C and 770 °C. In case of DTA and DTG graph the height or depth of the peaks expresses reactivity intensity [55].

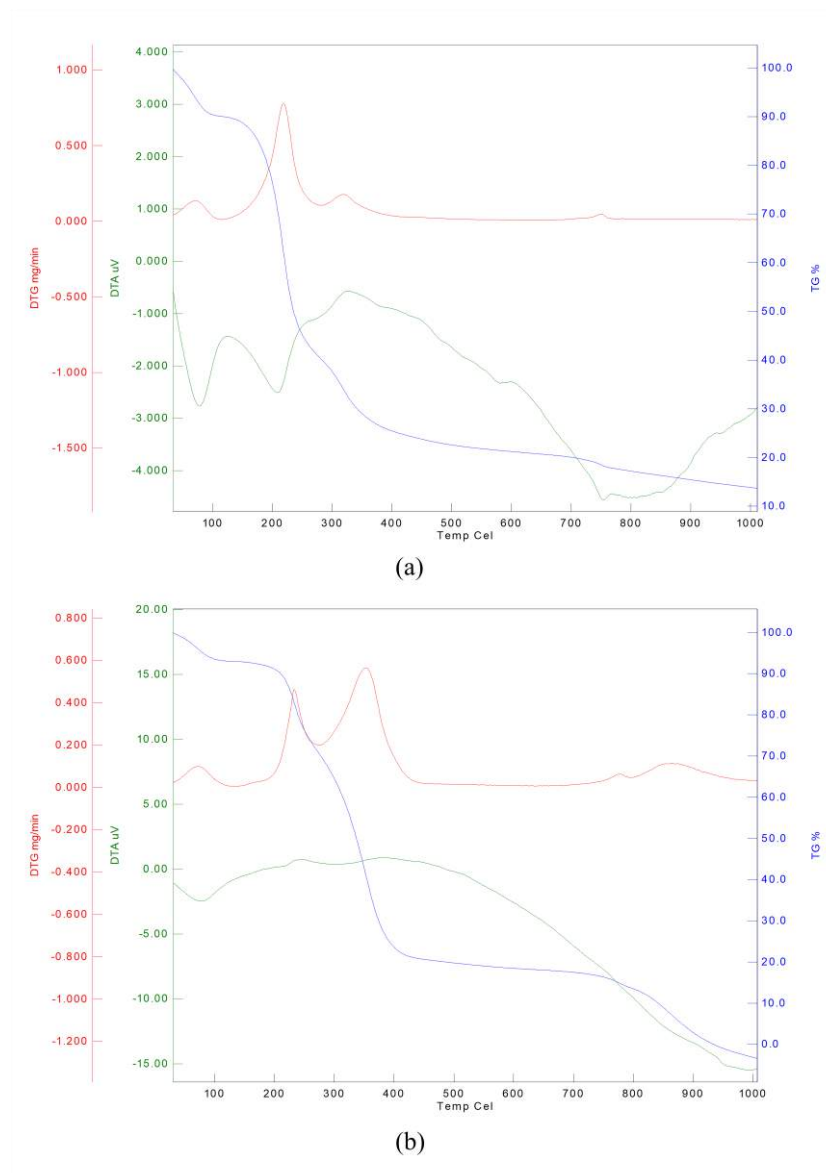
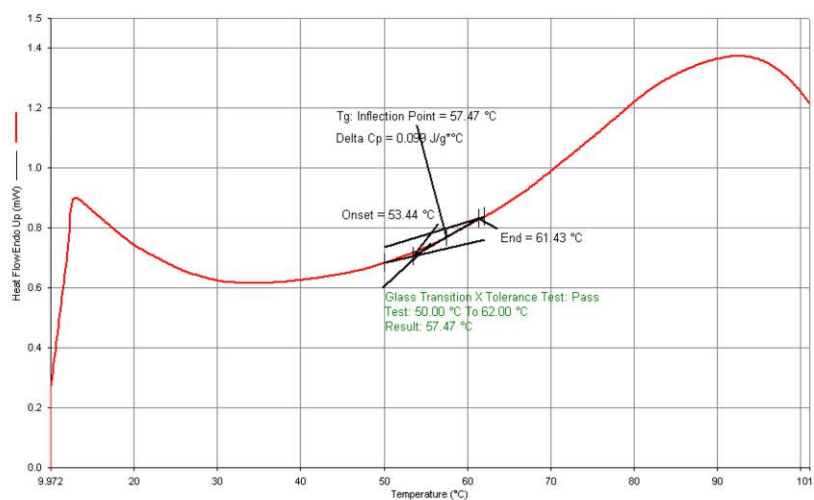


Figure 5. The graphical representation of TGA/DTA analysis (a) HGY and (b) HPEG

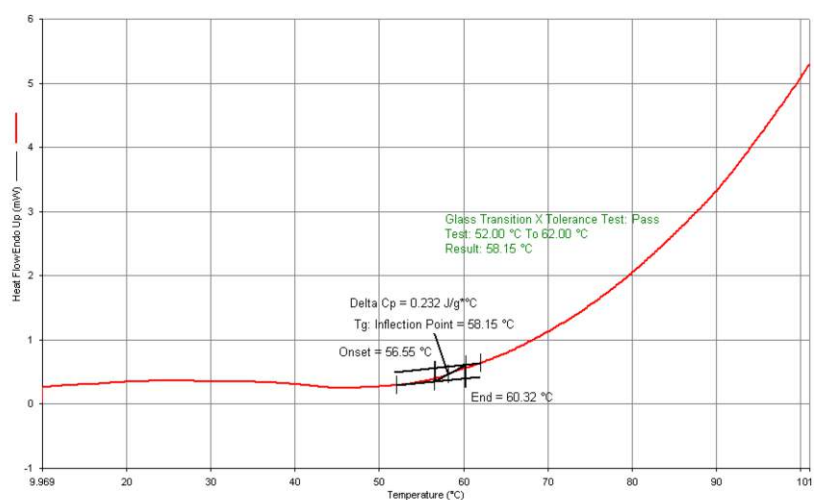
In figure 5(b), the initial degradation of HPEG occurs from 220 °C continues till 420 °C. The first weight loss percentage of HPEG is 70% whereas the second degradation of HPEG occurs at 820 °C and continued till 920 °C with the second weight-loss percentage of HPEG as 12%. The DTA graph plot of HPEG symbolizes the endothermic degradation. The first degradation of HPEG is detected at 70 °C which is an endothermic reaction where degradation occurs owing to evaporation of water molecules intensely enclosed to the sample [52]. At 220 °C a small peak of the endothermic reaction was observed representing the further degradation. At 300 °C a small broad peak is observed representing endothermic reaction of HPEG. On additional heating, a small broad endothermic peak was detected at 940 °C which completes the final breakdown of the polymer. The DTG graph plot approves the breakdown of the sample and denotes the precise temperature at which the breakdown starts and ends [52]. The breakdown of HPEG owing to loss of water occurs from 10 °C to 100 °C.

Correspondingly, the chief breakdown of the polymer happens at 210 °C to 280 °C and 280 °C to 450 °C. On additional heating, two broad peaks were detected at 760 °C to 820 °C and 820 °C to 950 °C which signify dehydration reaction and final degradation of HPEG [55].

So, according to the above discussion, an inference can be drawn that HPEG has more thermal stability than HGY. As HPEG roughly degrade at 300 °C and the complete degradation occurs at almost 950 °C, thus it has high thermostability which has valuable utility in industries.



(a)



(b)

Figure 6. The graphical depiction of DSC analysis (a) HGY and (b) HPEG

3.5. Thermal analysis using Differential Scanning Calorimetry (DSC)

Thermal analysis method such as DSC is used for evaluating first and second order thermal analysis like glass transition (Tg) phenomena, melting (Tm) and crystallization (Tc)h [52]. Tg temperature

represents the mobility of molecules. Tg in lower temperature represent smooth molecule movement and at higher temperature rough molecular movement [53]. HGY (figure 6(a)) has Tg value 57.5 °C whereas in case of HPEG (figure 6(b)) Tg value is 58.15 °C which are nearly similar. The Tg value of HGY and HPEG indicates that the materials are amorphous in nature as lower the temperature of Tg value higher the molecular mobility. The plasticizer molecules helps in arranging the polymer chains away from each other and upsurges the free volume which helps in easy motion of the polymer chain on top of each other at low temperature preceding in the decline of Tg of the polymer [54]. The above mentioned XRD enquiry also approves the amorphous nature of the hydrogel (HGY and HPEG) similar to DSC analysis.

3.6. Swelling properties

Table 1 describe the investigation of the degree of swelling (DOS) of HGY which is considered as standard as compared to HPEG in water and diverse pH. DOS in case of the water of HPEG is 5.54 which is slightly more than DOS in case of the water of HGY which is 5.10. With growing pH the DOS value rises to pH 5.5 and declines from pH 6 which discloses the pH-sensitive nature of hydrogel. DOS value of HPEG is highest as 12.09 at pH 5 whereas HGY has maximum DOS value of 18.87 at pH 5. As glycerol has short polymer chain and PEG 400 has long polymer chain thus glycerol forms more space in the hydrogel which effects the swelling property of hydrogels [56]. Thus HGY has comparatively more DOS than HPEG. But as discussed earlier in TGA/DTG/DTA section PEG 400 provides thermal stability to the polymer thus, in summary, though HPEG has slightly low DOS value than HGY but have more enhanced property than HGY. The properties of HPEG is probably an operational drug delivery method over body parts which has a mean pH of 5 to 5.5 [57]. Other than this, the high entrapment capability, porosity and swelling properties makes it capable to entrap pollutants from the air such as dust particles, microorganism and pathogens entrap into droplets which generally spread by sneezing and more. The DOS value of HPEG is significantly high as compared to literature study and thus it has significant industrial value [14, 58].

Table 1. DOS value in water and different pH buffers of HGY and HPEG

Sample	DOS in water	DOS in pH 4.5	DOS in pH 5	DOS in pH 5.5	DOS in pH 6	DOS in pH 6.5	DOS in pH 7	DOS in pH 7.5
PCGY	5.10±0.12	6.53±0.22	18.87±0.07	16.12±0.27	14±0.63	Dissolved	Dissolved	Dissolved
PCPEG	5.54±0.08	6.07±0.24	12.09±0.27	8.75±0.61	3.18±0.24	Dissolved	Dissolved	Dissolved

Symbol “±” signifies standard deviation where $n = 4$

3.7. Cell compatibility studies

The cytocompatibility of HGY and HPEG was measured by observing the change of survivability of WI-38 cells after cultivation with HGY and HPEG for diverse time intervals using MTT assay. The survival percentage at different time intervals is shown in figure 7. HPEG showed high survival percentage from 24 hours to 48 hours and decrease by 72 hours similarly as in HGY. Owing to the percolation of Cu^{2+} from gradually breakdown of hydrogels with respect to time because of alkaline pH of the media, the rate of cell survival decrease at 72 hours [59]. The literature study has revealed

good cell compatibility of glycerol base hydrogel with CMC and pectin thus, HGY reveals good cytocompatibility [14] but, PEG 400 with pectin and CMC are not studied. Thus, HPEG shows good cytocompatibility of PEG 400 based hydrogel.

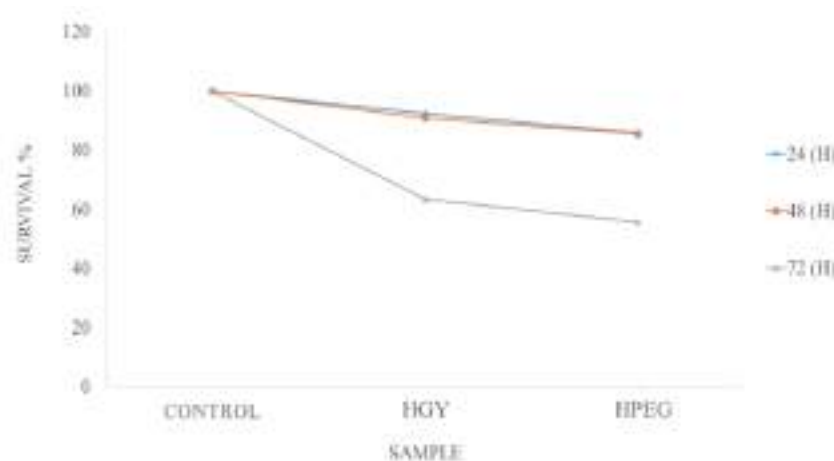


Figure 7. The graphical depiction of the survival percentage of HGY and HPEG with respect to time.

4. Conclusion

As discussed earlier the efficacious manufacture of hydrogel scaffold has accompanied. HGY which is made-up by means of pectin, CMC with glycerol as the plasticizer is considered as standard hydrogel in comparison with HPEG which is made-up by means of pectin, CMC with PEG 400 as a plasticizer which is the interest of study. HGY and HPEG are both amorphous in nature as confirmed by DSC and XRD analysis which reveals that interaction of plasticizers has resulted in the loss of crystalline nature of pectin and CMC molecules. FTIR peaks confirm the satisfactory interaction among the CMC and pectin in both HGY and HPEG. PEG 400 have more reactive $-OH$ groups than glycerol which effects the bond formation and the intensity of the peaks of HPEG. As discussed earlier the increase in the intensity of peak absorbance is directly correlated to the increase in the number of bonds formation at that particular wavelength. The higher intensity of HPEG signifies intense bond formation at that particular wavelengths. TGA/DTG/DTA confirms the high thermal stability of HPEG than HGY due to the presence of PEG 400 as the plasticizer in HPEG. As HPEG approximately degrade at $300\text{ }^{\circ}\text{C}$ and the complete degradation occurs at approximately $950\text{ }^{\circ}\text{C}$, thus it conveys high thermal stability. The pore size of HGY is $41.38\text{ }\mu\text{m}$ and HPEG is $6 - 98\text{ }\mu\text{m}$. The pore size of HGY is less than HPEG but are uniformly spread whereas HPEG is a combination heterogeneous pore size. PEG400 avoid nonspecific bindings as stated in the above context thus, this property of PEG 400 provides excellent property to HPEG. HGY and HPEG both have high DOS as 18.87 and 12.09 respectively at pH 5 which is due to glycerol and PEG 400 as plasticizer respectively.

The high and heterogeneous porosity of the HPEG provide its unique features by providing the capability to entrap molecules with small to large size. Other than this, HPEG is cytocompatible and nontoxic with a high degree of swelling which enables it to absorb moisture and the pollutants along with this moisture from the environment. The Cu^{2+} ion used for crosslinking hydrogel has biocidal property along with thermostability which is helpful for easy sterilization. The pH sensitivity of the hydrogel can be applied to discharge the entrap particles in a specific pH media and also enable easy degradation and therefore is eco-friendly in nature. The conversion of hydrogel into scaffold by lyophilize can be utilized to form thin film of hydrogel scaffold with application as filters for masks and more.

Thus, as discussed earlier HPEG is thermo-stable, pH sensitive, have high porosity, avoids nonspecific binding, high swelling property, and cytocompatibility makes it excellent hydrogel scaffold for its industrial use as compared to HGY. Hence, PEG 400 as a plasticizer enhances the properties of hydrogel and the above discussed results suggested that HPEG hydrogel has varied applications in biomedical sectors.

Acknowledgments

The authors of this paper are thankful to Department of Metallurgy, IIT Kharagpur for providing research facility.

Funding: This research did not receive any specific grant from funding agencies in the public, commercial, or not-for-profit sectors.

Conflict of Interest: The authors declare that they have no conflict of interest.

References

- [1] Gad Y H 2008 Preparation and characterization of poly(2-acrylamido-2-methylpropane-sulfonic acid)/Chitosan hydrogel using gamma irradiation and its application in wastewater treatment. *Radiat. Phys. Chem.* **77**, 1101-1107.
- [2] Crini G 2005 Recent developments in polysaccharide-based materials used as adsorbents in wastewater treatment. *PROG POLYM SCI* **30**, 38-70.
- [3] Lutcmiah K A R D, Verliefde K, Roest L C, Rietveld and E R Cornelissen 2014 Forward osmosis for application in wastewater treatment: A review. *Water Res* **58**, 179-197.
- [4] Souza G R, Molina J R, Raphael R M, Ozawa M G, Stark D J, Levin C S, Bronk L F, Ananta J S, Mandelin J, Georgescu M-M, Bankson J A, Gelovani J G, Killian T C, Arap W and Pasqualini R 2010 Three-dimensional tissue culture based on magnetic cell levitation. *Nat. Nanotechnol.* **5**, 291.
- [5] Landers R, Hübner U, Schmelzeisen R and Mülhaupt R 2002 Rapid prototyping of scaffolds derived from thermoreversible hydrogels and tailored for applications in tissue engineering. *Biomaterials* **23**, 4437-4447.
- [6] Seliktar D 2012 Designing Cell-Compatible Hydrogels for Biomedical Applications. *Science* **336**, 1124-1128.
- [7] Drury J L and Mooney D J 2003 Hydrogels for tissue engineering: scaffold design variables and applications. *Biomaterials* **24**, 4337-4351.
- [8] Lee K Y and Mooney D J 2001 Hydrogels for Tissue Engineering. *Chem. Rev.* **101**, 1869-1880.
- [9] Peppas N A, Bures P, Leobandung W and Ichikawa H 2000 Hydrogels in pharmaceutical formulations. *EUR J PHARM BIOPHARM* **50**, 27-46.
- [10] Van Tomme S R, Storm G and Hennink W E 2008 In situ gelling hydrogels for pharmaceutical and biomedical applications. *Int. J. Pharm.* **355**, 1-18.
- [11] Gupta P, Vermani K and Garg S 2002 Hydrogels: from controlled release to pH-responsive drug delivery. *Drug Discov. Today* **7**, 569-579.
- [12] Malafaya P B, Silva G A and Reis R L 2007 Natural-origin polymers as carriers and scaffolds for biomolecules and cell delivery in tissue engineering applications. *Adv. Drug Deliv. Rev.* **59**, 207-233.
- [13] Vieira M G A, da Silva M A, dos Santos L O and Beppu M M 2011. Natural-based plasticizers and biopolymer films: A review. *Eur. Polym. J.* **47**, 254-263.
- [14] Ninan N, Muthiah M, Park I-K, Elain A, Thomas S and Grohens Y 2013. Pectin/carboxymethyl cellulose/microfibrillated cellulose composite scaffolds for tissue engineering. *Carbohydr. Polym.* **98**, 877-885.

- [15] Nazarov R, Jin H-J and Kaplan D L 2004 Porous 3-D Scaffolds from Regenerated Silk Fibroin. *Biomacromolecules* **5**, 718-726.
- [16] Chung T W, Yang J, Akaike T, Cho K Y, Nah J W, Kim S I and Cho C S 2002 Preparation of alginate/galactosylated chitosan scaffold for hepatocyte attachment. *Biomaterials* **23**, 2827-2834.
- [17] Sheridan M H, Shea L D, Peters M C and Mooney D J 2000 Bioabsorbable polymer scaffolds for tissue engineering capable of sustained growth factor delivery. *J CONTROL RELEASE* **64**, 91-102.
- [18] Luu Y K, Kim K, Hsiao B S, Chu B and Hadjiargyrou M 2003 Development of a nanostructured DNA delivery scaffold via electrospinning of PLGA and PLA-PEG block copolymers. *J CONTROL RELEASE* **89**, 341-353.
- [19] Agrawal C M and Ray R B 2001 Biodegradable polymeric scaffolds for musculoskeletal tissue engineering. *J. Biomed. Mater. Res.* **55**, 141-150.
- [20] Mao J S, Zhao L G, Yin Y J and Yao K D 2003 Structure and properties of bilayer chitosan-gelatin scaffolds. *Biomaterials* **24**, 1067-1074.
- [21] Xiao W, He J, Nichol J W, Wang L, Hutson C B, Wang B, Du Y, Fan H, and Khademhosseini A 2011 Synthesis and characterization of photocrosslinkable gelatin and silk fibroin interpenetrating polymer network hydrogels. *Acta Biomater.* **7**, 2384-2393.
- [22] Chen M-C, Tsai H-W, Liu C-T, Peng S-F, Lai W-Y, Chen S-J, Chang Y and Sung H-W 2009 A nanoscale drug-entrapment strategy for hydrogel-based systems for the delivery of poorly soluble drugs. *Biomaterials* **30**, 2102-2111.
- [23] Bhattarai N, Gunn J and Zhang M 2010 Chitosan-based hydrogels for controlled, localized drug delivery. *Adv. Drug Deliv. Rev.* **62**, 83-99.
- [24] He H, Cao X, and Lee L J 2004 Design of a novel hydrogel-based intelligent system for controlled drug release. *J CONTROL RELEASE* **95**, 391-402.
- [25] Soppimath K S, Kulkarni A R and Aminabhavi T M 2000 Controlled release of antihypertensive drug from the interpenetrating network poly(vinyl alcohol)-guar gum hydrogel microspheres. *J. Biomater. Sci. Polym. Ed.* **11**, 27-43.
- [26] Williams C G, Malik A N, Kim T K, Manson P N and Elisseff J H 2005 Variable cytocompatibility of six cell lines with photoinitiators used for polymerizing hydrogels and cell encapsulation. *Biomaterials* **26**, 1211-1218.
- [27] Mann B K, Gobin A S, Tsai A T, Schmedlen R H and West J L 2001 Smooth muscle cell growth in photopolymerized hydrogels with cell adhesive and proteolytically degradable domains: synthetic ECM analogs for tissue engineering. *Biomaterials* **22**, 3045-3051.
- [28] Kobayashi H and Ikacia Y 1991 Corneal cell adhesion and proliferation on hydrogel sheets bound with cell-adhesive proteins. *Curr. Eye Res.* **10**, 899-908.
- [29] Banerjee A, Arha M, Choudhary S, Ashton R S, Bhatia S R, Schaffer D V and Kane R S 2009 The influence of hydrogel modulus on the proliferation and differentiation of encapsulated neural stem cells. *Biomaterials* **30**, 4695-4699.
- [30] Basak S, Nandi N, Paul S, Hamley I W and Banerjee A 2017 A tripeptide-based self-shrinking hydrogel for waste-water treatment: removal of toxic organic dyes and lead (Pb²⁺) ions. *ChemComm* **53**, 5910-5913.
- [31] Ninan N, Muthiah M, Park I-K, Kalarikkal N, Elain A, Wui Wong T, Thomas S and Grohens Y 2014 Wound healing analysis of pectin/carboxymethyl cellulose/microfibrillated cellulose based composite scaffolds. *Mater. Lett.* **132**, 34-37.
- [32] Akalin G O and Pulat M 2018 Preparation and Characterization of Nanoporous Sodium Carboxymethyl Cellulose Hydrogel Beads *J. Nanomater.* **2018**, 12.
- [33] Borkow G 2014 Using Copper to Improve the Well-Being of the Skin. *Curr Chem Biol* **8**, 89-102.

- [34] Sothornvit R and Krochta J M 2001 Plasticizer effect on mechanical properties of β -lactoglobulin films. *J. Food Eng.* **50**, 149-155.
- [35] Baiardo M, Frisoni G, Scandola M, Rimelen M, Lips D, Ruffieux K and Wintermantel E 2003 Thermal and mechanical properties of plasticized poly(L-lactic acid). *Appl. Polym. Sci.* **90**, 1731-1738.
- [36] Srinivasa, Ramesh P C, Tharanathan M N, R N 2007 Effect of plasticizers and fatty acids on mechanical and permeability characteristics of chitosan films. *Food Hydrocoll.* **21**, 1113-1122.
- [37] Péan J-M, Boury F, Venier-Julienne M-C, Menei P, Proust J-E and Benoit J-P J P R 1999 Why Does PEG 400 Co-Encapsulation Improve NGF Stability and Release from PLGA Biodegradable Microspheres? *Pharm Res.* **16**, 1294-1299.
- [38] D'souza A A and Shegokar R 2016 Polyethylene glycol (PEG): a versatile polymer for pharmaceutical applications. *EXPERT OPIN DRUG DEL* **13**, 1257-1275.
- [39] Charles P T, Stubbs V R, Soto C M, Martin B D, White B J and Taitt C R 2009 Reduction of Non-Specific Protein Adsorption Using Poly(ethylene) Glycol (PEG) Modified Polyacrylate Hydrogels In Immunoassays for Staphylococcal Enterotoxin B Detection. *Sensors* **9**, 645-655.
- [40] Chiu Y-C, Larson J C, Isom A Jr, Brey E M 2010 Generation of porous poly(ethylene glycol) hydrogels by salt leaching. *Tissue Eng Part C Methods.* **16**, 905-912.
- [41] Strzelczyk A K, Wang H, Lindhorst A, Waschke J, Pompe T, Kropf C, Luneau B and Schmidt S 2017 Hydrogel Microparticles as Sensors for Specific Adhesion: Case Studies on Antibody Detection and Soil Release Polymers. *Gels.* **3**, 31.
- [42] Sadeghi M J A J B A S 2011 Synthesis and Investigation of Swelling Behavior Natural Based Superabsorbent Composites with High Thermal Resistance. *AJBAS* **5**, 887-895.
- [43] Liu Y, Peterson D A, Kimura H and Schubert D 1997 Mechanism of Cellular 3-(4,5-Dimethylthiazol-2-yl)-2,5-Diphenyltetrazolium Bromide (MTT) Reduction. *J Neurochem.* **69**, 581-593.
- [44] Mishra R K, Datt M and Banthia A K 2008 Synthesis and characterization of pectin/PVP hydrogel membranes for drug delivery system. *AAPS PharmSciTech* **9**, 395-403.
- [45] Yang J, Duan J, Zhang L, Lindman B, Edlund H and Norgren M J C 2016 Spherical nanocomposite particles prepared from mixed cellulose–chitosan solutions. *Cellulose* **23**, 3105-3115.
- [46] Coldea T E, Socaciu C, Fetea F, Ranga F A, Pop R M and Florea M 2013 Rapid Quantitative Analysis of Ethanol and Prediction of Methanol Content in Traditional Fruit Brandies from Romania, using FTIR Spectroscopy and Chemometrics. *Notulae Botanicae Horti Agrobotanici Cluj-Napoca.* **41**, 143-149.
- [47] Luna-Martínez J F, Hernández-Uresti D B, Reyes-Melo M E, Guerrero-Salazar C A, González-González V A and Sepúlveda-Guzmán S 2011 Synthesis and optical characterization of ZnS–sodium carboxymethyl cellulose nanocomposite films. *Carbohydr. Polym.* **84**, 566-570.
- [48] Munajad A, Subroto C and Suwarno S J E 2018 Fourier Transform Infrared (FTIR) Spectroscopy Analysis of Transformer Paper in Mineral Oil-Paper Composite Insulation under Accelerated Thermal Aging. *Energies* **11**, 364.
- [49] Bandara K, Ekanayake C, Saha T K and Annamalai P K 2016 Understanding the ageing aspects of natural ester based insulation liquid in power transformer. *IEEE Transactions on Dielectrics and Electrical Insulation.* **23**, 246-257, doi: 10.1109/TDEI.2015.004744..
- [50] Bhattacharya R, Phaniraj T N and Shailaja D 2003 Polysulfone and polyvinyl pyrrolidone blend membranes with reverse phase morphology as controlled release systems: experimental and theoretical studies. *J MEMBRANE SCI* **227**, 23-37.

- [51] Saravana S, Bheemaneni G and Kandaswamy R 2018 Effect of Polyethylene glycol on Mechanical, Thermal, and Morphological Properties of Talc Reinforced Polylactic Acid Composites. *Materials Today: Proceedings* **5**, 1591-1598.
- [52] Malik N S, Ahmad M and Minhas M U 2017 Cross-linked beta-cyclodextrin and carboxymethyl cellulose hydrogels for controlled drug delivery of acyclovir. *PloS one* **12**, e0172727.
- [53] Hale A 2002 In: *Handbook of Thermal Analysis and Calorimetry*. ed. S. Z. D. Cheng, 3, 295-354. (Elsevier Science B.V).
- [54] Jadhav N R, Gaikwad V L, Nair K J, Kadam H M 2009 Glass transition temperature: Basics and application in pharmaceutical sector. *Asian J. Pharm.* **3**.
- [55] Palermo P J 2001 In: *Separation Science and Technology*. eds. S. Ahuja and S. Scypinski, 3, 235-267. (Academic Press).
- [56] Lee S and Wan V C H 2006 In: *Edible films and coatings*. Food Science And Technology- New York-Marcel Dekker-, 149(3), 135.
- [57] Lambers H, Piessens S, Bloem A, Pronk H and Finkel P 2006 Natural skin surface pH is on average below 5, which is beneficial for its resident flora. *Int. J. Cosmet.* **28**, 359-370.
- [58] Sadeghi M 2011 Synthesis, and Investigation of Swelling Behavior Natural Based Superabsorbent Composites with High Thermal Resistance. *Aust. J. Basic & Appl. Sci.* **5**, 887-895.
- [59] Lang F and Hoffmann E K 2012 Role of ion transport in control of apoptotic cell death. *Compr. Physiol.* **2**, 2037-2061.



Protective effect of indomethacin on vanadium-induced adrenocortical and testicular damages in rat

Rituparna Ghosh & Samudra Prosad Banik

To cite this article: Rituparna Ghosh & Samudra Prosad Banik (2021): Protective effect of indomethacin on vanadium-induced adrenocortical and testicular damages in rat, Toxicology Mechanisms and Methods, DOI: [10.1080/15376516.2021.1973169](https://doi.org/10.1080/15376516.2021.1973169)

To link to this article: <https://doi.org/10.1080/15376516.2021.1973169>



Published online: 21 Sep 2021.



Submit your article to this journal



Article views: 9



View related articles



View Crossmark data

RESEARCH ARTICLE



Protective effect of indomethacin on vanadium-induced adrenocortical and testicular damages in rat

Rituparna Ghosh^a and Samudra Prosad Banik^b

^aDepartment of Physiology, Bhairab Ganguly College, Belghoria, Kolkata, India; ^bDepartment of Microbiology, Maulana Azad College, Kolkata, India

ABSTRACT

Vanadium toxicity is a globally recognized threat to the reproductive health of man and animal. However the mechanism of vanadium-induced damage to the testicular and adrenocortical tissues is not fully characterized. It was hypothesized that prostaglandins may partially mediate the inflammatory response to vanadate damage. In this study prostaglandin (PG) mediated effects of vanadate on testicular and adrenocortical functions was substantiated by using indomethacin to block prostaglandin synthesis. Significant inhibition of spermatogenesis, decreased serum level of testosterone and gonadotropins in the vanadium-exposed group of rats indicated the damaging effects of vanadium-induced reactive oxygen species. This was also reflected in the appreciable increase in testicular lipid peroxidation (LPO) level and decline in the activities of steroidogenic and antioxidant enzymes. Histopathological studies revealed regressive and degenerative changes in testis. However, inhibition of cyclooxygenase activity by indomethacin increased steroid hormone production, gonadotropin level, elevated the specific activities of enzymes and decreased LPO level in rat testis exposed to vanadium. Vanadium also caused prostaglandin mediated adrenocortical hyperactivity, as inhibition of PG synthesis abolished these adrenal responses to vanadium. The studies showed that vanadium toxicity is directly linked to stimulation of prostaglandin synthesis. Therefore, indomethacin can be a good prospect to alleviate vanadium induced male infertility.

Abbreviations: V: vanadium; i.p.: intraperitoneal; ASg: type A spermatogonia; pLSc: preleptotene spermatocytes; mPSc: mid pachytene spermatocytes; 7Sd: step 7 spermatids; LH: luteinizing hormone; FSH: follicle stimulating hormone; HSD: hydroxysteroid dehydrogenase; NAD: nicotinamide adenine dinucleotide phosphate; LPO: lipid peroxidation; TBARS: thiobarbituric acid reactive substances; MDA: malondialdehyde; SOD: superoxide dismutase; CAT: catalase; EDTA: ethylenediamine tetraacetic acid; BSA: bovine serum albumin; GPx: glutathione peroxidase; NSAIDS: nonsteroidal anti-inflammatory drugs; COX: cyclooxygenase

ARTICLE HISTORY

Received 23 March 2021
Revised 16 August 2021
Accepted 19 August 2021

KEYWORDS

Indomethacin; male infertility; prostaglandin synthesis; vanadium induced toxicity

1. Introduction

Vanadium, a group V element of the periodic table is required by our body in trace amounts and is associated with a handful of health augmenting effects (Ghosh et al. 2020). However, its toxic effects at higher concentrations are significantly more documented (Zwolak 2020). Vanadium is a chief industry-borne contaminant of soil and water bodies and is known to exert significant damage especially to the male reproductive system (Wilk et al. 2017). The toxicity of vanadium increases with valency of the metal; subsequently, the pentavalent forms are the most toxic species of the element to enter the human body. Vanadium compounds are known to cause partial degeneration of the epithelium of the seminiferous tubules in the testes and therefore poses a threat to affect fertility.

Prostaglandins are distributed throughout the reproductive tract of the male and hold a key position in the common pathway through which hormones and drugs exert control

over different aspects of reproduction. The enzymes cyclooxygenase (COX) catalyzes the first two steps in the biosynthesis of prostaglandins (PGs) from the substrate arachidonic acid. COX activity serves as an important rate limiting and commitment step in the prostaglandin synthesis pathway. Since the increase of prostaglandins attributes to the inflammatory response, nonsteroidal anti-inflammatory drugs (NSAIDS) reduce inflammation and pain by inhibiting the cyclooxygenase activities. There are two isoforms of the cyclooxygenase, COX-1 and COX-2 (Versteeg et al., 1999). COX-1 is a constitutively active enzyme that produces prostaglandins on the endoplasmic reticulum, which is then excreted and used for signaling purposes. COX-1 is expressed in various tissues at a constant level. The second isoform, COX-2 is normally absent in cells and is induced by growth factors, tumor promoters, or cytokines. In some tissue such as the brain, testes, and macula densa of the kidneys, COX-2 serves specialized functions, and is expressed regardless of stimulation. It is expressed in high concentration at sites of

inflammation and in monocytes and macrophages (Vane and Botting 1998).

Prostaglandins have an inhibitory effect on testicular steroidogenesis and spermatogenesis *in vivo*, as well as on sperm motility *in vitro*. Prostaglandins of E and F series also exert antifertility effects (Conte et al. 1985). These observations suggest a negative regulatory effect of prostaglandins on testicular and spermatozoal function. Several lines of evidence indicate that vanadate also induces stimulation of prostaglandin release alongside its other effects including inhibition of various phosphohydrolases and phosphotyrosine phosphatases, stimulation of adenylyl cyclase and specific protein kinases, vasoconstriction and regulation of carbohydrate metabolism, cell proliferation and gene expression (Plass et al. 1992). All these information suggest the possible involvement of increased prostaglandin release in vanadium-induced testicular impairment in rats which can be further substantiated by blocking prostaglandin with non-steroidal anti-inflammatory drug. NSAIDs produce their therapeutic activities through inhibition of cyclooxygenase (COX), the enzyme that makes prostaglandins (PGs). COX-1 inhibition is based on hydrogen bonding, thus the process is instantaneous and reversible. COX-2 inhibition on the other hand has a more complicated binding mechanism which involves covalent binding and secondary conformational changes in the channel. Indomethacin, is a non-steroidal anti-inflammatory drug (NSAID) with anti-inflammatory, analgesic, and antipyretic properties. Structurally, it is an indole-acetic acid derivative with the chemical name 1-(p-chlorobenzoyl) 25-methoxy-2-methylindole-3-acetic acid (Lucas 2016). Indomethacin with its anti-inflammatory and anti-pyretic properties is primarily used in the management of Rheumatoid Arthritis, gout and other related disorders. However, its role on the reversal of vanadium induced toxicity has not been systematically studied till date.

The present study has been designed to understand whether the effect of vanadium on male reproduction is mediated through an increased release of prostaglandin. In this context, the role of indomethacin, a specific inhibitor of prostaglandin synthesis, (Kirch et al. 1989), on the reversal of vanadium-induced toxicity has been investigated.

2. Materials and methods

2.1. Animals

Three-month old male albino rats of Sprague Dawley strain *Rattus norvegicus* weighing 200 ± 10 g were used in the present study. The animals were maintained as per national guidelines and protocols, approved by the Institutional Ethics Committee. They were housed in clean polypropylene cages and in a controlled environment (temperature $22 \pm 2^\circ\text{C}$ and relative humidity 40–60%) in the animal house with constant 12 h light and 12 h dark schedule. The animals were fed on standardized normal diet (20% protein) which consisted of 70% wheat, 20% Bengal gram, 5% fish meal powder, 4% dry yeast powder, 0.75% refined til oil, and 0.25% shark liver oil and water *ad libitum* (Chandra et al. 2007a).

2.2. Reagents

Sodium metavanadate (NaVO_3) was purchased from Riedel-de-Haen. Bovine serum albumin (BSA), thiobarbituric acid (TBA), NADPH, Triton X, triethanol amine, diethanolamine, EDTA, MnCl_2 were purchased from Sigma Chemical Company, St. Louis, M.O., USA. Inmecin-25 (Indomethacin) was purchased from E.M. Pharmaceuticals Pvt. Ltd., India. All other reagents were purchased from Sisco Research Laboratories (SRL), Mumbai, India and were of analytical grade.

2.3. Animal treatment

The rats were divided into four groups. Each group consists of 8 animals. Group I: control rats were injected with sterile distilled water intraperitoneally (i.p) daily for 26 days as vehicle. Group II: rats received i.p. injection of sodium metavanadate (NaVO_3) dissolved in sterile distilled water at a dose of 0.4 mgV/kg body weight daily for 26 days. Group III: rats were treated with indomethacin (1 mg/kg body weight) alone without vanadium for 26 days. Group IV: rats were pre-treated with indomethacin dissolved in vegetable oil at a dose of 1 mg/kg body weight orally (Abbatiello et al. 1975) and then NaVO_3 was administered (20 min after indomethacin treatment) (Plass et al. 1992) at a dose of 0.4 mgV/kg body weight daily i.p. for 26 days.

2.4. Body and organ weights

The body weights of the experimental animals were recorded on the first day before injection (initial) and the day of sacrifice (final). The testicles and adrenal gland were dissected out, trimmed off the attached tissues and weighed. The relative weight of organs was expressed per 100 g body weight. The left testis of each rat was used for histological study and the right for other biochemical measurements.

2.5. Histopathological study of testis

Immediately after removal, the testes were fixed in Bouin's fluid and embedded in paraffin. Sections of 5 μm thickness were taken from the mid portion of each testis and stained with hematoxylin-eosin and examined under a light microscope. Quantitative analysis of spermatogenesis was carried out by counting the relative number of each variety of germ-cells at stage VII of the seminiferous epithelium cycle, i.e. type-A spermatogonia (ASg), preleptotene spermatocytes (pLSc), mid pachytene spermatocytes (mPSc) and step 7 spermatids (7Sd), according to the method of Leblond and Clermont (1952). Stage VII spermatogenesis was analyzed because this stage is highly susceptible to testosterone deficiency and also reflects the final stages of spermatid maturation and thus provides evidence of spermatogenesis as a whole (Clermont and Harvey 1967). Diameters of seminiferous tubules of testes were measured by ocular micrometer under light microscope.

2.6. Sperm analysis

The sperm count was determined by counting in a hemocytometer following the method of Majumder and Biswas (1979). Sperm samples were collected from the cauda epididymis. For the study of sperm morphology, a drop of sperm suspension was placed on a slide for observation. Eosin-Nigrosin (0.1: 1 g in 100 ml 5% sucrose solution for 30 s) stained air-dried slides were used to analyze sperm morphology according to the criteria described by Wyrobek and Bruce (1975) with some modifications, to report the percentage of abnormal forms found.

2.7. ELISA of serum testosterone

Serum testosterone was assayed using ELISA kit obtained from Equipar Diagnostici, SRL, Italy (code no. 74010). The absorbance was read against blanking well at 450 nm within 30 min in ELISA Reader (Merck). The sensitivity of the testosterone assay was 5 pg/ml and inter and intra-run precision had a coefficient of variation of 3.9 and 6.2%, respectively.

2.8. RIA of follicle stimulating hormone (FSH) and luteinizing hormone (LH)

Serum levels of FSH and LH were assayed by RIA (Moudgal and Madhawa 1974) using reagents supplied by Rat Pituitary Distribution and NIDDK (Bethesda, MD, USA). Carrier free ^{125}I for hormone iodination was obtained from Bhabha Atomic Research Center (BARC), Mumbai, India. Pure rat FSH (NIDDK-r FSH-I-11) and LH (NIDDK-r LH-I-11) were iodinated using chloramines-T (Sigma Chemical Company, St. Louis, M.O., USA) as the oxidizing agent following the procedure of Greenwood et al., (1963). NIDDK anti-rat FSH-S-11 and anti-rat LH-S-11 in rabbit were used as antiserum at a final dilution of 1:35,000 and 1:70,000, respectively. The second antibody was goat anti-rabbit γ -globulin purchased from Indo-Medicine (Friendswood, TX, USA). The intra-assay variation for FSH and LH was 5.0 and 4.5%, respectively. All samples were run in one assay to avoid inter-assay variation.

2.9. Spectrofluorimetric determination of serum corticosterone

Serum corticosterone was determined by spectrofluorimetric method (Glick et al. 1964; Silber 1966). The fluorescence was measured at 463 nm (excitation), 518 nm (emission) by setting the instrument at a spectrofluorimetric reading 80 with a standard corticosterone solution having 1.6 $\mu\text{g}/\text{ml}$ concentrations. A minimum of 1.6 μg corticosterone/100 ml serum can be measured by this method.

2.10. Assay of steroidogenic enzymes activity

2.10.1. Testicular and adrenal $\Delta^53\beta$ -hydroxysteroid dehydrogenase enzyme activity ($\Delta^53\beta$ -HSD)

To study testicular $\Delta^53\beta$ -HSD enzyme activity, tissues were homogenized in 20% spectroscopic-grade glycerol

containing 5 mM of potassium phosphate and 1 mM of EDTA and centrifuged at 10,000 g for 30 min at 4°C. The supernatant was used as enzyme extract for the assay of 3β -HSD. The reaction mixture contained 1 ml of 100 μM sodium pyrophosphate buffer (pH 8.9) and 20 μl of 30 μM 17β -Estradiol, 1 ml of 0.5 μM NAD. The absorbance at 340 nm was measured immediately after the addition of enzyme extract at 15 s intervals for 3 min in a spectrophotometer against blank (Talalay 1962). One unit of enzyme activity is equivalent to a change in absorbance of 0.001/min at 340 nm.

2.10.2. Testicular 17β -hydroxysteroid dehydrogenase enzyme activity (17β -HSD)

For measurements of testicular 17β -HSD enzyme activity (Jarabak et al. 1962), the same supernatant fluid (200 μl) (prepared as described above) was added with 1.5 ml of 440 μM sodium pyrophosphate buffer (pH 8.9), 0.5 ml of bovine serum albumin (25 mg crystalline BSA) and 40 μl of 0.3 μM 17β -estradiol, 1 ml of 1.35 μM NAD. The absorbance at 340 nm was measured at 15 s intervals for 3 min in a spectrophotometer against blank. One unit of enzyme activity is equivalent to a change in absorbance of 0.001/min at 340 nm.

2.11. Determination of lipid peroxidation (LPO) level

Lipid peroxidation was measured by the method of Buege and Aust (1978). The level of LPO in the testicular homogenate was measured based on the formation of thiobarbituric acid-reactive substances (TBARS). Malondialdehyde (MDA) forms adducts with thiobarbituric acid, which is measured spectrophotometrically at 532 nm against a blank. MDA, a product of LPO, was used as a standard. An extinction coefficient of $156,000 \text{ M}^{-1} \text{ cm}^{-1}$ was applied for calculation.

2.12. Assay of antioxidant enzymes activity

2.12.1. Superoxide dismutase (SOD)

The method described by Paoletti and Mocali (1990) was used for the assay of SOD activity. This method consists of purely chemical reaction sequence, which generates superoxide from molecular oxygen in the presence of EDTA, manganese (II) chloride, and mercaptoethanol. NAD(P)H oxidation is linked to the availability of superoxide anions in the medium. The decrease in absorbance at 340 nm was monitored for 20 min at 5-min interval in a spectrophotometer. In this assay system, 1 unit of SOD activity is defined as the amount of enzyme required to inhibit the rate of NADPH oxidation of the control by 50%.

2.12.2. Catalase (CAT)

The activity of catalase was assayed by the method of Aebi (1974). In the ultraviolet range H_2O_2 shows a continual increase in absorption with decreasing wavelength. The decomposition of H_2O_2 can be correctly followed by monitoring the decrease in absorbance at 240 nm for 60 s in spectrophotometer. The change in absorbance is the measure of

the catalase activity and was expressed as nmols/mg protein/s. The extinction coefficient of H_2O_2 at 240 nm is $40 \text{ M}^{-1} \text{ cm}^{-1}$.

2.12.3. Glutathione peroxidase (GPx)

The activity of glutathione peroxidase was determined by the method of Rotruck et al. (1973). GPx converts reduced glutathione (GSH) into oxidized form using hydrogen peroxide during its reaction. The amount of GSH utilized is estimated by measuring it in the assay mixture before and after the enzyme activity. GSH reacts with DTNB to give yellow color, which was then measured at 412 nm. The enzyme activity was expressed as units/mg protein.

2.13. Analysis of tissue vanadium concentrations

One testis per animals was processed as described (Nurnberg 1983). Samples were analyzed using a graphite furnace Atomic Absorption Spectrometer (Perkin-Elmer A Analyst 400). Blanks were analyzed to identify metal contamination from this source. Accuracy was assured by three random determinations of five standard solutions. The wavelength was 213.86 nm; the detection limit was 0.37 ppm and the slit 2.7/0.8 nm. Results were expressed as $\mu\text{g/g}$ of wet tissues.

2.14. Determination of protein

Proteins were estimated by the method of Lowry et al. (1951) using bovine serum albumin (BSA) as the standard protein.

2.15. Statistical analysis

Results were expressed as mean \pm standard deviation. One-way analysis of variance (ANOVA) test was first carried out to test for any differences between the mean values of all groups. If differences between groups were established, the values of the treated groups were compared with those of the control group by a post hoc *t*-test. A value of $p < 0.05$ was interpreted as statistically significant (Fisher and Yates 1974).

3. Results

The administration of vanadium resulted in a significant reduction of total body weight and all reproductive organ weights (testis, 34.4%; epididymis, 28.3%; prostate, 30.8%; seminal vesicle, 31.6%) over the control values (Table 1).

Epididymal sperm number in vanadium treated rats was significantly decreased (46.2%) along with the increase in sperm morphological abnormalities. Testicular sections from rats treated with repetitive intraperitoneal injection of vanadate showed a significant reduction in diameters of seminiferous tubules and testicular lesions ranging from absence of elongated spermatids to reduction of postspermatogonial germ cells (Figure 1). However, all these negative effects of vanadium were significantly alleviated by pretreatment with indomethacin.

Sodium metavanadate treatment significantly reduced the number of spermatogonia A (29.4%), preleptotene spermatocytes (19.5%), mid pachytene spermatocytes (31.1%) and step 7 spermatid (41.9%) over the control values. The ratio of mPSc: 7Sd was 1:2.82 after vanadium treatment; the ratio of the control group was 1:3.34. The percentage spermatid degeneration (29.5%) was highly significant after vanadium treatment when compared with those of the control (16.5%). However, pretreatment with COX inhibitor, indomethacin to vanadium-treated rats showed normal cellular counts and spermatid degeneration (20.25%) was significantly reduced (Table 2).

The decrease in the activities of testicular $\Delta^5\beta$ -HSD (34.8%) and 17β -HSD (52.2%) was observed in vanadium treated rats (Figure 2). Vanadium treatment caused a statistically significant inhibition in the activity of SOD (50.9%), CAT (52.6%) and GPx (48.9%) and sharp increase in lipid peroxidation level (2.1-folds) over the respective control values. However, these negative effects of vanadium on the above parameters were significantly alleviated by pretreatment with indomethacin. (Figure 3).

Vanadium treatment lowered serum levels of LH (49.7%), FSH (46.4%) and testosterone (56.1%). However, pretreatment with indomethacin in vanadium exposed animals retrieved the serum hormones at near normal level. The testicular concentration of vanadium increased in rats that were treated with sodium metavanadate but pretreatment with indomethacin significantly reduced the tissue vanadium concentration (Figure 4).

The weight of the adrenals of vanadium-treated rats was significantly greater (31.7%) than the corresponding value for the control rats. There was a significant increase in the adrenal $\Delta^5\beta$ -HSD activity (24.4%) and serum corticosterone level (41.6%) over control value. Pretreatment with indomethacin counteracted the effect of vanadium on adrenal gland by normalizing all the above parameters. Moreover, no negative influence of indomethacin alone on sperm and endocrine parameters was observed in the present study (Table 3).

Table 1. Alterations in the body and organ weights of rats subjected to different treatment.

Group	Body weight (g)		Testes ^c (pair)	Seminal vesicle ^d (without fluid)	Ventral prostate ^d	Coagulating gland ^d	Cauda epididymis ^d
	Initial	Final					
Control	200.0 \pm 6.93	257.75 \pm 7.19	1.22 \pm 0.04	156.72 \pm 6.15	214.13 \pm 17.95	48.97 \pm 3.41	174.65 \pm 9.76
V	203.0 \pm 7.86	235.25 \pm 4.78	0.80 \pm 0.15 ^a	107.23 \pm 6.47 ^a	148.25 \pm 10.45 ^a	33.16 \pm 4.69 ^a	125.19 \pm 6.37 ^a
Indo	210.0 \pm 4.66	267.0 \pm 7.33	1.21 \pm 0.04 ^b	153.73 \pm 9.07 ^b	208.03 \pm 13.39 ^b	49.72 \pm 5.81 ^b	172.0 \pm 10.89 ^b
V + Indo	204.5 \pm 5.09	248.5 \pm 7.98	1.14 \pm 0.09 ^b	148.47 \pm 10.17 ^b	192.44 \pm 10.17 ^{ab}	47.74 \pm 4.58 ^b	163.82 \pm 7.73 ^{ab}

Data is presented as the mean \pm SD, $n = 8$. Values bearing superscripts are significantly different by ANOVA at $p < 0.05$. ^aControl vs. other groups; ^bV vs. Indo or V + Indo. ^cg/100 g body weight, ^dmg /100 g body weight. Indo: indomethacin.

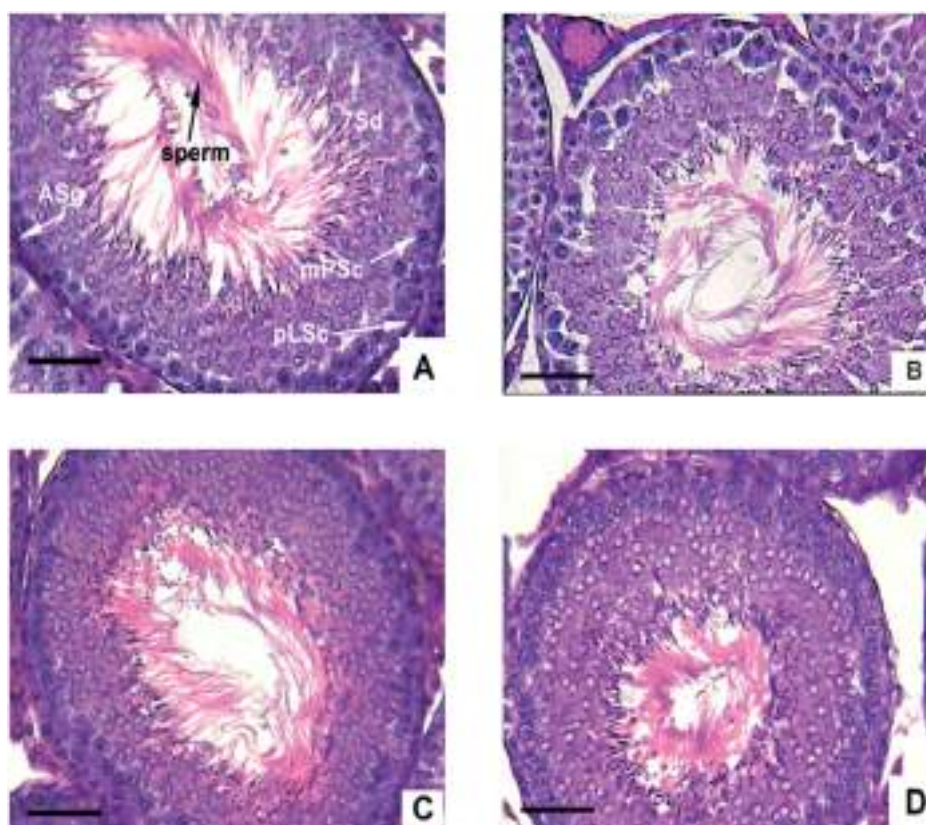


Figure 1. Photomicrographs of paraffin-embedded H&E-stained rat testicular sections showing the effect of indomethacin pretreatment in vanadium exposed animals. (A) Rat testicular section (400 \times) from control animals. (B) Testis section (400 \times) from vanadate-treated animals (0.4 mg/kg, i.p. for 26 days). (C) Testis section (400 \times) from rats treated with indomethacin (1 mg/kg, oral for 26 days). (D) Testis section (400 \times) from rats treated with indomethacin at a dose of 1 mg/kg, oral for 26 days and sodium metavanadate (0.4 mg/kg, i.p. for 26 days). ASg: spermatogonia A; pLSc: preleptotene spermatocytes; mPSc: mid pachytene spermatocytes; 7Sd: step 7 spermatid. Scale bars are equal to 50 μ m.

Table 2. Effect of indomethacin (Indo) pretreatment on testicular seminiferous tubular diameter, sperm count, sperm morphological abnormalities, and the relative number of germ cells per tubular cross section at stage VII of the seminiferous epithelial cycle in vanadium-treated rats.

Parameters	Control	V	Indo	V + Indo
Diameter of seminiferous tubule (μ m)	264.13 \pm 13.54	207.0 \pm 10.23 ^a	264.38 \pm 9.49 ^b	239.0 \pm 6.99 ^{ab}
Sperm count ^c	131.37 \pm 6.16	70.64 \pm 3.79 ^a	127.18 \pm 2.76 ^b	121.68 \pm 6.20 ^{ab}
% Abnormal sperm	3.96 \pm 0.78	11.77 \pm 1.89 ^a	3.93 \pm 0.59 ^b	6.36 \pm 0.86 ^{ab}
ASg	0.68 \pm 0.04	0.48 \pm 0.02 ^a	0.67 \pm 0.04 ^b	0.66 \pm 0.02 ^b
pLSc	18.5 \pm 1.2	14.9 \pm 0.7 ^a	18.1 \pm 1.30 ^b	17.8 \pm 1.31 ^b
mPSc	19.3 \pm 1.3	13.3 \pm 0.4 ^a	19.1 \pm 1.9 ^b	18.2 \pm 1.8 ^b
7Sd	64.5 \pm 1.8	37.5 \pm 1.4 ^a	62.9 \pm 1.21 ^b	58.22 \pm 1.7 ^{ab}
mPSc: 7Sd	1:3.34	1:2.82	1:3.29	1:3.19
7Sd degeneration (%)	16.5	29.5	17.75	20.25
Effective 7Sd degeneration	–	+13.0	+1.25	+3.75

Data is presented as the mean \pm SD, $n = 8$. Values bearing superscripts are significantly different by ANOVA at $p < 0.05$. ^aControl vs. other groups; ^bV vs. Indo or V + Indo. ^cMillion cells/ cauda epididymis. ASg: spermatogonia A; pLSc: preleptotene spermatocytes; mPSc: mid pachytene spermatocytes; 7Sd: step 7 spermatid.

4. Discussion

Vanadium is a persistent and bioaccumulative environmental toxicant. Previous studies had highlighted the toxicity of vanadium including reproductive toxicity (Ghosh and Banik 2016). The specific mechanisms by which the metal exerts its effects have also been mostly delineated (Ghosh et al. 2020). Vanadium derivatives act as generator of free radicals, that impair testicular functions, spermatogenesis and sperm maturation in rats. Moreover, a strong correlation exists between vanadate-induced reproductive toxicity and increase in lipid peroxidation (Chandra et al. 2007a, 2007b, 2007c; 2010).

Several lines of evidences also indicate that stimulation of prostaglandin release is one of the chief mechanisms of vanadate action (Plass et al. 1992). Evidences from the present studies also confirmed that vanadate induces testicular toxicity in rats by stimulating prostaglandin release.

The broad functions of NSAIDs are mediated through the prostaglandin and thromboxane pathways, which act on numerous biological and physiological processes, including reproduction. We wanted to explore the potential of one of such NSAIDs, indomethacin, in alleviation of vanadium induced toxicity to reproductive system. The synthesis of prostaglandin begins with the release of the precursor lipid,

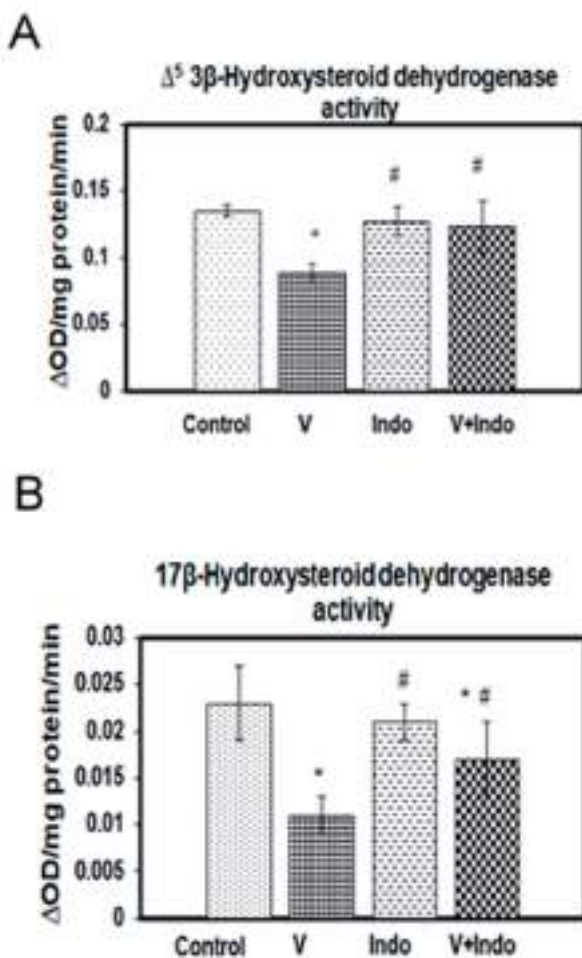


Figure 2. Effect of indomethacin (Indo) pretreatment on testicular $\Delta^5\beta$ -HSD (A), 17β -HSD (B) activity. Each bar denotes mean \pm standard deviation of 8 animals per group. Mean values are significantly different by ANOVA at $p < 0.05$, ^aControl vs. other groups; [#]V vs. Indo or V + Indo.

arachidonic acid, from the plasma membrane phospholipids by either phospholipase A2 or phospholipase C. The enzyme cyclooxygenase (COX) converts it to prostaglandin G2 and subsequently it is peroxidized to prostaglandin H2 by the same enzyme. Studies in recent years have demonstrated important roles for the COX enzyme in steroidogenesis and steroid hormone-regulated physiological functions in both human and animals (Wang et al. 2003). The present studies demonstrated that inhibition of COX activity by indomethacin dramatically increased steroid hormone production in rat testis exposed to vanadate. The increase in steroid output may be attributable to an increase in the activity of the steroidogenic enzymes $\Delta^5\beta$ -HSD and 17β -HSD. The data suggested that enhanced testosterone production in COX inhibitor-supplemented rats showed a significant improvement in the growth of testes and accessory sex organs as these organs are highly androgen-dependent. However indomethacin alone could induce neither increase in steroidogenic enzyme activities nor a significant increase in testosterone production. The observations cumulatively suggested that the inhibitor itself did not have a direct stimulatory effect on steroid production, but rather, lowered the threshold of cAMP-stimulated steroidogenesis (Wang et al. 2003). Some studies have indicated the toxic effects associated with the use of NSAIDs like indomethacin, especially on male reproductive viability (Uzun et al. 2015; Bagoji et al. 2017). We carried out a dose-response curve for choosing the working concentration of indomethacin and found that concentrations in excess of 3 mg/kg of body weight decreased sperm count, sperm motility, serum gonadotropin and testosterone concentrations. Therefore, a single sub-toxic concentration of 1 mg/kg of body weight was selected for the studies.

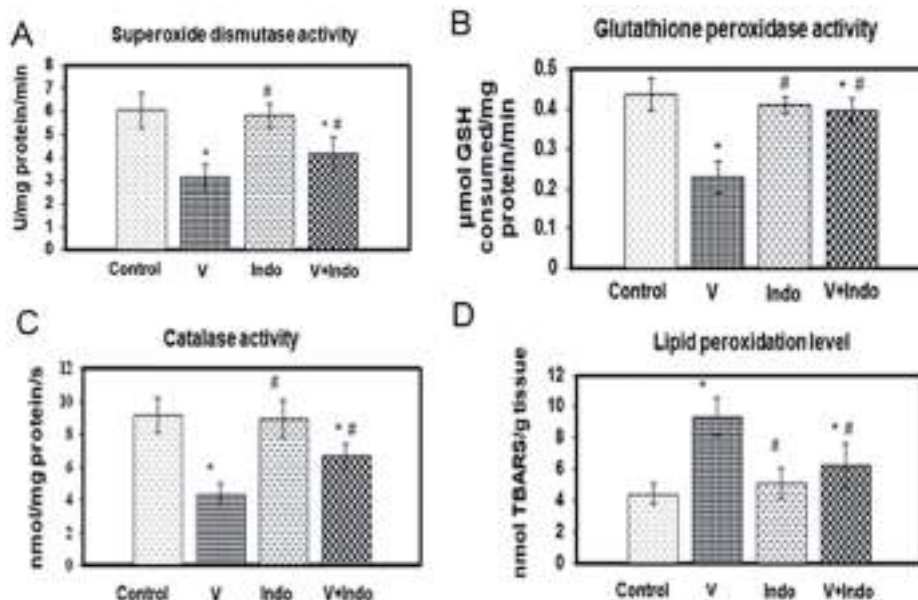


Figure 3. Effect of indomethacin (Indo) pretreatment on testicular antioxidant (SOD, CAT, GPx) enzymes activity and testicular lipid peroxidation level in vanadium-treated rats. (A) SOD (B) CAT (C) GPx (D) lipid peroxidation level each bar denotes mean \pm standard deviation of 8 animals per group. Mean values are significantly different by ANOVA at $p < 0.05$, ^aControl vs. other groups; [#]V vs. Indo or V + Indo.

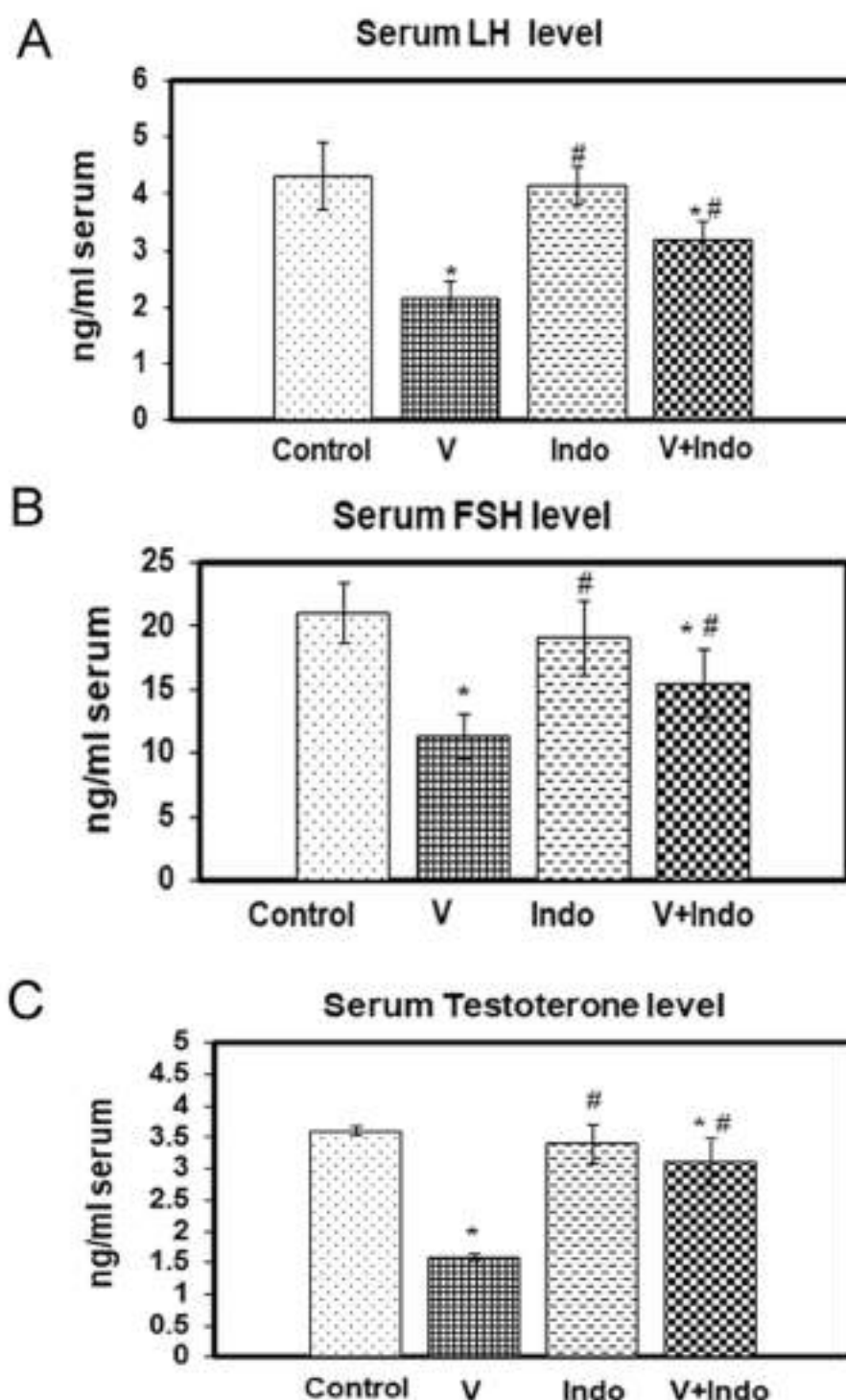


Figure 4. Effect of indomethacin (Indo) pretreatment on serum hormone (A) LH, (B) FSH, (C) Testosterone levels and testicular vanadium incorporation in vanadium-treated rats. Each bar denotes mean \pm standard deviation of 8 animals per group. Mean values are significantly different by ANOVA at $p < 0.05$, ^aControl vs. other groups; ^bV vs. Indo or V + Indo.

Table 3. Effect of indomethacin (indo) pretreatment on adrenal gland weight, adrenal steroidogenic enzyme activity and serum level of corticosterone in vanadium-treated rats.

Parameters	Control	V	Indo	V + Indo
Adrenal weight ^c	12.38 \pm 0.79	16.31 \pm 0.83 ^a	11.86 \pm 1.31 ^b	12.47 \pm 1.46 ^b
Adrenal $\Delta^5\beta$ -HSD ^d	0.164 \pm 0.01	0.204 \pm 0.01 ^a	0.169 \pm 0.006 ^b	0.174 \pm 0.008 ^{ab}
Serum corticosterone ^e	30.33 \pm 1.77	42.96 \pm 1.49 ^a	31.73 \pm 3.06 ^b	35.23 \pm 0.77 ^{ab}

Data is presented as the mean \pm SD, $n = 8$. Values bearing superscripts are significantly different by ANOVA at $p < 0.05$.

^aControl vs. other groups; ^bV vs. Indo, or V + Indo; ^cmg/100 g body wt; ^d Δ OD/min/mg protein; ^e μ g/dl serum.

Prostaglandins have an inhibitory effect on spermatogenesis *in vivo*. The prostaglandin synthetase system is also located primarily in the interstitial cells and the seminiferous tubules (Ellis et al. 1975). These may suggest a negative regulatory effect of prostaglandins on testicular and spermatozoal function in vanadium treated rats. Spermatogenic failure after vanadium treatment was characterized by the suppression of spermatocytes populations and abolition of round spermatids beyond stage VII, with the numbers of earlier germ cells being severely reduced which might be due to depressed level of serum FSH. Indomethacin pretreatment produced a marked increase in spermatogenesis in vanadium treated rats. The number of post meiotic germ cells increased significantly over the controls with serum FSH levels returning to near normal level. The present findings establish that vanadium can cause a strong induction of testicular prostaglandin production, which might help to explain the well-known antispermato-genic effect of this metal.

Vanadium induced a depression of the hypothalamus-pituitary-testis (HPT) system, mediated by the activated hypothalamus-pituitary-adrenocortical (HPA) system, resulting in a fall in plasma LH and testosterone levels. Decreased plasma concentrations of testosterone, independent of gonadotropins, can be induced by corticosteroids. Vanadium decreased feedback sensitivity which may allow hypersecretion throughout the HPA system as evidenced by increased adrenal gland weight and elevated secretion of serum concentration of corticosterone. It is also evident that PGE₂ caused an increase in corticosterone synthesis from adrenal gland (Delarue et al. 1990). Results suggest that effects of vanadate on adrenocortical activities may be mediated at least in part by prostaglandins, as inhibition of prostaglandin synthesis by indomethacin abolished these responses. Evidence is available that this nonsteroidal anti-inflammatory drug influences the hypothalamo-pituitary-axis via changes in prostaglandin metabolism (Barkay et al. 1984) and markedly reduced the effects of vanadate on male reproductive systems.

Cyclooxygenase, which catalyzes the initial oxidation step of arachidonate to prostaglandins and is induced under inflammatory conditions, is also well known ROS-generating enzyme (Baud and Ardaillou 1986). In the present study, vanadium treatment increased testicular lipid peroxidation and decreased the specific activities of antioxidant enzymes such as SOD, CAT, and GPx in vanadium exposed rats, indicating an imbalance in pro-oxidant and antioxidant system and leading to oxidative stress which could be attributed to an increase in PG secretion. This was effectively reversed by pretreatment with COX-inhibitor, indomethacin. Moreover, the detailed and comprehensive analysis of all factors used for characterization of male reproductive functions showed no evidence for a negative influence of indomethacin alone on sperm and endocrine parameters.

5. Conclusion

The studies cumulatively indicated that vanadate induces testicular toxicity and adrenocortical hyperactivity in rats by

stimulating prostaglandin release. It also showed that indomethacin, within the permissible limit, can be effectively used as a successful therapeutic agent to counteract reproductive toxicities induced by environmental pollutants like vanadium. However, attempts to exploit the therapeutic potential of indomethacin can only be initiated after a detailed characterization of the basis of indomethacin induced reversal of prostaglandin release, including real time analysis of COX transcript levels at various time points before and after application of indomethacin in vanadium treated subjects.

Acknowledgement

The authors thank Dr. Syed N. Kabir, Scientist, Cell Biology & Physiology Division, Indian Institute of Chemical Biology (IICB), Kolkata, India for his help in conducting RIA of FSH and LH. Sincere thanks is also due to Principal, Maulana Azad College for providing all sorts of infrastructural support.

Disclosure statement

No potential conflict of interest was reported by the author(s).

References

- Abbatiello ER, Kaminsky M, Weisbroth S. 1975. The effect of prostaglandins and prostaglandin inhibitors on spermatogenesis. *Int J Fertil*. 20(3):177–182.
- Aebi H. 1974. Catalase. In: Bergmeyer HU, editors. *Methods in enzymatic analysis*. Vol. 2. New York: Academic Press; p. 673–678.
- Bagoji IB, Hadimani GA, Yendigeri SM, Das KK. 2017. Sub-chronic indomethacin treatment and its effect on the male reproductive system of albino rats: possible protective role of black tea extract. *J Basic Clin Physiol Pharmacol*. 28(3):201–207.
- Barkay J, Harpaz-Kerpel S, Ben-Ezra S, Gordon S, Zuckerman H. 1984. The prostaglandin inhibitor effect of anti-inflammatory drugs in the therapy of male infertility. *Fertil Steril*. 42(3):406–411.
- Baud L, Ardaillou R. 1986. Reactive oxygen species: production and role in the kidney. *Am J Physiol*. 251:765–776.
- Buege JA, Aust SD. 1978. Microsomal lipid peroxidation. *Methods Enzymol*. 52:302–310.
- Chandra AK, Ghosh R, Chatterjee A, Sarkar M. 2007a. Amelioration of vanadium-induced testicular toxicity and adrenocortical hyperactivity by vitamin E acetate in rats. *Mol Cell Biochem*. 306(1–2):189–200.
- Chandra AK, Ghosh R, Chatterjee A, Sarkar M. 2007b. Vanadium-induced testicular toxicity and its prevention by oral supplementation of zinc sulphate. *Toxicol Mech Methods*. 17(4):175–187.
- Chandra AK, Ghosh R, Chatterjee A, Sarkar M. 2010. Protection against vanadium-induced testicular toxicity by testosterone propionate in rats. *Toxicol Mech Methods*. 20(6):306–315.
- Chandra AK, Ghosh R, Chatterjee A, Sarkar M. 2007c. Effects of vanadate on male rat reproductive tract histology, oxidative stress markers and androgenic enzyme activities. *J Inorg Biochem*. 101(6):944–956.
- Clermont Y, Harvey SC. 1967. Effect of hormones on spermatogenesis in the rat. *Ciba Found Colloq Endocrinol*. 16:173–196.
- Conte D, Nordio M, Romanelli F, Manganelli F, Giovenco P, Dondero F, Isidori A. 1985. Role of seminal prostaglandins in male fertility. II. Effects of prostaglandin synthesis inhibition on spermatogenesis in man. *J Endocrinol Invest*. 8(4):289–291.
- Delarue C, Delton I, Fiorini F, Homo-Delarche F, Fasolo A, Braquet P, Vaudry H. 1990. Endothelin stimulates steroid secretion by frog adrenal gland *in vitro*: evidence for the involvement of prostaglandins and extracellular calcium in the mechanism of action of endothelin. *Endocrinology*. 127(4):2001–2008.

- Ellis LC, Sorenson DK, Buhrley LE. 1975. Mechanisms and interactions in testicular steroidogenesis and prostaglandin synthesis. *J Steroid Biochem.* 6(6):1081–1085.
- Fisher RA, Yates R. 1974. Statistical tables for biological, agricultural and medical research. London: Longman Group.
- Ghosh R, Banik SP. 2016. Dual effects of vanadium: toxicity analysis in developing therapeutic lead-ups. In: Bagchi D, Swaroop A, Stohs SJ, editors. *Food toxicology*. p. 337–354. Boca Raton (FL): CRC Press.
- Ghosh R, Das A, Bandyopadhyay A, Majumder R, Banik SP. 2020. Vanadium toxicity revisited. striking the right balance between potential new generation therapeutics and adverse side effects. In: Bagchi D, Bagchi M, editors. *Metal toxicology handbook*. p. 323–344. Boca Raton (FL): CRC Press.
- Glick D, Redlich DV, Levine S. 1964. Fluorometric determination of corticosterone and cortisol in 0.02–0.05 milliliters of plasma or submilligram samples of adrenal tissue. *Endocrinology*. 74:653–655.
- Jarabak J, Adams JA, Williams-Ashman HG, Talalay P. 1962. Purification of a 17β hydroxysteroid dehydrogenase of human placenta and studies on its transhydrogenase function. *J Biol Chem.* 237:345–357.
- Kirch W, Stroemer K, Hoogkamer JF, Kleinbloesem CH. 1989. The influence of prostaglandin inhibition by indomethacin on blood pressure and renal function in hypertensive patients treated with cilazapril. *Br J Clin Pharmacol.* 27(2):297S–301S.
- Leblond PC, Clermont Y. 1952. Definition of the stages of the cycle of the seminiferous epithelium in the rat. *Ann N Y Acad Sci.* 55(4): 548–573.
- Lowry OH, Rosebrough NJ, Farr AL, Randall RJ. 1951. Protein measurement with phenol reagent. *J Biol Chem.* 193(1):265–275.
- Lucas S. 2016. The pharmacology of indomethacin. *Headache*. 56(2): 436–446.
- Majumder GC, Biswas R. 1979. Evidence for the occurrence of an ecto-(adenosine triphosphatase) in rat epididymal spermatozoa. *Biochem J.* 183(3):737–743.
- Moudgal NR, Madhawa RHG. 1974. Pituitary gonadotropin. In: Jaffe BM, Behrman HR, editors. *Methods of hormone radioimmunoassay*. New York: Academic Press; p. 57–85.
- Nurnberg HW. 1983. Processing biological samples for metal analysis. In: Brown SS, Savory J, editors. *International union of pure and applied chemistry*. New York: Academic Press; p. 31–44.
- Paoletti F, Mocali A. 1990. Determination of superoxide dismutase activity by purely chemical system based on NAD(P)H oxidation. *Methods Enzymol.* 186:209–220.
- Plass H, Roden M, Wiener H, Turnheim K. 1992. Vanadium-induced Cl-secretion in rabbit descending colon is mediated by prostaglandins. *Biochim Biophys Acta.* 1107(1):139–142.
- Rotruck JK, Pope AL, Ganther HE, Swanson AB, Hafeman DG, Hoekstra WG. 1973. Selenium: biochemical role as a component of glutathione peroxidase. *Science.* 179(4073):588–590.
- Silber RH. 1966. Fluorometric analysis of corticoids. In: Glick D, editors. *Methods of biochemical analysis*. New York: Interscience Publishers; p. 63–78.
- Talalay P. 1962. Hydroxy Steroid Dehydrogenase. In: Colowick SP, editors. *Methods in Enzymology*. New York: Academic Press; p. 513–532.
- Uzun B, Atli O, Perk B, Burukoglu D, Ilgin S. 2015. Evaluation of the reproductive toxicity of naproxen sodium and meloxicam in male rats. *Hum Exp Toxicol.* 34(4):415–429.
- Vane JR, Botting RM. 1998. Anti-inflammatory drugs and their mechanism of action. *Inflamm Res.* 47(Suppl 2):S78–S87.
- Versteeg HH, van Bergen En Henegouwen PM, van Deventer SJ, Peppelenbosch MP. 1999. Cyclooxygenase-dependent signalling: molecular events and consequences. *FEBS Lett.* 445(1):1–5.
- Wang X, Dyson MT, Jo Y, Stocco DM. 2003. Inhibition of cyclooxygenase-2 activity enhances steroidogenesis and steroidogenic acute regulatory gene expression in MA-10 mouse Leydig cells. *Endocrinology.* 144(8):3368–3375.
- Wilk A, Dagmara Szypulska K, Wiszniewska B. 2017. The toxicity of vanadium on gastrointestinal, urinary and reproductive system, and its influence on fertility and fetuses malformations. *Postepy Hig Med Dosw.* 71(0):850–859.
- Wyrobek AJ, Bruce WR. 1975. Chemical induction of sperm abnormalities in mice. *Proc Natl Acad Sci USA.* 72(11):4425–4429.
- Zwolak I. 2020. Protective effects of dietary antioxidants against vanadium-induced toxicity: a review. *Oxid Med Cell Longev.* 2020: 1490316.



Effective body recomposition vs. misconceptions of the traditional weight loss strategies: TRCAP21 - a novel technological breakthrough in body recomposition

Debasis Bagchi^{1,2*}, Bernard W. Downs², Samudra P. Banik³, Manashi Bagchi⁴, Steve Kushner⁵, Sanjoy Chakraborty⁶, Bruce S. Morrison⁷, Stephen Hesson⁸

¹College of Pharmacy and Health Sciences, Texas Southern University, Houston, TX, USA; ²Victory Nutrition International, Inc., Department of Research and Development, Bonita Springs, FL, USA; ³Department of Microbiology, Maulana Azad College, Kolkata, India; ⁴Dr. Herbs LLC, Concord, CA, USA; ⁵ALM Research and Development, Oldsmar, FL, USA; ⁶Department of Biological Sciences, New York City College of Technology/CUNY, Brooklyn, NY, USA; ⁷Morrison Family and Sports Medicine, Huntingdon Valley, PA, USA; ⁸PFHIX Inc., Neenah, WI, USA.

***Corresponding Author:** Debasis Bagchi, ¹College of Pharmacy and Health Sciences, Texas Southern University, Houston, TX, USA; ²Victory Nutrition International, Inc., Department of Research and Development, Bonita Springs, FL, USA

Submission Date: February 18th, 2022; **Acceptance Date:** March 15th, 2022; **Publication Date:** April 1st, 2022

Please cite this article as: Bagchi D., Downs B.W., Banik S.P., Bagchi M., Kushner S., Chakraborty S., Morrison B.S., Hesson S. Effective Body Recomposition vs. Misconceptions of the Traditional Weight Loss Strategies: TRCAP21 - A Novel Technological Breakthrough in Body Recomposition. *Functional Foods in Health and Disease* 2022; 12(4): 134-150. DOI: <https://www.doi.org/10.31989/ffhd.v12i3.905>

ABSTRACT

Background: The prevalence of obesity has increased an astounding 30.5% to 42.2% over the last two decades despite numerous weight loss products and programs, thus qualifying it as an epidemic. Fat is the lightest of macromolecules, the highest energy reserve of the body, and the last reservoir of survival insurance to be expended. Water, muscle, and electrolytes are diminished prior to the expenditure of fat resources, the primary cause of rapid weight loss. Contrary to popular belief that only “weight gain” is the sole and correct parameter for evaluating healthy body recomposition, there are no less than 10 additional factors that contribute to a reduction in metabolic rate and an increase in fat storage. These are mostly ignored from considerations regarding the etiology of obesity. Our laboratory developed a novel formulation of D-ribose nicotinamide, alpha glycerol phosphorylcholine and four other evidence-based botanical constituents encapsulated in a Prodosomed stimulant- and sugar-free TRCAP21 (TrimRox™) formulation that effectively addresses those contributing factors. To investigate the feasibility of doing a 90-day randomized, double-blind placebo-controlled investigation, we conducted a 21-day concept validation pilot study on TRCAP21 in 9 subjects to assess changes in various body parts, including chest, upper arms, waist/belly, hips, and thighs, as well as body weight.

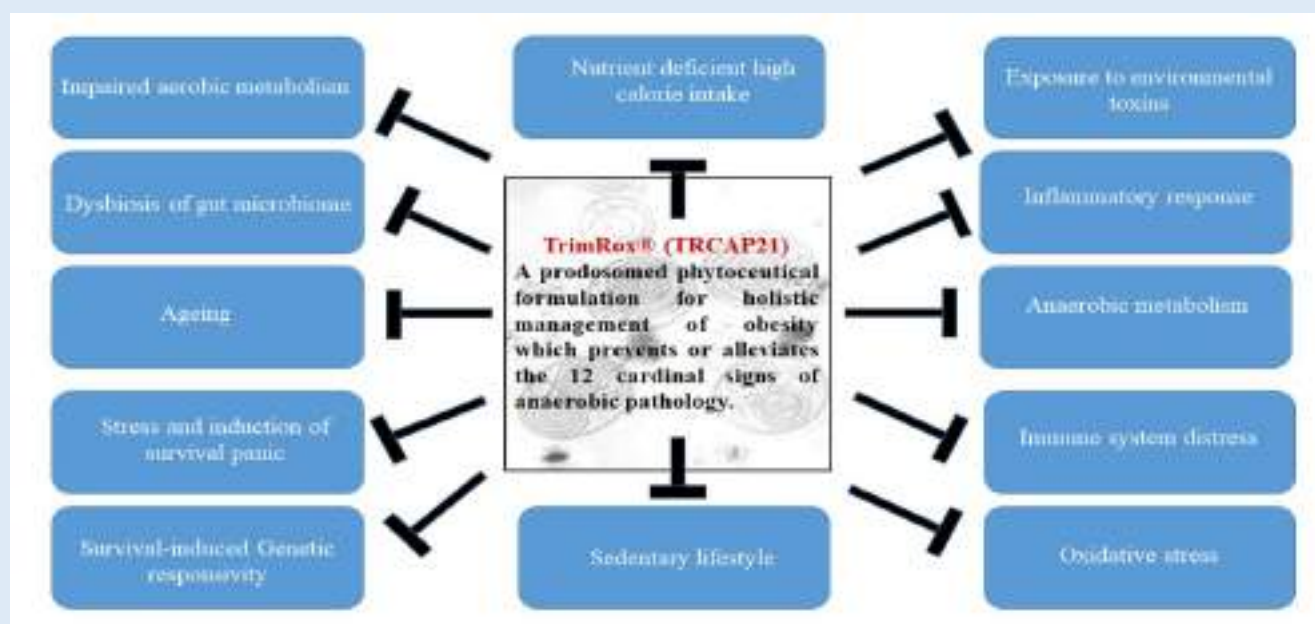
Objective: This physician-supervised 21-day concept validation pilot study on TRCAP21 was conducted on 9 subjects to determine changes in anthropometric parameters including chest, upper arms, waist/belly, hips, and thighs, as well as body weight, and determine the effect of TRCAP21 on energy, mood, satiety, and sugar cravings.

Materials and Methods: The study was conducted on nine male and female subjects (age: 47-70 years) to assess the efficacy of TrimRox™ over a period of 21 consecutive days. Body weights and anthropometric measurements were conducted at the initiation and termination of the study. The effect of TRCAP21 was evaluated on energy level, mood elevation, satiety level, sugar cravings, overall health, and adverse events in the subjects.

Results: The results demonstrated that all subjects experienced a reduction in size of one or more these body parts. In addition, it also led to significant improvements in mood elevation, satiety, reduced sugar cravings, elevated energy levels and overall mental and physical health. Intake of 1 packet twice a day (BID) before meals resulted in a significantly greater reduction of body measurements than consuming it once a day (OID). Surprisingly, body weight was reduced in all nine subjects from 2 lbs. to 11 lbs. The randomized double-blind placebo-controlled study is underway to confirm and further substantiate these findings.

Conclusion: The TRCAP21 Prodosomed nutraceutical formulation combines the evidence-based efficacy of 6 key constituents, mostly of botanical origin, that act synergistically to restore aerobic cellular metabolism, boost energy level, mood elevation, improve satiety, reduce sugar cravings, reduce body fat in various body compartments as well as weight and improve overall health. Owing to the encapsulation of the components in unique concentric layers of liposome, their release takes place in a sustained and sequential manner. It will be worthwhile to explore its effect on the Gut-Brain Axis, especially the associated microbiome in order to obtain further insights to more accurately define the multiple mechanisms of action.

Keywords: obesity, weight management, body recomposition, Aerobic body homeostasis, prodosome®, herbal nutraceuticals



©FFC 2021. This is an Open Access article distributed under the terms of the Creative Commons Attribution 4.0 License (<http://creativecommons.org/licenses/by/4.0>)

INTRODUCTION

The prevalence of obesity in USA was 42.4% during 2017-2018, while that of severe obesity was 9.2% [1]. Interestingly, obesity prevalence was 40% in adults of age group 20-39 years, while obesity prevalence was 44.8% in age group between 40 to 59 years. However, there was

a lower trend of 42.8% in adults over 60 years. Consequences of obesity are associated with a diverse number of diseases including type 2 diabetes, coronary heart disease (CHD), stroke, hypertension; gallbladder disease; breast, endometrial and colon cancers; osteoarthritis and premature death [2]. In USA, an

estimated annual medical cost of adult obesity ranges from \$ 147 BN to nearly \$ 210 BN [3]. Taken together, the obesity epidemic is alarmingly increasing at a skyrocketing pace in the USA.

In both medical and scientific communities, the most common terminologies are either “weight loss” or “weight management”. However, a more focused and accurate indicator should specify changes in body composition, body size, or a reduction in fat mass instead of weight reduction only [4]. Specifically, “weight loss” is not at all a focused or reliable indicator as it specifically focuses on the heaviness of the body but doesn’t reflect the healthy changes in body composition/size, or metabolic homeostasis [5]. Muscle mass, bone and body fluids are comparatively much heavier than fat, while fat is the lightest of macromolecules, and in the body recomposition process, fat is usually metabolized last to be eliminated from the body [5]. Thus, short-term expectations of weight loss from fat loss are erroneous.

Diverse factors such as hormonal balance, genetics and genetic predispositions, gut microbiota, neurotransmitters, and lifestyle have a major impact on energy metabolism, metabolic homeostasis, and fat metabolism [6]. Existing commercial weight loss strategies have greatly failed to achieve and maintain sustainable weight loss and enhance greater healthy fat loss.

MATERIALS AND METHODS

Study Protocol: This concept validation pilot study was supervised by Dr. Bruce S. Morrison, DO. All subjects were critically reviewed and included in this investigation. All subjects duly reviewed the detailed protocol and signed consent forms, which were endorsed by Dr. Morrison.

Study Subjects: The study was conducted in a total of nine volunteers [male = 3; female = 6; age = 47-70 Y] over a period of 21 consecutive days (Table 1). Adverse event monitoring was strictly enforced. All subjects maintained a daily diary and submitted it at the completion of the investigation.

Treatment Strategy: Eight subjects took a single dose of TrimRox™ 6.75 g per day in the morning in an empty stomach over a period of 21 consecutive days, while the ninth subject took two doses of 6.75 g per day, the first dose in an empty stomach in the AM and the second dose in an empty stomach in the afternoon, a total of 13.5 g per day, over a period of 21 consecutive days.

Anthropometric Measurements: Anthropometric measurements were conducted on changes in chest (inches), upper arm/bicep right and left (inches), hips (inches), thighs right and left (inches), and waist (inches) in addition to evaluating changes in body weights.

Behavioral Parameters: Effect of TRCAP21 on energy level, mood elevation, satiety level, sugar cravings, and overall health was regularly monitored over these 21 consecutive days of supplementation.

Adverse event monitoring: Adverse event monitoring was critically supervised. Daily diaries were critically checked and verified.

RESULTS:

Table 1 demonstrates the changes on diverse anthropometric parameters including changes in chest (inches), upper arm/bicep right and left (inches), hips (inches), thighs right and left (inches), and waist (inches) in these subjects following treatment with TrimRox™ over a period of 21 consecutive days. Modest reductions in all these parameters were observed (Table 1). Surprisingly, no increases were observed. In addition, body weight reduced in all nine subjects from 2 lbs. to 11 lbs. Table 2 demonstrates the effect of TRCAP21 on energy level, mood elevation, satiety level, sugar cravings, and overall health over these 21 consecutive days of supplementation.

No adverse events were reported.

Table 1. Effect of TRCAP21 on multiple anthropometric parameters as well as body weight in male and female subjects

Gender (Age)	Dose (g)	Anthropometric Measurements																
		Chest (Inches)		Upper Arm/Bicep (Inches)				Hips (Inches)		Thighs (Inches)				Waist/Belly (Inches)		Body Weight (lbs)		
		Initial	Final	Right		Left		Initial	Final	Right		Left		Initial	Final	Initial	Final	Δ Change
				Initial	Final	Initial	Final			Initial	Final	Initial	Final					
F (55)	6.75	41.25	40.5	13.5	13.5	13	13	44.5	44.5	26.5	26	26.25	25.75	44.5	44.25	178	176	-2.0
F (62)	6.75	42	41	13	12.5	13	12.5	43.5	43	23.5	22	23.5	22	41	40	178	175	-3.0
F (47)	6.75	49	48	15	13.25	13	12.75	47.5	47	25.5	24.75	24.5	24	43	41.5	208	197	-11.0
M (54)	6.75	50.5	49.5	14	14	13.75	14	46	45.5	23	22	22.75	21.5	52.5	50	280	272	-8.0
M (54)	6.75	43	43	14.5	14	14.5	14	44	41	23	24	23	24	41	40	214	210	-4.0
F (70)	6.75	46.5	45.5	16	15	16	15.5	51	49.75	27.25	26.5	27.25	26.5	50.75	48.5	229	224	-5.0
F (65)	6.75	43.5	42	13.75	13.75	14	13.5	49	47.5	26.25	26.25	25.5	25.25	49.5	48.5	173	167	-6.0
F (54)	6.75	45	42	12.75	11.75	12	11	41	40	24	24	24.5	23.5	40.5	38	176	170.5	-5.5
M (55)*	13.5	53.5	51	16	15	15.5	14.5	52	50.5	26	24	26.5	23.5	56.5	53.5	306	300	-6.0

*An employee of VNI Inc, Bonita Springs, FL; M= Male; F = Female

Table 2. Effect of TRCAP21 on energy, mood, satiety, and sugar cravings in subjects

	Gender (Age)	Dose (g)	Energy Level	Mood Improvement	Satiety Level	Sugar Cravings	Sleep	Overall Health	Adverse Events
1	F (55 Y)	6.75	+++	+++	+++	Reduced sugar cravings	+++	Improved	None
2	F (62 Y)	6.75	++	+++	+++	Reduced sugar cravings	+++	Improved	None
3	F (47 Y)	6.75	++	NR	+++	No Effect	+++	Improved	None
4	M (54 Y)	6.75	+++	NR	+++	NR	NR	Improved	None
5	M (54 Y)	6.75	+++	+++	+++	Reduced sugar cravings	+++	Improved	None
6	F (70 Y)	6.75	++	+++	+++	Reduced sugar cravings	+++	Improved	None
7	F (65 Y)	6.75	++	NR	+++	Reduced sugar cravings	NR	Improved	None
8	F (54 Y)	6.75	+++	+++	+++	Reduced sugar cravings	+++	Improved	None
9	M (55 Y)*	13.50	+++	NR	+++	Reduced sugar cravings	NR	Improved	None

*An employee of VNI Inc, Bonita Springs, FL; M= Male; F = Female; NR = None reported

Key: + = modest improvement; ++ = better improvement; +++ = significantly better improvement

Overall, this 21-day concept validation pilot study demonstrates that TRCAP21 enhanced healthy body recomposition observed as a reduction in size of various body parts, increased energy levels, elevated mood, enhanced satiety, reduced sugar cravings, improved restful sleep, and improved overall health. Interestingly, consistent, but varying amounts of weight loss were observed, although, Crawford et al. [7] have reported earlier that a healthy and effective body recomposition strategy can result in a small net gain in weight due to an increase in exercise-induced muscle density, while resulting in a loss of size and improvements in healthy

body recomposition. Subjects in the study made no other changes to their lifestyle.

Cascade of Events: Overindulgence of healthy/unhealthy foods, sedentary lifestyle and lack of exercise are the critical factors leading to overweight and obesity. However, there are additional significant contributory factors not addressed by conventional weight loss/management products and programs. It is essential to have a decent lifestyle with a regular, healthy, nutritious, and balanced diet with limited amounts of alcoholic beverages, poultry, fish and red meat,

moderate amount of exercise, and restful sleep to maintain good health. Implementation of a healthy lifestyle in conjunction with TrimRox™ (TRCAP21) Prodosomed nutraceutical technology will contribute to obtaining a healthy improvement in body composition with reduced fat and water storage, improved muscularity, and even some weight loss.

Obesity is associated with several lifestyle factors including (i) genetics, (ii) poor, unhealthy, and sedentary lifestyle, (iii) chronic stress, (iv) toxic environmental exposure, and (v) disruption in energy homeostasis. Furthermore, chronic stress, trauma, infection, and allergen/antigen insults induce tissue hypoxia or hypoxic/anaerobic events leading to a massive inflammatory response and survival panic [8].

TrimRox™ (TRCAP21) Prodosomed nutraceutical formulation effectively and discretely addresses the salient features, as outlined in Table 1, involved in obesity. The basis or prime objective of this formulation was to restore aerobic metabolic cellular homeostasis to optimize oxygen utilization and hydration status, mitigate oxidative stress, and improve body composition parameters, i.e., promote body recomposition [9-11].

DISCUSSION

Obesity is thus often related directly to the lack of sufficient physical activity, lack of energy homeostasis, and poor dietary habits. However, a lot of other intrinsic and extrinsic factors also play an equally pertinent role in regulating predisposition to excess fat accumulation. A major cause of obesity is metabolic dysfunction leading to a loss of physiological homeostasis, enhanced dependence on anaerobic pathways, accumulation of ROS, and elicitation of inflammatory responses, all culminating in a significant increase in survival-induced

energy conservation; a decline in the basal/resting metabolic rate and the rate of lipid oxidation; and increased fat storage [5,6].

Energy Homeostasis: Three discrete forms of survival insurance are genetically preprogrammed in a human body which includes (a) Fat, (b) Sugar as glycogen, and (c) water. An upregulation of these survival insurance storage components takes place when the body is placed in a “survival panic” mode along with a retardation in energy expenditure [12,13]. As stated elsewhere, chronic degenerative disorders are induced by anaerobic pathologies and in turn cause genetically triggered survival panic. As stated earlier, several intricate factors induce the incidence of obesity and metabolic syndrome. Following are the causative factors that play a regulatory role in the pathophysiology of obesity:

- (a) Overindulgence of high-fat, carbohydrate-filled nutrient-deficient junk foods.
- (b) Lack of physical activity and sedentary lifestyle.
- (c) Continued exposure to structurally diverse environmental pollutants, toxic chemicals, fertilizers, fungicides, insecticides, herbicides, toxic heavy metals, antibiotics, pigments, and colorants.
- (d) Compromised digestive health, gut dysbiosis, inflammatory bowel disorders (IBD), and hyperacidity.
- (e) Enhanced anaerobic metabolism.
- (f) Increased inflammatory response leading to an increase in insulin resistance and enhanced fat accumulation around the belly.
- (g) Increased fat storage.
- (h) Compromised and increased energy conservation.

- (i) Increased oxidative stress and oxidative DNA damage.
- (j) Compromised immune system
- (k) Chronic stress, impaired cognition, depression, and elevated sadness.
- (l) Advancing age and premature aging.
- (m) Impaired aerobic homeostasis, enhancing anaerobic glycolysis and compromising metabolic homeostasis, leading to deficiency in circulating AMPK; all of these contribute to energy disruption, abdominal (and other body compartments) fat deposition and storage.

Of these 13 vital parameters, the “weight management” industries are basically targeting only the first two prime factors of overindulgence of unhealthy foods, and sedentary lifestyle/lack of exercise.

Selected strategies may help in enhancing fat metabolism. These include: (i) minimize sugar, gluten, and fast-food consumption, (ii) improve healthy lifestyle, nutritious balanced diet, and moderate exercise, and (iii) consumption of appropriate research-driven dietary supplements. All of these can optimize energy production, maximize cellular metabolism, and the removal of cellular wastes leading to a more desirable body composition, enhanced lean body mass, healthy muscle mass and optimal health.

It is quite evident that conventional weight loss strategies/techniques completely failed to appropriately address the biological, genetic, and metabolic consequences that occur with advancing age. Several factors are critically important to control the obesity epidemic including: (i) optimize hormonal levels, (ii) minimize anaerobic pathologies caused by cellular oxygen deprivation, (iii) optimize metabolic homeostasis

and enhance fat metabolism/oxidation, (iv) optimize cardiovascular, gastrointestinal, neuromuscular, and kidney health, and (v) promote healthy gut microbiome.

Detrimental effect of anaerobic pathologies on fat

metabolism: A broad spectrum of anaerobic pathologies has been demonstrated to induce an inability to effectively utilize oxygen leading to an increased anaerobic metabolism and lactate accumulation [9]. A disruption in oxidative pathologies, in conjunction with increased lactate production, led to an upsurge in H⁺ increasing cellular acid burden with a reduction in blood pH leading to progressive acidemia. All these will induce a metabolic transition towards cellular anaerobic glycolysis, and a compensatory expenditure of alkalinizing histidine molecules from the heme protein of deconjugated hemoglobin (Hb), which in turn releases iron. These cause an upsurge of anaerobic/acidic cellular events, which cause a series of pathological manifestations including a perturbation of fat metabolism, inflammatory sequela, compromised cardiovascular function, and vaso-occlusive incidences [10].

Influence of inflammatory response on fat metabolism:

Chronic inflammatory conditions exert an array of anaerobic sequela including a disruption in the glucose-insulin system, upregulation of white adipose tissue, and macrophage-associated inflammatory sequela, all of which lead to obesity [11].

Enhanced production of oxygen free radicals, oxidative injury, and fat metabolism: An increase in anaerobic metabolic events causes an upsurge of oxidative stress,

inflammatory sequela, and adipose tissue hypoxia that further induces an array of anaerobic pathologies including mitochondrial dysfunctions, development of type 2 diabetes mellitus, adipose hypertrophy, and a massive disruption in energy homeostasis [11-13]. Therefore, an inability to effectively utilize cellular oxygen (i.e., \uparrow anaerobic metabolism) increases the production of ROS and enhances fat storage.

Immune distress and its impact on fat metabolism: An array of inflammatory sequela play an instrumental role in enhanced fibrosis, angiogenesis, altered lipid metabolism including lipids, cholesterol, and fatty acids; and immune cell activation and immune distress [14-15].

Influence of stress on fat metabolism: Increased stress induces significant stress on cells, potentially impairing cellular oxygen utilization, and exerting massive demands on cells. This cascade of events induces an increase in hunger and appetite for high-fat, sweet, and salty foods [16].

Effect of unpropitious gene expression of hormones and neurotransmitters on fat metabolism **Leptin:** Research studies have demonstrated that increased obesity, T1D, T2D, infertility, and Rabson-Mendenhall Syndrome can occur because of leptin resistance or deficiency [17-18]. Energy homeostasis, hunger/appetite, metabolism, endocrine functions, and fat storage in adipocytes are regulated by leptin, a 167 amino acid adipocytokine. Appropriate regulation of leptin will potentially decrease fat storage in adipocytes and provide significant benefits in the regulation of obesity, body weight, and metabolic syndrome, as well as improve reproductive health,

hematopoiesis, blood pressure, hypertension, lymphoid organ homeostasis, bone density and bone mass [17-18].

Ghrelin (Hunger hormone): Under the influence of excessive stress and sufficient physiological disruption, anaerobic/hypoxic metabolic events are induced that trigger a state of genetically mediated “survival panic”. This then increases energy conservation and ultimately potentiates hunger signaling [19-20]. A conventional corrective strategy includes regulating/inhibiting ghrelin release and enhancing leptin release [19-20], to restore aerobic metabolism and terminate “survival panic” signaling.

Reproductive hormones: The hypothalamus is a key component that regulates energy homeostasis, specifically energy intake and energy expenditure [21]. An injury in the hypothalamus causes a perturbation in energy homeostasis. The hypothalamus is equipped with two nuclear estrogen receptor (ER) proteins, viz. ER α and ER β , which regulate food intake and body weight. For example, as an activation of ER α reduces food intake, body weight, and meal size, as well as promotes synthesis of AMPK and adipose tissue triglyceride lipase (ATGL)-mediated lipolysis providing free fatty acids as a fuel to activate UCP-1. These estrogen receptors are available in multiple peripheral tissues including adipose tissue [22-23]. The availability of estrogens in the adipose tissue causes anti-inflammatory activities in the peripheral tissues and in the central nervous system, which prevents women from experiencing multiple inflammatory consequences. Thus, some additional estrogen may provide a therapeutic benefit in regulating obesity and anti-inflammatory efficacy [22-24].

Thyroid hormones and neurotransmitters: Two major hormones including triiodothyronine (T3) and tetraiodothyronine (thyroxine or T4) are produced and released by the thyroid gland, which are important for (i) metabolic homeostasis, (ii) cardiac functions, (iii) digestive functions, (iv) muscle control, (v) neuronal development and function, and (v) bone function. The third active thyroid hormone, 3,5-Diiodothyronine (3,5-T₂) or just T2, stimulate the TRb receptor of thyroid hormones that controls energy expenditure [25-28].

Two prime neurotransmitters: serotonin and dopamine: It has been extensively demonstrated that an interruption/dysfunction in feeding signals by neuronal cells plays a vital role in obesity. Neurotransmitters are basically chemical messengers that transmit signals to multiple target cells including different neurons, muscle cells, or gland cells [29]. Serotonin is specifically involved in the transmission of nerve impulses and plays a major role in appetite control/suppression [29-30].

Deficiency of dopamine in obese individual can be easily characterized by increased food intake and food consumption behaviors [31]. Dopamine not only regulates food cravings, but also motivation and reward circuitry.

Consequential effects of premature aging on fat metabolism: An upsurge in oxidative stress, increased cellular lactic acid production, and anaerobic glycolysis

are pioneering hallmarks of impaired cellular metabolism. All these events lead to chronic degenerative disorders/disease including accelerated premature aging and, are classic pathophysiological characteristics of anaerobic/hypoxic events. Thus, restoring aerobic glycolysis must be an important anti-aging objective to reduce the anaerobic cellular metabolic requirement that induces a concomitant increase in anaerobic-induced lactic acid production [32].

Accordingly, we hypothesize that the Prodosomed TRCAP21 phytoceutical technology should minimize anaerobic-based metabolic impairments and combat a full spectrum of etiological obesogenic factors.

Role of AMPK (adenosine monophosphate-activated kinase) on fat metabolism: AMPK is a key enzyme known to regulate cellular energy balance. However, it declines with advancing age. AMPK enhances fat oxidation and energy production (ATP), however, a decline in AMPK enhances the conversion of sugar into fat along with a concomitant increase in fat storage [33-36]. Thus, in a successful body recomposition strategy, rejuvenating AMPK synthesis and metabolism should be a most important objective.

A synergistic botanical formulation - TRCAP21: This novel formulation was designed using the following Prodosomed six research-affirmed nutraceutical ingredients (Figure 1).

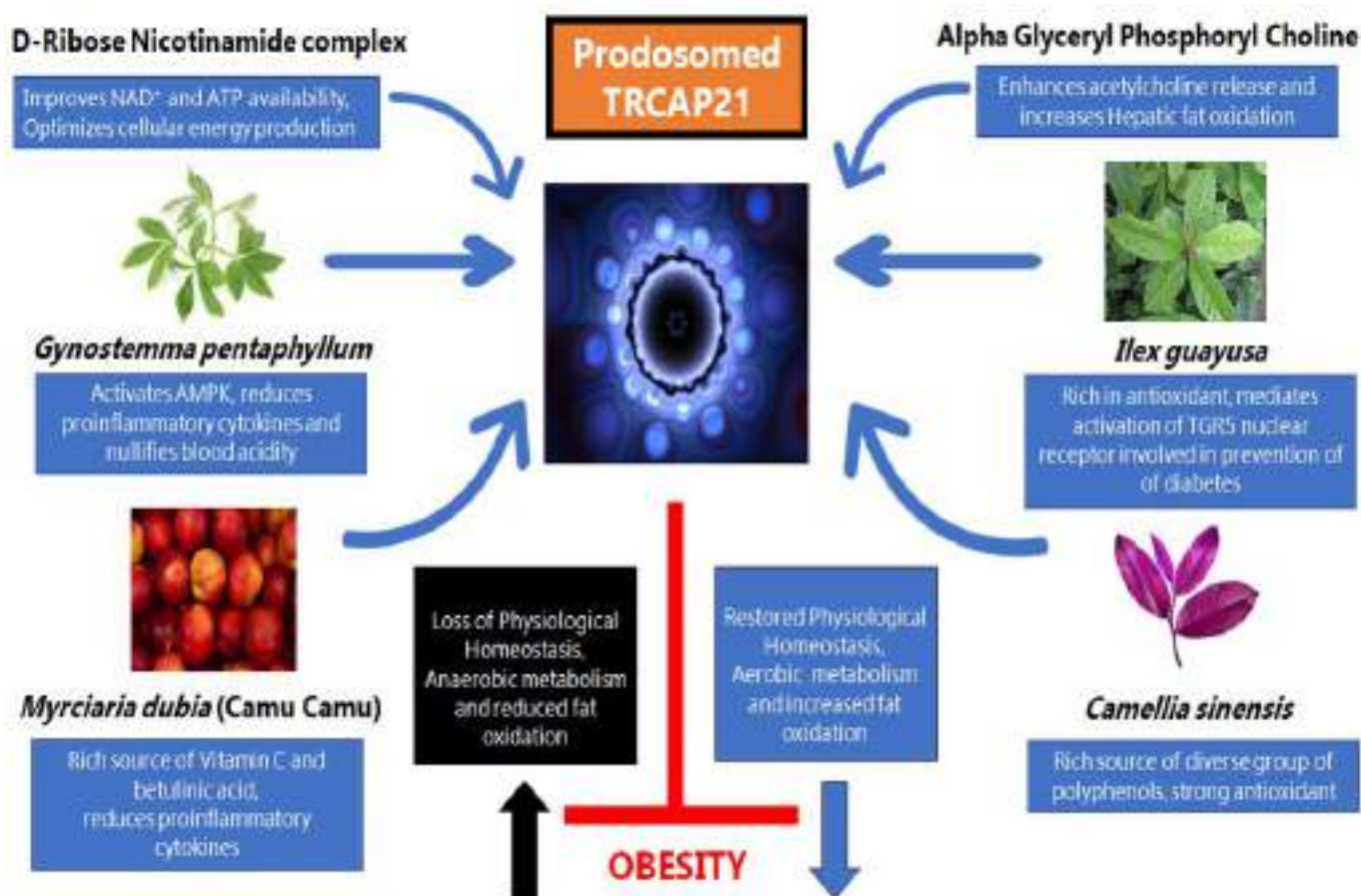


Fig 1. Prodosomed TRCAP21 as a novel anti-obesity formulation: A major cause of obesity is metabolic dysregulation and dysfunction leading to loss of physiological homeostasis, enhanced dependence on anaerobic pathways, accumulation of Reactive Oxygen Species and elicitation of inflammatory response, all culminating in a significant decline in the rate of lipid oxidation. Prodosomed TRCAP21 is a proprietary formulation consisting of extracts of six vital plant derived constituents that collectively ensure restoration of normal physiological homeostasis thus mitigating obesogenic factors. Abbreviations: NAD⁺ - Nicotinamide Adenine Dinucleotide, ATP – Adenosine Triphosphate, AMPK - Adenine Mono Phosphate activated Protein Kinase, TGR5 – Takeda G Protein Coupled Receptor/G-Protein Coupled Bile Acid Receptor

D-Ribose nicotinamide complex (RiaGev; Source: Bioenergy): In a clinical investigation, a proprietary blend of D-ribose and nicotinamide exhibited enhanced bioavailability and effectively promoted the synthesis of nicotinamide adenine dinucleotide (NAD)[37]. A pilot study in one human volunteer demonstrated that blood NAD⁺ can elevate up to 2.7-fold following the administration of a single dose of RiaGev. A pharmacokinetic study in twelve human volunteers demonstrated that administration of a single dose of 100, 300 and 1,000 mg of RiaGev can enhance blood NAD⁺

metabolome significantly [38]. It is important to mention that maximum concentration of NAD, a coenzyme in redox reactions and a donor of ADP-ribose moieties in ADP-ribosylation reactions, is in the mitochondria and is important to optimize cellular energy production. The safety and efficacy of RiaGev was also investigated in 18 subjects (age = 35-65 years) in a single-center, randomized, double-blind, comparator controlled, cross-over study. Interestingly, both ATP and ADP levels increased by approximately 7.3%, while both NAD⁺ and NADP⁺ levels increased by approximately 15%, and

glutathione level (GSH) increased by 11% and maintained redox homeostasis. Improvements in muscle and brain performance were observed along with GSH. Furthermore, increases in insulin response and glucose tolerance were also observed along with a steady reduction in salivary cortisol. Quality of life, attention, focus, and motivation levels improved significantly as well. In conclusion, RiaGev provides effective benefits to all tissues as well as a synergistic dose-response was observed between RiaGev and NAD metabolites in the liver, muscle, and brain tissues [39].

***Gynostemma pentaphyllum* (GP) leaf extract:** This leaf extract activates and increases AMPK level, which is instrumental in regulating cellular energy balance. It also enhances fat oxidation, energy production, and glucose homeostasis; and inhibits cholesterol synthesis [38,40,34,36]. In cellular mitochondria, AMPK activation enhances conversion of ingested food molecules into ATP. Moreover, it upregulates catabolic pathways through glycolysis and fatty acid oxidation to boost energy homeostasis (ATP) [33-36].

GP also reduces cytokine production and activates NF- κ B and STAT3 signaling in lipopolysaccharide-induced macrophages, without affecting their viability [40]. GP extract has been reported to exhibit multiple beneficial effects including maintenance of healthy cholesterol and blood glucose levels; increasing hemoglobin, liver glycogen, and muscle glycogen concentrations; decreasing blood lactic acid (BLA) levels and blood urea nitrogen (BUN) concentrations; boosting immunity; and protecting cells from mutations [41-44]. Park et al. [45] conducted a randomized, double-blind, placebo-

controlled clinical investigation in 80 obese subjects (age: 40.08 ± 10.60 years; weight: 74.58 ± 9.19 kg; BMI: 27.53 ± 1.22 kg m⁻²) using a GP extract (450 mg/day) over a period of 12 consecutive weeks. Body weight, body fat mass, percent body fat, and BMI were significantly decreased in the treatment group. No adverse events were observed [45].

***Myrciaria dubia* (JS0208 Camu Camu) whole-berry extract (MD):** Camu Camu is a potent antioxidant containing considerable amounts of vitamin C, betulinic acid, beta-carotene, riboflavin, thiamine, niacin, cyanidin 3-glucoside, delphinidin 3-glucoside, ellagic acid, kaempferol, myricetin, quercetin, quercitrin, rutin, and micronutrients. It protects genomic DNA integrity, enhances energy level and immune competence, and exhibits anti-inflammatory benefits by downregulating cytokine production and c-reactive proteins (CRP), and suppresses water retention (inhibits edema formation). It also facilitates tissue reconstruction and repair and provides protection against allergens and mutagens [46-49].

***Ilex guayusa* Loes. (Family Aquifoliaceae) (Guayusa) leaf extract (GL):** GL leaf extract contains potent structurally diverse antioxidants and phytonutrients including chlorogenic acid, ursolic acid, as well as caffeine [50,51]. Especially, ursolic acid exerts a pronounced mechanistic role in the activation of nuclear receptor TGR5, which in turn is instrumental in the management of metabolic syndrome by enhancing energy expenditure and insulin sensitization [51-53].

In a battery of safety studies, GL leaf extract demonstrated broad spectrum safety with no genotoxicity, and secured FDA-notified GRAS (Generally Recognized as Safe) status in 2019 [54].

GL leaf extract has been demonstrated to elevate mood and enhance cognition and focus, promote brain function, restful sleep, alleviate stress, promote cardiovascular health, antiviral potential against herpes simplex virus, and protect against potential neurotoxins and hepatotoxicity [55].

It was observed that the action of Guayusa caffeine source distinctly differs from other natural and synthetic caffeine sources as it did not induce a significant effect on epinephrine (adrenaline). This can explain its reduced adrenaline-related side effects compared to other caffeine sources. Also, no significant effect of Guayusa was observed on dopamine, norepinephrine, or GABA levels [56].

Purple Tea (PT; HS1222 *Camellia sinensis* extract; PurpleForce™): This “purple” variation of *Camellia sinensis* extract was derived from plants grown in a high-altitude mountain area exposed to strong UV rays, which increase the protective properties of the plants. PT has high polyphenol content including delphinidin content and exerts higher antioxidant activity compared to other tea extracts [57].

PT exhibits diverse beneficial antioxidant and anti-inflammatory effects including: (i) improves nitric oxide production, (ii) restores blood flow, (ii) improves recovery from exercise-induced muscular injury by decreasing creatine kinase, oxidative injury, and exercise-induced soreness, (iii) and promotes exercise recovery

[58]. In a clinical study, PT exhibited a significant reduction in body weight, BMI, abdominal fat, triglycerides in serum and hepatic tissues; and suppression of fat absorption, increasing hepatic fat metabolism, and enhanced expression of carnitine palmitoyl transferase (CPT) 1A [59]. Another study assessed the efficacy of supplemental PT (100 mg/day) in 30 healthy exercising men after strenuous and stressful exercise over a period of 8 consecutive days [59]. Muscle endurance performance was remarkably improved and lactate dehydrogenase level, a marker of muscular injury, was significantly reduced. Overall, these results strengthen the pronounced role of PT in human health and well-being.

Alpha Glyceryl phosphoryl choline (Alpha-GPC; AlphaSize®): The cholinergic system is the largest neurotransmitter system in the body regulating brain-to-muscle communication, intestinal peristalsis, and locomotion; attention, higher-order cognitive processing, and emotions [60-62]. Alpha-GPC is a safe, non-stimulating endurance-enhancing ergogenic supplement, and exhibited to improve memory, focus, learning, cognition, mood, and physiological performance in athletes [62]. Following administration of Alpha-GPC, choline and growth hormone secretion, and hepatic fat oxidation significantly increased. Alpha-GPC was shown to boost endurance and performance, while preventing the reduction of choline levels [63-64].

The Prodosomed TRCAP21 is a proprietary formulation (Figure 1) comprised of D-ribose nicotinamide, alpha-GPC and four botanical extracts rich in a diverse range of phytochemical components, including

phytosaccharides, theobromine, (and other dimethylxanthines viz. paraxanthine and theophylline), amino acids, gallic acid, guanidine, isobutyric acid, B-vitamins, vitamin C, nitric oxide, chlorogenic acid, ellagic acid, triterpenes and pentacyclic triterpenoid acids, saponins (such as gypenosides), and alcohols, including ursolic acid (0.7–1%) and amyirin esters (up to 0.5%), betulinic acid; bioactive phenolic compounds including anthocyanins (cyanidin-3-O-glucoside and delphinidin-3-O-glucoside), flavonols (myricetin, quercetin), ellagic acid, ellagitannins, proanthocyanidins, and carotenoids (lutein, carotene, violaxanthin and luteoxanthin), etc., that collectively act to mitigate obesogenic factors and restore aerobic metabolism and normal physiological homeostasis [65].

Overall, this unique and proprietary TRCAP21 formulation technology exerted significant benefits and improvement in overall body composition in these nine volunteers as evident from the reduced anthropometric measurements of the chest, bicep, hips, thighs, and waist, as well as modest, varying, but noteworthy reductions in body weight. Energy levels, mood, and restful sleep were improved. Moreover, reduced appetite or appetite correction was reported by all subjects, and sugar cravings were also reduced. Overall health improved and no adverse events were reported.

This pilot concept validation study motivated us to do a full-fledged IRB (Institutional Review Board)-approved randomized, double-blind, placebo-controlled study, with clinicaltrials.gov approval (#NCT05283525), which is now in progress.

CONCLUSION

It has been difficult for any therapeutics/food supplements/nutraceuticals to make significant headway into the management of obesity owing to human being's

general insufficient physical activity and inherent craving for sweet, salty, fatty, tasty, and fried junk foods. As incidences of obesity and associated ailments continue to rise even faster, the need of the hour is to explore more unique and effective natural remedies instead of synthetic ones and use them in correct synergistic proportions to plan anti-obesity regimens and achieve a healthy and balanced lifestyle. Since the management of obesity also depends to a significant extent on the mental health and wellness of the affected person, it will be worthwhile to investigate the effect of the constituents of TrimRox™ over the communication network of the Gut-Brain Axis [66], particularly on the associated microbiome to understand how nutraceuticals influence the complex human-microbe associations for ensuring optimal body homeostasis, both mentally as well as physically.

List of Abbreviations: ACh: Acetylcholine; ADP: Adenosine diphosphate; Alpha-GPC: Alpha Glyceryl phosphoryl choline; ATGL: Adipose tissue triglyceride lipase; AMPK: Adenosine monophosphate-activated kinase; ATP: Adenosine triphosphate; BID: Twice a day BMI: Body mass index; BN: Billion; CHD: Coronary heart disease; CNS: Central nervous system; CPT: Carnitine palmitoyl transferase; CRP: C-Reactive protein; DNA: Deoxyribonucleic acid; ER: Estrogen receptor; FDA: Food and Drug Administration; GABA: Gamma amino butyric acid; GHG: 1,2-Di-O-galloyl-4,6-O-(S)-hexahydroxy-diphenoyl-β-D-glucose; GL: Guayusa (*Ilex guayusa* Loes.) leaves; GP: *Gynostemma pentaphyllum*; GRAS: Generally recognized as safe; GSH: Glutathione; Hb: Hemoglobin; IBD: Inflammatory bowel disease; IRB: Institutional review board; MD: *Myrciaria dubia* (also known as Camu Camu); NAD⁺: Nicotinamide adenine dinucleotide⁺; NADH: Nicotinamide adenine dinucleotide (NAD) + hydrogen (H); OID: Once a day; PT: Purple tea; ROS:

Reactive oxygen species; T1D: Type 1 diabetes mellitus; T2 or 3,5-T2z; 3,5-Diiodothyronine; T2D: Type 2 diabetes mellitus; T3: Triiodothyronine; T4 or thyroxine: Tetraiodothyronine; UCP-1: Uncoupling protein-1

Authors' Contribution: DB, BD, SK, MB, SB, and SC significantly contributed to designing and drafting the manuscript. Dr. Bruce Morrison was intricately associated with the clinical investigation and data

Acknowledgment: The authors thank Ms. Kim Downs for her generous assistance towards the completion of the manuscript.

Funding: Bioscience Division of Victory Nutrition International, Inc., Bonita Springs, FL, USA.

REFERENCES

1. Adult Obesity Facts: Obesity is a common, serious, and costly disease. Feb 11, 2021. <https://www.cdc.gov/obesity/data/adult.html>. Retrieved Feb 28, 2022.
2. Wolf AM, Colditz GA. Current Estimates of the Economic Cost of Obesity in the United States. *Obesity Research*, 1998; 6(2): 97-106. <https://doi.org/10.1002/j.1550-8528.1998.tb00322.x>.
3. Strategies to Overcome and Prevent Obesity Alliance. Obesity School of Public Health and Health Services. 2021. The George Washington University. <https://stop.publichealth.gwu.edu/sites/stop.publichealth.gwu.edu/files/documents/Fast%20Facts%20Cost%20of%20Obesity.pdf>. Retrieved Feb 11, 2022.
4. World Health Organization (WHO): Obesity and Overweight. <https://www.who.int/news-room/fact-sheets/detail/obesity-and-overweight>. Retrieved Feb 21, 2022.
5. Managing overweight and obesity in adults; Systematic evidence review from the obesity expert panel, 2013. US Dept of Health and Human Services, NIH; <https://www.nhlbi.nih.gov/health-topics/managing-overweight-obesity-in-adults>. Retrieved Feb 11, 2022.
6. Finkelstein EA, Trogdon JG, Cohen JW, Dietz W. 2009. Annual Medical Spending Attributable to Obesity: Payer-And Service-Specific Estimates. *Health Affairs*; Vol 28:

analyses. SH standardized the ingredients and cooperated in designing the formulation.

Competing Interests: Commercial Division of Victory Nutrition International (VNI), Inc., Bonita Springs, FL, USA, is involved in marketing this product. BD is an employee of Research and Development Division of VNI Inc., Bonita Springs, FL, USA. DB, SK, and MB are scientific consultants. BM is an independent physician. SH is an ingredient designers and manufacture

Supplement

1

<https://www.healthaffairs.org/doi/10.1377/hlthaff.28.5.w8>

22. Retrieved Feb 26, 2021.

7. Crawford V, Scheckenbach R, Preuss HG. Effects of niacin-bound chromium supplementation on body composition in overweight African-American women. *Diabetes, Obesity and Metabolism*, 1999; 1(6): 331-337. <https://doi.org/10.1046/j.1463-1326.1999.00055.x>.
8. Downs BW, Corbier JR, Speight N, Kushner S, Aloisio T, Bagchi M, Bagchi D. Anemia: Influence of Dietary Fat, Sugar, and Salt on Hemoglobin and Blood Health. In: Dietary Sugar, Salt, and Fat in Human Health. Editors: Preuss HG, Bagchi D eds. (2020) Boston (MA): Elsevier/ Academic Press, pp. 103-128.
9. Baillie-Hamilton PF. Chemical Toxins: A Hypothesis to Explain the Global Obesity Epidemic. *The Journal of Alternative and Complementary Medicine*, 2002; 8(2): 185-192. <https://doi.org/10.1089/107555302317371479>.
10. Hyman MA. Environmental toxins, obesity, and diabetes: An emerging risk factor. *Alternative Therapy in Health and Medicine*, 2010; 16(2): 56-58. PMID: 20232619
11. Brown K, DeCoffe D, Molcan E, Gibson DL. Diet-induced dysbiosis of the intestinal microbiota and the effects on immunity and disease. *Nutrients*, 2012; 4(8): 1095-1119. <https://doi.org/10.3390/nu4081095>.
12. Boulangé CL, Neves AL, Chilloux J, Nicholson JK, Dumas ME. 2016. Impact of the gut microbiota on inflammation, obesity, and metabolic disease. *Genome Medicine*, 2016; 8:42 <https://doi.org/10.1186/s13073-016-0303-2>.
13. Phipers B, Pierce T. Lactate physiology in health and disease. *Continuing Education in Anesthesia and Critical Care and Pain*, 2006; 6(3): 128-132. <https://doi.org/10.1093/bjaceaccp/mkl018>.
14. Corbier JR, Downs BW, Kushner S, Aloisio T, Bagchi D, Bagchi M. VMP35 MNC, a novel iron-free supplement, enhances cytoprotection against anemia in human subjects: a novel

- hypothesis. *Food and Nutrition Research*, 2019; 63: 3410
<https://doi.org/10.29219/fnr.v63.3410>.
15. Xu H, Barnes GT, Yang Q, Tan G, Yang D, Chou CJ, Sole J, Nichols A, Ross JS, Tartaglia LA, Chen H. Chronic inflammation in fat plays a crucial role in the development of obesity-related insulin resistance. *Journal of Clinical Investigation*, 2003; 112(12): 1821-1830.
<https://doi.org/10.1172/JCI19451>
 16. Netzer N, Gatterer H, Faulhaber M, Burtscher M, Pramsohler S, Pesta D. Hypoxia, oxidative stress and fat. *Biomolecules*, 2015; 5(2): 1143-1150
<https://doi.org/10.3390/biom5021143>
 17. Zhang Y, Chua S Jr. Leptin function and regulation. *Comprehensive Physiology*, 2017; 8(1): 351-369.
<https://doi.org/10.1002/cphy.c160041>.
 18. Triantafyllou GA, Paschou SA, Mantzoros CS. Leptin and hormones: energy homeostasis. *Endocrinology and Metabolism Clinics of North America*, 2016; 45(3): 633-645.
<https://doi.org/10.1016/j.ecl.2016.04.012>.
 19. Akki R, Raghay K, Errami M. Potentiality of ghrelin as antioxidant and protective agent. *Redox Report*, 2021; 26(1):71–79.
<https://doi.org/10.1080/13510002.2021.1913374>.
 20. Downs BW, Bagchi M, Morrison BS, Galvin J, Kushner S, Bagchi D. PerformLyte – A Prodosomed PL425 PEC Phytoceutical-Enriched Electrolyte Supplement – Supports Nutrient Repletion, Healthy Blood pH, Neuromuscular Synergy, Cellular and Metabolic Homeostasis. In: Antioxidants and Functional Foods for Neurodegenerative Disorders: Uses in Prevention and Therapy. Editors: Kumar A, Bagchi D (2021) Boca Raton (FL): CRC Press/ Taylor & Francis, pp. 399-424.
 21. Leeners B, Geary N, Tobler PN, Asarian L. Ovarian hormones and obesity. *Human Reproduction Update*, 2017; 23(3): 300-321. <https://doi.org/10.1093/humupd/dmw045>.
 22. Lainez NM, Coss D. Obesity, Neuroinflammation, and Reproductive Function. *Endocrinology*, 2010; 160(11): 2719-2736. <https://doi.org/10.1210/en.2019-00487>.
 23. Santollo J, Wiley MD, Eckel LA. Acute activation of ER alpha decreases food intake, meal size, and body weight in ovariectomized rats. *American Journal of Physiology: Regulatory, Integrative and Comparative Physiology*, 2007; 293(6):R2194-201.
<https://doi.org/10.1152/ajpregu.00385.2007>.
 24. Santos RS, Frank AP, Fatima LA, Palmer BF, Oz OK, Clegg DJ. Activation of estrogen receptor alpha induces beiging of adipocytes. *Molecular Metabolism*, 2018; 18: 51–59.
<https://doi.org/10.1016/j.molmet.2018.09.002>.
 25. Brown LM, Gent L, Davis K, Clegg DJ. Metabolic impact of sex hormones on obesity. *Brain Research*, 2010; 1350: 77-85.
<https://doi.org/10.1016/j.brainres.2010.04.056>.
 26. Goglia F. The effects of 3,5-diiodothyronine on energy balance. *Frontiers in Physiology*, 2014; 5:528.
<https://doi.org/10.3389/fphys.2014.00528>.
 27. Lombardi A, Senese R, De Matteis R, Busiello RA, Cioffi F, Goglia F, Lanni A. 2015. 3,5-Diiodo-L-thyronine activates brown adipose tissue thermogenesis in hypothyroid rats. *PLOS ONE*, 2015; 10 (2): e0116498. Bibcode:2015PLoS One.1016498L
<https://doi.org/10.1371/journal.pone.0116498>.
 28. Jonas W, Lietzow J, Wohlgemuth F, Hoefig CS, Wiedmer P, Schweizer U, Köhrle J, Schürmann A. 3,5-Diiodo-L-thyronine (3,5-T2) exerts thyromimetic effects on hypothalamus-pituitary-thyroid axis, body composition, and energy metabolism in male diet-induced obese mice. *Journal of Endocrinology*, 2015; 156(1): 389–99.
<https://doi.org/10.1210/en.2014-1604>.
 29. Miller GD. Appetite Regulation: Hormones, Peptides, and Neurotransmitters and Their Role in Obesity. *American Journal of Lifestyle Medicine*, 2019; 13(6): 586–601.
<https://doi.org/10.1177/1559827617716376>.
 30. Blum K, Febo M, Badgaiyan RD. 2016. Fifty Years in the Development of a Glutaminergic-Dopaminergic Optimization Complex (KB220) to Balance Brain Reward Circuitry in Reward Deficiency Syndrome: A Pictorial. *Austin Addiction Science*, 2016; 1(2): 1006. PMCID: PMC5103643. NIHMSID: NIHMS822953. PMID: 27840857.
 31. Wang GJ, Volkow ND, Logan J, Pappas NR, Wong CT, Zhu W, Netusil N, Fowler FS. Brain dopamine and obesity. *Lancet*, 2001; 357(9253): 354-357. [https://doi.org/10.1016/s0140-6736\(00\)03643-6](https://doi.org/10.1016/s0140-6736(00)03643-6).
 32. Chung KW. Advances in understanding of the role of lipid metabolism in aging. *Cells*, 2021; 10: 880.
<https://doi.org/10.3390/cells10040880>.
 33. Carling D. The AMP-activated protein kinase cascade—a unifying system for energy control. *Trends in biochemical sciences*, 2004; 29(1): 18-24.
<https://doi.org/10.1016/j.tibs.2003.11.005>.
 34. Fogarty S, Hardie DG. Development of protein kinase activators: AMPK as a target in metabolic disorders and cancer. *Biochimica Biophysica Acta*, 2010; 1804(3): 581-591.
<https://doi.org/10.1016/j.bbapap.2009.09.012>.
 35. Hardie DG. AMPK: a key regulator of energy balance in the single cell and the whole organism. *International Journal of*

- Obesity* (London), 2008; 32 (Suppl 4): S7-S12. <https://doi.org/10.1038/ijo.2008.116>.
36. Zhang BB, Zhou G, Li C. AMPK: an emerging drug target for diabetes and the metabolic syndrome. *Cell Metabolism*, 2009; 9(5): 407-416. <https://doi.org/10.1016/j.cmet.2009.03.012>.
 37. Trammell SAJ, Schmidt MS, Weidemann BJ, Redpath P, Jaksch F, Dellinger RW, Li Z, Abel ED, Migaud ME, Benner C. Nicotinamide riboside is uniquely and orally bioavailable in mice and humans. *Nature Communications*, 2016; 7:12948; 1-14. <https://doi.org/10.1038/ncomms12948>.
 38. Hopp AK, Grüter P, Michael O, Hottiger MO. Regulation of Glucose Metabolism by NAD⁺ and ADP-Ribosylation. *Cells*, 2019; 8(8): 890. <https://doi.org/10.3390/cells8080890>.
 39. Dölle C, Rack JGM, Ziegler M. NAD and ADP-ribose metabolism in mitochondria. *FEBS J.*, 2013; 280(15): 3530-3541. <https://doi.org/10.1111/febs.12304>.
 40. Wong WY, Lee MLL, Chan BD, Ma VWS, Zhang W, Yip TTC, Wong WT, Tai WCS. Gynostemma pentaphyllum saponins attenuate inflammation in vitro and in vivo by inhibition of NF- κ B and STAT3 signaling. *Oncotarget*, 2017; 8(50): 87401–87414. <https://doi.org/10.18632/oncotarget.20997>.
 41. Megalli S, Davies NM, Roufogalis BD. Anti-hyperlipidemic and hypoglycemic effects of Gynostemma pentaphyllum in the Zucker fatty rat. *Journal of Pharmacy and Pharmaceutical Sciences*, 2006; 9(3): 281-291. PMID: 17207412
 42. Yeo J, Kang YJ, Jeon SM, Jung UJ, Lee MK, Song H, Choi MS. Potential hypoglycemic effect of an ethanol extract of Gynostemma pentaphyllum in C57BL/KsJ-db/db mice. *Journal of Medical Foods*, 2008; 11(4): 709-716. <https://doi.org/10.1089/jmf.2007.0148>
 43. Lu HF, Chen YS, Yang JS, Chen JC, Lu KW, Chiu TH, Liu KC, Yeh CC, Chen GW, Lin HJ, Chung JG. Gypenosides induced G0/G1 arrest via inhibition of cyclin E and induction of apoptosis via activation of caspases-3 and 29 in human lung cancer A-549 cells. *In Vivo*, 2008; 22(2): 215-221. PMID: 18468406
 44. Razmovski-Naumovski V, Huang THW, Tran VH, Li GQ, Duke CC, Roufogalis BD. Chemistry and pharmacology of Gynostemma pentaphyllum. *Phytochemistry Reviews*, 2005; 4: 197-219. <https://doi.org/10.1007/s11101-005-3754-4>
 45. Park SH, Huh TL, Kim SY, Oh MR, Pichiah T, Chae SW, Cha YS. Antiobesity effect of Gynostemma pentaphyllum extract (Actiponin): A randomized, double-blind, placebo-controlled trial. *Obesity*, 2014; 22(1): 63-71. <https://doi.org/10.1002/oby.20539>.
 46. Langley PC, Pergolizzi JV Jr, Taylor R Jr, Ridgway C. Antioxidant and associated capacities of Camu camu (*Myrciaria dubia*): a systematic review. *Journal of Alternative and Complementary Medicine*, 2015; 21(1): 8-14. <https://doi.org/10.1089/acm.2014.0130>.
 47. Fracassetti D, Costa C, Moulay L, Tomás-Barberán FA. Ellagic acid derivatives, ellagitannins, proanthocyanidins and other phenolics, vitamin C and antioxidant capacity of two powder products from camu-camu fruit (*Myrciaria dubia*). *Food Chemistry*, 2013; 139(1-4): 578-588. <https://doi.org/10.1016/j.foodchem.2013.01.121>.
 48. Yazawa K, Suga K, Honma A, Shirosaki M, Koyama T. Anti-inflammatory effects of seeds of the tropical fruit camu-camu (*Myrciaria dubia*). *Journal of Nutritional Science and Vitaminology* (Tokyo), 2011; 57(1): 104-107. <https://doi.org/10.3177/jnsv.57.104>.
 49. Inoue T, Komoda H, Uchida T, Node T. Tropical fruit camu-camu (*Myrciaria dubia*) has anti-oxidative and anti-inflammatory properties; A randomized controlled trial. *Journal of Cardiology*, 2008; 52(2):127-132. <https://doi.org/10.1016/j.jicc.2008.06.004>.
 50. Dueñas JF, Jarrett C, Cummins I, Logan-Hines E. Amazonian guayusa (*Ilex guayusa* Loes.): A historical and ethnobotanical overview. *Economic Botany*, 2016; 70: 85–91. https://ayusa.com.au/wp-content/uploads/Duenas_et al2016.pdf
 51. García-Ruiz A, Baenas N, Benítez-González AM, Stinco CM, Meléndez-Martínez AJ, Moreno DA, Rualesa J. Guayusa (*Ilex guayusa* L.) new tea: Phenolic and carotenoid composition and antioxidant capacity. *J Sci Food Agric.*, 2017; 97(12): 3929–3936. <https://doi.org/10.1002/jsfa.8255>.
 52. Brinckmann J, Brendler T. Herb Profile: Guayusa (*Ilex guayusa* family: Aquifoliaceae). *Herbalgram* 2019; 6: Issue 124. <https://www.herbalgram.org/resources/herbalgram/issues/124/table-of-contents/hg124-herbprofile-guayusa/>.
 53. Chianesea G, Golin-Pachecob SD, Taglialatela-Scafati O, Collado JA, Muñoz E, Appendino G, Pollastro F. Bioactive triterpenoids from the caffeine-rich plants guayusa and mate'. *Food Research International*, 2019; 115: 504–510. <https://doi.org/10.1016/j.foodres.2018.10.005>.
 54. GRAS Notice (GRN) No. 835 from the Food Additive Safety. <https://www.fda.gov/food/generally-recognized-safe-gras/gras-notice-inventory> (Retrieved Feb 8, 2022).
 55. Gamboa F, Muñoz CC, Numpaque G, Sequeda-Castañeda LG, Gutierrez SJ, Ellez N. Antimicrobial Activity of *Piper marginatum* Jacq and *Ilex guayusa* Loes on Microorganisms Associated with Periodontal Disease. *International Journal*

- of Microbiology, 2018; Article ID 4147383: 9 pages <https://doi.org/10.1155/2018/4147383>.
56. Kreiger DR, Kalman DS, Feldman S, Arnillas L, Goldberg D, Gisbert O, Nader S. The safety, pharmacokinetics, and nervous system effects of two natural sources of caffeine in healthy adult males. *Clinical and Translational Science*. 2016; 9(5): 246–251. <https://doi.org/10.1111/cts.12403>
57. Cesario K, Ziegenfuss T, Raub B, Sandrock J, Lopez H. Effects of Purple tea on muscle hyperemia and oxygenation, serum markers of nitric oxide production and muscle damage, and exercise performance. *Journal of Exercise and Nutrition*, 2020; 3(3): 13 ISSN 2640-2572. <https://www.journalofexerciseandnutrition.com/index.php/JEN/article/view/71>
58. Harty PS, Zabriskie HA, Erickson JL, Molling PE, Kerkick CM, Jagim AR. Multi-ingredient pre-workout supplements, safety implications, and performance outcomes: a brief review. *Journal of International Society of Sports Nutrition*, 2018; 15(1):41. <https://doi.org/10.1186/s12970-018-0247-6>.
59. Shimoda H, Hito S, Nakamura S, Matsuda H. Purple tea and its extract suppress diet-induced fat accumulation in mice and human subjects by inhibiting fat absorption and enhancing hepatic carnitine palmitoyl transferase expression. *International Journal of Biomedical Sciences*, 2015; 11(2): 67-75. PMCID: PMC4502735 PMID: 26199579.
60. Teipel SJ, Meindell T, Grinberg L, Grothe M, Cantero JL, Reiser MF, Moller HJ, Heinsen H, Hempel H. The cholinergic system in mild cognitive impairment and Alzheimer's disease: An in vivo MRI and DTI study. *Hum Brain Mapp.*, 2011; 32(9): 1349–1362. <https://doi.org/10.1002/hbm.21111>.
61. Avila DS, Gubert P, Roos DH, Puntel R, Aschner M. Manganese: Encyclopedia of Food and Health. Editors: Caballero B, Finglas PM, Toldra F (2016) Boston (MA): Elsevier/ Academic Press, pp. 637-640.
62. Parnetti L, Abate G, Bartorelli L, Cucinotta D, Cuzzupoli M, Maggioni M, Villardita C, Senin U. Multicentre study of l- α -glyceryl-phosphorylcholine vs ST200 among patients with probable senile dementia of Alzheimer's type. *Drugs Aging*, 1993; 3(2): 159-164 <https://doi.org/10.2165/00002512-199303020-00006>.
63. Kawamura, T, Okubo T, Sato K, Fujita S, Goto K, Hamaoka T, Iemitsu M. 2012. Glycerophosphocholine enhances growth hormone secretion and fat oxidation in young adults; a clinical trial. *Nutrition*, 2012; 28(11-12):1122-1126. <https://doi.org/10.1016/j.nut.2012.02.011>.
64. Ziegenfuss T, Landis J, Hofheins J. Acute supplementation with α -glycerylphosphorylcholine augments growth hormone response to, and peak force production during resistance exercise. *Journal of International Society of Sports Nutrition*, 2008; 5(Suppl 1): P15 <https://doi.org/10.1186/1550-2783-5-S1-P15>.
65. Bondia-Pons I, Ryan L, Martinez JA. Oxidative stress and inflammation interactions in human obesity. *Journal of Physiology and Biochemistry*, 2012; 68: 701–711. <https://doi.org/10.1007/s13105-012-0154-2>.
66. Appleton J. The gut-brain axis: Influence of microbiota on mood and mental health. *Integrative Med. (Encinitas)*, 2018; 17(4): 28–32. PMCID: PMC6469458 PMID: 31043907



Enhanced production of biohydrogen from lignocellulosic feedstocks using microorganisms: A comprehensive review

Rituparna Saha^{a,b}, Debalina Bhattacharya^c, Mainak Mukhopadhyay^{a,*}

^a Department of Biotechnology, JIS University, Kolkata, West Bengal, 700109, India

^b Department of Biochemistry, University of Calcutta, Kolkata, West Bengal, 700019, India

^c Department of Microbiology, Maulana Azad College, Kolkata, West Bengal, 700013, India

ARTICLE INFO

Keyword:

Biohydrogen
Renewable energy
Lignocellulosic feedstock
Biological
Pretreatment
Photofermentation
Dark fermentation

ABSTRACT

Biohydrogen (BioH₂) is a low-carbon fuel with high energy efficiency. Although it can be produced using various technologies, the biological method has been deemed more sustainable and economically feasible. Extensive research has also led to identifying of lignocellulosic feedstocks (LCFs) as the highly abundant and renewable raw material for BioH₂ production. Although there are many hurdles, the use of microbes-dependent processes for BioH₂ production could bring down the operational cost and waste produced, and is efficient enough to meet future energy demands. In this review, the latest developments made in recent years regarding the biological conversion of LCFs to BioH₂ are discussed. The microorganisms involved in the technologies of biological pretreatment, photo- and dark fermentation are presented. The recent developments made with genetic engineering and other factors (like pH, temperature, external additives, and nanomaterials) for enhancing the BioH₂ production from microorganisms using the LCFs are discussed in detail. Each parameter has been explored and analysed to highlight its effects on maximizing hydrogen yield and enhancing the production rate. This aims to contribute to the ongoing research about the potential of these individual parameters to improve BioH₂ production. Furthermore, future perspectives on integration and improvement required to enhance the lignocellulosic-biohydrogen production process are also reviewed.

1. Introduction

The global rise in population and economic development has put an unprecedented demand on energy supply. Improvement in human civilization and advancement in technology has more than doubled energy consumption per capita. The rise in energy demand is set to increase by 50% by the year 2030 and has put a strain on fuel sources that are becoming unable to keep up with the consumer demand in the public market and the industry [1]. Since the early dawn of industrialization, fossil fuels have played the role of the sole supplier for meeting our energy needs. Over the years, our growing dependency on fossil fuels has led to over-exploitation of the non-renewable resources causing depletion of the fossil fuel reserves and thereby dwindling the availability of the fuels. Moreover, scientists have identified fossil fuels as one of the main contributors to global warming [2]. The increasing CO₂ concentration in the atmosphere due to fossil fuels has led to adverse environmental effects and has resulted in climate change [3]. With the escalation in weather catastrophes and rise in geopolitical conflicts,

policymakers and scientists have now understood the danger of relying solely upon fossil fuels and therefore have commenced looking for alternatives that can ultimately replace fossil fuels and meet our rising energy demands [4].

Renewable energy sources have proved to be a highly viable alternative that can help curb carbon emissions and greenhouse gases released due to the utilization of fossil fuels. Scientists have claimed that the use of renewables can help protect the environment and assist in achieving energy security for the masses and ultimately give rise to a sustainable economy [5]. The major types of renewables that have gained popularity over the years include solar, wind, hydropower, and geothermal energy. The use of renewables has increased most predominantly in the electricity and transport sectors. However, the lack of advancement in the prerequisite technology required for extensive adaptation of the energy sources has halted the growth of the renewable energy sector [6]. However, another renewable resource that has slowly risen to prominence and has been used significantly is biofuels. Compared to other renewable sources, biofuels have found more

* Corresponding author.

E-mail address: mainak.mukhopadhyay12@gmail.com (M. Mukhopadhyay).

<https://doi.org/10.1016/j.ecmx.2021.100153>

Received 14 September 2021; Received in revised form 9 November 2021; Accepted 29 November 2021

Available online 4 December 2021

2590-1745/© 2021 The Authors. Published by Elsevier Ltd. This is an open access article under the CC BY license (<http://creativecommons.org/licenses/by/4.0/>).

acceptances and have seen a rapid surge in their overall production especially in developed countries. Extensive research into optimizing and increasing the production efficiency of biofuels has made it one of the most consumed renewable energy resources [7].

Biofuels include fuels derived from biomasses and their residuals; containing energy acquired from atmospheric carbon fixation [8]. The ability to produce biofuels from various biomasses has made them highly accessible, reliable, and sustainable fuels. Moreover, properties exhibited by the biofuels with the likes of high energy content, low emissions of greenhouse gases with little to zero harmful effects produced on the environment has made them the most likely to replace fossil-derived fuels [9]. Biofuels, which are net-zero carbon emitters, have been categorized into four different types based on the feedstocks from which they are derived and their availability in the near future [11]. The development and production of 'First generation' biofuels provides CO₂ benefits as well as encompasses the ability to blend with petroleum-based fuels partially, but the use of food crops such as sugarcane, corn, soya bean, and others have raised concerns with increasing food prices, competition in land use and effects on biodiversity along with the 'food vs. fuel' debate [10]. In comparison, 'Second generation' biofuels, although derived from plant biomass, primarily include lignocellulosic feedstocks such as agricultural and forestry residues, which are among the cheapest non-food materials available from plants in abundance. The use of lignocellulosic feedstocks provides several advantages, including complete replacement of petroleum-sourced fuels, non-existent competition with food sources, and rapid technological advancement that can ultimately reduce the overall costs of conversion and production of these 'Second generation' biofuels [11]. 'Third generation' biofuels are produced from algal biomass with a short harvesting cycle and high growth rate and require much lesser and simpler processing techniques for a much higher yield of the finished product [12]. Whereas 'Fourth generation' biofuels involve genetically modified algal biomass with features properties like improved photosynthetic efficiency, increased light penetration ability and significantly reduced photoinhibition, to achieve enhanced production of biofuels [13]. Some of the most common biofuels used most excessively and in high demand include bioethanol, biodiesel, biohydrogen, biogas and other synthetic biofuels [14].

In the past decade, biohydrogen (BioH₂) has become one of the most promising low-carbon alternative fuels derived from renewable and sustainable energy sources [15]. Among all the other biofuels, BioH₂ is considered one of the cleanest fuels with high energy efficiency. BioH₂ can be easily produced from various types of waste biomass and other feedstocks. However, one of the significant problems that have plagued BioH₂ production is its low yield [16]. Various biological processes have been used over the years for improved BioH₂ production. Integration of microorganisms has been the most effective way to boost bioprocessing efficiency and enhance BioH₂ production. The BioH₂ produced has the highest energy density, produces no pollution, and has no negative impact on the environment [17]. The market demand for BioH₂ has gone up steadily over the past few years and has received widespread attention as a next-generation energy carrier [18].

Recently, many studies have been carried out with a vast array of microorganisms by fixating on utilizing their metabolic and enzymatic activities to enhance BioH₂ production. Remarkably, one of the common factors that have linked them all is using lignocellulosic feedstocks (LCFs) as the substrate. Many previous reviews have discussed general BioH₂ production from LCFs using different pretreatments as well as through photo- and dark fermentation and other hydrogen production pathways. However, to the best of our knowledge, the review based on enhancing BioH₂ production utilizing and alternating different properties of microorganisms in the presence of LCFs as the substrate has been sparse. As a result, with this current review article we hope to provide an in-depth understanding and contribute a better insight into the process of enhanced BioH₂ production from LCFs. This review article will focus on the different LCFs used for BioH₂ production with a brief introduction to the properties and characteristics of the biofuel itself. The variety of

microorganisms used in the production process, from biological pretreatment to different fermentation techniques, will be summarized and actions taken to enhance microbially assisted BioH₂ production will be discussed in detail.

2. Biohydrogen – a novel renewable energy resource

Hydrogen is one of the most abundant elements on the planet formed from water under natural conditions and is a non-toxic, colourless, odourless, and highly combustible gas in normal atmospheric conditions [19]. Along with being the lightest element, hydrogen produces water vapour during combustion and is highly efficient in its conversion to produce energy [20]. The clean and green nature of hydrogen has made it especially valuable in the electric and transportation sector. In addition, hydrogen has also found its use in various applications in the chemical industry, oil refineries, and other industrial processes. Globally, hydrogen is mostly produced using conventional processes that involve electrical, thermal, and biochemical methods and are extracted from fossil fuels like methane, oil, and coal [21].

With the shift to renewables and introduction of waste-to-energy technologies, synthesis of BioH₂ has become an increasingly lucrative and sustainable option. A large amount of organic waste biomass generated every year has attracted scientists' attention to develop methods to convert these natural biological energy sources into chemical energy [22]. Different technologies involving physical, chemical and biological processes have been investigated. Biological processes include the use of microorganisms to carry out reactions like pretreatment and fermentation (photofermentation and dark fermentation) [23]. The microorganisms used have their unique characteristics and the ability to decompose the complex waste and produce BioH₂ simultaneously. Developing and utilizing the biological methods is highly cost-effective for industrial production of BioH₂ and is the most significant way to reduce and eliminate the use and production of hazardous chemicals during the designing, manufacturing and application process [24].

3. Lignocellulosic feedstocks – potentially sustainable sources for biohydrogen production

The utilization and growing demand for biofuels have generated widespread interest in a biomass-based economy. Biomass has been one of the most attractive and sustainable renewable resources that can be obtained from plants, animals, and microorganisms and used to produce biofuels. These carbon-based feedstocks have the capacity to replace the current fossil-fuel based energy systems and the petrochemical products required for various applications across the industry [25].

Lignocellulosic biomass has been the most promising feedstock for the production of eco-friendly biofuels, biochemicals as well as carbon-neutral bio-materials [26]. It is a renewable woody feedstock and a highly abundant terrestrial plant biomass, which consists of non-edible plant materials and therefore produces no competition with food crops and agricultural lands. LCFs are harvested mainly from agricultural and forestry residues, although different industrial and municipal wastes also provide other potential sources [27].

Different types of LCFs exhibit different types of characteristics with regards to their appearance and strength, but they are mainly composed of three basic components which make up approximately 90% of their dry weight. These are the homopolymeric cellulose (35–55 wt%), heteropolymeric hemicellulose (20–40 wt%), and lignin (10–25 wt%) (Fig. 1). The lignocellulosic polymers are linked with each other and form a mesh-like network through the formation of specific bonds between them, and play a role in providing both the physical appearance and the strength of the various LCFs [28]. The main component cellulose is a crystalline polysaccharide made up of D-glucose subunits linked together by β -1,4 glycosidic bonds, van der Waals forces and hydrogen bonds. It is one of the most abundant organic polymers available on

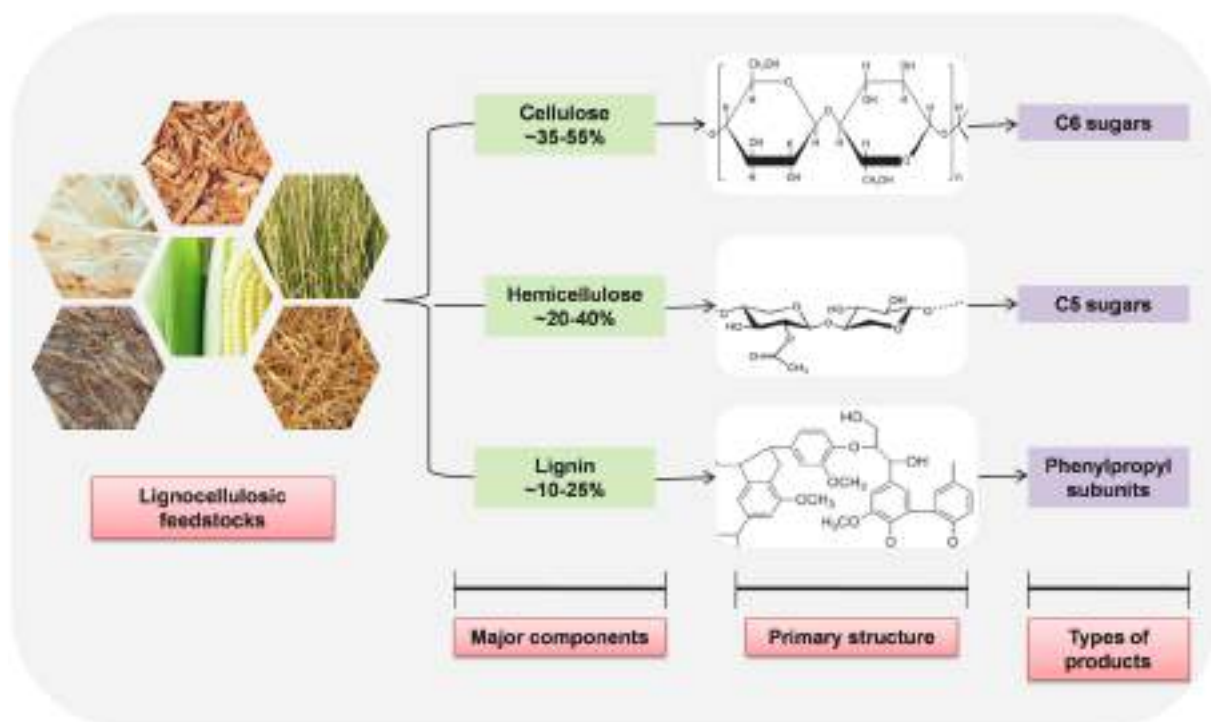


Fig. 1. Components of lignocellulosic feedstocks and the primary classes of products generated on hydrolysis.

earth and forms the basic building subunit of the plant cell walls. The long unbranched polymeric chains that makeup cellulose readily form microfibril structures that remain packed together with inter- and intra-molecular hydrogen bonding, allowing the formation of either a crystalline or amorphous structure. In comparison, hemicellulose is a complex and branched polysaccharide made up of heterogeneous mixtures of hexoses, pentoses and sugar acids which are all linked together by the much weaker α - and β -glycosidic bonds. The composition of this complex carbohydrate varies from hardwood to softwood structures, and is mainly responsible for forming cross-links with the cellulosic microfibrils and lignin. The final component which completes the structure of LCF is lignin – a recalcitrant heteropolymer composed of phenylpropanoid subunits linked together by aryl-ether (C-O-C) and carbon-carbon (C-C) bonds to various quantities. It is made up of three monolignol monomers, namely *p*-coumaryl alcohol, coniferyl alcohol and sinapyl alcohol, which together are responsible for the formation of lignin precursors which are *p*-hydroxyphenyl, guaiacyl and syringyl units that constitutes the phenylpropane subunits. The branched, polymeric and cross-linked structure of lignin provides structural rigidity and impermeability to the entire lignocellulosic polymer, therefore making it extremely hard to extract the cellulose and hemicellulose for the production of fermentable sugars [29-31].

Recently, LCFs have been adopted for biohydrogen production due to the presence of a high concentration of carbohydrates in the form of cellulose and hemicellulose. The most common LCFs used are corncobs, corn stover, corn stalk, switchgrass, rice straw, sugarcane bagasse, and wheat straw (Table 1 [29,31]). However, the complexity of the LCFs prevents the utilization of the lignocellulosic materials, making it impossible to produce BioH₂. Therefore, in order to digest or remove the lignin polymer, and increase the digestibility of the cellulose and hemicellulose during fermentation, several pretreatment processes including physical, chemical and biological methods have been developed. Physical pretreatment operations are costly and require a high energy input, whereas chemical methods requires not only hazardous chemicals but also produces toxic compounds that have a negative impact on the environment. In comparison, biological pretreatment process involves microorganisms and utilizes the enzymatic hydrolysis

Table 1

Composition of some common lignocellulosic feedstocks used for biohydrogen production.

Lignocellulosic feedstocks	Lignin (wt%)	Cellulose (wt%)	Hemicellulose (wt%)	Ash (wt %)	Extractives (wt%)
Corncoobs	15	45	35	–	–
Corn stover	18	40	22	–	–
Rice straw	18	32.1	24	–	–
Sugarcane bagasse	20.8	42.4	35.3	1.6	–
Switchgrass	5–20	30–50	10–40	4.5	–
Wheatstraw	16.3	39.1	24.1	1.3	19.2

of lignin which is more efficient and needs low energy input and has ultimately proven to be a cost-effective method with a wide range of applications and a higher yield of the final product [32]. The removal of the lignin polymer by the naturally occurring microorganisms not only help in the production of lignocellulosic BioH₂ after proper fermentation reactions but also help in the production of several value-added products.

4. Lignocellulosic biohydrogen production process

The less energy intensive and environment friendly properties have made the biological process for BioH₂ production to be highly beneficial. The utilization of microorganisms and their natural biochemical machinery has been proven to play an important role in the bioconversion of LCFs to BioH₂. The biological processes employed during BioH₂ production include the biological pretreatment process followed with either a photofermentation (PF) or dark fermentation (DF) reaction (Fig. 2. Table 2 summarizes the major differences between the three biological processes that are employed for lignocellulosic BioH₂ production.

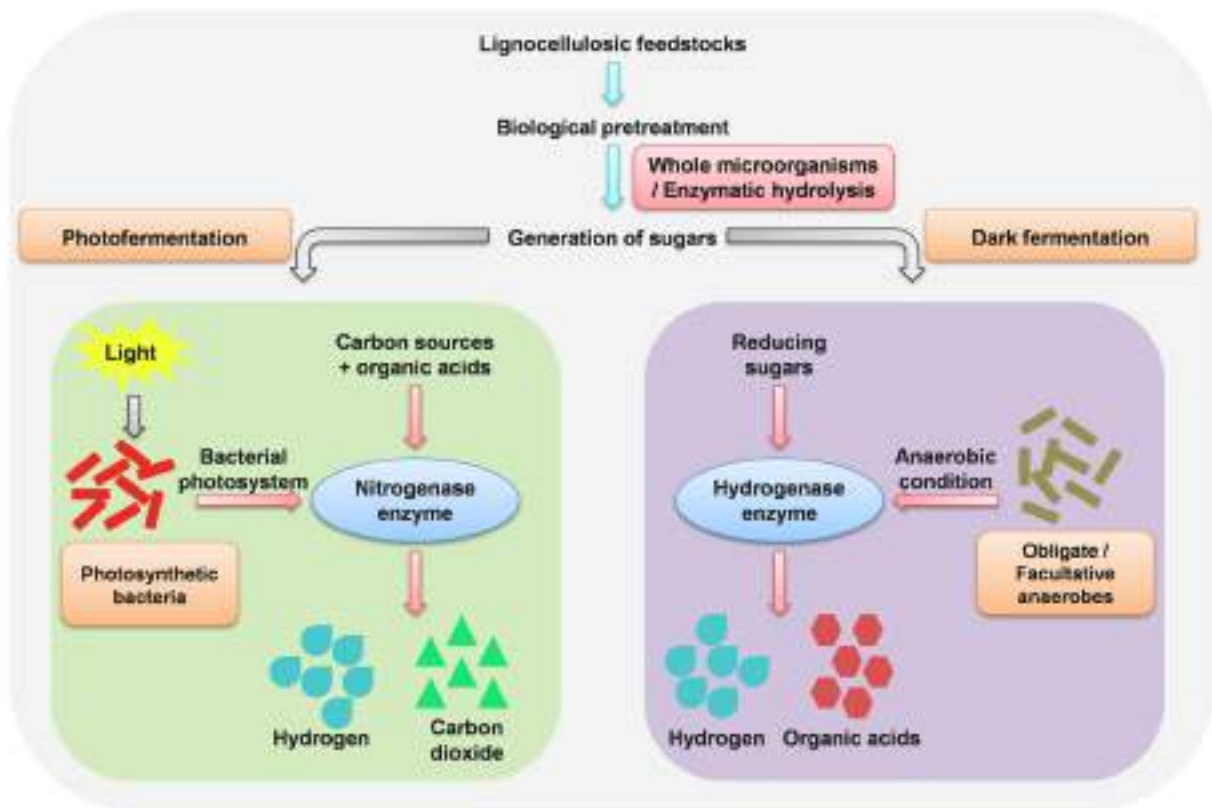


Fig. 2. Different pathways of photo- and dark fermentation that are involved in biohydrogen production from lignocellulosic feedstocks.

Table 2

Comparison between different lignocellulosic biohydrogen production processes.

Characteristics	Biological pretreatment	Photofermentation	Dark fermentation
Main substrates	Lignin and hemicellulose	Sugars and volatile fatty acids	Carbohydrates, proteins and glycerol
Key enzymes	Ligninolytic and cellulolytic enzymes	Hydrogenase and nitrogenase enzyme systems	Only hydrogenase enzyme system
End products	Degradation of lignin and hemicellulose	Hydrogen and carbon dioxide	Hydrogen, carbon dioxide, organic acids and alcohol
Maintenance of continuous operation	Easy	Difficult	Easy
Operational cost	For whole cell – Low For enzymatic - High	High	Medium
Types of microorganisms	Cellulolytic bacteria, ascomycetes and basidiomycetes fungi	Photosynthetic bacteria	Fermentative bacteria
Examples of microorganisms	Cellulolytic bacteria - <i>Cellulomonas fimi</i> and <i>Thermomonospora fusca</i> , ligninolytic bacteria - <i>Azospirillum lipoferum</i> and <i>Bacillus subtilis</i> , ascomycetes fungi - <i>Aspergillus</i> sp., <i>Penicillium</i> sp., and <i>Trichoderma</i> sp., basidiomycetes fungi - <i>Schizophyllum</i> sp., and <i>Fomitopsis palustris</i>	<i>Rhodobium</i> sp., <i>Rhodobacter</i> sp., <i>Rhodospirillum</i> sp., and <i>Rhodopseudomonas</i> sp.	<i>Clostridium</i> sp., such as <i>C. butyricum</i> , <i>C. acetobutylicum</i> , <i>C. beijerinckii</i> , and <i>C. thermocellum</i> , and lactic acid bacteria such as <i>Cellulomonas</i> , <i>Klebsiella pneumoniae</i>
Advantages	<u>Whole cell</u> <ul style="list-style-type: none"> Low energy input required Economically friendly <u>Enzymatic</u> <ul style="list-style-type: none"> Inhibitor generation is negligible No harsh conditions required 	<ul style="list-style-type: none"> A broad spectrum of light energy is used Has the ability to use a wide variety of substrates 	<ul style="list-style-type: none"> No external light energy is required for hydrogen production Different carbon sources can be used as substrates Produces highly valuable metabolites as by-products
Disadvantages	<u>Whole cell</u> <ul style="list-style-type: none"> Rate of hydrolysis is low Presence of contamination proves to be problematic <u>Enzymatic</u> <ul style="list-style-type: none"> Catalytic activity is slow Inhibition of substrate and product cause problems 	<ul style="list-style-type: none"> Light conversion efficiency is low Oxygen acts as a strong inhibitor of hydrogenase enzyme system 	<ul style="list-style-type: none"> High energy input is required Large amounts of by-products are produced Final gas produced contains carbon dioxide which needs to be separated

4.1. Biological pretreatment

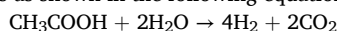
In biological pretreatment, ligninolytic microorganisms or enzymes are used for the depolymerization of LCFs. This first step towards BioH₂ production acts as a precursor to the subsequent hydrolysis and fermentation reactions. Biological pretreatment of biomass primarily

involves four distinct techniques, such as (i) pretreatment using microorganisms (e.g., fungal and bacterial), (ii) pretreatment using microbial consortium, (iii) ensilaging, and (iv) pretreatment using enzymes [33]. The microorganisms that are utilized depolymerize lignin by secreting extracellular ligninolytic enzymes involved in catalysing various biochemical reactions. The microbial inoculum subsequently grows on

the biomass and ultimately results in lignin degradation. However, the incubation time and depolymerization rate varies from microbes to microbes and sometimes ranges from weeks to months [32]. In order to avoid this, enzymes are purified from bacteria and fungi, which are then used directly for the pretreatment technique. Although, enzymatic production and optimization along with purification may prove to be costly, thus increasing the overall costs of the process. The use of microbial consortia greatly reduces the pretreatment time and is advantageous due to improved hydrolytic efficiency, high adaptability, and increased substrate utilization rate. The synergistic action of the enzymes produced from different species of bacteria and fungi together is particularly effective to bring about lignin degradation [34–36]. Ensilaging is another advanced technology developed for biological pretreatment which involves the use of anaerobic fermentation by lactic acid bacteria resulting in the breakdown of macromolecules producing different organic acids and preventing microbial contamination. But factors like biomass composition, microorganisms and dry matter content, greatly affect the final yield in the ensilaging process [33]. Biological pretreatment is a highly effective and efficient method, although more detailed investigation is required in order to decrease the overall time required for the process.

Photofermentation

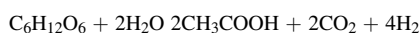
PF is accomplished in the presence of sunlight with the help of anaerobic photosynthetic bacteria which mostly includes purple non-sulphur bacteria [34]. These bacteria facilitate the PF process by utilizing the nitrogenase enzyme to produce hydrogen and carbon dioxide by metabolizing volatile organic acids. The photosynthetic bacteria only has photosystem I and uses external organic acids like acetate, lactate, malate, and butyrate, as suitable electron donors to produce hydrogen gas as shown in the following equation [35]:



The nitrogenase enzyme catalyses the reaction of protons and electrons with adenosine triphosphate (ATP) to produce ammonia, hydrogen, adenosine diphosphate (ADP) and inorganic phosphate (Pi). The use of organic substrates has increased the applicability of the purple non-sulphur bacteria to a wide range of waste biomass for BioH₂ production [37]. These bacteria have the capacity to liberate almost 100% of the electrons from the biomass in presence of light to generate hydrogen and carbon dioxide by using the nitrogenase enzyme system. In addition, advantages like high substrate conversion efficiency, great metabolic versatility and ability to withstand a wide range of light intensity, has facilitated the use of the PF process for BioH₂ production [38].

4.3. Dark fermentation

DF is performed in the absence of sunlight by utilizing obligate or facultative anaerobes to produce hydrogen from organic substrates and waste biomass [35]. Pretreatment of biomass followed by hydrolysis produces reducing sugars which are used as substrates for the anaerobic production of hydrogen, and other high-value intermediates such as carbon dioxide, organic acids, and alcohol [39]. The hydrogenase enzyme system carries out the oxidation of electrons along with subsequent reduction of protons to produce hydrogen [40]. Pyruvate is a key metabolite produced during the anaerobic fermentation process for hydrogen generation, which can be further enzymatically converted to acetyl CoA. Other notable metabolites produced in the fermentation process are acetic acid and butyric acid alongside the hydrogen gas [41]:



In comparison to PF, DF is highly advantageous as it is inexpensive, requires less maintenance, with no light source, and requires smaller bioreactors [37]. However, a major stumbling block in this fermentation

process has been the substrate's organic load, which is not fully converted during the reaction process, thus resulting in a low hydrogen yield [39].

5. Engineering of microorganisms for enhanced biohydrogen production

LCFs have always been deemed as the most sustainable source for the generation of BioH₂. Moreover, the integration of microorganisms for successful hydrolysis and fermentation of LCFs has received tremendous attention in the recent years in order to boost BioH₂ production in an economically cost-effective way (Fig. 3). This is why it is highly essential to focus on the wild type and recombinant microbial strains responsible for the efficient bioprocessing of LCFs to BioH₂.

5.1. Biological pretreatment

In the biological pretreatment method, the cellulose and hemicellulose counterparts in the biomass get hydrolysed into monomeric sugars and simultaneously degrade the lignin polymer. Microorganisms used solely for the biological process secrete a wide range of enzymes that fall into three categories: cellulolytic, hemicellulolytic, and ligninolytic enzymes. Mainly ascomycetes and basidiomycetes fungi and several bacteria have been identified to possess the enzymes required for the hydrolysis of LCFs [42].

The most common bacterial strains which have proved to be highly efficient in the pretreatment process belongs to the *Clostridium* sp., *Cellulomonas* sp., *Bacillus* sp., *Thermomonospora* sp., and *Streptomyces* sp., etc. Some notable cellulolytic bacteria that have been extensively studied for their high cellulase production are *Cellulomonas fimi* and *Thermomonospora fusca*. Other bacterial strains such as *Azospirillum lipoferum* and *Bacillus subtilis* have been identified to produce the ligninolytic enzyme laccase which can carry out lignin depolymerization [32]. Recently, there has been an increased interest in screening for extremophiles due to their much faster pace of BioH₂ production from LCFs [43]. The newly isolated thermophilic strain *Thermoanaerobacterium* sp. strain F6 produced 1822.6 and 826.3 mL H₂/L of hydrogen using corn cob and sugarcane bagasse respectively [44]. Another study utilized a thermophilic consortium consisting of *Thermoanaerobacterium* sp., *Clostridia* sp., and *Geobacillus* sp., for production of BioH₂ from prairie cordgrass. Optimized treatment conditions of the biomass by the consortium increased the hydrogen production from 1.07 mmol H₂/g to 2.2 mmol H₂/g of the biomass [45].

In addition to bacteria, fungi also possess distinct lignocellulolytic enzymes for LCFs degradation. The various species of fungi used for biological pretreatment includes ascomycetes (e.g. *Aspergillus* sp., *Penicillium* sp., and *Trichoderma* sp.) as well as basidiomycetes (e.g. *Schizophyllum* sp., and *Fomitopsis palustris*) [32]. The most studied ligninolytic enzymes producing fungi are *Phanerochaete chrysosporium* and *Pleurotus* sp. Fungi have been really useful for their ability to degrade the lignin polymer directly without any help. Several mixed cultures of fungi have been grown together in order to increase the lignin depolymerization rate [46]. The extracellular production of most enzymes has led to the utilization of crude enzyme lysates and pure enzymes directly onto the LCFs. Newly identified thermostable laccase from the fungus *Trichoderma asperellum* strain BPLMBT1 has been able to remove approximately 76.93% of lignin from sweet sorghum stover biomass resulting in 402.01 mL of BioH₂ production, which was found to be 3.26-fold higher in comparison to control which didn't have any form of enzymatic pretreatment [47]. Overall, biological pretreatment has turned out to be an increasingly attractive and sustainable process for BioH₂ production.

5.1.1. Use of different additives

Decreasing the microbial treatment time and simultaneously increasing the final yield of BioH₂ has always been the main focus of the biological pretreatment process. This has resulted in the addition of

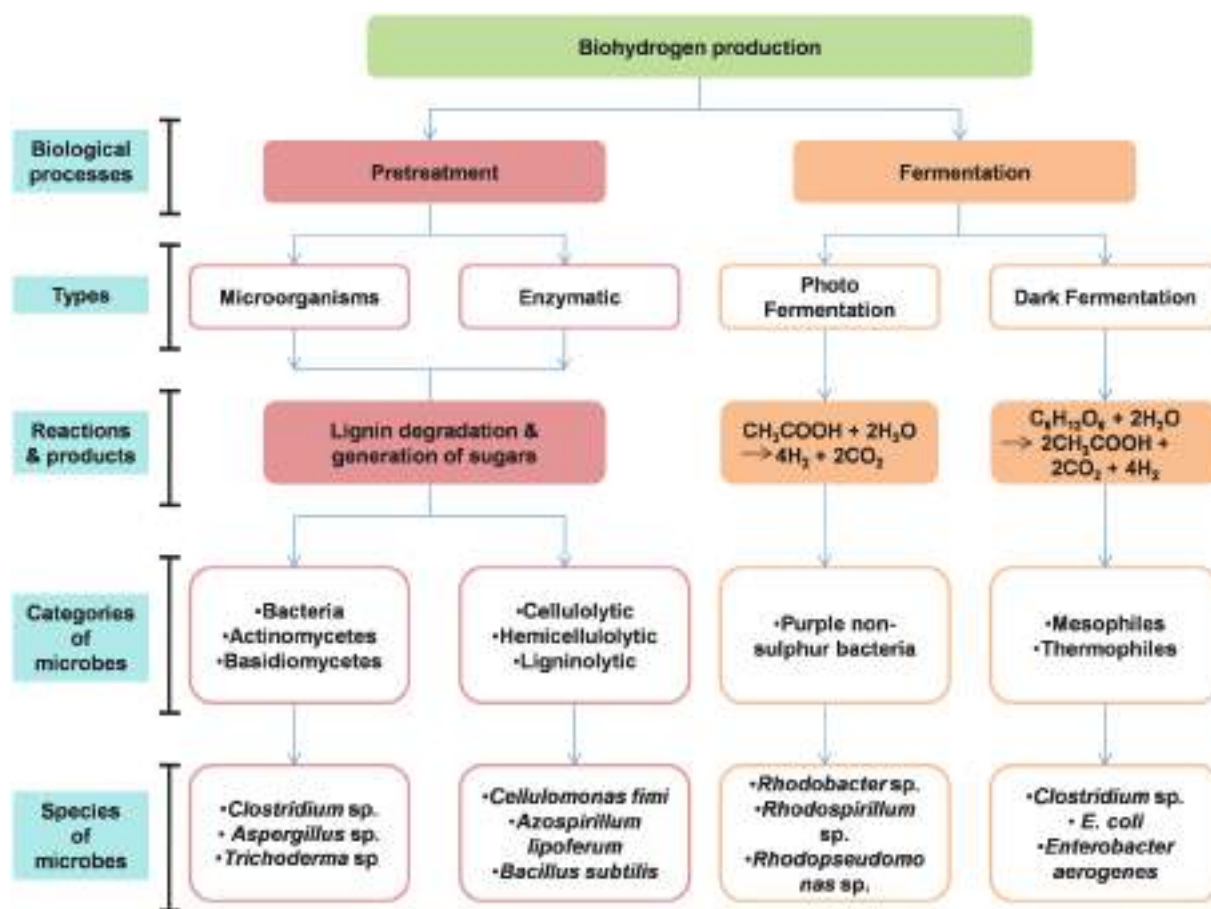


Fig. 3. General bioconversion processes and the microorganisms employed for biohydrogen production.

different types of additives ranging from chemical to biological along with the microbes during the pretreatment method for rapid degradation of the LCFs in order to produce biohydrogen (Table 3).

In a study, a combination of sodium carbonate and sodium sulphide was used along with the crude enzyme lysate produced by the *Streptomyces* sp. MDS for the pretreatment of sugarcane bagasse. This not only resulted in a higher yield of reducing sugars amounting to 592 mg/g but subsequent hydrolysis using the microbial strain *Clostridium beijerinckii* KCTC1785 led to a cumulative hydrogen production of 1485 mL/L with a production rate of 61.87 mL/L/h [48]. Cumulative addition of 0.75% Triton X-100 and 15 mM of sodium carbonate with the bacterium *Clostridium thermocellum* ATCC 27,405 utilizing waste date seeds as the substrate, led to a 40.6% increase in the total hydrogen yield [49]. In another study, a co-culture formed between the hydrolytic microbe *Clostridium cellulovorans* and the fermentative microbe *Clostridium acetobutylicum* led to a 2- to 3-fold improvement in BioH₂ production using wheat straw as substrate [50].

Another enhancement study involved the use of microorganisms present in bovine ruminal fluid in presence of *Clostridium acetobutylicum* resulting in the yield of greater than 40 g/L glucose from agave biomass ultimately leading to a total yield of 150 L of hydrogen per Kg of the biomass [51]. In comparison, corncob treated with 2% sulphuric acid before the addition of bovine ruminal fluid with *Clostridium acetobutylicum* were able to produce 575 mL of hydrogen which was equivalent to 132 L H₂/Kg of biomass [52]. Hydrogen production from the organic fraction of the municipal solid waste pretreated with *Bacillus subtilis* in a combination of bacteria/sludge ratio of 0.25 led to a volumetric hydrogen production of 564.4 ± 10.9 mL [53]. The thermophilic bacterium *Thermoanaerobacterium thermosaccharolyticum* W16 was used for the pretreatment of corn stover hydrolysate by mixing the inoculum

with three different types of seed sludge – which were rotten corn stover, cow dung compost and sludge from anaerobic digestion. Hydrogen yield increased from 8.78 to 9.17 mmol H₂/g utilized sugar in presence of rotten corn stover, 8.18–8.42 mmol H₂/g utilized sugar in presence of cow dung compost, and 8.55–9.17 mmol H₂/g utilized sugar in presence of sludge. Analysis on the microbial communities that dominated this different sludge turned out to be mostly *Thermoanaerobacterium* spp. and *Clostridium* spp. which are predominantly responsible for BioH₂ production [54]. Moreover, a combination of the thermo-anaerobic bacteria *Ruminiclostridium thermocellum* strain M3 with domestic sewage sludge increased the cumulative hydrogen production in a variety of LCFs like rice straw (0.66–6.42 mmol H₂/g substrate), corncob (0.61–5.55 mmol H₂/g substrate), and pine wood waste (0.58–5.32 mmol H₂/g substrate) [55].

5.2. Photofermentation

In PF, BioH₂ production is carried out by the purple non-sulphur photosynthetic bacteria which grows under anaerobic or microaerobic conditions, and has the capacity to use a wide range of organic compounds as their substrates. The most common photosynthetic bacteria used for BioH₂ production belongs to the *Rhodobium* sp., *Rhodobacter* sp., *Rhodospirillum* sp., and *Rhodopseudomonas* sp., out of which the *Rhodobacter* species have been extensively studied and widely used for photofermentative hydrogen production [56–58].

In a recent study, *Rhodobacter sphaeroides* was used for BioH₂ production by photofermentation using brewery waste. It was observed that *R. sphaeroides* had a higher growth rate in the presence of diluted brewery waste which resulted in a ~ 2.5 fold increase in hydrogen production [59]. Use of *Rhodopseudomonas pseudopalustris* DSM 123 on

Table 3
Summary of different additives used for enhancing biohydrogen production.

Microorganisms	Lignocellulosic feedstock	Additives	Productivity		References
			Increase in biohydrogen production	Final yield of biohydrogen	
Biological pretreatment					
<i>Streptomyces</i> sp. MDS followed with dark fermentation by <i>Clostridium beijerinckii</i> KCTC1785	Sugarcane bagasse	Sodium carbonate and sodium sulphide	–	0.733 mmol H ₂ /g of sugarcane bagasse	[48]
<i>Clostridium thermocellum</i> ATCC 27,405	Waste date seeds	0.75% Triton X-100 and 15 mM of sodium carbonate	~40.6%	146.19 mmol/L	[49]
Co-culture between the hydrolytic microbe <i>Clostridium cellulovorans</i> and the fermentative microbe <i>Clostridium acetobutylicum</i>	Wheat straw	Microbes had a inoculation ratio of 5:3	~2–3 fold	128 mL/L	[50]
<i>Clostridium acetobutylicum</i>	Agave biomass	Bovine ruminal fluid	–	150 L H ₂ /Kg of biomass	[51]
<i>Clostridium acetobutylicum</i>	Corncob	2 % sulphuric acid	–	132 L H ₂ /Kg of biomass	[52]
<i>Bacillus subtilis</i>	Organic fraction of municipal solid waste	Bacteria/sludge ratio used was 0.25	–	1.61 L H ₂ /L of substrate	[53]
<i>Thermoanaerobacterium thermosaccharolyticum</i> W16	Corn stover hydrolysate	Rotten corn stover Cow dung compost Sludge	–	8.78 – 9.17 mmol H ₂ /g utilized sugar 8.18–8.42 mmol H ₂ /g utilized sugar 8.55–9.17 mmol H ₂ /g utilized sugar	[54]
<i>Ruminiclostridium thermocellum</i> strain M3	Rice straw Corncob Pine wood waste	Domestic sewage sludge	–	0.66–6.42 mmol H ₂ /g substrate 0.61–5.55 mmol H ₂ /g substrate 0.58–5.32 mmol H ₂ /g substrate	[55]
Photofermentation					
<i>Rhodopseudomonas palustris</i>	–	Acetate Butyrate Lactate	–	1.58 mol H ₂ /mol 4.92 mol H ₂ /mol 2.57 mol H ₂ /mol	[67]
<i>Rhodobacter sphaeroides</i> MDC6521	–	Succinate and acetate	~2–3 fold	~6.5 mmol H ₂ /g of biomass	[68]
HAU-M1 microbial consortium	Duckweed and corn straw biomass	Carbon to nitrogen ratio (5:1)	–	85.6 mL/g of biomass	[69]
HAU-M1 microbial consortium	Cornstalk	Potassium phosphate buffer (pH 6.5)	–	23.96 mL/h	[70]
HAU-M1 microbial consortium	Cornstalk	Sodium phosphate buffer (pH 6)	–	132.69 mL/g of corn stalk	[71]
<i>Rhodopseudomonas palustris</i> ATH 2.1.37	–	40° C	~4 fold	11.0 ± 0.9 mL/h	[72]
HAU-M1 microbial consortium	Cornstalk	Zeolite (0.2 g/g of cornstalk) Kieselguhr (0.2 g/g of cornstalk)	~33.33% ~15.93%	160.4 ± 2.7 mL/g of cornstalk	[73]
HAU-M1 microbial consortium	<i>Arundo donax</i> L.	Glycerol (15 g/L)	~294%	–	[74]
HAU-M1 microbial consortium	Corn straw	Basalt fiber	~5.23%	323.94 mL	[75]
<i>Rhodopseudomonas palustris</i> CGA009	Hydrolysate of brewers spent grain	Syringaldehyde (0.03 g/L)	~1.4 fold	960 mL	[76]
HAU-M1 microbial consortium	Corn straw	Nano-TiO ₂ (300 mg/L)	~27.9%	–	[77]
Dark fermentation					
<i>Clostridium thermosaccharolyticum</i>	Sweet sorghum stalks	Dilute sulphuric acid	~76% hydrogen, ~84% acetic acid, ~113% butyric acid	5.77 mmol/g substrate, 2.17 g/L acetic acid, 2.07 g/L butyric acid	[86]
<i>Clostridium</i> sp.	<i>Lolium perenne</i> L.	FeSO ₄ (400 mg/L)	~49.6%	72.8 mL/g-dry grass	[87]
<i>Lachnospiraceae</i>	Pretreated sugarcane bagasse	Biochar	~317.1%	–	[88]
<i>Thermoanaerobacterium thermosaccharolyticum</i> M18	Cornstalk	Biochar, derived from residue cornstalk	–	286.1 mL H ₂ /g substrate	[89]
<i>Clostridium</i> and <i>Lactobacillus</i> , <i>Blautia</i> and <i>Propionibacterium</i>	80% tequila vinasse and 20% nixtamalization wastewater (w/w)	pH reduced from 6.5 to 5.8	~17%	–	[90]
Anaerobic granular sludge used as the microbial source	Hydrolysate of <i>Agave tequilana</i> bagasse	Activated carbon(1% p/v)	~33%	–	[91]
<i>Enterobacter cancerogeous</i> HG6 2Aand <i>Enterobacter homaechei</i> 83 at a ratio of 0.9:1	–	Activated carbon	~259%	–	[92]
<i>Enterobacter aerogenes</i>	Date-palm fruit wastes	Fe ₃ O ₄ nanoparticles	~3 fold	238.7 mL/g of substrate	[95]

tequila vinasses produced 860 mL H₂/L during PF reactions [60]. Single-stage PF process carried out with *Rp. palustris* on the sucrose-based wastes i.e. sugar beet molasses have a maximum of hydrogen productivity of 0.55 mmol/L h [61]. Newly isolated *R. capsulatus* produced a hydrogen yield of 1.96 mol H₂/moles sugar under optimized conditions using raw sugarcane bagasse as the main feedstock [62]. A novel photosynthetic bacterial strain identified as *Rubrivax benzoatilyticus* TERI-CHL1 produced 86.4 mmol/L of cumulative hydrogen under optimized conditions from spent effluent with a 75% H₂ yield efficiency [63].

A co-culture of photosynthetic bacteria containing *Rs. rubrum*, *R. capsulatus* and *Rp. palustris* produced hydrogen with a maximum yield of 642 ± 22 mL using starch based agricultural residues as substrates [64]. Utilizing the cellulolytic bacterium, *Cellulomonas fimi* in combination with *Rp. palustris* on low-cost cellulosic substrate generated hydrogen with a yield of 44 mmol H₂/L at the highest substrate concentration of 5 g/L [65]. A mixed consortium of photosynthetic bacteria containing 27% *Rs. rubrum*, 25% *Rp. capsulatus*, 28% *Rp. palustris*, 9% *R. sphaeroides*, and 11% *R. capsulatus*(HAU-M1), was used for hydrogen production from corn stover biomass with separate saccharification photofermentation (SSP) and separate hydrolysis photofermentation (SHP) methods. The consortium gave a hydrogen yield of 83.87 mL H₂/g corn stover with SSP method that was 27.8% higher than that of SHP [66].

5.2.1. Use of different additives

Extensive research into several photosynthetic bacteria has revealed that crucial factors like pH, lighting conditions, substrate concentrations, chemical and biological additives, and different biological pretreatment conditions, enhances BioH₂ production via the PF process utilizing LCFs (Table 3).

A study reported that the photosynthetic bacteria *Rp. palustris* mediated hydrogen production was affected in presence of different lighting conditions and a variety of carbon sources. Incandescent light led to an increased rate of cell growth followed by enhanced hydrogen yields of 1.58, 4.92 and 2.57 mol H₂/mol when acetate, butyrate and lactate were respectively used as carbon sources [67]. In comparison, a mixture of succinate and acetate as a carbon mixture with the bacterium *R. sphaeroides* MDC6521 enhanced the hydrogen production approximately ~ 2–3 fold with a cumulative yield of ~ 6.5 mmol H₂/g of biomass [68]. Co-digestion of duckweed and corn straw biomass with the HAU-M1 microbial consortium in the presence of a high carbon to nitrogen ratio (5:1) enhanced the final hydrogen yield from 78 mL/g of biomass to 85.6 mL/g of biomass [69].

Change in pH also has an effect on photofermentative hydrogen production. The HAU-M1 consortium produces hydrogen from biomass in presence of potassium phosphate buffer with pH values ranging from 5 to 7. pH 6.5 produced the maximum hydrogen production rate that was 23.96 mL/h in comparison to the rate of 5.59 and 5.42 mL/h produced in presence of pH 5 and 7.5 respectively [70]. In comparison, a pH 6 sodium phosphate buffer led to an increase in conversion efficiency by 9.84% with a hydrogen yield of 132.69 mL/g of corn stalk using the HAU-M1 consortia [71]. In another study, increasing the temperature optima of a *Rp. palustris* strain to 40 °C enhanced the hydrogen production upto ~ 4 fold as compared to 300C [72]. Addition of the catalysts zeolite and kieselguhr separately to the HAU-M1 consortia increased the hydrogen yield from corn stalk by 33.33% and 15.93% respectively, in comparison to control [73]. A correlation was also found between glycerol addition and hydrogen production in HAU-M1 consortia. Utilizing *Arundo donax* L. as a substrate, the consortia enhanced hydrogen production by 294% in presence of 15 g/L of optimal glycerol concentration [74]. Even the presence of basalt fiber has been observed to promote bacterial growth and enhanced the bioconversion rate of corn straw by 5.23% with a maximum hydrogen yield of 323.94 mL [75]. Another study reported, the addition of compounds such as syringaldehyde (0.03 g/L) to steam explosion hydrolysate of brewers

spent grain in the fermentation media of *Rp. palustris* CGA009 enhanced BioH₂ production by 1.4 fold to 960 mL, in contrast to vanillin-containing media [76].

Addition of the photocatalyst nano-TiO₂ (300 mg/L) to the HAU-M1 consortia produced significant effects on the photo-fermentative hydrogen production from corn straw. Nano-TiO₂ promoted the metabolism of butyric acid and acetic acid and reduced the concentration of intermediary products. This resulted in an increase in the cumulative hydrogen volume by 32.6% along with the maximum hydrogen production rate and average hydrogen content by 27.9% and 8.3%, respectively in comparison to the control [77]. Although the use of photocatalytic nanoparticles has recently been identified to impact the production of BioH₂ using photosynthetic bacteria, research with photofermentative reaction utilizing LCFs has been sparse.

5.2.2. Use of genetic engineering

Genetic engineering has been a powerful tool to utilize for the photofermentative bacteria in order to enhance the BioH₂ production process. Different methods have been employed to produce mutant strains of naturally occurring photosynthetic bacteria and increase the production yield of BioH₂ (Table 4).

In a recent study, a mutant strain (*Hup*[−]) of the bacterium *R. sphaeroides* HY01 was generated which increased the growth rate and enhanced the hydrogen production rate up to 4.62 mol H₂/mol of reducing sugar generated from maize straw hydrolysate [78]. The growth in presence of NH₄Cl was repressed in case of a double deletion mutant generated from *R. sphaeroides* HY01 (*cbbR*[−], *pycA*[−]); whereas the growth as well as the hydrogen yields of a transposon mutant with an inactivated *pycA* gene (*cbbR*[−], Δ *pycA*) was enhanced by 2%, 10.5%, and 26.8% in the presence of 0.6, 1.2, and 1.8 mM NH₄Cl respectively. The hydrogen production rates were also improved by 15.9%, 6.2% and 46.1% in presence of the three concentrations of NH₄Cl [79]. A mutant of the *R. capsulatus* strain JL1 with a *cheR2* gene deletion changed its pH from faintly acidic to weakly alkaline condition, and gave a maximum hydrogen yield of 4406.7 ± 45.9 mL/L and 54.1 ± 1.6 mL/L in presence of acetate and butyrate as direct carbon sources, which accounted for an enhancement of 36.3% and 12.3% over the wild type strain. With corn stalk hydrolysate as a substrate, the mutant generated hydrogen up to 224.85 ± 5.18 mL-H₂/g of biomass which resulted in a 171.43% increase in comparison to the wild type strain [80]. A temperature-tolerant mutant strain of *R. capsulatus* MX01 exhibited an increased hydrogen production at a higher culture temperature of 33° C and light intensity of 5000 lx. Using corn stalk hydrolysate, the mutant strain had an enhanced BioH₂ yield of 3.64 ± 0.18 mol-H₂/g of biomass and a production rate of 40.07 ± 1.70 mmol-H₂/(h.g-cornstalk) along with an energy conversion efficiency of 10.6% [81]. Another ammonium-tolerant mutant strain of *R. capsulatus* strain WH02 was produced through transposon mutagenesis. Batch experiments with optimized ammonia concentration (2–8 mmol/L) showed an increased hydrogen yield by 3.74 folds. With sugarcane bagasse containing high ammonium concentration (87.94 ± 2.22 mmol/L) the maximum hydrogen production amounted to 153.96 ± 1.98 mL-H₂/g of the bagasse along with an energy conversion efficiency which increased by 10.95%, thereby making it highly feasible to produce BioH₂ from LCFs containing high ammonium [82].

5.3. Dark fermentation

In DF, the type of microorganism used plays an essential parameter as the hydrogen yield consecutively depends on the bacterial metabolism. A wide variety of obligate and facultative anaerobes are used for the DF reaction. Although cocultures are mostly used but pure cultures make it easy to discern any metabolic shift that might takes place while utilizing LCFs as substrates for BioH₂ production. The most extensively studied anaerobes belong to the *Clostridium* sp., such as *C. butyricum*, *C. acetobutylicum*, *C. beijerinckii*, and *C. thermocellum*. *Clostridium* sp. is

Table 4
Summary of different genetic engineering used for enhancing biohydrogen production.

Microorganisms	Lignocellulosic feedstock	Genetic modification	Productivity		References
			Increase in biohydrogen production	Final yield of biohydrogen	
Photofermentation					
<i>Rhodobacter sphaeroides</i> HY01	Maize straw hydrolysate	<i>Hup</i> [−]	–	4.62 mol H ₂ /mol reducing sugar	[78]
<i>Rhodobacter sphaeroides</i> HY01	–	<i>cbbR</i> [−] , Δ <i>pycA</i>		–	[79]
		0.6 mM NH ₄ Cl, 1.2 mM NH ₄ Cl, 1.8 mM NH ₄ Cl	~2% ~10.5% ~26.8%		
<i>Rhodobacter capsulatus</i> JL1	Corn stalk hydrolysate	Δ <i>cheR2</i>	~171.43%	224.85 ± 5.18 mL-H ₂ /g of biomass	[80]
<i>Rhodobacter capsulatus</i> MX01	Corn stalk hydrolysate	Temperature-tolerant mutant. Cultured at a temperature of 33 °C and light intensity of 5000 lx	–	3.64 ± 0.18 mol-H ₂ /g of biomass	[81]
<i>Rhodobacter capsulatus</i> WH02	Sugarcane bagasse	Ammonium-tolerant mutant	–	153.96 ± 1.98 mL-H ₂ /g of bagasse	[82]
Dark fermentation					
<i>Enterobacter aerogenes</i>	–	Irradiation with ⁶⁰ Co γ -rays	~81.8%	–	[97]
<i>Enterobacter aerogenes</i>	Acid pretreated biomass of <i>Alternanthera philoxeroides</i>	Irradiation with ⁶⁰ Co γ -rays	~31.8%	–	[98]

the most dominant hydrogen producing bacteria in the DF process. Some facultative anaerobes which are also capable of producing hydrogen are *E. coli*, *E. cloacae*, and *E. aerogenes*, among others [83,84]. Other lesser known bacteria used for hydrogen production through the dark fermentative process includes *Bacillus subtilis*, the lactic acid bacteria – *Cellulomonas*, *Klebsiella pneumoniae*, and some thermophilic archaea like *Caldicellulosiruptor saccharolyticus* and *Thermotoga neapolitana* [85].

5.3.1. Use of different additives

Similar to PF, the microorganisms utilized for the DF process has also been characterized on the basis of several additive factors which bring about the amplified BioH₂ generation while using various LCFs as substrates (Table 3).

Research into the addition of a dilute acid treatment in between a two-step DF process revealed the additional step plays a potential role in hydrogen production. Sweet sorghum stalks were used as the substrate for carrying out the fermentation process using the *C. thermosaccharolyticum* bacterium. After the initial step of the fermentation with the biomass, a 1 h treatment with dilute sulphuric acid at an optimum concentration of 1.5% (w/v) at 120 °C with 10 g/L of substrate increased the production of hydrogen by 76%, acetic acid by 84%, and butyric acid by 113%. The total yield after the two-step process amounted to 5.77 mmol/g-substrate of hydrogen, 2.17 g/L acetic acid and 2.07 g/L butyric acid [86]. In a study, microbial communities present in seed sludge were used directly for BioH₂ production from grass (*Lolium perenne* L.). Addition of Fe²⁺ significantly improved the microbial activity on the biomass as well as enriched hydrogen producers, making *Clostridium* sp. the dominant bacteria. Moreover, Fe²⁺ (400 mg/L) also increased the utilization of organics by the hydrogen producers from 15.9% to 20.6%. This subsequently led to an increased yield of BioH₂ production from 48.7 mL/g-dry grass in the control group to 72.8 mL/g-dry grass in Fe²⁺ added group, which was relatively 49.6% higher [87]. Biochar, produced by the thermal decomposition of carbonaceous biomass, has generated research interests as a suitable additive for improving the performance of the anaerobic digestion during dark fermentative reaction and influencing hydrogen production. In a study it was observed that biochar boosted hydrogen production by 317.1% in the presence of pretreated sugarcane bagasse and a heat-shocked consortium derived from sewage sludge. Biochar was found to stimulate bacterial growth especially that of cellulolytic *Lachnospiraceae*, and improve critical enzymatic activities and manipulate the NADH/NAD⁺ ratio, thereby increasing the electron

transfer efficiency of the fermentation system [88]. Another study proposed quite an innovative approach to utilize biochar in the hydrogen production process. Biochar, derived from residue cornstale that was left after BioH₂ production, was implemented on cornstale along with the thermophilic bacterium *Thermoanaerobacterium thermosaccharolyticum* M18. After 96 h of fermentation, the BioH₂ production rate increased from 3.5 to 5.7 mL H₂/g substrate/h, and the hydrogen production potential was enhanced from 156.2 to 286.1 mL H₂/g substrate, resulting from increased cellulolytic enzyme activity which subsequently promoted a highly efficient substrate conversion to BioH₂ [89].

BioH₂ production was also found to be affected by change in pH. When a two-step dark co-fermentation was carried out using a mixed culture by utilizing 80% tequila vinasse and 20% nixtamalization wastewater (w/w), it was observed that reducing the pH from the first step (pH 6.5) to the second step (pH 5.8) reduced the operational time along with enhancing the hydrogen production by 17%. This pH shift also induced the syntrophy between *Clostridium* and *Lactobacillus* while reducing the proliferation of *Blautia* and *Propionibacterium*, thereby increasing the efficiency of BioH₂ conversion [90]. Detoxification carried out with activated carbon (1% p/v) on the hydrolysates of *Agave tequilana* bagasse, using an anaerobic granular sludge as the microbial source for carrying out the fermentation process, promoted the removal of acetic acid by 89% with minimal losses of fermentable sugars and increasing the hydrogen yield by 33% in comparison to the undetoxified biomass [91]. Cell immobilization carried out with *Enterobacter cancerogeous* HG6 2A and *E. homaechei* 83 at a ratio of 0.9:1 on activated carbon improved the yield of BioH₂ by 259% in comparison to the system where cell suspension was used, proving immobilization to be a highly effective method for amplifying hydrogen production [92].

To increase the quality and quantity of the produced hydrogen from DF reactions utilizing LCFs as substrates, another prominent external alterations that have been introduced to conventional fermentation reactions are inorganic nanoparticles such as silver, iron, nickel, and titanium oxide, etc., metal oxide nanoparticles such as Fe₂O₃, NiCo₂O₄, CuO, ZnO, and CoO, etc., and nanocomposites along with graphene-based nanomaterials among others, which have been studied for their role in influencing different parameters which are involved in enhancing BioH₂ production [93,94]. Fe₃O₄ nanoparticles were used in a DF process involving the bacterium *E. aerogenes* and the substrate date-palm fruit wastes in a recent study. Fe₃O₄ nanoparticles were added in a fermentation media, whereas date seed activated nanocomposites formed with Fe₃O₄ nanoparticles were added to another fermentation

media, in comparison to control where no nanoparticles were added. Optimal dosage of 150 mg/L and fermentation time of 24 h revealed a maximum hydrogen yield of 238.7 mL/g in the nanocomposites containing media which was found to be 65.7% higher than the media containing only the nanoparticles, along with a cumulative ~ 3 fold increase in the total yield compared to control, implying use of nanocomposites could have significant impact in the industrial applications that are concerned with BioH₂ production [95].

5.3.2. Use of genetic engineering

The use of genetic engineering for producing recombinant strains through over-expressing or activating genes of interest in order to enhance hydrogen production during the fermentation process has been deemed to have great potential for industrial applications. The majority of genetic modifications have been limited to the *Clostridium* sp., *Enterobacter* sp., and *E. coli* [96]. But the use of these mutant strains for BioH₂ production involving LCFs as substrate has been very few (Table 4).

Besides modifying genes of interest, use of nuclear irradiation to produce mutants of hydrogen-producing bacteria has been another promising method. Irradiation with ⁶⁰Co γ -rays produced mutants of *E. aerogenes* which enhanced the hydrogenase activity. This led to the increase in production of hydrogen yield by 81.8% more than the wild type strain. The mutant had a hydrogen production rate of 27.2 mL/(L.h) which was higher by 40.9% [97]. In another study, irradiated mutant of *E. aerogenes* enhanced the hydrogen yield by 31.8% from acid pretreated biomass of *Alternanthera philoxeroides* [98]. In order to lay emphasis on enhanced BioH₂ production through DF, several novel molecular techniques like restriction fragment length polymorphism

(RFLP), quantitative real-time PCR (q-PCR), fluorescent in-situ hybridization (FISH), and next generation sequencing (NGS) are being used in order to perform extensive research into the genes and the associated metabolic pathways in the microorganisms for efficient generation of BioH₂ [99].

6. Future perspectives

The urgent need to replace fossil fuels for reducing carbon emissions has made BioH₂ a very attractive biofuel. Nonetheless, hydrogen is mostly synthesized from fossil fuel sources to meet the need for industrial applications. Use of alternative methods for hydrogen production especially from renewable sources has become highly essential to meet future needs and demands. Lignocellulosic-based BioH₂ generation using microorganisms is steadily becoming one of the emerging technologies which are highly sustainable. Use of biological pretreatment, photo- and dark fermentation methods represents environmentally friendly and sustainable approaches for production of biohydrogen. Extensive research has been made into the three biological methods in order to develop and improve the yield and production rate of hydrogen production but only in laboratory scale. Therefore more research is required to (1) make these methods economically feasible and highly efficient, (2) to develop a common and effective saccharification technology for all feedstocks, (3) to isolate more microorganisms that have the capability to carry out the efficient production of reducing sugars from the biomass, (4) reduce the treatment time required for the biomass saccharification, (5) and to have a detailed understanding of the genes and the metabolic pathways involved in the processes for a robust production of BioH₂ required for industrial applications (Fig. 4).

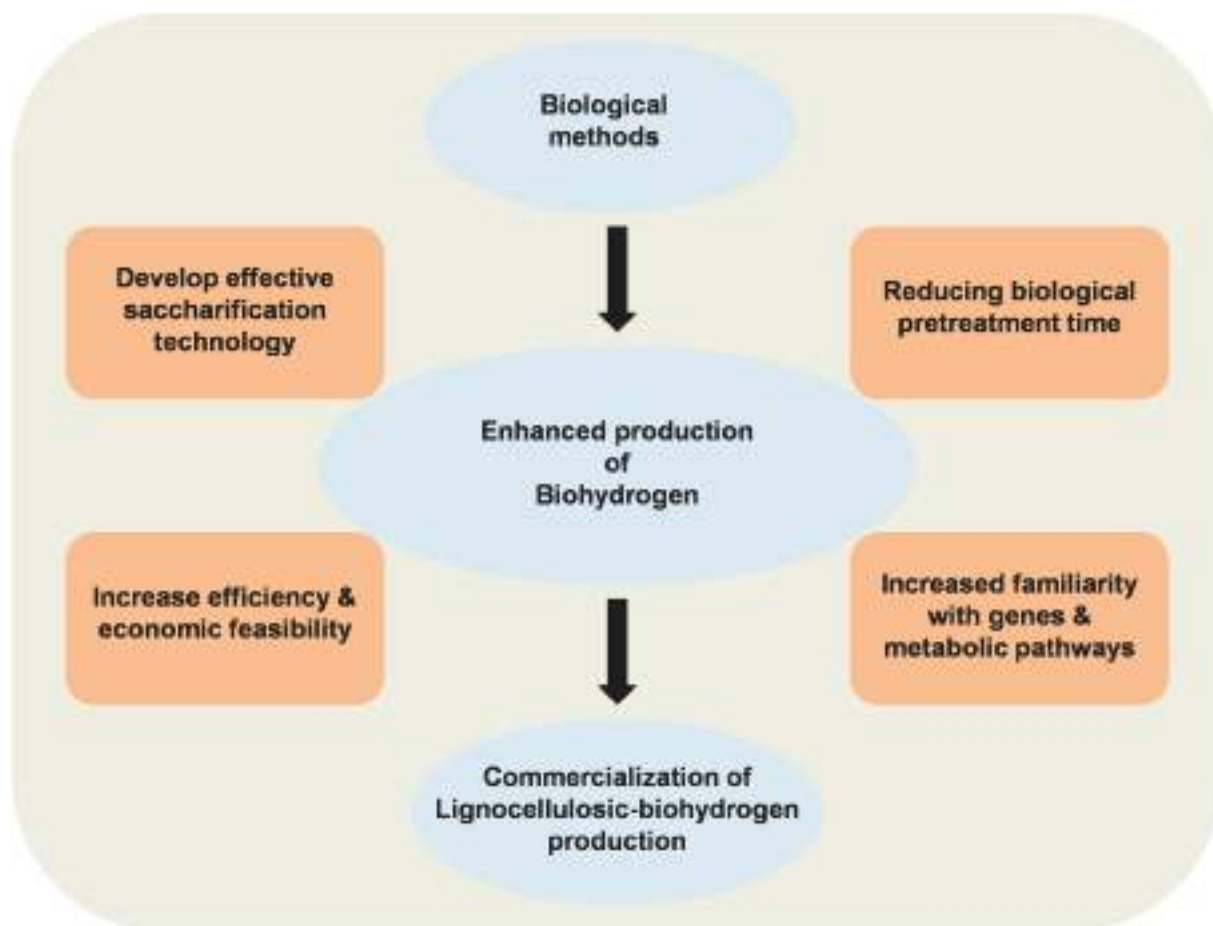


Fig. 4. Future developments required for enhancement and commercialization of lignocellulosic-biohydrogen production.

Developments in integrative biorefinery approaches are also required to commercialize the biological processes, amplify the BioH₂ production from lab scale to industrial scale, and produce more value-added products for their utilization in the industry [41,100,101].

7. Conclusion

The studies carried out in recent years with lignocellulosic-based BioH₂ production have revealed the prospects as well as the limitations of the biological methods. It has also shed light on the improvements that are absolutely required in order to develop this nascent technology in an industrial scale. This review article reported on the biological pretreatment, photo- and dark fermentation methods utilized for BioH₂ production with LCFs as substrates. Several key external factors and engineering methods used on the microorganisms for enhancing BioH₂ production were discussed. The methods in combination have the ability to become one of the key alternative technologies for the advancement of BioH₂ production. Therefore, it is highly crucial to continue doing extensive research to increase the efficiency, yield, and productivity rate of BioH₂ production. Constant tracking and analysis of the biological systems could help overcome the limitations that hinder the use of this technology on a wide scale. The prospect of producing hydrogen from renewable sources could help to improve the techno-economic aspects of green energy.

CRediT authorship contribution statement

Rituparna Saha: Conceptualization, Investigation, Visualization, Writing - original draft, Writing - review & editing. **Debalina Bhattacharya:** Conceptualization, Visualization, Writing - review & editing, Supervision. **Mainak Mukhopadhyay:** Conceptualization, Visualization, Writing - review & editing, Supervision.

Declaration of Competing Interest

The authors declare that they have no known competing financial interests or personal relationships that could have appeared to influence the work reported in this paper.

References

- [1] Shuba ES, Kifle D. Microalgae to biofuels: 'Promising' alternative and renewable energy, review. *Renew Sustain Energy Rev* 2018;81:743–55. <https://doi.org/10.1016/j.rser.2017.08.042>.
- [2] Oh Y, Hwang K, Kim C, Kim JR, Lee J. Recent development and key barriers to advanced biofuels: a short review. *Bioresour Technol* 2018;257:320–33. <https://doi.org/10.1016/j.biortech.2018.02.089>.
- [3] Unglert M, Bockey D, Bofinger C, Buchholz B, Fisch G, Luther R, et al. Action areas and the need for research in biofuels. *Fuel* 2020;268:117227. <https://doi.org/10.1016/j.fuel.2020.117227>.
- [4] Keasling J, Martin HG, Lee TS, Mukhopadhyay A, Singer SW, Sundstrom E. Microbial production of advanced biofuels. *Nat Rev Microbiol* 2021. <https://doi.org/10.1038/s41579-021-00577-w>.
- [5] Sinsel SR, Riemke RL, Hoffmann VH. Challenges and solution technologies for the integration of variable renewable energy sources – a review. *Renew Energy* 2020; 145:2271–85. <https://doi.org/10.1016/j.renene.2019.06.147>.
- [6] Liu Y, Cruz-Morales P, Zargar A, Belcher MS, Pang B, Englund E, et al. Biofuels for a sustainable future. *Cell* 2021;184:1636–1647. <https://doi.org/10.1016/j.cell.2021.01.052>.
- [7] Gaurav N, Sivasankari S, Kiran GS, Ninawe A, Selvin J. Utilization of bioresources for sustainable biofuels: A review. *Renew Sustain Energy Rev* 2017;73:205–214. <https://doi.org/10.1016/j.rser.2017.01.070>.
- [8] Tang DYY, Yew GY, Koyande AK, Chew KW, Vo DN, Show PL. Green technology for the industrial production of biofuels and bioproducts from microalgae: a review. *Environ Chem Lett* 2020;18:1967–85. <https://doi.org/10.1007/s10311-020-01052-3>.
- [9] Bórawski P, Beldycka-Bórawska A, Szymańska EJ, Jankowski KJ, Dubis B, Dunn JW. Development of renewable energy sources market and biofuels in the European Union. *J Clean Prod* 2019;228:467–84. <https://doi.org/10.1016/j.jclepro.2019.04.242>.
- [10] Nanda S, Rana R, Sarangi PK, Dalai AK, Kozinski JA. A broad introduction to First-, Second-, and Third-generation Biofuels. In: Sarangi P, Nanda S, Mohanty P, editors. *Recent Advancements in Biofuels and Bioenergy Utilization*. Springer: Singapore; 2018. p. 1–25.
- [11] Aron NSM, Khoo KS, Chew KW, Show PL, Chen W, Nguyen THP. Sustainability of the four generations of biofuels – a review. *Int J Energy Res* 2020;44:1–17. <https://doi.org/10.1002/er.5557>.
- [12] Chowdhury H, Loganathan B. 3rd generation biofuels from microalgae: a review. *Curr Opin Green Sustain Chem* 2019. <https://doi.org/10.1016/j.cogsc.2019.09.003>.
- [13] Abdullah B, Muhammad SAFS, Shokravi Z, Ismail S, Kassim KA, Mahmood AN, et al. Fourth generation biofuel: a review on risks and mitigation strategies. *Renew Sustain Energy Rev* 2019;107:37–50. <https://doi.org/10.1016/j.rser.2019.02>.
- [14] Callegari A, Bolognesi S, Ceconet D, Capodaglio AG. Production technologies, current role, and future prospects of biofuel feedstocks: a state-of-the-art review. *Crit Rev Environ Sci Technol* 2019;1–53. <https://doi.org/10.1080/10643389.2019.1629801>.
- [15] Mona S, Kumar SS, Kumar V, Parveen K, Saini N, Deepak B, et al. Green technology for sustainable biohydrogen production (waste to energy): a review. *Sci Total Environ* 2020;728:138481. <https://doi.org/10.1016/j.scitotenv.2020.138481>.
- [16] Shanmugam S, Hari A, Pandey A, Mathimani T, Felix L, Pugazhendhi A. Comprehensive review on the application of inorganic and organic nanoparticles for enhancing biohydrogen production. *Fuel* 2020;270:117453. <https://doi.org/10.1016/j.fuel.2020.117453>.
- [17] Preethi, Usman TMM, Banu JR, Gunasekaran M, Kumar G. Biohydrogen production from industrial wastewater: An overview. *Bioresour Technol Rep* 2019;7:100287. <https://doi.org/10.1016/j.biteb.2019.100287>.
- [18] Srivastava RK, Shetti NP, Reddy KR, Aminabhavi TM. Biofuels, biodiesel and biohydrogen production using bioprocesses. A review. *Environ Chem Lett* 2020. <https://doi.org/10.1007/s10311-020-00999-7>.
- [19] Boodhun BSF, Mudhoo A, Kumar G, Kim S, Lin C. Research perspectives on constraints, prospects and opportunities in biohydrogen production. *Int J Hydrog Energy* 2017;42:27471–81. <https://doi.org/10.1016/j.ijhydene.2017.04.077>.
- [20] Nagarajan D, Lee D, Chang J. Recent insights into consolidated bioprocessing for lignocellulosic biohydrogen production. *Int J Hydrog Energy* 2019;44:14362–79. <https://doi.org/10.1016/j.ijhydene.2019.03.066>.
- [21] Tian H, Li J, Yan M, Tong YW, Wang C, Wang X. Organic waste to biohydrogen: A critical review from technological development and environmental impact analysis perspective. *Appl Energy* 2019;265:113961. <https://doi.org/10.1016/j.apenergy.2019.113961>.
- [22] Singh H, Das D. Biofuels from Microalgae: Biohydrogen. In: Jacob-Lopes E, Queiroz Zepka L, Queiroz M, editors. *Energy from Microalgae*. Springer, Cham: Green Energy and Technology; 2018. p. 201–28. https://doi.org/10.1007/978-3-319-69093-3_10.
- [23] Plante L, Sheehan NP, Bier P, Murray K, Quell K, Ouellette C, et al. Bioenergy from biofuel residues and waste. *Water Environ Res* 2019;91:1199–204. <https://doi.org/10.1002/wer.1214>.
- [24] Prabakar D, Manimudi VT, K SS, Sampath S, Mahapatra DM, Rajendran K, et al. Advanced biohydrogen production using pretreated industrial waste: Outlook and prospects. *Renew Sustain Energy Rev* 2018;96:306–324. <https://doi.org/10.1016/j.rser.2018.08.006>.
- [25] Kucharska K, Rybarczyk P, Hołowacz I, Lukajtis R, Glinka M, Kamiński M. Pretreatment of lignocellulosic materials as substrates for fermentation processes. *Molecules* 2018;23:2937. <https://doi.org/10.3390/molecules23112937>.
- [26] Zhu P, Abdelaziz OY, Hultberg CP, Riisager A. New synthetic approaches to biofuels from lignocellulosic biomass. *Curr Opin Green Sustain Chem* 2020;21: 16–21. <https://doi.org/10.1016/j.cogsc.2019.08.005>.
- [27] Tu W, Hallett JP. Recent advances in the pretreatment of lignocellulosic biomass. *Curr Opin Green Sustain Chem* 2019;20:11–7. <https://doi.org/10.1016/j.cogsc.2019.07.0004>.
- [28] Kumar B, Bhardwaj N, Agrawal K, Chaturvedi V, Verma P. Current perspective on pretreatment technologies using lignocellulosic biomass: An emerging biorefinery concept. *Fuel Process Technol* 2020;199:106244. <https://doi.org/10.1016/j.fuproc.2019.106244>.
- [29] Okolie JA, Nanda S, Dalai AK, Kozinski JA. Chemistry and specialty industrial applications of lignocellulosic biomass. *Waste Biomass Valor* 2021;12:2145–69. <https://doi.org/10.1007/s12649-020-01123-0>.
- [30] Zabel HM, Akter S, Yun J, Zhang G, Awad FN, Qi X, et al. Recent advances in biological pretreatment of microalgae and lignocellulosic biomass for biofuel production. *Renew Sustain Energy Rev* 2019;105:105–28. <https://doi.org/10.1016/j.rser.2019.01.048>.
- [31] Kumar G, Sivagurunathan P, Sen B, Mudhoo A, Davila-Vasquez G, Wang G, et al. Research and development perspectives of lignocellulose-based biohydrogen production. *Int Biodeterior Biodegrad* 2017;119:225–38. <https://doi.org/10.1016/j.ibiod.2016.10.030>.
- [32] Sharma HK, Xu C, Qin W. Biological pretreatment of lignocellulosic biomass for biofuels and bioproducts: An overview. *Waste Biomass Valor* 2017. <https://doi.org/10.1007/s12649-017-0059-y>.
- [33] Zabel H, Sultana S, Sahu JN, Qi X. An overview on the application of lignolytic microorganisms and enzymes for pretreatment of lignocellulosic biomass. In: Sarangi P, Nanda S, Mohanty P, editors. *Recent advancements in biofuels and bioenergy utilization*. Singapore: Springer; 2018. p. 53–72. https://doi.org/10.1007/978-981-13-1307-3_3.
- [34] Yadav M, Paritosh K, Vivekanand V. Lignocellulose to bio-hydrogen: An overview on recent developments. *Int J Hydrog Energy* 2019. <https://doi.org/10.1016/j.ijhydene.2019.10.027>.
- [35] Chozhavendhan S, Rajamehala M, Karthigadevi G, Praveen Kumar R, Bharathiraja B. A review on feedstock, pretreatment methods, influencing factors,

- production and purification processes of bio-hydrogen production. CSCEE 2020; 2:100038. <https://doi.org/10.1016/j.cscee.2020.100038>.
- [36] Phan PT, Nguyen B, Nguyen T, Kumar A, Nguyen V. Lignocellulose-derived monosugars: a review of biomass pre-treating techniques and post-methods to produce sustainable hydrogen. Biomass Convers Biorefin 2020. <https://doi.org/10.1007/s13399-020-01161-7>.
- [37] Sarangi PK, Nanda S. Biohydrogen production through dark fermentation. Chem Eng Technol 2020;43:601–12. <https://doi.org/10.1002/ceat.201900452>.
- [38] Zhang Q, Zhang Z. Biological hydrogen production from renewable resources by photofermentation. Advances in Bioenergy, Elsevier 2018:137–60. <https://doi.org/10.1016/b.s.aibe.2018.03.001>.
- [39] Radhakrishnan S, Prasad S, Kumar S, Subramanian D. Production of biohydrogen from lignocellulosic feedstocks. In: Ingle AP, Chandel AK, da Silva SS, editors. Lignocellulosic biorefining technologies, Wiley; 2020. 10.1002/9781119568858.ch4.
- [40] Liu Y, Min J, Feng X, He Y, Liu J, Wang Y, et al. A review of biohydrogen productions from lignocellulosic precursor via dark fermentation: Perspective on hydrolysate composition and electron-equivalent balance. Energies 2020;13: 2451. <https://doi.org/10.3390/en13102451>.
- [41] Bhatia SK, Jagtap SS, Bedekar AA, Bhatia RK, Rajendran K, Pugazhendhi A, et al. Renewable biohydrogen production from lignocellulosic biomass using fermentation and integration of systems with other energy generation technologies. Sci Total Environ 2021;765:144429. <https://doi.org/10.1016/j.scitotenv.2020.144429>.
- [42] Rajendran K, Drielak E, Varma VS, Muthusamy S, Kumar G. Updates on the pretreatment of lignocellulosic feedstocks for bioenergy production – a review. Biomass Conv Bioref 2017;8:471–83. <https://doi.org/10.1007/s13399-017-0269-3>.
- [43] Rao R, Sani RK, Kumar S. Biohydrogen production from lignocellulosic feedstocks using extremophiles. In: Sani R, Krishnaraj RN, editors. Extremophilic microbial processing of lignocellulosic feedstocks to biofuels, value-added products, and usable power, Springer, Cham; 2018, p. 79–96. 10.1007/978-3-319-74459-9_5.
- [44] Jiang Y, Lu J, Lv Y, Wu R, Dong W, Zhou J, et al. Efficient hydrogen production from lignocellulosic feedstocks by a newly isolated thermophilic *Thermoanaerobacterium* sp. strain F6. Int J Hydrog. Energy 2019;44:14380–6. <https://doi.org/10.1016/j.ijhydene.2019.01.226>.
- [45] Bibra M, Kumar S, Wang J, Bhalla A, Salem DR, Sani RK. Single pot bioconversion of prairie cordgrass into biohydrogen by thermophiles. BioresourTechnol 2018; 266:232–41. <https://doi.org/10.1016/j.biortech.2018.06.046>.
- [46] Tian S, Zhao R, Chen Z. Review of the pretreatment and bioconversion of lignocellulosic biomass from wheat straw materials. Renew Sustain Energy Rev 2018;91:483–9. <https://doi.org/10.1016/j.rser.2018.03.113>.
- [47] Shanmugam S, Hari A, Ulaganathan P, Yang F, Krishnaswamy S, Wu Y. Potential of biohydrogen generation using the delignified lignocellulosic biomass by a newly identified thermostable laccase from *Trichoderma asperellum* strain BPLMBT1. Int J Hydrog Energy 2018;43:3618–28. <https://doi.org/10.1016/j.ijhydene.2018.01.016>.
- [48] Saratale GD, Saratale RG, Kim SH, Kumar G. Screening and optimization of pretreatments in the preparation of sugarcane bagasse feedstock for biohydrogen production and process optimization. Int J Hydrog Energy 2018;43:11470–83. <https://doi.org/10.1016/j.ijhydene.2018.01.187>.
- [49] Rambabu K, Show P, Bharath G, Banat F, Naushad M, Chang J. Enhanced biohydrogen production from date seeds by *Clostridium thermocellum* ATCC 27405. Int J Hydrog Energy 2019. <https://doi.org/10.1016/j.ijhydene.2019.06.133>.
- [50] Valdez-Vasquez I, Castillo-Rubio LG, Pérez-Rangel M, Sepúlveda-Gálvez A, Vargas A. Enhanced hydrogen production from lignocellulosic substrates via bioaugmentation with *Clostridium* strains. Ind Crops Prod 2019;137:105–11. <https://doi.org/10.1016/j.indcrop.2019.05.023>.
- [51] Morales-Martínez TK, Medina-Morales MA, Ortiz-Cruz AL, Rodríguez-De la Garza JA, Moreno-Dávila M, López-Badillo CM, et al. Consolidated bioprocessing of hydrogen production from agave biomass by *Clostridium acetobutylicum* and bovine ruminal fluid. Int J Hydrog Energy 2019. <https://doi.org/10.1016/j.ijhydene.2019.11.089>.
- [52] Medina-Morales MA, De la Cruz-Andrade LE, Paredes-Peña LA, Morales-Martínez TK, Rodríguez-De la Garza JA, Moreno-Dávila IM, et al. Biohydrogen production from thermochemically pretreated corn cob using a mixed culture bioaugmented with *Clostridium acetobutylicum*. Int J Hydrog Energy 2021;46:25974–25984. 10.1016/j.ijhydene.2021.04.046.
- [53] Sharma P, Melkania U. Effect of bioaugmentation on hydrogen production from organic fraction of municipal solid waste. Int J Hydrog Energy 2018;43:7290–8. <https://doi.org/10.1016/j.ijhydene.2018.03.031>.
- [54] Zhang K, Cao G, Ren N. Bioaugmentation with *Thermoanaerobacterium thermosaccharolyticum* W16 to enhance thermophilic hydrogen production using corn stover hydrolysate. Int J Hydrog Energy 2019. <https://doi.org/10.1016/j.ijhydene.2019.01.045>.
- [55] Sheng T, Meng Q, Wen X, Sun C, Yang L, Li L. Bioaugmentation with *Ruminiclostridium thermocellum* strain M3 to enhance thermophilic hydrogen production from agricultural solid waste. J Chem Technol Biotechnol 2021;96: 1623–31. <https://doi.org/10.1002/jctb.6602>.
- [56] Hitam CNC, Jalil AA. A review on biohydrogen production through photo-fermentation of lignocellulosic biomass. Biomass Conv Bioref 2020. <https://doi.org/10.1007/s13399-020-01140-y>.
- [57] Reungsang A, Zhong N, Yang Y, Sittijunda S, Xia A, Liao Q. Hydrogen from photo fermentation. In: Liao Q, Chang J, Herrmann C, Xia A, editors. Bioreactors for microbial biomass and energy conversion. Singapore: Springer; 2018. p. 221–317. https://doi.org/10.1007/978-981-10-7677-0_7.
- [58] Sagir E, Hallenbeck PC. Photofermentative hydrogen production. Biohydrogen (Second Edition) – Biomass, Biofuels, Biochemicals, Elsevier 2019:141–57. <https://doi.org/10.1016/B978-0-444-64203-5.00006-X>.
- [59] Hakobyan L, Gabrielyan L, Blbulyan S, Trchounian A. The prospects of brewery waste application in biohydrogen production by photofermentation of *Rhodobacter sphaeroides*. Int J Hydrog Energy 2020. <https://doi.org/10.1016/j.ijhydene.2020.09.184>.
- [60] García-Sánchez R, Ramos-Ibarra R, Guatemala-Morales G, Arriola-Guevara E, Toriz-González G, Corona-González RI. Photofermentation of tequila vinasses by *Rhodopseudomonas pseudopalustris* to produce hydrogen. Int J Hydrog Energy 2018. <https://doi.org/10.1016/j.ijhydene.2018.07.015>.
- [61] Sagir E, Ozgur E, Gunduz U, Eroglu I, Yucel M. Single-stage photofermentative biohydrogen production from sugar beet molasses by different purple non-sulfur bacteria. Bioprocess Biosyst Eng 2017;40:1589–601. <https://doi.org/10.1007/s00449-017-1815-x>.
- [62] Mirza SS, Qazi JI, Liang Y, Chen S. Growth characteristics and photofermentative biohydrogen production potential of purple non sulfur bacteria from sugar cane bagasse. Fuel 2019;255:115805. <https://doi.org/10.1016/j.fuel.2019.115805>.
- [63] Verma D, Kumar NR, Subudhi S. Isolation and characterization of a novel photoheterotrophic strain 'Rubrivax benzoatilyticus TERI-CHL1': Photo fermentative hydrogen production from spent effluent. Int J Hydrog Energy 2020; 45:14245–54. <https://doi.org/10.1016/j.ijhydene.2020.03.133>.
- [64] Hu B, Li Y, Zhu S, Zhang H, Jing Y, Jiang D, et al. Evaluation of biohydrogen yield potential and electron balance in the photo-fermentation process with different initial pH from starch agricultural leftover. BioresourTechnol 2020;305:122900. <https://doi.org/10.1016/j.biortech.2020.122900>.
- [65] Hitit ZY, Lazaro CZ, Hallenbeck PC. Single stage hydrogen production from cellulose through photo-fermentation by a co-culture of *Cellulomonas fimi* and *Rhodopseudomonas palustris*. Int J Hydrog Energy 2017;42:6556–66. <https://doi.org/10.1016/j.ijhydene.2016.12.035>.
- [66] Wang Y, Zhou X, Hu J, Jing Y, Wu Q, Chang J, et al. A comparison between simultaneous saccharification and separate hydrolysis for photofermentative hydrogen production with mixed consortium of photosynthetic bacteria using corn stover. Int J Hydrog Energy 2017;42:30613–20. <https://doi.org/10.1016/j.ijhydene.2017.11.008>.
- [67] Hu C, Choy S, Giannis A. Evaluation of lighting systems, carbon sources, and bacteria cultures on photofermentative hydrogen production. Appl Biochem Biotechnol 2018;185:257–69. <https://doi.org/10.1007/s12010-017-2655-5>.
- [68] Hakobyan L, Gabrielyan L, Trchounian A. Biohydrogen by *Rhodobacter sphaeroides* during photo-fermentation: Mixed vs. sole carbon sources enhance bacterial growth and H₂ production. Int J Hydrog Energy 2018. 10.1016/j.ijhydene.2018.11.082.
- [69] Zhang X, Jiang D, Zhang H, Wang Y, Zhang Z, Lu C, et al. Enhancement of the biohydrogen production performance from mixed substrate by photo-fermentation: Effects of initial pH and inoculation volume ratio. Bioresour Technol 2021;319:124153. 10.1016/j.biortech.2020.124153.
- [70] Guo S, Lu C, Wang K, Wang K, Wang J, Zhang Z, et al. Enhancement of pH values stability and photo-fermentation biohydrogen production by phosphate buffer. Bioengineered 2020;11:291–300. <https://doi.org/10.1080/21655979.2020.173639>.
- [71] Lu C, Tahir N, Li W, Zhang Z, Jiang D, Guo S, et al. Enhanced buffer capacity of fermentation broth and biohydrogen production from corn stalk with Na₂HPO₄/NaH₂PO₄. BioresourTechnol 2020;313:123783. <https://doi.org/10.1016/j.biortech.2020.123783>.
- [72] Du Toit J, Pott RWM. Heat-acclimatised strains of *Rhodopseudomonas palustris* reveal higher temperature optima with concomitantly enhanced biohydrogen production rates. Int J Hydrog Energy 2021;46:11564–72. <https://doi.org/10.1016/j.ijhydene.2021.01.068>.
- [73] Lu C, Li W, Zhang Q, Liu L, Zhang N, Qu B, et al. Enhancing photo-fermentation biohydrogen production by strengthening the beneficial metabolic products with catalysts. J Clean Prod 2021;317:128437. <https://doi.org/10.1016/j.jclepro.2021.128437>.
- [74] Jiang D, Zhang X, Ge X, Yue T, Zhang T, Zhang Y, et al. Insights into correlation between hydrogen yield improvement and glycerol addition in photo-fermentation of *Arundodonax* L. BioresourTechnol 2021;321:124467. <https://doi.org/10.1016/j.biortech.2020.124467>.
- [75] He C, Qi B, Song H, Zhang H, Lan M, Jiao Y, et al. Enhanced biohydrogen production from corn straw by basal fiber addition. BioresourTechnol 2021;338: 125528. <https://doi.org/10.1016/j.biortech.2021.125528>.
- [76] Mabutyana L, Pott RWM. Photo-fermentative hydrogen production by *Rhodopseudomonas palustris* CGA009 in the presence of inhibitory compounds. Int J Hydrog Energy 2021. <https://doi.org/10.1016/j.ijhydene.2020.12.189>.
- [77] Zhang T, Jiang D, Li Y, Zhang H, Zhang Z, Petracchini F, et al. Study of the interrelationship between nano-TiO₂ addition and photo-fermentative biohydrogen production of corn straw. Bioresour Technol 2021;338:125549. <https://doi.org/10.1016/j.biortech.2021.125549>.
- [78] Wang X, Fang Y, Wang Y, Hu J, Zhang A, Ma X, et al. Single-stage photo-fermentative hydrogen production from hydrolysed straw biomass using *Rhodobacter sphaeroides*. Int J Hydrog Energy 2018;43:13810–20. <https://doi.org/10.1016/j.ijhydene.2018.01.057>.
- [79] Feng J, Yang H, Wang X, Guo L. Enhanced hydrogen production performance of cbbR & pycA inactive *R. sphaeroides* mutant by improving the ammonium tolerance. Int J Hydrog Energy 2018. <https://doi.org/10.1016/j.ijhydene.2018.07.196>.

- [80] Feng J, Li Q, Zhang Y, Yang H, Guo L. High $\text{NH}_3\text{-N}$ tolerance of a cheR2-deletion *Rhodobacter capsulatus* mutant for photo-fermentative hydrogen production using cornstarch. *Int J Hydrog Energy* 2018;44:15833–41. <https://doi.org/10.1016/j.ijhydene.2018.09.015>.
- [81] Wei X, Feng J, Cao W, Li Q, Guo L. Photo-biological hydrogen production by a temperature-tolerant mutant of *Rhodobacter capsulatus* isolated by transposon mutagenesis. *Bioresour Technol* 2021;320:124286. <https://doi.org/10.1016/j.biortech.2020.124286>.
- [82] Wei X, Feng J, Cao W, Guo L. Enhanced biohydrogen production by an ammonium-tolerant *Rhodobacter capsulatus* from sugarcane bagasse. *Fuel* 2021;300:121009. <https://doi.org/10.1016/j.fuel.2021.121009>.
- [83] Toledo-Alarcón J, Capson-Tojo G, Marone A, Paillet F, Júnior AD. Basics of biohydrogen production by dark fermentation. In: Chatellard L, Bernet N, Trably E, editors. *Bioreactors for Microbial Biomass and Energy Conversion*, Springer, Singapore; 2018, p. 199–220. 10.1007/978-981-10-7677-0_6.
- [84] Bundhoo ZMA. Potential of bio-hydrogen production from dark fermentation of crop residues: A review. *Int J Hydrog Energy* 2018. <https://doi.org/10.1016/j.ijhydene.2018.11.098>.
- [85] Sampath P, Brijesh, Reddy KR, Reddy CV, Shetti NP, Kulkarni RV, et al. Biohydrogen production from organic waste – A review. *ChemEngTechnol* 2020;43:1240–1248. 10.1002/ceat.201900400.
- [86] Islam MS, Guo C, Liu C. Enhanced hydrogen and volatile fatty acid production from sweet sorghum stalks by two-steps dark fermentation with dilute acid treatment in between. *Int J Hydrog Energy* 2018;43:659–66. <https://doi.org/10.1016/j.ijhydene.2017.11.059>.
- [87] Yang G, Wang J. Enhancement of biohydrogen production from grass by ferrous ion and variation of microbial community. *Fuel* 2018;233:404–11. <https://doi.org/10.1016/j.fuel.2018.06.067>.
- [88] Bu J, Wei H, Wang Y, Cheng J, Zhu M. Biochar boosts dark fermentative H_2 production from sugarcane bagasse by selective enrichment/colonization of functional bacteria and enhancing extracellular electron transfer. *Water Res* 2021;202:117440. <https://doi.org/10.1016/j.watres.2021.117440>.
- [89] Zhao L, Wang Z, Ren H, Chen C, Nan J, Cao G, et al. Residue cornstarch derived biochar promotes direct bio-hydrogen production from anaerobic fermentation of cornstarch. *Bioresour Technol* 2021;320:124338. <https://doi.org/10.1016/j.biortech.2020.124338>.
- [90] García-Depraet O, Rene ER, Gómez-Romero J, López-López A, León-Becerril E. Enhanced biohydrogen production from the dark co-fermentation of tequila vinasse and nixtamalization wastewater: Novel insights into ecological regulation by pH. *Fuel* 2019;253:159–66. <https://doi.org/10.1016/j.fuel.2019.04.147>.
- [91] Valdez-Guzmán BE, Toro EER, Cardenas-López RL, Méndez-Acosta HO, González-Alvarez V, Arreola-Vargas J. Enhancing biohydrogen production from Agave tequilana bagasse: Detoxified vs. undetoxified acid hydrolysates. *BioresourTechnol* 2019;276:74–80. <https://doi.org/10.1016/j.biortech.2018.12.101>.
- [92] Zhang C, Kang X, Liang N, Abdullah A. Improvement of biohydrogen production from dark fermentation by cocultures and activated carbon immobilization. *Energy Fuels* 2017;31:12217–22. <https://doi.org/10.1021/acs.energyfuels.7b02035>.
- [93] Kumar G, Mathimani T, Rene ER, Pugazhendhi A. Application of nanotechnology in dark fermentation for enhanced biohydrogen production using inorganic nanoparticles. *Int J Hydrog Energy* 2019;44:13106–13. <https://doi.org/10.1016/j.ijhydene.2019.03.131>.
- [94] Srivastava N, Srivastava M, Malhotra BD, Gupta VK, Ramteke PW, Silva RN, et al. Nanoengineered cellulosic biohydrogen production via dark fermentation: A review. *Biotech Adv* 2019;37:107384. <https://doi.org/10.1016/j.biotechadv.2019.04.006>.
- [95] Rambabu K, Bharath G, Banat F, Hai A, Show PL, Nguyen THP. Ferric oxide/date seed activated carbon nanocomposites mediated dark fermentation of date fruit wastes for enriched biohydrogen production. *Int J Hydrog Energy* 2021;44:16631–43. <https://doi.org/10.1016/j.ijhydene.2020.06.108>.
- [96] Dahiya S, Chatterjee S, Sarkar O, Mohan SV. Renewable hydrogen production by dark fermentation: Current status, challenges and perspectives. *BioresourTechnol* 2020. <https://doi.org/10.1016/j.biortech.2020.124354>.
- [97] Chen J, Liu M, Song W, Ding L, Liu J, Zhang L, et al. Enhanced hydrogen production of *Enterobacter aerogenes* mutated by nuclear irradiation. *Bioresour Technol* 2017;227:50–5. <https://doi.org/10.1016/j.biortech.2016.12.033>.
- [98] Song W, Ding L, Liu M, Cheng J, Zhou J, Li Y. Improving biohydrogen production through dark fermentation of steam-heated acid pretreated *Alternanthera philoxeroides* by mutant *Enterobacter aerogenes* ZJU1. *Sci Total Environ* 2019. <https://doi.org/10.1016/j.scitotenv.2019.134695>.
- [99] Kumar G, Mathimani T, Sivaramakrishnan R, Shanmugam S, Bhatia SK, Pugazhendhi A. Application of molecular techniques in biohydrogen production as a clean fuel. *Sci Total Environ* 2020. <https://doi.org/10.1016/j.scitotenv.2020.137795>.
- [100] Ren N, Zhao L, Chen C, Guo W, Cao G. A review on bioconversion of lignocellulosic biomass to H_2 : Key challenges and new insights. *Bioresour Technol* 2016;215:92–9. <https://doi.org/10.1016/j.biortech.2016.03.124>.
- [101] Banu JR, Usman TMM, SK, Kannah RY, K N Y, P S, Bhatnagar a, Kumar G. A critical review on limitations and enhancement strategies associated with biohydrogen production. *Int J Hydrog Energy* 2021;46:16565–16590. 10.1016/j.ijhydene.2021.01.075.



A hydrogel sheet mask with tea tree essential oil entrapment and targeted dose delivery capability

Biva Ghosh^a, Debalina Bhattacharya^b, Mainak Mukhopadhyay^{a,*}

^a Department of Biotechnology, JIS University, 81, Nilgunj Road, Agarpara, Kolkata 700109, West Bengal, India

^b Department of Microbiology, Maulana Azad College, 8 Rafi Ahmed Kidwai Road, Kolkata 700013, West Bengal, India

ARTICLE INFO

Article history:

Available online 7 February 2022

Keywords:

Antimicrobial activity
β-cyclodextrin
Chitosan oligosaccharide
Hydrogel scaffold
Skin treatment

ABSTRACT

Skin is a very aesthetic organ of our body which is significant for personal health. Skin problem specially face skin problem has the psychosocial effect. Skin problems like acne is one of the most common problems among adolescents. Commonly these are treated with benzoyl peroxide and erythromycin by physicians, but tea tree oil also has equal efficacy similar to them. But these oils are hard to administer because the essential oil composition are volatile and thus, does not stay over the skin for long duration as well as a larger dose of this oil is known to irritate the skin. Since hydrogel is well-known for its targeted drug delivery system, therefore, hydrogel patch or scaffold sheet can be used to deliver the tea tree oil to the skin in optimum quantity. But hydrogels are hydrophilic and cannot absorb essential oils. β-cyclodextrin has the capability to entrap volatile, unstable molecules inside its hydrophobic interior and can release on the target site. Whereas, chitosan oligosaccharide has the antimicrobial activity. Therefore, the present study deal with the formulation of hydrogel with β-cyclodextrin and chitosan oligosaccharide along with pectin and carboxymethyl cellulose (CMC) to enable this hydrogel to entrap essential oil and show enhanced antimicrobial activity. The synthesized hydrogel HCCHB1 has very good cytocompatibility according to MTT assay. The antimicrobial activity of tea tree oil entrapped HCCHB1 is greater than the tea tree oil alone. Hence, it can be helpful to deliver reduced dose of tea tree oil over the skin and minimize irritation without compromising the antimicrobial activity of the tea tree oil. The HCCHB1 has good porosity and high swelling property in water, pH 5.5 and essential oil with 1001%, 1033% and 94% respectively. Additionally, the successful interaction of polymers among each other has occurred successfully as represented by FTIR.

Copyright © 2022 Elsevier Ltd. All rights reserved.

Selection and peer-review under responsibility of the scientific committee of the International Symposium on Materials of the Millennium: Emerging Trends and Future Prospects.

1. Introduction

Skin is the largest organ of our body with various functions among which providing protection to the inner tissues by acting as barrier towards entry of infectious agent. Therefore, skin health is a major aspect of the personal health. It provides an aesthetic look to our body and hence also affects the psychosocial and communications of a person in the public [1]. Skin are of various types depending on the lifetime and sebum secretion [2]. Various skin needs to be managed differently. There are various types of skin problem, among which acne is one of the common problems among the adolescents. Acne is a chronic inflammatory disease

which is caused by the combination of multiple factors such as excessive sebum production, infection by *Propionibacterium acnes* bacteria and anomalous follicular epithelium desquamation [3,4]. About 90% adolescents suffer from acne among which 5% adults suffer from insistent or late-onset acne [5-7]. Acne results in physical discomfort and scarring over the skin. This also brings psychological and emotional stress to the suffering person [8]. There are various medications available in the market to treat acne. Among them benzoyl peroxide and erythromycin gel are some of the most common medications [9,10]. But these medications have side effects like burning sensation and scaling of skin, etc. [11]. Most people opt for self-treatment of acne and prefer tea tree essential oil for the same. Tea tree essential oil is the extract of *Melaleuca alternifolia*, a native Australian plant. It consists of terpinen-4-ol in minimum and 1, 8-cineole in maximum quantity. Among these

* Corresponding author.

E-mail address: mainak.mukhopadhyay12@gmail.com (M. Mukhopadhyay).

terpinen-4-ol is the main cause of versatile antimicrobial activity against bacteria, fungus, virus and protozoa which affects the skin and mucosa. Even tea tree oil is used as a treatment for the acne vulgaris, seborrheic dermatitis, chronic gingivitis oral candidiasis, tinea, onychomycosis, molluscum contagiosum and many more [12]. Other than this, tea tree oil also exhibits anti-inflammatory, anti-oxidant and anti-cancer effect over the skin [13]. The antibacterial effect of tea tree oil is done by the non-specific cell membrane damage [14]. Tea tree oil is well known to show efficacy of acne curing similar to 2.5% benzoyl peroxide and 2% erythromycin gel [9,10]. But tea tree oil is volatile in nature and has a low penetration in human skin and therefore, the application of tea tree oil is limited [15]. But this problem can be solved by the use of hydrogels. Hydrogels are a three-dimensional network of polymers crosslinked physically or chemically, capable of holding large amount of water and having high porosity and entrapment capability [16]. They are well-known for targeted drug delivery system [17–20]. But hydrogels are hydrophilic in nature and thus essential oil entrapment is tough. β -cyclodextrins are well-known for its entrapment capability of volatile, sparingly water soluble and unstable molecules. β -cyclodextrins are cyclic compounds of seven glucose subunits with hydrophobic inside and hydrophilic outside. The volatile, sparingly water soluble and unstable molecules can be entrapped in the inner side of the β -cyclodextrins and can be delivered to the targeted site [21–23]. Therefore, use of β -cyclodextrins in the fabrication of the hydrogel can be useful to entrap essential oils such as tea tree oil. Other than this, large dose of tea tree oil application can irritate the skin, therefore, to reduce the dose of tea tree oil, but still maintain its antimicrobial property, the antimicrobial hydrogel can be prepared which has its own property to combat infection and can be helpful for the treatment [11,24,25]. Therefore, chitosan oligosaccharide can be used in the synthesis of the hydrogel since, chitosan oligosaccharide has antimicrobial activity as well as is water soluble, which can be blended with other natural polymers such as pectin and carboxymethyl cellulose (CMC) properly [26]. The antimicrobial property of chitosan oligosaccharide is due to number of NH_2 group exposed during deacetylation of acetyl-D-glucosamine [27]. Pectin and CMC are known to provide good physical strength and also consist of $-\text{COOH}$ group which is useful for initiation of crosslinking among the polymer by the copper sulphate as a crosslinker [28]. The copper sulphate also has biocidal property and plays an important role in skin regeneration and wound healing which can provide vital properties to the hydrogel [29]. Other than this, use of plasticizer can be done for proper alignment of polymer chains to attain good porosity. Good porosity of hydrogel is significant in many aspects such as swelling properties, entrapment of molecules in polymer networks and release of the same, and proliferation of the cells, etc. [30–33]. Polyethylene glycol 400 (PEG 400) is small molecular size plasticizer with the capability to provide good porosity by forming three-dimensional H-bonding with the polymer molecules and arranging them in proper alignment [34–36]. PEG 400 has various applications in pharmaceutical industries and are also cytocompatibility, non-immunogenic, flexible, and water-soluble.

Therefore, fabrication of hydrogel scaffold with β -cyclodextrins, chitosan oligosaccharide, pectin and CMC along with PEG 400 as plasticizer and copper sulphate as crosslinker can have potential application in the tropical delivery of tea tree oil over the skin in optimum quantity for the treatment of skin infection such as acne. The hydrogel scaffold thus formed can be used as a sheet mask or patches for the treatment of acne and other skin infection [1,37]. Since, it is a hydrogel therefore, it can also deliver other therapeutic molecules essential for healthy skin and skin repair. β -cyclodextrins can be useful in entrapping vitamins and stabilize them by protecting them from environmental stress as well as deli-

ver them in the targeted site [21–23]. The pH sensitivity of the hydrogel can be an effective tool for targeted drug delivery. Hence, allowing this hydrogel scaffold sheet mask or patch to have potential application in dermatology and cosmetology. This study aims in the fabrication of above discussed hydrogel scaffold and study its properties.

2. Materials and methods

2.1. Materials

The synthesis of the hydrogel was done by using polyethylene glycol 400 (PEG 400), chitosan oligosaccharide (water-soluble chitosan (WSC)), β -cyclodextrins, pectin and carboxymethyl cellulose (CMC), copper sulfate pentahydrate ($\text{CuSO}_4 \cdot 5\text{H}_2\text{O}$). The other chemicals used are Tris-buffer, hydrochloric acid, ethanol. All the chemicals are brought from Merck, Sisco Research laboratories and Hi-media. Distilled water was collected from the department of chemistry, JIS University, Kolkata.

2.2. Synthesis of hydrogel

The solutions of polymers such as pectin, CMC, WSC, β -cyclodextrins, CuSO_4 and PEG 400 in a percentage of 4%, 2%, 1%, 1%, 2% and 4%, respectively. All these components were mixed uniformly in various ratios for the fabrication of hydrogel. Among these hydrogels depending on their physical properties two hydrogels were chosen which are HCCHB1 and HCCHB2 with a ratio of 1:1:0.8:0.8 and 1:1:0.8:0.1 in a composition pectin: CMC: WSC: β -cyclodextrins respectively. In this preparation 4% PEG 400 acted as plasticizer and 2% CuSO_4 as crosslinker. The hydrogels prepared were washed with distilled water and stored in -20°C for overnight and lyophilized next day at room temperature.

2.3. Characterization

The structural study of the hydrogel samples was done using scanning electron microscope (SEM) (MIRA3 TESCAN) and field emission scanning electron microscopy (FESEM) (JEOLUESR) using 1X1 cm lyophilized hydrogel scaffold. The interaction among the polymers and new bond formations of the hydrogel scaffolds was analyzed using Fourier transform infrared spectra (FTIR) (Agilent, Cary 630, USA) at a scanning frequency of $400\text{--}4000\text{ cm}^{-1}$.

2.4. Water uptake capability

To study the swelling property of the hydrogel scaffolds is represented as a percentage of degree of swelling (DOS%). W_i represents the initial weight of the dried hydrogel which are cut into small pieces and dipped in water and different pH solutions at room temperature. When the hydrogel swells completely after seven days, they are removed from the respective solutions and the final weight is taken to represent as W_f . The degree of swelling percentage is represented as below in Eqn 1.

$$\text{Degree of swelling \% (DOS\%)} = \frac{W_f - W_i}{W_i} \times 100 \quad (1)$$

2.5. Cell compatibility studies

The cell compatibility study is done by using MTT 3-(4,5-dimethylthiazol-2-yl)-2,5-diphenyl tetrazolium bromide (MTT) assay. In this assay the mitochondrial succinate dehydrogenase present in the live cells reduces MTT compound into insoluble purple color formazan compound. Now, these cells with the dark color com-

pound are dissolved in DMSO solution and measured at 590 nm using a spectrophotometer. The viability of the cells is determined on the basis that only metabolically active cells can convert MTT into purple color compounds [38]. For this process, WI-38 cells are cultured in 96 well plates with DMEM media and incubated with hydrogels for 24 h, 48 h and 72 h at 37 °C in 5% CO₂ incubator. The survival percentage is calculated on the basis of hydrogel untreated cells as controlled versus hydrogel treated cells where the viability of hydrogel untreated cells survival is considered as 100%.

2.6. Antibacterial activity study

To study the antibacterial activity of hydrogel HCCHB1 infused with tea tree essential oil, *Pseudomonas* sp. was used as test organism along with tea tree oil as control. Here the spread plate technique is used to inoculate the three plates with *Pseudomonas* sp. Among these plates, one *Pseudomonas* sp. plate was cut with a small hole in the middle of the plate and 10 µl of tea tree oil was poured. The other two plates of *Pseudomonas* sp. were treated with equal weight hydrogel scaffold piece, one infused with tea tree essential oil and another hydrogel scaffold without tea tree oil in the middle of the plates respectively. All the *Pseudomonas* sp. plates were incubated at 15 °C. The experiment was repeated thrice in the duplicates and the area of the zone of incubation (cm²) was noted as mentioned in Eqn 2 [39].

$$\text{Area of zone of inhibition} = \frac{1}{4} \times 3.14 \times (\text{diameter (d)})^2 \quad (2)$$

3. Result and discussion

3.1. Structural analysis of hydrogel

The structural analysis of the hydrogel scaffold HCCHB1 and HCCHB2 is done by the scanning electron microscope (SEM) and field emission scanning electron microscopy (FESEM). Fig. 1 (a) and (b) represents SEM whereas Fig. 1 (c) and (d) represents FESEM of HCCHB1 and HCCHB2 respectively. The average pore size of HCCHB1 is 25.16 µm and for HCCHB2 is 6721.86 µm. Both the hydrogels HCCHB1 and HCCHB2 has good porosity but in case of HCCHB1 the pores are small in size, but numerous in number, whereas, the pores of HCCHB2 are big in size and are not uniform and has merged with each other. For better understanding of the morphology of the hydrogel scaffolds and its porosity, Supplementary Figure 1 with more image of HCCHB1 and HCCHB2 is provided. The change in pore size is due to the change in the ratio of β-cyclodextrin in the hydrogel composite. The HCCHB2 has less β-cyclodextrin with respect to HCCHB1. The –OH group of the outer shell of the cyclic β-cyclodextrin form dense networks with the other polymers resulting in small pore size of the HCCHB1. The porosity of the hydrogel plays important role in swelling properties, entrapment capability and cytocompatibility.

3.2. Energy dispersive X-Ray (EDX) composition analysis

Tables 1a and 1b represents the EDX composition analysis of the HCCHB1 and HCCHB2 respectively. Both the hydrogel scaffolds have approximately same mass% of the elements. The only difference seen among the composition of HCCHB1 and HCCHB2 is in the case of mass% of copper. In case of the HCCHB1, the mass% of the copper is 10.38 whereas, in case of the HCCHB2 it is 2.45. The higher copper content in the HCCHB1 explains the strong and dense crosslinking among the polymer molecules due to copper ions. The denser the crosslinking the smaller the pore size of

the hydrogel scaffold. Therefore, the pore size of the hydrogel HCCHB1 is smaller than HCCHB2 which can be correlated with the FESEM analysis. The supplementary data 2 (a) and (b) provide the graphical representation of the EDX analysis of HCCHB1 and HCCHB2 respectively for better understanding.

3.3. FTIR spectroscopy analysis

The Fig. 2 (a) and (b) represents the FTIR analysis of HCCHB1 and HCCHB2 respectively which studies the interaction among the polymer molecules. In Fig. 2 (a) the peak 3894 cm⁻¹ to 3649 cm⁻¹ represents the presence of –OH bonds and simultaneous H-bonding between the polymers. The sharp peak at 2366 cm⁻¹ and 2321 cm⁻¹ represent the C≡N of carboxylic acid derivatives. The peak from 1693 cm⁻¹ to 1647 cm⁻¹ represents C=O of –COOCH₃. The strong peaks from 1562 cm⁻¹ to 1515 cm⁻¹ represent the NH₂ group of chitosan oligosaccharide. The peaks from 1336 cm⁻¹ to 1262 cm⁻¹ represent the CH₃ and CH₂ bending.

Similarly, in Fig. 2 (b) 3893 cm⁻¹ to 3698 cm⁻¹ represent the presence of –OH bonds and H-bonding between the polymers. The sharp peak at 2863 cm⁻¹ represents the strong presents of CH₃, CH₂ and CH. The two peaks at 2364 cm⁻¹ and 2321 cm⁻¹ C≡N of derivatives of carboxylic acid. The peak at 1693 cm⁻¹ to 1646 cm⁻¹ represent C=O of –COOCH₃. The peak from 1532 cm⁻¹ 1462 cm⁻¹ represents the NH₂ group of chitosan oligosaccharide. The peak from 1425 cm⁻¹ to 1340 cm⁻¹ represent the CH₃ and CH₂ bending. The peak at 1248 cm⁻¹ to 1015 cm⁻¹ represents C-O bonds.

The shift in the peak position is due to the interaction among the polymer molecules due to cross linking by copper ion. The change in the peak patterns in case of both the hydrogels are due to the variation in the concentration of the β-cyclodextrins. The FTIR analysis demonstrates the strong presence of H-bonding among the NH₂ group with the other functional groups creating an N-H wagging. The free presence of NH₂ group and cross linking with copper ion is the key reason of antimicrobial activity. The presence C≡N, C=O and C-O of carboxymethyl group represents the cross-linking interaction among the polymers and formation of different derivatives due to the presence of –COOCH₃. Hence, the successful interaction among the polymer molecules is observed and the fabrication of hydrogel was successful.

3.4. Swelling properties

The swelling properties of the HCCHB1 and HCCHB2 is measured in terms of degree of swelling percentage (DOS %) (Table 2). From the Table 2 it can be inferred that the DOS% of HCCHB2 is comparatively higher than the DOS% of HCCHB1. The highest DOS% in HCCHB1 and HCCHB2 are 1001% and 1348% in water and 1033% and 1601% in pH 5.5 respectively. The DOS% of the HCCHB2 is higher due to its large pore size. Other than this, it also contains less amount of β-cyclodextrins which also effect the swelling property of the hydrogel. β-cyclodextrins has both hydrophilic and hydrophobic moiety in its structure. The hydrophilic moiety is present on the outer surface of the cyclic structure, whereas, the hydrophobic moiety is present on the inner surface of the structure of β-cyclodextrins. This hydrophobic moiety resists water to enter in the hydrogel scaffold. Since, HCCHB1 has a comparatively high amount of β-cyclodextrins therefore, the DOS% in water and other pH solution is comparatively less than the HCCHB2. But in the case of tea tree essential oil, the DOS% of HCCHB1 is 94%, which is higher than the DOS% of HCCHB2. This high DOS% of HCCHB1 in tea tree essential oil is due to the presence of high amount of β-cyclodextrins. The hydrophobic moiety of β-cyclodextrins has the capability to entrap essential oil, vitamins and sparingly water sol-

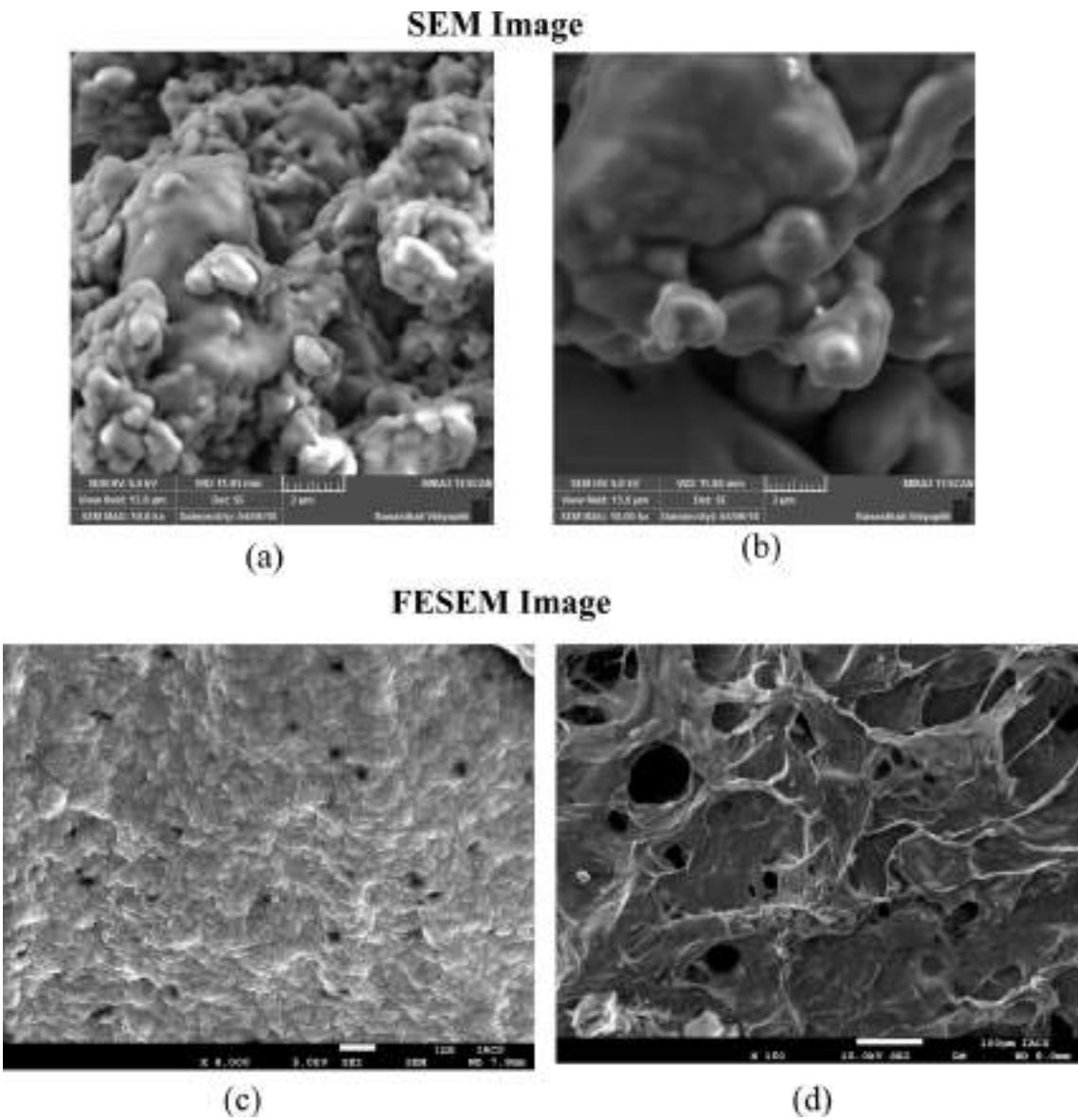


Fig. 1. Structural analysis of hydrogel: SEM image of (a) HCCHB1 and (b) HCCHB2; FESEM image of (c) HCCHB1 and (d) HCCHB2.

Table 1a
The EDX analysis of the HCCHB1.

Element	(keV)	Mass%	Sigma	Atom%	Compound	Mass%	Cation	K
C K	0.277	50.81	0.12	62.25				46.3233
N K	0.392	6.53	0.13	6.86				5.0630
O K	0.525	29.68	0.19	27.30				26.2453
S K	2.307	2.61	0.04	1.20				5.2555
Cu K	8.040	10.38	0.26	2.40				17.1130
Total		100.00		100.00				

Table 1b
The EDX analysis of the HCCHB2.

Element	(keV)	Mass%	Sigma	Atom%	Compound	Mass%	Cation	K
C K	0.277	57.03	0.15	64.34				67.0271
N K	0.392	7.78	0.21	7.53				5.0047
O K	0.525	32.45	0.30	27.49				23.8510
S K	2.307	0.28	0.03	0.12				0.5222
Cu K	8.040	2.45	0.22	0.52				3.5949
Total		100.00		100.00				

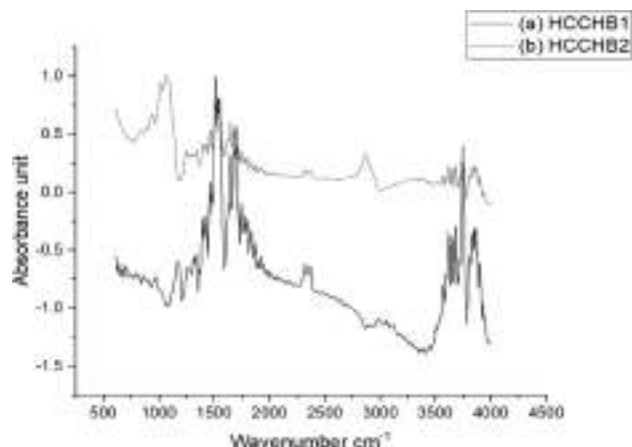


Fig. 2. The graphical representation of FTIR spectroscopy of (a) HCCHB1 and (b) HCCHB2.

uble and volatile molecules in its cyclic structure. It can also stabilize and solubilize it in water with the help of its hydrophilic moiety present in the outer surface of the structure. Since, the HCCHB1 has significantly high swelling property in tea tree essential oil, water and pH 5.5, therefore, it can be a very good candidate to entrap essential oil and deliver it over the skin. Hence, preparation of a hydrogel sheet mask can deliver the essential oil in a very user-friendly method.

3.5. Cell compatibility study

The cell cytocompatibility (Fig. 3) of the HCCHB1 and HCCHB2 is measured by conducting the MTT assay with WI-38 cells. Both

Table 2

Degree of swelling percentage (DOS%) of HCCHB1 and HCCHB2 in water, tea tree essential oil and different pH.

Sample	DOS% in tea tree essential oil	DOS% in water	DOS% in pH. 4.5	DOS% in pH. 5	DOS% in pH. 5.5	DOS% in pH. 6	DOS% in pH. 6.5	DOS% in pH. 7	DOS% in pH. 7.5
HCCHB1	94 ± 0.036	1001 ± 0.089	614 ± 0.02	620 ± 0.068	1033 ± 0.065	496 ± 0.034	481 ± 0.025	0	0
HCCHB2	43 ± 0.023	1348 ± 0.078	725 ± 0.041	980 ± 0.056	1601 ± 0.075	506 ± 0.042	0	0	0

*Where “±” denotes standard deviation with n = 5.

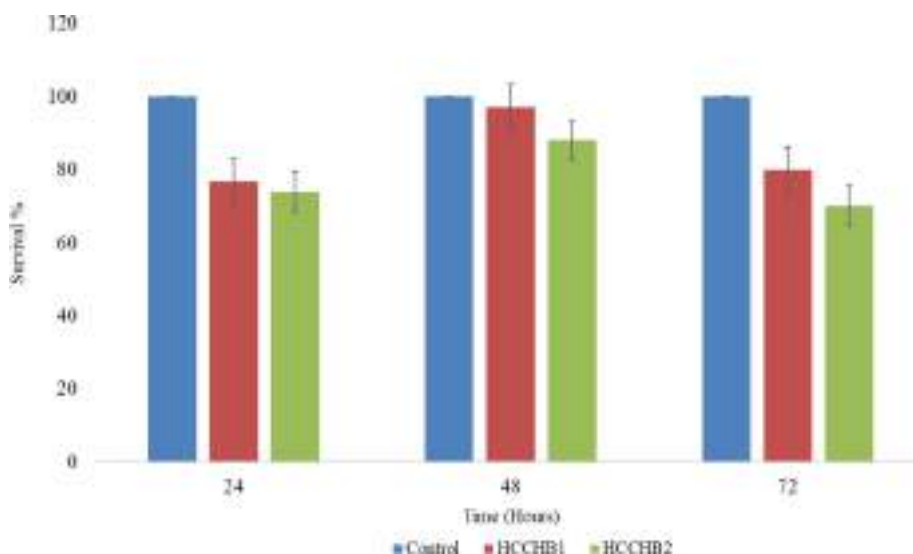


Fig. 3. The graphical representation of cytocompatibility study of HCCHB1 and HCCHB2.

hydrogels, HCCHB1 and HCCHB2 are non-toxic and cytocompatible. But HCCHB1 has highest cytocompatibility compared to HCCHB2. This is due to the largely spread small pores over the HCCHB1 which allows proper transport of oxygen, nutrients and allows the cells to proliferate over the hydrogel matrix. Whereas, in case of HCCHB2 the pore size is big but are not evenly spread and are not uniform in structure which is not a good property for hydrogel scaffold to act as a matrix for cell growth. Hence, HCCHB1 has higher cytocompatibility in overall. The highest cytocompatibility is seen at 48 h and at 72 h. The reduction in cytocompatibility is due to the degradation of hydrogel scaffold in high pH medium and loss of its structure. The cytocompatibility of the HCCHB1 is advantageous for the skin therapy and also will allow the skin cells to repair along with the delivery of tea tree essential oil over the skin. This oil is well known for the antimicrobial activity and acne treatment. Along with this the CuSO_4 which is used as crosslinker here is also advantageous for the skin repair. Hence, the non-toxic hydrogel sheet mask prepared can be helpful for infection and acne treatment over the skin.

3.6. Antibacterial activity study

The *Pseudomonas* sp. cultured plates which were incubated with HCCHB1 infused with tea tree essential oil showed comparatively higher antibacterial activity than the control plates incubated with alone tea tree essential oil and hydrogel scaffold without tea tree essential oil (Fig. 4). The area of the zone of inhibitions (cm^2) are recorded in Fig. 4 (ii). The area of the zone of inhibition in the case of HCCHB1 infused with tea tree essential oil is 6.15 cm^2 , which is higher than the control plates. The zone of inhibition in case of control plates with only tea tree essential oil is 3.14 cm^2 and with only HCCHB1 is 2.54 cm^2 . Thus, we can infer that the hydrogel has enhanced the antibacterial activity in combination with the tea

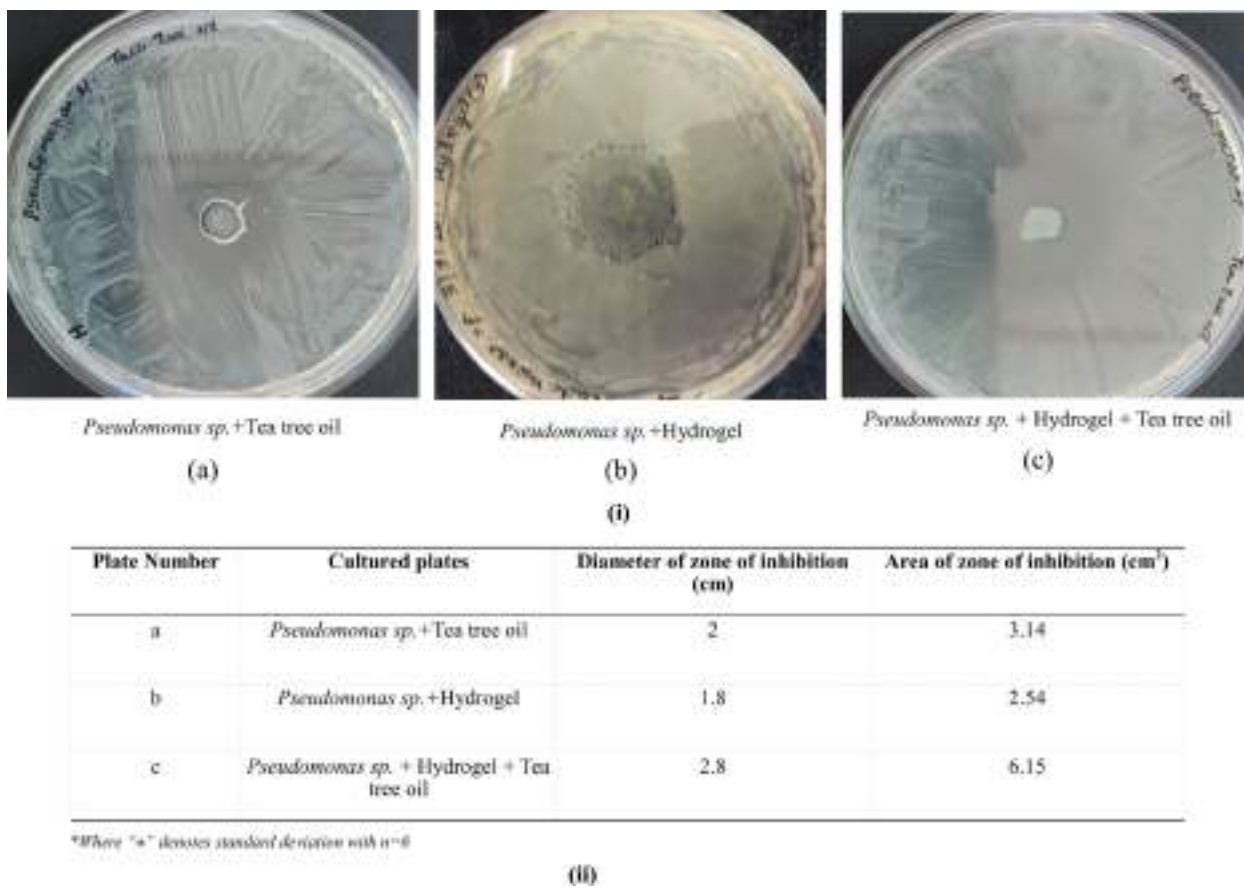


Fig. 4. (i) The image of antimicrobial activity of HCCHB1 (a) *Pseudomonas sp.* + Tea tree oil, (b) *Pseudomonas sp.* + Hydrogel (HCCHB1) and (c) *Pseudomonas sp.* + Hydrogel (HCCHB1) + Tea tree oil; (ii) Diameter and area of zone of inhibition (cm²).

tree essential oil. The enhanced antibacterial activity of HCCHB1 is due to the presence of copper ion as cross linker and chitosan oligosaccharide as one of the components of the polymer mixture. Therefore, this HCCHB1 can be used as sheet masks to deliver tea tree essential oil and treat infections and acne over the skin.

4. Conclusion

According to the above discussion, it can be concluded that though the HCCHB2 has higher pore size than HCCHB1 but has low cytocompatibility compared to HCCHB1. The pore size of HCCHB1 is 25.16 μm which is substantial. Even the cytocompatibility of HCCHB1 is higher due to its widely spread pores. Other than this, though the swelling property of HCCHB2 is considerable higher than HCCHB1 in water and different pH, but the swelling property of HCCHB1 in tea tree oil is 94% which is significant for industrial use. Even the DOS% of HCCHB1 in other mediums is also significant. The different DOS% of the hydrogels in different pH buffer represents the pH sensitivity. The highest DOS% of HCCHB1 is in the water and pH5.5 which allows its application over the skin. The HCCHB1 also shown enhanced antibacterial activity when coupled with tea tree essential oil. Hence, the hydrogel HCCHB1 can deliver tea tree essential oil in a more efficient way with better antibacterial activity and no toxicity. The FTIR analysis reveals the bond formation and successful interaction among the polymer molecules while fabrication of hydrogel. Therefore, the sheet of HCCHB1 can be used as a sheet mask to deliver tea tree essential oil and treat infection and acne over the skin.

CRediT authorship contribution statement

Biva Ghosh: Conceptualization, Formal analysis, Investigation, Data curation, Methodology, Writing – original draft. **Debalina Bhattacharya:** Conceptualization, Formal analysis, Investigation, Resources, Data curation, Writing – review & editing. **Mainak Mukhopadhyay:** Supervision, Conceptualization, Validation, Visualization, Writing – review & editing.

Declaration of Competing Interest

The authors declare that they have no known competing financial interests or personal relationships that could have appeared to influence the work reported in this paper.

Acknowledgements

The authors of this paper are thankful to the IACS Kolkata and Banasthali Vidyapith University, Jaipur for providing research facility regarding FTIR, SEM, FESEM and EDX analysis.

Funding

This research did not receive any specific grant from funding agencies in the public, commercial, or not-for-profit sectors.

Appendix A. Supplementary data

Supplementary data to this article can be found online at <https://doi.org/10.1016/j.matpr.2022.01.349>.

References

- [1] M.A. Nilforoushzadeh, M.A. Amirkhani, P. Zarrintaj, A.S. Moghaddam, T. Mehrabi, S. Alavi, M.M. Sisakht, J. Cosmet. Dermatol. 17 (5) (2018) 693–702.
- [2] S.W. Youn, S.J. Kim, I.A. Hwang, K.C. Park, Skin Res. Technol. 8 (3) (2002) 168–172.
- [3] I. Kurokawa, F.W. Danby, Q. Ju, X. Wang, L.F. Xiang, L. Xia, W.C. Chen, I. Nagy, M. Picardo, D.H. Suh, R. Ganceviciene, S. Schagen, F. Tsatsou, C.C. Zouboulis, Exp. Dermatol. 18 (10) (2009) 821–832.
- [4] H.C. Williams, R.P. Dellavalle, S. Garner, Lancet 379 (9813) (2012) 361–372.
- [5] V. Stathakis, M. Kilkeny, R. Marks, Australas. J. Dermatol. 38 (3) (1997) 115–123.
- [6] W.J. Cunliffe, D.J. Gould, Br. Med. J. 1 (6171) (1979) 1109–1110.
- [7] B. Dréno, A. Layton, C.C. Zouboulis, J.L. López-Estebarez, A. Zalewska-Janowska, E. Bagatin, V.A. Zampeli, Y. Yutskovskaya, J.C. Harper, J. Eur. Acad. Dermatol. Venereol. 27 (9) (2013) 1063–1070.
- [8] L. Misery, J. Invest. Dermatol. 131 (2) (2011) 290–292.
- [9] A.W. Armstrong, S. Cheeney, J. Wu, C.T. Harskamp, C.W. Schupp, Am. J. Clin. Dermatol. 13 (6) (2012) 405–416.
- [10] R. Darabi, M. Hafezi, N. Akbarloo, Clin. Microbiol. Infect. Suppl. (2005) 11.
- [11] K.A. Hammer, Int. J. Antimicrob. Agents 45 (2) (2015) 106–110.
- [12] E. Markum, J. Baillie, J. Drugs Dermatol. 11 (3) (2012) 349–354.
- [13] N. Pazyar, R. Yaghoobi, N. Bagherani, A. Kazerouni, Int. J. Dermatol. 52 (7) (2013) 784–790.
- [14] C.F. Carson, B.J. Mee, T.V. Riley, Antimicrob. Agents Chemother. 46 (6) (2002) 1914–1920.
- [15] S.E. Cross, M. Russell, I. Southwell, M.S. Roberts, Eur. J. Pharm. Biopharm. 69 (1) (2008) 214–222.
- [16] E.M. Ahmed, J. Adv. Res. 6 (2) (2015) 105–121.
- [17] M.-C. Chen, H.-W. Tsai, C.-T. Liu, S.-F. Peng, W.-Y. Lai, S.-J. Chen, Y. Chang, H.-W. Sung, Biomaterials 30 (11) (2009) 2102–2111.
- [18] N. Bhattarai, J. Gunn, M. Zhang, Adv. Drug Deliv. Rev. 62 (1) (2010) 83–99.
- [19] H. He, X. Cao, L.J. Lee, J. Control Release 95 (3) (2004) 391–402.
- [20] K.S. Soppimath, A.R. Kulkarni, T.M. Aminabhavi, J. Biomater. Sci. Polym. Ed. 11 (1) (2000) 27–43.
- [21] B.N. Estevinho, F. Rocha, in: Nanotechnology Applications in Food, Elsevier, 2017, pp. 1–19, <https://doi.org/10.1016/B978-0-12-811942-6.00001-7>.
- [22] C. Sebaaly, C. Charcosset, S. Fourmentin, H. Greige-Gerges, in: Role of Materials Science in Food Bioengineering, Elsevier, 2018, pp. 187–234, <https://doi.org/10.1016/B978-0-12-811448-3.00006-1>.
- [23] G. Tiwari, R. Tiwari, A.K. Rai, J. Pharm. Bioallied Sci. 2 (2) (2010) 72–79.
- [24] I.B. Bassett, R.S.C. Barnetson, D.L. Pannowitz, Med. J. Aust. 153 (8) (1990) 455–458.
- [25] H.H. Kwon, J.Y. Yoon, S.Y. Park, S. Min, D.H. Suh, Dermatology 229 (2) (2014) 102–109.
- [26] X. Liu, W. Xia, Q. Jiang, Y. Xu, P. Yu, J. Agric. Food Chem. 62 (1) (2014) 297–303.
- [27] Y.-J. Jeon, S.-K. Kim, J. Microbiol. Biotechnol. 11 (2) (2001) 281–286.
- [28] B. Ghosh, D. Bhattacharya, A. Kotal, A. Kuila, M. Mukhopadhyay, J. Solgel Sci. Technol. 94 (3) (2020) 616–627.
- [29] G. Borkow, Curr. Chem. Biol. 8 (2) (2014) 89–102.
- [30] T.R. Hoare, D.S. Kohane, Polymer 49 (8) (2008) 1993–2007.
- [31] S. Gerecht, S.A. Townsend, H. Pressler, H. Zhu, C.L.E. Nijst, J.P. Bruggeman, J.W. Nichol, R. Langer, Biomaterials 28 (32) (2007) 4826–4835.
- [32] I. Martin, B. Obradovic, S. Treppo, A.J. Grodzinsky, R. Langer, L.E. Freed, G. Vunjak-Novakovic, Biorheology 37 (1–2) (2000) 141–147.
- [33] L. Yildirimer, N.T.K. Thanh, A.M. Seifalian, Trends Biotechnol. 30 (12) (2012) 638–648.
- [34] A. Domján, J.N. Bajdik, K. Pintye-Hódi, Macromolecules 42 (2009).
- [35] A.A. D'souza, R. Shegokar, Expert Opin. Drug Deliv. 13 (9) (2016) 1257–1275.
- [36] S. Saravana, G. Bheemaneni, R. Kandaswamy, Mater. Today: Proc. 5(1, Part 1) (2018) 1591–1598.
- [37] T.-W. Lee, J.-C. Kim, S.-J. Hwang, Eur. J. Pharm. Biopharm. 56 (3) (2003) 407–412.
- [38] Y. Liu, D.A. Peterson, H. Kimura, D. Schubert, J. Neurochem. 69 (2) (1997) 581–593.
- [39] H.S. Bhargav, S.D. Shastri, S.P. Poornav, K.M. Darshan, M.M. Nayak, Measurement of the Zone of Inhibition of an Antibiotic, in: 2016 IEEE 6th International Conference on Advanced Computing (IACC), 2016.



Advances in modified antimicrobial peptides as marine antifouling material

Rituparna Saha^{a,b}, Debalina Bhattacharya^c, Mainak Mukhopadhyay^{a,*}

^a Department of Biotechnology, JIS University, Kolkata, West Bengal 700109, India

^b Department of Biochemistry, University of Calcutta, Kolkata, West Bengal 700019, India

^c Department of Microbiology, Maulana Azad College, Kolkata, West Bengal, 700013, India

ARTICLE INFO

Keywords:

Marine biofouling
Biofilm
Antimicrobial peptides
Modifications
Antifouling

ABSTRACT

Biofouling is the undesirable attachment of organisms and their by-products on surfaces. It has become a severe problem in the industries that utilize devices and facilities in the marine environment. Several antifouling strategies have been developed, but many have adverse effects on numerous species, the surrounding environment, and marine devices. However, antimicrobial peptides (AMPs) have emerged as a promising non-toxic biomaterial that can modify the submerged surfaces to inhibit biofouling. AMPs are getting recognized as a highly potent material as they exhibit strong antimicrobial activity against fouling organisms and resistance towards biofilm formation. This review discusses the latest developments made in recent years regarding applying AMPs as prominent marine antifouling material. The various properties of AMPs, including structural, functional characteristics, and mechanism of action, are presented. Different types of modification of AMPs to improve their stability, efficacy, and activity against fouling organisms are discussed in detail. Furthermore, future perspectives and significant improvements required to make AMPs an integrative part of the marine antifouling process are reviewed.

1. Introduction

The exponential rise in world population in the recent decades has led to extraordinary levels of industrial development. This has increased general economic prosperity and created an immense demand for necessities, putting tremendous pressure on natural resources. The most prominent of them is water resources which are one of the most vital commodities in the world. Access to the wide variety of riches provided by the water-based ecosystems is directly related to human health, agriculture, energy, and many industrial activities [1]. Commercial enterprises like fisheries, offshore gas and oil, transportation, cooling systems, and canalizations are well-known marine industries that positively impact the world economy. Irrespective of all the advantages, the limited availability of fresh- and clean water has made water scarcity one of the most prominent issues of the 21st century. The situation is rapidly worsening due to geopolitical conflicts and extreme weather conditions, which have increased water demands in many industrial sectors [2]. This has led numerous scientists and policymakers to look for alternatives like desalination technologies and membrane bioreactors to treat, recycle, and produce clean water to meet the rising demands and ultimately solve the water crisis.

However, there are severe problems associated with marine-based technologies and industries which thwart production efficiency and quality and cause substantial operating costs. One such complication quickly becoming a critical global issue is marine fouling. Although different types of fouling occur in marine-based systems, biofouling is considered the major and the most dominant fouling mechanism [3]. The phenomenon of 'Biofouling' is the undesirable attachment and colonization of organisms and their by-products on the surfaces. It gets initiated when biomolecules such as polysaccharides and proteins adhere to the surfaces, supporting bacterial accumulation. The attachment of bacteria leads to forming of a well-defined bacterial network known as biofilm [4,5]. In the biofilm, the bacterial aggregates can exchange nutrients and signals. The biofilm also encapsulates the entire bacterial population in an extracellular matrix, making it more resistant to the surrounding environment and eventually acquiring antibiotic resistance. In addition, the biofilm also helps other organisms like fungi, algae, barnacles, mollusks, and sponges, to adhere to the surface, thereby causing a significant setback for different machine systems (Fig. 1) [6,7].

Several industries and other water-dependent technologies use various naval devices whose metallic surfaces remain submerged in

* Corresponding author.

E-mail address: m.mukhopadhyay85@gmail.com (M. Mukhopadhyay).

<https://doi.org/10.1016/j.colsurfb.2022.112900>

Received 1 July 2022; Received in revised form 19 September 2022; Accepted 1 October 2022

Available online 3 October 2022

0927-7765/© 2022 Elsevier B.V. All rights reserved.

water wholly unprotected. The attachment of fouling organisms to these surfaces increases the corrosion. It reduces the speed of the devices, ultimately limiting their service life and producing terrible economic and environmental consequences. Biofouling costs several billion US dollars to the marine industry per year [8,9]. Therefore, various strategies have been explored to tackle biofouling and develop environment-friendly antifouling strategies that remain a significant challenge. Most of the approaches are typically based on the physical, chemical, and topographical modifications in the surfaces [10,11]. Overall, the strategies can be divided into 'Anti-biofouling,' which includes modifications that prevent the adhesion of the organisms to the surfaces, and 'Anti-microbials,' which are materials that kill the accumulated bacteria. Some of the anti-biofouling solutions include chemical modifications with natural products, zwitterionic polymers, hydrophilic or amphiphilic polymers, organic-inorganic hybrid systems, polymer-peptide conjugates, self-assembly of low molecular weight peptides, and immobilization of protein-repelling polymers like polyethylene glycol (PEG) and oligoethylene glycol (OEG) [12–14].

Although many antifouling materials have been identified and developed over the years, many have shared common disadvantages like lacking long-term stability and expelling other surrounding organisms. Thus, it has been necessary to synthesize and extract highly efficient antifouling agents that can inhibit the attachment of bacteria and biofilm formation and ultimately block biofouling [5]. One class of biomolecules that has shown promise as effective antifouling coatings on surfaces is 'Antimicrobial peptides' (AMPs). AMPs have garnered particular attention due to their ability to kill bacteria and serve as antibiotics [15]. They are generally produced by various organisms such as animals, plants, fungi, bacteria, and viruses. Most organisms produce many AMPs as an arsenal against intruding pathogens [16]. These peptides have been demonstrated to produce their impact by either disrupting the cell membrane's integrity or entering the cells and attacking specific intracellular targets. In most cases, the peptides act through charge interaction due to their amphiphilic structure, damaging the bacteria and killing them. Therefore, using AMPs coatings on surfaces can help to reduce the surface adsorption of biomolecules, bacteria, and other organisms, thus proving to be a highly desirable solution to the marine biofouling problem [17,18].

Since the late 1950 s, biofouling and corrosion have been prevented

by using biocide-containing antifouling paints as coatings for submerged surfaces which proved to be highly effective against fouling organisms. But their broad-spectrum impact on marine organisms raised environmental concerns, leading to restrictions limiting their use [14]. In recent years, studies on surfaces immobilized with non-toxic AMPs have shown great potential as antimicrobial and antifouling coatings. Scientists have developed various strategies by taking a modern and bio-friendly approach to employing AMPs as useful marine antifouling material [19]. Biomimicry has been identified as a promising strategy that includes isolating, synthesizing and modifying natural antifouling compounds produced by marine organisms to protect surfaces by inhibiting biofilm formation [20]. Surfaces modified by AMPs are more stable, which changes bacterial orientation and kills them once coming in contact. Surface topology is another crucial strategy that uses artificially designed surface microstructures with AMPs to reduce fouling attachment by decreasing surface attachment points [21]. AMPs have gained enormous importance as amphiphilic coatings due to their tuneable structural and functional characteristics, which can be modified by controlling the exact addition of amino acids and, therefore, the location and concentration of hydrophilic and hydrophobic moieties. This precise control has immensely helped in optimizing the antifouling performances of AMPs, which have been found to be closely related to their surface composition [22,23].

Recently, many studies have been carried out involving a wide range of AMPs which have been demonstrated as suitable antifouling coatings. In addition, several AMPs have also been modified to enhance their chemical characteristics for their application to prevent bacterial growth. Many previous reviews have discussed different AMPs that are used for a multitude of applications. However, to the best of our knowledge, any reviews discussing AMPs focusing on their modified forms have been sparse. As a result, in this review article, we hope to provide an in-depth understanding of AMPs and how their functionality forms one of the fundamental properties of antifouling. In addition, the variety of AMPs that are explicitly used as marine antifouling agents will be summarized, and the modifications in the peptides which bring change in their structure and function will be discussed in detail.

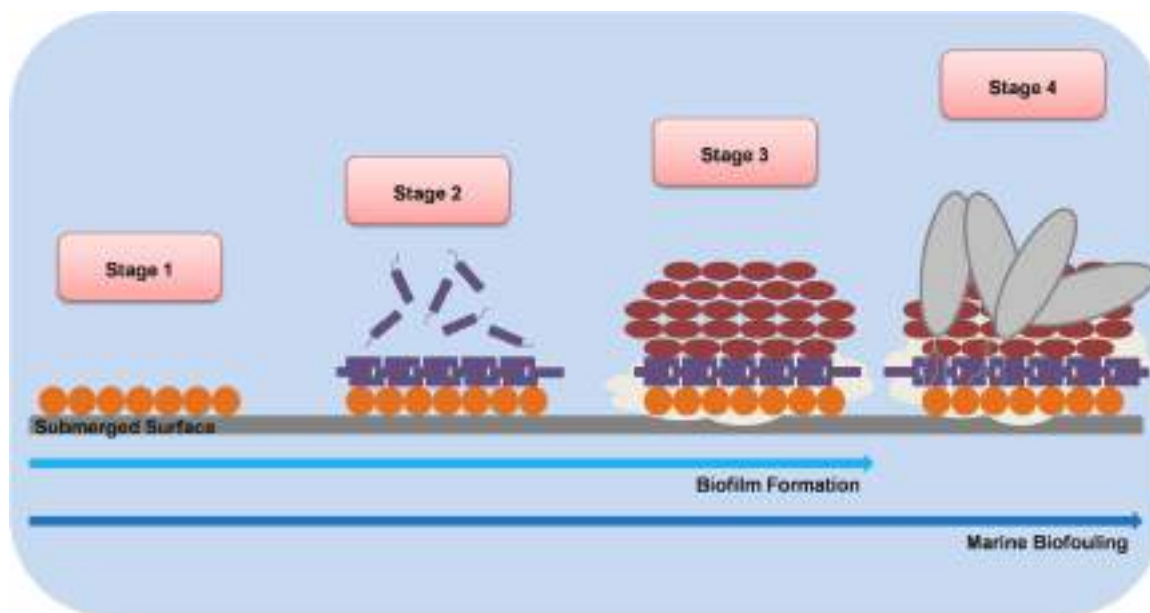


Fig. 1. Marine Biofouling process. Stage 1: Surface conditioning with organic and inorganic macromolecules, Stage 2: transport and attachment of bacteria to the surface, Stage 3: Formation of a complex biofilm strengthening the attachment of bacteria to the surface, Stage 4: After enough biofilm forms, large organisms attach and develop a more complex strategy.

2. Antimicrobial peptides

The growing use of antibiotics in multiple industries has led to the emergence of drug-resistant pathogenic microorganisms. This has resulted in a worldwide quest to develop a new generation of antibiotics. Currently, AMPs are considered the alternative to conventional antibiotics as they lead to bacteria developing little to no resistance [24]. AMPs, also known as host defense peptides, are diverse biological molecules that exhibit a broad spectrum of activity against microorganisms. Discovered over 70 years ago, AMPs are oligopeptides consisting of 5–100 amino acids with a molecular weight of 2–10 kDa [25, 26]. They are highly abundant and form an essential part of the innate immune system, and generally are expressed in response to any attack by pathogenic microorganisms [27]. These peptides differ in the number of amino acids, peptide structure, net charge, physicochemical properties, and their mechanism of action.

2.1. Diversity

AMPs are produced by various organisms, ranging from bacteria to fungi, plants, vertebrates, and invertebrates. Nearly all bacterial species produce AMPs whose primary function is to kill other bacterial species competing for nutrients and the same habitat. One of the first peptides isolated from bacteria was Gramicidin D, synthesized by a multienzyme complex containing D-amino acids. Gramicidin kills bacteria by increasing the permeability of their cell membranes to monovalent cations, thereby destroying the intracellular ion gradient. These AMPs are highly active against Gram-positive bacteria and very few Gram-negative organisms [28]. Nisin, another prominent bacterial peptide, is a member of the lantibiotic family, characterized by the presence of uncommon amino acids. Nisin was isolated from *Lactococcus lactis* and contained a single lanthionine molecule and two β -methyl lanthionine rings. Nisin acts by forming pores on the cell membrane and inhibiting peptidoglycan synthesis. Compared to Gramicidin, nisin exhibits a broad spectrum of activity against several Gram-positive and Gram-negative pathogenic bacteria [29]. Other standard bacterial AMPs include microcins, tyrothricins, gageotetrins, and polymyxin B, which exhibit their distinctive activity spectrum on pathogenic organisms [30].

Even though bacterial AMPs are pretty common, a significant proportion of AMPs studied extensively belong to eukaryotes. In the case of fungi, most of the peptides extracted belong to the peptaibols peptide family, which is identified by the presence of non-proteinogenic amino acids, like α -aminoisobutyric acid (Aib). They also consist of acetylated N-terminal residues along with the presence of amino alcohol like phenylalanine or leucinol at their C-terminus. Alamethicin, produced by *Trichoderma viride*, is the most common peptaibol, exhibiting a broad spectrum of action ranging from bacteria, fungi, and animals to insect cells. Trichogen GA IV is a lipopeptaibol with an Aib residue, leucinol at its C-terminal end but differs from alamethicin due to a lipophilic acyl chain at the N-terminal end. Tricholongins B and Saturninins SA are some of the other peptaibols which are effective against Gram-positive and Gram-negative bacteria [29,30].

Plants produce several different types of AMPs as they play an essential role in their innate immunity offering protection from infection by bacteria and fungi. These peptides are found in leaves, flowers, seeds, and tubers and are rich in cysteine with numerous disulfide bonds. The most relevant groups of plant AMPs are Purothionins, Defensins, and Cyclotides. Purothionins are cationic peptides toxic to mammalian cells and against several pathogenic bacteria, whereas defensins are cationic peptides but exhibit antifungal activity. In comparison, cyclotides are amphipathic peptides that provide resistance against insect infections and have antibacterial and antifungal activity [31–33].

Like plants, invertebrates also lack an adaptive immune system, so they depend entirely on their innate immune response. AMPs have been isolated from almost all invertebrates studied to date. The AMP family of Discodermins produced in sponges are active against bacteria and fungi.

Aurelin, isolated from jellyfish, has antibacterial activity. Marine mollusks produce several cysteine-rich peptides which exhibit antifungal activity. Gram-negative bacteria are more sensitive toward the family of AMPs, i.e., Cecropins isolated from the hemolymph of the giant silk moth. The Ceratotoxins family of peptides also has the same activity. However, they belong to the sex-specific family of AMPs as they are produced only in the female reproductive accessory glands of the Mediterranean fruit fly [29,30,34].

Compared to other organisms, vertebrates consist of both innate and adaptive immunity. Most AMPs have been isolated from various vertebrates, like fish, reptiles, amphibians, birds, and mammals. The most prominent ones that have been characterized belong to the Cathelicidins and Defensins family of peptides. They have been isolated from intestines and different white blood cells of fishes, skins of different amphibians, bodily fluids, mouth, and lungs of reptiles, birds, and mammals. These peptides generally exhibit a broad spectrum of antimicrobial activity [30].

2.2. Structural features

AMPs are a distinct and diverse range of biomolecules. Like their familiar counterparts, they also consist of definite structural properties that could be classified into primary and secondary structures.

The primary structure of AMPs is defined by their sequence length and amino acid composition. With over 2500 AMPs identified and sequenced, it has become easier to investigate the relationship between their structure and activity. The sequence lengths of most peptides vary from 10 to 60 amino acid residues, with shorter lengths generally having a decreased tendency to form secondary structures and therefore compromising their interaction with bacteria [35]. In comparison, long-chain peptides often exhibit much higher hemolytic and cytotoxic activity. Concerning their amino acid composition, AMPs mainly include cationic residues like arginine, lysine, and histidine and hydrophobic residues composed of aliphatic and aromatic amino acids. In addition, cysteine and proline residues are highly conserved in natural AMPs. The positively charged amino acids serve to interact with the negatively charged components of the bacterial cell wall. In contrast, the hydrophobic amino acids get incorporated into the lipid bilayer to increase membrane permeability and ultimately cause disruption to ion channels, which leads to cell death [36,37].

AMPs could be classified into three subgroups when it comes to secondary structures. The first is the α -helices which are found in a high proportion among peptides and have been derived from different species ranging from insects, amphibians, fish, plants, and mammals. Many studies have reported that most of the peptides that act on cell membranes acquire the α -helical structure in order to segregate the charged residues from hydrophobic amino acids so that the positively charged amino acids could interact through electrostatic interactions with the negatively charged molecules present in the bacterial cell wall and exhibit its antimicrobial activity [38]. The second principal structure which AMPs predominantly adopts is a β -sheet structure. Interestingly, β -sheet peptides have multiple cysteine residues, which are conserved and participate in the formation of disulfide bridges that stabilize their bioactive conformation and protect against protease degradation. Studies have shown that β -sheet and α -helical peptides with equal hydrophobicity and charge impart similar antimicrobial activities, but β -structures tend to exhibit much greater cell selectivity [28]. The third and final subgroup of secondary structure includes extended structures. Most AMPs that possess this structure have a higher proportion of proline and glycine residues. Proline-rich extended peptides mostly have 15–39 residues and are isolated from mammals and insects. In comparison, glycine-rich extended peptides have been extracted from various insect species, and their size varies from 8 to 30 kDa [39].

2.3. Functional characteristics

Three significant parameters determine the functional characteristics of any AMPs. The first feature is the net positive charge present in any amphipathic peptides. Most cationic peptides have a positive charge ranging from + 2 to + 9 as the interaction between the peptides and the cell membranes depends upon the electrostatic attraction. The net positive charge carried by any peptides generally impacts its antimicrobial activity. Studies have indicated that enhancing the positive charge of an AMP results in a greater affinity between the microbial membrane and the peptide, whereas introducing negative charges decreases the antimicrobial activity of AMPs [40]. The second important parameter involved is hydrophobicity, which is responsible for the antimicrobial activity and cell selectivity of AMPs. Peptides with high hydrophobicity easily damage the membrane structure resulting in cell lysis or helping to form transient pores in the membranes for the peptides to enter and interact with intracellular targets. The third parameter responsible for the antimicrobial activity of AMPs is its amphipathicity which results from the segregation of the polar and hydrophobic residues on the opposite faces of the molecular framework. The amphipathic nature enables AMPs to form α -helical structures and exhibit a broad spectrum of antimicrobial activity. Studies have revealed that increasing the amphipathicity of peptides tends to enhance both the bactericidal effects and cytotoxicity [39,41].

2.4. Mechanism of action

The antimicrobial activity is one of the most fundamental mechanisms of action of all AMPs. It is highly complex and difficult to characterize as some AMPs can act on multiple targets at once. However,

studies have provided clear evidence of two significant pathways sufficient to cause cell death (Fig. 2).

One of the primary pathways by which AMPs affect organisms is interacting through their cell membranes. The peptides can achieve the amphipathic conformation when it meets the negatively charged membranes. The Gram-positive and Gram-negative bacteria membrane composition makes them highly susceptible to peptide attack [42]. Once the peptides bind to the membranes, they cross the polysaccharides and other components before interacting with the cytoplasmic membrane in Gram-positive bacteria. In comparison, peptides gain access to the inner and outer membranes by displacing the divalent cations, destabilizing Gram-negative bacteria's molecular assembly [43]. In addition, some peptides keep attaching themselves to the target surface until they reach a threshold concentration. As the concentration increases, the peptides continue interacting with the lipid headgroups, folding, and orienting themselves perpendicularly to the lipid molecules, then inserting themselves by partitioning in the hydrophobic core of the bilayer. As they reach the required threshold concentration, the peptides undergo conformation changes and alter the bilayer topology through pore formation or membrane disintegration [28,44].

Another prominent pathway involves AMPs exerting their antimicrobial activity by targeting intracellular targets. Certain peptides can enter the organisms through the membranes by keeping them intact and mitigating their activity by interacting with the anionic cellular nucleic acids or intracellular enzymes involved in crucial metabolic activities [35].

2.5. Synthetic AMPs

Generally, the production of cationic AMPs cannot be enhanced by

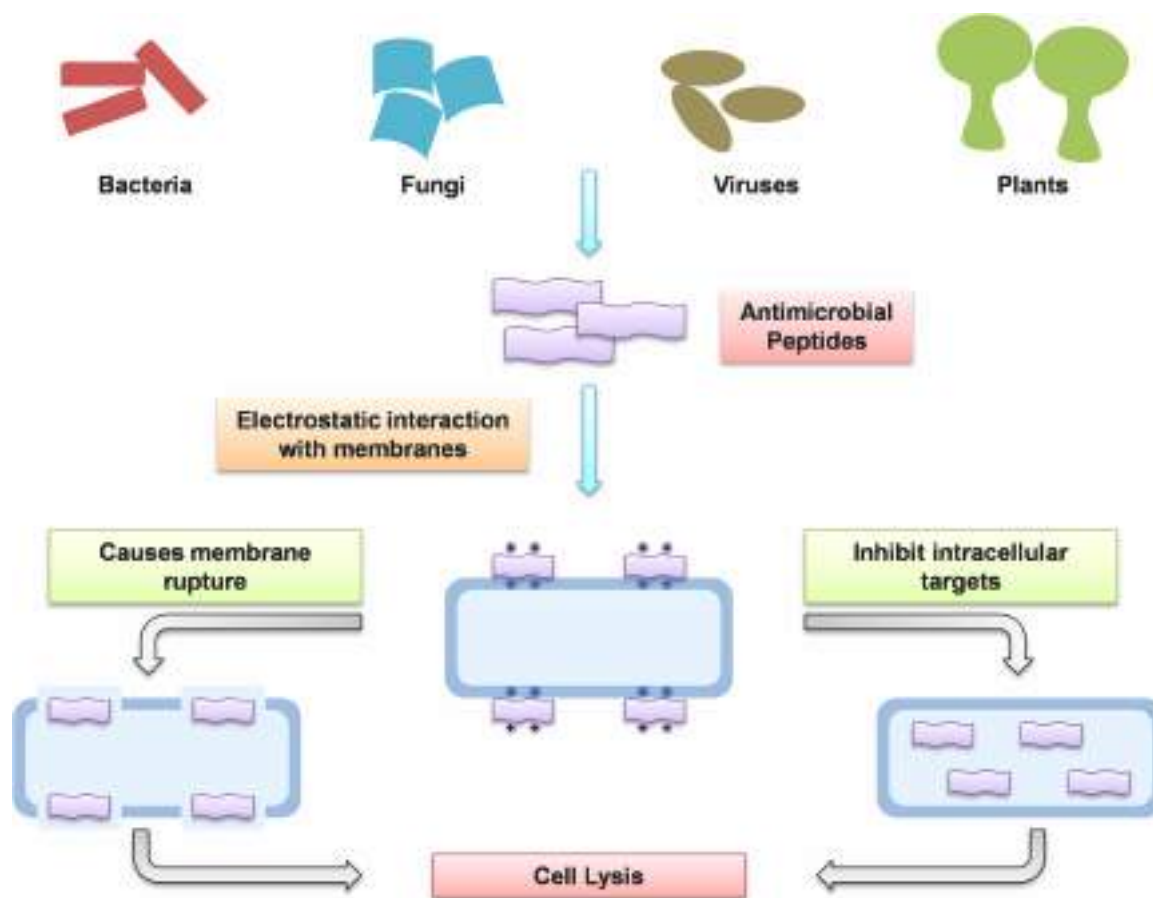


Fig. 2. Mechanisms of action of antimicrobial peptides.

recombinant expression as they are toxic to the cells. Therefore, most peptides are synthesized chemically, while some are expressed in bacteria as part of fusion proteins, tandem multimers, or inclusion bodies [45]. Research has pioneered the synthesis of synthetic hybrid peptides based on natural AMPs, which increase the activity of the compounds and can be made to change the targets and decrease their cytotoxicity. Some peptides are also produced as synthetic analogs of natural AMPs [46]. These synthetic analogs are designed to have a broad spectrum of activity and cell selectivity compared to their natural counterparts. In addition, synthetic cationic AMPs are also designed not based on natural sequences and could be imparted with features like better attachment with membranes and having a particular secondary structure that effectively increases the potency of its antimicrobial activity [30].

3. Development of modified AMPs as marine antifouling material

Biochemical modification of different marine-based surfaces has become crucial to avoid biofouling. Although many different strategies have been developed, AMPs as an antifouling material have quickly gained increased attention in recent years. Generally, various AMPs are available, but their finite antibacterial activity limits their use universally. Research into the modification of the evolutionary design of these peptides has helped not only improve amphipathicity and introduce flexibility in their conformation. However, it has also enhanced their antibacterial activity and selectivity over a broad spectrum, establishing greatly improved structure-activity and structure-selectivity relationships (Fig. 3) [47,48].

3.1. Direct modification to AMPs

Rapid colonization of submerged metallic structures by a host of organisms affects the material's performance and causes early deterioration. Natural biofilm formation is highly complex and involves interaction between the microorganism, submerged surfaces, and the chemical components naturally present in the seawater. One of the

initial actions taken for biofilm inhibition is the attachment of AMPs to surfaces to fight against marine biofouling (Table 1). Natural peptides were extracted from snow crabs to reduce biofilm formation in submerged mild steel surfaces in a study. Five different AMPs were extracted, mainly composed of D-amino acids like D-tyrosine, D-leucine, D-tryptophan, and D-methionine, which can inhibit biofilm formation in a solid medium as well as a liquid medium. The snow crab AMPs combined with the natural organic matter present in seawater produced an antifouling effect on the organisms' cellular arrangement and viability, thereby affecting the formation of conditioning film, the first stage of biofilm formation [8]. Another study extracted Portoamides which are cyclic peptides produced by the cyanobacterium *Phormidium* sp. LEGE 05292 demonstrated high effectiveness against mussel larvae settlement and bioactivity towards biofilm disruption of bacterial strains, revealing broad-spectrum bioactivity towards a range of biofouling species [49].

A metal-binding peptide with the sequence NLNPNTASAMHV was used as the target peptide to prepare a hydrophobic/hydrophilic metal surface on stainless steel. Experiments on surface morphology, roughness, and Fourier-Transform Infrared Spectroscopy (FTIR) revealed that changes occurred on the steel surface, making the surface coarser and some organic groups' appearance in the modified steel surface, endowing the metal surface protection against biofouling [50]. In another study, a peptide derived from the receptor-binding domain of *Pseudomonas aeruginosa* type IV pilin with the sequence ACTSNADN-KYLPKTCQT was used to modify the surface of the stainless steel surface. Scanning Electron Microscopy (SEM) and FTIR demonstrated that the peptide got successfully bound to the steel surface and illustrated antimicrobial activity against *Staphylococcus aureus* when tested, presenting valuable information for peptide-dependent marine anti-biofouling approaches [51]. AMPs were covalently attached to membrane surfaces involved in water purification processes like desalination. The photo-reactive 3-(4-benzoylphenyl)alanine was incorporated into the AMP sequence RWRWRWA, attached to the surface by filtration, and subsequently irradiated with UV light. The modification increased the surface hydrophilicity and moderately altered the membrane's performance. The modification also decreased bacterial viability by 55 % and

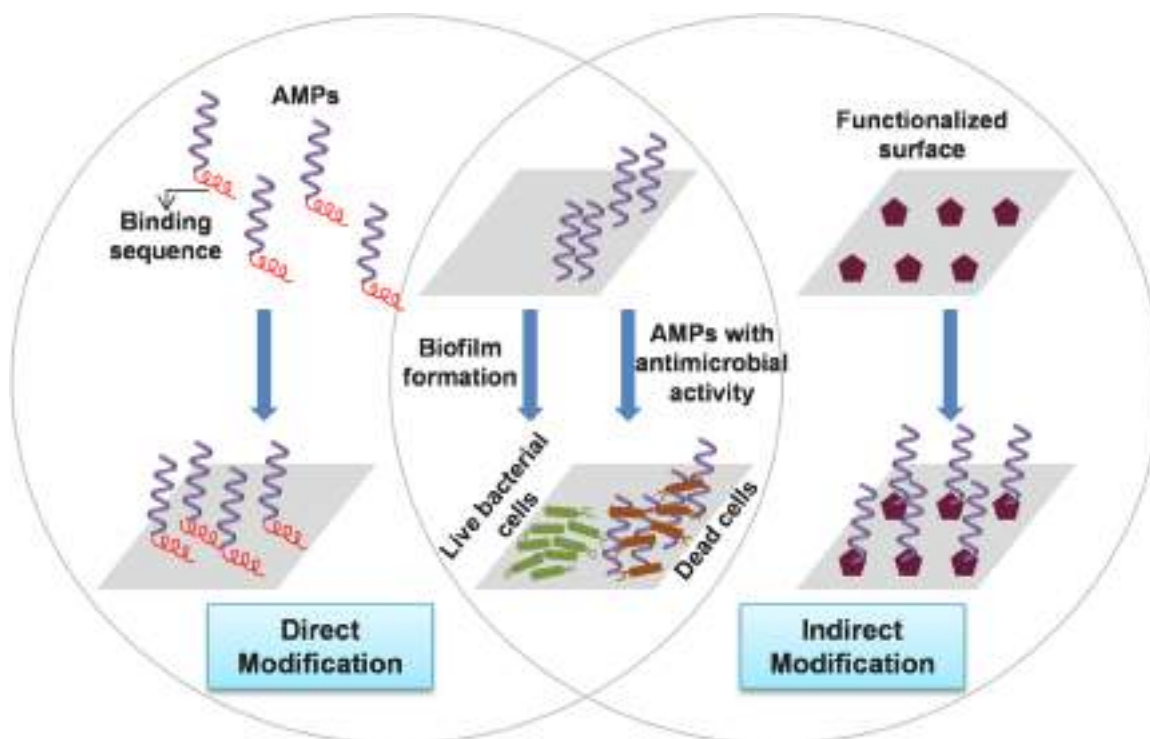


Fig. 3. Major types of modifications of antimicrobial peptides for use as marine antifouling agents.

Table 1

Summary of directly modified AMPs developed as marine antifouling material.

AMPs	Origin	Structure	Modification	Mechanism	Antifouling activity	References
Composed of D-amino acids like D-tyrosine, D-leucine, D-tryptophan, and D-methionine	Snow crab (<i>Chionoecetes opilio</i>)	–	Combined with natural organic matter	Affects organisms' cellular arrangement and viability	Inhibits formation of conditioning film	[8]
Portoamides	<i>Phormidium</i> sp. LEGE 05292	Cyclic dodecapeptides		Broad-spectrum bioactivity	Mussel larvae settlement and bioactivity towards biofilm disruption of bacterial strains	[49]
NLNPNTASAMHV	Synthetic	–	Metal-binding peptide	Imparts hydrophobicity to its attached metal surface on stainless steel	Prevents biofilm formation	[50]
ACTSNADNKYLPKTCQT	<i>Pseudomonas aeruginosa</i> type IV pilin	–	Metal-binding peptide	Inhibits organisms' cellular viability	Antimicrobial activity against <i>Staphylococcus aureus</i>	[51]
RWRWRWA	Synthetic	–	Photoreactive 3-(4-benzoylphenyl)alanine was incorporated and irradiated with UV light	Affects organisms' cellular viability by 55 %	Inhibits biofilm formation against <i>Pseudomonas aeruginosa</i>	[52]
NCLNPNTASACMHV	Synthetic	–	–	Antimicrobial and anti-algal activity	Reduces biofilm formation and exerts strong anti-algal performance against <i>Chlorella pyrenoidosa</i> and <i>Phaedactylum tricornutum</i> , at a rate of 78.56 % and 87.80 %, respectively	[53]
Melittin	–	α -helical peptide	Charge conversion mechanism	After attachment of bacteria, produces a acidic microenvironment affecting cell viability	Antimicrobial activity against a wide range of Gram-positive and Gram-negative bacteria	[54]
Equinatoxin II	Beadlet anemone (<i>Actinia equine</i>)	Cyclic peptides	Attachment of a hydrophobic palmitic acid	Inhibits settlement of mixed marine microbial consortium	Prevents biofilm formation over 24 h	[55]
Zwitterionic peptides	Synthetic	–	Block charge distributions	–	Broad-spectrum antifouling activity	[56]
Zwitterionic peptides	Synthetic	–	Incorporated amino acid spacers like serine, glycine, and leucine	–	Leucine inserted peptides significantly increased protein adhesion, while serine reduced the interaction between the peptide monolayer and various protein foulants	[57]
Zwitterionic peptides	Synthetic	–	Self-assembled monolayers (SAMs)	–	Low rate of barnacle larvae settlement, with SAMs exhibiting exceptionally favorable antifouling properties	[58]
Fluorinated and non-fluorinated oligopeptide	Synthetic	–	Two triblock amphiphilic polymers - one containing a hydrophobic middle block and another hydrophilic middle block	–	Copolymers exerted both antifouling and fouling release properties against the cells of the diatom <i>Navicula incerta</i> and the green algae <i>Ulva linza</i>	[59]
2,5-diketopiperazine	–	–	Pharmacophore derived from amphiphilic micropeptides	Broad-spectrum activity	Against various fouling organisms but in low micromolar range	[60]
21 amino acid long peptide	Synthetic	–	Adhesive group in the form of the amino acid 3,4-dihydroxy-L-phenylalanine (L-DOPA) was added	Inhibits bacterial colonization	–	[61]
Amphiphilic peptide	Synthetic	–	Lysine placed adjacent to the L-DOPA residue for better adhesion, adding a linear fluorinated N-terminal to improve the film's packing density, along with placing L-DOPA at the C-terminal	–	Antifouling properties was enhanced by 30 %	[62]
Sarcosine	Synthetic	–	Grafting density and the side chain was varied	–	Increased antifouling performance	[63]
Analogin	Synthetic	–	Incorporated into a polymer scaffold	–	Increased the release of the fouling organisms <i>Ulva linza</i> and <i>Navicula incerta</i>	[64]
D-enantiomers containing peptides	Synthetic	–	Incorporated with non-proteinogenic Aib	–	Resistant towards the diatoms <i>Navicula</i>	[65]

(continued on next page)

Table 1 (continued)

AMPs	Origin	Structure	Modification	Mechanism	Antifouling activity	References
Peptide-terminated SAMs	Synthetic	–	A serine residue was replaced with an alanine residue The bulky Aib molecule was inserted	Change with alanine altered the hydrophilicity of the peptide Inclusion of Aib decreased the overall packing density by almost 17–37 % and changed the structure from a mixture of β -sheet/random coil to completely random coil Showed antimicrobial activity by inhibiting cellular viability	<i>perminuta</i> and <i>Cobetia marina</i> Reduced fouling by <i>N. perminuta</i> 50–84 % better against the settlement of <i>U. linza</i> and 100 % resistant against the enzymatic degradation by trypsin	[66]
14-mer peptide containing an amino acid sequence derived from the sea anemone <i>Actinia equina</i>	Synthetic	–	Combined with tetrakis (hydroxymethyl) phosphonium sulfate (THPS)		Demonstrated a 2-log reduction, 1-log reduction, and 1-log reduction in sessile sulfate-reducing bacteria cell count, sessile acid-producing bacteria cell count, and sessile general heterotrophic bacteria cell count, respectively	[67]

inhibited biofilm formation against *Pseudomonas aeruginosa* [52].

Treatment of a surface with a peptide containing sequence NCLNPNTASACMHV brought changes in the surface chemical composition and surface topology, which slightly reduced biofilm formation but exerted strong anti-algal performance, with the rate reaching 78.56 % and 87.80 % for anti-*Chlorella pyrenoidosa* and anti-*Phaedactylum tricornutum*, respectively [53]. Another study used the α -helical peptide melittin constructed with a charge conversion mechanism. The pH-sensitive moieties immobilized on the surface involved an acrylic acid polymer brush grafted on the surface using UV light and benzophenone as a photoinitiator. The surface was modified with ethylenediamine and 2,3-dimethylmaleic anhydride, following which the melittin was fixed using electrostatic interaction. This modified surface allowed bacteria to grow exponentially, accumulate, and ultimately attach to the surface. This triggers an acidic micro-environment which leads the pH-responsive surface to ultimately release the peptide, exhibiting antimicrobial activity against a wide range of Gram-positive and Gram-negative bacteria [54]. In addition, noncovalent interactions have also immobilized cyclic peptides with a hydrophobic palmitic acid attaching them to membranes. The adsorbed peptides could disperse already established biofilms, withstand significant stress, remain active, and prevent biofilm formation for over 24 h [55].

Zwitterionic peptides are a class of AMPs considered highly favorable candidates for antifouling processes. A study revealed that surface-tethered zwitterionic peptides with multiple zwitterionic lysine and glutamic acid residues exhibit better antifouling performance. However, the same amount of positive and negative charge affects the structure of the peptide molecule but does not change its antifouling properties at all [56]. Another study incorporated neutral amino acid spacers like serine, glycine, and leucine, which have different hydrophobicities, into zwitterionic peptides. Analysis revealed that the hydrophilicity of the neutral spacers affects the structure as well as the antifouling performance of the peptide. Hydrophobic leucine inserted peptides significantly increased protein adhesion, while hydrophilic serine reduced the interaction between the peptide monolayer and various protein foulants [57]. Zwitterionic peptide-based fouling resistant self-assembled monolayers (SAMs) were subjected to presentation of surface-attached pheromones for barnacle larvae. The analysis confirmed the low rate of barnacle larvae settlement, but SAMs exhibited exceptionally favorable antifouling properties [58].

A study demonstrated the modification of a fluorinated and non-fluorinated non-natural oligopeptide with two triblock amphiphilic polymers – one containing a hydrophobic middle block and another hydrophilic middle block. Surfaces coated with these copolymers

exerted both antifouling and fouling release properties against the cells of the diatom *Navicula incerta* and the green algae *Ulva linza* [59]. Incorporation of pharmacophore derived from amphiphilic micro-peptides into a 2,5-diketopiperazine scaffold displayed broad-spectrum activity in the low micromolar range and against various fouling organisms [60]. A 21 amino acid long peptide containing antifouling and antibacterial group attached to a peptide backbone was synthesized in a study. An adhesive group in the form of the amino acid 3,4-dihydroxy-L-phenylalanine (L-DOPA) was added, making the peptide capable of getting adsorbed onto titanium surfaces overnight. Microscopy, bacterial staining, and colony-forming-unit counting method confirmed that the peptide could inhibit bacterial colonization while preventing bovine serum albumin adhesion, demonstrating the peptide's antifouling properties [61]. In another study, an amphiphilic peptide was manipulated by changing the position of certain individual amino acids. This included positioning lysine adjacent to the L-DOPA residue for better adhesion, adding a linear fluorinated N-terminal to improve the film's packing density, and ultimately placing L-DOPA at the C-terminal. This modification resulted in the enhancement of the antifouling properties of the amphiphilic peptide by 30 % [62].

AMPs as molecules also exist in varied structural forms, which have their unique functions as antifouling materials. One such variant is 'Peptoids' which are novel poly(*N*-substituted glycine) mimics consisting of side chains attached to amide nitrogens. A study revealed that varying the grafting density and the side chain of the simplest peptoid residue, i.e., Sarcosine, exhibited high antifouling performance. Using polysarcosine with a small polymer chain cross-section led to extended chain conformations and lowered the overall electrostatic potential, which promoted chain flexibility and increased hydration [63]. Incorporating a newly synthesized non-hydrogen bonding peptoid analog in a polymer scaffold was better suited to resist marine fouling and increased the release of the fouling organisms *Ulva linza* and *Navicula incerta* compared to a hydrogen-bonding peptoid analog [64].

Most of the peptides used for surface functionalization are made up of L-amino acids and exhibit high resistance toward non-specific adsorption of proteins but are very prone to degradation by protease. In order to improve their stability towards proteolytic degradation, the mirror image of two peptides was synthesized using all D-amino acids and incorporated with the non-proteinogenic Aib. Experiments revealed that the D-enantiomers containing peptides maintained the same non-specific adsorption of proteins and resistance towards the diatoms *Navicula perminuta* and *Cobetia marina* but enhanced the protection against proteolytic degradation [65]. A study determined the altered properties of peptide-terminated SAMs by exchanging a serine with an

alanine residue and inserting the bulky Aib molecule. The change with alanine altered the hydrophilicity of the peptide and reduced fouling by *N. perminuta*, whereas the inclusion of Aib decreased the overall packing density by almost 17–37 % and brought about structural changes from a mixture of β -sheet/random coil to completely random coil structure. In addition, the peptide containing Aib were over 50–84 % better against the settlement of *U. linza* and 100 % resistant against the enzymatic degradation by trypsin [66]. Peptides have also been modified to enhance the efficacy of biocides. A chemically synthesized 14-mer peptide containing an amino acid sequence derived from the sea anemone *Actinia equina* exhibited antimicrobial activity against an oil-field biofilm consortium grown on C1018 carbon steel. The peptide, along with tetrakis(hydroxymethyl) phosphonium sulfate (THPS), led to an additional 2-log reduction, 1-log reduction, and 1-log reduction in sessile sulfate-reducing bacteria cell count, sessile acid-producing bacteria cell count, and sessile general heterotrophic bacteria cell count, respectively [67].

3.2. Indirect modification to AMPs

Extensive studies were made in which AMPs used for antifouling on immersed surfaces were modified indirectly using different support structures, which added to the effect produced on biofilm formation (Table 2). In one study, the AMP nisin was grafted on a previously coated surface with the repelling polysaccharide hyaluronic acid in the hydrolyzed form. Another modification involved coupling the nisin peptide with the polysaccharide in solution before grafting it on the surfaces. Results demonstrated a more significant antibacterial activity

of nisin when grafted to the hydrolyzed hyaluronic acid, which subsequently turned out to be a better combination exhibiting both anti-adhesive and biocidal properties [68]. A group of three cyclotides, namely P1, P2, and P3, were extracted and purified from *Viola philippica* Cav. and further utilized for modifying steel surfaces by using polydopamine as a coupling agent. Assessment of the antimicrobial activity of surfaces modified with the three peptides revealed that P3 has a more significant activity than P1 and P2, with P3 exerting the most robust antibiofilm capacity [69]. Attachment of nisin on a glass microstructural surface via dopamine exhibited antiadhesive and antibiofilm formation against the algae *Phaeodactylum tricornutum* and the bacteria *Bacillus* sp. [70]. Another study applied a combinatorial surface modification procedure using dopamine and two synthetic peptides on a 304 stainless steel surface. The modified surface showed a higher antibiofilm effect and antibacterial activity against *Staphylococcus aureus* than the untreated and dopamine-only surface [71]. Magainin is a highly common AMP that exhibits a broad-spectrum antimicrobial capacity, whereas polydopamine (DA) possess substantial adhesive property to almost all kinds of organic and inorganic surface in a weak alkaline aquatic environment. In a study, MAG II was used in conjugation with dopamine to modify the surface of stainless steel. Analysis revealed that the peptide bond successfully to the surface with remarkable change observed in both the topology and wettability of the steel surface. The antibacterial performance indicated that the modified surface decreased adhesion against two marine bacteria, *Vibrio natriegens* and *Citrobacter farmer*, by 99.79 % and 99.33 %, respectively [5]. Two additional modification studies were carried out with MAG II and DA for creating antibacterial surfaces. One involved grafting MAG II onto a DA modified 304 stainless

Table 2
Summary of indirectly modified AMPs developed as marine antifouling material.

AMPs	Origin	Structure	Modification	Mechanism	Antifouling activity	References
Nisin	–	–	Grafted on a previously coated surface with the repelling polysaccharide hyaluronic acid in its hydrolyzed form	High antibacterial activity	Exhibited both antiadhesive and biocidal properties	[68]
P1, P2, and P3	<i>Viola philippica</i> Cav.	Cyclotides	Polydopamine (DA) was used as a coupling agent	–	P3 demonstrated a more significant activity than P1 and P2, with P3 exerting the most robust antibiofilm capacity	[69]
Nisin	–	–	Dopamine was used as a coupling agent	–	Demonstrated antiadhesive and antibiofilm formation against the algae <i>Phaeodactylum tricornutum</i> and the bacteria <i>Bacillus</i> sp.	[70]
2 peptides	Synthetic	–	Dopamine was used as a coupling agent	–	High antibiofilm effect and antibacterial activity against <i>Staphylococcus aureus</i>	[71]
Magainin II (MAG II)	–	–	Dopamine was used as a coupling agent	The peptide brought a remarkable change in both the topology and wettability of the steel surface which made a significant increase in its antibacterial performance	The modified surface decreased adhesion against two marine bacteria, <i>Vibrio natriegens</i> and <i>Citrobacter farmer</i> , by 99.79 % and 99.33 %, respectively	[5]
MAG II	–	–	MAG II was grafted onto a DA modified 304 stainless steel surface (SS-DA-MAG). A combination of MAG II and DA was grafted onto the surface (SS-MAG-DA).	Physicochemical and antibacterial properties of the SS-MAG-DA were far superior to the SS-DA-MAG modified surface	Both the modified surfaces exhibited strong antibacterial capacity against <i>V. natriegens</i> with an efficiency of 98.07 % and 99.79 % by SS-DA-MAG and SS-MAG-DA, respectively.	[72]
Nisin	–	–	Nisin was grafted onto a polysulfone and poly(dopamine methyl acrylamide) (PDMA) modified surface	–	Demonstrated antimicrobial activity against <i>S. aureus</i>	[73]
MAG II	–	–	Hydrophilic coatings containing zwitterionic, neutral, positively charged poly (ethylene glycol) (PEG) polymers were grafted along with the covalently attached MAG II peptide on the surface	–	Demonstrated antimicrobial activity against <i>Pseudomonas aeruginosa</i> and inhibited biofilm formation	[74]
Andoligopeptoid	Synthetic	Oligopeptide	Poly (dimethylsiloxane) (PDMS)- and poly (ethylene oxide) (PEO)-based copolymer coatings were functionalized with the peptoid side chains	–	The surface containing the peptoid-PEO coatings demonstrated much lower adhesion strength and initial attachment property of <i>N. incerta</i>	[75]

steel surface (SS-DA-MAG). Another consisted of grafting a combination of MAG II and DA onto the surface (SS-MAG-DA). Observation of film thickness and surface topology revealed that both the grafts were immobilized on the surface successfully. However, both the modified surfaces exhibited strong antibacterial capacity against *V. natriegens* with an efficiency of 98.07 % and 99.79 % by SS-DA-MAG and SS-MAG-DA, respectively. However, physicochemical and antibacterial properties of the SS-MAG-DA were far superior to the SS-DA-MAG modified surface [72].

Another highly used modification technique is using various polymers combined with peptides to modify surfaces to develop antibacterial coatings. In a study, nisin was immobilized on the surface of ultrafiltration membranes based on polysulfone and poly(dopamine methyl acrylamide) (PDMA). The grafting was accomplished through the reaction between the amino groups of nisin and the catechol groups of PDMA. The resulting attachment of nisin on the membranes showed resistance to fouling and flux recovery ability due to the hydrophilic properties of PDMA moiety. In contrast, the nisin moiety exerted excellent antimicrobial activity against *S. aureus* [73]. In another study, various hydrophilic coatings consisting of zwitterionic, neutral, positively charged poly (ethylene glycol) (PEG) polymers were grafted along with the covalently attached MAG II peptide on the surface of the membranes. All AMP-modified membranes were found to have activity against *Pseudomonas aeruginosa* and enhance < 20 % of biofilm volume on the surfaces and subsequent inhibition of biofilm formation [74]. Poly (dimethylsiloxane) (PDMS)- and poly (ethylene oxide) (PEO)-based block copolymer coatings were functionalized with non-natural oligopeptide and oligopeptoid side chains. Analysis to measure the biofouling performance revealed that peptoid chains facilitate the removal of *U. linza* sporelings from the PDMS coatings. The non-hydrogen bonding peptoid backbone primarily contributes to the low adhesion strength to the modified surfaces. However, the adhesion strength and initial attachment property of *N. incerta* were much lower on the surface containing the peptoid-PEO coatings, therefore establishing the conjugation of peptide-polymer coatings as highly essential for use in marine antifouling applications [75].

4. Future prospects

Marine fouling has become a highly potent problem for industries that utilize marine resources and various submerged surfaces for their daily functions. Although several antifouling strategies exist, their inherent toxicity to the machinery and the surrounding environment and being costly has made many of them redundant [76]. However, biomaterials have become a superior choice in solving the biofouling problem. To this effect, AMPs have rapidly gained attention as a molecule that repels the settlement and permanent attachment of fouling organisms. Since then, many peptides have been discovered, yet only a specific few have been applied for marine antifouling purposes [77]. The reason might be attributed to the structure-function relationship, which significantly affects the physicochemical properties of the peptides. The variation in structural conformation in the aqueous environment relative to the membrane environment is also another potential problem. Any structural modifications introduced to improve its efficacy or any other property becomes difficult as no standard protocol exists. Therefore, more effort and extensive research are required for structural modification [78]. As far as the mechanisms of action of the AMPs are concerned, several are known, and their overall targets have also been identified, but the exact precise mechanism is barely known. The entire process of microorganism attachment to biofilm formation is complex, and it becomes essential to identify the precise targets that the AMPs act on. Studies have established different modification techniques and chemical synthesis methods for AMPs [79]. However, a more rational design and universal modification protocol is required to develop more powerful peptides that are both chemically stable and environmentally friendly. Approaches could be made to utilize novel

formulations like liposomes, micelles, and nano-embedded structures to impart more stability and efficiency to AMPs.

In addition, coatings with modified AMPs have shown promising results, but they remain expensive and challenging to produce [80]. And the fouling models studied to date have mainly been carried out under laboratory conditions proving insufficient in comparison to the complexity of the marine environment with its variety of biofouling organisms [81]. Utilizing AMPs for submerged surfaces is an emerging strategy. Studies have been limited with field tests being hardly carried out and few getting tested in river and aquarium environments under a restricted test period producing results that require further investigation. Although it is expected that more research is going to emerge in the future, there need to be two universal standards that should be maintained in marine field tests [82]. Firstly, biofouling in the marine environment has shown spatiotemporal variation under different seasons, with variations in temperatures, salinity, and light regimes; thus, more extended field tests throughout the seasons in diverse conditions will reveal the durability and stability of the coatings. Secondly, a more extended test period will also help to understand the antifouling capabilities of the AMPs coatings [7,83]. The development of novel strategies for simple, low-cost, and efficient synthesis techniques will benefit the production and practical applications of AMPs as a potent antifoulant for submerged surfaces in marine facilities.

A practical approach that can play an essential role in future studies is the molecular dynamics (MD) simulation technique. Many researchers have recently utilized MD simulation with AMPs to analyze the peptides' attachment behaviors on different surfaces [84]. The simulation results could easily be used to understand the distribution of surface atoms and their influence on the performance of the peptides. These can contribute to a better understanding of the interactions between the surfaces and the peptides and could prove to be of great significance for using AMPs as marine antifouling material [85].

5. Conclusion

AMPs have gained the most attention as a prominent marine antifouling material. Extensive studies were carried out to reveal the prospects and the limitations associated with applying AMPs. It has also shed light on the improvements and new approaches that need to be developed to gain a better outlook on the performance and properties of the peptides—this review article reported on the antimicrobial peptides and the many characteristics associated with them. Several modification methods involved in improving AMPs, their structure, stability, and antimicrobial activity were discussed. A more rational design for peptide modification could prove to be highly crucial for developing efficient and cost-effective antifouling biomaterials. The prospect of utilizing AMPs as the significant antifouling material could turn the tide for the marine industries in the future.

Funding

The authors declare that no funds, grants, or other support were received during the preparation of this manuscript.

Declaration of Competing Interest

The authors declare that they have no known competing financial interests or personal relationships that could have appeared to influence the work reported in this paper.

Data availability

No data was used for the research described in the article.

References

- [1] H. Oh, C. Lee, Origin and evolution of quorum quenching technology for biofouling control in MBRs for wastewater treatment, *J. Membr. Sci.* 554 (2018) 331–345, <https://doi.org/10.1016/j.memsci.2018.03.019>.
- [2] S.S. Bucs, N. Farhat, J.C. Kruihof, C. Picioreanu, M.C.M. van Loosdrecht, J. S. Vrouwenvelder, Review on strategies for biofouling mitigation in spiral wound membrane systems, *Desalination* 434 (2018) 189–197, <https://doi.org/10.1016/j.desal.2018.01.023>.
- [3] P.A. Vinagre, T. Simas, E. Cruz, E. Pinori, J. Svenson, Marine biofouling: a European database for the marine renewable energy sector, *J. Mar. Sci. Eng.* 8 (2020) 495, <https://doi.org/10.3390/jmse8070495>.
- [4] H. Flemming, Biofouling and me: my Stockholm syndrome with biofilms, *Water Res.* 173 (2020), 115576, <https://doi.org/10.1016/j.watres.2020.115576>.
- [5] P. Cao, C. Du, X. He, C. Zhang, C. Yuan, Modification of a derived antimicrobial peptide on steel surface for marine bacterial resistance, *Appl. Surf. Sci.* 510 (2020), 145512, <https://doi.org/10.1016/j.apsusc.2020.145512>.
- [6] H. Jin, L. Tian, W. Bing, J. Zhao, L. Ren, Bioinspired marine antifouling coatings: status, prospects, and future, *Prog. Mater. Sci.* 124 (2022), 100889, <https://doi.org/10.1016/j.pmatsci.2021.100889>.
- [7] H. Jin, J. Wang, L. Tian, M. Gao, J. Zhao, L. Ren, Recent advances in emerging integrated antifouling and anticorrosion coatings, *Mater. Des.* 213 (2022), 110307, <https://doi.org/10.1016/j.matdes.2021.110307>.
- [8] K. Doiron, L. Beaulieu, R. St-Louis, K. Lemarchand, Reduction of bacterial biofilm formation using marine natural antimicrobial peptides, *Colloids Surf. B Biointerfaces* 167 (2018) 524–530, <https://doi.org/10.1016/j.colsurfb.2018.04.051>.
- [9] P. Cao, D. Liu, Y. Liu, H. Wang, C. Zhang, C. Yuan, X. Liu, Marine antifouling behaviour of the surfaces modified by dopamine and antibacterial peptide, *J. Ocean. Limnol.* (2022), <https://doi.org/10.1007/s00343-021-1270-z>.
- [10] G.P. Sakala, M. Reches, Peptide-based approaches to fight biofouling, *Adv. Mater. Interfaces* (2018) 1800073, <https://doi.org/10.1002/admi.201800073>.
- [11] T. Lou, X. Bai, X. He, W. Liu, Y. Yang, C. Yuan, Antifouling performance and mechanism analysis of marine peptide modified aluminium alloy surface, *Surf. Coat. Technol.* 445 (2022), 128742, <https://doi.org/10.1016/j.surfcoat.2022.128742>.
- [12] A. Saha, S. Nir, M. Reches, Amphiphilic peptides with dual functionality resists biofouling, *Langmuir* 36 (2020) 4201–4206, <https://doi.org/10.1021/acs.langmuir.9b03997>.
- [13] N.S. Kandiyote, G. Mohanraj, C. Mao, R. Kasher, C.J. Arnusch, Synergy on surfaces: anti-Biofouling interfaces using surface-attached antimicrobial peptides PGLa and Magainin-2, *Langmuir* 34 (2018) 11147–11155, <https://doi.org/10.1021/acs.langmuir.8b01617>.
- [14] H. Qiu, K. Fang, A. Gapeeva, K. Meurisch, S. Kaps, X. Li, L. Yu, Y.K. Mishra, R. Adelung, M. Baum, Functional polymer materials for modern marine biofouling control, *Prog. Polym. Sci.* 127 (2022), 101516, <https://doi.org/10.1016/j.progpolymsci.2022.101516>.
- [15] Y.E. Hwang, S. Im, H. Kim, J. Sohn, B. Cho, J.H. Cho, B.H. Sung, S.C. Kim, Adhesive antimicrobial peptides containing 3,4-dihydroxy-L-phenylalanine residues for direct one-step surface coating, *Int. J. Mol. Sci.* 22 (2021) 11915, <https://doi.org/10.3390/ijms222111915>.
- [16] J.S.M. Svendsen, T.M. Grant, D. Rennison, M.A. Brimble, J. Svenson, Very short and stable lactoferrin-derived antimicrobial peptides: design principles and potential uses, *Acc. Chem. Res.* 52 (2019) 749–759, <https://doi.org/10.1021/acs.accounts.8b00624>.
- [17] S. Rigo, D. Hürlimann, L. Marot, M. Malmsten, W. Meier, C.G. Palivan, Decorating nanostructured surfaces with antimicrobial peptides to efficiently fight bacteria, *ACS Appl. Bio Mater.* 3 (2020) 1533–1543, <https://doi.org/10.1021/acsabm.9b01154>.
- [18] S.S. Griesser, M. Jasieniak, K. Vasilev, H.J. Griesser, Antimicrobial peptides grafted onto a plasma polymer interlayer platform: performance upon extended bacterial challenge, *Coatings* 11 (2021) 68, <https://doi.org/10.3390/coatings11010068>.
- [19] H. Zhang, S. Zhu, J. Yang, A. Ma, Advancing strategies of biofouling control in water-treated polymeric membranes, *Polymers* 14 (2022) 1167, <https://doi.org/10.3390/polym14061167>.
- [20] L. Chen, Y. Duan, M. Cui, R. Huang, R. Su, W. Qi, Z. He, Biomimetic surface coatings for marine antifouling: natural antifoulants, synthetic polymers and surface microtopography, *Sci. Total Environ.* 766 (2021), 144469, <https://doi.org/10.1016/j.scitotenv.2020.144469>.
- [21] Y. Guo, C. Liu, H. Liu, J. Zhang, H. Li, C. Zhang, Contemporary antibiofouling modifications of reverse osmosis membranes: state-of-the-art insights on mechanisms and strategies, *Chem. Eng. J.* 429 (2022), 132400, <https://doi.org/10.1016/j.cej.2021.132400>.
- [22] A. Kumar, A. AL-Jumaili, O. Bazaka, E.P. Ivanova, I. Levchenko, K. Bazaka, M. V. Jacob, Functional nanomaterials, synergisms, and biomimicry for environmentally benign marine antifouling technology, *Mater. Horiz.* 8 (2021) 3201–3238, <https://doi.org/10.1039/D1MH01103K>.
- [23] X. Zhang, J. Ma, J. Zheng, R. Dui, X. Wang, Z. Wang, Recent advances in nature-inspired antifouling membranes for water purification, *Chem. Eng. J.* 432 (2022), 134425, <https://doi.org/10.1016/j.cej.134425>.
- [24] H. Moravej, Z. Moravej, M. Yazdanparast, M. Heiat, A. Mirhosseini, M. Moghaddam, R. Mirnejad, Antimicrobial peptides: features, action, and their resistance mechanisms in bacteria, *Microb. Drug Resist.* 24 (2018) 747–767, <https://doi.org/10.1089/mdr.2017.0392>.
- [25] A.K. Mishra, J. Choi, E. Moon, K. Baek, Tryptophan-rich and proline-rich antimicrobial peptides, *Molecules* 23 (2018) 815, <https://doi.org/10.3390/molecules23040815>.
- [26] M. Yasir, M.D.P. Willcox, D. Dutta, Action of antimicrobial peptides against bacterial biofilms, *Materials* 11 (2018) 2468, <https://doi.org/10.3390/ma11222468>.
- [27] L.S. Biswaro, M.G. da Costa Sousa, T.M.B. Rezende, S.C. Dias, O.L. Franco, Antimicrobial peptides and nanotechnology, recent advances and challenges, *Front. Microbiol.* 9 (2018) 855, <https://doi.org/10.3389/fmicb.2018.00855>.
- [28] M.E. Büyükkiraz, Z. Kesmen, Antimicrobial peptides (AMPs): a promising class of antimicrobial compounds, *J. Appl. Microbiol.* (2021), <https://doi.org/10.1111/jam.15314>.
- [29] P. Kumar, J.N. Kizhakkedathu, S.K. Straus, Antimicrobial peptides: diversity, mechanism of action and strategies to improve the activity and biocompatibility in vivo, *Biomolecules* 8 (2018) 4, <https://doi.org/10.3390/biom8010004>.
- [30] J.M. Ageitos, A. Sánchez-Pérez, P. Calo-Mata, T.G. Villa, Antimicrobial peptides (AMPs): ancient compounds that represent novel weapons in the fight against bacteria, *Biochem. Pharmacol.* 133 (2017) 117–138, <https://doi.org/10.1016/j.bcp.2016.09.018>.
- [31] S. Tang, Z.H. Prodhan, S.K. Biswas, C. Le, S.D. Sekaran, Antimicrobial peptides from different plant sources: isolation, characterisation, and purification, *Phytochemistry* 154 (2018) 94–105, <https://doi.org/10.1016/j.phytochem.2018.07.002>.
- [32] B. Shanmugaraj, C.J.I. bualon, A. Malla, W. Phoolcharoen, Biotechnological insights on the expression and production of antimicrobial peptides in plants, *Molecules* 26 (2021) 4032, <https://doi.org/10.3390/molecules26134032>.
- [33] O.O. Bakare, A. Gokul, A.O. Fadaka, R. Wu, L. Niekerk, A.M. Barker, M. Keyster, A. Klein, Plant antimicrobial peptides (PAMPs): features, applications, production, expression, and challenges, *Molecules* 27 (2022) 3073, <https://doi.org/10.3390/molecules27123703>.
- [34] M.H. Semreen, M. El-Gamal, S. Abdin, H. Alkharaji, L. Kamal, S. Hammad, F. El-Awady, D. Waleed, L. Kourbaj, Recent updates of marine antimicrobial peptides, *Saudi Pharm. J.* 26 (2018) 396–409, <https://doi.org/10.1016/j.sjps.2018.01.001>.
- [35] J. Wang, X. Dou, J. Song, Y. Lyu, X. Zhu, L. Xu, W. Li, A. Shan, Antimicrobial peptides: promising alternatives in the post-feeding antibiotic era, *Med. Res. Rev.* (2018), <https://doi.org/10.1002/med.21542>.
- [36] Y. Liu, J. Shi, Z. Tong, Y. Jia, B. Yang, Z. Wang, The revitalization of antimicrobial peptides in the resistance era, *Pharmacol. Res.* 163 (2021), 105276, <https://doi.org/10.1016/j.phrs.2020.105276>.
- [37] A.B. Hafeez, X. Jiang, P.J. Bergen, Y. Zhu, Antimicrobial peptides: an update on classifications and databases, *Int. J. Mol. Sci.* 22 (2021) 11691, <https://doi.org/10.3390/ijms222111691>.
- [38] J. Koebach, D.J. Craik, The vast structural diversity of antimicrobial peptides, *Trends Pharmacol. Sci.* 40 (2019) 517–528, <https://doi.org/10.1016/j.tips.2019.04.012>.
- [39] T.A.E. Ahmed, R. Hammani, Recent insights into structure-function relationships of antimicrobial peptides, *J. Food Biochem.* (2018), e12546, <https://doi.org/10.1111/jfbc.12546>.
- [40] M.E. Büyükkiraz, Z. Kesmen, Antimicrobial peptides (AMPs): a promising class of antimicrobial compounds, *J. Appl. Microbiol.* 132 (2022) 1573–1596, <https://doi.org/10.1111/jam.15314>.
- [41] Y. Liu, J. Shi, Z. Tong, Y. Jia, B. Yang, Z. Wang, The revitalization of antimicrobial peptides in the resistance era, *Pharmacol. Res.* (2020), 105276, <https://doi.org/10.1016/j.phrs.2020.105276>.
- [42] Y. Luo, Y. Song, Mechanisms of antimicrobial peptides: antimicrobial, anti-inflammatory and antibiofilm activities, *Int. J. Mol. Sci.* 22 (2021) 11401, <https://doi.org/10.3390/ijms222111401>.
- [43] Q. Zhang, Z. Yan, Y. Meng, X. Hong, G. Shao, J. Ma, X. Cheng, J. Liu, J. Kang, C. Fu, Antimicrobial peptides: mechanism of action, activity and clinical potential, *Mil. Med. Res.* 8 (2021) 48, <https://doi.org/10.1186/s40779-021-00343-2>.
- [44] S. Mallapragada, A. Wadhwa, P. Agrawal, Antimicrobial peptides: the miraculous biological molecules, *J. Indian Soc. Periodo* 21 (2017) 434–438, <https://doi.org/10.4103/jisp.jisp.325.16>.
- [45] P.G. Lima, J.T.A. Oliveira, J.L. Amaral, C.D.T. Freitas, P.F.N. Souza, Synthetic antimicrobial peptides: characteristics, design, and potential as alternative molecules to overcome microbial resistance, *Life Sci.* 278 (2021), 119647, <https://doi.org/10.1016/j.ifs.2021.119647>.
- [46] T. Vanzolini, M. Bruschi, A.C. Rinaldi, M. Magnani, A. Fraternali, Multitalented synthetic antimicrobial peptides and their antibacterial, antifungal and antiviral mechanisms, *Int. J. Mol. Sci.* 23 (2022) 545, <https://doi.org/10.3390/ijms23010545>.
- [47] J. Rodríguez-Hernández, Antimicrobial/Antifouling surfaces obtained by Surface modification. *Polymers Against Microorganisms*, Springer, Cham, 2017, https://doi.org/10.1007/978-3-319-47961-3_5.
- [48] D. Juretić, J. Simunić, Design of α -helical antimicrobial peptides with a high selectivity index, *Expert Opin. Drug Disco* (2019) 1–11, <https://doi.org/10.1080/17460441.2019.1642322>.
- [49] J. Antunes, S. Pereira, T. Ribero, J.E. Plowman, A. Thomas, S. Clerens, A. Campos, V. Vasconcelos, J.R. Almeida, A multi-bioassay integrated approach to assess the antifouling potential of the cyanobacterial metabolites portoamides, *Mar. Drugs* 17 (2019) 111, <https://doi.org/10.3390/md17020111>.
- [50] C. Ma, C. Yuan, P. Cao, A facile method to prepare a hydrophilic/hydrophobic metal surface by peptide, *Materials* 11 (2018) 1289, <https://doi.org/10.3390/ma11081289>.

- [51] P. Cao, X. He, J. Xiao, C. Yuan, X. Bai, Peptide-modified stainless steel with resistance capacity of *Staphylococcus aureus* biofilm formation, *Surf. Interface Anal.* (2018), <https://doi.org/10.1002/sia.6531>.
- [52] C. Mao, G. Mohanraj, N.S. Kandiyote, R. Kasher, C.J. Arnusch, UV mediated attachment of short Arginine-Tryptophan antimicrobial peptides on reverse osmosis membrane surfaces inhibit *Pseudomonas aeruginosa*, *Desalination* 431 (2018) 73–79, <https://doi.org/10.1016/j.desal.2017.12.027>.
- [53] P. Cao, D. Liu, Y. Liu, Y. Zhang, C. Yuan, C. Zhang, Combining topography and peptide to inhibit algae attachment: preparation of peptide-modified microstructured surfaces, *Surf. Interface Anal.* (2021), <https://doi.org/10.1002/sia.7000>.
- [54] J. Zhang, W. Zhu, B. Xin, S. Lin, L. Jin, H. Wang, Development of an antibacterial surface with a self-defensive and pH-responsive function, *Biomater. Sci.* (2019), <https://doi.org/10.1039/c9bm00670b>.
- [55] M. Herzberg, M. Berglin, S. Eliahu, L. Bodin, K. Agrenius, A. Zlotkin, J. Svenson, Efficient prevention of marine biofilm formation employing a surface-grafted repellent marine peptide, *ACS Appl. Bio Mater.* 4 (2021) 3360–3373, <https://doi.org/10.1021/acsabm.0c1672>.
- [56] C. Li, C. Liu, M. Li, X. Xu, S. Li, W. Qi, R. Su, J. Yu, Structures and antifouling properties of self-assembled zwitterionic peptide monolayers: effects of peptide charge distributions and divalent cations, *Biomacromolecules* 21 (2020) 2087–2095, <https://doi.org/10.1021/acs.biomac.0c00062>.
- [57] C. Li, M. Li, W. Qi, R. Su, J. Yu, Effect of hydrophobicity and charge separation on the antifouling properties of surface-tethered zwitterionic peptides, *Langmuir* 37 (2021) 8455–8462, <https://doi.org/10.1021/acs.langmuir.1c00803>.
- [58] T. Ederth, M. Lerm, B. Orihuela, D. Rittschof, Resistance of zwitterionic peptide monolayers to biofouling, *Langmuir* 35 (2019) 1818–1827, <https://doi.org/10.1021/acs.langmuir.8b01625>.
- [59] D.R. Calabrese, B.M. Wenning, H. Buss, J.A. Finlay, D. Fischer, A.S. Clare, R. A. Segalman, C.K. Ober, Oligopeptide-modified hydrophobic and hydrophilic polymers as antifouling coatings, *Green. Mater.* 5 (2017) 31–43, <https://doi.org/10.1680/jgrma.17.00006>.
- [60] J. Svenson, T.M. Grant, D. Rennison, G. Cervin, H. Pavia, C. Hellio, V. Foulon, M. A. Brimble, P. Cahill, Towards eco-friendly marine antifouling biocides – nature inspired tetrasubstituted 2,5-Diketopiperazines, *SSRN* (2021), <https://doi.org/10.2139/ssrn.3967417>.
- [61] A. Saha, S. Nir, M. Reches, Amphiphilic peptide with dual functionality resists biofouling, *Langmuir* 36 (2020) 4201–4206, <https://doi.org/10.1021/acs.langmuir.9b03997>.
- [62] S.L. Gaw, G. Sakala, S. Nir, A. Saha, Z.J. Xu, P.S. Lee, M. Reches, Rational design of Amphiphilic peptides and its effect on antifouling performance, *Biomacromolecules* 19 (2018) 3620–3627, <https://doi.org/10.1021/acs.biomac.8b00587>.
- [63] D.L. Cheung, K.H.A. Lau, Atomistic study of Zwitterionic peptoid antifouling brushes, *Langmuir* 35 (2019) 1483–1494, <https://doi.org/10.1021/acs.langmuir.8b01939>.
- [64] M.E. Barry, E.C. Davidson, C. Zhang, A.L. Patterson, B. Yu, A.K. Leonardi, N. Duzen, K. Malaviya, J.L. Clarke, J.A. Finlay, A.S. Clare, Z. Chen, C.K. Ober, R. A. Segalman, The role of hydrogen bonding in peptoid-based marine antifouling coatings, *Macromolecules* 52 (2019) 1287–1295, <https://doi.org/10.1021/acs.macromol.8b02390>.
- [65] C.D. Beyer, M.L. Reback, N. Heinen, S. Thavalingam, A. Rosenhahn, N. Metzler-Nolte, Low fouling peptides with an all (D) amino acid sequence provide enhanced stability against proteolytic degradation while maintaining low antifouling properties, *Langmuir* 36 (2020) 10996–11004, <https://doi.org/10.1021/acs.langmuir.0c01790>.
- [66] C.D. Beyer, M.L. Reback, S.M. Gopal, K.A. Nolte, J.A. Finlay, A.S. Clare, L. V. Schäfer, N. Metzler-Nolte, A. Rosenhahn, α -Aminoisobutyric acid-stabilized peptide SAMs with low non-specific protein adsorption and resistance against marine biofouling, *ACS Sustain. Chem. Eng.* 8 (2020) 2665–2671, <https://doi.org/10.1021/acssuschemeng.9b05889>.
- [67] R. Jia, D. Yang, W. Dou, J. Liu, A. Zlotkin, S. Kumseranee, S. Punpruk, X. Li, T. Gu, A sea anemone-inspired small synthetic peptide at sub-ppm concentrations enhanced biofilm mitigation, *Int. Biodeterior. Biodegrad.* 139 (2019) 78–85, <https://doi.org/10.1016/j.ibiod.2018.11.009>.
- [68] J. Paris, D. Seyer, T. Jouenne, P. Thébaud, Various methods to combine hyaluronic acid and antimicrobial peptides coatings and evaluation of their antibacterial behaviour, *Int. J. Biol. Macromol.* 139 (2019) 468–474, <https://doi.org/10.1016/j.ijbiomac.2019.07.188>.
- [69] P. Cao, Y. Yang, F.I. Uche, S.R. Hart, W. Li, C. Yuan, Coupling plant-derived cyclotides to metal surfaces: an antibacterial and antibiofilm study (<https://doi.org/>), *Int. J. Mol. Sci.* 19 (2018) 793, <https://doi.org/10.3390/ijms19030793>.
- [70] T. Lou, X. Bai, X. He, C. Yuan, Antifouling performance analysis of peptide-modified glass microstructural surfaces, *Appl. Surf. Sci.* 541 (2021), 148384, <https://doi.org/10.1016/j.apsuc.2020.148384>.
- [71] P. Cao, W. Li, A.R. Morris, P.D. Horrocks, C. Yuan, Y. Yang, Investigation of the antibiofilm capacity of peptide-modified stainless steel, *R. Soc. Open Sci.* 5 (2018), 172165, <https://doi.org/10.1098/rsos.172165>.
- [72] P. Cao, K. Liu, X. Liu, W. Sun, D. Wu, C. Yuan, X. Bai, C. Zhang, Antibacterial properties of Magainin II peptide onto 304 stainless steel surfaces: a comparison study of two dopamine modification methods, *Colloids Surf. B: Biointerfaces* 194 (2020), 111198, <https://doi.org/10.1016/j.colsurfb.2020.111198>.
- [73] J. Kim, K. Kim, Y. Choi, H. Kang, D.M. Kim, J. Lee, Polysulfone based ultrafiltration membranes with dopamine and nisin moieties showing antifouling and antimicrobial properties, *Sep. Purif. Technol.* 202 (2018) 9–20, <https://doi.org/10.1016/j.seppur.2018.03.033>.
- [74] N.S. Kandiyote, T. Avidis, C.J. Arnusch, R. Kasher, Grafted polymer coatings enhance fouling inhibition by an antimicrobial peptide on reverse osmosis membranes, *Langmuir* 35 (2019) 1935–1943, <https://doi.org/10.1021/acs.langmuir.8b03851>.
- [75] A.L. Patterson, B. Wenning, G. Rizis, D.R. Calabrese, J.A. Finlay, S.C. Franco, R. N. Zuckermann, A.S. Clare, E.J. Kramer, C.K. Ober, R.A. Segalman, Role of backbone chemistry and monomer sequence in amphiphilic oligopeptide- and oligopeptoid-functionalized PDMS- and PEO-based block copolymers for marine antifouling and fouling release coatings, *Macromolecules* 50 (2017) 2656–2667, <https://doi.org/10.1021/acs.macromol.6b02505>.
- [76] I.C. Nwuzor, C.I. Idumah, S.C. Nwanonyi, O.E. Ezeani, Emerging trends in self-polishing anti-fouling coatings for marine environment, *Saf. Extrem. Environ.* 3 (2021) 9–25, <https://doi.org/10.1007/s42797-021-00031-3>.
- [77] L. Tian, Y. Yin, W. Bing, E. Jin, Antifouling technology trends in marine environmental protection, *J. Bionic. Eng.* 18 (2021) 239–263, <https://doi.org/10.1007/s42235-021-0017-z>.
- [78] X. Liu, J. Yang, D. Rittschof, J.S. Maki, J. Gu, redirecting marine antibiofouling innovations from sustainable horizons, *Trends Ecol. Evol.* 37 (2022) 469–472, <https://doi.org/10.1016/j.tree.2022.02.009>.
- [79] Y. Bhoj, M. Tharmavaram, D. Rawtani, A comprehensive approach to antifouling strategies in desalination, marine environment, and wastewater environment, *Chem. Phys. Impact* 2 (2021), 100008, <https://doi.org/10.1016/j.chphi.2020.100008>.
- [80] D. Zabiegaj, F. Hajirasouliha, A. Duilio, S. Guido, S. Caserta, M. Kostoglou, M. Petala, T. Karapantsios, A. Trybala, Wetting/spreading on porous media and on deformable, soluble structured substrates as a model system for studying the effect of morphology on biofilms wetting and for assessing anti-biofilm methods, *Curr. Opin. Colloid Interface Sci.* 53 (2021), 101426, <https://doi.org/10.1016/j.cocis.2021.101426>.
- [81] H. Jin, L. Tian, W. Bing, J. Zhao, L. Ren, Bioinspired marine antifouling coatings: status, prospects, and future, *Prog. Mater. Sci.* 124 (2022), 100889, <https://doi.org/10.1016/j.pmatsci.2021.100889>.
- [82] C. Wu, J. Wang, S. Song, Z. Wang, S. Zhao, Antifouling and anticorrosion performance of the composite coating made of tetrabromobisphenol-A epoxy and polyaniline nanowires, *Prog. Org. Coat.* 148 (2020), 105888, <https://doi.org/10.1016/j.porgcoat.2020.105888>.
- [83] C.S. Lim, M.L. Neo, S.Z.Z. Rahim, R.C.T. Andre, S.L.M. Teo, Investigating the effect of temporal variation on fouling settlement using a rapid assay method, *J. Coat. Technol. Res.* 16 (2019) 761–769, <https://doi.org/10.1007/s11998-018-00153-7>.
- [84] N. Palmer, J.R.M.A. Maasch, M.D.T. Torres, C. de la Fuente-Nunez, Molecular dynamics for antimicrobial peptide discovery, *Infect. Immun.* 89 (2021), <https://doi.org/10.1128/IAI.00703-20>.
- [85] P.G.A. Aronica, L.M. Reid, N. Desai, J. Li, S.J. Fox, S. Yadahalli, J.W. Essex, C. S. Verma, Computational methods and tools in antimicrobial peptide research, *J. Chem. Inf. Model* 61 (2021) 3172–3196, <https://doi.org/10.1021/acs.jcim.1c00175>.



Exosomal long noncoding RNAs – the lead thespian behind the regulation, cause and cure of autophagy-related diseases

Sougata Ghosh Chowdhury¹ · Debalina Bhattacharya² · Parimal Karmakar¹

Received: 10 February 2022 / Accepted: 25 April 2022 / Published online: 2 June 2022
© The Author(s), under exclusive licence to Springer Nature B.V. 2022

Abstract

Recent advances in exosome biology have revealed significant roles of exosome and their contents in intercellular communication. Among various exosomal content, long non-coding RNAs (lncRNAs), which have a large size (> 200 nt) and lack protein coding potential, are known to play key roles in intercellular communication and novel biomarkers of various metabolic disorders. Moreover, long non-coding RNAs are often involved in the regulation of various cellular processes such as autophagy, apoptosis, cell proliferation. On the other hand, autophagy is the central regulating point that controls the various metabolic functions of the body. This process is known to prevent diseases and promote longevity. Therefore, the present review discusses the relationship between diseases and autophagy, and also look into the biological functions of exosome-associated lncRNAs in regulating autophagy. Furthermore, this review will summarize some of the studies that provide novel insights into the pathogenesis of autophagy-related diseases followed by the non-canonical roles played by autophagy and related proteins in the development of exosome biogenesis.

Keywords Exosome · Long non-coding RNAs (lncRNAs) · Autophagy · Autophagy related diseases

Introduction

Autophagy is a commonly used metabolic process that occurs in most eukaryotic cells to promote cell survival. It involves the removal of damaged organelles and proteins through the fusion of lysosome and a double-membrane vesicle [1]. It refers to the process of lysosomal degradation in a cellular environment. It can be generally categorized as macroautophagy, chaperone-mediated autophagy, and microautophagy [2]. Macroautophagy involves the fusion of the lysosomal enzymes with the cytoplasm of a double-walled membrane. The lysosomal enzymes help in the degradation of sequestered products. Microautophagy is a process where the lysosomes engulf cytoplasmic cargo. Chaperone mediated autophagy is the only mode where proteins are targeted to the lysosomes using signal

peptide. A successful autophagy system consists of several key components, including mitophagy, ERphagy, lipophagy, and xenophagy. These components are responsible for maintaining the cellular homeostasis. Basal autophagy is a process that occurs during physiological conditions. It helps to maintain cellular metabolism and homeostasis. However, dysregulation in autophagy can contribute to the development of various diseases. Under severe stress, insufficient autophagy can result in the accumulation of toxic substances which contribute to the development of various diseases like cancers, metabolic disorder and neurodegeneration [3]. Autophagy can be divided into two groups: basal autophagy and induced autophagy. The former provides a blueprint for eukaryotes to maintain their cellular homeostasis. Compared with basal autophagy, induced autophagy is a defensive response that can cause cell death. This process is triggered by the body's response to external stimuli. In humans, autophagy is the central regulating point that controls the various metabolic functions of the body. This process is known to prevent diseases and promote longevity by removing the cellular garbage [4]. Exosomes are small vesicles that come out of every cell type in the environment. Studies have shown that they can serve as a type of intercellular communication channel [5]. The intricate relationship

✉ Parimal Karmakar
pkarmakar_28@yahoo.co.in

¹ Department of Life Science and Biotechnology, Jadavpur University, 700032 Kolkata, India

² Department of Microbiology, Maulana Azad College, 700013 Kolkata, India

between the exosomal pathways and autophagy can have important implications for human diseases and physiology. This relationship is also influenced by the environment.

Exosomes are membrane bound microvesicles with diameter 30–150 nm procured from late endosomes of eukaryotic cells [6]. They are known to serve as a bridge between cells and their recipients. Exosomes are embodied with various kinds of RNAs like mRNA, tRNA, miRNA. They can also carry a wide range of lncRNAs, which can transmit different information to neighbouring cells [7]. The exact role of exosomal RNAs has not been fully explored. Further, it has been discovered that exosomes play a crucial role in the secretion of damaged protein and RNAs and maintain cellular fitness. The crosstalk between exoplasmic and autophagic pathways is a complex process that varies greatly in various diseases [8]. There are numerous examples of autophagy-related protein complexes that can serve as scaffolds for exosome biogenesis. The role of exosome biogenesis and autophagy in maintaining cellular homeostasis has been acknowledged.

Non-coding RNAs are often referred to as long non-coding RNAs (lncRNAs), microRNAs (miRNAs), and circular RNAs (circRNAs). They play key roles in cellular metabolism by modifying the structure of DNA and transferring protein translation [9]. It is widely believed that these RNAs are actively transcribed from the human genome and play important roles in the development and regulation of various diseases. Among these, involvement of long non-coding RNAs (lncRNAs) seen in the regulation of various diseases has been observed. Their discovery has led to the development of novel diagnostic and therapeutic targets. The effects of lncRNAs on cellular functions include the induction of apoptosis, cell proliferation, and the evasion of tumor suppressors proteins [10]. As a matter of fact, lncRNAs are known to play key roles in the regulation of transcription of protein-coding genes. Additionally, recent studies suggest that they can also contribute to the diseases originated from deregulated autophagy [11]. Evidence showed that lncRNA H19 and lncRNA HOTAIR can target various autophagy-related signaling pathways. In this review, we will discuss the relationship between diseases and autophagy, and also look into the biological functions of exosome-associated lncRNAs in regulating autophagy. This review will also summarize some of the studies that provide novel insights into the pathogenesis of autophagy-related diseases followed by the non-canonical roles played by autophagy and related proteins in the development of exosome biogenesis. This topic is based on the discovery that a subset of the autophagy proteins can function in the exosome.

Interplay between autophagy and exosome

Autophagy is a complex process involving a set of proteins and molecules that can be affected by abnormalities in one gene or another. The intersection points of the mTOR and Beclin1 signalling pathways are key factors in the regulation of autophagy. The two main pathways that regulate autophagy are the PI3K-Akt-mTOR and AMPK-mTOR pathways (Fig. 1 A). The mTOR and PI3K/Akt activation are known to suppress autophagy [12]. The activation of AMPK activates autophagy either by inactivating mTOR and associated proteins or by inducing expression of autophagy related proteins [13]. A defect in any of these pathways can prevent the efficient digestion of protein aggregates and cause exosome release to alleviate proteotoxic stresses. The crosstalk between exosome and autophagic pathways has been observed in the development of diseases. The core mammalian protein complex known as PI3K is involved in the endocytosis and autophagy stages. The complex consists of three components known as VPS34, p150 and Beclin 1 [14]. The association between the PI3K complex and the Beclin1-Interacting protein has been shown to suppress endocytosis and autophagy. The effects of exosomal processing on the autophagic activity are not consistent with current studies. Since the exosomal cargo can regulate the signaling pathways of the autophagic system [8]. It is important to understand the role of exosomes in this process. An important exosomal cargo miRNA are non-coding RNAs that can regulate the expression of target genes. Li et al. showed that overexpression of miR-221/222 impairs the level of PTEN, activates the Akt signaling pathway and reduced the expression of several key signaling hallmarks that are associated with autophagy [15]. Liu et al. revealed that miRNA-223, which is a novel class of molecules that can augment the autophagy of H9C2 cells, prevented hypoxia-induced apoptosis in new-born rats [16]. Arslan et al. showed that the presence of MCS-exo can augment the protection of individuals from cardiac dysfunction caused by the activation of the PI3K/Akt pathway [17]. Yang et al. stated that, by inhibiting exosomal miR-30a, they were able to prevent the induction of apoptosis in cardiomyocytes subjected to hypoxia [18]. The exosomal miR-30a could also contribute to the development of a novel pathway of autophagy. Nair et al. showed that the fusion of autophagosome with membranes depends on the activity of the SNARE family proteins, which includes VAMP7, syntaxin 7, and syntaxin 8 [19]. VAMP7 is a key component of the exosome secretion pathway. Its role in this process is evidenced by its activity as a SNAREs. ATG proteins can be found in the assembly of autophagosomes through the use of a MVB associate protein known as Rab11 [20]. ALIX has been shown to interact with exosomal cargo. It has been suggested that this

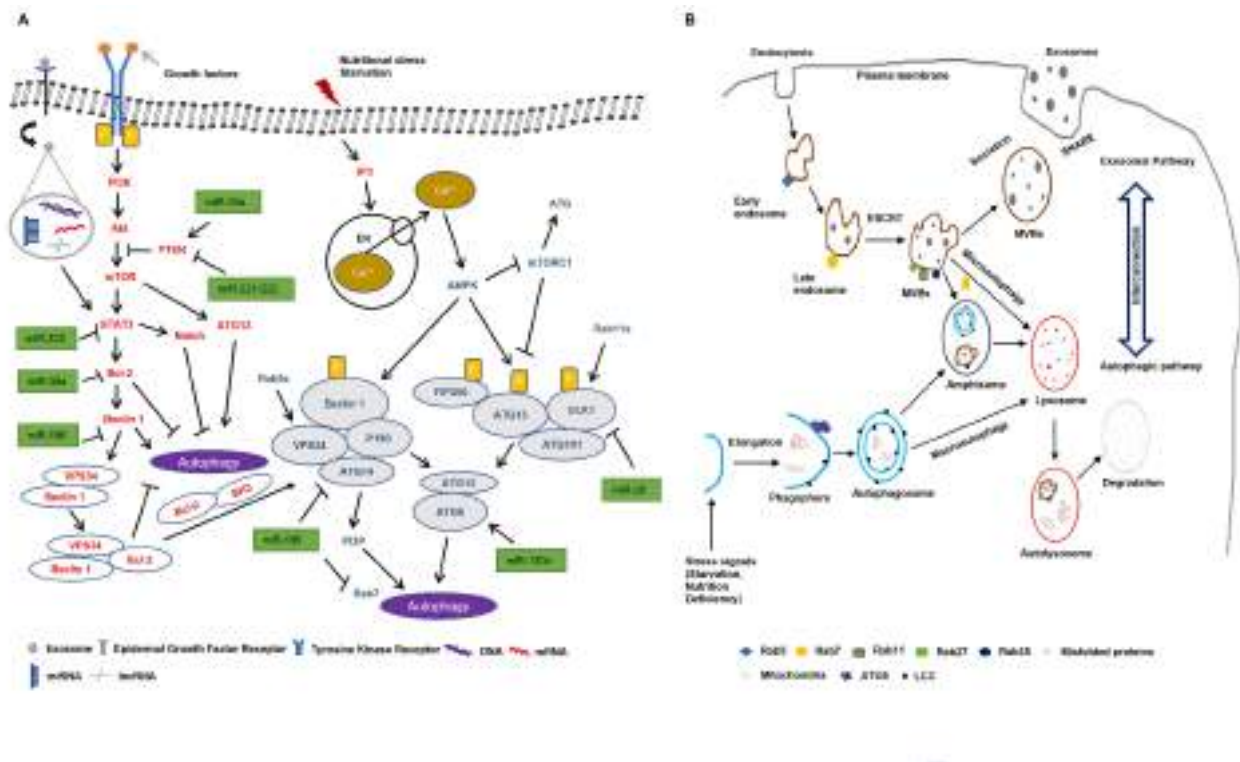


Fig. 1 (A) A schematic diagram of the signaling pathways involved in exosome-mediated autophagy. Exosomes can also contribute to the induction of this process by interacting with the epidermal growth factor receptor (EGFR). Binding of growth factors to the tyrosine kinase receptor activates the complex, which then recruits and activates the PI3K protein, which phosphorylates the Akt. One of the main targets of the phosphorylated AKT protein is the mTOR pathway. Different exosomal miRNAs also target the epidermal growth factor receptor and inactivate the mTOR pathway. During starvation, the ULK1 complex is activated by autophosphorylation and phosphorylates ATG13, FIP200. AMPK can trigger the activation of ULK1, which can be initiated by negatively regulating mTORC1 or phosphorylating ULK1. Red colour for Akt/mTOR signaling pathway, blue colour for AMPK/mTOR signal pathway and green colour for exosomal miRNAs mediated pathway. (B) The proposed mechanism involves the cross-regulation of the exosome and autophagic pathways. As the endosome matures, it forms into multivesicular bodies (MVBs) that can fuse with the plasma membrane and are secreted as exosomes. In response to environmental stress, the protein assembly site extends to form the phagophore. As the phagophore continues to grow, it engulfs damaged organelles and proteins. The phagophore then forms a bilayered membrane, which is the autophagosome. Alternatively, the MVBs can form hybrid organelles, amphisome with autophagosomes. The lysosome and the autophagosome fuse together to form the autolysosome, which is a degradation centre for harmful components in the body

association could play a role in the exosomal secretory pathways involved in lysosomal degradation (Fig. 1B). ALIX inhibition revealed a decrease in autophagy, which is a major step in the exosome biogenesis pathway. This decrease in autophagy is associated with the crosslink arrangement between the exosome biogenesis and the autophagy pathway [21]. ATG5 has been shown to play a crucial role in the exosome biogenesis pathway and the autophagy pathway. It has also been shown that the dissociation of vacuolar protons from MVBs allows MVB–PM fusion [22, 23]. The ATG5 knockout significantly reduces the exosome release and attenuated the exosomal enrichment of LC3B [23, 24]. This effect is important since the formation of autophagosomal cells does not require the exosome release. The ATG7 knockout did not affect the release of exosome proteins. It has been suggested that the absence of LC3B lipidation or the formation of autophagosomes does not require exosome

release. The study shows that LC3B, which is a type of protein involved in the development of exosome biogenesis, plays a crucial role in the fate of MVBs. The ATG12–ATG3 complex, which is a component of the LC3B conjugation pathway, plays a crucial role in exosome biogenesis. It is also known to interact with the ALIX protein to regulate the exosome biogenesis [21]. The loss of ATG12–ATG3 disrupted late endosome trafficking and exosome biogenesis, but not starvation induced autophagy. Despite the loss of ALIX, starvation-induced autophagy remained intact. This suggests that the various regulatory machineries that control this process regulate different aspects of autophagy [21].

LncRNAs and autophagy

The commonly used classifications for lncRNAs are based on their genomic location, function, and the presence of repeat elements. They are known to play key roles in various biological processes such as cell growth, differentiation, and metabolism [25]. These small molecules can be bound to various transcription factors to regulate the activity of their host genes. Also, their downstream effector molecules can interact with different signaling pathways to provide information to the platform. These modes of action are not independently coordinated and interacted with each other. For example, lncRNA-p21 is an intergenic non-coding RNA that was induced by the p53 tumor suppressor protein to suppress its tumor suppression function during DNA damage [26]. lncRNA-p21 localizes to p53 target genes and prevents their transcription. A number of studies suggested that lncRNAs could suppress or induce autophagy through the ATGs [11, 27]. In addition, studies revealed that HOTAIR can promote cancer progression and drug resistance [28]. For instance, in human HCC cells, increasing HOTAIR expression can trigger the induction of autophagy by ATG3 and ATG7 [29]. Xu et al. was confirmed that lncRNA GAS5 promotes autophagy by upregulating the expression of certain autophagic regulators like ATG5, ATG12 [30]. Huang et al. discovered that the expression of PVT1 activates ULK1, which is an autophagy-activating protein. It was also hypothesized that MEG3 could regulate the cellular autophagy process and promote BDC proliferation [31]. On the other hand, down-regulation of H19 can increase the expression of ATG7, which is a good indicator of the association between the two. Another study shows that the upregulation of HOTAIR in the cell proliferation promotes the growth of HCC cells by enhancing ATG3 and ATG7 expressions.

Exosomal lncRNA and autophagy

Long Non-coding RNA has been proven to regulate cell autophagy. This is a major factor in the pathogenesis of diseases. lncRNA can also target autophagy-related proteins by sponging some miRNAs [11]. For example, lncRNA APF can regulate the expression of ATG7 and miR-188-3p, which is an autophagy factor. lncRNA TTGF2-OT1 can regulate the expression of various autophagy-related proteins by binding to various regulators of the protein expression. These include the CERS1, LARP1, and NAT8L.

Autophagy protects cancer cells from cellular stress. It is believed that cancer cells can use autophagy to maintain their fuel supply and survival. Researchers have found that lncRNAs are important regulators of autophagy, which

helps cancer cells to avoid cellular stress and chemotherapy. The lncRNA-CAF plays a crucial role in the survival and proliferation of tumor cells. It prevents the degradation of the pro-inflammatory cytokine IL-33 by suppressing p62-dependent autophagy. Normal stromal fibroblasts have high levels of lncRNA-CAF, which can promote tumor proliferation. The positive feedback loop occurs in the tumor microenvironment when cancer cells secrete lncRNA-CAF which is known to promote the growth of tumor cells. Higher levels of lncRNA-CAF in the tumor microenvironment are also associated with poor prognosis in patients with OSCC. lncRNA ANRIL that promotes autophagy in endothelial cells through the upregulation of Beclin1. This is a mechanism that promotes cell proliferation and angiogenesis [32]. A novel approach to treat uremic cardiovascular disease could involve the release of lncRNA ANRIL, which can regulate the autophagy of cardiomyocytes [33]. A study shows that high glucose levels decrease the level of lncRNA H19, which leads to the onset of autophagy [29]. Autophagy has been linked to a negative cardiac function response. H19 may decrease hypoxia-induced injury through the activation of the PI3K/Akt pathway [34]. Overexpression of H19 can help alleviate this effect by reducing the risk of cardiac failure. Downregulation of H19 can increase the expression of ATG7 and Beclin 1 in response to hypoxia [29]. According to Wang et al., lncRNA H19 impairs the cell viability of cultured cells by triggering the autophagy process through a mechanism involving DUSP5-ERK1/2 axis [35]. This study supports the notion that H19 is associated with autophagy.

Metastasis-associated lung adenocarcinoma transcript 1 (MALAT1) is a transcriptional regulator that plays an important role in cancer development. The presence of MALAT1 in the pancreatic ductal adenocarcinoma was a diagnostic marker for the disease. The ability to inhibit autophagy and tumor proliferation was exhibited by the expression of MALAT1. The inhibition of autophagy by MALAT1 silencing was associated with the reduction of tumor growth and metastasis [36]. A study shows that suppressing the MALAT1 protein elevates p62 and lowers LAMP2 expression, which is important for the fusion of lysosomes and autophagosomes [29]. Additionally, it can trigger autophagy by deactivating the expression of the Beclin 1 protein. A new study reports that the MALAT1 knockdown can reduce the expression of the Beclin 1 protein in multiple myeloma tissues [29]. lncRNA MALAT1 is an autophagy inducer that prevents the reoxygenation of cerebral microvascular endothelial cells. This impairs the ability of these cells to repair the damage caused by the upregulation of ULK2 [37]. A study revealed that downregulation of MALAT1 can prevent the death of neurons by suppressing the expression of the miR-30a [38].

It has been hypothesized that the role of the antisense lncRNA known as HOTAIR in regulating gene expression is linked to the coordination of the polycomb repressive complex 2 (PRC2) and the chromosomal remodelling [39]. In patients with hepatocellular carcinoma, overexpression of HOTAIR in the tissues leads to the activation of autophagy, which promotes cell proliferation [40]. This effect is also evidenced by the up regulation of ATG3 and ATG7 expression. Studies revealed that the silencing of HOTAIR inhibited the drug resistance of NSCLC cells by suppressing autophagy through the activation of the ULK1 protein [41]. Studies have shown that the downregulation of lncRNA HOTAIRM1 can block autophagy and inhibit the degradation of the PML-RARA protein by alltrans retinoic acid (ATRA) in PML cells [42]. Studies also showed that the upregulation of the LC3-II/LC3-I, Beclin 1 proteins can increase the level of cellular autophagy by lncRNA HOTAIR [43]. The other lncRNA HULC expression was higher in epithelial ovarian cancer tissues than in normal samples, which promoted the tumorigenesis of the cancer by suppressing autophagy through inhibiting ATG7 [44]. The activation of one more lncRNA MEG3 by the p53 pathway increases bladder cancer cell proliferation by suppressing autophagy [45]. Like in the case of pathogen infection, cancer cells can also trigger autophagy to survive stress

through the repression of MEG3. This impairs the cell's ability to generate and sustain autophagy. Another study shows that over-expression of MEG3, which is known to induce autophagy, can inhibit the growth and progression of human ovarian cancer by regulating the ATG3 protein [46]. The PTENP1 is a member of the lncRNA family and plays a crucial role in the regulation of PTEN expression. The presence of the sustained PTENP1 expression level in hepatocellular carcinoma cells upregulates the PTEN expression and also involved in the induction of autophagy by suppressing the signaling cascade of PI3K/AKT protein [47]. LncRNA SNHG1 is known to inhibit the activities of the miR-16-5p which is involved in p38 MAPK pathway and can alleviate the inflammatory symptoms of osteoarthritis [48].

Exosomal lncRNA and autophagy related diseases

Due to the rapid emergence of high-throughput gene-chip technology, the number of studies investigating the molecular mechanisms of lncRNA has greatly increased. Its involvement in the pathophysiology of diseases such as cancer and Alzheimer's has been widely studied. In this section, we will discuss the role of the exosomal lncRNA-mediated

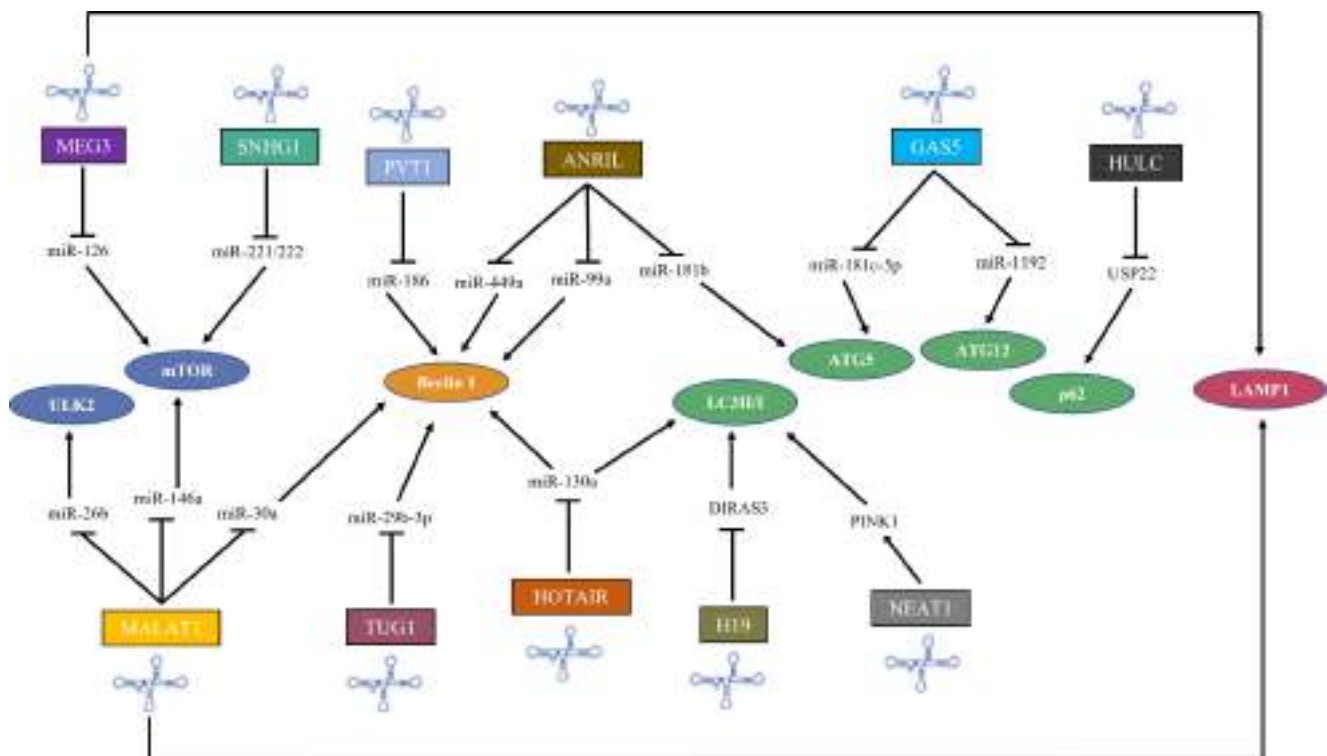


Fig. 2 The complex network of miRNAs and exosomal lncRNAs in regulating autophagy. LncRNAs can function as a sponge for miRNAs and can act as a competing endogenous RNA. See Text and Table 1 for detailed molecular mechanism explanations. Rectangular box represents exosomal lncRNAs; blue oval represents regulatory initiation proteins; orange oval represents regulatory nucleation protein; green oval represents regulatory elongation proteins; pink oval represents regulatory fusion protein in autophagy pathway

autophagy pathway (Fig. 2) in the pathogenesis of various diseases such as cancer, Alzheimer's, Parkinson's, and vascular diseases (Fig. 3) (Table 1).

Alzheimer's Disease (AD)

Alzheimer's disease is a type of neuropathological disorder that affects the memory and cognitive abilities of people over age. It is believed that the hallmark of this condition is the accumulation of tau and β -amyloid protein. The lncRNA17A is known to be expressed by the human brain.

It was found that the expression of this protein was upregulated in the brains of patients with AD [49]. The researchers discovered that the knockdown of lncRNA17A in cells led to an increase in the expression of LC3-II, which is a sign of autophagosome formation [50]. Also, the downregulation of lncRNA17A promoted autophagy prevented the accumulation of protein aggregations in AD. NEAT1 is upregulated in the brain tissue of patients with AD. The study showed that overexpression of lncRNA NEAT1 can improve the interaction between the NEDD4L and PINK1, facilitate

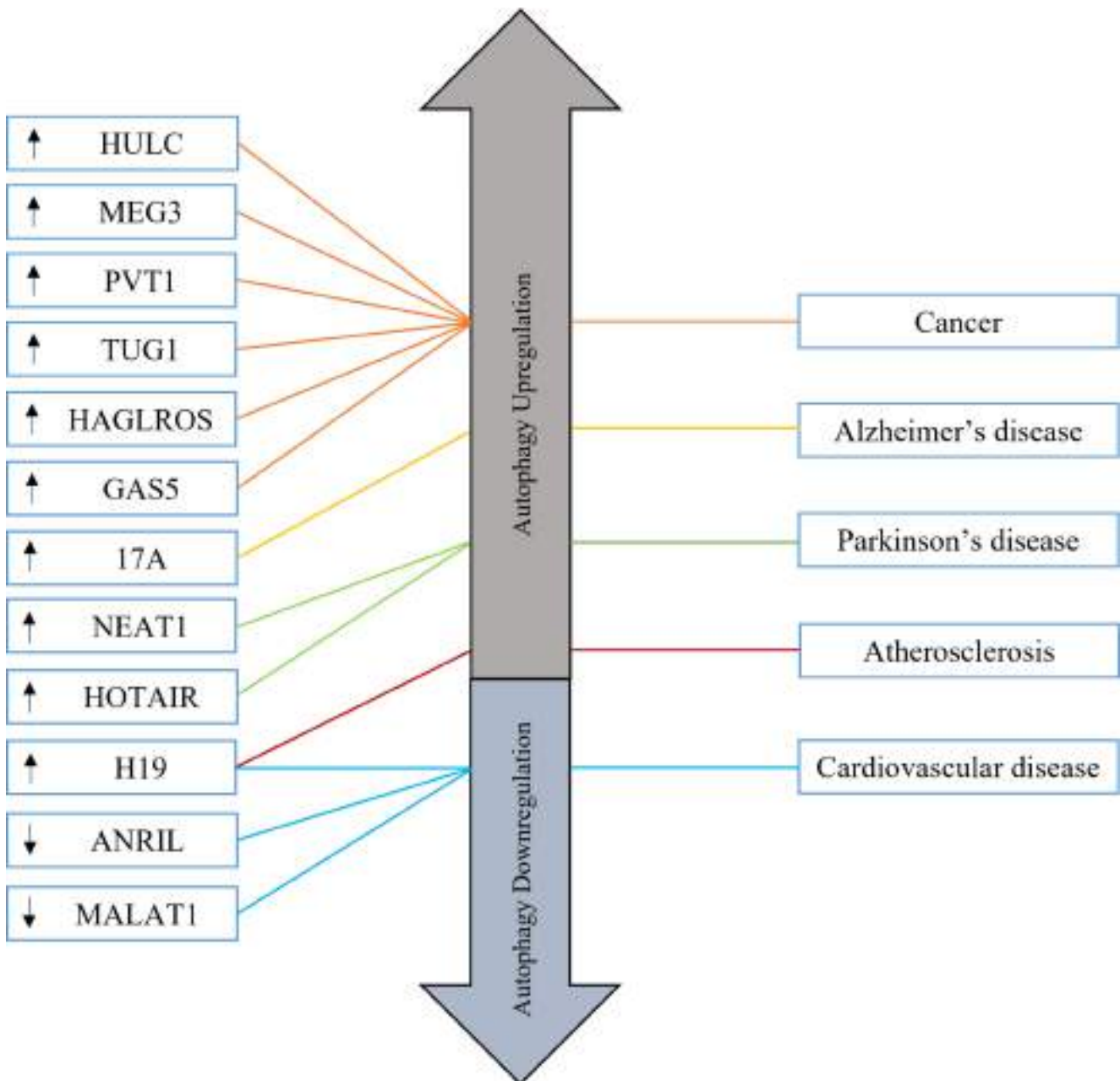


Fig. 3 Autophagy modulating exosomal lncRNAs in different diseases. Most of the lncRNAs are overexpressed and they induce autophagy to promote or suppress diseases. Conversely, downregulated lncRNAs induce or suppress autophagy to promote or inhibit diseases

Table 1 List of autophagy modulating exosomal lncRNAs and their roles in various diseases

Exosomal lncRNAs	Regulation	Target	Pathways	Autophagy-associated diseases	References
ANRIL	Down	miR-181b	ATG5 (↓), Beclin1 (↓), LC3II/I (↓), p62 (↑)	Cardiovascular disease	33
	Up	miR-99a, miR-449a	Beclin1 (↑)	Angiogenesis, Thrombosis	32
MALAT1	Up	miR-26b	ULK2 (↑)	Ischemia	37
	Down	miR-146a	PI3K/AKT/mTOR (↓)	Liver Cancer	68
	Down	miR-30a	Beclin1 (↓)	Ischemic stroke	38
	Down	miR-384	GOLM1 (↓)	Glioma	80
H19	Up	DUSP5	ERK1/2 (↑)	Cerebral ischemia-reperfusion injury	35
	Up	ACP5	WNT/ β -catenin	Atherosclerosis, Ischemic stroke	61
	Up	DIRAS3	ATG7 (↓), LC3-II (↓), Beclin1 (↓)	Diabetic cardiomyopathy	62
HULC	Up	miR15a	p62 (↑)	Liver Cancer	70
	Up	USP22	SIRT1 (↑), p62 (↓), LC3-II (↑)	Liver Cancer	71
HOTAIR	Up	miR-126-5p	Unknown	Parkinson's disease	57
	Up	LRRK2	ERK/MAPK (↑)	Parkinson's disease	56
	Up	miR-130a	Beclin1 (↑), p62 (↓), LC3II/I (↑)	Gastrointestinal stromal tumor	43
MEG3	Up	miR-205-5p	LC3-II (↑), ATG3 (↑), LAMP1 (↑), p62 (↓)	Ovarian Cancer	76
	Down	P53	LC3II/I (↑)	Bladder Cancer	45
17 A	Up	GABABR2	LC3II/I (↑)	Alzheimer's disease	50
NEAT1	Down	PINK1	Unknown	Alzheimer's disease	51
	Up	PINK1	LC3-II/I (↑)	Parkinson's disease	53
SNHG1	Down	miR-221/222	mTOR (↑)	Parkinson's disease	11
	Up	miR-16-5p	p-ERK1/2 (↓), p-p38 (↓), p-p65 (↓)	Osteoarthritis	48
PVT1	Up	miR-20a-5p	ULK (↑)	Pancreatic ductal adenocarcinoma	31
	Up	miR-186	ATG7 (↑), Beclin1 (↑)	Glioma	78
TUG1	Up	miR-29b-3p	Beclin1 (↑)	Ovarian Cancer	72
HAGLROS	Up	miR-5095	PI3K/Akt/mTOR (↑)	Liver Cancer	64
	Up	mTORC1	ATG9A (↓), ATG9B (↓)	Gastric Cancer	63
GAS5	Up	mTOR	LC3II (↓), p62 (↑)	Glioma	81
	Up	miR-222-3p	LC3B (↑), Beclin1 (↑)	Colorectal Cancer	75

the ubiquitination of the latter which can then inhibit the mitophagy process and reduce the risk of Alzheimer's disease [51].

Parkinson's Disease (PD)

The loss of dopaminergic neurons in the brain's substantia nigra region can also lead to the development of a disease known as Parkinson's. This impairs the movement of the body. Recent studies revealed that the lncRNA plays a crucial role in the pathogenesis of Parkinson's disease. It has been known that lncRNA NEAT1 plays a key role in the pathogenesis of PD [52]. The level of lncRNA NEAT1, which is known to increase with time, can also be regulated by MPTP. MPTP can increase the expression level of PINK1, LC3-II in vitro and/or in vivo models of PD [11]. The accumulated PINK1 can increase the accumulation of LC3-II within mitochondria. This phenomenon, known as abnormal mitochondria autophagy, is caused by the accumulation of LC3. It was hypothesized that lncRNA NEAT1,

which is a downstream regulatory factor, could trigger abnormal autophagy by stabilizing the PINK1 protein [53].

It has been discovered that the level of SNHG1 in patients with PD is upregulated [54]. Also, it has been demonstrated that its promotion of α -synuclein aggregation could cause neurotoxicity. The role of lncRNA SNHG1 in promoting α -synuclein aggregation and neurotoxic effects has been highlighted in animal models [55]. It is a key component of the mTOR pathway and plays a role in the autophagy process. It has been shown that it can reduce the toxicity of dopamine neurons in patients with PD. Studies have shown that lncRNA HOTAIR can increase the stability and upregulate the expression of LRRK2 in people with PD [56]. The silencing of HOTAIR would not only improve the cell viability but would also prevent autophagy-related alterations. The lncRNA HOTAIR prevents the interaction between RAB3IP and the miR-126-5p, which could inhibit autophagy and cause the accumulation of the α -synuclein protein in dopaminergic neurons [57].

Atherosclerosis

The overexpression of MALAT1 led to the suppression of the miR-558 target and increased cell death. It also upregulates the ULK1 protein to promote the protective autophagy [58]. MALAT1 targets the miR-15b-5p to increase the level of MAPK1 expression [59]. This pathway enhances the progression of Atherosclerotic heart disease. MALAT1 inhibition promotes the growth and survival of endothelial progenitor cells, which are vulnerable to Atherosclerosis. Studies have shown that the involvement of lncRNAs in the progression of AS is vital. One particular study revealed that the upregulation of lncRNA TUG1 in the peripheral blood of subjects with CHD led to its promotion [60]. Studies have also shown that the defective autophagy in vascular walls cells can inhibit the progression of AS. This impairs the ability of the cells to generate new blood vessels. The studies revealed that the presence of the lncRNA H19 can increase the expression of the ACP5 protein and contribute to atherosclerosis [61]. The researchers discovered that lncRNA H19 could inhibit the autophagy-related activities of cardiomyocytes by silencing the DIRAS3 gene [62].

Cancer

The overexpression of lncRNA HAGLROS is associated with poor clinical outcome in patients with gastric cancer. In gastric cancer, the expression of the transcription factor STAT3 led to the upregulation of the lncRNA HAGLROS. STAT3 can inhibit autophagy by suppressing the mTOR pathway. As for autophagy, HAGLROS can also activate the mTORc1 signaling pathway, which is a negative signal of autophagy [63]. It can also promote cell proliferation by blocking the migration of cancer cells. A study revealed that expression of HAGLROS can also enhance autophagy in human liver cancer cells by regulating miR-5095/ATG12 signals. The study also showed that ATG12, which is a key protein in the development of autophagosomes, is a target of miR-5095 and could provide new insights into the treatment of liver cancer [64]. The human plasmacytoma variant 1 (PVT1) is known to be an oncogene that can predict poor survival in patients with various cancers. This gene is also known to be associated with the ULK1 protein in pancreatic ductal adenocarcinoma. It was revealed that PVT1 can promote cyto-protective autophagy by restoring the expression of ULK1. In addition, PVT1 enhanced autophagy by suppressing ATG3 expression [65]. It has been shown that suppressing the expression of miR-485 by lncRNA PVT1 can promote cell migration and invasion. The expression of lncRNA MALAT1 was increased in gastric and colorectal cancer cells, and it was associated with autophagy activity. A study revealed that MALAT1 could regulate the

autophagosome's maturation through a mechanism. This could contribute to the chemoresistance of colon and gastric cancers. MALAT1 enhanced the CDDP resistance of gastric cancer cells by suppressing the expression of miR-30b [66]. It also sequestered the miR-30e and miR-30b and upregulates ATG5 expression. In colon cancer, MALAT1 promoted autophagy by acting as a ceRNA with miR-101 [67]. MALAT1 silencing can also impair liver cancer cell proliferation and viability when it is subjected to induced autophagy [68]. This effect was triggered by the presence of ATG4D, which is a member of the ATG4 family. NEAT1 was also known to promote poor cancer cell survival such as hepatocellular carcinoma, colorectal cancer. It was also involved in the development of autophagy-related pathways. NEAT-mediated chemoresistance was also promoted by targeting the autophagy-related genes miR-204/ATG3 in colon and anaplastic thyroid cancers [69]. These pathways are involved in lysosome localization, autophagy, and autophagocytosis. Studies also revealed that lncRNA HULC is upregulated in liver cancer cells which increases the amount of p62 expression by decreasing miR-15a [70]. Researchers discovered that the presence of HULC can trigger the autophagy of liver cancer cells by stabilizing the Sirt1 protein [71]. The discovery of a role for HULC in the regulation of autophagy has revealed a potential link between the chemoresistance of human cancer cells and the development of ovarian cancer. The study shows that the absence of the TUG1 protein in ovarian cancer cells can decrease the formation of autophagosomes [72].

The lncRNA PTENP1, which is a pseudogene of PTEN, was down regulated in different cell lines. It can increase the expression of certain miRNA targets, which can promote pro-death autophagy in cells. In addition, PTENP1 overexpression prevented the invasion and migration of cells in the HCC through the use of decoying miR-193a-3p [73]. In a study, Chen et al. discovered that the downregulated lncRNA PTENP1 can be used as a targeted anti-tumor agent by reducing the migration and proliferation of human HCC cells by activating autophagy in PI3K/Akt pathways [74]. lncRNA GAS5 upregulates the expression of PTEN by suppressing colorectal cancer cell migration and invasion [75].

Glioma is a primary brain tumor that has poor prognosis and high mortality. It is considered one of the most common types of central nervous system tumors. lncRNA MEG3 is a widely recognized tumor suppressor gene. It was discovered that it is downregulated in glioma cells and tissues. This impairs the ability of certain microRNAs to interact with their target mRNAs. After discovering that overexpression of the lncRNA MEG3 suppressed the proliferation and migration of U251 cells [76]. In addition, lncRNA MEG3 overexpression decreased the levels of key enzymes in the

PI3K/Akt/mTOR pathways, [77] which are involved in the degeneration of certain cellular components and suggests that the inactivation of these pathways is associated with the upregulation of Sirt7 mediated autophagy. In addition, the expression levels of various vascular endothelial cells, including ATG7, Beclin1 and LC3-II/LC3-I, were upregulated by lncRNA PVT1 [11]. It was also observed that the presence of lncRNA PVT1 led to the expansion of the vascular cell population and the formation of new blood vessels. Further studies reveal that lncRNA PVT1, which is bound to miR-186, can prevent the negative effects of various vascular regulators (ATG7, Beclin 1) on autophagy [78]. The study shows that lncRNA PVT1 promotes the proliferation and migration of vascular cells through the regulation of the miR-186-ATG7/Beclin1 expression. It has been hypothesized that the expression of lncRNA MALAT1 in glioma tissues is an indicator of poor prognosis in patients with glioma. The regulatory mechanism of this gene is also unknown in humans. Its elevated expression was associated with the LC3-II level [79]. In vitro experiments revealed that lncRNA MALAT1, which is a major promoter of autophagy, promoted the proliferation and survival of glioma cells. The study revealed that the lncRNA MALAT1 was a miRNA sponge that regulated the autophagy of glioma cells. The discovery of the GOLM1 downstream target led to the discovery of lncRNA MALAT1, which promoted autophagy and invasion by upregulating GOLM1 [80]. GOLM1, which is a part of the miR-384 family, was also identified to promote the autophagy by upregulating the protein kinase Akt. Huo et al. showed that GAS5 was decreased in glioma cells and the exposure to cisplatin increased the cell sensitivity to it [81]. The author also showed that this process triggered excessive autophagy by increasing LC3-II/LC3-I and suppressing p62 accumulation.

Conclusions

The significance of autophagy has been widely revealed by a growing body of studies. This process of energy metabolism plays a crucial role in the development and maintenance of human health. Various studies have shown that lncRNAs and miRNAs can be utilized as molecular diagnostic tools and therapeutic targets for diseases. Although the role of lncRNAs and microRNAs in autophagy has been acknowledged, the interactions between them and the regulatory complexity of the cellular process are still not yet fully understood. This review aims to summarize the current research on the interactions between these two components of autophagy. Although it has been hypothesized that the presence of lncRNAs in exosomes can serve as disease markers, the lack of adequate research related to their

discovery and development has hindered the progress of this field as a result of which we have only limited knowledge about the mechanisms that regulate the interaction between autophagy and exosomal lncRNAs. Various aspects of the effects of lncRNAs on cancer cells are still being studied. Although the cancer-suppressing properties of lncRNAs have been proven, their effects on the carcinogenesis are still controversial and the effects of lncRNAs on autophagy are still unclear.

Abbreviations

ACP5	Acid Phosphatase 5
AD	Alzheimer's Disease
ANRIL	Antisense ncRNA in the INK4 Locus
APF	Animal Protein Factor
CAF	Cancer-Associated Fibroblast
CERS1	Ceramide Synthase 1
CHD	Coronary Heart Disease
DIRAS3	GTP-binding protein Di-Ras3
ERK	Extracellular Signal-Regulated Kinase
GAS5	Growth Arrest-Specific 5
GMEC	Goat Mammary Epithelial Cells
GOLM1	Golgi Membrane Protein 1
HCC	Hepato Cellular Carcinoma
HOTAIR	HOX Transcript Antisense RNA
HULC	Highly Upregulated in Liver Cancer
LAMP2	Lysosome-Associated Membrane Protein 2
LncRNAs	Long noncoding RNAs
MALAT1	Metastasis-related Lung Adenocarcinoma Transcript 1
MCS	Mesenchymal Stem Cell
MEG3	Maternally Expressed Gene 3
MPTP	Mitochondrial Permeability Transition Pore
MVBs	Multivesicular Bodies
MVB-PM	MVB-Plasma Membrane
NEAT1	Nuclear Enriched Abundant Transcript 1
PD	Parkinson's Disease
PI3K	Phosphoinositide 3-kinase
PML-RARA	Promyelocytic Leukemia Retinoic Acid Receptor Alpha
PRC2	Polycomb Repressive Complex 2
PTEN	Phosphatase and Tensin Homolog deleted on Chromosome 10
PVT1	Plasmacytoma Variant Translocation 1
SNARE	SNAP Receptor
SNHG1	Small Nucleolar RNA Host Gene 1
STAT3	Signal Transducer and Activator of Transcription 3
TGFB2-OT1	Transforming Growth Factor Beta-2 Organic Anion Transporter
TUG1	Taurine Upregulated Gene 1
ULK	Unc-51 Like Autophagy Activating Kinase

VAMP7 Vesicle Associated Membrane Protein 7
VPS34 Vacuolar Protein Sorting 34

Acknowledgements Authors would like to acknowledge the academic fellowship grant from Department of Science and Technology and Biotechnology, Govt. of West Bengal.

Author contribution SGC performed the literature research and drafted the manuscript; DB, PK participated in modifying the article.

Funding This work is financially supported by the Department of Science and Technology and Biotechnology (Sanction no.BT/ST/P/S&T/2G-13/2017), Govt. of West Bengal.

Data Availability Not applicable.

Declarations

Conflict of interest The authors declare no competing interests.

Ethical approval and consent to participate Not applicable.

Consent for publication All the authors approved the publication.

References

- Parzych KR, Klionsky DJ (2014) An overview of autophagy: morphology, mechanism, and regulation. *Antioxid Redox Signal* 20(3):460–473. doi:<https://doi.org/10.1089/ars.2013.5371>
- Badadani M (2012) Autophagy Mechanism, Regulation, Functions, and Disorders. *International Scholarly Research Notices* 2012. <https://doi.org/10.5402/2012/927064>
- Mathew R, Wadsworth VK, White E (2007) Role of autophagy in cancer. *Nat Rev Cancer* 7(12):961–967. doi:<https://doi.org/10.1038/nrc2254>
- Aman Y, Medina TS, Hansen M et al (2021) Autophagy in healthy aging and disease. *Nat Aging* 634–650. <https://doi.org/10.1038/s43587-021-00098-4>
- Jella KK, Nasti TH, Li Z, Malla SR, Buchwald ZS, Khan MK (2018) Exosomes, Their Biogenesis and Role in Inter-Cellular Communication, Tumor Microenvironment and Cancer Immunotherapy. *Vaccines (Basel)* 6(4):69. doi:<https://doi.org/10.3390/vaccines6040069>
- Chowdhury SG, Ray R, Bhattacharya D, Karmakar P (2022) DNA damage induced cellular senescence and its PTEN-armed exosomes-the warriors against prostate carcinoma cells. *Med Oncol* 39(3):34. doi:<https://doi.org/10.1007/s12032-021-01614-7>
- Redzic JS, Balaj L, van der Vos KE, Breakefield XO (2014) Extracellular RNA mediates and marks cancer progression. *Semin Cancer Biol* 28:14–23. doi:<https://doi.org/10.1016/j.semcancer.2014.04.010>
- Hassanpour M, Rezaabakhsh A, Rezaie J, Nouri M, Rahbarghazi R (2020) Exosomal cargos modulate autophagy in recipient cells via different signaling pathways. *Cell Biosci* 10(1):1–6. <https://doi.org/10.1186/s13578-020-00455-7>
- Zhou X, Jiang L, Fan G, Yang H, Wu L, Huang Y, Xu N, Li J (2019) Role of the ciRS-7/miR-7 axis in the regulation of proliferation, apoptosis and inflammation of chondrocytes induced by IL-1 β . *Int Immunopharmacol* 71:233–240. doi:<https://doi.org/10.1016/j.intimp.2019.03.037>
- Fang Y, Fullwood MJ (2016) Roles, Functions, and Mechanisms of Long Non-coding RNAs in Cancer. *Genomics Proteome Bioinf* 14(1):42–54. doi:<https://doi.org/10.1016/j.gpb.2015.09.006>
- Xu X, Cui L, Zhong W, Cai Y (2020) Autophagy-Associated lncRNAs: Promising Targets for Neurological Disease Diagnosis and Therapy. *Neural Plast* 2020. doi:<https://doi.org/10.1155/2020/8881687>
- Li X, Hu X, Wang J, Xu W, Yi C, Ma R, Jiang H (2018) Inhibition of autophagy via activation of PI3K/Akt/mTOR pathway contributes to the protection of hesperidin against myocardial ischemia/reperfusion injury. *Int J Mol Med* 42(4):1917–1924. doi:<https://doi.org/10.3892/ijmm.2018.3794>
- Alers S, Löffler AS, Wesselborg S, Stork B (2012) Role of AMPK-mTOR-Ulk1/2 in the regulation of autophagy: cross talk, shortcuts, and feedbacks. *Mol Cell Biol* 32(1):2–11. doi:<https://doi.org/10.1128/MCB.06159-11>
- Sun Q, Fan W, Zhong Q (2009) Regulation of Beclin 1 in autophagy. *Autophagy* 5(5):713–716. doi:<https://doi.org/10.4161/auto.5.5.8524>
- Li B, Lu Y, Wang H, Han X, Mao J, Li J, Yu L, Wang B, Fan S, Yu X, Song B (2016) miR-221/222 enhance the tumorigenicity of human breast cancer stem cells via modulation of PTEN/Akt pathway. *Biomed Pharmacother* 79:93–101. doi:<https://doi.org/10.1016/j.biopha.2016.01.045>
- Liu X, Deng Y, Xu Y, Jin W, Li H (2018) MicroRNA-223 protects neonatal rat cardiomyocytes and H9c2 cells from hypoxia-induced apoptosis and excessive autophagy via the Akt/mTOR pathway by targeting PARP-1. *J Mol Cell Cardiol* 118:133–146. doi:<https://doi.org/10.1016/j.yjmcc.2018.03.018>
- Arsalan F, Lai RC, Smeets MB, Akeroyd L, Choo A, Aguor EN et al (2013) Mesenchymal stem cell-derived exosomes increase ATP levels, decrease oxidative stress and activate PI3K/Akt pathway to enhance myocardial viability and prevent adverse remodeling after myocardial ischemia/reperfusion injury. *Stem Cell Res* 10(3):301–312. doi:<https://doi.org/10.1016/j.scr.2013.01.002>
- Yang Y, Li Y, Chen X, Cheng X, Liao Y, Yu X (2016) Exosomal transfer of miR-30a between cardiomyocytes regulates autophagy after hypoxia. *J Mol Med (Berl)* 94(6):711–724. doi:<https://doi.org/10.1007/s00109-016-1387-2>
- Nair U, Jotwani A, Geng J, Gammoh N, Richerson D, Yen WL et al (2011) SNARE Proteins Are Required for Macroautophagy. *Cell* 146(2):290–302. doi:<https://doi.org/10.1016/j.cell.2011.06.022>
- Puri C, Vicinanza M, Ashkenazi A, Gratian MJ, Zhang Q, Bento CF, Renna M, Menzies FM, Rubinshtein DC (2018) The RAB11A-positive compartment is a primary platform for autophagosome assembly mediated by WIPI2 recognition of PI3P-RAB11A. *Dev Cell* 45(1):114–131. <https://doi.org/10.1016/j.devcel.2018.03.008>
- Murrow L, Malhotra R, Debnath J (2015) ATG12-ATG3 interacts with Alix to promote basal autophagic flux and late endosome function. *Nat Cell Biol* 17(3):300–310. doi:<https://doi.org/10.1038/ncb3112>
- Salimi L, Akbari A, Jabbari N, Mojarad B, Vahhabi A, Szafert S, Kalashani SA, Soraya H, Nawaz M, Rezaie J (2020) Synergies in exosomes and autophagy pathways for cellular homeostasis and metastasis of tumor cells. *Cell Biosci* 10:1–8. <https://doi.org/10.1186/s13578-020-00426-y>
- Gurunathan S, Kang MH, Kim JH (2021) A Comprehensive Review on Factors Influences Biogenesis, Functions, Therapeutic and Clinical Implications of Exosomes. *Int J Nanomedicine* 16:1281–1312. doi:<https://doi.org/10.2147/IJN.S291956>
- Papademetrio DL, Garcia MN, Grasso D, Alvarez É (2021) Autophagy-Mediated Exosomes as Immunomodulators of Natural Killer Cells in Pancreatic Cancer Microenvironment. *Front Oncol* 10:622956. doi:<https://doi.org/10.3389/fonc.2020.622956>
- Yan X, Ma L, Yang M (2020) Identification and characterization of long non-coding RNA (lncRNA) in the developing seeds of

- Jatropha curcas*. *Sci Rep* 10(1):1–10. <https://doi.org/10.1038/s41598-020-67410-x>
26. Jin S, Yang X, Li J, Yang W, Ma H, Zhang Z (2019) p53-targeted lincRNA-p21 acts as a tumor suppressor by inhibiting JAK2/STAT3 signaling pathways in head and neck squamous cell carcinoma. *Mol Cancer* 18(1):38. <https://doi.org/10.1186/s12943-019-0993-3>
 27. Khan MZI, Tam SY, Law HKW (2019) Autophagy-modulating long non-coding RNAs (lncRNAs) and their molecular events in cancer. *Front Genet* 9:750. doi:<https://doi.org/10.3389/fgene.2018.00750>
 28. Xin X, Li Q, Fang J, Zhao T (2021) LncRNA HOTAIR: A Potential Prognostic Factor and Therapeutic Target in Human Cancers. *Front Oncol* 2904. doi:<https://doi.org/10.3389/fonc.2021.679244>
 29. Yang L, Wang H, Shen Q, Feng L, Jin H (2017) Long non-coding RNAs involved in autophagy regulation. *Cell Death Dis* 8(10):e3073. doi:<https://doi.org/10.1038/cddis.2017.464>
 30. Xu T, Xu X, Chu Y, Jiang D, Xu G (2021) Long-chain non-coding RNA GAS5 promotes cell autophagy by modulating the miR-181c-5p/ATG5 and miR-1192/ATG12 axes. *Int J Mol Med* 48(6):209. doi: <https://doi.org/10.3892/ijmm.2021.5042>
 31. Huang F, Chen W, Peng J, Li Y, Zhuang Y, Zhu Z, Shao C, Yang W, Yao H, Zhang S (2018) LncRNA PVT1 triggers Cyto-protective autophagy and promotes pancreatic ductal adenocarcinoma development via the miR-20a-5p/ULK1 Axis. *Mol Cancer* 17(1):1–6. doi:<https://doi.org/10.1186/s12943-018-0845-6>
 32. Zeng R, Song XJ, Liu CW, Ye W (2019) LncRNA ANRIL promotes angiogenesis and thrombosis by modulating microRNA-99a and microRNA-449a in the autophagy pathway. *Am J Transl Res* 11(12):7441–7448
 33. Xu Y, Chen J, Wang M, Yu R, Zou W, Shen W (2021) Mechanism of lncRNA-ANRIL/miR-181b in autophagy of cardiomyocytes in mice with uremia by targeting ATG5. *PLoS ONE* 16(9):e0256734. doi:<https://doi.org/10.1371/journal.pone.0256734>
 34. Yuan L, Yu L, Zhang J, Zhou Z, Li C, Zhou B, Hu X, Xu G, Tang Y (2020) Long noncoding RNA H19 protects H9c2 cells against hypoxia-induced injury by activating the PI3K/AKT and ERK/p38 pathways. *Mol Med Rep* 21(4):1709–1716. doi:<https://doi.org/10.3892/mmr.2020.10978>
 35. Wang J, Cao B, Han D, Sun M, Feng J (2017) Long Non-coding RNA H19 Induces Cerebral Ischemia Reperfusion Injury via Activation of Autophagy. *Aging Dis* 8(1):71–84. doi:<https://doi.org/10.14336/AD.2016.0530>
 36. Li X, Zhao J, Zhang H, Cai J (2020) Silencing of lncRNA metastasis-associated lung adenocarcinoma transcript 1 inhibits the proliferation and promotes the apoptosis of gastric cancer cells through regulating microRNA-22-3p-mediated ErbB3. *Onco Targets Ther* 13:559–571. doi:<https://doi.org/10.2147/OTT.S222375>
 37. Li Z, Li J, Tang N (2017) Long noncoding RNA Malat1 is a potent autophagy inducer protecting brain microvascular endothelial cells against oxygen-glucose deprivation/reoxygenation-induced injury by sponging miR-26b and upregulating ULK2 expression. *Neuroscience* 354:1–10. doi: <https://doi.org/10.1016/j.neuroscience.2017.04.017>
 38. Guo D, Ma J, Yan L, Li T, Li Z, Han X, Shui S (2017) Down-Regulation of Lncrna MALAT1 Attenuates Neuronal Cell Death Through Suppressing Beclin1-Dependent Autophagy by Regulating Mir-30a in Cerebral Ischemic Stroke. *Cell Physiol Biochem* 43(1):182–194. doi: <https://doi.org/10.1159/00048033>
 39. Zhang K, Sun X, Zhou X, Han L, Chen L, Shi Z, Zhang A, Ye M et al (2015) Long non-coding RNA HOTAIR promotes glioblastoma cell cycle progression in an EZH2 dependent manner. *Oncotarget* 6(1):537–546. doi:<https://doi.org/10.18632/oncotarget.2681>
 40. Yang L, Zhang X, Li H, Liu J (2016) The long noncoding RNA HOTAIR activates autophagy by upregulating ATG3 and ATG7 in hepatocellular carcinoma. *Mol BioSyst* 12(8):2605–2612. doi:<https://doi.org/10.1039/c6mb00114a>
 41. Yang Y, Jiang C, Yang Y, Guo L, Huang J, Liu X, Wu C, Zou J (2018) Silencing of LncRNA-HOTAIR decreases drug resistance of Non-Small Cell Lung Cancer cells by inactivating autophagy via suppressing the phosphorylation of ULK1. *Biochem Biophys Res Commun* 497(4):1003–1010. doi: <https://doi.org/10.1016/j.bbrc.2018.02.141>
 42. Chen ZH, Wang WT, Huang W, Fang K, Sun YM, Liu SR, Luo XQ, Chen YQ (2017) The lncRNA HOTAIRMI1 regulates the degradation of PML-RARA oncoprotein and myeloid cell differentiation by enhancing the autophagy pathway. *Cell Death Differ* 24(2):212–224. doi:<https://doi.org/10.1038/cdd.2016.111>
 43. Zhang J, Chen K, Tang Y et al (2021) LncRNA-HOTAIR activates autophagy and promotes the imatinib resistance of gastrointestinal stromal tumor cells through a mechanism involving the miR-130a/ATG2B pathway. *Cell Death Dis* 12(4):367. <https://doi.org/10.1038/s41419-021-03650-7>
 44. Chen S, Wu DD, Sang XB, Wang LL, Zong ZH, Sun KX, Liu BL, Zhao Y (2017) The lncRNA HULC functions as an oncogene by targeting ATG7 and ITGB1 in epithelial ovarian carcinoma. *Cell Death Dis* 8(10):e3118. doi:<https://doi.org/10.1038/cddis.2017.486>
 45. Ying L, Huang Y, Chen H, Wang Y, Xia L, Chen Y, Liu Y, Qiu F (2013) Downregulated MEG3 activates autophagy and increases cell proliferation in bladder cancer. *Mol BioSyst* 9(3):407–411. <https://doi.org/10.1039/C2MB25386K>
 46. Xiu YL, Sun KX, Chen X, Chen S, Zhao Y, Guo QG, Zong ZH (2017) Upregulation of the lncRNA Meg3 induces autophagy to inhibit tumorigenesis and progression of epithelial ovarian carcinoma by regulating activity of ATG3. *Oncotarget* 8(19):31714–31725. doi:<https://doi.org/10.18632/oncotarget.15955>
 47. Li W, Zhang T, Guo L, Huang L (2018) Regulation of PTEN expression by noncoding RNAs. *J Exp Clin Cancer Res* 37(1):1–12. doi:<https://doi.org/10.1186/s13046-018-0898-9>
 48. Lei J, Fu Y, Zhuang Y, Zhang K, Lu D (2019) LncRNA SNHG1 alleviates IL-1 β -induced osteoarthritis by inhibiting miR-16-5p-mediated p38 MAPK and NF- κ B signaling pathways. *Biosci Rep* 39(9):BSR20191523. doi:<https://doi.org/10.1042/BSR20191523>
 49. Asadi MR, Hassani M, Kiani S, Sabaie H, Moslehian MS, Kazemi M, Ghafouri-Fard S, Taheri M, Rezazadeh M (2021) The Perspective of Dysregulated LncRNAs in Alzheimer's Disease: A Systematic Scoping Review. *Front Aging Neurosci* 13:582. doi:<https://doi.org/10.3389/fnagi.2021.709568>
 50. Wang X, Zhang M, Liu H (2019) LncRNA17A regulates autophagy and apoptosis of SH-SY5Y cell line as an invitro model for Alzheimer's disease. *Biosci Biotechnol Biochem* 83(4):609–621. doi:<https://doi.org/10.1080/09168451.2018.1562874>
 51. Huang Z, Zhao J, Wang W, Zhou J, Zhang J (2020) Depletion of LncRNA NEAT1 Rescues Mitochondrial Dysfunction Through NEDD4L-Dependent PINK1 Degradation in Animal Models of Alzheimer's Disease. *Front Cell Neurosci* 14:28. doi:<https://doi.org/10.3389/fncel.2020.00028>
 52. Boros FA, Vécsei L, Klivényi P (2021) NEAT1 on the Field of Parkinson's Disease: Offense, Defense, or a Player on the Bench? *J Parkinsons Dis* 11(1):123–138. doi:<https://doi.org/10.3233/JPD-202374>
 53. Yan W, Chen ZY, Chen JQ, Chen HM (2018) LncRNA NEAT1 promotes autophagy in MPTP-induced Parkinson's disease through stabilizing PINK1 protein. *Biochem Biophys Res Commun* 496(4):1019–1024. doi: <https://doi.org/10.1016/j.bbrc.2017.12.149>
 54. Zhou S, Yu X, Wang M, Meng Y, Song D, Yang H, Wang D, Bi J, Xu S (2021) Long Non-coding RNAs in Pathogenesis of Neurodegenerative Diseases. *Front Cell Dev Biol* 9:2416. doi:<https://doi.org/10.3389/fcell.2021.719247>

55. Chen Y, Lian YJ, Ma YQ, Wu CJ, Zheng YK, Xie NC (2018) LncRNA SNHG1 promotes α -synuclein aggregation and toxicity by targeting miR-15b-5p to activate SIAH1 in human neuroblastoma SH-SY5Y cells. *Neurotoxicology* 68:212–221. doi:<https://doi.org/10.1016/j.neuro.2017.12.001>
56. Wang S, Zhang X, Guo Y, Rong H, Liu T (2017) The long noncoding RNA HOTAIR promotes Parkinson's disease by upregulating LRRK2 expression. *Oncotarget* 8(15):24449–24456. doi:<https://doi.org/10.18632/oncotarget.15511>
57. Lin Q, Hou S, Dai Y, Jiang N, Lin Y (2019) LncRNA HOTAIR targets miR-126-5p to promote the progression of Parkinson's disease through RAB31P. *Biol Chem* 400(9):1217–1228. doi:<https://doi.org/10.1515/hsz-2018-0431>
58. Guo X, Wu X, Han Y, Tian E, Cheng J (2019) LncRNA MALAT1 protects cardiomyocytes from isoproterenol-induced apoptosis through sponging miR-558 to enhance ULK1-mediated protective autophagy. *J Cell Physiol* 234(7):10842–10854. doi:<https://doi.org/10.1002/jcp.27925>
59. Zhu Y, Yang T, Duan J, Mu N, Zhang T (2019) MALAT1/miR-15b-5p/MAPK1 mediates endothelial progenitor cells autophagy and affects coronary atherosclerotic heart disease via mTOR signaling pathway. *Aging* 11(4):1089–1109. doi:<https://doi.org/10.18632/aging.101766>
60. You G, Long X, Song F, Huang J, Tian M, Xiao Y, Deng S, Wu Q (2020) Metformin activates the AMPK-mTOR pathway by modulating lncRNA TUG1 to induce autophagy and inhibit atherosclerosis. *Drug Des Devel Ther* 14:457–468. doi:<https://doi.org/10.2147/DDDT.S233932>
61. Huang Y, Wang L, Mao Y, Nan G (2019) Long Noncoding RNA-H19 Contributes to Atherosclerosis and Induces Ischemic Stroke via the Upregulation of Acid Phosphatase 5. *Front Neurol* 10:32. doi:<https://doi.org/10.3389/fneur.2019.00032>
62. Zhuo C, Jiang R, Lin X, Shao M (2017) LncRNA H19 inhibits autophagy by epigenetically silencing of DIRAS3 in diabetic cardiomyopathy. *Oncotarget* 8(1):1429–1437. doi:<https://doi.org/10.18632/oncotarget.13637>
63. Chen JF, Wu P, Xia R, Yang J, Huo XY, Gu DY, Tang CJ, De W, Yang F (2018) STAT3-induced lncRNA HAGLROS overexpression contributes to the malignant progression of gastric cancer cells via mTOR signal-mediated inhibition of autophagy. *Mol Cancer* 17(1):6. doi:<https://doi.org/10.1186/s12943-017-0756-y>
64. Wei H, Hu J, Pu J, Tang Q et al (2019) Long noncoding RNA HAGLROS promotes cell proliferation, inhibits apoptosis and enhances autophagy via regulating miR-5095/ATG12 axis in hepatocellular carcinoma cells. *Int Immunopharmacol* 73:72–80. doi: <https://doi.org/10.1016/j.intimp.2019.04.049>
65. Yang L, Peng X, Jin H, Liu J (2019) Long non-coding RNA PVT1 promotes autophagy as ceRNA to target ATG3 by sponging microRNA-365 in hepatocellular carcinoma. *Gene* 697:94–102. doi:<https://doi.org/10.1016/j.gene.2019.02.036>
66. Xi Z, Si J, Nan J (2019) LncRNA MALAT1 potentiates autophagy-associated cisplatin resistance by regulating the microRNA-30b/autophagy-related gene 5 axis in gastric cancer. *Int J Oncol* 54(1):239–248. <https://doi.org/10.3892/ijo.2018.4609>
67. Si Y, Yang Z, Ge Q, Yu L, Yao M, Sun X, Ren Z, Ding C (2019) Long non-coding RNA Malat1 activated autophagy, hence promoting cell proliferation and inhibiting apoptosis by sponging miR-101 in colorectal cancer. *Cell Mol Biol Lett* 24(1):1–12. doi:<https://doi.org/10.1186/s11658-019-0175-8>
68. Peng N, He J, Li J et al (2020) Long noncoding RNA MALAT1 inhibits the apoptosis and autophagy of hepatocellular carcinoma cell by targeting the microRNA-146a/PI3K/Akt/mTOR axis. *Cancer Cell Int* 20:165. doi:<https://doi.org/10.1186/s12935-020-01231-w>
69. Li X, Zhou Y, Yang L, Ma Y, Peng X, Yang S, Li H, Liu J (2019) LncRNA NEAT1 promotes autophagy via regulating miR-204/ATG3 and enhanced cell resistance to sorafenib in hepatocellular carcinoma. *J Cell Physiol* 235:3402–3413. doi: <https://doi.org/10.1002/jcp.29230>
70. Xin X, Wu M, Meng Q et al (2018) Long noncoding RNA HULC accelerates liver cancer by inhibiting PTEN via autophagy cooperation to miR15a. *Mol Cancer* 17(1):94. <https://doi.org/10.1186/s12943-018-0843-8>
71. Xiong H, Ni Z, He J et al (2017) LncRNA HULC triggers autophagy via stabilizing Sirt1 and attenuates the chemosensitivity of HCC cells. *Oncogene* 36(25):3528–3540. <https://doi.org/10.1038/onc.2016.521>
72. Gu L, Li Q, Liu H, Lu X, Zhu M (2020) Long Noncoding RNA TUG1 Promotes Autophagy-Associated Paclitaxel Resistance by Sponging miR-29b-3p in Ovarian Cancer Cells. *Onco Targets Ther* 13:2007–2019. doi:<https://doi.org/10.2147/OTT.S240434>
73. Qian YY, Li K, Liu QY, Liu ZS (2017) Long non-coding RNA PTENP1 interacts with miR-193a-3p to suppress cell migration and invasion through the PTEN pathway in hepatocellular carcinoma. *Oncotarget* 8(64):107859. doi:<https://doi.org/10.18632/oncotarget.22305>
74. Chen CL, Tseng YW, Wu JC, Chen GY, Lin KC, Hwang SM, Hu YC (2015) Suppression of hepatocellular carcinoma by baculovirus-mediated expression of long non-coding RNA PTENP1 and MicroRNA regulation. *Biomaterials* 44:71–81. doi:<https://doi.org/10.1016/j.biomaterials.2014.12.023>
75. Liu L, Wang HJ, Meng T et al (2019) lncRNA GAS5 Inhibits Cell Migration and Invasion and Promotes Autophagy by Targeting miR-222-3p via the GAS5/PTEN-Signaling Pathway in CRC. *Mol Ther Nucleic Acids* 17:644–656. doi:<https://doi.org/10.1016/j.omtn.2019.06.009>
76. Tao P, Yang B, Zhang H, Sun L, Wang Y, Zheng W (2020) The overexpression of lncRNA MEG3 inhibits cell viability and invasion and promotes apoptosis in ovarian cancer by sponging miR-205-5p. *Int J Clin Exp Pathol* 13(5):869–879 PMID: PMC7270692
77. He Y, Dan Y, Gao X, Huang L, Lv H, Chen J (2021) DNMT1-mediated lncRNA MEG3 methylation accelerates endothelial-mesenchymal transition in diabetic retinopathy through the PI3K/AKT/mTOR signaling pathway. *Am J Physiol Endocrinol Metab* 320(3):E598–608. doi:<https://doi.org/10.1152/ajpendo.00089.2020>
78. Ma Y, Wang P, Xue Y, Qu C, Liu X, Ma J (2017) PVT1 affects growth of glioma microvascular endothelial cells by negatively regulating miR-186. *Tumor Biol* 39(3):1010428317694326. doi: <https://doi.org/10.1177/1010428317694326>
79. Shao G, Zhao Z, Zhao W, Hu G, Zhang L, Li W, Xing C, Zhang X (2020) Long non-coding RNA MALAT1 activates autophagy and promotes cell proliferation by downregulating microRNA-204 expression in gastric cancer. *Oncol Lett* 19(1):805–812. doi:<https://doi.org/10.3892/ol.2019.11184>
80. Ma R, Zhang BW, Zhang ZB, Deng QJ (2020) LncRNA MALAT1 knockdown inhibits cell migration and invasion by suppressing autophagy through miR-384/GOLM1 axis in glioma. *Eur Rev Med Pharmacol Sci* 24(5):2601–2615. doi:https://doi.org/10.26355/eurrev_202003_20529
81. Huo JF, Chen XB (2019) Long noncoding RNA growth arrest-specific 5 facilitates glioma cell sensitivity to cisplatin by suppressing excessive autophagy in an mTOR-dependent manner. *J Cell Biochem* 120(4):6127–6136. doi: <https://doi.org/10.1002/jcb.27900>

Publisher's note Springer Nature remains neutral with regard to jurisdictional claims in published maps and institutional affiliations.

PERSPECTIVE

Glycation-induced Amyloid Formation in Proteins: An Emerging Perspective to Explore Diabetes Associated Onset of Neurodegenerative Symptoms

Samudra Prosad Banik^{1,*}

¹Department of Microbiology, Maulana Azad College, Kolkata 700013, India

Abstract: Non-enzymatic protein glycation occurs spontaneously *via* the formation of sugar-protein Schiff adducts. The end products of this pathway are terminally misfolded proteins popularly known as Advanced Glycation End (AGE) Products. Glycated proteins account for a diverse spectrum of physiological maladies including arteriosclerosis, renal failure, diabetic complications, obesity, and neurological disorders. AGEs not only jeopardise the functionality of modified proteins but also induce the formation of Covalent protein cross-links. Glycation has the potential to induce the unfolding and refolding of globular proteins into cross- β structures thus resembling many amyloid deposits like amyloid beta, tau protein, and prions. However, glycation-induced amyloid formation is not a generic property of proteins; instead, it is guided by the nature and conformation of the protein, the type of glycation agent as well as the solution conditions governing the glycation reaction. The half-lives of AGE adducts are prolonged by their impaired proteasomal clearance since glycation modifies the lysine residues and renders them unavailable for ubiquitination. AGEs are cleared *via* sequestration with specific cell surface receptors (RAGE); subsequently, downstream signalling events involving MAPK and NF- κ B result in the activation of inflammatory response or the apoptotic pathway. This perspective article discusses the current developments in understanding the various facets of glycation-associated protein aggregation and the corresponding development of amyloid-like entities.

ARTICLE HISTORY

Received: September 04, 2022

Revised: January 22, 2023

Accepted: January 23, 2023

DOI:

10.2174/1573401319666230224094812

Keywords: Advanced glycation end product, protein aggregation, amyloid plaques, diabetes, neurodegenerative disorders, arteriosclerosis.

1. INTRODUCTION

Almost all neurodegenerative disorders share the signature pathophysiology of accumulation of misfolded protein aggregates termed as amyloid plaques. Alzheimer's disease is characterised by neurofibrillary tangles of brain tissue, constituted of amyloid β and hyperphosphorylated τ proteins [1]; in Parkinson's disease the culprit is alpha-synuclein [2], the most significant pre-synaptic chaperone and in Huntington's disease, misfolding of the protein huntingtin is caused by expansion of glutamines [3]. Three major factors have been chiefly accountable for the aggregation of proteins; high hydrophobicity, high propensity to convert from alpha-helical to beta-sheet structures, and low net charge [4]. However, the entire set of intrinsic and extrinsic factors which are accountable for the toxic aggregation of these resident body proteins remains to be deciphered completely. A chief reason accounting for the non-native aggregation of proteins that has emerged over the last few decades is the spontaneous attachment of sugar residues to protein, a phenomenon termed as glycation [5].

Glycation is brought about by the persistence of dietary sugars inside the body over a long time period and the chief targets of this process are cellular macromolecules including proteins, lipids as well as nucleic acids. The process involves the formation of Schiff bases between the carbonyl groups of reducing sugars and amino groups in the side chains of proteins involving lysine or histidine. The Schiff base undergoes subsequent Amadori rearrangements to form glycated adducts known as Early Maillard products. The glycated adduct eventually results in the formation of a terminally misfolded protein aggregate termed as Advanced Glycation End product (AGE) [6]. Since carbohydrate is the most important staple food and the most significant constituent of diet across the globe, the formation of glycated adduct inside the body occurs unavoidably as part of the normal metabolic process. Under physiological conditions as well as most clinical settings, glucose is the primary glycation agent and Schiff base formation with glucose AGEs accumulated in low concentration seldom poses any significant threat to the maintenance of body homeostasis since these adducts are quickly removed from the circulation by dedicated receptors expressed by macrophages, dendritic cells and certain other immune cells [7]. However, sustained consumption of sugary and junk foods as well as several other lifestyle habits may sig-

*Address correspondence to this author at the Department of Microbiology, Maulana Azad College, Kolkata 700013, India; Tel: +91 33-22260995; E-mail: samudrapb@gmail.com

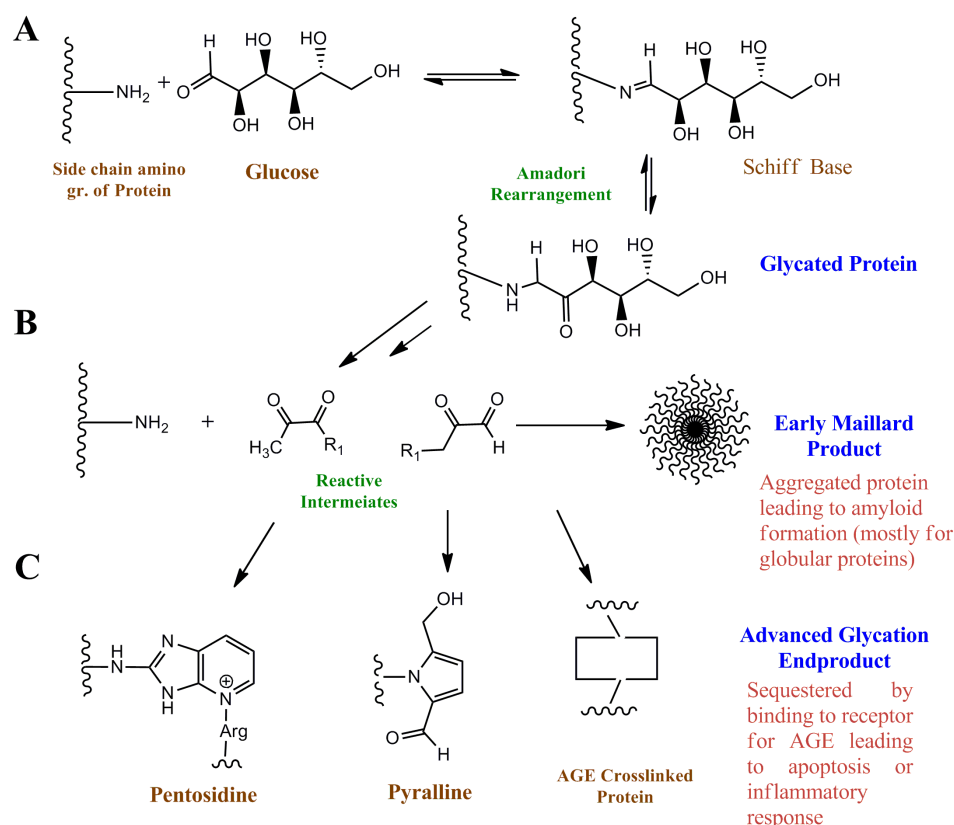


Fig. (1). A schematic outline of the progression of protein glycation: The entire process consists of three distinctively identifiable stages (A) The reaction is initiated by Schiff base formation of sugar with lysine/arginine residue of proteins (B) The reaction progresses through Amadori rearrangement of the Schiff base involving the formation of early Maillard Product; for some proteins, the early Maillard products eventually develop into Thio-T positive amyloids (C) The reaction ends with the formation of various terminally misfolded protein-sugar adducts including cross-linked adducts collectively known as Advanced Glycation End-products (AGEs). AGE molecules are sequestered by membrane-bound and soluble forms of specific receptors termed RAGE which may eventualize into elicitation of inflammatory response or apoptosis of the concerned cell.

nificantly increase the burden of AGEs leading to their deposition with corresponding AGE-mediated cross-linking of proteins (Fig. 1).

1.1. Diabetes and Neurodegenerative Disorders: Exploring Newer Frontiers of Glycation-induced Toxicity

Insulin resistance has long been associated with the development of various metabolic syndromes, impairment of cognitive function, and development of dementia [8]. Apart from metabolic complications arising from insulin resistance, enhanced production of amyloid Beta precursor protein under elevated glucose concentration has also been traced to be a key reason for the development of amyloidosis in diabetic patients [9, 10]. Also, there have been several lines of concrete evidences suggesting that Insulin resistance in brain cells augments the development of amyloid beta and tau pathologies implicated in Alzheimer's Disease [11]. A very recent observation in this respect has been the development of similar aggregates from glycated proteins at various extracellular locations which resemble amyloid plaques typical of neurodegenerative disorders [12]. This perspective article is based on the current advances in our understanding of glycation-associated amyloid formation and resultant cellular toxicity.

1.2. Primary and Secondary Sources of Glycation and its Management

As mentioned earlier, AGEs accumulate in the body as part of unavoidable normal metabolism; toxic effects are recognized only when they go beyond the critical level in circulation and tissue fluids. In addition, many food products also contain a substantial amount of AGE (chiefly in the form of Carboxymethyl Lysine, CML, or Methyl Glyoxal, MG). CMLs are already present naturally in raw foods from animal sources, and cooking especially involving roasting, boiling, grilling and frying accelerate the process of new AGE formation [13]. Recent studies on animal models have established that dietary AGEs (dAGE) constitute a substantial part of the total AGE content of the body [14]. Besides diet, tobacco smoking also leads to co-valent adduct formation in the low-density lipoproteins (LDL) of plasma, structural proteins of the vascular wall as well as the eye lens chaperone protein crystallin [15], and these adducts show striking resemblance with AGEs [16]. A high concentration of these adducts has been detected in smokers as well as in patients affected with periodontitis, in an inflammasome complex together with other inflammatory markers such as matrix metalloproteinases-9 (MMP-9), tumour necrosis fac-

tor-alpha (TNF- α) and nod-like receptor family pyrin domain-containing protein-3 (NLRP3) complex [17]. This is again strong evidence that AGE molecules are elicitors of oxidative stress and inflammatory response in the body [18]. The burden of AGEs can be significantly curtailed by the consumption of a Mediterranean diet including fruits, vegetables, legumes and sea-foods while minimising intake of animal fats and proteins including dairy products and processed foods as well as foods rich in sugar and salt with low nutrients [19]. Alongside reducing AGE load, sticking to this healthy regimen maintains body homeostasis and reduces susceptibility to other ailments such as Cardio-Vascular Disease (CVD), Chronic Kidney Disease (CKD), and many other life-threatening conditions [20].

2. GLYCATION-INDUCED AGGREGATION AND AMYLOID FORMATION IN PROTEINS

The most significant and vulnerable biomolecules susceptible to glycation are proteins. Although glycation occurs generously on side chains of arginine and lysine residues, N terminal amino groups of proteins and free thiol groups of cysteines are additional sites where the sugar adducts can also initiate. Glycated proteins slowly accumulate *in vivo* and can lead to several physiological maladies apart from diabetes including cardiovascular complications, gut microbiome-associated illnesses, liver or neurodegenerative diseases, cancer arteriosclerosis, renal failure, and neurological disorders [21]. Along with jeopardising the structure and function of proteins, AGE adducts also induce their cross-linking. A direct consequence of AGE-induced crosslinking is the formation of crosslinked Type IV collagen leading to vascular stiffness [22]. During the progression of the glycation reaction, the affected proteins adopt various misfolded and aggregated conformations depending on the native conformation of the protein as well as the glycating sugar. Several such aggregated forms have been shown to develop into unique amyloid-like plaques, a phenomenon reported by different independent groups over the last two decades [23-25] and extensively studied thereafter by the group of Ianuzzi and Sirangelo [26, 27]. However, this unique glycation-induced amyloid formation is not a universally observed phenomenon for all proteins; from reports obtained thus far, it seems that the pathway towards amyloidogenic transition is heavily biased for globular proteins like albumin [28], Hen Egg White Lysozyme [27], insulin [29] amylin [30] and many others. Understandably enough, glycation is more prominent on proteins with a higher number of solvent-accessible histidine and lysine residues. Additionally, solution conditions are also known to modulate the amyloidogenic transition pathway. Reducing conditions promote amyloid formation in glycated insulin whereas, under non-reducing environments, glycation hinders amyloidogenic transition [29]. Choice of sugar also is a major determinant of the extent of glycation, at least for *in vitro* glycated proteins. Whereas agents like Methyl Glyoxal and ribose has been shown to have the highest *in vitro* glycation efficiency, the reaction occurs rather slowly with other sugars such as glucose [31]. Interestingly enough, the effect of glycation on conventional amyloidogenic proteins is markedly different.

Glycation has been shown to significantly decrease the fibrillation kinetics of amyloid-beta peptides implicated in Alzheimer's disease [32-34]. Therefore, it has been almost an uphill task for scientists to understand and predict the glycation-induced amyloidogenic behaviour of certain proteins accounting for so many factors simultaneously. A representative list of the differential effects of glycation has been shown in Table 1.

2.1. Accounting for Proper Controls During *in vitro* Glycation Reactions

In vitro glycation requires incubation of the protein at 37°C for a week. Sustained thermal incubation for long periods is bound to inflict major or minor structural changes in the protein often leading to their aggregation [35, 36]. However, not many reports have systematically addressed the issue of keeping proper controls during the development of *in vitro* glycated protein models to discriminate between glycation-induced aggregation and thermal aggregation of proteins. A recent study in our laboratory involving *in vitro* ribosylated albumin from bovine serum has been able to shed some light on this crucial aspect in deciphering the structural changes associated with glycation. Using a combination of ANS binding and Dynamic Light Scattering, two widely used tools for studying the aggregation of proteins, it was shown that glycation actually hinders and delays hydrophobicity-driven thermal aggregation of proteins [28]. Thermally aggregated proteins (formed by incubation at 37°C and representing the control of glycation reaction) also showed insignificant Thioflavin-T binding suggesting that they were mechanistically different from glycation-induced amyloidogenic aggregation.

2.2. Glycation-induced Amyloids Arising out of Globular Proteins Often Lack Fibrillar Cross-beta Morphology

The glycation adducts bind Thioflavin T typical of amyloid plaques implicated in neurological disorders such as the beta-amyloid, tau, prions, *etc.* [27]. This striking resemblance of hyperglycemia-induced AGE-adducts with amyloid plaques led to the establishment of one of the several significant causes accounting for the strong clinical correlation between diabetes and neurological disorders. However, glycation adducts arising especially from globular proteins do not necessarily reflect all hallmark features of a typical amyloid plaque. A stage-by-stage biophysical characterisation of AGE adducts in our laboratory using ribosylated serum albumin as a model protein has indicated that attachment of ribose molecules results in the structural transition of the albumin from a predominantly alpha-helical form to the beta-pleated sheet like conformation with enhanced Thioflavin-T binding [28]. Parallely, the adducts also acquire enhanced thermostability. Peculiarly though, these amyloids did not show any Congo-red birefringence and therefore lacked the cross-beta fibrillar architecture. These unique Thio-T positive Congo-red negative amyloids formed out of glycation of globular proteins were termed globular amyloids according to their appearance under TEM [28, 37, 38]. However, as the reaction progresses, the glycated protein loses its

Table 1. Amyloids/amyloid like adducts formed by protein glycation and their unique structural features.

Protein	Glycating agent	Feature	References
Islet Amyloid Polypeptide	Derivatized CML	Conformational change from random coil to β -sheet fibrillar	[21]
Bovine Serum Albumin	Glucose-6-phosphate	Loss of globular structure, bind to both Thio-T and Congo-red	[27]
Bovine Serum Albumin	Ribose	Loss of alpha-helicity but retainment of globular structure, Thio-T positive but Congo red negative	[22, 24]
Camel Serum Albumin	Methyl glyoxal	Thio-T positive but no significant loss in secondary structure	[28]
Human insulin	Methyl Glyoxal	Thio-T positive showing characteristic fibril formation	[29]
Alpha crystallin	Fructose, Methyl Glyoxal	Significant alteration in secondary structure	[11]
Amyloid Beta peptide	Methyl Glyoxal	Fibrillation is significantly slower	[25]
Alpha synuclein	Ribose	Transformation into globules	[26]
Tau	Glucose	Changes aggregation propensity in different tau isoforms	[30]

amyloid-like behaviour as well as secondary structure and transforms into a terminally misfolded glycated protein aggregate, typically called AGE.

3. AGE-SPECIFIC RECEPTOR (RAGE) AS A CELLULAR DEFENCE MECHANISM

Since glycation occurs preferentially on lysine residues which are also the sites of protein ubiquitination, these misfolded aggregates are often recalcitrant to proteasomal degradation and therefore impose severe toxicity on cells through the generation of Reactive Oxygen Species [37, 38]. A proteome-wide identification of glycation sites from a breast cancer cell line revealed that most of the potential sites of glycation also coincided with ubiquitination and acetylation sites [39]. In order to prevent these toxic AGE adducts from jeopardising the cellular environment, cells have evolved a receptor-based response pathway to trap, sequester, and nullify the threat posed by AGEs, although sometimes at the cost of serious damage to the host in terms of heightened oxidative stress and inflammatory response.

Most of the cellular pathophysiological alterations leading to oxidative stress and subsequent inflammatory response have been linked to the initial recognition of the AGEs by specific cell surface receptors (RAGE), originally described as a 35 kDa AGE-binding protein belonging to the immunoglobulin superfamily [40]. Subsequently, the mitogen-activated protein kinases (MAPKs) such as extracellular signal-regulated kinase (ERK) and c-Jun N terminal kinase (JNK) were discovered to be the components of the AGE-RAGE signalling pathway [41]. Downstream effectors of this pathway are the transcription factors like nuclear factor-kappa B (NF- κ B) whose activation turns on the expression of genes implicated in oxidative stress and proinflammatory immune response leading to a host of pathophysiological maladies such as diabetic complications, Alzheimer disease, arthritis, myocardial infarction, renal failures, hypoxia and other peripheral vascular diseases. Under conditions of

heightened AGE accumulation, AGE-RAGE signalling also leads to apoptosis of the host cell in order to block uncontrolled inflammatory response [42]. The intensity of the signal transduction depends on the binding of AGEs to RAGE, as blocking RAGE with either an excess of soluble RAGE (s-RAGE) or with an anti-RAGE antibody prevents cellular activation [43]. The original hypothesis that the evolution of RAGE has occurred as a protective response of the body has been supported by several lines of evidence [44]. In fact, the binding of amyloids by RAGE has been shown to arrest its further aggregation [45]. Alongside, RAGE has also emerged as a potential therapeutic target for the treatment of a plethora of ailments where AGEs are implicated [46]. The involvement of the AGE-RAGE axis in numerous cell signalling pathways leading to diverse physiological effector responses has thus baffled scientists in deciphering its true role, whether as a protective response mediator, as a harbinger of cellular catastrophes, or simply as a biomarker for predicting the onset of diseases. The resemblance of many AGEs to amyloids, at least in their intermediate stages of progression has complicated the scenario; under the circumstances, in spite of a thrust of research to arrest the development of amyloids in prediabetic patients, it has not been possible for the scientific community to delink these two dreaded diseases.

CONCLUSION AND FUTURE IMPLICATIONS

Glycation-induced formation of amyloid plaques is a complex phenomenon dependent upon both the structure and sequence of the target protein as well as the type of sugar involved. Therefore, predicting the consequence or prognosis of a diabetic individual towards neuronal abnormalities and subsequently developing a therapeutic strategy for arresting the same has remained a coveted achievement for scientists and clinicians. Carboxy Methyl Lysine (CML) and Methyl Glyoxal (MG) have emerged as the gold standard for the clinical detection of AGE either by ELISA-based fluorescence or by Mass Spectrometry [47]. However, the mode of

structural transition induced by both CML and MG seems to be different for each of the cellular proteins if not unique. Additionally, exactly at which stage a sugar-protein adduct acquire RAGE recognition attributes also remains to be deciphered. Unless we acquire sufficient knowledge about the biophysical attributes of the glycated adducts during each and every stage of their progression, designing effective therapeutics to uncover and arrest the missing link will keep eluding us.

CONSENT FOR PUBLICATION

Not applicable.

FUNDING

Some studies reported in this article were funded by the University Grants Commission, Government of India. UGC-Major Research Project No. 43-69/2014 (SR) dated 23rd July, 2015.

CONFLICT OF INTEREST

The author(s) declare no conflict of interest, financial or otherwise.

ACKNOWLEDGEMENTS

Declared none.

REFERENCES

- [1] Rajmohan R, Reddy PH. Amyloid-beta and phosphorylated tau accumulations cause abnormalities at synapses of alzheimer's disease neurons. *J Alzheimers Dis* 2017; 57(4): 975-99. <http://dx.doi.org/10.3233/JAD-160612> PMID: 27567878
- [2] Min JO, Strohäker T, Jeong BC, Zweckstetter M, Lee SJ. Chicago sky blue 6B inhibits α -synuclein aggregation and propagation. *Mol Brain* 2022; 15(1): 27. <http://dx.doi.org/10.1186/s13041-022-00913-y> PMID: 35346306
- [3] Daldin M, Fodale V, Cariulo C, *et al.* Polyglutamine expansion affects huntingtin conformation in multiple Huntington's disease models. *Sci Rep* 2017; 7(1): 5070. <http://dx.doi.org/10.1038/s41598-017-05336-7> PMID: 28698602
- [4] Iannuzzi C, Irace G, Sirangelo I. Differential effects of glycation on protein aggregation and amyloid formation. *Front Mol Biosci* 2014; 1: 9. <http://dx.doi.org/10.3389/fmolb.2014.00009> PMID: 25988150
- [5] Rabbani N, Thornalley PJ. Protein glycation – biomarkers of metabolic dysfunction and early-stage decline in health in the era of precision medicine. *Redox Biol* 2021; 42: 101920. <http://dx.doi.org/10.1016/j.redox.2021.101920> PMID: 33707127
- [6] Gkogkolou P, Böhm M. Advanced glycation end products. *Dermatoendocrinol* 2012; 4(3): 259-70. <http://dx.doi.org/10.4161/derm.22028> PMID: 23467327
- [7] Jud P, Sourij H. Therapeutic options to reduce advanced glycation end products in patients with diabetes mellitus: A review. *Diabetes Res Clin Pract* 2019; 148: 54-63. <http://dx.doi.org/10.1016/j.diabres.2018.11.016> PMID: 30500546
- [8] Lee HJ, Seo HI, Cha HY, Yang YJ, Kwon SH, Yang SJ. Diabetes and Alzheimer's disease: Mechanisms and nutritional aspects. *Clin Nutr Res* 2018; 7(4): 229-40. <http://dx.doi.org/10.7762/cnr.2018.7.4.229> PMID: 30406052
- [9] Díez R, Madero M, Gamba G, Soriano J, Soto V, Renal AA. Renal AA amyloidosis in patients with type 2 diabetes mellitus. *Nephron Extra* 2014; 4(2): 119-26. <http://dx.doi.org/10.1159/000363625> PMID: 25337080
- [10] Chao AC, Lee TC, Juo SHH, Yang DI. Hyperglycemia increases the production of amyloid beta-peptide leading to decreased endothelial tight junction. *CNS Neurosci Ther* 2016; 22(4): 291-7. <http://dx.doi.org/10.1111/cns.12503> PMID: 26842741
- [11] de la Monte SM. Contributions of brain insulin resistance and deficiency in amyloid-related neurodegeneration in Alzheimer's disease. *Drugs* 2012; 72(1): 49-66. <http://dx.doi.org/10.2165/11597760-000000000-00000> PMID: 22191795
- [12] Ko SY, Ko HA, Chu KH, *et al.* The possible mechanism of advanced glycation end products (AGEs) for alzheimer's disease. *PLoS One* 2015; 10(11): e0143345. <http://dx.doi.org/10.1371/journal.pone.0143345> PMID: 26587989
- [13] Uribarri J, Woodruff S, Goodman S, *et al.* Advanced glycation end products in foods and a practical guide to their reduction in the diet. *J Am Diet Assoc* 2010; 110(6): 911-6. <http://dx.doi.org/10.1016/j.jada.2010.03.018>
- [14] Goldberg T, Cai W, Peppia M, *et al.* Advanced glycoxidation end products in commonly consumed foods. *J Am Diet Assoc* 2004; 104(8): 1287-91. <http://dx.doi.org/10.1016/j.jada.2004.05.214> PMID: 15281050
- [15] Kumar PA, Kumar MS, Reddy GB. Effect of glycation on α -crystallin structure and chaperone-like function. *Biochem J* 2007; 408(2): 251-8. <http://dx.doi.org/10.1042/BJ20070989> PMID: 17696877
- [16] Rungratanawanich W, Qu Y, Wang X, Essa MM, Song BJ. Advanced glycation end products (AGEs) and other adducts in aging-related diseases and alcohol-mediated tissue injury. *Exp Mol Med* 2021; 53(2): 168-88. <http://dx.doi.org/10.1038/s12276-021-00561-7> PMID: 33568752
- [17] Ali D, AlAhmari F, Mikami T, Baskaradoss JK. Increased expression of advanced glycation endproducts in the gingival crevicular fluid compromises periodontal status in cigarette-smokers and waterpipe users. *BMC Oral Health* 2022; 22(1): 206. <http://dx.doi.org/10.1186/s12903-022-02240-z> PMID: 35614406
- [18] van der Lugt T, Weseler A, Gebbink W, Vrolijk M, Opperhuizen A, Bast A. Dietary advanced glycation endproducts induce an inflammatory response in human macrophages *in vitro*. *Nutrients* 2018; 10(12): 1868. <http://dx.doi.org/10.3390/nu10121868> PMID: 30513810
- [19] Gutierrez-Mariscal FM, Cardelo MP, la Cruz S, *et al.* Reduction in circulating advanced glycation end products by mediterranean diet is associated with increased likelihood of type 2 diabetes remission in patients with coronary heart disease: From the cordioprev study. *Mol Nutr Food Res* 2021; 65(1): 1901290. <http://dx.doi.org/10.1002/mnfr.201901290> PMID: 32529753
- [20] Fotheringham AK, Gallo LA, Borg DJ, Forbes JM. Advanced glycation end products (ages) and chronic kidney disease: Does the modern diet AGE the kidney? *Nutrients* 2022; 14(13): 2675. <http://dx.doi.org/10.3390/nu14132675> PMID: 35807857
- [21] Kuzan A. Toxicity of advanced glycation end products (Review). *Biomed Rep* 2021; 14(5): 46. <http://dx.doi.org/10.3892/br.2021.1422> PMID: 33786175
- [22] McKay TB, Priyadarsini S, Karamichos D. Mechanisms of collagen crosslinking in diabetes and keratoconus. *Cells* 2019; 8(10): 1239. <http://dx.doi.org/10.3390/cells8101239> PMID: 31614631
- [23] Bouma B, Kroon-Batenburg LMJ, Wu YP, *et al.* Glycation induces formation of amyloid cross-beta structure in albumin. *J Biol Chem* 2003; 278(43): 41810-9. <http://dx.doi.org/10.1074/jbc.M303925200> PMID: 12909637
- [24] Miranda HV, Outeiro TF. The sour side of neurodegenerative disorders: The effects of protein glycation. *J Pathol* 2010; 221(1): 13-25. <http://dx.doi.org/10.1002/path.2682> PMID: 20186922
- [25] Hsu YH, Chen YW, Wu MH, Tu LH. Protein glycation by glyoxal promotes amyloid formation by islet amyloid polypeptide. *Biophys J* 2019; 116(12): 2304-13. <http://dx.doi.org/10.1016/j.bpj.2019.05.013> PMID: 31155148
- [26] Iannuzzi C, Borriello M, Irace G, Cammarota M, Di Maro A, Sirangelo I. Vanillin affects amyloid aggregation and non-enzymatic glycation in human insulin. *Sci Rep* 2017; 7(1): 15086. <http://dx.doi.org/10.1038/s41598-017-15503-5> PMID: 29118444

- [27] Sirangelo I, Iannuzzi C. Understanding the role of protein glycation in the amyloid aggregation process. *Int J Mol Sci* 2021; 22(12): 6609.
<http://dx.doi.org/10.3390/ijms22126609> PMID: 34205510
- [28] Das A, Basak P, Pramanik A, *et al.* Ribosylation induced structural changes in bovine serum albumin: Understanding high dietary sugar induced protein aggregation and amyloid formation. *Heliyon* 2020; 6(9): e05053.
<http://dx.doi.org/10.1016/j.heliyon.2020.e05053> PMID: 33015393
- [29] Alavi P, Yousefi R, Amirghofran S, Karbalaee-Heidari HR, Moosavi-Movahedi AA. Structural analysis and aggregation propensity of reduced and nonreduced glycosylated insulin adducts. *Appl Biochem Biotechnol* 2013; 170(3): 623-38.
<http://dx.doi.org/10.1007/s12010-013-0207-1> PMID: 23584594
- [30] Milordini G, Zacco E, Percival M, *et al.* The role of glycation on the aggregation properties of IAPP. *Front Mol Biosci* 2020; 7: 104.
<http://dx.doi.org/10.3389/fmolb.2020.00104> PMID: 32582762
- [31] Muraoka MY, Justino AB, Caixeta DC, Queiroz JS, Sabino-Silva R, Salmen Espindola F. Fructose and methylglyoxal-induced glycation alters structural and functional properties of salivary proteins, albumin and lysozyme. *PLoS One* 2022; 17(1): e0262369.
<http://dx.doi.org/10.1371/journal.pone.0262369> PMID: 35061788
- [32] Emendato A, Milordini G, Zacco E, *et al.* Glycation affects fibril formation of A β peptides. *J Biol Chem* 2018; 293(34): 13100-11.
<http://dx.doi.org/10.1074/jbc.RA118.002275> PMID: 29959224
- [33] Khan MS, Dwivedi S, Priyadarshini M, *et al.* Ribosylation of bovine serum albumin induces ROS accumulation and cell death in cancer line (MCF-7). *Eur Biophys J* 2013; 42(11-12): 811-8.
<http://dx.doi.org/10.1007/s00249-013-0929-6> PMID: 24218080
- [34] Liu K, Liu Y, Li L, *et al.* Glycation alter the process of Tau phosphorylation to change Tau isoforms aggregation property. *Biochim Biophys Acta Mol Basis Dis* 2016; 1862(2): 192-201.
<http://dx.doi.org/10.1016/j.bbadis.2015.12.002> PMID: 26655600
- [35] Rondeau P, Armenta S, Caillens H, Chesne S, Bourdon E. Assessment of temperature effects on β -aggregation of native and glycosylated albumin by FTIR spectroscopy and PAGE: Relations between structural changes and antioxidant properties. *Arch Biochem Biophys* 2007; 460(1): 141-50.
<http://dx.doi.org/10.1016/j.abb.2007.01.014> PMID: 17320036
- [36] Hanczyc P, Słota P, Radzewicz C, Fita P. Two-photon excited laser for detection of amyloids in brain tissue. *J Photochem Photobiol B* 2022; 228: 112392.
<http://dx.doi.org/10.1016/j.jphotobiol.2022.112392> PMID: 35086026
- [37] Wei Y, Chen L, Chen J, Ge L, He RQ. Rapid glycation with D-ribose induces globular amyloid-like aggregations of BSA with high cytotoxicity to SH-SY5Y cells. *BMC Cell Biol* 2009; 10(1): 10.
<http://dx.doi.org/10.1186/1471-2121-10-10> PMID: 19216769
- [38] Chen L, Wei Y, Wang X, He R. Ribosylation rapidly induces alpha-synuclein to form highly cytotoxic molten globules of advanced glycation end products. *PLoS One* 2010; 5(2): e9052.
<http://dx.doi.org/10.1371/journal.pone.0009052> PMID: 20140223
- [39] Sun F, Suttapitugsakul S, Xiao H, Wu R. Comprehensive analysis of protein glycation reveals its potential impacts on protein degradation and gene expression in human cells. *J Am Soc Mass Spectrom* 2019; 30(12): 2480-90.
<http://dx.doi.org/10.1007/s13361-019-02197-4> PMID: 31073893
- [40] Buckley ST, Ehrhardt C. The receptor for advanced glycation end products (RAGE) and the lung. *J Biomed Biotechnol* 2010; 2010: 1-11.
<http://dx.doi.org/10.1155/2010/917108> PMID: 20145712
- [41] Ramasamy R, Yan SF, Herold K, Clynes R, Schmidt AM. Receptor for advanced glycation end products: fundamental roles in the inflammatory response: winding the way to the pathogenesis of endothelial dysfunction and atherosclerosis. *Ann N Y Acad Sci* 2008; 1126(1): 7-13.
<http://dx.doi.org/10.1196/annals.1433.056> PMID: 18448789
- [42] Mahali S, Raviprakash N, Raghavendra PB, Manna SK. Advanced glycation end products (AGEs) induce apoptosis via a novel pathway: involvement of Ca²⁺ mediated by interleukin-8 protein. *J Biol Chem* 2011; 286(40): 34903-13.
<http://dx.doi.org/10.1074/jbc.M111.279190> PMID: 21862577
- [43] Yan SF, Ramasamy R, Schmidt AM. Soluble RAGE: Therapy and biomarker in unraveling the RAGE axis in chronic disease and aging. *Biochem Pharmacol* 2010; 79(10): 1379-86.
<http://dx.doi.org/10.1016/j.bcp.2010.01.013> PMID: 20096667
- [44] Kang R, Tang D, Schapiro NE, *et al.* The Receptor For Advanced Glycation End Products (RAGE) sustains autophagy and limits apoptosis, promoting pancreatic tumor cell survival. *Cell Death Differ* 2010; 17(4): 666-76.
<http://dx.doi.org/10.1038/cdd.2009.149> PMID: 19834494
- [45] Chaney MO, Stine WB, Kokjohn TA, *et al.* RAGE and amyloid beta interactions: Atomic force microscopy and molecular modeling. *Biochim Biophys Acta Mol Basis Dis* 2005; 1741(1-2): 199-205.
<http://dx.doi.org/10.1016/j.bbadis.2005.03.014> PMID: 15882940
- [46] Guo WA, Knight PR, Raghavendran K. The receptor for advanced glycation end products and acute lung injury/acute respiratory distress syndrome. *Intensive Care Med* 2012; 38(10): 1588-98.
<http://dx.doi.org/10.1007/s00134-012-2624-y> PMID: 22777515
- [47] Ashraf JM, Ahmad S, Choi I, *et al.* Recent advances in detection of AGEs: Immunochemical, bioanalytical and biochemical approaches. *IUBMB Life* 2015; 67(12): 897-913.
<http://dx.doi.org/10.1002/iub.1450> PMID: 26597014

DISCLAIMER: The above article has been published, as is, ahead-of-print, to provide early visibility but is not the final version. Major publication processes like copyediting, proofing, typesetting and further review are still to be done and may lead to changes in the final published version, if it is eventually published. All legal disclaimers that apply to the final published article also apply to this ahead-of-print version.

Antibiotics; the Miracle Drugs, also a Predisposing Factor of Obesity

Tuhina Nasrin Ali¹, Malay Mitra² and Avishek Ghosh^{3*}

¹Department of Clinical Nutrition & Dietetics, KPC Medical College (Kolkata) India.

²Department of Food & Nutrition, Netaji Nagar College for Women (Kolkata) India.

³Department of Microbiology, Maulana Azad College (Kolkata) India.

(Corresponding author: Avishek Ghosh*)

(Received: 08 February 2023; Revised: 13 April 2023; Accepted: 18 April 2023; Published: 20 May 2023)

(Published by Research Trend)

ABSTRACT: We live in the era of antibiotics. This particular group of medicines has remarkable efficiency to treat infections with reduced morbidity and mortality and thus conquer the title of miracle drugs. But their enormous use without proper guidelines is a precursor of antibiotic resistance as well as is a raising concern of long-term metabolic changes in our body. In this review we emphasis on the impact of dysbiosis resulting from antibiotic exposure on body weight gain. Evidences tell us early life repeated exposures are unlikely to be a predisposing factor of offspring obesity. Pre-natal antibiotic use is also a contributory to this. Sex-specific effect is there: boys are more vulnerable compare to girls. Although the mechanisms underlining the association remain unexplained, the little we found out is this action is due to the byproducts of microbial fermentation, gut hormone alteration, metabolic entoxemia and fasting induced adipocyte factor (Fiaf). Since randomized control trial (RCT) deals with the safety of the participants, it would be ethical concern in this regard and consumption of antibiotic doesn't show immediate effect on body mass index (BMI) while it usually increases the body fat at the later stages of life, additional well-designed longitudinal prospective cohort studies have been undertaken. More similar type of researches involving human regarding this issue necessitate for better explanation and ultimately to control the global epidemic obesity.

Keywords: Antibiotics, Dysbiosis, Obesity, BMI, SCFA, Bacterial components.

INTRODUCTION

The penicillin introduction by Alexander Fleming began the era of antibiotics, a compound produced by a microorganism possessing growth inhibiting or killing ability against other microbes and since then these have been recognized as the “miracle drugs” in the field of medical science. Right from invention they have been successfully used for treating different infections and to reduce morbidity and mortality (Rayanoothala *et al.*, 2021; Tan and Tatsumura 2015; Zaffiri *et al.*, 2012). Their remarkable effectiveness and easy availability make them famous worldwide but since their introduction, undoubtedly, they have been consumed freely and most of the time when they are not necessary (Del Fiol *et al.*, 2018). So what happens usually, the innumerable use is followed by the dark side of the so called ‘miracle drugs’ (Shekhar and Petersen 2020). The bacterial communities are colonized in the human body, mainly in the GI tract plays an important role in metabolism and immunity of the host (Aversa *et al.*, 2021). Antibiotics target these microbiota, decrease their amount significantly even in some cases they completely remove specific bacterial community (Angelakis *et al.*, 2014) and hamper the gut-microbiota homeostasis (Shekhar and Petersen 2020). It has been hypothesized that this imbalance in gut microbiota, also known as dysbiosis is linked to overweight or obesity Ali *et al.*,

by different mechanisms especially due to the exposure of antibiotics at early stages of life (Leong *et al.*, 2018; Sejersen *et al.*, 2019).

The term ‘overweight’ defined by WHO as BMI ≥ 25 kg/m² and ‘obesity’ as ≥ 30 kg/m², stand as the leading public health problem in current scenario (Vallianou *et al.*, n.d.). Research evidences have shown the relationship between the abuse of antibiotics and the development epidemic obesity parallelly, during the last few decades. Now the epidemic has been transformed into a pandemic very fast (Del Fiol *et al.*, 2018). A commonly followed and most effective treatment procedure for obese individuals is the gastric bypass surgery. The change in the gut microbial composition after gastric bypass surgery has also been indicated to be connected to obesity. The high population of the family Prevotellaceae prior to surgery in obese individuals could be observed and following the surgery number of Prevotellaceae was reduced in lean subjects along with increase of the members of family Enterobacteriaceae and genus *Akkermansia* strengthening the fact that change in gut microbiota composition has fair connection with gain and loss of weight (Zhang *et al.*, 2009). Since antibiotic administration alters the gut microbiota composition, this review will emphasise on the effect of antibiotic consumption on body weight, intestinal gut microbiota,

and how dysbiosis occurs due to antibiotic exposure related to obesity.

Antibiotic use in the modern era. Unnecessary worldwide prescription and consumption of antibiotics have been reported in recent times by numerous studies- it may be considered as abuse these chemotherapeutic agents. One study demonstrate that there is an increase of 46% of global antibiotic consumption which rate from 2000 to 2018 (9.8 defined daily doses (DDD)/1000 population/day at 2000, 14.3 DDD/1000 population/day) in low income and middle income countries (Browne *et al.*, 2021). According to The State of World's Antibiotic report in 2021, Global Antibiotic Consumption from 2000 to 2015 has been increased by 65% and if there is no alteration in this trend, it will be increased by 200% in the next 15 years. They also found that percentage change in per capita antibiotic use is 35.12% from 2010 to 2020 globally. In India, per capita antibiotic use is 5.74 DDD in 2020, whereas it was 4.40 DDD in 2010 (*The State of the World's Antibiotics 2021 A Global Analysis of Antimicrobial Resistance and Its Drivers*, n.d.). Children with same infection take different rates of antibiotics irrespective of their age, co-morbidities and socioeconomic factors. The overuse of antibiotics has been associated with antimicrobial resistance. World Health Organization (WHO) has identified this problem as "one of three greatest threat to human health" (Vangay *et al.*, 2015).

Development of gut microbiome. Human gut is crowded with heterogeneous microorganisms including bacteria, viruses, archaea, protozoa etc. (Leong *et al.*, 2018). The initiation of introduction of microbes in human gut occurs during the birth i.e. at the time of delivery. The mode of delivery is the most predisposing factor for the development of gut microbiome as most of the microorganisms come from vagina, fecal sources and skin microbiome, along with the other factors like prematurity, infant diet (breast fed, formula fed), hygiene etc also contribute to the gut microbiome development (Vangay *et al.*, 2015). The initial pH of stomach ranges between 6-8 before birth and within the first hours of delivery decreases to ~1.5-2.5 but due to the buffering capabilities of milk it comes back to 7-7.6. This higher pH may support transition of ingested bacteria those colonized in the lower GI tract (Vangay *et al.*, 2015). Development of gut microbiome follows Darwin Dynamics where facultative aerobes colonize in the gut first reducing oxygen level in gut and enhancing the growth of strict anaerobes (Bezirtzoglou, 1997). Due to the introduction of breast milk as the first food for the infant, Proteobacteria and Firmicutes initially colonise in gut, followed by Actinobacteria (Sela *et al.*, 2008). There is a decline of *Proteobacteria* and Actinobacteria and increase in the count of Bacteroidetes by 6 months (Koenig *et al.*, 2011; Vaishampayan *et al.*, 2010). At the age of 1 year, Bacteroidetes and Firmicutes dominate infant gut. This dramatic change in the composition in gut microbiome continues throughout the first two years of life (Yatsuneneko *et al.*, 2012). Firmicutes, Bacteroidetes, Proteobacteria,

Fusobacteria, Spirochaetae and Verrucomicrobia are the dominating bacteria in the adult human gut (Chan *et al.*, 2013).

Effect of antibiotics on gut microbiome. The word antibiotic means against living organisms. These are the drugs used to treat infections either killing the bacteria or by inhibiting their growth and reproduction. So, it is obvious that they have an impact on the living things in the gut. Identification of the composition of this microbiome employs the modern genomic techniques since microbial culture technique possesses disadvantages like they can only identify a few species of bacteria in the intestinal gut. 16S rDNA and metagenomic sequencing are the modern techniques to know the composition and diversity of gut microbiome (Arslan, 2014). It is a culture independent analysis suited for viable but non-cultivable microorganisms and provides in-depth, extensive information of microbial community (Jo *et al.*, 2016).

Bacteroidetes and Firmicutes constitute approximately 90% of the total microbial content of gut (Arslan, 2014). Administration of Doxycycline and Hydroxychloroquine in endocarditis patients resulted in a decline in the concentration of Bacteroidetes ($p=0.002$) and Firmicutes ($p=0.01$) and also in total bacterial count. This phylum level gut alteration could play a key role in the weight gain (Angelakis *et al.*, 2014). Another study showed that children less than 3 years of age exposed with multiple antibiotic exposure courses causing less microbial diversity than the unexposed children (Yassour *et al.*, 2016). Antibiotic type, consumer's age, route of administration can influence gut microbiome. Along with these the other contributory factors are diet, consumption of other medicines, lifestyles, probiotic consumptions etc. (Leong *et al.*, 2018).

Obesity is a global epidemic. Obesity, the global epidemic is a complex metabolic disorder resulting from the energy imbalance which can lead to excess accumulation of fat in our body. This is a risk factor for a number of significant co morbidities such as type 2 diabetes, hypertension, CVDs *etc.* at later stages of life. Most of the people live in those countries where obesity kills more people than underweight. Irrespective of socio economic status, the prevalence of overweight has increased dramatically over the past few decades. Since 1975 the worldwide obesity has nearly tripled (Goyal and Julka 2014; Huang *et al.*, 2010; Thompson-McCormick *et al.*, 2010). Over 340 million children and adolescents aged 5-19 were overweight or obese in 2016 globally (World Health Organisation). In India more than 135 million people were affected by obesity (Ahirwar and Mondal 2019). Since 2006, genome wide association studies have found 50 genes correlated with obesity. The thrifty gene hypothesis or Gianfranco's hypothesis was proposed by geneticist James V. Neel and said that in order to survive the famine we have procured efficient food and evolved genes for fat deposition. Rarely, obesity transpires in families according to an inheritance pattern due to change in a single gene. Generally, the implicated gene is MC4R,

which encrypt the melanocortin 4 receptor. MC4R bound by alpha-melanocyte stimulating hormone that stimulates appetite (Walley *et al.*, 2009). Although genetics play an important role, obesity epidemic does not have only genetic basis; lifestyle modifications during the last century has created an obesogenic environment that influence the genetic factor (Herrera and Lindgren 2010). Hence it is a metabolic disorder and it is very much associated with diet (Pitsavos *et al.*, 2006).

Effect of microbiome on body weight. Gut microbiome has an effect on the physiological status of the host as it can influence the metabolism of the hosts (Arslan, 2014; Leong *et al.*, 2018). Low level of Bacteroidetes and high level of Firmicutes with reduced bacterial diversity in human intestine is associated with obesity (Arslan, 2014). Numerous randomized, double blinded placebo control studies were conducted at different parts of the world (Canada, Russia, Japan) on adult person who were overweight or obese or having metabolic syndrome. Results indicated that, when adults' diet supplemented with different species of probiotics, there had been a decline of body weight and fat mass (Sanchez *et al.*, 2014; Sharafedinov *et al.*, 2013; Takahashi *et al.*, 2016). Similar kinds of findings were also found in the children. Nicolucci *et al.* (2017) treated overweight and obese children with oligofructose enriched inulin and after 16 weeks there was a reduction in body weight Z-Score (-3.10%) and body fat percentage (-2.40%) (Nicolucci *et al.*, 2017). Biofidobacteria and members of *Lactobacillus* ssp. are

found to be major candidates for managing the body weight and obesity in both human and experimental models. As a medication strategy use of *Lactobacillus* ssp. has been satisfactory owing to the fact that administration of it led to prolonged satiety and satiation including less fat deposition and food intake (Ameho and Christina 2021).

Antibiotic exposure can cause obesity. Animal and human studies provide supporting evidences that antibiotic use is associated with obesity though in this review we only focus on the human researches. Several epidemiological studies demonstrate that the use of antibiotics resulting in weight gain. Most of the studies done in this regards were either prospective or retrospective cohort and some were randomized control trials. Study findings indicate that the increase in BMI is more in boys and early life exposure has greater effect. Repeated exposure and broader spectrum of antibiotics are responsible for enhancing the BMI too. Undernourished children treated with Aureomycin shows significant difference in weight gain in the treated group with placebo group. Even prenatal antibiotic use also increases risk of obesity in their children (Table 1). This phenomenon is found in case of adults too, both in men and women. Ranitide and clarithromycin intake twice a day for 6 months increase the mean BMI of them. Patients of endocarditis, pulmonary diseases treated with different antibiotics (Vancomycin, Azithromycin, Doxycycline, Hydroxychloroquine etc.) put extra weight during the treatment (Table 2).

Table 1: Evidence showing the relation between early life antibiotic exposures and obesity.

Study	Studied subjects	Sample size	Study design	Exposure & Duration	Follow up	Outcomes	Remarks
(Macdougall, 1957) Africa	Undernourished African children (avg. Age 2 years)	n=72 38 received treatment, 34 placebo	Randomized Control Trial	Low dose of Aureomycin 50mg	2-7 weeks	Wight gain shows with highly significant differences Aureomycin treated- 45.3gm/day Placebo treated-14.1gm/day	Yes
Aversa <i>et al.</i> (Aversa <i>et al.</i> , 2021) US	Children	n=14572 7026 girls, 7546 boys	Prospective cohort	Antibiotic exposure (< 2 years)	14 years	Overweight (12873 subjects, 4856 events, HR 1.22, 95% CI, p<0.001) Obesity (13649 subjects, 2567 events, HR 1.20, 95% CI, p<0.001)	Yes
Kenyon <i>et al.</i> (Kenyon <i>et al.</i> , 2020)UK, USA	Children from USA and Europe		Ecological study	Macrolides and total antibiotics consumption	5 years	Positively associated with obesity Europe- Coef 0.03, SE 0.005, p<0.001 USA- Coef 0.003, Se 0.0006, p<0.001	Yes
(Sejersens <i>et al.</i> , 2019) Denmark	Mother-child cohort	n=700	Prospective cohort	Antibiotic exposure < 1 year	6 years	No association with BMI Z score -0.06 (95% CI: 0.17:0.06) No sex differences (p=0.48)	No
(Stark <i>et al.</i> , 2019) US	Children	n=241502	Cohort	Antibiotic exposure (in first 2 years of life)	7 years	Association with obesity (HR 1.26, 95% CI) Regardless to antibiotic class and strengthen with each class	Yes
(Zhang <i>et al.</i> , 2019) North Carolina, US	Infants	n=454	Prospective cohort	Prenatal antibiotic exposure by their mother	12 months	2 nd trimester exposure associated with higher infant WFL-z and skin fold thickness 0.21 (95% CI 0.02, 0.41) higher WFL-z-at 12 months	Yes

						0.28(95% CI 0.02,0.55) higher WFL-z-second trimester exposure	
(Block <i>et al.</i> , 2018)	Children <72 months of age in 35 health care institutions	n=362550	Cohort	>=1 antibiotic prescription (before 24 months)	6 years	28% of study subjects develop overweight or obesity Body weight slightly increase (mean BMI Z-score 0.40[SD1.19])	Yes
(Cassidy- Bushrow <i>et al.</i> , 2018) US	Pregnant Women	n=303	Cohort	Antibiotic use (during pregnancy)	2 years	Prenatal antibiotic use associated with BMI Higher mean BMI Z-score 0.20+-0.10(p=0.046) 1 st and 2 nd trimester exposure were more strongly associated	Yes
(Ville <i>et al.</i> , 2017) USA	Latino children	n=97	Prospective cohort	Antibiotic use (infancy)	2 years	Weight gain (OR 6.42, 95% CI) Obesity at the age 2 years (OR 6.15, 95% CI)	Yes
(Poulsen <i>et al.</i> , 2017) Pennsylvania	Mothers and singleton children	n=8793	Cohort	Prenatal antibiotic use Antibiotic use of children (first 3 years)	6 years	Significantly associated with higher BMIZ in children Prenatal antibiotic use->=3 antibiotic order β [CI] (1 order:0.027, 2 order:0.034, >=3 order:0.117; p=0.006) 1 st year antibiotic exposure- >=2 antibiotic order β [CI] (1 order: 0.021, 2 order:0.088, >=3 order: 0.104; p<0.001) 2 nd or 3 rd year antibiotic use- >=6 antibiotic order β [CI] (1 order: 0.015, 2-3 order: 0.053, 4-5 order:0.054, >=6 order: 0.123; p=0.003)	Yes
(Scott <i>et al.</i> , 2016) UK	Children of the health improvement network	n=21714	Retrospective cohort	Antibiotic exposure	4 years	\uparrow risk of obesity at 4 years (OR=1.21; 95% CI, 1.07- 1.38) \uparrow odd ratios with repeated exposures For 1-2 prescriptions (OR=1.07, 95% CI, 0.91- 1.23) For 3-5 prescriptions (OR=1.41, 95% CI, 1.20- 1.65) For >=6 prescriptions (OR=1.47, 95% CI, 1.19- 1.82)	Yes
(Li <i>et al.</i> , 2017) California, USA	Infants in Kaiser permanent north California (born between 01.01.1997- 31.03.2013)	n=260556	Retrospective cohort	Antibiotic use in infections	18 years	Infant with untreated infections antibiotic use not increase risk of obesity Infections without antibiotic use associated with obesity compared with controls without infections (OR=1.25, 95% CI) Neither broad spectrum nor narrow spectrum antibiotics associated with obesity	No
(Gerber <i>et al.</i> , n.d.) USA	Children with birth weight >=2000g	n=38614 (38522 singleton, 92 twins)	Retrospective cohort	Systematic antibiotic use (first 6 months)	7 years	Exposure not significantly associated with weight change Singleton children (0.7%, 95% CI, P=0.07) Twins (-0.09kg, 95% CI, P=0.30)	No
(Mbakwa <i>et al.</i> , 2016) Netherland	Children	n=979	Prospective cohort	Antibiotic exposure	10 years	One course antibiotic exposure \uparrow weight (adj β 0.54, 95% CI) \uparrow height (adj β 0.23, 95% CI) Later life exposure not	Yes/No

						associated Specific antibiotic use not associated	
(Schwartz <i>et al.</i> , 2016) USA	Children aged 3-18 years	n=163820	Retrospective cohort	Antibiotic exposure	11 years	Short time BMI ↑ (p<0.001)	Yes
(Edmonson and Eickhoff 2017) USA	Children with vesicoureteral reflux (2-71 months with a median age 12 months)	n=607 antibiotic treated group=302; placebo=305	Randomized control trial	Trimethoprim-sulfamethoxazole-1 tab daily	2 years	No significant difference in weight gain between these two groups (change in weight for age Z-score SD +0.14[0.83]- in treated group; SD + 0.18[0.85]- in the placebo group)	No
(Saari <i>et al.</i> , 2015) Finland	Boys and girls of first 24 months	n=12062	Prospective cohort	Antibiotic treatment		Exposed children heavier than unexposed BMI-for-Age Z Score Boys 0.13 SD, 95% CI, 0.07-0.19, p<0.001 Girls 0.07 SD, 95% CI, 0.01-0.13, p<0.05 Effect more pronounced after exposure to macrolides before 6 months of age Boys 0.28SD Girls 0.23SD >1 exposure Boys 0.20SD Girls 0.13SD	Yes
(Mueller <i>et al.</i> , 2015) USA	Mother child dyads	n=436	Prospective cohort	Prenatal antibiotic use	7 years	85% higher risk of obesity with antibiotic exposure during 2 nd & 3 rd trimester ↑ BMI Z Score, waist circumference % of body fat (p<0.05)	Yes
(Mor <i>et al.</i> , 2015) Denmark	School children	n=3250	Prospective cohort	Prenatal antibiotic exposure	11 years	Exposure associated with overweight (1.26, 95% CI) Obesity (1.29, 95% CI) Among girls (1.16, 95% CI)-for overweight (1.27, 95% CI)-for obesity Among boys (1.37, 95% CI)-for overweight (1.29, 95% CI)-for obesity	Yes
(Bailey <i>et al.</i> , 2014) Philadelphia, Pennsylvania USA	0-59 months children	n=64580	Prospective cohort	Antibiotic exposure (during 0-23 months)	5 years	Cumulative exposure to antibiotics associated with obesity (RR 1.11, 95% CI)>=4 episodes Effect stronger for broad spectrum of antibiotics (RR 1.16, 95% CI) Early exposure 0-5m (RR 1.11, 95% CI), 6-11m (RR 1.09, 95% CI)	Yes
(Azad <i>et al.</i> , 2014) Canada	Children from Canadian longitudinal birth cohort	n=1047 (at the age 9, n=616; at the age 12, n=431)	Prospective cohort	Antibiotic exposure (1 st year of life)	12 years	Overweight later in childhood (P=0.002) Association persisted more in boys At the age 12-Boys (OR=5.35, 95% CI); Girls (OR=1.13, 95% CI) At the age 9-Boys (OR=2.19, 95% CI); Girls (OR=1.20, 95% CI)	Yes
(Murphy <i>et al.</i> , 2014) International	Children of 38 centers of 18 countries	n=74946	Cross-sectional	Antibiotic-Paracetamol (first 12 months of life)	8 years	↑ BMI in boys (+0.107 kg m ² , P<0.0001) No association in girls (-0.008 kg m ² , P=0.75)	Yes/No
(Trasande <i>et al.</i> , 2013) UK	Children birth weight >=2.5kg in avon	n=11532	Prospective cohort	Exposure of antibiotics at three different ages (<6months, 6-14months, 15-	7 years	↑Body Mass exposure of an, tibiotic<6months (↑ weight for length Z Score +0.105 s.d unit, P=<0.001 at 10 months	Yes/No

				23months)		+0.083 s.d unit, P=0.001 at 20 months BMI Z Score +0.067 s.d units, P=0.009 at 38 months) No association exposure of antibiotic at 6-14 months Positive association exposure of antibiotics at 15-23months (BMI Z Score +0.049 s.d units, P=0.050 at age 7 years)	
(Saiman <i>et al.</i> , 2003)	Cystic fibrosis patients >=6 years (87 active group, 98 placebo group)	n=185	Randomized control trial	Azithromycin 3 days in a week (for 168 days)	1.5 years	Average weight ↑ 0.7kg in patients than placebo group (95% CI, 0.1-1.4kg, P=0.02)	Yes
(Ajslev <i>et al.</i> , 2011) Denmark	Mother child dyads of Danish National Birth Cohort, infants before 6 months	n=28354	Prospective cohort	Antibiotic exposure	7 years	Children of normal weight mother, ↑ risk of overweight (OR 1.54, 95% CI) Children of normal weight mother, ↓ risk of overweight (OR 0.54, 95%CI) Children of normal weight mother, ↓ risk of overweight (OR 0.85, 95%CI)	Yes/No
(Saiman, 2010) US & Canada	Pediatric cystic fibrosis patients	n=260 Antibiotic treated group 131, placebo group 129	Randomized control trial (double blinded placebo control)	Azithromycin 3 days per week		↑ body weight (0.58 95% CI)	Yes

Table 2: Studies showing the association between antibiotic exposures in adulthood with obesity.

Study	Studied subjects	Sample size	Study design	Exposure & Duration	Follow up	Outcomes	Remarks
(Pirzada <i>et al.</i> , 2003) UK	Patients with pulmonary disease	n=40 20 patients 20 controls	Prospective cohort	Azithromycin 250 mg daily	12 months	↑ Body mass by a mean of 1.2 in the Azithromycin group	Yes
(Thuny <i>et al.</i> , 2010) France	Infected endocarditis patients	n=96 48 IE patients, 48 controls	Case Control	Vancomycin treatment	1 year	↑ BMI in treated group but not in controls (mean [+/- SE]kg/m ² , 2.3[0.9], p=0.03)	Yes
(Lane <i>et al.</i> , 2011) England, UK	20-59 years aged people	n=1558	Randomized Control Trial	Ranitidin bismuth citrate 400mg, Clarithromycin 500mg twice a day	6 months	Participants gain >=3kg in the intervention group compared to placebo group (OR 1.57, 95% CI) Mean BMI ↑ Intervention group:27.5-27.8 kg/m ² Placebo group:27.0-27.2 kg/m ²	Yes
(Francois <i>et al.</i> , 2011) NewYork, USA	18 years adults and more	n=92 38 H. Pylorie negative, 44 H.pylori positive, 10 interminate	Prospective cohort	H. pylori eradication therapy (Amoxicillin 1000mg, Clarithromycin 500mg, Omeprazole 20mg, Rabeprazole or Esomeprazole 20mg)	7 months	BMI ↑ (5 +- 2%, p=0.008) Post prandial acylated ghrelin ↑ 6 fold than pre-eradication (p=0.005) ↑ leptin 20% (p<0.001)	Yes
(Angelakis <i>et al.</i> , 2014) France	Q fever endocarditis patients	n=82	Prospective cohort	Doxycycline and Hydroxychloroquine treatment (for atleast 18 months)	1 year after treatment	Weight gain among 23% treated patients (P=0.001)	Yes
(Mikkelsen <i>et al.</i> , 2015) Denmark	Adult men 18-40 years	n=12	Intervention study	Antibiotic course with Vancomycin 500 mg, Gentamycin 40 mg, Meropenem 500 mg once in a day	1 year	Increase in body weight 1.3 kg (78.1-79.4), p=0.04 Increase in BMI 0.3 kg/m ² (22.6-22.9), p=0.04	Yes

				(6 months)			
(Mikkelsen <i>et al.</i> , 2015) USA	Women ages 35-74 years	n=50237	Prospective cohort	Penicillins, Quinolones, Bactericidal, Tetracyclines exposure		Antibiotic use during 4 th decade of life associated with obesity Penicillin (OR 2.00, 95% CI) Bactericidals (OR 1.71, 95% CI) Tetracycline	Yes

Association of antibiotic with obesity. The purpose of antibiotic use is to eradicate certain bacterial taxa; therefore, antibiotic exposures directly affect the gut microbial biodiversity leading to dysbiosis, which turn into predisposing factors of obesity by multiple mechanisms. Antibiotics-induced obesity primarily caused by shifts in functional capabilities of gut and then long lasting metabolic shifts resulting in irreversible recovery to the normal trajectory (Vangay *et al.*, 2015). On the basis of animal and human studies several hypothesis have been made in this regard.

Byproducts of microbial fermentation. Microbial fermentation of indigestible polysaccharides yields short chain fatty acids (SCFAs) such as propionate, acetate, L-lactate, butyrate. These SCFAs play very crucial role in energy metabolism and adipose tissue expansion like acetate is used as a precursor of cholesterol and fatty acids and propionate acts as a neoglucogenic substrate (Delzenne *et al.*, 2005; Delzenne and Cani 2011). SCFAs are ligands of G-protein coupled receptor GPR43 and activation of GPR43 inhibit lipolysis and differentiation of adipocytes (Arslan, 2014). Byproducts of microbial fermentation activate hepatic carbohydrate response element binding protein (ChREBP) increasing the transcription of regulators involving in lipogenesis, leading to accumulation of hepatic fat (Le Poul *et al.*, 2003). As microbial fermentation yields 80-200 kcal energy per day (Bell, 2015), change in the composition of gut microbiome i.e. 20% increase in Firmicutes with corresponding 20% decrease in Bacteroidetes count can create additional 150kcal energy on a regular basis, can be a contributing factor for gaining weight (Leong *et al.*, 2018).

Alteration of gut hormones. Entero-endocrine system is regulated by gut microbial diversity like the abundance of *Bifidobacterium* though it is not the dominating phylum in gut but play an instrumental role on host metabolism (Arslan, 2014; Cani *et al.*, 2007). Dietary fructo-oligosaccharides increase the abundance of *Bifidobacterium* resulted into increased colonic fermentation as well as the level of glucagon like peptide (GLP-I) and decreased ghrelin (the hunger hormone), with subsequent decreased food intake and fat accumulation (Daubioul *et al.*, 2000; Delzenne *et al.*, 2005). Reduced *Bifidobacterium* and following a high fat diet yield increased secondary inflammatory activity, resulted in increase of fat mass and insulin resistance. SCFAs alter the secretion of Peptide YY (PYY) and GLP-I directly influencing satiety (Festi *et al.*, 2014). Reduction in PYY causes increase in intestinal transit time and reduction of harvesting

dietary energy (Arslan, 2014). Gut bacteria induced bile acid metabolism that act as ligands of G-protein coupled bile acid receptor 1 and nuclear farnesoid X receptor (FXR). These two are also involved in gut hormone regulation related to glucose and lipid metabolism (Leong *et al.*, 2018).

Metabolic endotoxaemia. Gut bacteria can disrupt the mucosal barrier of the gut and expose the host's immune system to microbial products like lipopolysaccharide (LPSs), lipopeptides that have hepatotoxic effects and induced inflammation called metabolic endotoxaemia. With increased permeability, endotoxemia causes greater inflammation, a predisposing factor for weight gain. Gut microbiome have some microbe-associated molecules namely pathogen associated molecular patterns (PAMPs) and some endogenous products called damage-associated molecular patterns (DAMPs), those are noticed by pattern recognised receptor TLRs (toll-like receptors). Amongst the total 13 identified TLRs, TLR2, TLR4, TLR9 help in the development of non-alcoholic fatty liver disease (NAFLD). Bacterial components like LPS, flagellum, structural lipids, peptidoglycan create inflammatory response which ultimately lead to insulin resistance obesity (Abu-Shanab and Quigley 2010; Leong *et al.*, 2018; Machado and Cortez-Pinto 2012). It was observed that TLR4 led to inflammation, resulting weight gain in rats (de La Serre *et al.*, 2010).

Fasting-induced adipocyte factor (Fiaf). Dysbiosis causes reduction of Angiopoietin-like protein factor 4 (ANGPTL4), also known as fasting-induced adipocyte factor, that inhibit lipoprotein lipase (Bäckhed *et al.*, 2004). Hindrance of lipoprotein lipase blocked the separation of fatty acids from triglycerides for tissue uptake and promote fatty acid oxidation-thus reduce fat storage (Mandard *et al.*, 2004).

DISCUSSION

Though most of the studies implicit that the antibiotic exposure during infancy causing overweight or obesity in children in their later life (Bailey *et al.*, 2014; Saari *et al.*, 2015; Scott *et al.*, 2016), some contraindication are there (Gerber *et al.*, n.d.; Sejersen *et al.*, 2019). Overall the studies those found the association between antibiotic exposures with obesity for the children identified the early stage of life as the key period. Bailey *et al.* found that effect of antibiotic exposure in 0-5 months was stronger than the exposure in 6-11 months. Similar findings by Sarri *et al.* (2015) support this evidence, who found effect was more pronounced for exposure before 6 months of age (Bailey *et al.*, 2014; Saari *et al.*, 2015). This may be due to the reason

that infancy is the key period for microbial development in human gut. Azad *et al.* conducted a longitudinal study in Canada on antibiotic exposure during 1st year of life and note the results at 9th and 12th year. Similar kind of study was done by Sarri *et al.* (2015) on 6114 boys and 5948 girls. Both identified boys as a more vulnerable group for gaining more weight (Azad *et al.*, 2014; Saari *et al.*, 2015). Another thing is that the frequency of exposure of antibiotics. Scott *et al.* (2016) found that the odd ratio is more for ≥ 6 prescriptions than 3-5 and 1-2 prescriptions, supported by the findings of Bailey *et al.* and Poulsen *et al.* (Bailey *et al.*, 2014; Poulsen *et al.*, 2017; Scott *et al.*, 2016). An interesting finding came out from a Danish mother child dyads cohort study on early antibiotic exposure that, it was observed in the children of normal weight mother had increase the risk of overweight, where the risk of overweight was decreasing for the children of overweight or obese mother; indicating maternal pre-pregnancy BMI influence the body weight of their children in their later life (Ajslev *et al.*, 2011). In case of prenatal exposure of antibiotics where Muller *et al.* indicated that, antibiotic use during the last two had more impact on their children's body weight (Mueller *et al.*, 2015), Cassidy-Bushrow said 1st and 2nd trimester exposure was more strongly associated (Cassidy-Bushrow *et al.*, 2018). Another observation identify the second trimester exposure as the key period regarding this purpose (Zhang *et al.*, 2019). There are many studies showing the clear association between antibiotic exposure in adulthood during treatment with weight gain (Angelakis *et al.*, 2014; Pirezada *et al.*, 2003; Thuny *et al.*, 2010) that indicate the consumption of antibiotic causing weight gain is irrespective of age but early life exposure has more impact on it.

CONCLUSIONS

This review has demonstrated that antibiotic exposure is a predisposing factor of obesity. Association is more marked for early life repeated exposures and particularly for the male child. We found out the children of the mother having a history of antibiotic use during pregnancy are also vulnerable. We are having still many unanswered questions such as class, dose, timing and mechanism. The little we know is use of antibiotics altering the biodiversity of gut microbiota and metabolites of them led to weight gain by their effect on body metabolisms. Randomized control trials would be unethical in this regards, further longitudinal human studies where these kinds of effects are secondary outcomes could elicit explanation.

FUTURE SCOPE

In this review article, the antibiotic exposure to children and consequent obesity was emphasised. Exposure to various types of antibiotics during early childhood and also antibiotic treatment to carrying mothers resulted in significant subsequent weight gain for the children after birth and in latter lives. In present scenario, this particular study may be significant since obesity is a

global issue and this review shows that, right after birth of a child or even before birth administration of antibiotics is a cause of weight gain. Antibiotic may be more judiciously administered to control the weight gain and subsequent obesity in future. Further research is to be undertaken to correlate the antibiotic exposure during pregnancy and neonatal periods with other obesity induced diseases in their later lives.

Acknowledgement. The authors sincerely acknowledge the Principal, Maulana Azad College, Kolkata and Principal, Netaji Nagar College for Women, Kolkata for allowing the particular study to be conducted smoothly.

Conflict of Interest. None.

REFERENCES

- Abu-Shanab, A. and Quigley, E. M. M. (2010). The role of the gut microbiota in nonalcoholic fatty liver disease. *Nature Reviews. Gastroenterology & Hepatology*, 7(12), 691–701.
- Ahirwar, R. and Mondal, P. R. (2019). Prevalence of obesity in India: A systematic review. *Diabetes & Metabolic Syndrome*, 13(1), 318–321.
- Ajslev, T. A., Andersen, C. S., Gamborg, M., Sørensen, T. I. A. and Jess, T. (2011). Childhood overweight after establishment of the gut microbiota: the role of delivery mode, pre-pregnancy weight and early administration of antibiotics. *International Journal of Obesity*, 35(4), 522–529.
- Ameho, S. and Christina, E. (2021). A Review on the Therapeutic Roles of Selected Thermophilic Secondary Metabolites. *Biological Forum-An International Journal*, 13(2), 83.
- Angelakis, E., Million, M., Kankoe, S., Lagier, J. C., Armougom, F., Giorgi, R. and Raoult, D. (2014). Abnormal Weight Gain and Gut Microbiota Modifications Are Side Effects of Long-Term Doxycycline and Hydroxychloroquine Treatment. *Antimicrobial Agents and Chemotherapy*, 58(6), 3342–3347.
- Arslan, N. (2014). Obesity, fatty liver disease and intestinal microbiota. *World Journal of Gastroenterology*, 20(44), 16452.
- Aversa, Z., Atkinson, E. J., Schafer, M. J., Theiler, R. N., Rocca, W. A., Blaser, M. J. and LeBrasseur, N. K. (2021). Association of Infant Antibiotic Exposure With Childhood Health Outcomes. *Mayo Clinic Proceedings*, 96(1), 66–77.
- Azad, M. B., Bridgman, S. L., Becker, A. B. and Kozyrskyj, A. L. (2014). Infant antibiotic exposure and the development of childhood overweight and central adiposity. *International Journal of Obesity*, 38(10), 1290–1298.
- Bäckhed, F., Ding, H., Wang, T., Hooper, L. V., Koh, G. Y., Nagy, A., Semenkovich, C. F. and Gordon, J. I. (2004). The gut microbiota as an environmental factor that regulates fat storage. *Proceedings of the National Academy of Sciences of the United States of America*, 101(44), 15718–15723.
- Bailey, L. C., Forrest, C. B., Zhang, P., Richards, T. M., Livshits, A. and DeRusso, P. A. (2014). Association of Antibiotics in Infancy With Early Childhood Obesity. *JAMA Pediatrics*, 168(11), 1063.
- Bell, D. S. H. (2015). Changes seen in gut bacteria content and distribution with obesity: causation or association? *Postgraduate Medicine*, 127(8), 863–868.
- Bezirtzoglou, E. (1997). The intestinal microflora during the

- first weeks of life. *Anaerobe*, 3(2–3), 173–177.
- Block, J. P., Bailey, L. C., Gillman, M. W., Lunsford, D., Daley, M. F., Eneli, I., Finkelstein, J., Heerman, W., Horgan, C. E., Hsia, D. S., Jay, M., Rao, G., Reynolds, J. S., Rifas-Shiman, S. L., Sturtevant, J. L., Toh, N. S., Trasande, L., Young, J., Forrest, C. B. and PCORnet Antibiotics and Childhood Growth Study Group. (2018). Early Antibiotic Exposure and Weight Outcomes in Young Children. *Pediatrics*, 142(6).
- Browne, A. J., Chipeta, M. G., Haines-Woodhouse, G., Kumaran, E. P. A., Hamadani, B. H. K., Zarea, S., Henry, N. J., Deshpande, A., Reiner, R. C., Day, N. P. J., Lopez, A. D., Dunachie, S., Moore, C. E., Stergachis, A., Hay, S. I. and Dolecek, C. (2021). Global antibiotic consumption and usage in humans, 2000–18: a spatial modelling study. *The Lancet Planetary Health*, 5(12), e893–e904.
- Cani, P. D., Amar, J., Iglesias, M. A., Poggi, M., Knauf, C., Bastelica, D., Neyrinck, A. M., Fava, F., Tuohy, K. M., Chabo, C., Waget, A., Delmée, E., Cousin, B., Sulpice, T., Chamontin, B., Ferrières, J., Tanti, J. F., Gibson, G. R., Casteilla, L. and Burcelin, R. (2007). Metabolic endotoxemia initiates obesity and insulin resistance. *Diabetes*, 56(7), 1761–1772.
- Cassidy-Bushrow, A. E., Burmeister, C., Havstad, S., Levin, A. M., Lynch, S. V., Ownby, D. R., Rundle, A. G., Woodcroft, K. J., Zoratti, E. M., Johnson, C. C. and Wegienka, G. (2018). Prenatal antimicrobial use and early-childhood body mass index. *International Journal of Obesity*, 42(1), 1–7.
- Chan, Y. K., Estaki, M. and Gibson, D. L. (2013). Clinical Consequences of Diet-Induced Dysbiosis. *Annals of Nutrition and Metabolism*, 63(Suppl. 2), 28–40.
- Daubioul, C. A., Taper, H. S., De Wispelaere, L. D. and Delzenne, N. M. (2000). Dietary oligofructose lessens hepatic steatosis, but does not prevent hypertriglyceridemia in obese Zucker rats. *The Journal of Nutrition*, 130(5), 1314–1319. <https://doi.org/10.1093/jn/130.5.1314>
- de La Serre, C. B., Ellis, C. L., Lee, J., Hartman, A. L., Rutledge, J. C. and Raybould, H. E. (2010). Propensity to high-fat diet-induced obesity in rats is associated with changes in the gut microbiota and gut inflammation. *American Journal of Physiology. Gastrointestinal and Liver Physiology*, 299(2), G440–8.
- Del Fiol, F. S., Balcão, V. M., Barberato-Fillho, S., Lopes, L. C. and Bergamaschi, C. C. (2018). Obesity: A New Adverse Effect of Antibiotics? In *Frontiers in Pharmacology* (Vol. 9). Frontiers Media S.A.
- Delzenne, N. M. and Cani, P. D. (2011). Interaction between obesity and the gut microbiota: relevance in nutrition. *Annual Review of Nutrition*, 31, 15–31.
- Delzenne, N. M., Cani, P. D., Daubioul, C., & Neyrinck, A. M. (2005). Impact of inulin and oligofructose on gastrointestinal peptides. *The British Journal of Nutrition*, 93 Suppl 1, S157–61. <https://doi.org/10.1079/bjn20041342>
- Edmonson, M. B. and Eickhoff, J. C. (2017). Weight Gain and Obesity in Infants and Young Children Exposed to Prolonged Antibiotic Prophylaxis. *JAMA Pediatrics*, 171(2), 150.
- Festi, D., Schiumerini, R., Eusebi, L. H., Marasco, G., Taddia, M. and Colecchia, A. (2014). Gut microbiota and metabolic syndrome. *World Journal of Gastroenterology*, 20(43), 16079.
- Francois, F., Roper, J., Joseph, N., Pei, Z., Chhada, A., Shak, J. R., de Perez, A. Z. O., Perez-Perez, G. I. and Blaser, M. J. (2011). The effect of *H. pylori* eradication on meal-associated changes in plasma ghrelin and leptin. *BMC Gastroenterology*, 11, 37.
- Gerber, J. S., Bryan, M., Ross, R. K., Daymont, C., Parks, E. P., Localio, A. R., Grundmeier, R. W., Stallings, V. A., and Zaoutis, T. E. (n.d.). Antibiotic Exposure During the First 6 Months of Life and Weight Gain During Childhood. *JAMA*, 315(12), 1258–1265.
- Goyal, R. and Julka, S. (2014). Impact of breakfast skipping on the health status of the population. *Indian Journal of Endocrinology and Metabolism*, 18(5), 683–687.
- Herrera, B. M. and Lindgren, C. M. (2010). The Genetics of Obesity. *Current Diabetes Reports*, 10(6), 498–505.
- Huang, C. J., Hu, H.-T., Fan, Y.-C., Liao, Y.-M., & Tsai, P.-S. (2010). Associations of breakfast skipping with obesity and health-related quality of life: evidence from a national survey in Taiwan. *International Journal of Obesity*, 34(4), 720–725.
- Jo, J. H., Kennedy, E. A. and Kong, H. H. (2016). Research Techniques Made Simple: Bacterial 16S Ribosomal RNA Gene Sequencing in Cutaneous Research. *The Journal of Investigative Dermatology*, 136(3), e23–e27.
- Kenyon, C., Laumen, J., Manoharan-Basil, S. S. and Buyze, J. (2020). Strong association between adolescent obesity and consumption of macrolides in Europe and the USA: An ecological study. *Journal of Infection and Public Health*, 13(10), 1517–1521.
- Koenig, J. E., Spor, A., Scalfone, N., Fricker, A. D., Stombaugh, J., Knight, R., Angenent, L. T. and Ley, R. E. (2011). Succession of microbial consortia in the developing infant gut microbiome. *Proceedings of the National Academy of Sciences*, 108(supplement_1), 4578–4585.
- Lane, J. A., Murray, L. J., Harvey, I. M., Donovan, J. L., Nair, P. and Harvey, R. F. (2011). Randomised clinical trial: *Helicobacter pylori* eradication is associated with a significantly increased body mass index in a placebo-controlled study. *Alimentary Pharmacology & Therapeutics*, 33(8), 922–929.
- Le Poul, E., Loison, C., Struyf, S., Springael, J. Y., Lannoy, V., Decobecq, M. E., Brezillon, S., Dupriez, V., Vassart, G., Van Damme, J., Parmentier, M. and Detheux, M. (2003). Functional characterization of human receptors for short chain fatty acids and their role in polymorphonuclear cell activation. *The Journal of Biological Chemistry*, 278(28), 25481–25489.
- Leong, K. S. W., Derraik, J. G. B., Hofman, P. L. and Cutfield, W. S. (2018). Antibiotics, gut microbiome and obesity. *Clinical Endocrinology*, 88(2), 185–200.
- Li, D.-K., Chen, H., Ferber, J. and Odouli, R. (2017). Infection and antibiotic use in infancy and risk of childhood obesity: a longitudinal birth cohort study. *The Lancet Diabetes & Endocrinology*, 5(1), 18–25.
- MACDOUGALL, L. G. (1957). The effect of aureomycin on undernourished African children. *Journal of Tropical Pediatrics (London, England : 1955)*, 3(2), 74–81.
- Machado, M. V. and Cortez-Pinto, H. (2012). Gut microbiota and nonalcoholic fatty liver disease. *Annals of Hepatology*, 11(4), 440–449.
- Mandard, S., Zandbergen, F., Tan, N. S., Escher, P., Patouris, D., Koenig, W., Kleemann, R., Bakker, A., Veenman, F., Wahli, W., Müller, M. and Kersten, S. (2004). The direct peroxisome proliferator-activated receptor target fasting-induced adipose factor (FIAF/PGAR/ANGPTL4) is present in blood plasma as a truncated protein that is increased by fenofibrate treatment. *The Journal of Biological Chemistry*,

- 279(33), 34411–34420.
- Mbakwa, C. A., Scheres, L., Penders, J., Mommers, M., Thijs, C. and Arts, I. C. W. (2016). Early Life Antibiotic Exposure and Weight Development in Children. *The Journal of Pediatrics*, 176, 105–113.e2.
- Mikkelsen, K. H., Frost, M., Bahl, M. I., Licht, T. R., Jensen, U. S., Rosenberg, J., Pedersen, O., Hansen, T., Rehfeld, J. F., Holst, J. J., Vilsbøll, T. and Knop, F. K. (2015). Effect of Antibiotics on Gut Microbiota, Gut Hormones and Glucose Metabolism. *PLOS ONE*, 10(11), e0142352.
- Mor, A., Antonsen, S., Kahlert, J., Holsteen, V., Jørgensen, S., Holm-Pedersen, J., Sørensen, H. T., Pedersen, O. and Ehrenstein, V. (2015). Prenatal exposure to systemic antibacterials and overweight and obesity in Danish schoolchildren: a prevalence study. *International Journal of Obesity*, 39(10), 1450–1455.
- Mueller, N. T., Whyatt, R., Hoepner, L., Oberfield, S., Dominguez-Bello, M. G., Widen, E. M., Hassoun, A., Perera, F. and Rundle, A. (2015). Prenatal exposure to antibiotics, cesarean section and risk of childhood obesity. *International Journal of Obesity*, 39(4), 665–670.
- Murphy, R., Stewart, A. W., Braithwaite, I., Beasley, R., Hancox, R. J. and Mitchell, E. A. (2014). Antibiotic treatment during infancy and increased body mass index in boys: an international cross-sectional study. *International Journal of Obesity*, 38(8), 1115–1119.
- Nicolucci, A. C., Hume, M. P., Martínez, I., Mayengbam, S., Walter, J. and Reimer, R. A. (2017). Prebiotics Reduce Body Fat and Alter Intestinal Microbiota in Children Who Are Overweight or With Obesity. *Gastroenterology*, 153(3), 711–722.
- Pirzada, O. M., McGaw, J., Taylor, C. J. and Everard, M. L. (2003). Improved lung function and body mass index associated with long-term use of Macrolide antibiotics. *Journal of Cystic Fibrosis*, 2(2), 69–71.
- Pitsavos, C., Panagiotakos, D., Weinem, M. and Stefanadis, C. (2006). Diet, Exercise and the Metabolic Syndrome. *The Review of Diabetic Studies*, 3(3), 118–118.
- Poulsen, M. N., Pollak, J., Bailey-Davis, L., Hirsch, A. G., Glass, T. A. and Schwartz, B. S. (2017). Associations of prenatal and childhood antibiotic use with child body mass index at age 3 years. *Obesity*, 25(2), 438–444.
- Rayanoothala, P., Mahapatra, S. and Das, S. (2021). A Review on Mode of Action of Antibiotics : Paved the Path to Evolution of Antibiotic Resistance and their Mechanisms in Phytobacterial Disease Management. *Biological Forum-An International Journal*, 13, 29–31.
- Saari, A., Virta, L. J., Sankilampi, U., Dunkel, L. and Saxen, H. (2015). Antibiotic exposure in infancy and risk of being overweight in the first 24 months of life. *Pediatrics*, 135(4), 617–626.
- Saiman, L. (2010). Effect of Azithromycin on Pulmonary Function in Patients With Cystic Fibrosis Uninfected With *Pseudomonas aeruginosa*. *JAMA*, 303(17), 1707. <https://doi.org/10.1001/jama.2010.563>
- Saiman, L., Marshall, B. C., Mayer-Hamblett, N., Burns, J. L., Quittner, A. L., Cibene, D. A., Coquillotte, S., Fieberg, A. Y., Accurso, F. J., Campbell, P. W. and Macrolide Study Group. (2003). Azithromycin in patients with cystic fibrosis chronically infected with *Pseudomonas aeruginosa*: a randomized controlled trial. *JAMA*, 290(13), 1749–1756.
- Sanchez, M., Darimont, C., Drapeau, V., Emady-Azar, S., Lepage, M., Rezzonico, E., Ngom-Bru, C., Berger, B., Philippe, L., Ammon-Zuffrey, C., Leone, P., Chevrier, G., St-Amand, E., Marette, A., Doré, J. and Tremblay, A. (2014). Effect of *Lactobacillus rhamnosus* CGMCC1.3724 supplementation on weight loss and maintenance in obese men and women. *The British Journal of Nutrition*, 111(8), 1507–1519.
- Schwartz, B. S., Pollak, J., Bailey-Davis, L., Hirsch, A. G., Cosgrove, S. E., Nau, C., Kress, A. M., Glass, T. A. and Bandeen-Roche, K. (2016). Antibiotic use and childhood body mass index trajectory. *International Journal of Obesity*, 40(4), 615–621.
- Scott, F. I., Horton, D. B., Mamtani, R., Haynes, K., Goldberg, D. S., Lee, D. Y. and Lewis, J. D. (2016). Administration of Antibiotics to Children Before Age 2 Years Increases Risk for Childhood Obesity. *Gastroenterology*, 151(1), 120–129.e5.
- Sejersen, T. S., Vinding, R. K., Stokholm, J., Chawes, B., Bønnelykke, K., Krakauer, M. and Bisgaard, H. (2019). Antibiotic exposure in infancy and development of BMI and body composition in childhood. *EClinicalMedicine*, 17, 100209.
- Sela, D. A., Chapman, J., Adeuya, A., Kim, J. H., Chen, F., Whitehead, T. R., Lapidus, A., Rokhsar, D. S., Lebrilla, C. B., German, J. B., Price, N. P., Richardson, P. M. and Mills, D. A. (2008). The genome sequence of *Bifidobacterium longum* subsp. infantis reveals adaptations for milk utilization within the infant microbiome. *Proceedings of the National Academy of Sciences of the United States of America*, 105(48), 18964–18969.
- Sharafedinov, K. K., Plotnikova, O. A., Alexeeva, R. I., Sentsova, T. B., Songisepp, E., Stsepetova, J., Smidt, I. and Mikelsaar, M. (2013). Hypocaloric diet supplemented with probiotic cheese improves body mass index and blood pressure indices of obese hypertensive patients - a randomized double-blind placebo-controlled pilot study. *Nutrition Journal*, 12(1), 138.
- Shekhar, S. and Petersen, F. C. (2020). The Dark Side of Antibiotics: Adverse Effects on the Infant Immune Defense Against Infection. In *Frontiers in Pediatrics* (Vol. 8). Frontiers Media S.A.
- Stark, C. M., Susi, A., Emerick, J. and Nylund, C. M. (2019). Antibiotic and acid-suppression medications during early childhood are associated with obesity. *Gut*, 68(1), 62–69.
- Takahashi, S., Anzawa, D., Takami, K., Ishizuka, A., Mawatari, T., Kamikado, K., Sugimura, H. and Nishijima, T. (2016). Effect of *Bifidobacterium animalis* ssp. lactis GCL2505 on visceral fat accumulation in healthy Japanese adults: a randomized controlled trial. *Bioscience of Microbiota, Food and Health*, 35(4), 163–171.
- Tan, S. and Tatsumura, Y. (2015). Alexander Fleming (1881–1955): Discoverer of penicillin. *Singapore Medical Journal*, 56(07), 366–367.
- The State of the World's Antibiotics 2021 A Global Analysis of Antimicrobial Resistance and Its Drivers. (n.d.).
- Thompson-McCormick, J. J., Thomas, J. J., Bainivualiku, A., Khan, A. N. and Becker, A. E. (2010). Breakfast skipping as a risk correlate of overweight and obesity in school-going ethnic Fijian adolescent girls. *Asia Pacific Journal of Clinical Nutrition*, 19(3), 372–382.
- Thuny, F., Richet, H., Casalta, J. P., Angelakis, E., Habib, G. and Raoult, D. (2010). Vancomycin Treatment of Infective Endocarditis Is Linked with Recently

- Acquired Obesity. *PLoS ONE*, 5(2), e9074.
- Trasande, L., Blustein, J., Liu, M., Corwin, E., Cox, L. M. and Blaser, M. J. (2013). Infant antibiotic exposures and early-life body mass. *International Journal of Obesity*, 37(1), 16–23.
- Vaishampayan, P. A., Kuehl, J. V., Froula, J. L., Morgan, J. L., Ochman, H., and Francino, M. P. (2010). Comparative metagenomics and population dynamics of the gut microbiota in mother and infant. *Genome Biology and Evolution*, 2, 53–66.
- Vallianou, N., Dalamaga, M., Stratigou, T., Karampela, I., Tsigalou, C. and Tsigalou xtsigalou, C. (n.d.). *Do Antibiotics Cause Obesity Through Long-term Alterations in the Gut Microbiome? A Review of Current Evidence*.
- Vangay, P., Ward, T., Gerber, J. S. and Knights, D. (2015). Antibiotics, Pediatric Dysbiosis, and Disease. *Cell Host & Microbe*, 17(5), 553–564.
- Ville, A. P., Heyman, M. B., Medrano, R. and Wojcicki, J. M. (2017). Early Antibiotic Exposure and Risk of Childhood Obesity in Latinos. *Childhood Obesity*, 13(3), 231–235.
- Walley, A. J., Asher, J. E. and Froguel, P. (2009). The genetic contribution to non-syndromic human obesity. *Nature Reviews. Genetics*, 10(7), 431–442.
- Yassour, M., Vatanen, T., Siljander, H., Hämäläinen, A.-M., Härkönen, T., Ryhänen, S. J., Franzosa, E. A., Vlamakis, H., Huttenhower, C., Gevers, D., Lander, E. S., Knip, M., DIABIMMUNE Study Group and Xavier, R. J. (2016). Natural history of the infant gut microbiome and impact of antibiotic treatment on bacterial strain diversity and stability. *Science Translational Medicine*, 8(343), 343ra81.
- Yatsunencko, T., Rey, F. E., Manary, M. J., Trehan, I., Dominguez-Bello, M. G., Contreras, M., Magris, M., Hidalgo, G., Baldassano, R. N., Anokhin, A. P., Heath, A. C., Warner, B., Reeder, J., Kuczynski, J., Caporaso, J. G., Lozupone, C. A., Lauber, C., Clemente, J. C., Knights, D. and Gordon, J. I. (2012). Human gut microbiome viewed across age and geography. *Nature*, 486(7402), 222–227.
- Zaffiri, L., Gardner, J. and Toledo-Pereyra, L. H. (2012). History of antibiotics. From salvarsan to cephalosporins. *Journal of Investigative Surgery : The Official Journal of the Academy of Surgical Research*, 25(2), 67–77.
- Zhang, H., DiBaise, J. K., Zuccolo, A., Kudrna, D., Braidotti, M., Yu, Y., Parameswaran, P., Crowell, M. D., Wing, R., Rittmann, B. E. and Krajmalnik-Brown, R. (2009). Human gut microbiota in obesity and after gastric bypass. *Proceedings of the National Academy of Sciences*, 106(7), 2365–2370.
- Zhang, M., Differding, M. K., Benjamin-Neelon, S. E., Østbye, T., Hoyo, C. and Mueller, N. T. (2019). Association of prenatal antibiotics with measures of infant adiposity and the gut microbiome. *Annals of Clinical Microbiology and Antimicrobials*, 18(1), 18.

How to cite this article: Tuhina Nasrin Ali, Malay Mitra and Avishek Ghosh (2023). Antibiotics; the Miracle Drugs, also a Predisposing Factor of Obesity. *Biological Forum – An International Journal*, 15(5): 169-179.

TOPICAL REVIEW • OPEN ACCESS

Recent developments in photodynamic therapy and its application against multidrug resistant cancers

To cite this article: Debalina Bhattacharya *et al* 2023 *Biomed. Mater.* **18** 062005

View the [article online](#) for updates and enhancements.

You may also like

- [Functionalised biomimetic hydroxyapatite NPs as potential agent against pathogenic multidrug-resistant bacteria](#)
Debbethi Bera, Kunal Pal, Souravi Bardhan et al.
- [Management of multidrug-resistant tuberculosis in human immunodeficiency virus patients](#)
K F Jamil
- [Multidrug-resistant organisms \(MDRO\) patterns of GICU patients in Dr Mohammad Hoesin Hospital Palembang](#)
Phey Liana, Venny Patricia and Cornelia Agatha



The Breath Biopsy® Guide
Fourth edition

FREE

DOWNLOAD THE FREE E-BOOK

BREATH BIOPSY

GILLETTE MEDICAL

Biomedical Materials



TOPICAL REVIEW

OPEN ACCESS

RECEIVED
13 June 2023

REVISED
6 October 2023

ACCEPTED FOR PUBLICATION
12 October 2023

PUBLISHED
24 October 2023

Original content from
this work may be used
under the terms of the
[Creative Commons
Attribution 4.0 licence](#).

Any further distribution
of this work must
maintain attribution to
the author(s) and the title
of the work, journal
citation and DOI.



Recent developments in photodynamic therapy and its application against multidrug resistant cancers

Debalina Bhattacharya¹, Mainak Mukhopadhyay², Kumar Shivam³, Satyajit Tripathy^{4,5}, Ranjan Patra^{3,6} and Arindam Pramanik^{7,8,*}

¹ Department of Microbiology, Maulana Azad College, Kolkata, West Bengal 700013, India

² Department of Biotechnology, JIS University, Kolkata, West Bengal 700109, India

³ Amity Institute of Click Chemistry Research & Studies, Amity University, Noida 201301, India

⁴ Department of Pharmacology, University of Free State, Bloemfontein, Free State, 9301, South Africa

⁵ Amity Institute of Allied Health Science, Amity University, Noida 201301, India

⁶ Department of Chemistry, Pohang University of Science and Technology, Pohang 37673, Republic of Korea

⁷ School of Medicine, University of Leeds, Leeds, LS9 7TF, United Kingdom

⁸ Amity Institute of Biotechnology, Amity University, Noida 201301, India

* Author to whom any correspondence should be addressed.

E-mail: arindampramanik87@gmail.com

Keywords: multidrug resistant cancer, nanoparticles, photosensitizers, photodynamic therapy

Abstract

Recently, photodynamic therapy (PDT) has received a lot of attention for its potential use in cancer treatment. It enables the therapy of a multifocal disease with the least amount of tissue damage. The most widely used prodrug is 5-aminolevulinic acid, which undergoes heme pathway conversion to protoporphyrin IX, which acts as a photosensitizer (PS). Additionally, hematoporphyrin, bacteriochlorin, and phthalocyanine are also studied for their therapeutic potential in cancer. Unfortunately, not every patient who receives PDT experiences a full recovery. Resistance to different anticancer treatments is commonly observed. A few of the resistance mechanisms by which cancer cells escape therapeutics are genetic factors, drug–drug interactions, impaired DNA repair pathways, mutations related to inhibition of apoptosis, epigenetic pathways, etc. Recently, much research has been conducted to develop a new generation of PS based on nanomaterials that could be used to overcome cancer cells' multidrug resistance (MDR). Various metal-based, polymeric, lipidic nanoparticles (NPs), dendrimers, etc, have been utilized in the PDT application against cancer. This article discusses the detailed mechanism by which cancer cells evolve towards MDR as well as recent advances in PDT-based NPs for use against multidrug-resistant cancers.

1. Introduction

The current need for therapeutic oncology is to develop a cytotoxic drug that effectively eliminates cancer cells while protecting vital host cells and their activities. If not for the issue of human cancer's resistance to chemotherapy or the drugs' non-specific cytotoxicity, cancer treatment would have been analogous to antibacterial treatment, in which complete eradication of infection is frequently observed. One of the key issues with cancer therapy is innate (inherited) or acquired resistance [1]. A tumor's initial inability to respond to a specific therapy is referred to as natural resistance, and the unresponsiveness of

a drug that develops following an initial successful course of treatment is referred to as acquired resistance. Mutations that arise during treatment can also contribute to acquired drug resistance, as can a variety of other adaptive responses like elevated levels of the therapeutic target and stimulating substitute compensatory signaling pathways in previously sensitive tumors [2]. Drug resistance has been associated with a wide variety of molecular mechanisms, including elevated drug efflux rates, drug target mutations, and changes in drug metabolism [3]. Chemoresistance has also been linked to epigenetic changes and the impact of the surrounding tumor microenvironment (TME). Because cancer stem cells

are inherently resistant to many therapeutic modalities, their presence in some situations has recently been linked to treatment failure [4].

One of the less invasive techniques that could be employed for cancer therapy is photodynamic therapy (PDT). PDT can be used as another option for surgical cancer treatment [5]. In this therapy, a photosensitizer (PS) that has been applied to the patient builds up in the tumor, where it causes significant damage when exposed to the right wavelength of oxygen and light, resulting in the death of cancer cells and tumor vascularity. PDT also triggers immune and inflammatory reactions against tumor cells. Currently, 5-aminolevulinic acid (5-ALA) is the most commonly used medication for PDT [6]. Unfortunately, not all patients experience full recovery post-treatment with PDT. The primary factor in anticancer PDT therapy failure is the development of resistance. The PDT resistance mechanisms attributed to the PS are likely similar to general drug resistance mechanisms and involve altered intracellular trafficking or efflux rates and altered drug uptake [7]. Alternately, upregulated antioxidant detoxifying enzymes and heat shock protein activation are linked to the deactivation of reactive oxygen species (ROS) and PDT resistance. An increased level of DNA damage repair and decreased PS levels in tumor cells may also lead to multidrug resistance (MDR).

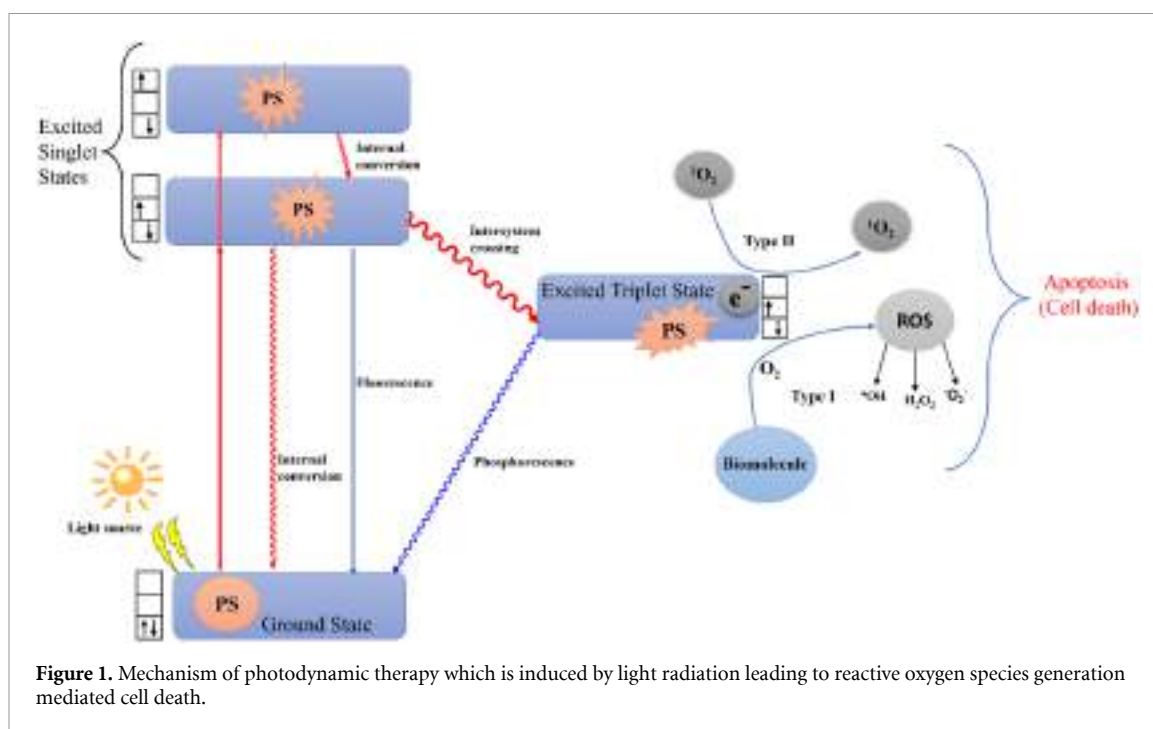
2. Photodynamic therapy (PDT)

The most widely employed treatment modalities for various types of cancer are surgery, chemotherapy, radiation therapy, and immunotherapy. Recently, small-molecule-based therapy has also been successfully applied [8]. However, these traditional treatments have major disadvantages in terms of their selectivity against cancer cells. Chemotherapy is frequently associated with systemic adverse effects and an elevated risk of recurrence following surgical excision of malignancies, whereas radiation therapy is constrained by the combined dose of radiation [9]. As a result, research has concentrated on creating alternative therapy approaches that are very specific and selective, safe, powerful, and economical. Additionally, it should only damage the cancerous cells while sparing the surrounding healthy cells and tissues. A new, non-invasive alternative to traditional tumor-ablative therapies for the treatment of a variety of malignancies is PDT [10]. PDT is made up of three main parts: (1) light, (2) PSs, and (3) oxygen in their molecular states (figure 1). PDT makes ROS more likely to form in two different ways. In the type I pathway, the PS moves electrons to make free radicals [11]. In the type II pathway scenario, it transfers energy to produce the highly reactive singlet oxygen ($^1\text{O}_2$) and the triplet ground-state molecular oxygen ($^3\text{O}_2$) [12]. A ground-state PS is propelled into a

high-energy electronic state by the absorption of light (photon) [13, 14]. According to Lucky *et al* following intersystem crossing, the PS's excited singlet state can produce a persistently excited triplet state [15]. This excited triplet state can then come back to the ground singlet state by releasing energy in the form of fluorescence, heat, or other forms of energy. The excited triplet state transfers energy to surrounding oxygen molecules or other substrate molecules, which in turn induces the creation of singlet oxygen ($^1\text{O}_2$) or other ROS. When PDT is performed, the formation of ROS such as hydrogen peroxide (H_2O_2), hydroxyl radical ($\text{OH}\cdot$), and superoxide anion radical ($\text{O}_2\cdot$) reacts with biological molecules such as lipids, DNA, and proteins to eradicate tumor cells by necrosis and/or apoptosis. However, the killing mechanisms of radiotherapy and chemotherapy are predominantly immunosuppressive, destroying tumor vasculatures as an anti-angiogenesis effect and stimulating the host immune system to find, locate, and kill any remaining tumor cells [16]. Additionally, PDT can be locally applied to a specific region of tumors by selectively illuminating the lesion without affecting the normal tissues. Therefore, PDT is much more advantageous than radiotherapy and chemotherapy, which exert toxicity. PDT is more effective than traditional treatments because it is less invasive, can be done more than once without causing toxicity, has better functional and cosmetic effects, has less long-term morbidity, and improves the patient's quality of life. PDT has been successful in treating skin cancer [17], Barrett's esophagus [18], head and neck malignancies [19], lung cancer, and bladder cancer [20] over the past 40 years. PDT is well tolerated by patients because of its selective action. PDT procedures are pleasant, and their straightforward application enables outpatient use.

2.1. Light source

For a PDT reaction to take place, the PS is required to be turned on by a light source with a wavelength of <800 nm. Above 800 nm, PS cannot be turned on and cannot make enough singlet oxygen because its triplet state is beneath the energy threshold of singlet oxygen [21]. In the earlier days, photosensitization had been performed with high-power traditional metal halogen lights that put out radiation between 600 and 800 nm [22]. In the next generation of PDT, laser lights were used for photosensitization instead of gas lights. There are two types of lasers used in PDT: dye-lasers and diode-lasers. An organic dye molecule, such as rhodamine or kiton red, that produces light in the 600–650 nm spectral region serves as the lasing medium in dye lasers. This is done to coincide with a particular PS's absorption wavelength [23]. To prevent overheating, the dye substance is often a liquid that is constantly circulated. Due to circulation, only a part of the dye is ever lasing in the cavity at any



given time. Light is produced by electron-hole recombination in semiconductor devices called diode lasers. Since diode lasers have a fixed wavelength, a different laser unit is required for each PS that absorbs at a different excitation wavelength. Irradiance from clinical diode lasers can reach 1 W cm^{-2} . PDT commonly uses diode lasers with output wavelengths in the 415–690 nm range [23]. But light-emitting diodes (LEDs) are now widely used instead of lasers as light sources for photosensitization because they are easier to operate and last longer than lasers [24]. Due to the dynamic interactions between light, PS, and oxygen, PDT dosimetry is complicated. The clinical effectiveness of PDT is determined by the type of complex dosimetry used, the overall dose, the length of light exposure, the delivery mechanism, and the fractionation scheme. Direct dosimetry, explicit dosimetry, biophysical/biological tissue response monitoring, and implicit dosimetry are the four dosimetric methods that can be employed for PDT dosimetry. A single metric can combine two or more of the treatment parameters. PDT dosage is one such metric, which is calculated as the sum of the PS concentration and light fluence (J cm^{-2}) [23].

2.2. Photosensitizers (PSs)

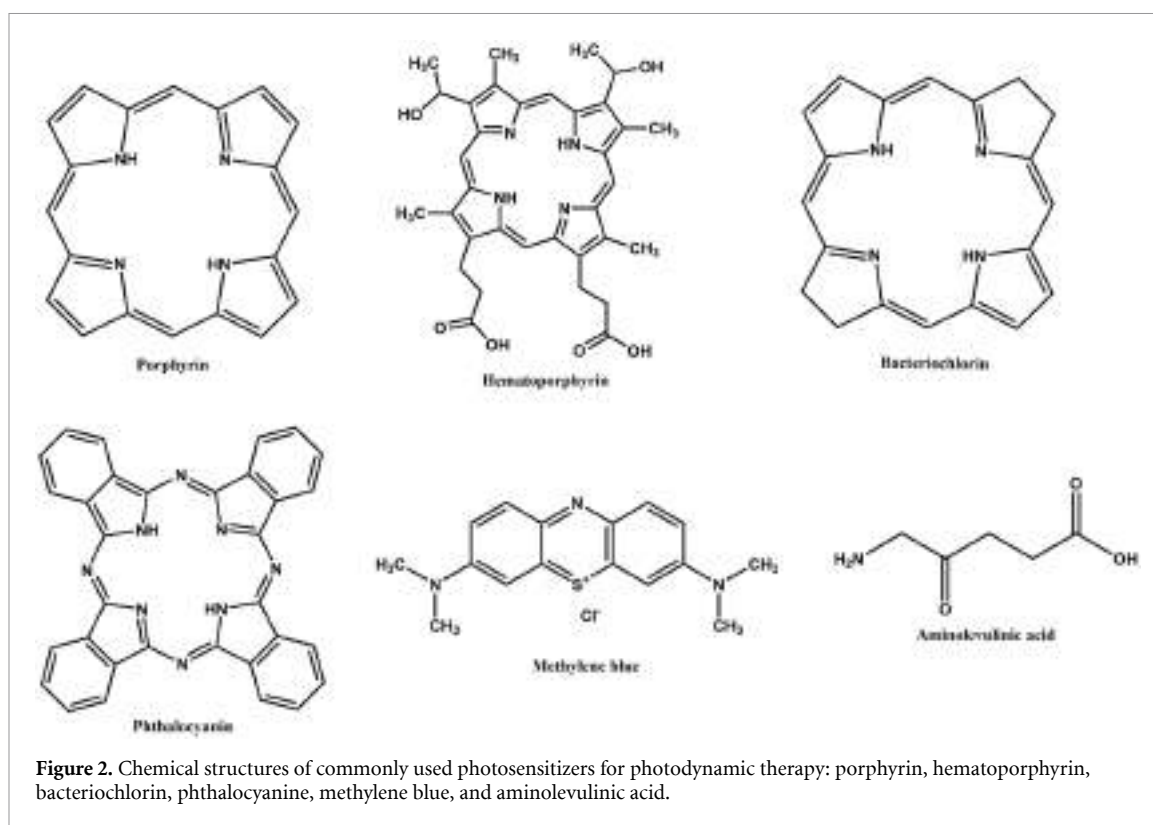
Scientists have studied three different types of PSs. At first, a hematoporphyrin derivative was used to detect tumors and emit fluorescence (figure 2). Later, Meyer-Betz found that porphyrins might also have phototoxic effects and could be used to kill cancer cells [25]. So, the first-generation PSs are porphyrins, hematoporphyrin, and their derivatives, such as Photosan and Photocan, as well as Photofrin.

The monomeric, dimeric, and oligomeric parts of each derivative are different [26].

The pure synthetic compounds made of an aromatic macrocycle are second-generation PSs such as chlorins, bacteriochlorins, benzo-porphyrins, and some common dyes such as rose Bengal (RB) [27], eosin Y [28], or methylene blue (MB) [29] that produce a high absorbance ($85\,000 \text{ M}^{-1} \text{ cm}^{-1}$) at 664 nm. Third-generation PSs are distinguished by the fusion of second and first-generation PS with targeting ligands, such as antibodies, carbohydrates, amino acids, and peptides, or by their encapsulation within carriers like liposomes, micelles, and nanoparticles (NPs). This strategic approach aims to enhance the concentration of PSs specifically at the intended tumor sites, building upon the advancements seen in second-generation PS. Figure 3 represents the mechanism of utilizing third-generation PSs for cancer treatment using PDT. A list of clinically approved photosensitizers or under trial for PDT in cancers has been provided in table 1.

2.3. Limitations of PDT

Although PDT is one of the most effective techniques for the therapy and management of various types of cancer, its fundamental limitation is that it can only be used to treat superficial, flat lesions, initial lesions, or lesions accessible by endoscopic instruments. However, PDT cannot be used to treat solid, bulky, or deeply embedded tumors. This is because light cannot penetrate the deep tissues inside our body, and whole-body irradiation is not possible with the PDT technique. Moreover, the organic PSs in PDT do not exhibit high selectivity for cancer cells, and



they have a complicated structure. It is easily degraded by enzymes and is not cost-effective. Although PDT is used for cancer treatment, it has toxic side effects. The PS does cause a significant amount of toxicity to the local tissue when exposed to light. Although reactive oxygen is thought to be the major cytotoxic agent in PDT, other ROS, like the superoxide anion and hydroxyl radicals, could cause biological damage to healthy tissue in the nearby locations around tumors. So, to solve the drawbacks of this classic PS, a better alternative, such as nanomaterial-mediated PDT, has been developed.

3. NPs and PDT

Nanomaterials can be synthesized from a wide variety of starting materials, which are both natural and synthetic. NPs are simple to create, allowing for the targeted delivery of several theranostic agents [46, 47]. NPs are extensively used as carriers for PSs in PDT [47]. This is because of the following factors:

- (1) Due to their high surface area-to-volume ratio, they can significantly enhance PS delivery to the cells being targeted.
- (2) If PS is enclosed in NPs, early PS discharge in healthy tissues and potential medication inactivation by plasma components may be prevented [48].
- (3) NPs loaded with PS can be transported efficiently through the circulatory system to the site of the tumor.

- (4) Compared to organic PS, NPs exhibit increased permeability and retention (EPR) within tumor tissue.
- (5) To enhance the biological distribution, pharmaceutical kinetics, cellular absorption, and targeting properties of the NPs, different functional groups or targeting moieties can be added to the surface of the particles.

Based on these above-mentioned properties, researchers have classified NPs as non-biodegradable and biodegradable NPs that can be used as PSs in PDT [49, 50]. Figure 4 shows different types of non-polymeric and polymeric NPs applied in PDT.

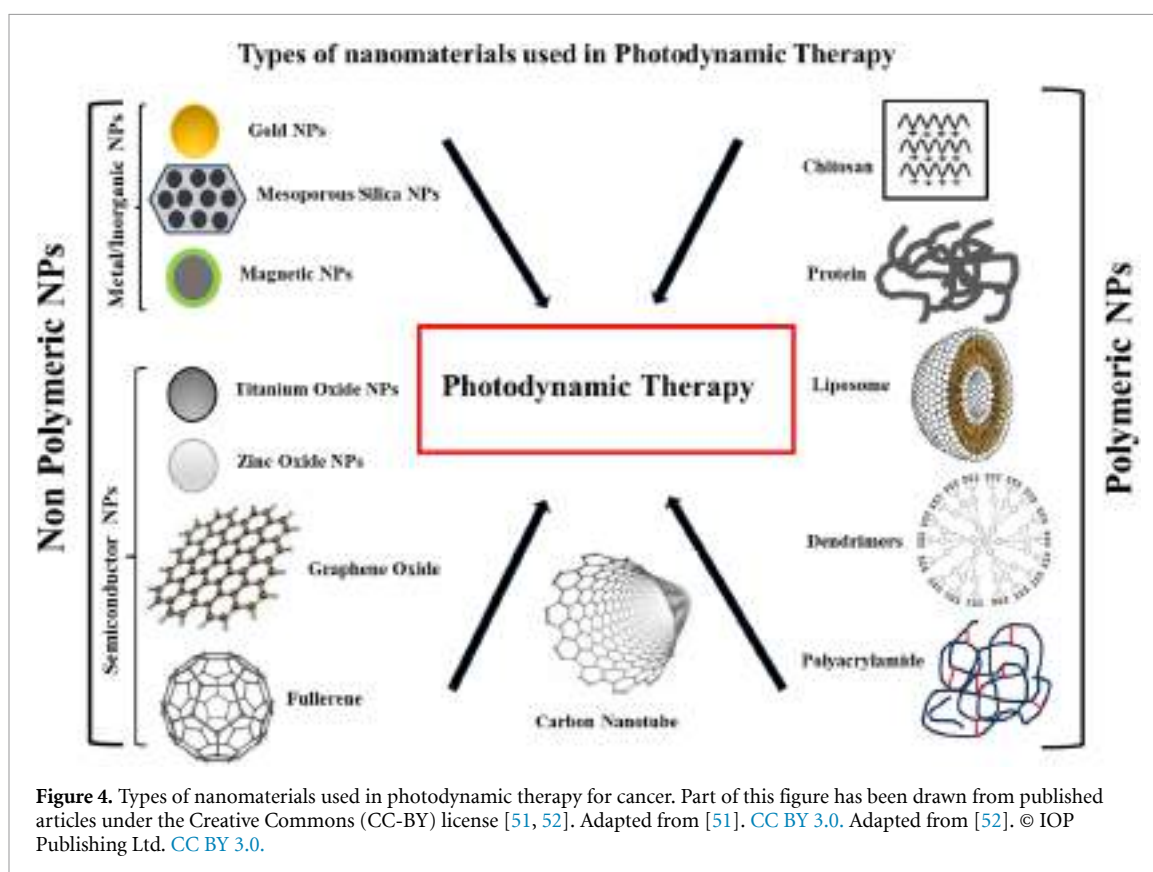
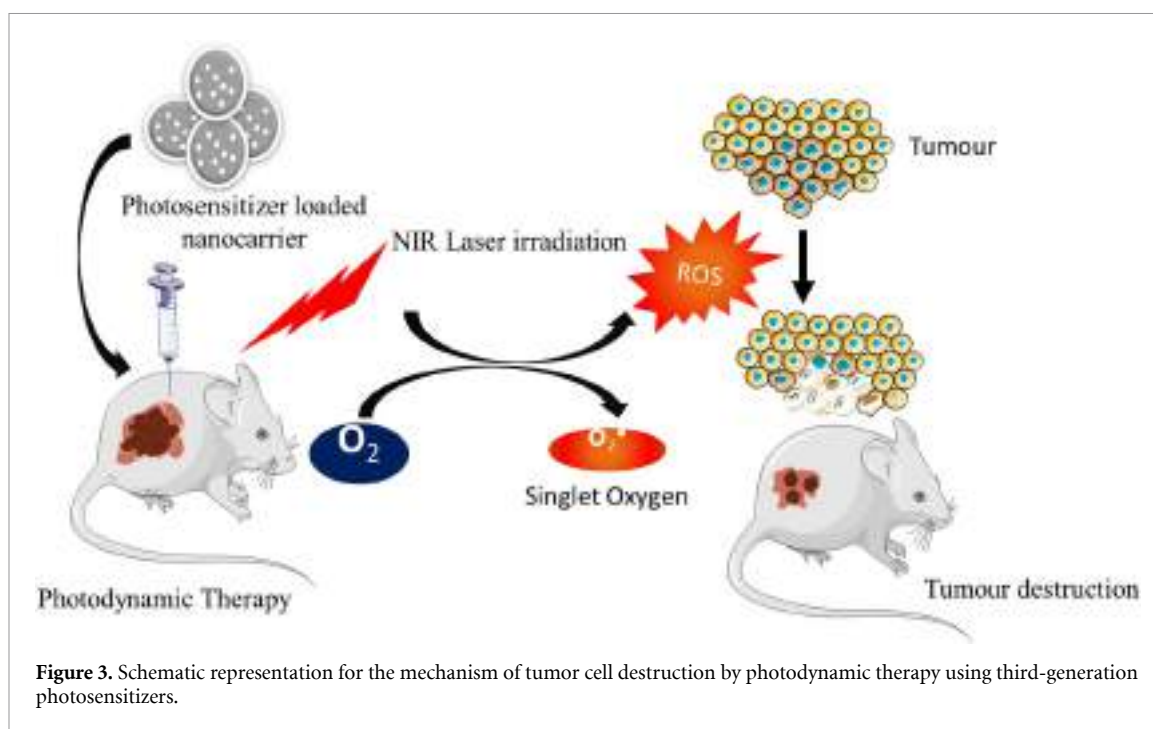
3.1. Non-biodegradable NPs

NPs that are not biodegradable have gained much attention in the area of PDT as potential multimodal theranostic vehicles because of the unique traits they possess, including their optical characteristics, their form, their size, their porosity, and so on. Nonbiodegradable NPs encompass inorganic, metallic, or hybrid NPs.

When light interacts with metallic NPs, a phenomenon known as localized surface plasmon resonance (LSPR) occurs in which the free electrons in the metal collectively oscillate at a particular frequency [53]. The local electromagnetic field around the NP may be strengthened by this oscillation, increasing light scattering and absorption. Even though PSs themselves have relatively low absorption at the desired wavelength, they can effectively absorb the

Table 1. List of photosensitizers clinically approved or under trial for PDT applications in cancer.

Generic name/trade name	Chemical compound	Approved or in trail	Cancer types	References
Clinically approved drug				
(Photofrin®)	Porfimer sodium porphyrin	World wide	PDT of esophageal cancer, lung adenocarcinoma, endobronchial cancer, gastric and recurrent bladder cancers	[30]
Levulan	5-Aminolevulinic acid	Worldwide	PDT of skin, bladder, brain, and esophagus cancers	[31]
Cysview®	Hexaminolevulinate (HAL)	EMEA & USA	PDT of skin and bladder cancer	[32]
Metvix®	Methyl ALA ester (MAL)	USA, Europe	PDT of actinic keratosis and basal cell carcinoma (BCC)	[33]
Laserphyrin®	N-aspartyl choline E6	Japan	PDT of early centrally located lung cancer	[34]
Redaporfin®	Bacteriochlorin	USA	PDT of biliary tract cancer	[35]
Photogem®	Porphyrin	Russia	PDT of BCC	[36]
Photosens®	Aluminum phthalocyanine tetrasulfonate	Russia	PDT of breast, lung, stomach, and skin cancers	[37]
Photolon®	Chlorin E6	Belarus, Russia, Kazakhstan, Ukraine	PDT of skin melanoma and mucosal malignancy	[38]
Photochlor®	2-(1-Hexyloxyethyl)-2-devinyl pyropheophorbide-a (HPPH)	USA	PDT of BCC, head and neck cancer, and lung cancer	[39]
In clinical trail				
Verteporfin®	Chlorin	Approved in China and Norway, trial in the UK	PDT of BCC, lung and skin cancers	[40]
Temoporfin (Foscan®)	Chlorin	Approved in Europe, trial in USA	PDT of advanced head and neck cancer, lung, brain, skin, and bile duct cancers	[41]
Talaporfin®	Chlorin	Approved in Japan, trail in USA	PDT of lung cancer, colorectal neoplasms, liver metastasis, and glioma	[34]
Radachlorin	Chlorin	Belarus, Russia	PDT of skin cancer, nasopharyngeal sarcoma	[42]
Purlytin	Tin ethyl etiopurpurin	USA	PDT of metastatic breast cancer	[43]
Padoporfin (TOOKAD)	Palladium-bacteriopheophorbide	USA	PDT of prostate cancer Phase II and III	[44]
Motexafin lutetium (Lutex)	Texaphyrin	USA	PDT of breast cancer	[45]



enhanced electromagnetic field when placed close to plasmonic NPs. This enhanced light absorption improves the chances that PSs will capture photons, which results in more effective photosensitizing molecule excitation. Table 2 represents different non-polymeric NPs in PDT of cancers.

3.1.1. Gold nanoparticles (AuNPs)

AuNPs have played a significant role in the advancement of a synergistic hyperthermia-phototherapy technique because of their surface plasmon resonance (SPR) feature, their capacity to convert photoenergies into thermal energy for PDT applications, and their

Table 2. List of different types of nonpolymeric nanoparticles and photosensitizers for photodynamic therapy in cancers.

Nonpolymeric nanoparticles	Photosensitizers	Cancers	Light wavelength/intensity	References
AuNPs	Chlorophyll b (Chl b)	Human breast carcinoma cell line and liver carcinoma cell line (MCF7 & HepG2)	650 nm/15 mW cm ⁻²	[54]
MSN	BODIPY	Human cervical cancer cell line (HeLa)	455 nm, 518 nm and 655 nm/10–15 J cm ⁻²	[55]
	Methylene blue	Breast cancer	660 nm/15 mW cm ⁻²	[56]
SPION	Protoporphyrin IX	Mouse mammary carcinoma cell line (4T1)	632 ± 3 nm/5 mW cm ⁻²	[57]
TiO ₂ NPs	Porphyrin	Human breast carcinoma cell line MCF7	980 nm/0.72 W cm ⁻²	[58]
	Phthalocyanine	HeLa xenograft tumor model	420–800 nm/0.25 W cm ⁻²	[59]
SWCNT	Chlorin e6	Mouse squamous cancer cell line (SCC-7)	630 nm/0.15 W cm ⁻² 808 nm/1 W cm ⁻²	[60]
MWCNT	m-tetrahydroxyphenylchlorin	Ovarian cancer cell line (SKOV3)	650 nm/125 mW cm ⁻² (for PDT) 808 nm/2.3 W cm ⁻² (for PTT)	[61]
GO NPs	Tetraphenylethylene-Red	Bladder cancer cell line (UMUC3)	450 nm/200 mW cm ⁻²	[62]
rGO NPs	Manganese dioxide (MnO ₂)	Human cervical cancer cell line (HeLa)	980 nm/0.4 W cm ⁻²	[63]
C60 Fullerene	Black Phosphorous	Mouse mammary tumor cells (4T1)	650 nm/0.5 W cm ⁻²	[64]
	Tirapazamine (TPZ)	Cancer cell	500 nm	[65]

enzyme mimetic activity [66]. Based on these properties, a metal nano-organic framework was developed, where AuNPs act as catalysts like nano enzymes and the PS chlorin e6 is encapsulated to mitigate tumor hypoxia and reinforces PDT under 660 nm laser irradiation. This nano-delivery platform is stable in blood circulation and can easily penetrate and accumulate in tumors [66]. Similarly, in another study, AuNPs conjugated with 5-ALA showed enhanced PDT in cutaneous squamous cell carcinoma under 621 nm irradiation using LED for 1.5 h [67]. It was observed that 5-ALA-AuNPs not only suppressed cancer cell viability but also increased cell apoptosis and produced more singlet oxygen compared to PDT with 5-ALA alone [67]. In addition, to improve the PS's excitation effectiveness, LSPRs surrounding AuNPs may be utilized. Singlet oxygen generation in several AuNP morphologies has been investigated [68]. These include spherical AuNPs with hollow structures, gold nanocages (AuNCs), gold nanorods (AuNRs), and gold nanospheres [68].

As an optical contrast agent, AuNRs were used by Kuo *et al* to kill A549 cancer cells [69]. The cancer cells were exposed to PDT and hyperthermia simultaneously after their treatment with AuNR conjugated PS indocyanine green (ICG) under an 808 nm NIR laser for 30 s to 3 min. The results showed that the combined approach successfully eliminated cancer cells when compared to PDT or photothermal treatment (PTT) alone [70]. On the other hand, Wang and Lu hypothesized that coordinating an early-phase PDT impact with a late-phase PTT effect would boost the synergistic therapeutic efficacy of AuNPs [71]. To do this, they conjugated Ce6 molecules into polyethylene glycol (PEG) chains to create PEGylated AuNRs, which they evaluated in breast cancer cells *in vitro* and a xenograft model in mice using MDA-MB-435 [71]. After 4 h of intratumoral delivery of the nanoconjugates, researchers used a 671 nm laser (1.0 W cm⁻²) to treat the tumor for 6 min. Tumor volume was significantly reduced by laser therapy with Ce6-loaded PEGylated AuNRs compared to the respective control groups [71]. This

research proved that the combinatorial method of PDT/PTT of AuNPs is more effective against cancer. A pH-stimulus-responsive drug delivery system based on chitosan-coated AuNPs was developed by Zhang *et al* [72]. This system too has applications for both PDT and PTT [72]. Due to the SPR absorption in the visible region and its nonlinear features, PTT using gold nanospheres can be accomplished using pulsed or continuous wave lasers in the near-infrared (NIR) and visible (Vis) wavelength spectrums [73–75].

3.1.2. Silica NPs (SNPs)

Different SNP varieties, including organically modified silica, mesoporous silica NPs (MSNPs), and Stöber SNPs, have recently been investigated as PDT vectors. This is because SNPs tend to be chemically inactive, have a porous structure that does not grow or change when the pH changes, and have a clear matrix that lets light in and out. They are very useful and can be made using a wide range of ingredients and easy-to-use synthesis methods. Changes can be made to the NPs' density, ability to spread out, size, and shape. Their surfaces can also be changed by several functional chemicals, polymers like PEG, or biomolecules that target cancer cells in particular. In an investigation, Cornell prime dots (C' dots), which are extremely tiny PEGylated fluorescent core-shell SNPs, were employed to provide a potential targeted platform for PDT usage in oncology [76]. MSNPs are better for delivering drugs because they have a large surface area and a high pore volume that can be reached [77]. Spherical and rod-shaped MSNPs were created to be used as third-generation PSs in a trial on the bladder cancer model using UM-UC-3 and HT-1376 cell lines. Cells were exposed to white light at 8.4 mW cm^{-2} for 40 min [78].

To target cancer cells precisely, MSN was functionalized by a biomolecule that can bind to cancer cells. The absorption of the NPs by receptors would be enhanced if the particles were functionalized to target certain receptors that are overexpressed on the surface of cancer cells in many malignancies. Based on this idea a unique MSN was made where the water-soluble PS and cancer cell-targeting mannose covalently attached to the mesoporous silica matrix for PDT application in MDA-MB 231 breast cancer cells. Results showed that without irradiation MSN conjugated with mannose and PS had only 19% cytotoxicity but when cells were irradiated under 630–680 nm NIR exposure at 6 mW cm^{-2} for 40 min 99% cell death occurred [79]. On the other hand, tests on nude tumor-bearing mice were used to assess *in vivo* biodistribution of protoporphyrin IX (PpIX)-silica NPs loaded with the DID (dioctadecyl tetramethyl indodicarbocyanine chloro benzene) tracer [80]. Up to 24 h after the NPs' tail vein injection, photographs of the biodistribution were taken. The three cancer

models under research (HCT 116, A 549, and glioblastoma) showed significant tumor uptake of PpIX-silica NPs with good phototoxicity under 630 nm NIR irradiation at 4 mW cm^{-2} , but the peak accumulations occurred at different times: 2 h for glioblastoma models, 16 h for A549, and 20 h for HCT 116 models. Other types of SNPs have been used to encase PS in PDT [80]. In another report, silica nanospheres with a 130 nm diameter that are hollow and porous were synthesized [81]. The NPs were created by carefully hydrolyzing N-(b-aminoethyl)-a-aminopropyl triethoxysilane under the influence of ammonia. Hypocrellin A was not surface adsorbing but rather embedded, according to fluorescence quenching experiments. It was found that the particles have high thermal and light stability. These SNPs were efficiently absorbed by HeLa cancer cells and had higher PDT efficacy than hypocretin A.

3.1.3. Magnetic NPs

Out of all nanomaterials and NPs, superparamagnetic iron oxide NPs (SPIONs) are the ones that have been studied most profoundly in combination with PDT [82]. In a study, iron oxide (Fe_3O_4) NPs, or MNPs, were conjugated with Zn phthalocyanine derivatives. At first folic acid (FA) and amine-functionalized magnetic NPs were covalently linked to Complexes 1 (Zn mono cinnamic acid phthalocyanine) and 2 (Zn mono carboxyphenoxy phthalocyanine), respectively [83]. Next, they were evaluated in the human breast carcinoma cell line MCF7 for enhanced PDT at a fixed irradiation dosimetry of 170 J cm^{-2} at 680 nm. These complexes exert significant singlet oxygen generation and better bioavailability and toxicity on MCF7 cells [83]. Huo *et al* synthesized iron oxide (Fe_3O_4) NPs in the presence of triphenylphosphine (TPP)-grafted dextran. Here $\text{Fe}^{2+}/\text{Fe}^{3+}$ ions have a magnetic resonance imaging (MRI) effect [84]. Next, the PSs protoporphyrin IX (PpIX) and glutathione (GSH)-responsive mPEG-ss-COOH are grafted on $\text{Fe}_3\text{O}_4@\text{Dex-TPP}$ NPs to form $\text{Fe}_3\text{O}_4@\text{Dex/TPP/PpIX/ss-mPEG}$ NPs [84]. After internalization, these nano platforms increase the oxygen concentration in tumor cells by the Fenton reaction and produce ROS around the mitochondrial surface under illumination with a 637 nm laser which leads to disruption of mitochondrial membrane permeability. Therefore, this nano platform can serve as a Fenton reaction-assisted PDT for tumor therapeutic efficacy [83, 84]. In another study, a magnetic core and silica layer were combined to create hybrid nanomaterials. A single or double silica coating was applied for the synthesis of SPIONs. Following its entrapment in the silica layer, the PS molecule methyl blue decomposed on the surface of SPIONs. Upon exposure to light of a visible wavelength ($\lambda = 532 \text{ nm}$ or $\lambda = 633 \text{ nm}$), this hybrid

nanomaterial successfully generates singlet oxygen and highlights the potential use of MNPs in PDT [85]. The use of ferroptosis inducers in ferroptosis therapy to cause lethal lipid peroxidation and kill tumor cells is an intriguing option for the administration of chemotherapy for cancer. Chen *et al* created a NP-driven system where ferric oxide (Fe_3O_4) and chlorin E6 (Ce6) are combined in polylactic-co-glycolic acid to create a potent ferroptosis-photodynamic anticancer treatment [86]. The Fe_3O_4 -PLGA-Ce6 NP is capable of breaking down in the acidic TME, releasing Ce6, ferrous (Fe^{+2}), and ferric ions (Fe^{+3}). The Fenton reaction may be carried out by extracellular hydrogen peroxide (H_2O_2) and release ferrous and ferric ions to create hydroxyl radicals ($\text{OH}\cdot$) and induce ferroptosis in cancer cells [87]. When exposed to laser light under 660 nm, 0.5 W cm^{-2} for 3 min, the discharge of Ce6 may promote the production and accumulation of ROS to provide PDT that can improve ferroptosis in 4T1 breast cancer cells [87]. Additionally, this Fe_3O_4 -PLGA-Ce6 nanosystem has good MRI characteristics, extremely effective anticancer activity, and high *in vivo* biocompatibility [87].

3.2. Semiconductor NPs

In the present, semiconductor NPs are also used as PDT PSs. The gap between the valence and conduction bands should be filled by stimulating light energy. The energy of excitation can be transferred to an organic PS or molecules of oxygen in their ground state using a fluorescence resonance energy transfer mechanism.

3.2.1. Titanium dioxide NPs

Titanium dioxide (TiO_2) is an oxide of titanium that is found in nature. It is also called titania. TiO_2 is used in many different ways, such as photodegradation, photocatalysis, cleaning up the environment, dividing water for hydrogen fuel, reducing CO_2 , making surfaces that clean themselves, electrochromic gadgets, sensors, and cheap solar cells. TiO_2 has lately been thought of as a possible photosensitizing compound for PDT due to its low toxicity, biochemical inertness, notable biocompatibility, and unusual photocatalytic properties [88]. Photoinduced hole-electron pairs are made when UV radiation with higher energy than the band gap of TiO_2 excites electrons in TiO_2 's valence band. The strong reduction and oxidation characteristics of these photoinduced electrons and holes allow them to interrelate with nearby oxygen and water molecules to produce ROS [89]. Based on these properties, TiO_2 NPs were utilized for PDT of cancers. The survival of human cervical cancer cells (HeLa) was reduced by TiO_2 NPs upon solar and ultraviolet (UV) irradiation [89]. When these TiO_2 nanocrystals were doped with metal (cobalt) and non-metal (nitrogen) the photoactivation of doped- TiO_2 NPs was significantly enhanced

in the Vis/NIR region [89]. However, these nanocrystals were not significantly cytotoxic compared to PEGylated undoped- TiO_2 . Therefore, this study showed that water-soluble PEGylated TiO_2 NPs may be a good candidate for the PDT of cervical cancer cells [89]. Afterward, multiple cell lines of human carcinoma, including monocytic leukemia cells (U937), colon carcinoma cells (LS-174-t), bladder cancer cells (T24), adenocarcinoma cells (SPC-A1), glioma cells (U87), and breast carcinoma cells (MDA-MB-468, MCF-7), were investigated to discover the accurate mechanism of TiO_2 NPs' UV-induced phototoxic effect [90]. TiO_2 NPs have only rarely been used *in vivo* for PDT applications. This is because TiO_2 is insoluble and forms aggregates in the physiological environment; as a result, it is easily recognized by cells and removed from circulation, which in turn reduces its accumulation in the tumor.

3.2.2. Zinc oxide NPs

ZnO has a similar photocatalytic activity and band gap energy (3.2 eV) as TiO_2 . It has been established that ZnO quantum dots, which have an average diameter of 11.6 nm, produce singlet oxygen as well as other forms of ROS when exposed to blue (400–500 nm) light [91]. There was no triplet signal in the ZnO samples that had not been exposed to radiation. Considering application in combination photothermal theory (PTT) as well as PDT for cancer, Vasuki and Manimekalai investigated the anticancer effect of ternary modified ZnO nanocomposites with NIR absorbance on the MCF-7 breast carcinoma cell line [92]. The nanocomposites showed significant cytotoxicity against cancer cells, and therefore, they can be used for combined cancer therapy [92]. In another study, it was shown that ZnO nanorods (NRs) can be used as a PS and biomarker for PDT on cervical cancer cell lines. This is because ZnO NRs are a source of NIR light for deep tissue penetration and have more surface plasmon resonance light absorption than ZnO NPs [93]. Through the use of laser scanning confocal microscopy and fluorescence spectroscopy with excitation at 488 and 514 nm wavelengths, it was possible to analyze the fluorescence and light activation of ZnO NRs in cancer cells. The fluorescence of the ZnO NRs was conjugated with the well-known PDT PS 5-ALA, and the results demonstrated that ZnO NRs are potent tumor necrosis candidates under the right light activation and are a good candidate for PDT of malignancies [93]. According to studies, Ultraviolet A radiation (20 mW cm^2 for 15 min) combined with ZnO NP doses of 0.2 and 2 g ml^{-1} can effectively destroy cancer cells by causing late apoptosis and necrosis. In this aspect, Hariharan *et al* synthesized PEGylated ZnO NPs conjugated with doxorubicin (DOX), which generates ROS under UV irradiation for potential antitumor activity [94]. It has also been reported that

ROS are produced when light energy is absorbed by PEG-functionalized Ag-doped semiconductor NPs of ZnO and transferred to water and molecular oxygen molecules in the biological environment [95, 96].

3.3. Carbon nanomaterials

There are three different types of carbon nanomaterials, such as zero-dimensional (0D)–structure fullerene, one-dimensional (1D) carbon nanotubes (CNTs), and two-dimensional (2D) graphene. Carbon nanomaterials are widely used in electronic and electrical fields, biosensors, medical treatments, environmental applications, etc. Due to their unique structure and large surface area, carbon nanomaterials, especially CNTs and graphene, are widely used in drug delivery for cancer therapy [97].

3.3.1. Carbon nanotubes (CNTs)

Graphene sheets roll up CNTs into hollow cylindrical structures with both ends open. The carbon atoms are exclusively organized in rings similar to those found in benzene. The armchair, zigzag, and chiral structural representations of CNT include allotropic forms of both sp² planar and sp³ cubic [98]. CNTs are classified as single-walled CNTs (SWCNTs), which have an inner diameter of 1–3 nm and an outer diameter of 2–100 nm, and multi-walled CNTs (MWCNTs), which have an inner diameter of 1–3 nm and an outer diameter ranging from 0.2 to several micrometers, respectively, based on the layer formation [97]. CNTs play a special function as nanocarriers for medicines, polymers, PSs, and particular ligands that target siRNA and DNA [97]. SWCNTs penetrate the cells directly, whereas MWCNTs enter through the endocytosis pathway. Based on this property, CNTs are widely used in cancer therapy as novel drug carriers. To treat cancer effectively and specifically, researchers are now concentrating on combination therapies using CNTs and PDT. To improve solubility and bioavailability and to target only cancer cells, PSs are combined with CNTs. For efficient PDT of colon cancer cells, Sundaram and Abrahamse created SWCNTs combined with hyaluronic acid (HA) and chlorin e6 (Ce6) [98]. This nanocomposite induces morphological changes in colon cancer cells using PDT at a fluence of 5 J cm⁻² and 10 J cm⁻² after 24 h followed by LDH cytotoxicity and cell death [98].

3.3.2. Graphene, graphene oxide (GO), and reduced graphene oxide (rGO) NPs

A 2D network of carbon atoms with sp² hybridization makes up graphene. Graphene undergoes an oxidation-reduction process to produce rGO and GO. The finding that graphene can be used as PSs in PDT and effectively kill cancer cells has been demonstrated in several studies [99, 100]. Considering its capacity to absorb light in the NIR range, graphene has been the subject of extensive *in vivo* and *in vitro* studies into

its potential use in cancer imaging and phototherapy [101, 102]. Hosseinzadeh *et al* developed a nanocomposite for PDT using GO and MB and evaluated its cytotoxicity on the triple-negative breast cancer cell line MDA-MB-231 by MTT assay [103]. In dark conditions cell viability was reduced by up to 60% for the PS using a concentration of 20 µg ml⁻¹; however, under irradiation with a red LED light of 630 nm for 30 min, a reduction of up to 80% was obtained using the same dose of PS [103]. This is because, in the presence of red LED light, MB-GO nanocomposites could penetrate more inside the tumor cells and exert toxicity. rGO NPs have also been used in PDT for cancer in the last few years. To test the photodynamic activity in the human breast cancer cell line MCF7, Vinothini and coworkers (2020) created an rGO-based nanocomposite with magnetic NPs (Fe₃O₄), camptothecin, 4-hydroxycoumarin, and allylamine [104]. The rGO hybrid exerts cytotoxicity by producing ROS against MCF7 cells under 365 nm of laser irradiation of 20 mW cm⁻² for 3 min [104].

3.3.3. Fullerenes

Fullerenes (also known as bucky balls) are closed convex polyhedra composed of an even number -of carbon nanostructures with a high triplet yield, and a high molar absorption coefficient and are made of sp² hybridized carbon atoms. Fullerenes have multiple types but the most renowned forms are C₆₀, C₇₀, etc because of their important uses. Fullerenes are particularly effective at creating photoexcited singlet oxygen (¹O₂) in organic solvents or hydrophobic environments, but in an aqueous environment, they convert to type 1 photochemistry and produce HO• and superoxide anions [105]. Although pristine C₆₀ fullerenes are insoluble in water, the cage can be easily functionalized with polar groups such as carboxylic acids and quaternary amino groups to increase solubility and biological compatibility [105]. Various pristine C₆₀ fullerenes as well as their functionalized derivatives, have been extensively used as PSs for *in vitro* cancer cell killing [106]. Fullerene C₇₀ is also used in PDT of cancers due to its extended π system [107]. Guan and his team created fullerene C₇₀ nanovesicles (abbreviated FCNVs) using C₇₀-oligo ethylene glycol-Ce6 and comprised of both hydrophilic and hydrophobic components [46]. These constructs efficiently absorb light in the NIR region within 660 nm (20 mW cm⁻²) and exert strong anticancer activity in the lung carcinoma cell line A549 [46]. Fullerene C₆₀ dyads are also reported for PDT in cancers. In one study four novel glucose-BODIPY-fullerene dyads with styryl units were created. The organic detergent Tween 80 helps to produce nanomicelles, which measure 14–17 nm [108]. When exposed to UV light, glucose-BODIPY-fullerene nanomicelles (14–17 nm) effectively produce singlet oxygen and

ROS [108]. K562 human chronic myelogenous leukemia suspension cells were used to examine the molecules' *in vitro* anti-cancer efficacy under the influence of light and the absence of light for PDT [108].

Porphyrin-fullerene dyads have gained increasing interest due to their interesting optoelectronic properties and their potential applications in PDT. These dyads are created by joining organic molecules that donate electrons, like porphyrins, with molecules that accept them, like fullerene derivatives [109]. The efficient intramolecular photoinduced charge separation that the donor-acceptor dyads can undergo has sparked extensive research on the practical use of these materials. Additionally, it has been demonstrated that fullerene functions as a quencher, minimizing the photobleaching of the porphyrin component during PDT. A PS's therapeutic efficacy may be diminished due to photobleaching, which is the irreversible destruction of PSs upon exposure to light. In overextended PDT treatment sessions, the fullerene aids in preserving the stability and activity of the PS by quenching the excited states of the porphyrin. In 2021, Vallecorsa *et al* assessed the *in vitro* photoactivity of a porphyrin coupled to a fullerene and four meso-substituted porphyrins. The results suggest that the porphyrin-fullerene dyad TCP-C 604 has potential in PDT application as compared to fullerene dyad alone under 600 nm NIR radiation with a fluence rate between 10 and 220 mJ cm⁻² and the power density 0.5 mW cm⁻² [110]. Although porphyrin-fullerene dyads show great promise in anticancer applications, it is important to note that further study is required to improve their characteristics and guarantee their safety and efficacy in clinical settings.

3.4. Biodegradable NPs

Biodegradable NPs are mainly polymeric NPs. Polymeric NPs are naturally occurring, exhibit greater photodynamic efficacy for tumor killing, and have reduced photosensitivity [111]. Polymeric NP encapsulation of PSs can significantly improve their solubility and dispersibility in a hydrated environment, enhancing their pharmacokinetic properties. Additional paybacks of utilizing biodegradable NPs made of polymers include their capacity to carry a respectable payload of different agents to the tumor while protecting it from early blood leakage and maintaining photoactive agents' and fluorophores' photostability. These agents include therapeutic PS and diagnostic PS. Several types of polymeric NPs have been used for PDT in cancers. Table 3 represents different polymeric NPs and PS in PDT of cancers.

3.4.1. Chitosan

Chitosan is a polymer. It is obtained from chitin, which is usually found in crab and insect shells. It is made up of N-acetyl-glucosamine and glucosamine

repeating units. Chitosan has a positive charge and is unable to dissolve at pH 7, but it dissolves at an acidic pH [122]. The amphiphilic nature of chitosan has promoted them to serve as carriers for hydrophobic anticancer therapeutics [123]. For PDT, the PS was either confined inside the inner core of self-constructed NPs of chitosan or it formed a covalent or ionic connection with chitosan, which was then assembled into a NP. Chitosan NPs (CNPs) can encapsulate protoporphyrin IX (PpIX), a PS, and vitamin B9 (PpIX-B9) and transport it to tumor cell masses for effective PDT [124]. In a different investigation, ICG-loaded hydrophilic sulfhydryl NPs of chitosan (SA-CS-NAC@ICG NPs) were developed by Yang *et al* using a self-assembly and self-crosslinking method for PDT [125]. Traditional PS carriers have drawbacks due to their poor chemical stability, inadequate loading, and single-responsive PS release. These drawbacks are resolved by these unique pH/GSH multi-responsive chitosan NPs. ROS are reduced by the SA-CS-NAC@ICG NPs when exposed to 808 nm laser light. *In vitro* cell experiments verified that these novel NPs had a great capacity for cellular absorption, low toxicity, and effective cancer inhibition [125]. Chitosan NPs with ALA derivatives, such as prodrugs 5-ALA and 8-ALA, have the synergistic effect of combining conventional PDT with electrochemotherapy for the treatment of melanoma cancer [126]. In a different study, a nano-code delivery of chitosan/tripolyphosphate (CS-TPP) was made by combining a PS 5-ALA and methylenetetrahydrofolate dehydrogenase 1-like (MTHFD1L) shRNA for PDT. By triggering apoptosis and producing ROS *in vitro* under 635 nm, 10 J cm⁻², this CS-TPP-(shMTHFD1L-ALA)-PDT demonstrated potent anticancer efficacy in oral squamous cell carcinoma (OSCC) [127].

3.4.2. Albumin

Human serum albumin (HSA) is an acidic, positively charged plasma protein with a wide variety of roles. HSA is a globular, amphoteric protein that maintains its structure between pH 4 and 9 [128]. NPs created using HSA have recently attracted attention as prospective theranostic drug carriers, especially for the administration of lipophilic drugs. Hydrophobic medicines can be transported by HSA-based NPs without the use of potentially hazardous solvents [128]. Additionally, HSA-based NPs can target the tumor by endogenous albumin pathways with massive doses of chemotherapeutic medications and can avoid the problem of the accrual of drug NPs elsewhere in the body. Abraxane® (albumin-bound paclitaxel NPs) is another example of a medication that utilizes HSNP-binding technology. In a medical facility, this technique is employed to provide paclitaxel for the treatment of pancreatic, breast,

Table 3. List of different types of polymeric nanoparticles and photosensitizers for photodynamic therapy in cancers.

Polymeric nanoparticles	Photosensitizers	Cancers	Light wavelength/intensity	Reference
CNPs	Zinc Phthalocyanine	Cutaneous squamous cell carcinoma	660 nm/5 J cm ⁻²	[112]
	Protoporphyrin IX	Adenocarcinoma	635 nm/0.2 W cm ⁻²	[113]
HSA NPs	Indocyanine green	Oral squamous cell carcinoma (OSCC)	808 nm/2 W cm ⁻²	[114]
	Chlorin e6	Bladder cancer	660 nm/0.15 W cm ⁻²	[115]
Gelatin NPs	Zinc phthalocyanine (ZnPc)	Mouse macrophage carcinoma cell line (J774 A-1)	660 nm/0.2 W cm ⁻²	[116]
	Chlorin E6	Mouse mammary tumor model	650 nm/580 mW cm ⁻²	[117]
PAA NPs	Methylene blue	Prostate cancer	630 nm	[118]
Liposomal NPs	HPPH	Triple negative breast cancer	660 nm/50 mW cm ⁻²	[119]
2,2-bis(hydroxymethyl) propionic acid (Bis-MPA) hyperbranched PEG-OH dendrimers	Pyropheophorbide a	Mouse mammary tumor cells (4T1)	660 nm/1 J cm ⁻²	[120]
PAMAM & PEG dendrimers	Chlorin E6 & indocyanine green	Mouse mammary tumor cells (4T1)	660 nm/0.1 W cm ⁻² (for PDT)	[121]

and pulmonary malignancies [128]. For the combined phototherapy and chemotherapy of breast cancer, flexible hollow human serum albumin NPs (HHSAs) were produced and coupled with two distinct DOX therapeutics and the PS chlorin e6 (ce6) [129]. In *in vitro* conditions, it reduces the survival of 4T1 breast cancer cells without irradiation but it has remarkably higher toxicity under 660 nm irradiation. Additionally, these HHSADOX-ce6 NPs lower tumor metastasis *in vivo* [129]. ICG, a NIR fluorescent dye, has demonstrated significant possibilities in cancer PDT and PTT [130]. However this dye has some limitations that make it difficult to use effectively in PDT/PTT, such as the fact that it is insoluble in water, has a brief half-life, and has non-targeting accumulations. This is why Liu *et al* developed PEGylated-HSA-ICG-TAT to penetrate the nucleus of cancerous cells and get around ICG's drawbacks in the treatment of tumors [130]. They demonstrated that compared to free ICG, these ICG-loaded NPs had a greater cellular absorption rate and a stronger PDT/PTT impact. Moreover, these ICG-loaded NPs were easily metabolized in normal mice with no toxicity but in tumor-bearing mice, these NPs showed a significant reduction in tumor growth [130]. A similar NIR dye, IR780, and HSA NPs (HSA@IR780@DTX), which are loaded with docetaxel (DTX), were created for targeted imaging and PTT/PDT together with chemotherapeutic treatment of castration-resistant

prostate cancer [131]. In this study, prostate cancer cells were irradiated with a 1 W cm⁻² 808 nm laser for 2.5 min and produced a large amount of ROS. In another study, a tumor-targeted multifunctional theranostic medication for PTT and PDT applications was made using four therapeutically approved substances: artesunate (Arte), folic acid (FA), HSA, and ICG under a single NIR irradiation. The produced nanocomposites (FA-IHA NPs) displayed good physiological and photo-stability, excellent cellular absorption, and tumor accumulation *in vitro* and *in vivo* [132]. Additionally, when this nanocomposite (FA-IHA NPs) were irradiated under 808 nm NIR (1 W cm⁻²) Arte was released in the tumor cell and showed a chemotherapeutic effect [132]. C086 is a derivative of Curcumin and it is an inhibitor of heat shock protein 90 (HSP90). It has stronger antitumor activity than Curcumin. Based on this property He *et al* developed a C086-loaded HSA NP for PDT against cancer cells [133]. The anti-tumor PDT activity of C086@HSA NPs is applied to the human cervical cancer cell line HeLa. Upon 10 min blue light exposure at 450 nm (5 mW cm⁻²), it was found that C086@HSA NPs caused apoptosis and cell cycle arrest at the S and G2/M phase in HeLa cells. C086@HSA NPs were also tested for *in vivo* anticancer activity employing bright blue light (80 mW cm⁻²) using PDT in a 4T1 tumor-bearing mouse model [133].

3.4.3. Gelatin

Gelatin is a proteinaceous polymer that can be partially hydrolyzed from a pig or bovine collagen. It is a water-soluble macromolecule that is frequently used as a food additive. Gelatin NPs are now applied for PS delivery [134]. For *in vivo* PDT, the hydrophobic PS's water solubility must be increased, and its accumulation in tumor tissue must be increased. So Son *et al* have conjugated choline e6 (Ce6) with gelatin NPs for PDT applications [135]. The resulting conjugates were more water-soluble for an elongated period than hydrophobic Ce6, and upon laser irradiation under 658 nm (0.3 W, 200 J), they could produce singlet oxygen and destroy tumor cells. Additionally, the conjugates displayed an extended presence in the circulatory system and an exceedingly amplified assemblage in tumor tissue *in vivo*. Lee *et al* have developed self-assembled gelatin NPs containing both pheophorbide a (Pba) and thiabendazole (TPZ) to study the synergistic effect of drugs and their efficient delivery in tumor cells *in vivo* [136]. Gelatin polymer chains were coupled with PEG and Pba to create amphiphilic structures for self-assembly in aquatic conditions. These NPs were then loaded with TPZ to create TPZ-Pba-NPs. After laser irradiation at 95.1 J cm^{-2} , the efficacy of combination therapy employing TPZ-Pba-NPs was assessed in SCC7 tumor cells, and it was found that TPZ exerts toxicity in hypoxia. Additionally, in tumor-bearing mice, the *in vivo* therapeutic efficacy of combination therapy using TPZ-Pba-NPs was assessed [136].

3.4.4. Polyester and polyacrylamide NPs

Biopolyesters are biocompatible naturally occurring or synthetic polymers. PLA made from D- and/or L-lactic acid monomers (PLLA, PDLA), poly(-caprolactone), poly(hydroxyalkanoates), and poly(lactic acid with glycolic acid) copolymers (PLGA) are examples of naturally occurring polymers. Poly(orthoesters), poly(-amino esters) (PbAE), and poly(-hydroxy esters) are examples of synthetic polymers. Hydrophobic PLGA or PCL NPs that trap hydrophobic PSs are examples of simple polyester-based NPs produced for PDT applications. When second-generation PSs were coupled with PLGA NPs, they demonstrated good photodynamic activity, tumor-inhibiting activity, improved $^1\text{O}_2$ production, and increased plasma circulation duration. In one work, PLGA NPs were synthesized and conjugated with IR780 PSs for increased PDT against osteosarcoma HOS cells. These constructed NPs induce apoptosis and ferroptosis in HOS cells via excessive accumulation of ROS [137]. Similarly, in another study, Toluidine Blue was coupled as PSs in PLGA NPs (TB@PLGA), and it was proven that

TB@PLGA NPs may trigger apoptosis via a photodynamic mechanism and cause widespread necrosis of tumor cells when exposed to 660 nm laser irradiation. Furthermore, it was discovered that these TB@PLGA NPs have an excellent tumor suppression effect *in vivo* [138]. For increased PDT of malignancies, PLGA NPs are employed for the regulated release of PS MB with a PARP inhibitor, veliparib in a very low concentration [139]. These VMB NPs showed no toxicity in the dark but when they were irradiated with visible light they showed significant toxicity against B16F10-Nex2 cells [139].

PEG is a polymer that is used to conjugate polyester NPs and micelles for drug entrapment in both hydrophobic and hydrophilic environments. PEGylated polyesters, such as PEG-PLGA, PEG-PCL, and PEG-PLA, are used to make a variety of NPs. PEGylated polyesters in nano PDT have been tried as a delivery strategy for hydrophobic PSs by several researchers [111]. Trimethylene carbonate-based monomers were used to create light-responsive polycarbonates (LrPC) and PEGylated LrPC (LrPC-PEG) before being loaded with the PSs 5, 10, 15, and 20-tetrakis(m-hydroxyphenyl)chlorin (mTHPC) [140].

Polymerization of a nanoemulsion matrix yields hydrogel-like nanostructures known as polyacrylamide (PAA) NPs. Biodegradable polyacrylamide NPs have become prevalent in cancer therapeutics such as PDT, fluorescence imaging, and cancer targeting [141]. Both biodegradable and non-biodegradable cross-linkers can be used to produce hydrophilic PAA NPs and can have their surfaces functionalized with targeted ligands. The two simplest approaches for conjugating a PS into PAA NPs are encapsulation and post-loading, and depending on the PS's water solubility, both procedures may have varying effects on PDT activity. When PAA NPs are coupled with hydrophilic PSs like MB and its derivatives, they produce more $^1\text{O}_2$ under 808 nm laser at a power density of 1.5 W cm^{-2} for 2 min and increase cell death [142]. In another work amine-functionalized PAA NPs were loaded with hydrophobic PSs such as HPPH and NIR fluorescent organic dyes (NIRFDs). These NIRFDs can be excited in the first or second NIR windows of tissue optical transparency (NIR-I, $\sim 700\text{--}950 \text{ nm}$ and NIR-II, $\sim 1000\text{--}1350 \text{ nm}$) but the PS HPPH cannot absorb light. The result shows that these nano-shell conjugates produced the most $^1\text{O}_2$ and exhibited the highest phototoxicity *in vitro* and *in vivo* [143]. In an earlier study, tetrasulfonato-aluminum phthalocyanine-entrapped NPs coated with a second porphyrin-based PS and polylysine-bound tetrasulfonato-aluminum phthalocyanine (PCNP-P) were synthesized and were loaded with photodynamic PS. These two polyacrylamide-based NPs produce huge ROS in HT29 cells when

irradiated with 7 J cm^{-2} laser light and have good therapeutic potential [144].

3.4.5. Liposomal NPs

Concentrated phospholipid vesicles known as liposomes have several bilayered membranes composed of lipids derived from either natural or artificial sources. They make ideal therapeutic carriers since they have the unique capacity to store hydrophilic medicines in their aqueous interior and substances that are hydrophobic in their inner layers [145, 146]. Different PS has been used in specific commercial liposomal formulations, including benzo-porphyrin derivative (BPD)-MA, mTHPC, and zinc phthalocyanine (Zn-Pc) [147]. A PS-lipid combination called porphyrin-phospholipid leads to persistent, non-exchangeable inclusion into the liposome bilayer. Liang *et al* used nanoscale (20 nm) iron oxide-loaded porphyrin-grafted NPs of lipid to create a theranostic nano platform ($\text{Fe}_3\text{O}_4\text{@PGL}$ NPs) [148]. These nano platforms generate ROS to kill cancer cells and transfer Fe ions into tumor cells via the Fenton reaction [148]. In a different study, DOX, an effective chemotherapeutic agent, was added to porphyrin-imbedded lipid NPs for cooperative chemo-PDT. PGL-DOX NPs established exceptional cellular absorption, chemo-photodynamic reactions under 650 nm laser (0.2 W cm^{-2} , 10 min), and fluorescent imaging abilities in HeLa and PC3 cell lines. Porphyrin's usual ability to generate ROS with lower irradiation meaningfully blocked tumor growth *in vivo* once it united with the lethal potentials of the anticancer drug DOX [149]. Therefore from these studies, it can be stated that liposomal/lipid NPs can be used in PDT of cancers with suitable PSs.

3.4.6. Dendrimer NPs

Dendrimers have received a considerable amount of interest as PS vectors because of their unique architecture. It contains several functional groups on the surface that can connect various molecules or functional moieties. The size of these molecules and their lipophilicity can be modified to improve cellular absorption and tissue biodistribution. PAMAM dendrimers are the most promising and well-characterized dendrimers. PAMAM dendrimers are used in PDT for the transportation of PS in tumor tissues. They are frequently used as templates for preparing tiny NPs. To create self-assembled NPs, PAMAM dendrimers are treated with poly(ethylene glycol) cholesterol. The hydrophobic core of the NPs is enclosed with PS chlorin e6 (Ce6) and MnO_2 to increase the PDT. When exposed to a 670 nm laser, the developed DPCCM NPs act like enzymes that can catalyze the oxidation of H_2O_2 to produce O_2 and exert an

enhanced PDT effect [150]. Kojima *et al* used PEG-attached dendrimers to create nanocapsules with PSs for use in PDT [151]. They created two PEG-attached dendrimers from poly(amidoamine) (PEG-PAMAM) and poly(propylene imine) (PEG-PPI) and employed two PSs, RB and protoporphyrin IX (PpIX) at the same time. When compared to free PpIX, the combination of PpIX with PEG-PPI demonstrated efficient cytotoxicity by producing high levels of singlet oxygen under 530 nm light using a Xe lamp (400 W m^{-2}) and efficiently delivering this singlet oxygen to mitochondria [151]. Along with PAMAM dendrimers, other dendrimers like PPI, ALA, and anionic phosphorous dendrimers are also studied for PDT applications [152].

3.5. Nanoformulations of tetrapyrrole

To carry the tetrapyrrole-based PS for drug delivery systems, many nanocarriers have been created [153]. Bacteriochlorins are made up of tetrapyrrole, which is made up of two pyrrole and two reduced pyrrole units joined together by methine connections, with the two reduced pyrroles positioned diagonally across from one another [153]. Gomes *et al* investigated bacteriochlorophylls-loaded NPs synthesized by solvent evaporation. It was observed that this approach achieved 69% encapsulation [154]. It was also found that ROS generation was also enhanced and thus therapeutic efficacy [154]. Pantiushenko *et al* developed a novel nanomaterial composed of non-sulfur bacteriochlorophylls and their derivatives using AuNPs [155]. Gold NPs loaded with PS had a longer circulation time and better tumor absorption than free PSs due to nonspecific passive targeting. Ostroverkhov *et al* investigated the immobilization of a PS based on bacteriochlorin on a magnetic NP [156]. These bacteriochlorin-loaded magnetic NPs demonstrated cancer cell localization during *in vitro* testing, followed by photoinduced toxicity.

4. Mechanism associated with the development of drug resistance in cancer cells

Until now, the most prevalent cancer therapies are chemotherapy, which includes one or combinational drugs as part of the conventional treatment regime. These drugs either slow down or stop cancer cells from proliferating, infiltrating, and spreading [157]. However, a significant problem in clinical oncology is the effectiveness of chemotherapy, as drugs may fail to eliminate cancer cells for several reasons. Many times, cancer patients exhibit either inherent or acquired chemoresistance i.e., failing to respond to anticancer medications [158]. As per statistical data, the development of chemo/drug resistance is responsible

for more than 90% of cancer patients' deaths [159]. Because of the nearly universal prevalence of resistance to single medicines, several medications are typically employed [160]. Cancer cells can become resistant to multiple anticancer drugs depending on the mode of action of the drug and its structures. This effect is known as MDR and this makes the treatment strategy very difficult for clinicians. This challenge is particularly significant because most of the chemotherapeutic drugs only have a small therapeutic window and a narrow range of doses that will have a beneficial effect on the undesirable side effects [160]. Many individual factors could contribute to the development of MDR such as tumor-related, host-related, and host–tumor interactions as discussed below (figure 5).

4.1. Factors related to host

4.1.1. Drug resistance due to genetic variation

From several clinical studies on identifying molecular markers and studying genetic patterns in these years, it has been well established that genetic variability in patients accounts for a major difference in drug response among individuals. At the same time, gene variations in cancer cells also play an important role and are responsible for drug resistance to chemotherapy. Phase I drug metabolizing enzymes inactivate various chemotherapeutic drugs by hydrolysis, reduction, and oxidation [161]. Humanoid cytochrome P450 (CYP) consists of more than 50 enzymes that play a role in inactivation via the metabolism of Phase I drugs among which CYP2D6 is one of the key enzymes. Tamoxifen which is a commonly used chemotherapeutic drug for breast cancer is metabolized by CYP2D6 to produce endoxifen and 4-hydroxytamoxifen which are therapeutically ineffective and thus lose their therapeutic activity against breast cancer [162]. From research findings, it is evident that patients with a combination of some non-functional allele could decrease the metabolism of the breast cancer chemotherapeutic drug tamoxifen which could reduce the chances of disease-free survival (DFS) or recurrence-free survival and thus lowers the therapeutic efficacy [162]. Plasma membrane transporters are essential for both the absorption and efflux of several chemotherapeutic medicines, and they are closely related to drug resistance. Most drug's intracellular concentration is controlled by the big solute carrier (SLC) family of membrane transporters, which affects drug absorption. Contrarily, drug efflux is caused by the ATP-binding cassette (ABC) superfamily, and some of its members also take part in intracellular drug accumulation. These ABC transporter proteins which are controlled by ABCC1, ABCB1, or P-glycoprotein (p-gp) play a significant role in the development of drug resistance as they determine the drug distribution and

absorption by limiting the passage of drugs across the cell membranes [162]. Among different drug efflux proteins, ABCB1 has shown the highest clinical significance for the development of drug resistance from patient samples.

Many chemotherapy drugs, including platinum compounds, have cytotoxic effects that are caused by the production of various DNA adducts [163]. These adducts cause intra and inter-strand breaks, which stop DNA replication and cause cell death. However, various DNA damage repair mechanisms, such as nucleotide-excision repair and base-excision repair (BER), are available to cells to fix these defects. The clinical effectiveness of various medications, including cisplatin (CP), depends on the cancer cell's capacity to repair DNA damage caused by chemotherapy drugs. One of the members of the BER protein family 'XRCC1' can detect and repair DNA damage induced by CP [164]. As a consequence, cancer patients having upregulation of XRCC1 have shown decreased therapeutic responses towards CP and drug unresponsiveness. However, there are few cases of clinical studies where there is no connection observed between CP resistance and XRCC1 or genotypic relevance [164, 165]. In conclusion, several genetic markers have been studied for biomarkers of drug resistance in cancers, but the findings suggest that although some of them are linked with genetic variants but not all could be linked to it. Additionally, there must be other factors that have a key role in the development of drug resistance.

4.1.2. Drug interactions with another drug

Drug effectiveness or side effects are observed in case of parallel uptake of another medication which is linked to the pharmacodynamic and pharmacokinetic effects. Since cancer patients frequently take multiple medications, including anticancer medications, supportive care medications (such as antibiotics, anxiety relievers, gastrointestinal acid-reducing agents, and cholesterol-lowering statins), and other medications, they are particularly vulnerable to show these drugs non-responsiveness due to their inactivation by other [166]. Multiple studies have shown that cancer patients taking intravenous or oral administration of chemotherapy have shown drug inactivation due to another drug which is also a category of drug resistance or unresponsiveness observed [166–168]. Proton pump inhibitors (PPIs) are the most often prescribed stomach acid-reducing medications, and it is known that many cancer patients take them to treat their gastroesophageal reflux disease and dyspepsia symptoms. Tyrosine kinase inhibitors (TKIs) have poor bioavailability and solubility when taken orally. The uptake of TKIs largely depends on the pH and it decreases as stomach pH is raised by PPIs. Thus, PPIs have a role to play in

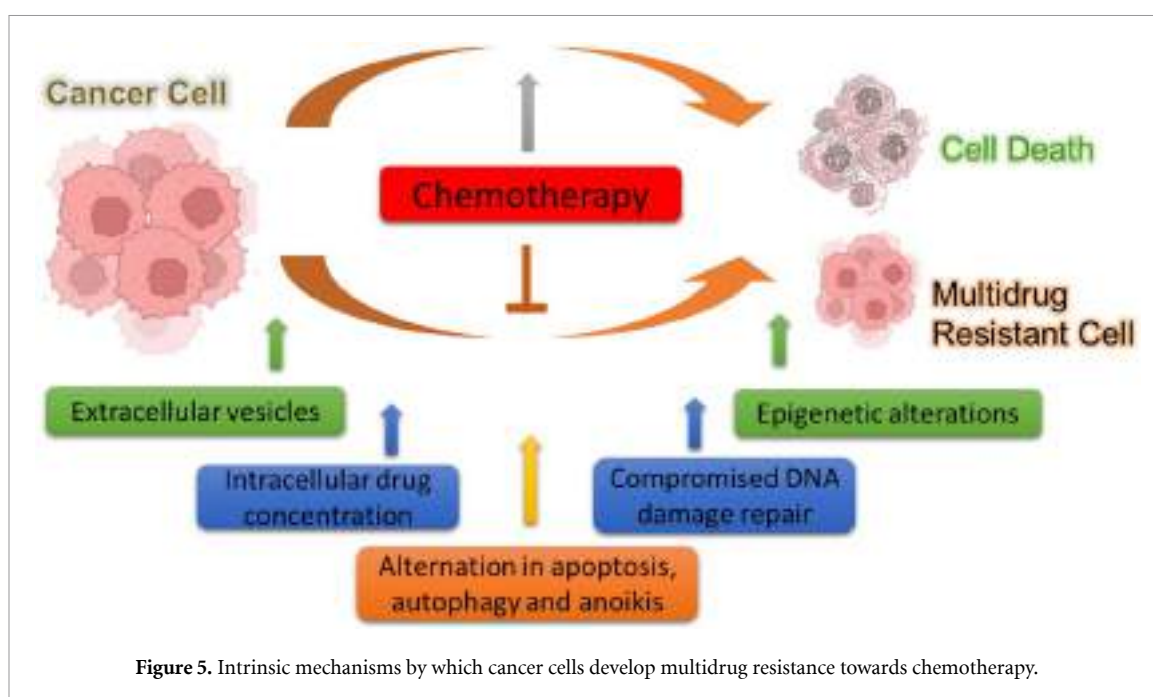


Figure 5. Intrinsic mechanisms by which cancer cells develop multidrug resistance towards chemotherapy.

reduced uptake and efficacy of TKIs class of drugs [169]. On the other hand, uptake of the TKIs is observed to enhance when taken alongside acidic beverages.

Although the gastrointestinal tract may be a site for drug absorption, the liver is the main location for drug biotransformation. Drugs that can activate human cytochrome P450 (CYPs) through higher transcription can lower the blood concentration of the induced enzymes' drug substrates. On the other hand, CYP inhibitors reduce the activity of a pro-drug that is converted into a pharmacologically active drug. Additionally, several CYP stimulants or inhibiting agents are also ABC transporter stimulants or inhibiting agents. In summary, DDIs should be crucially considered for cancer patients receiving medications as this leads to drug resistance and decreased effectiveness.

4.2. Factors related to tumors

4.2.1. Intracellular drug concentrations

To overcome drug resistance in cancers, escalating therapeutic drug dosage, and repeated administration has been major factor in the efficacy of present cancer therapies. Anticancer medications must be proactive and have high bioavailability in the tumor tissues to be therapeutically effective. Drugs that have targets within the cell must penetrate the plasma membrane to reach tumor cells [170]. Early research on drug resistance suggested that dysfunctional plasma membrane transporter proteins cause the inability of drug accumulation inside cells and this leads to drug resistance [171]. As discussed previously, cancer cells with drug resistance have an active efflux pump that ejects out hydrophobic molecules or metabolites including the

drugs through the plasma membrane which leads to decreased intracellular concentration of the drug and low therapeutic effect. One such drug efflux pump is the ABC transporter proteins [172, 173]. Cells exhibit lower intracellular drug concentration during the development of drug resistance and malignant transformation, which is primarily attained by decreased drug inflow, and increased outflow. Since the majority of common anticancer medications are weak bases with pKa between 7.4–8.4 and are hydrophobic, they permeate the cell membrane passively, but the rate of the same drugs is significantly impaired when the extracellular tumor surroundings are acidic because these medications become strongly protonated and pass the cellular membrane considerably less effectively when charged [174]. The decreased drug inflow via influx transporter proteins, which include SLCs, is one of the causes of the reduced intracellular drug levels found in chemo-resistant cancer cells. Additionally, it is widely acknowledged that ABC transporters like P-gp, MDR-associated protein 1 (MRP1), and BCRP are primarily responsible for increased drug efflux. Drug resistance has been linked to the overexpression of proteins of the ABC superfamily, including BCRP (ABCG2), MDR-associated protein 7 (MRP7/ABCC10) and P-gp, MRP1 (ABCC1) (figure 6) [175, 176]. Many neutral and cationic hydrophobic antitumor chemotherapy drugs, such as paclitaxel, DTX, etoposide, and teniposide acquire MDR when P-gp is overexpressed [177]. Patients with non-small cell lung cancer who were administered with paclitaxel had poor response rates when ABCB1 (P-gp) upregulation was present. During up-regulation of MRP1 cancer cells demonstrate MDR towards etoposide, teniposide, vinblastine, vincristine, and DOX

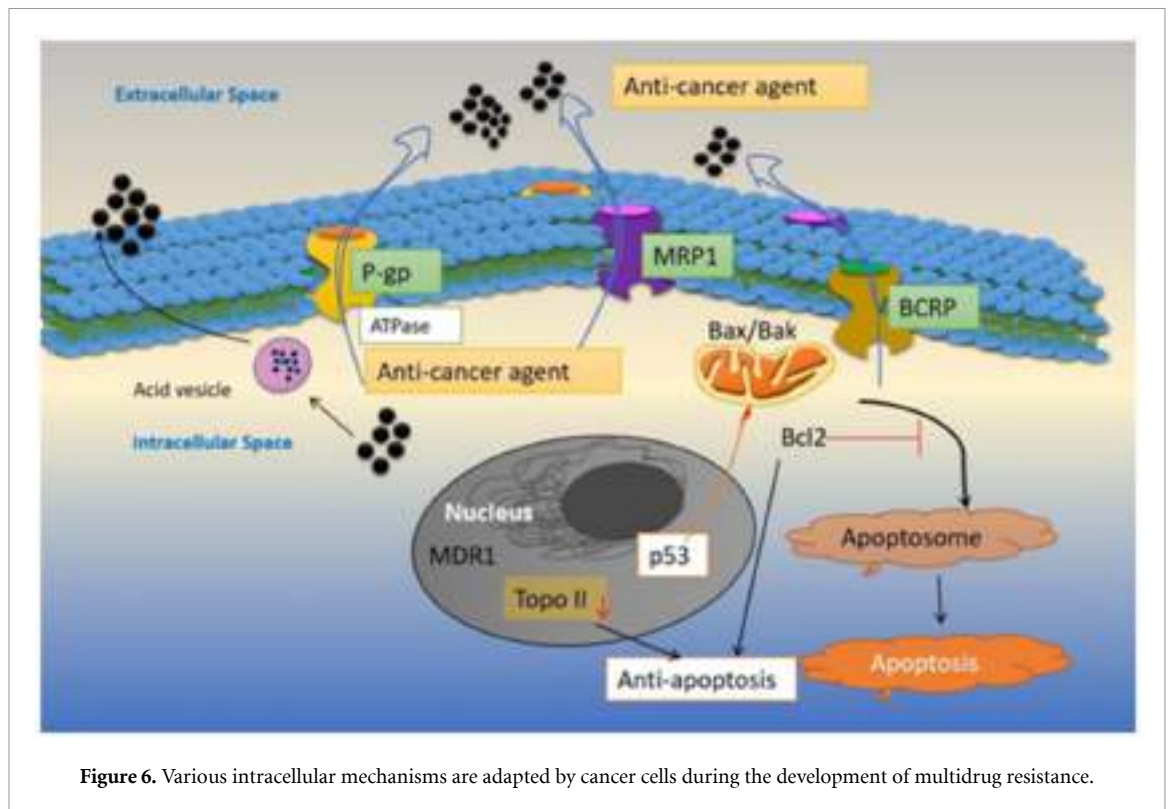


Figure 6. Various intracellular mechanisms are adapted by cancer cells during the development of multidrug resistance.

[178]. MDR towards methotrexate, DOX, and camptothecin is caused by upregulation in the BCRP gene (ABCG2) [179]. Since the upregulation of ABC transporters causes poor drug responses and outcomes in patients with many types of cancers, so inhibiting these transporter proteins could be an effective strategy to tackle multidrug resistant cancers and improve the therapeutic response in clinics.

4.2.2. Role of extracellular vesicles (EVs) in developing drug resistance

EVs have been well studied as a route for the development of MDR in cancers. EVs are phospholipid bilayer-enclosed NPs (25–1000 nm) which are incapable of replication. In the payload of EVs, drug efflux pumps like as P-gp, MRP1, and BCRP has been discovered [180]. It is thought that some of the membranes of the EVs ejected by MDR cells may have these drug transporters oriented inverted, which would facilitate the entry of medicines into the EVs [181]. The ability of EVs to enclose chemotherapy medicines in their payload is undoubted. EVs may expel medications into the extracellular environment once they have been liberated from tumor cells thus the bioavailability of the chemotherapeutic drug in the tumor cells is reduced and the therapeutic or drug response is inhibited [181, 182]. This unique mechanism of EVs-mediated therapeutic resistance is supported by *in vitro* research on the absorption of chemotherapy medicines within EVs. However, there is not much clinical evidence to support the fact that EVs play a role in the development of drug

resistance. Rituximab was administered to lymphoma patients in research that used fewer clinical samples [183]. Rituximab was shown to bind to EVs extracted from the patient's plasma, indicating a reduction in the drug's availability for therapeutic effect. In another clinical research, it was observed that EVs isolated from early-stage breast cancer patients of human epidermal growth factor receptor 2 (Her2) showed reduced absorption of trastuzumab compared to patients with advanced stages of the disease, indicating the role of EVs in reducing the availability of the drug and assisting in the development of chemotherapy resistance and poor outcome [184].

4.3. Disruption of apoptosis, autophagy, and anoikis as mechanisms of drug resistance

The potential of anti-cancer medications to cause cell death is what determines much of its cytotoxicity. Necrosis, autophagy, and apoptosis are the three main mechanisms of cell death, and these processes are primarily identified by the attributes of their morphology, biochemistry, and molecules [185]. Induction of autophagy-associated cell death, activation of pro-apoptotic receptors, ROS generation, DNA damage, and immune cell effector response are a few of the molecular and physiological mechanisms by which anticancer drugs can cause cell death [186]. On the other hand, cancer cells constantly adapt and evolve, giving them the capacity to avoid cell death (figure 6) [187]. The primary regulator of cell survival and the factor that determines how susceptible cancer cells

are to apoptosis is the delicate balance between pro-apoptosis and anti-apoptosis proteins. In this context, drug resistance develops during the overexpression of antiapoptotic proteins such as BCL2, MCL-1, and BCL-XL in tumor cells (figure 6) [188, 189]. In patients with bladder cancer, the expression of Bcl2 is considered a marker for poor prognosis in chemotherapy treatment [190]. Patients with estrogen receptor-positive breast cancer and low levels of BAD expression had significantly worse overall survival (OS) and DFS. Resistance to chemotherapy was also linked to death receptor pathways. In metastatic ovarian cancer, upregulation of FAS and TRAIL R1-R2 was linked to a reduced response to treatment [191]. Similarly in acute myeloid leukemia (AML) upregulation of TRAIL is found to be associated with poor therapeutic response in patients [192]. According to research, individuals with colorectal cancer (CRC) who had high TRAILR1 expression had worse DFS, worse OS, and shorter time to recurrence [193]. In AML, upregulation of XIAP, a protein that inhibits apoptosis, has been linked to a poor prognosis [194]. The tumor suppressor gene with the highest rate of mutation in human cancers is the p53 protein. Since p53 induces the expression of death receptors (like DR5, FAS), and inhibits the expression of antiapoptotic proteins (like survivin) and proapoptotic proteins (like BID, BAX), p53 can also contribute to apoptosis resistance (figure 6) [192]. Additionally, most cancer drugs cause cell death by inducing reactive oxygen production which leads to DNA damage and cell death [195]. However, upregulation of GSH, a crucial component of cellular antioxidant defense systems and numerous metabolic processes acts to lower the reactive oxygen production and thus is a major contributor to drug resistance [196].

4.3.1. Role of DNA damage repair in developing drug resistance

Any cell must have an effective DNA damage repair mechanism to sustain genomic stability, retain cellular homeostasis, and stop the growth of cancer. Mutations build up when the DDR's regular control is compromised, resulting in carcinogenesis, rapidly evolving tumors, and resistance to various DNA-damaging drugs. Platinum medicines including carboplatin, CP, and oxaliplatin are among the chemotherapy drugs used in the majority of traditional cancer therapies that cause DNA damage [197]. Some drugs, like nitrogen mustard or chloroethylnitrosoureas, create DNA adducts that prevent cancer cells from actively replicating DNA [197]. Replication stress is created when DNA replication fails and DNA damage cannot be repaired, which causes cells to undergo apoptosis. Deregulated activity in DNA damage repair pathways and significantly enhanced capacity of the cell to restore DNA damage and prevent apoptosis is closely linked with the emergence of drug resistance [198]. When a clinical

examination was performed for almost 62 susceptible genes in a cohort composed of 15 000 breast cancer patients and normal people, it was observed that almost 57 of the breast cancer patients were found to have lost function mutation in RAD51D which is a DNA damage repair gene [199]. On the other hand, less than 15 healthy people showed a similar mutation in RAD51D thus indicating the role of DDR genes in developing drug resistance [199].

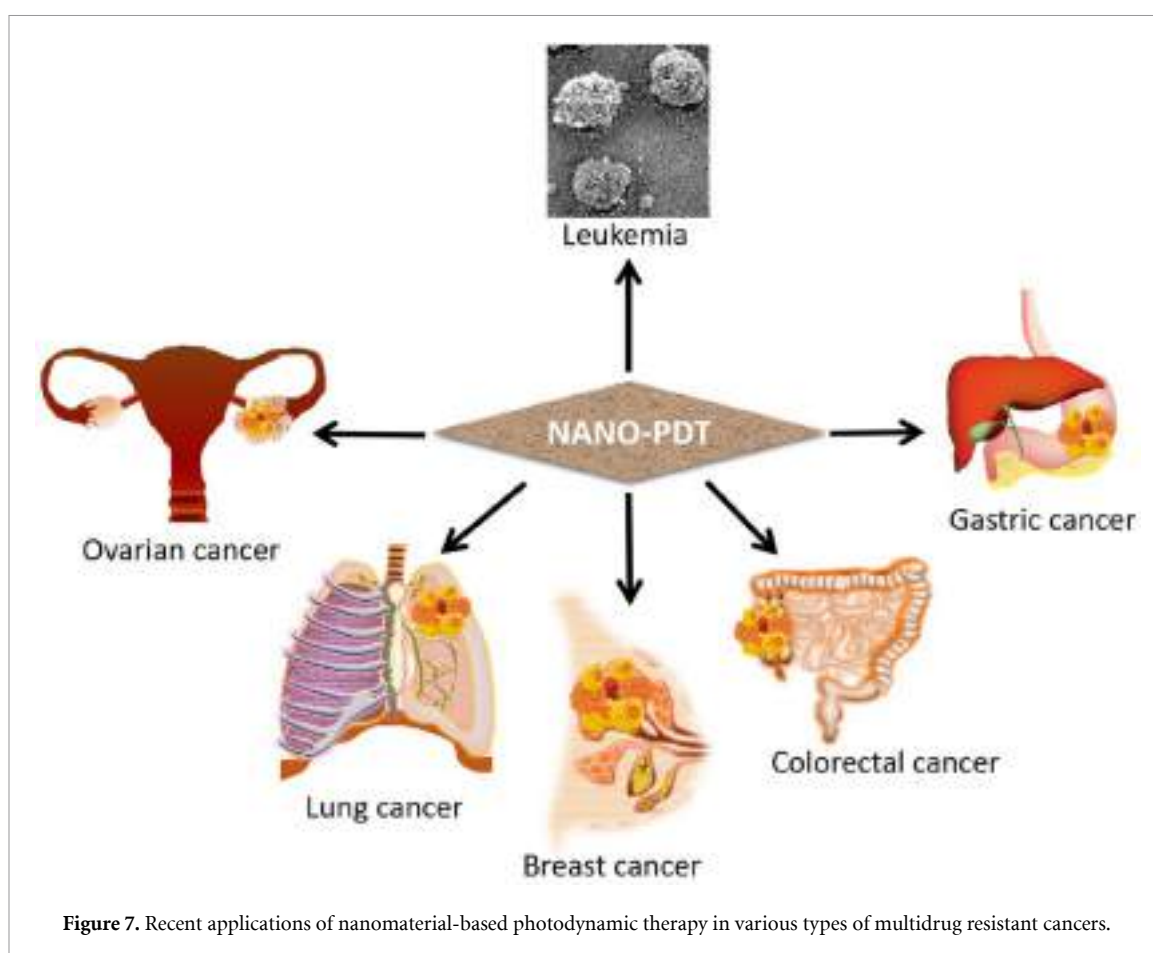
4.3.2. Epigenetic alteration

Alterations in DNA structure are known as epigenetic modifications, which do not involve sequence changes yet are persistently passed down from cell to cell. The epigenetic controls that contribute to treatment resistance in cancer include histone, DNA methylation, microRNA, and chromatin alterations [200]. Several MDR genes, pro-apoptotic genes (APAF-1) [201], including drug transporters (ABCB1) [202], histone modifiers [203], and DNA-repair proteins (MGMT) may have their expression altered after chemotherapy due to epigenetic processes.

One significant epigenetic change seen in many malignancies is DNA methylation which is carried out by DNA methyltransferase [204]. During methylation of the genome, a methyl group is bound to the cytosine residues at the 'CpG islands' thus helping to silence genes by inhibiting gene transcription. The majority of abnormal DNA methylation in cancer is connected to genes that regulate cell proliferation and differentiation, Wingless/Integrated (WNT), Mitogen-activated protein kinase (MAPK), p53, and Vascular endothelial growth factor (VEGF) signaling, or the production of cell cycle inhibitors [205]. Hypermethylation and MDR are highly associated with many malignancies [206]. Different promoter methylation patterns in testicular cancer can be identified from non-seminomas, reflecting particular clinical traits for MDR in patients [207]. Thus, to improve the efficacy of various treatment regimens and combat MDR, therapeutic targeting of epigenetic changes emerges as a crucial and promising method [208].

5. Therapeutic approaches of NP-mediated PDT in multi-drug resistant cancers

In contemporary years, several studies have investigated NP-based PDT for promoting cancer treatment and therapy. MDR, the primary process through which several malignancies acquire chemotherapeutic drug resistance, is an important cause of the ineffectiveness of several kinds of chemotherapy. It impacts those suffering from a range of cancers, including breast cancer, lung cancer, blood malignancies, oral cancer, etc [209]. The PDT technique lessens the need for extensive surgery and speeds up recovery; furthermore, it is capable of being performed without



accumulating adverse effects and may be used in conjunction with conventional therapies [8]. PDT is also effective against several drug-resistant malignancies, such as nasopharyngeal carcinoma [210], breast cancer [211], uterine sarcoma [212], and gastric cancer [213] as shown in (figure 7). In the next section, the mode of action of various NP-based photodynamic therapies for MDR malignancies will be discussed.

5.1. Lung cancer

MDR and malignant cell metastasis are two of the primary reasons why cancer treatments fail. Drug-selected MDR may emerge following chemotherapeutic medication and metastasis-associated MDR may develop resistance to drugs through cellular adaptation to microenvironmental shifts during metastasis. The expanding body of research suggests that cancer patients who have not received chemotherapy treatments may develop drug resistance and that the emergence of resistance to drugs is associated with the progression of cancer metastasis. It has been observed that 76%–79% of chemotherapy-naïve individuals with the third or fourth stage of non-small cell lung carcinoma were not able to become responsive to paclitaxel (Taxol) [214]. The metastasis-associated paclitaxel-resistant human lung cancer cell line H460

was demonstrated to behave similarly to circulating tumor cells in non-adherent and low-attachment culture conditions by functioning as floating cells [215]. Because of this, an *in vitro* model can be used to research how the development of MDR in a solid cancerous tumor is related to cancer spread. This study concluded that MDR cancer cells are caused by inappropriate medication selection and non-adherent culture conditions.

Small-sized pTHPP-PLHNPs were synthesized using a self-assembled nanoprecipitation technique. In an *in vitro* study, it was found that the formulated hybrid NPs exert photocytotoxicity of pTHPP by accumulating within the tumor cells, which generate superoxide anions and induce apoptosis in both A549 parental cells and its MDR variant irradiated with light of wavelength 653 nm for 12 min 45 s, at a light dose of 6 J cm^{-2} , by using an LED lamp, with no effect on P-gp overexpression in the MDR variant [216]. Moreover, these hybrid NPs (THPP-PLHNPs/PDT) can effectively eliminate MDR-floating lung cancer cells from circulation associated with metastasis. The key factor of pTHPP-PLHNPs/PDT was the targeted drug delivery capability based on the PLGA-lipid hybrid NPs, and this capability may also be advantageous for delivering non-PDT medicines. The pTHPP-PLHNPs nano platform is a promising

strategy for the PDT of MDR human lung carcinoma [216]. Another research group came up with a unique drug delivery approach (PTX/CQE) using paclitaxel (PTX), quercetin (QT), and chlorine e6 (Ce6) as a chemo-photodynamic treatment combination to stop breast cancer from spreading to the lungs and becoming resistant to multiple drugs. This nano platform can easily accumulate within tumors and shows good permeability and retention (EPR) effects. It was found that upon NIR light irradiation, PTX/CQE NPs can increase intracellular ROS production, which leads to decreased mitochondrial membrane potential followed by apoptosis [217]. In a unique plasmonic CuO/Cu₂O tapered nanocube-based theranostic nanomedicine, Shanmugam *et al* demonstrated that the nanomedicine may function as both a NIR fluorescence (NIRF) imaging agent and a MRI agent in the biological window II (1000–1500 nm) [218]. The MDR lung cancers are successfully destroyed by these nanomedicines, which effectively create singlet oxygen ($^1O^2$) and mediate a photodynamic therapeutic effect by absorbing NIR light at 1550 nm wavelength. A human small-cell lung cancer cell line called H69AR is a drug-resistant variation of the cell line. According to Shanmugam and colleagues, plasmonic CuO/Cu₂O TNCs-based nanomedicine does not cause drug resistance to develop in H69AR MDR-lung cancer cells [218].

5.2. Breast cancer

The world's deadliest disease for women is breast cancer. Breast malignancies were typically treated with chemotherapy, radiation, and surgical excision, but the main difficulty was to boost medication concentration in breast cancer cells while minimizing patient toxicity and adverse effects. About 90% of cancer patients experienced chemotherapy failure due to MDR of the medications, which hampered the advancement of chemotherapy. So, to decrease drug doses and overcome resistance to chemotherapeutic drugs, a novel, promising nanotechnology-based platform is developed. NP-mediated PDT is one of the outstanding applications to treat MDR breast cancers. Zeng *et al* have applied combined chemotherapy and NIR-triggered PDT to treat MDR breast tumors both *in vitro* and *in vivo*. They have synthesized folic acid (FA)-conjugated NaYF₄:Yb/Tm-TiO₂ nanocomposites loaded with the chemotherapeutic agent DOX [219]. This FA-targeting nanocarrier can easily be uptake by cells and can accumulate DOX within drug-sensitive MCF-7 and resistant MCF-7/ADR cells. As a result, the viability of MCF-7/ADR cells decreased by 53.5%, and the size of MCF-7/ADR tumors was inhibited up to 90.33%, compared with free DOX when a combination of chemotherapy and PDT was applied [219]. Therefore, it is evident that combined chemotherapy and PDT of FA-NPs-DOX nanocomposites under the irradiation of a

980 nm laser can defeat the MDR of breast tumors [219]. A breast cancer resistance protein (ABCG2) was discovered to be a PS called BPD. In light of this knowledge, porphyrin-lipid nanovesicles were developed as a novel method to increase PDT in three breast cancer cell lines by evading P-gp MRP1 and ABCG2-mediated efflux of BPD because researchers wanted to investigate how the P-gp and MRP1 facilitates the transport of BPD. So three breast cancer cell lines were developed as MCF-7 TX400 subline with P-gp overexpression, MCF-7 MX100 subline with ABCG2 overexpression, and MCF-7/VP subline with MRP1-overexpression which were chosen to receive 400 ng ml⁻¹ paclitaxel, 100 nM mitoxantrone (MTX), and 4 μ M etoposide respectively [220]. Interestingly it was observed that cells overexpressing P-gp and ABCG2 were involved in BPD transport only but cells overexpressing MRP1 have no role in BPD transport [220]. From this study, it was concluded that P-gp and ABCG2, but not MRP1, are capable of transporting BPD PSs with ease. Cancer cells are shielded against PDT with BPD by ABCG2 and P-gp. Lipidation promotes intracellular BPD retention for increased PDT effectiveness and conceals BPD to reduce P-gp and ABCG2-mediated efflux [220]. In another study, Rezaivala *et al* synthesized theranostic MNPs coated with spiky AuNPs (Au-CoFe₂O₄) [221]. Its star-shaped Au shell acts as a PS in PTT, and for combined chemotherapy with MTX, the chemotherapeutic agent is loaded in the core of the nanoshell [221]. These nanoshells were evaluated in the aggressive breast cancer cell line MDA-MB-231 for their cytotoxicity. It was found that cell death is mediated by the overlap of the absorption spectrum of the nanostructure and the emission spectrum of the light source [221]. Yu *et al* developed a strategy to combat MDR breast cancer [222]. They developed a new NIR-triggered co-release system based on the chemotherapeutic agent DOX and PS ICG on AuNCs through combined chemo, photothermal/PDT. MCF-7/ADR is an MDR human breast cancer cell. This nanosized co-release system kills MCF7/ADR cells by generating ROS and inducing apoptosis [222].

5.3. Gastric cancer

The fifth-most frequent cancer in the world is gastric cancer, also referred to as stomach cancer. It seriously endangers people's health. The primary adjuvant therapy for gastric cancer is chemotherapy followed by surgery. MDR is a major concern in postoperative chemotherapy for gastric cancer and has a detrimental impact on therapeutic outcomes. According to studies, ROS generation is an efficient way to treat tumors, and the TME is directly associated with the MDR mechanism. GRPR78 is an MDR-related protein overexpressed in stomach cancer. Through its attachment to GRP78, the extracellular absorption

peptide GMBP1 is capable of targeting MDR gastric cancer cells [223]. MRI was used by Zhan *et al* to observe MDR gastric cancer progression *in vivo*. They synthesized Mn_3O_4 nanoplates and conjugated them with GMBP1 peptide to form Mn_3O_4 @PEG-GMBP1 NPs [223]. *Ex vivo*, *in vitro*, and *in vivo* MRI experiments were performed in SGC7901/ADR tumor-bearing nude mice, as well as blocking studies, to confirm the selectivity of the resultant Mn_3O_4 @PEG-GMBP1 NPs to MDR gastric cancer cells [223]. To determine the cytotoxic parameters of these nanoplates, histological analyses, *in vitro* and *in vivo* toxicity tests, and other experiments were conducted. Therefore, it was concluded from these findings that Mn_3O_4 @PEG-GMBP1 NPs may act as a good MR contrast agent *in vivo* for monitoring MDR in gastric cancer [223]. In another study, GMBP1-modified pH/ H_2O_2 /GSH-responsive Mn_3O_4 multifunctional self-enhanced nano platform was developed [224]. To improve their biocompatibility within the tumor, Mn_3O_4 NPs were coated with polydopamine (PDA) to form Mn_3O_4 @PDA NPs. This nano platform efficiently delivers Fenton-like Mn^{2+} , shows GSH depletion properties, and combines chemo-photo thermal and photodynamic properties for *in vivo* instantaneous monitoring of MDR. This nano platform has potential for the medical treatment of MDR gastric/stomach cancer [224].

5.4. Other cancers

Barth *et al* constructed a nontoxic and nonaggregating nanocomposite for *in vivo* PDT of multi-drug resistant leukemia [225]. They synthesized calcium phosphosilicate NPs and encapsulated them with NIR-fluorescent dye ICG as PS. These nanocomposites generate ROS and induce apoptosis in leukemic cells upon 0.2 J cm^{-2} NIR light exposure [225].

In colorectal malignancies, MDR is extremely prevalent. High patient mortality is caused by it. One study combined the photothermal characteristics of AuNRs and the photodynamic features of the PS verteporfin to create a less invasive method to treat multi-drug resistant CRC. Gellan gum (GG) and lipoic acid are both naturally biodegradable compounds. To create a stable colloidal dispersion, AuNRs were encapsulated with lipoic acid and GG (AuNRs_{LA}, GG), then loaded with verteporfin (AuNRs_{LA}, GG/Vert). By combining PTT with PDT, this construct exhibits cytotoxicity against the human colon carcinoma cell line (HCT116) as well as against HCT116 mouse xenograft models [226].

One of the main issues with effective CRC chemotherapy is MDR. A therapeutic approach based on porphyrin/camptothecin/floxuridine triad microbubbles (PCF-MBs) has been developed by Chen *et al* [227]. This therapeutic composite features no early release, a large drug-carrying ability, and extremely

stable combined delivery of medications. It was interestingly discovered that HT-29 cancer tumor growth rate was suppressed up to 90% when ultrasound and laser irradiation were coupled with PCF-MBs. Therefore, a PCF-MB-based therapy approach to diminish multi-drug resistance in CRC is particularly promising [227].

AOT is an anions-based surfactant utilized as an excipient for intramuscular, topical, and oral medications. Alginate is a type of polysaccharide made from marine weeds that is widely utilized in tissue engineering and drug administration. According to Khair *et al* in an *in vitro* investigation, chemotherapy and PDT together with AOT-alginate NPs can easily accumulate inside tumor cells and kill multi-drug resistant ovarian cancer cells NCI/ADR-RES when irradiated with 50 J cm^{-2} dose of non-coherent light at 665 nm. In a different study, Busa *et al* devised a plan to combine chemotherapy and PDT to treat the MDR human uterine sarcoma cell line MES-SA/DX5 [228]. MSNPs, curcumin, and CP were used to create the nanocomposite [228]. IBN-1 NPs were first created with Cur embedded in them, and then the prodrug of CP was added to the carboxylate-modified surface (IBN-1-Cur-CP). In NP form, the Pluronic F127 triblock copolymer functions as a p-gp inhibitor. Excellent structural qualities can be found in these hybrid nanocomposites. They effectively transport Cur and CP molecules into the cytosol by endocytosis and generate large levels of cellular ROS after being irradiated with NIR radiation at 450 nm (15 mW cm^{-2}) for 5 min [228].

To transport PDT chemicals to the appropriate locations in the mitochondria and endoplasmic reticulum, a tumor-targeting nano platform was created. Following the initial synthesis and functionalization of molybdenum disulfide nanoflakes (MoS_2) using glucose-modified hyperbranched polyglycerol (hPG), organelle targeting PDT drugs were then loaded [229]. The enhanced concentration of PDT agents within MDR cells and correct subcellular localization of these new nano platform are visible. A HeLa MDR tumor mouse model experiences tumor reduction after NIR exposure due to intracellular ROS production. Apoptosis is followed by the release of cytochrome C when ROS-induced mitochondrial damage occurs [229]. Furthermore, ATP synthesis was also lowered as a result of mitochondrial damage, which led to the reversal of MDR. Therefore targeting tumors in subcellular organelles with the use of this nano platform's NIR-responsive characteristics is a promising method for MDR cancer treatment [229].

6. Conclusion

The four main types of cancer treatment, such as chemotherapy, radiation therapy, immunotherapy,

and surgery, have been extensively employed to treat several kinds of tumors successfully. However, there are some issues, like the radioactive damage caused by radiotherapy, the toxic side effects, drug tolerance of chemotherapy, the ineffectiveness of immunotherapy, and the recurrence of malignancies, which have diminished the therapeutic effects of cancer treatment and decreased patient quality of life. Therefore, a novel strategy must be developed to reduce these issues. PDT, a non-invasive approach to treat tumors, is more focused on its target and less harmful to surrounding healthy tissues. The primary mechanisms of PDT are to exert toxicity directly to the cancer cells, injury to tumor blood vessels, and anti-tumor immunological responses. However, PDT has several drawbacks. Only superficial lesions can be treated with it; solid, bulky, or deeply buried tumors cannot. This is because light cannot pass into our body's deep tissues, making whole-body irradiation with the PDT approach impossible. Additionally, the organic PSs used in PDT have a complex structure and do not display a high level of selectivity for cancer cells. Enzymes can quickly break it down, and it is pretty expensive. To address the shortcomings of this traditional PS, a highly promising PDT mediated by nanomaterials has been created. Nanomedicine's ability to perform several functions, transport PS molecules to particular regions, and modify photothermal conversion enables it to get around the limitations of conventional cancer treatments. In this study, we have covered the PDT with NPs used to treat malignancies that are resistant to many drugs. Additionally, according to our study, combining PDT with nanomaterials may increase the anti-tumor effects, reduce side effects, and improve quality of life, which could result in a significant survival benefit.

Data availability statement

All data that support the findings of this study are included within the article (and any supplementary files).

Conflict of interest

The authors declare no conflict of interest.

ORCID iD

Arindam Pramanik  <https://orcid.org/0000-0002-5827-6267>

References

- [1] Baxter D E, Allinson L M, Al Amri W S, Poulter J A, Pramanik A, Thorne J L, Verghese E T and Hughes T A 2021 MiR-195 and its target SEMA6D regulate chemoresponse in breast cancer *Cancers* **13** 5979
- [2] Holohan C, Van Schaeybroeck S, Longley D B and Johnston P G 2013 Cancer drug resistance: an evolving paradigm *Nat. Rev. Cancer* **13** 714–26
- [3] Fojo T and Bates S 2003 Strategies for reversing drug resistance *Oncogene* **22** 7512–23
- [4] Taylor S T, Hickman J A and Dive C 2000 Epigenetic determinants of resistance to etoposide regulation of Bcl-XL and Bax by tumor microenvironmental factors *J. Natl Cancer Inst.* **92** 18–23
- [5] Hillemanns P, Untch M, Dannecker C, Baumgartner R, Stepp H, Diebold J, Weingandt H, Pröve F and Korell M 2000 Photodynamic therapy of vulvar intraepithelial neoplasia using 5-aminolevulinic acid *Int. J. Cancer* **85** 649–53
- [6] Romiszewska A and Bombalska A 2018 The use of 5-aminolevulinic acid and its derivatives in photodynamic therapy and diagnosis *Biuletyn Wojskowej Akademii Technicznej* **67** 113–30
- [7] Casas A, di Venosa G, Hasan T and Batlle A 2011 Mechanisms of resistance to photodynamic therapy *Curr. Med. Chem.* **18** 2486–515
- [8] Agostinis P, Berg K, Cengel K A, Foster T H, Girotti A W, Gollnick S O, Hahn S M, Hamblin M R, Juzeniene A and Kessel D 2011 Photodynamic therapy of cancer: an update *Cancer J. Clin.* **61** 250–81
- [9] Lee H, Han J, Shin H, Han H, Na K and Kim H 2018 Combination of chemotherapy and photodynamic therapy for cancer treatment with sonoporation effects *J. Control. Release* **283** 190–9
- [10] Krajczewski J, Rucińska K, Townley H E and Kudelski A 2019 Role of various nanoparticles in photodynamic therapy and detection methods of singlet oxygen *Photodiagnosis Photodyn. Ther.* **26** 162–78
- [11] Tavakkoli F, Zahedifar M and Sadeghi E 2018 Effect of LaF₃: Ag fluorescent nanoparticles on photodynamic efficiency and cytotoxicity of Protoporphyrin IX photosensitizer *Photodiagnosis Photodyn. Ther.* **21** 306–11
- [12] Ishchenko A A and Syntugina A T 2023 Structure and photosensitizer ability of polymethine dyes in photodynamic therapy: a review *Theor. Exp. Chem.* **58** 1–29
- [13] Allison R R and Moghissi K 2013 Photodynamic therapy (PDT): PDT mechanisms *Clin. Endosc.* **46** 24–29
- [14] Karimi M, Sadeghi E, Bigdeli S K and Zahedifar M 2023 Optical properties, singlet oxygen, and free radical production ability with different UV irradiations and antimicrobial inhibitors against various bacterial species of ZnO: Eu nanoparticles *Radiat. Phys. Chem.* **212** 111132
- [15] Lucky S S, Soo K C and Zhang Y 2015 Nanoparticles in photodynamic therapy *Chem. Rev.* **115** 1990–2042
- [16] Zhou Z, Song J, Nie L and Chen X 2016 Reactive oxygen species generating systems meeting challenges of photodynamic cancer therapy *Chem. Soc. Rev.* **45** 6597–626
- [17] Tampa M, Sarbu M-I, Matei C, Mitran C-I, Mitran M-I, Caruntu C, Constantin C, Neagu M and Georgescu S-R 2019 Photodynamic therapy: a hot topic in dermatology-oncology *Oncol. Lett.* **17** 4085–93
- [18] Qumseya B J, David W and Wolfsen H C 2013 Photodynamic therapy for Barrett's esophagus and esophageal carcinoma *Clin. Endosc.* **46** 30–37
- [19] Ramsay D, Stevenson H and Jerjes W 2021 From basic mechanisms to clinical research: photodynamic therapy applications in head and neck malignancies and vascular anomalies *J. Clin. Med.* **10** 4404
- [20] Railkar R and Agarwal P K 2018 Photodynamic therapy in the treatment of bladder cancer: past challenges and current innovations *Eur. Urol. Focus* **4** 509–11
- [21] Weinberg B D, Allison R R, Sibata C, Parent T and Downie G 2010 Results of combined photodynamic therapy (PDT) and high dose rate brachytherapy (HDR) in treatment of obstructive endobronchial non-small cell lung cancer (NSCLC) *Photodiagnosis Photodyn. Ther.* **7** 50–58

- [22] Dhanalekshmi K I, Sangeetha K, Magesan P, Johnson J, Zhang X and Jayamoorthy K 2022 Photodynamic cancer therapy: role of Ag- and Au-based hybrid nano-photosensitizers *J. Biomol. Struct. Dyn.* **40** 4766–73
- [23] Kim M M and Darafsheh A 2020 Light sources and dosimetry techniques for photodynamic therapy *Photochem. Photobiol.* **96** 280–94
- [24] Huang A, Nguyen J K and Jagdeo J 2020 Light-emitting diode-based photodynamic therapy for photoaging, scars, and dyspigmentation: a systematic review *Dermatol. Surg.* **46** 1388–94
- [25] Meyer-Betz F 1913 Investigations on the biological (photodynamic) action of haematoporphyrin and other derivatives of blood and bile pigments *Deutsch. Arch. Klin. Med.* **112** 476–503
- [26] Kou J, Dou D and Yang L 2017 Porphyrin photosensitizers in photodynamic therapy and its applications *Oncotarget* **8** 81591
- [27] Lamberts J J M and Neckers D C 1985 Rose Bengal derivatives as singlet oxygen sensitizers *Tetrahedron* **41** 2183–90
- [28] Gandin E, Lion Y and van de Vorst A 1983 Quantum yield of singlet oxygen production by xanthene derivatives *Photochem. Photobiol.* **37** 271–8
- [29] Tardivo J P, del Giglio A, De Oliveira C S, Gabrielli D S, Junqueira H C, Tada D B, Severino D, de Fátima Turchiello R and Baptista M S 2005 Methylene blue in photodynamic therapy: from basic mechanisms to clinical applications *Photodiagnosis Photodyn. Ther.* **2** 175–91
- [30] Panjehpour M and Overholt B F 2006 Porfimer sodium photodynamic therapy for management of Barrett's esophagus with high-grade dysplasia *Lasers Surg. Med.* **38** 390–5
- [31] de Haas E R M, Kruijt B, Sterenborg H J C M, Neumann H A M and Robinson D J 2006 Fractionated illumination significantly improves the response of superficial basal cell carcinoma to aminolevulinic acid photodynamic therapy *J. Invest. Dermatol.* **126** 2679–86
- [32] Vallinayagam R, Schmitt E, Barge J, Wagnieres G, Wenger V, Neier R and Juillerat-Jeanneret L 2008 Glycoside esters of 5-aminolevulinic acid for photodynamic therapy of cancer *Bioconjug. Chem.* **19** 821–39
- [33] Kreutzer K, Bonnekoh B, Franke I and Gollnick H 2004 Photodynamic therapy with methylaminooxopentanoate (Metvix) and a broad band light source (PhotoDyn 501): practical experiences in problem-patients with actinic keratoses and basal cell carcinomas *J. German Soc. Dermatol.* **2** 992–9
- [34] Vicente M D G H and Smith K M 2023 Amino acid derivatives of chlorin-e6—a review *Molecules* **28** 3479
- [35] Mendes M I P and Arnaut L G 2023 Redaporfin development for photodynamic therapy and its combination with glycolysis inhibitors *Photochem. Photobiol.* **99** 769–76
- [36] Sokolov V V, Chissov V I, Filonenko E V, Sukhin G M, Yakubovskaya R I, Belous T A, Zharkova N N, Kozlov D N and Smirnov V V 1995 Photodynamic therapy of cancer with the photosensitizer PHOTOGEN *Proc. SPIE* **2325** 367–74
- [37] Sokolov V V, Chissov V I, Yakubovskaya R I, Aristarkhova E I, Filonenko E V, Belous T A, Vorozhtsov G N, Zharkova N N, Smirnov V V and Zhitkova M B 1996 Photodynamic therapy (PDT) of malignant tumors by photosensitizer photosens: results of 45 clinical cases *Proc. SPIE* **2625** 281–7
- [38] Efendiev K T, Alekseeva P M, Shiryayev A A, Skobeltsin A S, Solonina I L, Fatyanova A S, Reshetov I V and Loschenov V B 2022 Preliminary low-dose photodynamic exposure to skin cancer with chlorin e6 photosensitizer *Photodiagnosis Photodyn. Ther.* **38** 102894
- [39] Rigual N R, Shafirstein G, Frustino J, Seshadri M, Cooper M, Wilding G, Sullivan M A and Henderson B 2013 Adjuvant intraoperative photodynamic therapy in head and neck cancer *JAMA Otolaryngol.—Head Neck Surg.* **139** 706–11
- [40] Sato T, Kishi S, Matsumoto H and Mukai R 2010 Combined photodynamic therapy with verteporfin and intravitreal bevacizumab for polypoidal choroidal vasculopathy *Am. J. Ophthalmol.* **149** 947–54
- [41] Betz C S, Rauschnig W, Strnadko E P, Riabov M V, Albrecht V, Nifantiev N E and Hopper C 2008 Optimization of treatment parameters for Foscan®-PDT of basal cell carcinomas *Lasers Surg. Med.* **40** 300–11
- [42] Kochneva E V, Filonenko E V, Vakulovskaya E G, Scherbakova E G, Seliverstov O V, Markichev N A and Reshetnikov A V 2010 Photosensitizer Radachlorin®: skin cancer PDT phase II clinical trials *Photodiagnosis Photodyn. Ther.* **7** 258–67
- [43] Mang T S, Allison R, Hewson G, Snider W and Moskowitz R 1998 A phase II/III clinical study of tin ethyl etiopurpurin (Purlytin)-induced photodynamic therapy for the treatment of recurrent cutaneous metastatic breast cancer *Cancer J. Sci. Am.* **4** 378–84
- [44] Trachtenberg J, Weersink R A, Davidson S R H, Haider M A, Bogaards A, Gertner M R, Evans A, Scherz A, Savard J and Chin J L 2008 Vascular-targeted photodynamic therapy (padoporfin, WST09) for recurrent prostate cancer after failure of external beam radiotherapy: a study of escalating light doses *BJU Int.* **102** 556–62
- [45] Sessler J L and Miller R A 2000 Texaphyrins: new drugs with diverse clinical applications in radiation and photodynamic therapy *Biochem. Pharmacol.* **59** 733–9
- [46] Guan M, Ge J, Wu J, Zhang G, Chen D, Zhang W, Zhang Y, Zou T, Zhen M and Wang C 2016 Fullerene/ photosensitizer nanovesicles as highly efficient and clearable phototheranostics with enhanced tumor accumulation for cancer therapy *Biomaterials* **103** 75–85
- [47] Marzieh S, Ehsan S and Mostafa Z 2022 Fabrication, characterization, antibacterial properties, and the possibility of introducing silver tungstate nanoparticles with Zn as photosensitizers for photodynamic therapy *Appl. Phys. A* **128** 844
- [48] Chen W 2008 Nanoparticle fluorescence based technology for biological applications *J. Nanosci. Nanotechnol.* **8** 1019–51
- [49] Nann T 2011 Nanoparticles in photodynamic therapy *Nano Biomed. Eng.* **3** 137–43
- [50] Chatterjee D K, Fong L S and Zhang Y 2008 Nanoparticles in photodynamic therapy: an emerging paradigm *Adv. Drug Deliv. Rev.* **60** 1627–37
- [51] Song H, Su C, Cui W, Zhu B, Liu L, Chen Z and Zhao L 2013 Folic acid-chitosan conjugated nanoparticles for improving tumor-targeted drug delivery *Biomed. Res. Int.* **2013** 723158
- [52] Ealia S A M and Saravanakumar M P 2017 A review on the classification, characterisation, synthesis of nanoparticles and their application *IOP Conf. Ser.: Mater. Sci. Eng.* **263** 032019
- [53] Schasfoort R B M 2017 Introduction to surface plasmon resonance *Handbook of Surface Plasmon Resonance* 2nd Edition (The Royal Society of Chemistry) pp 1–26
- [54] Alexere S, ElZorkany H E, Abdel-Salam Z and Harith M A 2021 A novel synthesis of a chlorophyll b-gold nanoconjugate used for enhancing photodynamic therapy: *in vitro* study *Photodiagnosis Photodyn. Ther.* **35** 102444
- [55] Prieto-Montero R, Prieto-Castañeda A, Katsumiti A, Cajarville M P, Agarrabeitia A R, Ortiz M J and Martínez-Martínez V 2021 Functionalization of photosensitized silica nanoparticles for advanced photodynamic therapy of cancer *Int. J. Mol. Sci.* **22** 6618
- [56] Yang Y, Chen F, Xu N, Yao Q, Wang R, Xie X, Zhang F, He Y, Shao D and Dong W-F 2022 Red-light-triggered self-destructive mesoporous silica nanoparticles for cascade-amplifying chemo-photodynamic therapy favoring antitumor immune responses *Biomaterials* **281** 121368

- [57] Yan L, Amirshaghghi A, Huang D, Miller J, Stein J M, Busch T M, Cheng Z and Tsourkas A 2018 Protoporphyry IX (PpIX)-coated superparamagnetic iron oxide nanoparticle (SPION) nanoclusters for magnetic resonance imaging and photodynamic therapy *Adv. Funct. Mater.* **28** 1707030
- [58] Shi Z, Zhang K, Zada S, Zhang C, Meng X, Yang Z and Dong H 2020 Upconversion nanoparticle-induced multimode photodynamic therapy based on a metal–organic framework/titanium dioxide nanocomposite *ACS Appl. Mater. Interfaces* **12** 12600–8
- [59] Liang X, Xie Y, Wu J, Wang J, Petković M, Stepić M, Zhao J, Ma J and Mi L 2021 Functional titanium dioxide nanoparticle conjugated with phthalocyanine and folic acid as a promising photosensitizer for targeted photodynamic therapy *in vitro* and *in vivo* *J. Photochem. Photobiol. B* **215** 112122
- [60] Xie L, Wang G, Zhou H, Zhang F, Guo Z, Liu C, Zhang X and Zhu L 2016 Functional long circulating single walled carbon nanotubes for fluorescent/photoacoustic imaging-guided enhanced phototherapy *Biomaterials* **103** 219–28
- [61] Marangon I, Ménard-Moyon C, Silva A K A, Bianco A, Luciani N and Gazeau F 2016 Synergic mechanisms of photothermal and photodynamic therapies mediated by photosensitizer/carbon nanotube complexes *Carbon* **97** 110–23
- [62] Sun X, Zebibula A, Dong X, Zhang G, Zhang D, Qian J and He S 2018 Aggregation-induced emission nanoparticles encapsulated with PEGylated nano graphene oxide and their applications in two-photon fluorescence bioimaging and photodynamic therapy *in vitro* and *in vivo* *ACS Appl. Mater. Interfaces* **10** 25037–46
- [63] Kapri S and Bhattacharyya S 2018 Molybdenum sulfide–reduced graphene oxide p–n heterojunction nanosheets with anchored oxygen generating manganese dioxide nanoparticles for enhanced photodynamic therapy *Chem. Sci.* **9** 8982–9
- [64] Liu Y, Zhu D, Zhu X, Cai G, Wu J, Chen M, Du P, Chen Y, Liu W and Yang S 2020 Enhancing the photodynamic therapy efficacy of black phosphorus nanosheets by covalently grafting fullerene C₆₀ *Chem. Sci.* **11** 11435–42
- [65] Hong X, Xu X, Liu Z, Liu S, Yu J, Wu M, Ma Y and Shuai Q 2021 Hyaluronan–fullerene/AIEgen nanogel as CD44-targeted delivery of tirapazamine for synergistic photodynamic-hypoxia activated therapy *Nanotechnology* **32** 465701
- [66] Ma Y-C, Zhu Y-H, Tang X-F, Hang L-F, Jiang W, Li M, Khan M I, You Y-Z and Wang Y-C 2019 Au nanoparticles with enzyme-mimicking activity-ornamented ZIF-8 for highly efficient photodynamic therapy *Biomater. Sci.* **7** 2740–8
- [67] Chi Y-F, Qin J-J, Li Z, Ge Q and Zeng W-H 2020 Enhanced anti-tumor efficacy of 5-aminolevulinic acid-gold nanoparticles-mediated photodynamic therapy in cutaneous squamous cell carcinoma cells *Braz. J. Med. Biol.* **53** 8457–68
- [68] Vankayala R, Lin C-C, Kalluru P, Chiang C-S and Hwang K C 2014 Gold nanoshells-mediated bimodal photodynamic and photothermal cancer treatment using ultra-low doses of near infra-red light *Biomaterials* **35** 5527–38
- [69] Kuo W S, Chang C N, Chang Y T, Yang M H, Chien Y H, Chen S J and Yeh C S 2010 Gold nanorods in photodynamic therapy, as hyperthermia agents, and in near-infrared optical imaging *Angew. Chem., Int. Ed.* **49** 2711–5
- [70] Kuo W-S, Chang Y-T, Cho K-C, Chiu K-C, Lien C-H, Yeh C-S and Chen S-J 2012 Gold nanomaterials conjugated with indocyanine green for dual-modality photodynamic and photothermal therapy *Biomaterials* **33** 3270–8
- [71] Wang S and Lu G 2018 Applications of gold nanoparticles in cancer imaging and treatment *Noble and Precious Metals—Properties, Nanoscale Effects and Applications* vol 1 (IntechOpen) pp 291–309
- [72] Zhang Y, Li P, Su R, Wen F, Jia Z, Lv Y, Cai J and Su W 2022 Curcumin-loaded multifunctional chitosan gold nanoparticles: an enhanced PDT/PTT dual-modal phototherapeutic and pH-responsive antimicrobial agent *Photodiagnosis Photodyn. Ther.* **39** 103011
- [73] Jain S, Hirst D G and O’Sullivan J M 2012 Gold nanoparticles as novel agents for cancer therapy *Br. J. Radiol.* **85** 101–13
- [74] Huang X, Jain P K, El-Sayed I H and El-Sayed M A 2008 Plasmonic photothermal therapy (PPTT) using gold nanoparticles *Lasers Med. Sci.* **23** 217–28
- [75] Li J-L, Wang L, Liu X-Y, Zhang Z-P, Guo H-C, Liu W-M and Tang S-H 2009 *In vitro* cancer cell imaging and therapy using transferrin-conjugated gold nanoparticles *Cancer Lett.* **274** 319–26
- [76] Kohle F F E, Li S, Turker M Z and Wiesner U B 2019 Ultrasmall PEGylated and targeted core–shell silica nanoparticles carrying methylene blue photosensitizer *ACS Biomater. Sci. Eng.* **6** 256–64
- [77] Zhao Z X, Huang Y Z, Shi S G, Tang S H, Li D H and Chen X L 2014 Cancer therapy improvement with mesoporous silica nanoparticles combining photodynamic and photothermal therapy *Nanotechnology* **25** 285701
- [78] Borzęcka W, Pereira P M R, Fernandes R, Trindade T, Torres T and Tomé J P C 2022 Spherical and rod shaped mesoporous silica nanoparticles for cancer-targeted and photosensitizer delivery in photodynamic therapy *J. Mater. Chem. B* **10** 3248–59
- [79] Brevet D, Gary-Bobo M, Raehm L, Richeter S, Hocine O, Amro K, Look B, Couleaud P, Frochot C and Morère A 2009 Mannose-targeted mesoporous silica nanoparticles for photodynamic therapy *ChemComm* **12** 1475–7
- [80] Simon V, Devaux C, Darmon A, Donnet T, Thiénot E, Germain M, Honnorat J, Duval A, Pottier A and Borghi E 2010 Pp IX silica nanoparticles demonstrate differential interactions with *in vitro* tumor cell lines and *in vivo* mouse models of human cancers *Photochem. Photobiol.* **86** 213–22
- [81] Tang L and Cheng J 2013 Nonporous silica nanoparticles for nanomedicine application *Nano Today* **8** 290–312
- [82] Huang P, Li Z, Lin J, Yang D, Gao G, Xu C, Bao L, Zhang C, Wang K and Song H 2011 Photosensitizer-conjugated magnetic nanoparticles for *in vivo* simultaneous magnetofluorescent imaging and targeting therapy *Biomaterials* **32** 3447–58
- [83] Matlou G G, Oluwole D O, Prinsloo E and Nyokong T 2018 Photodynamic therapy activity of zinc phthalocyanine linked to folic acid and magnetic nanoparticles *J. Photochem. Photobiol. B* **186** 216–24
- [84] Hou H, Huang X, Wei G, Xu F, Wang Y and Zhou S 2019 Fenton reaction-assisted photodynamic therapy for cancer with multifunctional magnetic nanoparticles *ACS Appl. Mater. Interfaces* **11** 29579–92
- [85] Fudimura K A, Seabra A B, Santos M C and Haddad P S 2017 Synthesis and characterization of methylene blue-containing silica-coated magnetic nanoparticles for photodynamic therapy *J. Nanosci. Nanotechnol.* **17** 133–42
- [86] Chen Q, Ma X, Xie L, Chen W, Xu Z, Song E, Zhu X and Song Y 2021 Iron-based nanoparticles for MR imaging-guided ferroptosis in combination with photodynamic therapy to enhance cancer treatment *Nanoscale* **13** 4855–70
- [87] Chen W and Zhang J 2006 Using nanoparticles to enable simultaneous radiation and photodynamic therapies for cancer treatment *J. Nanosci. Nanotechnol.* **6** 1159–66
- [88] Zhang H, Shan Y and Dong L 2014 A comparison of TiO₂ and ZnO nanoparticles as photosensitizers in photodynamic therapy for cancer *J. Biomed. Nanotechnol.* **10** 1450–7
- [89] Shah Z, Nazir S, Mazhar K, Abbasi R and Samokhvalov I M 2019 PEGylated doped-and undoped-TiO₂ nanoparticles

- for photodynamic Therapy of cancers *Photodiagnosis Photodyn. Ther.* **27** 173–83
- [90] Lagopati N, Kitsiou P V, Kontos A I, Venieratos P, Kotsopoulou E, Kontos A G, Dionysiou D D, Pispas S, Tsilibary E C and Falaras P 2010 Photo-induced treatment of breast epithelial cancer cells using nanostructured titanium dioxide solution *J. Photochem. Photobiol. A* **214** 215–23
 - [91] Bhattacharya D, Santra C R, Ghosh A N and Karmakar P 2014 Differential toxicity of rod and spherical zinc oxide nanoparticles on human peripheral blood mononuclear cells *J. Biomed. Nanotechnol.* **10** 707–16
 - [92] Vasuki K and Manimekalai R 2019 NIR light active ternary modified ZnO nanocomposites for combined cancer therapy *Heliyon* **5** e02729
 - [93] Firdous S 2018 Development and imaging of zinc oxide nanorods as a photosensitizer for the diagnosis and treatment of cancer using lasers *Laser Phys. Lett.* **15** 095604
 - [94] Hariharan R, Senthilkumar S, Suganthi A and Rajarajan M 2012 Synthesis and characterization of doxorubicin modified ZnO/PEG nanomaterials and its photodynamic action *J. Photochem. Photobiol. B* **116** 56–65
 - [95] Sadeghi E, Mahmoodian Z and Zahedifar M 2019 Synthesis of nanoparticles of ZnS: Ag-L-cysteine-protoporphyrin IX conjugates and investigation its potential of reactive oxygen species production *J. Fluoresc.* **29** 1089–101
 - [96] Ma L, Zou X, Hossu M and Chen W 2016 Synthesis of ZnS: Ag, Co water-soluble blue afterglow nanoparticles and application in photodynamic activation *Nanotechnology* **27** 315602
 - [97] Lagos K J, Buzzá H H, Bagnato V S and Romero M P 2021 Carbon-based materials in photodynamic and photothermal therapies applied to tumor destruction *Int. J. Mol. Sci.* **23** 22
 - [98] Sundaram P and Abrahamse H 2020 Effective photodynamic therapy for colon cancer cells using chlorin e6 coated hyaluronic acid-based carbon nanotubes *Int. J. Mol. Sci.* **21** 4745
 - [99] Liu G, Qin H, Amano T, Murakami T and Komatsu N 2015 Direct fabrication of the graphene-based composite for cancer phototherapy through graphite exfoliation with a photosensitizer *ACS Appl. Mater. Interfaces* **7** 23402–6
 - [100] Roefinfard M, Zahedifar M, Darroudi M, Khorsand Zak A and Sadeghi E 2021 Synthesis of graphene quantum dots decorated with Se, Eu and Ag as photosensitizer and study of their potential to use in photodynamic therapy *J. Fluoresc.* **31** 551–7
 - [101] Gulzar A, Xu J, Yang D, Xu L, He F, Gai S and Yang P 2018 Nano-graphene oxide-UCNP-Ce6 covalently constructed nanocomposites for NIR-mediated bioimaging and PTT/PDT combinatorial therapy *Dalton Trans.* **47** 3931–9
 - [102] Roefinfard M, Zahedifar M, Darroudi M, Khorsand Zak A and Sadeghi E 2020 Preparation and characterization of selenium-decorated graphene quantum dots with high afterglow for application in photodynamic therapy *Luminescence* **35** 891–6
 - [103] Hosseinzadeh R, Khorsandi K and Hosseinzadeh G 2018 Graphene oxide-methylene blue nanocomposite in photodynamic therapy of human breast cancer *J. Biomol. Struct. Dyn.* **36** 2216–23
 - [104] Vinothini K, Rajendran N K, Rajan M, Ramu A, Marraiki N and Elgorban A M 2020 A magnetic nanoparticle functionalized reduced graphene oxide-based drug carrier system for a chemo-photodynamic cancer therapy *New J. Chem.* **44** 5265–77
 - [105] Kazemzadeh H and Mozafari M 2019 Fullerene-based delivery systems *Drug Discov. Today* **24** 898–905
 - [106] Yamakoshi Y, Aroua S and Yue M A 2023 Fullerenes (C60, C70) as photosensitizers for PDT *Photodiagnosis Photodyn. Ther.* **41** 103431
 - [107] Liu Q, Guan M, Xu L, Shu C, Jin C, Zheng J, Fang X, Yang Y and Wang C 2012 Structural effect and mechanism of C70-carboxyfullerenes as efficient sensitizers against cancer cells *Small* **8** 2070–7
 - [108] Gündüz E Ö, Gedik M E, Günaydin G and Okutan E 2022 Amphiphilic fullerene-BODIPY photosensitizers for targeted photodynamic therapy *ChemMedChem* **17** e202100693
 - [109] Milanesio M E, Alvarez M G, Rivarola V, Silber J J and Durantini E N 2005 Porphyrin-fullerene C60 dyads with high ability to form photoinduced charge-separated state as novel sensitizers for photodynamic therapy *Photochem. Photobiol.* **81** 891–7
 - [110] Vallecorsa P, di Venosa G, Ballatore M B, Ferreyra D, Mamone L, Sáenz D, Calvo G, Durantini E and Casas A 2021 Novel meso-substituted porphyrin derivatives and its potential use in photodynamic therapy of cancer *BMC Cancer* **21** 1–12
 - [111] Tirelli N, Lutolf M P, Napoli A and Hubbell J A 2002 Poly (ethylene glycol) block copolymers *Rev. Mol. Biotechnol.* **90** 3–15
 - [112] Karimi A R, Khodadadi A and Hadizadeh M 2016 A nanoporous photosensitizing hydrogel based on chitosan cross-linked by zinc phthalocyanine: an injectable and pH-stimuli responsive system for effective cancer therapy *RSC Adv.* **6** 91445–52
 - [113] Wang X, Li S and Liu H 2021 Co-delivery of chitosan nanoparticles of 5-aminolevulinic acid and shGBAS for improving photodynamic therapy efficacy in oral squamous cell carcinomas *Photodiagnosis Photodyn. Ther.* **34** 102218
 - [114] Wang Y, Xie D, Pan J, Xia C, Fan L, Pu Y, Zhang Q, Hong Ni Y, Wang J and Hu Q 2019 A near infrared light-triggered human serum albumin drug delivery system with coordination bonding of indocyanine green and cisplatin for targeting photochemistry therapy against oral squamous cell cancer *Biomater. Sci.* **7** 5270–82
 - [115] Luo J, Miao Z, Huang X, Yang Y, Liu M, Shen G and Yang T 2023 Translational albumin nanocarrier caging photosensitizer for efficient cancer photodynamic therapy *Front. Bioeng. Biotechnol.* **11** 1132591
 - [116] Carvalho J A, da Silva Abreu A, Tedesco A C, Junior M B and Simioni A R 2019 Functionalized photosensitive gelatin nanoparticles for drug delivery application *J. Biomater. Sci. Polym. Ed.* **30** 508–25
 - [117] Li X, Zhou Z, Zhou R, Yang J, Zhou M, Li Q, Li L and Huang Y 2021 Stimuli-responsive nanoparticles combining photodynamic therapy and mitochondria disruption suppressed tumor metastasis *Adv. Mater. Interfaces* **8** 2002200
 - [118] Jo J, Salfi E, Folz J, Udager A M, Keller E, Kopelman R, Kothapalli S-R, Xu G and Wang X 2023 Photoacoustic spectral analysis for evaluating the aggressiveness of prostate cancer labeled by methylene blue polyacrylamide nanoparticles *Biosensors* **13** 403
 - [119] Ding Y, Yang R, Yu W, Hu C, Zhang Z, Liu D, An Y, Wang X, He C and Liu P 2021 Chitosan oligosaccharide decorated liposomes combined with TH302 for photodynamic therapy in triple negative breast cancer *J. Nanobiotechnol.* **19** 147
 - [120] Zheng X, Pan D, Chen M, Dai X, Cai H, Zhang H, Gong Q, Gu Z and Luo K 2019 Tunable hydrophile-lipophile balance for manipulating structural stability and tumor retention of amphiphilic nanoparticles *Adv. Mater.* **31** 1901586
 - [121] Wang K, Tu Y, Yao W, Zong Q, Xiao X, Yang R-M, Jiang X-Q and Yuan Y 2020 Size-switchable nanoparticles with self-destructive and tumor penetration characteristics for site-specific phototherapy of cancer *ACS Appl. Mater. Interfaces* **12** 6933–43
 - [122] Ghosh D, Pramanik A, Sikdar N, Ghosh S K and Pramanik P 2010 Amelioration studies on optimization of low molecular weight chitosan nanoparticle preparation,

- characterization with potassium per sulfate and silver nitrate combined action with aid of drug delivery to tetracycline resistant bacteria *Int. J. Pharm. Sci. Drug Res.* **2** 247–53
- [123] Pramanik A, Laha D, Chattopadhyay S, Dash S K, Roy S, Pramanik P and Karmakar P 2015 Targeted delivery of “copper carbonate” nanoparticles to cancer cells *in vivo* *Toxicol. Res.* **4** 1604–12
- [124] Trejo-Santillan I, Mendoza-Guevara C C, Del Pilar Ramos-godínez M and Ramon-Gallegos E 2021 Synthesis of chitosan nanoparticles conjugated with protoporphyrin IX and vitamin B9 for their application in photodynamic therapy *IEEE Trans. Nanobiosci.* **21** 490–5
- [125] Yang Z, Li P, Chen Y, Gan Q, Feng Z, Jin Y, Zhou C, He Z, Wang C and Liu Y 2021 Construction of pH/glutathione responsive chitosan nanoparticles by a self-assembly/self-crosslinking method for photodynamic therapy *Int. J. Biol. Macromol.* **167** 46–58
- [126] M Ferreira D, Y Saga Y, Aluicio-Sarduy E and Tedesco A C 2013 Chitosan nanoparticles for melanoma cancer treatment by photodynamic therapy and electrochemotherapy using aminolevulinic acid derivatives *Curr. Med. Chem.* **20** 1904–11
- [127] Wang J, Wang K, Liang J, Jin J, Wang X and Yan S 2021 Chitosan-tripolyphosphate nanoparticles-mediated co-delivery of MTHFD1L shRNA and 5-aminolevulinic acid for combination photodynamic-gene therapy in oral cancer *Photodiagnosis Photodyn. Ther.* **36** 102581
- [128] Rapozzi V, Moret F, Menilli L, Guerrini A, Tedesco D, Naldi M, Bartolini M, Gani M, Zorzet S and Columbaro M 2022 HSA-binding prodrugs-based nanoparticles endowed with chemo and photo-toxicity against breast cancer *Cancers* **14** 877
- [129] Kang W, Shi Y, Yang Z, Yin X, Zhao Y, Weng L and Teng Z 2023 Flexible human serum albumin nanocapsules to enhance drug delivery and cellular uptake for photodynamic/chemo cancer therapy *RSC Adv.* **13** 5609–18
- [130] Liu J, Yin Y, Yang L, Lu B, Yang Z, Wang W and Li R 2021 Nucleus-targeted photosensitizer nanoparticles for photothermal and photodynamic therapy of breast carcinoma *Int. J. Nanomed.* **16** 1473
- [131] Lian H, Wu J, Hu Y and Guo H 2017 Self-assembled albumin nanoparticles for combination therapy in prostate cancer *Int. J. Nanomed.* **12** 7777
- [132] Yang H, Liu Z, Li X, Zhang Z, Chen D and Lian H 2018 Artesunate-loaded and near-infrared dye-conjugated albumin nanoparticles as high-efficiency tumor-targeted photo-chemo theranostic agent *Nanoscale Res. Lett.* **13** 1–10
- [133] He C, Zhang L, Liu W, Huang Y, Hu P, Dai T, Xu J and Chen Z 2021 Albumin-based nanoparticles combined with photodynamic therapy enhance the antitumor activity of curcumin derivative C086 *Dyes Pigm.* **189** 109258
- [134] Trindade A C et al 2022 Gelatin nanoparticles via template polymerization for drug delivery system to photoprocess application in cells *J. Biomater. Sci. Polym. Ed.* **33** 551–68
- [135] Son J, Yi G, Kwak M-H, Yang S M, Park J M, Lee B-I, Choi M-G and Koo H 2019 Gelatin–chlorin e6 conjugate for *in vivo* photodynamic therapy *J. Nanobiotechnology* **17** 1–12
- [136] Lee D, Jang S-Y, Kwon S, Lee Y, Park E and Koo H 2021 Optimized combination of photodynamic therapy and chemotherapy using gelatin nanoparticles containing tirapazamine and pheophorbide a *ACS Appl. Mater. Interfaces* **13** 10812–21
- [137] Wang Y, Zhang L, Zhao G, Zhang Y, Zhan F, Chen Z, He T, Cao Y, Hao L and Wang Z 2022 Homologous targeting nanoparticles for enhanced PDT against osteosarcoma HOS cells and the related molecular mechanisms *J. Nanobiotechnol.* **20** 1–28
- [138] Yang Y, Tang T, Liu B, Tian J, Wu H, Liu Z, Liu Z, Zhang L, Bao H and Liu T 2021 TB@ PLGA nanoparticles for photodynamic/photothermal combined cancer therapy with single near-infrared irradiation *Int. J. Nanomed.* **16** 4863
- [139] Magalhães J A, Arruda D C, Baptista M S and Tada D B 2021 Co-encapsulation of methylene blue and PARP-inhibitor into poly (lactic-co-glycolic acid) nanoparticles for enhanced PDT of cancer *Nanomaterials* **11** 1514
- [140] Anderski J, Mähler L, Sun J, Birnbaum W, Mulac D, Schreiber S, Herrmann F, Kuckling D and Langer K 2019 Light-responsive nanoparticles based on new polycarbonate polymers as innovative drug delivery systems for photosensitizers in PDT *Int. J. Pharm.* **557** 182–91
- [141] Wang H, Li L, Wang P, Wang X, Zhang K and Liu Q 2016 Comparison of photodynamic treatment produced cell damage between human breast cancer cell MCF-7 and its multidrug resistance cell *Photodiagnosis Photodyn. Ther.* **16** 1–8
- [142] Qin M, Hah H J, Kim G, Nie G, Lee Y-E K and Kopelman R 2011 Methylene blue covalently loaded polyacrylamide nanoparticles for enhanced tumor-targeted photodynamic therapy *Photochem. Photobiol. Sci.* **10** 832–41
- [143] Chepurina O M, Yakovliev A, Ziniuk R, Nikolaeva O A, Levchenko S M, Xu H, Losytskyy M Y, Bricks J L, Slominskii Y L and Vretik L O 2020 Core-shell polymeric nanoparticles co-loaded with photosensitizer and organic dye for photodynamic therapy guided by fluorescence imaging in near and short-wave infrared spectral regions *J. Nanobiotechnol.* **18** 1–15
- [144] Kuruppuarachchi M, Savoie H, Lowry A, Alonso C and Boyle R W 2011 Polyacrylamide nanoparticles as a delivery system in photodynamic therapy *Mol. Pharm.* **8** 920–31
- [145] Pramanik A et al 2022 Affimer tagged cubosomes: targeting of carcinoembryonic antigen expressing colorectal cancer cells using *in vitro* and *in vivo* models *ACS Appl. Mater. Interfaces* **14** 11078–91
- [146] Pramanik A, Xu Z, Ingram N, Coletta P L, Millner P A, Tyler A I I and Hughes T A 2022 Hyaluronic-acid-tagged cubosomes deliver cytotoxics specifically to CD44-positive cancer cells *Mol. Pharm.* **19** 4601–11
- [147] Moghassemi S, Dadashzadeh A, Azevedo R B, Feron O and Amorim C A 2021 Photodynamic cancer therapy using liposomes as an advanced vesicular photosensitizer delivery system *J. Control. Release* **339** 75–90
- [148] Liang X, Chen M, Bhattarai P, Hameed S, Tang Y and Dai Z 2021 Complementing cancer photodynamic therapy with ferroptosis through iron oxide loaded porphyrin-grafted lipid nanoparticles *ACS Nano* **15** 20164–80
- [149] Hameed S, Bhattarai P, Liang X, Zhang N, Xu Y, Chen M and Dai Z 2018 Self-assembly of porphyrin-grafted lipid into nanoparticles encapsulating doxorubicin for synergistic chemo-photodynamic therapy and fluorescence imaging *Theranostics* **8** 5501
- [150] Xu K-F, Jia H-R, Zhu Y-X, Liu X, Gao G, Li Y-H and Wu F-G 2019 Cholesterol-modified dendrimers for constructing a tumor microenvironment-responsive drug delivery system *ACS Biomater. Sci. Eng.* **5** 6072–81
- [151] Kojima C, Toi Y, Harada A and Kono K 2007 Preparation of poly (ethylene glycol)-attached dendrimers encapsulating photosensitizers for application to photodynamic therapy *Bioconjug. Chem.* **18** 663–70
- [152] Rout S R, Bandaru R, Kenguva G, Hasan N, Alam M S, Shukla R, Almalki W H, Kesharwani P and Dandela R 2023 Dendrimers in photodynamic therapy *Nanomaterials for Photodynamic Therapy* (Woodhead) pp 281–305
- [153] Pallavi P, Harini K, Anand Arumugam V, Gowtham P, Girigoswami K, Muthukrishnan S and Girigoswami A 2022 Nanoformulation of tetrapyrroles derivatives in photodynamic therapy: a focus on bacteriochlorin *Evid.-based Complement. Altern. Med.* **2022** 1–12
- [154] Gomes A J, Lunardi C N and Tedesco A C 2007 Characterization of biodegradable poly (D,

- L-lactide-co-glycolide) nanoparticles loaded with bacteriochlorophyll-a for photodynamic therapy *Photomed. Laser Surg.* **25** 428–35
- [155] Pantiushenko I V, Rudakovskaya P G, Starovoytova A V, Mikhaylovskaya A A, Abakumov M A, Kaplan M A, Tsygankov A A, Majouga A G, Grin M A and Mironov A F 2015 Development of bacteriochlorophyll a-based near-infrared photosensitizers conjugated to gold nanoparticles for photodynamic therapy of cancer *Biochemistry* **80** 752–62
- [156] Ostroverkhov P V, Semkina A S, Naumenko V A, Plotnikova E A, Melnikov P A, Abakumova T O, Yakubovskaya R I, Mironov A F, Vodopyanov S S and Abakumov A M 2019 Synthesis and characterization of bacteriochlorin loaded magnetic nanoparticles (MNP) for personalized MRI guided photosensitizers delivery to tumor *J. Colloid Interface Sci.* **537** 132–41
- [157] Engle K and Kumar G 2022 Cancer multidrug-resistance reversal by ABCB1 inhibition: a recent update *Eur. J. Med. Chem.* **239** 114542
- [158] Gonen N and Assaraf Y G 2012 Antifolates in cancer therapy: structure, activity and mechanisms of drug resistance *Drug Resist. Updat.* **15** 183–210
- [159] Bukowski K, Kciuk M and Kontek R 2020 Mechanisms of multidrug resistance in cancer chemotherapy *Int. J. Mol. Sci.* **21** 3233
- [160] Szakács G, Paterson J K, Ludwig J A, Booth-Gentle C and Gottesman M M 2006 Targeting multidrug resistance in cancer *Nat. Rev. Drug Discov.* **5** 219–34
- [161] Deenen M J, Cats A, Beijnen J H and Schellens J H M 2011 Part 2: pharmacogenetic variability in drug transport and phase I anticancer drug metabolism *Oncologist* **16** 820–34
- [162] Hertz D L, Snaveley A C, McLeod H L, Walko C M, Ibrahim J G, Anderson S, Weck K E, Magrinat G, Olajide O and Moore S 2015 *In vivo* assessment of the metabolic activity of CYP2D6 diplotypes and alleles *Br. J. Clin. Pharmacol.* **80** 1122–30
- [163] Zhou J, Kang Y, Chen L, Wang H, Liu J, Zeng S and Yu L 2020 The drug-resistance mechanisms of five platinum-based antitumor agents *Front. Pharmacol.* **11** 343
- [164] Li L-Y, Guan Y-D, Chen X-S, Yang J-M and Cheng Y 2021 DNA repair pathways in cancer therapy and resistance *Front. Pharmacol.* **11** 629266
- [165] Giovannetti E, Pacetti P, Reni M, Leon L G, Mambrini A, Vasile E, Ghidini M, Funel N, Lucchesi M and Cereda S 2011 Association between DNA-repair polymorphisms and survival in pancreatic cancer patients treated with combination chemotherapy *Pharmacogenomics* **12** 1641–52
- [166] Riechelmann R P, Tannock I F, Wang L, Saad E D, Taback N A and Krzyzanowska M K 2007 Potential drug interactions and duplicate prescriptions among cancer patients *J. Natl Cancer Inst.* **99** 592–600
- [167] van Leeuwen R W F, Swart E L, Boven E, Boom F A, Schuitenmaker M G and Hugtenburg J G 2011 Potential drug interactions in cancer therapy: a prevalence study using an advanced screening method *Ann. Oncol.* **22** 2334–41
- [168] van Leeuwen R W F, Brundel D H S, Neef C, van Gelder T, Mathijssen R H J, Burger D M and Jansman F G A 2013 Prevalence of potential drug–drug interactions in cancer patients treated with oral anticancer drugs *Br. J. Cancer* **108** 1071–8
- [169] Budha N R, Frymoyer A, Smelick G S, Jin J Y, Yago M R, Dresser M J, Holden S N, Benet L Z and Ware J A 2012 Drug absorption interactions between oral targeted anticancer agents and PPIs: is pH-dependent solubility the Achilles heel of targeted therapy? *Clin. Pharmacol. Ther.* **92** 203–13
- [170] Mansoori B, Mohammadi A, Davudian S, Shirjang S and Baradaran B 2017 The different mechanisms of cancer drug resistance: a brief review *Adv. Pharm. Bull.* **7** 339
- [171] Assaraf Y G and Schimke R T 1987 Identification of methotrexate transport deficiency in mammalian cells using fluoresceinated methotrexate and flow cytometry *Proc. Natl Acad. Sci.* **84** 7154–8
- [172] Kolata G 1986 Why do cancer cells resist drugs? Cancer cells that become resistant to one drug frequently become resistant to several other unrelated ones *Science* **231** 220–1
- [173] Ramu A, Pollard H B and Rosario L M 1989 Doxorubicin resistance in P388 leukemia—evidence for reduced drug influx *Int. J. Cancer* **44** 539–47
- [174] Manallack D T 2007 The pK_a distribution of drugs: application to drug discovery *Perspect. Med. Chem.* **1** 1177391X0700100003
- [175] Assaraf Y G 2007 Molecular basis of antifolate resistance *Cancer Metastasis Rev.* **26** 153–81
- [176] Hutchinson S A et al 2021 Liver x receptor alpha drives chemoresistance in response to side-chain hydroxycholesterols in triple negative breast cancer *Oncogene* **40** 2872–83
- [177] Gottesman M M and Ambudkar S V 2001 Overview: ABC transporters and human disease *J. Bioenerg. Biomembr.* **33** 453–8
- [178] Anreddy N, Gupta P, Kathawala R J, Patel A, Wurlpel J N D and Chen Z-S 2014 Tyrosine kinase inhibitors as reversal agents for ABC transporter mediated drug resistance *Molecules* **19** 13848–77
- [179] Mao Q 2005 Role of the breast cancer resistance protein (ABCG2) in drug transport *AAPS J.* **7** E118–E33
- [180] Mc Namee N and O'Driscoll L 2018 Extracellular vesicles and anti-cancer drug resistance *Biochim. Biophys. Acta* **1870** 123–36
- [181] Gong J, Luk F, Jaiswal R, George A M, Grau G E R and Bebawy M 2013 Microparticle drug sequestration provides a parallel pathway in the acquisition of cancer drug resistance *Eur. J. Pharmacol.* **721** 116–25
- [182] Samuel P, Fabbri M and Carter D R F 2017 Mechanisms of drug resistance in cancer: the role of extracellular vesicles *Proteomics* **17** 1600375
- [183] Aung T, Chapuy B, Vogel D, Wenzel D, Oppermann M, Lahmann M, Weinlage T, Menck K, Hupfeld T and Koch R 2011 Exosomal evasion of humoral immunotherapy in aggressive B-cell lymphoma modulated by ATP-binding cassette transporter A3 *Proc. Natl Acad. Sci.* **108** 15336–41
- [184] Ciravolo V, Huber V, Ghedini G C, Venturini E, Bianchi F, Campiglio M, Morelli D, Villa A, Mina P D and Menard S 2012 Potential role of HER2-overexpressing exosomes in countering trastuzumab-based therapy *J. Cell. Physiol.* **227** 658–67
- [185] Green D R and Llamby F 2015 Cell death signaling *Cold Spring Harb. Perspect. Biol.* **7** a006080
- [186] Tarasov V V, Chubarev V N, Ashraf G M, Dostdar S A, Sokolov A V, Melnikova T I, Sologova S S, Grigorevskikh E M, Makhmutova A and Kinzirsy A S 2019 How cancer cells resist chemotherapy: design and development of drugs targeting protein-protein interactions *Curr. Top. Med. Chem.* **19** 394–412
- [187] Indran I R, Tufo G, Pervaiz S and Brenner C 2011 Recent advances in apoptosis, mitochondria and drug resistance in cancer cells *Biochim. Biophys. Acta* **1807** 735–45
- [188] Campbell K J and Tait S W G 2018 Targeting BCL-2 regulated apoptosis in cancer *Open Biol.* **8** 180002
- [189] Wilson T R, Johnston P G and Longley D B 2009 Anti-apoptotic mechanisms of drug resistance in cancer *Curr. Cancer Drug Targets* **9** 307–19
- [190] Hussain S A, Ganesan R, Hiller L, Cooke P W, Murray P, Young I S and James N D 2003 BCL2 expression predicts survival in patients receiving synchronous chemoradiotherapy in advanced transitional cell carcinoma of the bladder *Oncol. Rep.* **10** 571–6
- [191] Dong H P, Kleinberg L, Silins I, Flørenes V A, Tropé C G, Risberg B, Nesland J M and Davidson B 2008 Death receptor expression is associated with poor response to chemotherapy and shorter survival in metastatic ovarian carcinoma *Cancer Interdiscip. Int. J. Am. Cancer Soc.* **112** 84–93

- [192] Costa A F O, Menezes D L, Pinheiro L H S, Sandes A F, Nunes M A P, Lyra Junior D P and Schimieguel D M 2017 Role of new immunophenotypic markers on prognostic and overall survival of acute myeloid leukemia: a systematic review and meta-analysis *Sci. Rep.* **7** 4138
- [193] Gundlach J-P, Hauser C, Schlegel F M, Böger C, Röder C, Röcken C, Becker T, Egberts J-H, Kalthoff H and Trauzold A 2018 Cytoplasmic TRAIL-R1 is a positive prognostic marker in PDAC *BMC Cancer* **18** 1–10
- [194] Tamm I, Richter S, Oltersdorf D, Creutzig U, Harbott J, Scholz F, Karawajew L, Ludwig W-D and Wuchter C 2004 High expression levels of x-linked inhibitor of apoptosis protein and survivin correlate with poor overall survival in childhood de novo acute myeloid leukemia *Clin. Cancer Res.* **10** 3737–44
- [195] Yang H, Villani R M, Wang H, Simpson M J, Roberts M S, Tang M and Liang X 2018 The role of cellular reactive oxygen species in cancer chemotherapy *J. Exp. Clin. Cancer Res.* **37** 1–10
- [196] Traverso N, Ricciarelli R, Nitti M, Marengo B, Furfaro A L, Pronzato M A, Marinari U M and Domenicotti C 2013 Role of glutathione in cancer progression and chemoresistance *Oxid. Med. Cell. Longev.* **2013** 1–10
- [197] Ghosh S 2019 Cisplatin: the first metal based anticancer drug *Bioorg. Chem.* **88** 102925
- [198] Yamanaka K, Chatterjee N, Hemann M T and Walker G C 2017 Inhibition of mutagenic translesion synthesis: a possible strategy for improving chemotherapy? *PLoS Genet.* **13** e1006842
- [199] Chen X, Li Y, Ouyang T, Li J, Wang T, Fan Z, Fan T, Lin B and Xie Y 2018 Associations between RAD51D germline mutations and breast cancer risk and survival in BRCA1/2-negative breast cancers *Ann. Oncol.* **29** 2046–51
- [200] Kagohara L T, Stein-O'Brien G L, Kelley D, Flam E, Wick H C, Danilova L V, Easwaran H, Favorov A V, Qian J and Gaykalova D A 2018 Epigenetic regulation of gene expression in cancer: techniques, resources and analysis *Brief. Funct. Genomics* **17** 49–63
- [201] Wilting R H and Dannenberg J-H 2012 Epigenetic mechanisms in tumorigenesis, tumor cell heterogeneity and drug resistance *Drug Resist. Updat.* **15** 21–38
- [202] Spitzwieser M, Pirker C, Koblmüller B, Pfeiler G, Hacker S, Berger W, Heffeter P and Cichna-Markl M 2016 Promoter methylation patterns of ABCB1, ABCC1 and ABCG2 in human cancer cell lines, multidrug-resistant cell models and tumor, tumor-adjacent and tumor-distant tissues from breast cancer patients *Oncotarget* **7** 73347
- [203] Ferraro A 2016 Altered primary chromatin structures and their implications in cancer development *Cell. Oncol.* **39** 195–210
- [204] Giri A K and Aittokallio T 2019 DNMT inhibitors increase methylation in the cancer genome *Front. Pharmacol.* **10** 385
- [205] Calvisi D F, Pascale R M and Feo F 2007 Dissection of signal transduction pathways as a tool for the development of targeted therapies of hepatocellular carcinoma *Rev. Recent Clin. Trials* **2** 217–36
- [206] Grasse S, Lienhard M, Frese S, Kerick M, Steinbach A, Grimm C, Hussong M, Rolff J, Becker M and Dreher F 2018 Epigenomic profiling of non-small cell lung cancer xenografts uncover LRP12 DNA methylation as predictive biomarker for carboplatin resistance *Genome Med.* **10** 1–16
- [207] Costa A L, Moreira-Barbosa C, Lobo J, Vilela-Salgueiro B, Cantante M, Guimarães R, Lopes P, Braga I, Oliveira J and Antunes L 2018 DNA methylation profiling as a tool for testicular germ cell tumors subtyping *Epigenomics* **10** 1511–23
- [208] Ahuja N, Sharma A R and Baylin S B 2016 Epigenetic therapeutics: a new weapon in the war against cancer *Annu. Rev. Med.* **67** 73–89
- [209] Dougherty T J, Gomer C J, Henderson B W, Jori G, Kessel D, Korbek M, Moan J and Peng Q 1998 Photodynamic therapy *J. Natl Cancer Inst.* **90** 889–905
- [210] Zhong Y, Bejjanki N K, Miao X, Weng H, Li Q, Zhang J, Liu T, Vannam R and Xie M 2021 Synthesis and photothermal effects of intracellular aggregating nanodrugs targeting nasopharyngeal carcinoma *Front. Bioeng. Biotechnol.* **9** 730925
- [211] Gustalik J, Aebischer D and Bartusik-Aebischer D 2022 Photodynamic therapy in breast cancer treatment *J. Appl. Biomed.* **20** 98–105
- [212] Cheung K K-Y, Chan J Y-W and Fung K-P 2013 Antiproliferative effect of pheophorbide a-mediated photodynamic therapy and its synergistic effect with doxorubicin on multiple drug-resistant uterine sarcoma cell MES-SA/Dx5 *Drug Chem. Toxicol.* **36** 474–83
- [213] Xu B, He P, Wang Y, Wang H, Zhang J, Zhu J, Pu W and Chen H 2023 PDT for gastric cancer—the view from China *Photodiagnosis Photodyn. Ther.* **42** 103366
- [214] Murphy W K, Fossella F V, Winn R J, Shin D M, Hynes H E, Gross H M, Davilla E, Leimert J, Dhingra H and Raber M N 1993 Phase II study of taxol in patients with untreated advanced non-small-cell lung cancer *J. Natl Cancer Inst.* **85** 384–8
- [215] Atjanasupatt K, Lirdprapamongkol K, Jantaree P and Svasti J 2015 Non-adherent culture induces paclitaxel resistance in H460 lung cancer cells via ERK-mediated up-regulation of β IVa-tubulin *Biochem. Biophys. Res. Commun.* **466** 493–8
- [216] Pramual S, Lirdprapamongkol K, Jouan-Hureaux V, Barberi-Heyob M, Frochet C, Svasti J and Niamsiri N 2020 Overcoming the diverse mechanisms of multidrug resistance in lung cancer cells by photodynamic therapy using pTHPP-loaded PLGA-lipid hybrid nanoparticles *Eur. J. Pharm. Biopharm.* **149** 218–28
- [217] Shi X, Yang X, Liu M, Wang R, Qiu N, Liu Y, Yang H, Ji J and Zhai G 2021 Chondroitin sulfate-based nanoparticles for enhanced chemo-photodynamic therapy overcoming multidrug resistance and lung metastasis of breast cancer *Carbohydrate Polym.* **254** 117459
- [218] Shanmugam M, Kuthala N, Vankayala R, Chiang C-S, Kong X and Hwang K C 2021 Multifunctional CuO/Cu₂O truncated nanocubes as trimodal image-guided near-infrared-III photothermal agents to combat multi-drug-resistant lung carcinoma *ACS Nano* **15** 14404–18
- [219] Zeng L, Pan Y, Tian Y, Wang X, Ren W, Wang S, Lu G and Wu A 2015 Doxorubicin-loaded NaYF₄: Yb/Tm–TiO₂ inorganic photosensitizers for NIR-triggered photodynamic therapy and enhanced chemotherapy in drug-resistant breast cancers *Biomaterials* **57** 93–106
- [220] Baglo Y, Liang B J, Robey R W, Ambudkar S V, Gottesman M M and Huang H-C 2019 Porphyrin-lipid assemblies and nanovesicles overcome ABC transporter-mediated photodynamic therapy resistance in cancer cells *Cancer Lett.* **457** 110–8
- [221] Rezaeivala Z, Imanparast A, Mohammadi Z, Najafabad B K and Sazgarnia A 2023 The multimodal effect of photothermal/photodynamic/chemo therapies mediated by Au-CoFe₂O₄@spiky nanostructure adjacent to mitoxantrone on breast cancer cells *Photodiagnosis Photodyn. Ther.* **41** 103269
- [222] Yu Y, Zhang Z, Wang Y, Zhu H, Li F, Shen Y and Guo S 2017 A new NIR-triggered doxorubicin and photosensitizer indocyanine green co-delivery system for enhanced multidrug resistant cancer treatment through simultaneous chemo/photothermal/photodynamic therapy *Acta Biomater.* **59** 170–80
- [223] Zhan W, Cai X, Li H, Du G, Hu H, Wu Y and Wang L 2020 GMBP1-conjugated manganese oxide nanoplates for *in vivo* monitoring of gastric cancer MDR using magnetic resonance imaging *RSC Adv.* **10** 13687–95
- [224] Li H, Cai X, Yi T, Zeng Y, Ma J, Li L, Pang L, Li N, Hu H and Zhan Y 2022 Tumor microenvironment responsive Mn₃O₄ nanoplateform for *in vivo* real-time monitoring of drug resistance and photothermal/chemodynamic

- synergistic therapy of gastric cancer *J. Nanobiotechnol.* **20** 1–22
- [225] Barth B M, Altinoglu E I, Shanmugavelandy S S, Kaiser J M, Crespo-Gonzalez D, DiVittore N A, McGovern C, Goff T M, Keasey N R and Adair J H 2011 Targeted indocyanine-green-loaded calcium phosphosilicate nanoparticles for *in vivo* photodynamic therapy of leukemia *ACS Nano* **5** 5325–37
- [226] Licciardi M, Varvarà P, Tranchina L, Puleio R, Cicero L, Cassata G and Giammona G 2022 *In vivo* efficacy of verteporfin loaded gold nanorods for combined photothermal/photodynamic colon cancer therapy *Int. J. Pharm.* **625** 122134
- [227] Chen M, Liang X, Gao C, Zhao R, Zhang N, Wang S, Chen W, Zhao B, Wang J and Dai Z 2018 Ultrasound triggered conversion of porphyrin/camptothecin-fluoroxymidine triad microbubbles into nanoparticles overcomes multidrug resistance in colorectal cancer *ACS Nano* **12** 7312–26
- [228] Busa P, Kankala R K, Deng J-P, Liu C-L and Lee C-H 2022 Conquering cancer multi-drug resistance using curcumin and cisplatin prodrug-encapsulated mesoporous silica nanoparticles for synergistic chemo-and photodynamic therapies *Nanomaterials* **12** 3693
- [229] Xu S, Zhang P, Heing-Becker I, Zhang J, Tang P, Bej R, Bhatia S, Zhong Y and Haag R 2022 Dual tumor-and subcellular-targeted photodynamic therapy using glucose-functionalized MoS₂ nanoflakes for multidrug-resistant tumor ablation *Biomaterials* **290** 121844

A critical assessment of the whole plant-based phytotherapeutics from *Withania somnifera* (L.) Dunal with respect to safety and efficacy vis-a-vis leaf or root extract-based formulation

Pawan Kumar, Samudra P. Banik, Apurva Goel, Sanjoy Chakraborty, Manashi Bagchi & Debasis Bagchi


To cite this article: Pawan Kumar, Samudra P. Banik, Apurva Goel, Sanjoy Chakraborty, Manashi Bagchi & Debasis Bagchi (2023) A critical assessment of the whole plant-based phytotherapeutics from *Withania somnifera* (L.) Dunal with respect to safety and efficacy vis-a-vis leaf or root extract-based formulation, *Toxicology Mechanisms and Methods*, 33:8, 698-706, DOI: [10.1080/15376516.2023.2242933](https://doi.org/10.1080/15376516.2023.2242933)

To link to this article: <https://doi.org/10.1080/15376516.2023.2242933>



Published online: 14 Aug 2023.



Submit your article to this journal 



Article views: 62



View related articles 



View Crossmark data 

REVIEW ARTICLE



A critical assessment of the whole plant-based phytotherapeutics from *Withania somnifera* (L.) Dunal with respect to safety and efficacy vis-a-vis leaf or root extract-based formulation

Pawan Kumar^a , Samudra P. Banik^b , Apurva Goel^c , Sanjoy Chakraborty^d , Manashi Bagchi^e  and Debasish Bagchi^f 

^aR&D Department, Chemical Resources (CHERESO), Panchkula, Haryana, India; ^bDepartment of Microbiology, Maulana Azad College, Kolkata, India; ^cRegulatory Department, Chemical Resources (CHERESO), Panchkula, Haryana, India; ^dDepartment of Biological Sciences, New York City College of Technology/CUNY, Brooklyn, NY, USA; ^eDepartment of R&D, Dr. Herbs LLC, Concord, CA, USA; ^fDepartment of Biology, College of Arts and Sciences, and Dept of Psychology, Gordon F. Derner School of Psychology, Adelphi University, Garden City, NY, USA

ABSTRACT

Withania somnifera (L.) Dunal, popularly known as Ashwagandha or Indian ginseng, is well acclaimed for its health-enhancing effects, including its potent immunomodulatory, anti-inflammatory, neuroprotective, and anti-tumorigenic properties. The prime biological effectors of these attributes are a diverse group of ergostane-based steroidal lactones termed withanolides. Withanones and withanosides are distributed differentially across the plant body, whereas withanolides and withanones are known to be more abundant in leaves, while withanosides are found exclusively in the roots of the plants. Standardized *W. somnifera* extract is Generally Recognized as Safe (GRAS)-affirmed, however, moderate to severe toxic manifestations may occur at high dosages. Withaferin A, which also happens to be the primary bioactive ingredient for the effectiveness of this plant. There have been contrasting reports regarding the distribution of withaferin A in *W. somnifera*. While most reports state that the roots of the plant have the highest concentrations of this phytochemical, several others have indicated that leaves can accumulate withaferin A in proportionately higher amounts. A comprehensive survey of the available reports suggests that the biological effects of Ashwagandha are grossly synergistic in nature, with many withanolides together mediating the desired physiological effect. In addition, an assorted formulation of withanolides can also neutralize the toxic effects (if any) associated with withaferin A. This mini-review presents a fresh take on the recent developments regarding the safety and toxicity of the plant, along with a critical assessment of the use of roots against leaves as well as whole plants to develop therapeutic formulations. Going by the currently available scientific evidence, it is safe to infer that the use of whole plant formulations instead of exclusively root or leaf recipes may present the best possible option for further exploration of therapeutic benefits from this novel medicinal plant.

HIGHLIGHTS

- Therapeutic potential of withanolides owes to the presence of α,β unsaturated ketone which binds to amines, alcohols, and esters and 5β , 6β epoxy group which react with side chain thiols of proteins.
- At concentrations above NOAEL (no observed adverse effect level), the same mechanisms contribute towards toxicity of the molecule.
- Although withanosides are found exclusively in roots, whole plants have higher contents of withanones and withanolides.
- Whole plant-based formulations have other metabolites which can nullify the toxicity associated with roots.
- Extracts made from whole plants, therefore can holistically impart all therapeutic benefits as well as mitigate toxicity.

ARTICLE HISTORY

Received 12 June 2023
Revised 26 July 2023
Accepted 26 July 2023

KEYWORDS

Withania somnifera;
Withanolides; Withaferin A;
safety; spatial distribution;
synergistic effect

1. Introduction

Withania somnifera (L.) Dunal or Ashwagandha is a popular member of the Solanaceae, or nightshade family of plants known widely for its multitude of therapeutic benefits. Its use has been in vogue in traditional Indian Ayurveda for centuries in the treatment of cancer, neurological disorders,

reproductive diseases, insomnia, and anxiety, as well as diverse chronic, debilitating conditions. The plant extract has also been successfully used in reducing stress (Speers et al. 2021), boosting immunity (Tharakan et al. 2021), improving memory (Gopukumar et al. 2021) and vigor (Bonilla et al. 2021), as well as a potent antioxidant to fight free-radical inflicted damage and injury (Sikandan et al. 2018). Recent

reports have unearthed cardioprotective, antimicrobial, anti-diabetic, and adaptogenic potentials of this phytochemical thus justifying its comparison with the Korean medicinal plant Ginseng (Mikulska et al. 2023).

The basis of the therapeutic potential of this plant is due to the presence of alkaloids, saponins, and a unique class of ergostane skeleton-based steroidal lactones termed withanolides. Currently, close to 600 naturally occurring withanolides have been discovered from the genus *Solanaceae* alone (Zhang et al. 2014) with modified or unmodified skeletons which differ with respect to their C-17 side chain leading to the more abundant C-22 hydroxyl/C-26 carboxylate δ -lactone/lactol or the less commonly encountered C-23/C-26 γ -lactone/lactol group with an additional hydroxyl group outside the lactone ring (White et al. 2016) (Figure 1).

Unique structural features such as the presence of the α,β -unsaturation in the A ring, 5 β ,6 β -epoxy in the B ring, two hydrogen bond donors, and six potential hydrogen bond acceptors form the mainstay of the high biological reactivity of the molecule (Sultana et al. 2021), especially with regards to its potential interaction with many components of the cellular signaling pathway (Fazil et al. 2021; Atteeq 2022). Owing to its versatility in treating human ailments, there has been a surge in the conduction of safety and toxicity studies to develop Ashwagandha as a therapeutic for human consumption (Patel et al. 2016; Tandon and Yadav 2020; Verma et al. 2021; Gupta et al. 2022).

Ashwagandha received self-affirmed Generally Regarded As Safe (GRAS) status in 2019 through a formulation developed by Ixoral Biomed in 2012 (<https://www.newhope.com/supply-news-amp-analysis/ksm-66-ashwagandha-gets-self-affirmed-gras-status>) for its use as a food supplement.

However, in the United States, Ashwagandha is not listed in FDA's GRAS inventory database in the Code of Federal Regulations (CFR) for incorporation in conventional food products (<https://www.herbalgram.org/resources/herbalgram/issues/99/table-of-contents/hg99-herbprofile-ashwagandha/>). Instead, United States Pharmacopoeia has developed guidelines for maintenance of quality standards in the manufacturing of Ashwagandha root based extract which requires a permit from FDA within a month of marketing of the product. The high propensity of withanolides to engage in biomolecular interactions has also brought to forefront several associated side effects. The first case of Ashwagandha-associated toxicity was reported by Inagaki in a 20-year-old man who developed jaundice due to consumption of a high uncontrolled dosage of Ashwagandha (Inagaki et al. 2017). Similar reports arising from excessive intake of Ashwagandha were also obtained from Iceland, USA, and Germany (Björnsson et al. 2020; Tóth et al. 2023). In addition, consumption of excessive Ashwagandha beyond prescribed dosage has been reported to result in minor illnesses such as drowsiness, stomach upset, diarrhea, and vomiting. Consumption of Ashwagandha is also prohibited in cases of pregnancy, surgery, autoimmune and thyroid disorders as well as in patients with high blood pressure (<https://www.nccih.nih.gov/health/ashwagandha>).

The toxicity of Ashwagandha has been primarily associated with withaferin A, its main constituent withanolide (Siddiqui et al. 2021). Most of the Ashwagandha-based dietary supplements are based on root extract instead of leaves (Chandrasekhar et al. 2012; Langade et al. 2019; Mikulska et al. 2023).

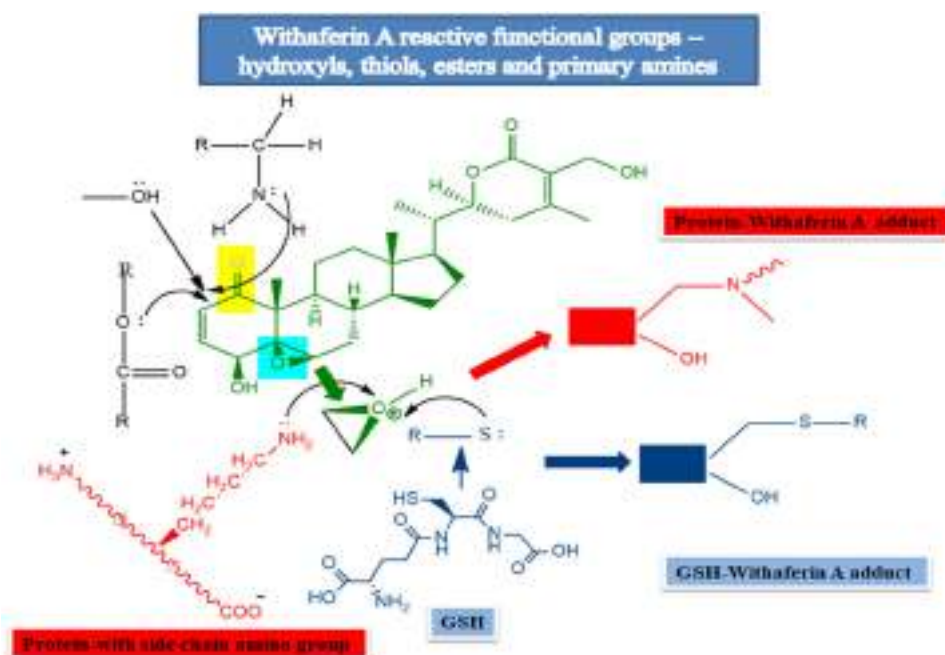


Figure 1. Main chemical attributes of Withaferin A's toxicity: Presence of several highly reactive sites including α,β -unsaturation in the A ring (highlighted in yellow) and 5 β ,6 β -epoxy in the B ring (highlighted in seablue) attract nucleophilic esters and primary amines present in abundance in biological molecules. The protein side-chain thiols and the cellular redox buffer GSH (reduced glutathione) are particularly susceptible to reaction with the epoxy group leading to irreversible covalent adducts with withaferin A. It is not very intriguing to note that the same mechanisms contribute to the therapeutic potential of this phytopharmaceutical within permissible limits.

However, intriguingly enough, the concentration of withaferin A in the roots of *Ashwagandha* has been found to be significantly higher than its distribution in other plant parts (Abouzid et al. 2010). Therefore, a fresh debate has been initiated regarding the safe use of the plant in the production of oral medicines and dietary supplements. In the subsequent sections of this mini-review, recent understandings of the safety and toxicity of *Ashwagandha* extract will be discussed along with the intrinsic advantages and disadvantages associated with the choice of the plant part to minimize its adverse effects.

1.1. Structure of withanolides: basis of cytotoxicity

Withanolides are built upon a 28-carbon triterpenoid ergostane with a lactone side chain. The big multi-ring assembly formed of four fused cyclo-alkane rings gives this compound ample scope of substitutions with richness in terms of biological activity. The cytotoxicity of withaferin A has been selectively utilized against cancer cells in many studies (Atteeq 2022; Kumar et al. 2023; Lee and Choi 2016). Withaferin A interferes with several signal transduction pathways of the cell including the NF- κ B pathway (Heyninck et al. 2014), the Notch-1 signaling pathway (Kakar et al. 2014), Bcl-2 (Mayola et al. 2011), STAT-3 (Choi and Kim 2015), p53-miR-27a/miR-10B (Lin et al. 2021) etc. and can selectively mediate cell cycle arrest (Tang et al. 2020) and promote apoptosis of cancer cells (Tang et al. 2020). A deeper insight into the structure of the compound reveals the presence of an α,β unsaturated ketone as well as the 5 β , 6 β epoxy group in the B ring as the chief mediators of macromolecular interactions. The α,β unsaturated ketone can act as a potent Michael acceptor which can effectively sequester nucleophiles including amines, alcohols and esters present in abundance in biomolecules (Figure 1).

In addition, the thiol side chains of proteins constitute sites of vulnerability for reaction with the epoxy center in the A ring leading to the formation of a β -hydroxy thioether linkage (Carioscia et al. 2007). In fact, most of the experimentally verified as well as *in silico* predicted interactions of withaferin A with cellular proteins target the cysteine residues of proteins (Antony et al. 2014; Heyninck et al. 2014; Grossman et al. 2017; Yang et al. 2019). Based on the emphasis and understanding of thiol-epoxide chemistry, protein pockets with thiols have emerged as hotspots for drug designing. The reaction can further proceed leading to the formation of reactive alcohols (Dadfar et al. 2021) thus opening additional centers for reactivity. The initial approach and docking of withaferin A to biomolecules is also facilitated by the presence of four potential hydrogen bond acceptors as well as two more groups which can additionally act as donors and hold the molecule within the range of nucleophilic attacks (Sudeep et al. 2020). The wide spectrum of withaferin A's biological effector response has been apparent in one study on its immunomodulatory activity where the compound inhibited the motility of human T-cells by arresting lymphocyte function-associated antigen-1 (LFA-1) integrin and its

ligand, intercellular adhesion molecule 1 (ICAM-1) through a pathway involving more than 250 proteins (Fazil et al. 2021).

The reactivity of withaferin A is also augmented by the type of substitution attached to the C17 side chain. In the majority of the naturally occurring withanolides, the C-22/C-26 δ -lactone predominates in the side chain whereas the C23-C28 γ -lactone is found scarcely (White et al. 2016). A study carried out on synthetic derivatives of withanolides from *Physalis sp.* revealed that the structure of the side chain lactone was an equally determinant factor governing the reactivity of withanolides (Ozawa et al. 2013). Although other structural analogues of withanolides such as paraminabeolides, capsisteroids, and chantriolides have been discovered from a plethora of other plants possessing both α,β -unsaturated ketone and/or epoxide, their biological effectivity and hence, the therapeutic potential of withanolides such as withaferin A have been found to be significantly superior (White et al. 2016). This proves beyond doubt the role played by the side chain lactones in collectively empowering the biological effectivity of withanolides.

1.2 Biosynthetic pathways of withanolides

Plants are unparalleled in the diversity of secondary metabolites produced which enable them to successfully interact and respond to various environmental stimuli (Erb and Kliebenstein. 2020), combat threats from various exogenous sources such as pathogens (Teoh 2015) as well as to mediate key events for the physiological development of the plant such as drawing pollinators, establishing symbiotic associations, and inducing vasculature (Ncube & Van Staden 2015). The biosynthesis and corresponding spatio-temporal distribution of these metabolites is under tight transcriptional control of the plant in response to various biotic and abiotic stressors (Jan et al. 2021, Sharma et al. 2023). In addition, many secondary metabolites are often species-specific in distribution and the plant species in question may be distributed to specific geographical location.

Plants from the Solanaceae family are prolific producers of tropane alkaloids, synthesized through the putrescine pathway and detected in *W. somnifera* much earlier than the discovery of the withanolides (Khanna et al. 1961). Biosynthesis of tropanes takes place in the roots from where they are transported into the leaves (Kohnen-Johannsen and Kayser 2019). Unlike the tropanes, withanolides are known to be synthesized significantly both in roots and leaves of plants under normal physiological conditions. Withanolides have triterpenoid backbones and hence require isopentenyl pyrophosphate (IPP) and dimethyl allyl pyrophosphate (DMAP) as precursors (Dhar et al. 2015). In Solanaceae, two independent routes for the synthesis of isoprene units have been traced. The mevalonate pathway (MVA) operates strictly in the cytosol with acetyl CoA as the primary precursor and is dedicated to the production of membrane sterols, steroidal hormones, and dolichol phosphate needed in N-linked glycosylation of proteins (Rodríguez-Concepción et al. 2004). The pathway is initiated by the enzyme 3-hydroxy-3-methylglutaryl-coenzyme A reductase (HMGR), which mediates the conversion of

hydroxymethylglutaryl coenzyme A (HMGCoA) into mevalonate, which is subsequently transformed into the two integral building blocks IPP and DMAP. The reactions proceed further through the squalene intermediate to lead to the synthesis of withanolides and withanolide glycosides.

The second 1-deoxy-D-xylulose 5-phosphate/2-methyl-D-erythritol 4-phosphate (DOXP/MEP) pathway, on the other hand, takes place only inside plastids and starts with pyruvate instead of acetyl CoA as the primary precursor. It involves the synthesis of 2-o-methyl-d-erythritol-4-phosphate from 1-deoxy-d-xylulose-5-phosphate catalyzed by 1-deoxy-D-xylulose-5-phosphate reductase (DXR) (Zhao et al. 2013) and ends with the synthesis of IPP and DMP which merge with the MVA pathway. The cytosolic mevalonate pathway is the major contributor of the total withanolides pool whereas the DOXP/MEP pathway contributes roughly one-fourth of the total withanolides biosynthesis (Chaurasiya et al. 2012). Therefore, it is apparent that the pyruvate route is less efficient than its cytosolic counterpart with respect to the production of IPP and DMP either due to the abundance of acetyl CoA funneled through sources other than glucose metabolism or due to enhanced expression of HMGR gene or both.

1.3 Distribution of withanolides across various plant tissues

The major withanolides present in *W. somnifera* are withaferin A, withanolide A, and withanone which differ from each other according to the position of the epoxy ring and hydroxyl groups in the main chain or lactone side chain. Withanone's epoxy group includes C6 and C7, unlike Withaferin A where the epoxy group comprises C5 and C6. Withanone has hydroxyl groups on C5 and C17 whereas withaferin A's hydrogen bond donors are on C4 and C27. Withanolide A's epoxy center shares the same location as that of the withanone, but it has hydroxyl groups on C5 and C21.

Although the backbone of withanolides might be synthesized ubiquitously across various plant tissues, several independent studies have reported the existence of spatiotemporal gradient as well as a tissue-specific distribution pattern of specific withanolides subtypes owing to the differential expression of genes responsible for the final substitution on the withanolide backbones (Agarwal et al. 2018; Gupta et al. 2013, 2021). Some studies have even suggested that there are distinct translocation mechanisms for a few withanolide molecules to unique locations from the site of synthesis. However, it has been often found that root withanolides are synthesized *de novo* in roots only and never imported from any other location (Sangwan et al. 2008).

Despite the presence of independent routes of synthesis of withanolides in roots and leaves, it has been found almost often that withanolides are enriched in leaves rather than roots (Siriwardane et al. 2013). This may be partly attributed to the fact that, in addition to the cytosolic mevalonate pathway contributing towards the bulk of withanolides synthesis, the minor 2-methyl-D-erythritol 4-phosphate (MEP) pathway

to produce withanolides which are initiated in the plastids, are more abundant in leaves (Nagella et al. 2010). Also, the roots and leaves vary in type, as does the constitution of withanolides. Whereas withaferins and withanolides are found in leaves in higher proportions (Chaurasiya et al. 2008), roots tend to accumulate more withanolide glycosides, which contain glycosyl substituents attached mostly to the A chain (Ha et al. 2022). An increase in withanolide biosynthesis in roots has only been possible through augmentation of root development with phytohormones such as Indole Acetic Acid (IAA) and Indole 3 Butyric Acid (IBA) through extrinsic manipulations as root-associated endophyte cultivation (Pandey et al. 2018) and adoption of suspension culture (Rangaraju et al. 2019).

Analysis of Kyoto Encyclopedia of Genes and Genomes (KEGG) pathway suggests that IAA promotes the influx of the metabolic intermediates Isopentenyl pyrophosphate (IPP) and Dimethyl-allyl pyrophosphate, the two primary precursors of withanolides biosynthesis. Withanolide levels are also found to be enhanced during reproductive stages of the plant being mediated directly by IAA and IBA (Srivastava et al. 2018; Thorat et al. 2022). IAA-mediated increase in withanolides biosynthesis clearly suggests that withanolides are intrinsically associated with plant growth promotion. In addition, the inclusion of agents such as chitosan and methyl salicylate has also resulted in enhanced synthesis, particularly of Withaferin A, by the plant (Singh et al. 2020). In a separate study, the biosynthetic pathway for withanolides was found to be upregulated under stress through enhanced expression of the genes dedicated to the synthesis of withanolides, such as CAS, SMT, DXR, and HMGR (Thorat et al. 2022) (Figure 2).

1.4. The root: leaf: whole plant debate for production of phytotherapeutics

Despite the increased contents of both withanones and withaferins in the leaves, there has been a trend amongst the nutraceutical industries to shift towards the development of root-based formulations of Ashwagandha, arising chiefly out of withanone-associated toxicity concerns with crude leaf extract (Lubarska et al. 2023; Siddiqui et al. 2021) and regulatory frameworks imposed by government agencies (Ministry of Ayush 2021). As a result, most of the documented safety studies have been conducted on root (Table 1). In addition to the withanolides, roots have other plant alkaloids such as withanins (Saleem et al. 2020), withanosides (Modi et al. 2022; Nile et al. 2019), and phytochemicals possessing anti-inflammatory (Orrù et al. 2023), anti-bacterial (Kumari and Gupta 2015) and antiviral activities (Singh et al. 2022). *W. somnifera* roots are also a significant source of withanolide glycosides (withanosides), a group of water-extractable molecules, responsible for a host of biological effector functions (Modi et al. 2022; Nile et al. 2019). The anti-SARS COV2 activity of a root extract of *W. somnifera* was also traced to be associated with withanoside V, a novel root derived withanolide glycoside *in vitro* (Singh et al. 2022).

On the contrary, leaves represent far more significant sources of withanolides and withanones than roots.

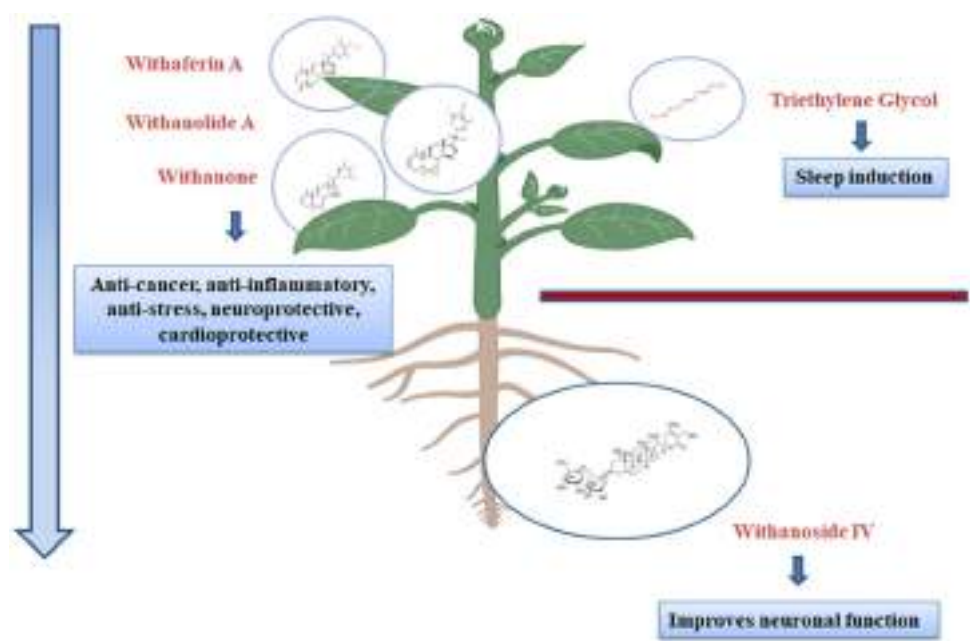


Figure 2. Distribution of biologically active metabolites across parts of Ashwagandha: The chief effector molecules of the plant’s phytotherapeutic potential, withaferin A, withanolide A, and withanone show a gradient in their distribution from leaves and stems to roots whereas certain equally significant metabolites are found exclusively in either roots (withanosides) or leaves (triethylene glycol). This goes to show that formulations developed from the whole plant will be more complete and optimized in terms of therapeutic potential in comparison to the ones based on roots or leaves only.

Table 1. Investigation of therapeutic potential of Ashwagandha in human volunteers.

Source tissue	Recommended dosage	Therapeutic effect/Toxicity	Reference
Root and leaf	400 mg daily for 30 days	Improved cognition and reduce stress/Nil	Remenapp et al. 2022
Root	300 mg twice daily for 8 weeks	Boosted sexual health in males/Nil	Chauhan et al. 2022
Root	300 mg twice daily for 8 weeks	Improved female sexual health/Nil	Ajgaonkar et al. 2022
Root	300 mg twice daily for 8 weeks	Improved cardiorespiratory endurance/Nil	Tiwari et al. 2021
Root	300 mg twice daily for 8 weeks	No adverse effect/Nil	Verma et al. 2021
Root	300 mg for 90 days	Reduce stress and improve cognitive functions/Nil	Gopukumar et al. 2021
Root and Leaf	240 mg daily for 60 days	Reduced stress/Nil	Lopresti et al. 2019
Root and Leaf	250 mg bid for 7 weeks	Reduced anxiety and stress/Nil	Pingali et al. 2014
Root and Leaf	250 mg twice daily for 12 weeks	Improved physical strength and endurance/Nil	Ziegenfuss et al. 2018

N.B. The above table is not exhaustive and gives a representative picture of data over the last five years. Although root extracts are predominant, leaf and whole plant extracts have also yielded promising results; however, none of the studies on human volunteers has tested the exclusive use of leaf extract.

Withanones are exclusively found in leaves and selectively induce apoptosis in cancer cells by upregulating the expression of p53 (Widodo et al. 2009). Intriguingly, withanones downregulate p53 in normal cells and thus act as anti-aging factors (Widodo et al. 2009). They are also implicated in imparting protection against several toxic environmental pollutants such as lead (Kumar et al. 2014) and methoxy acetic acid (Priyandoko et al. 2011) by mitigating reactive oxygen species-induced damage and switching on cellular defense pathways. Leaf extract has also been found to be more potent than root-derived components in the management of diabetes in a study conducted on glucose uptake by adipocytes. In addition, a leaf extract was also able to induce insulin secretion from the basal pancreatic beta cells (Gorelick et al. 2015). Apart from the withanolides, the leaves are also enriched in other bioactive components which are integral to the synergistic health-ameliorating effect of Ashwagandha. The plant is well known for the treatment of sleep disorders. Triethylene glycol, a water-extractable small molecule metabolite, found exclusively in leaves, was found to be the major effector of non-REM sleep (Kaushik et al. 2017). The leaf-

associated fraction was also able to neutralize withaferin A-induced toxicity in normal fibroblast cells (Widodo et al. 2009) plausibly by sequestering the toxicity of excess electrophilic withaferin A.

However, at higher concentrations, withanones can bind to thiols as glutathione (GSH) by virtue of their strong electrophilic property (Groeger and Freeman 2010) jeopardizing the endogenous antioxidant pathway leading to liver damage. In addition, it also forms adducts with the deoxy nucleosides dG, dA, and dC. In contrast not many significant and reportable toxic effects were found to be associated with the root extract of the plant except for mild symptoms of stomach upset, diarrhea, and vomiting. It must be stressed that irrespective of the root or leaf, the toxic effects are realized only at concentrations beyond the prescribed safe limit of the extract which is 500-2000 mg/kg body weight per day (Kumar et al. 2023).

It is generally accepted that the success of the therapeutic potential of Ashwagandha which is synergistic in nature and dependent upon the combination of withanolides, alkaloids, saponins, and other steroidal lactones (White et al. 2016),

with many of the active components still to be discovered (Speers et al. 2021). Either the roots or the leaves, individually, are not able to optimally highlight the therapeutic benefit of the plant. None of the studies carried out on safety analysis of the plant has reported adverse issues arising out of consumption of Ashwagandha extract within the admissible level of 500–2000 mg/kg of body weight (for human trials) for a period not exceeding three months. Therefore, discarding other parts of the plant for designing root-based phytotherapeutics not only adds up to the economic burden of the production process but additionally deprives the formulation of added health benefits.

The use of whole plant extract rather than only root or leaf-based formulation reported in only a handful of studies thus far has yielded much more promising results with no reported risk. One such studies conducted on animal models for a period of four weeks involving oral administration of the whole plant extract at a dosage of 1000 mg/kg of body weight proved to be safe and effective at the same time (Balkrishna et al. 2022). Based on the lack of adverse event reports with Ashwagandha whole plant formulations, three research-driven commercial products, WferinAmax ashwagandha, and two other whole plant-based phototherapeutics have successfully emerged into the market amidst the current popularity of root-based extracts. Toxicological profiling of WferinAmax ashwagandha has indicated that is free from harmful pesticides, heavy metals and pathogenic microbes (Kumar et al. 2023).

2. Concluding remarks

Since the discovery of the potential of the plant as a remedy for countless human ailments, extracts of *Withania somnifera* have been used by drug and pharmaceutical industries for developing phytotherapeutic formulations. While a small number of these have actually made it to the market, many more are in different phases of trial and are expected to be marketed soon. However, the debate over choosing roots over leaves as the raw material for extraction has grown to a sizable proportion, with reports of scientific studies presenting contrasting claims regarding their safety and efficacy. As indicated earlier, withanolides can modulate several metabolic as well as physiological pathways, including components of cell division, enzymes involved in metabolic pathways, and proteins involved in cellular signal transduction pathways. Therefore, it is not unprecedented that the therapeutic properties of these compounds will transform into toxic manifestations if the safety limits are not properly assessed.

Keeping in mind the complex compartmentalization of the various genes involved in the biosynthesis of the diverse spectra of withanolides and withanosides as well as the various environmental factors guiding their differential expressions, it may be safely inferred that it is never adequate to judge a withanolide-based phytotherapeutic formulation based on the tissue extracted. Rather, a holistic information database consisting of the time of collection, the status of

soil, and the use of nutrients, growth promoters, etc. should be adequately maintained and considered during the production process to achieve reproducibility of the desired phytochemical composition and effectiveness while simultaneously minimizing toxicity. Taking into consideration all the above factors, the safest approach for the development of herbal remedies from this plant from the present perspective appears to be the use of the whole plant instead of roots or leaves.

Funding

The author(s) reported there is no funding associated with the work featured in this article.

ORCID

Pawan Kumar  <http://orcid.org/0000-0002-2822-8133>
 Samudra P. Banik  <http://orcid.org/0000-0003-0075-7508>
 Apurva Goel  <http://orcid.org/0000-0003-2909-4226>
 Sanjoy Chakraborty  <http://orcid.org/0000-0002-6213-5483>
 Manashi Bagchi  <http://orcid.org/0000-0002-1527-6419>
 Debasis Bagchi  <http://orcid.org/0000-0001-9478-6427>

References

- Abouzid SF, El-Bassuony AA, Nasib A, Khan S, Qureshi J, Choudhary MI. 2010. Withaferin A production by root cultures of *Withania coagulans*. *Int J Appl Res Nat Prod*. 3(1): 23–27.
- Agarwal AV, Singh D, Dhar YV, Michael R, Gupta P, Chandra D, Trivedi PK. 2018. Virus-induced silencing of key genes leads to differential impact on withanolide biosynthesis in the medicinal plant, *Withania somnifera*. *Plant Cell Physiol*. 59(2):262–274. doi: [10.1093/pcp/pcx179](https://doi.org/10.1093/pcp/pcx179).
- Ajgaonkar A, Jain M, Debnath K. 2022. Efficacy and safety of Ashwagandha (*Withania somnifera*) root extract for improvement of sexual health in healthy women: A prospective, randomized, placebo-controlled study. *Cureus* 14(10): e30787. doi: [10.7759/cureus.30787](https://doi.org/10.7759/cureus.30787).
- Antony ML, Lee J, Hahm ER, Kim SH, Marcus AI, Kumari V, Ji X, Yang Z, Vowell CL, Wipf P, Uechi GT, Yates NA, Romero G, Sarkar SN, Singh SV. 2014. Growth arrest by the antitumor steroidal lactone withaferin A in human breast cancer cells is associated with down-regulation and covalent binding at cysteine 303 of β -tubulin. *J Biol Chem*. 289(3):1852–1865. doi: [10.1074/jbc.M113.496844](https://doi.org/10.1074/jbc.M113.496844).
- Atteeq M. 2022. Evaluating anticancer properties of withaferin A—a potent phytochemical. *Front Pharmacol*. 13: 975320. doi: [10.3389/fphar.2022.975320](https://doi.org/10.3389/fphar.2022.975320).
- Balkrishna A, Sinha S, Srivastava J, Varshney A. 2022. *Withania somnifera* (L.) Dunal whole-plant extract demonstrates acceptable non-clinical safety in rat 28-day subacute toxicity evaluation under GLP-compliance. *Sci Rep*. 12(1):11047. doi: [10.1038/s41598-022-14944-x](https://doi.org/10.1038/s41598-022-14944-x).
- Björnsson HK, Björnsson ES, Avula B, Khan IA, Jonasson JG, Ghabril M, Hayashi PH, Navarro V. 2020. Ashwagandha-induced liver injury: A case series from Iceland and the US Drug-Induced Liver Injury Network. *Liver Int*. 40(4): 825–829. doi: [10.1111/liv.14393](https://doi.org/10.1111/liv.14393).
- Bonilla DA, Moreno Y, Gho C, Petro JL, Odriozola-Martínez A, Kreider RB. 2021. Effects of Ashwagandha (*Withania somnifera*) on physical performance: Systematic review and Bayesian meta-analysis. *J Funct Morphol Kinesiol*. 6(1): 20. doi: [10.3390/jfmk6010020](https://doi.org/10.3390/jfmk6010020).
- Carioscia JA, Stansbury JW, Bowman CN. 2007. Evaluation and control of thiol-ene/thiol-epoxy hybrid networks. *Polymer (Guildf)*. 48(6):1526–1532. doi: [10.1016/j.polymer.2007](https://doi.org/10.1016/j.polymer.2007).
- Chandrasekhar K, Kapoor J, Anishetty S. 2012. A prospective, randomized double-blind, placebo-controlled study of safety and efficacy of a high-concentration full-spectrum extract of ashwagandha root in

- reducing stress and anxiety in adults. *Indian J Psychol Med.* 34(3): 255–262. doi: [10.4103/0253-7176.106022](https://doi.org/10.4103/0253-7176.106022).
- Chauhan S, Srivastava MK, Pathak AK. 2022. Effect of standardized root extract of ashwagandha (*Withania somnifera*) on well-being and sexual performance in adult males: a randomized controlled trial. *Health Sci Rep.* 5:e741. doi: [10.1002/hsr.2.741](https://doi.org/10.1002/hsr.2.741).
- Chaurasiya ND, Uniyal GC, Lal P, Misra L, Sangwan NS, Tuli R, Sangwan RS. 2008. Analysis of withanolides in root and leaf of *Withania somnifera* by HPLC with photodiode array and evaporative light scattering detection. *Phytochem Anal.* 19(2):148–154. doi: [10.1002/pca.1029](https://doi.org/10.1002/pca.1029).
- Chaurasiya ND, Sangwan NS, Sabir F, Misra L, Sangwan RS. 2012. Withanolide biosynthesis recruits both mevalonate and DOXP pathways of isoprenogenesis in Ashwagandha *Withania somnifera* L. (Dunal). *Plant Cell Rep.* 31(10):1889–1897. doi: [10.1007/s00299-012-1302-4](https://doi.org/10.1007/s00299-012-1302-4).
- Choi BY, Kim BW. 2015. Withaferin-A inhibits colon cancer cell growth by blocking STAT3 transcriptional activity. *J Cancer Prevent.* 20(3):185–192. doi: [10.15430/JCP.2015.20.3.185](https://doi.org/10.15430/JCP.2015.20.3.185).
- Dadfar SMM, Sekula-Neuner S, Trouillet V, Hirtz M. 2021. Protein microarray immobilization via epoxide ring-opening by thiol, amine, and azide. *Adv Mater Interfaces* 8, 2002117. doi: [10.1002/admi.200202117](https://doi.org/10.1002/admi.200202117).
- Dhar N, Razdan S, Rana S, Bhat WW, Vishwakarma R, Lattoo SK. 2015. A decade of molecular understanding of withanolide biosynthesis and in vitro studies in *Withania somnifera* (L.) Dunal: Prospects and perspectives for pathway engineering. *Front Plant Sci.* 6:1031. doi: [10.3389/fpls.2015.01031](https://doi.org/10.3389/fpls.2015.01031).
- Erb M, Kliebenstein DJ. 2020. Plant secondary metabolites as defenses, regulators, and primary metabolites: The blurred functional trichotomy. *Plant Physiol.* 184(1):39–52. doi: [10.1104/pp.20.00433](https://doi.org/10.1104/pp.20.00433).
- Fazil MHUT, Chirumamilla CS, Perez-Novo C, Wong BHS, Kumar S, Sze SK, Vanden Berghe W, Verma NK. 2021. The steroidal lactone withaferin A impedes T-cell motility by inhibiting the kinase ZAP70 and subsequent kinome signaling. *J Biol Chem.* 297(6): 101377. doi: [10.1016/j.jbc.2021.101377](https://doi.org/10.1016/j.jbc.2021.101377).
- Gopukumar K, Thanawala S, Somepalli V, Rao TSS, Thammatam VB, Chauhan S. 2021. Efficacy and safety of Ashwagandha root extract on cognitive functions in healthy, stressed adults: A randomized, double-blind, placebo-controlled study. *Evid Based Compl Alternat Med.* 2021: 8254344. doi: [10.1155/2021/8254344](https://doi.org/10.1155/2021/8254344).
- Gorelick J, Rosenberg R, Smotrich A, Hanuš L, Bernstein N. 2015. Hypoglycemic activity of withanolides and elicited *Withania somnifera*. *Phytochemistry.* 116:283–289. doi: [10.1016/j.phytochem.2015.02.029](https://doi.org/10.1016/j.phytochem.2015.02.029).
- Groeger AL, Freeman BA. 2010. Signaling actions of electrophiles: anti-inflammatory therapeutic candidates. *Mol Interv.* 10(1):39–50. doi: [10.1124/mi.10.1.7](https://doi.org/10.1124/mi.10.1.7).
- Grossman EA, Ward CC, Spradlin JN, Bateman LA, Huffman TR, Miyamoto DK, Kleinman JI, Nomura DK. 2017. Covalent ligand discovery against druggable hotspots targeted by anti-cancer natural products. *Cell Chem Biol.* 24(11): 1368–1376. e4. doi: [10.1016/j.chembiol.2017.08.013](https://doi.org/10.1016/j.chembiol.2017.08.013).
- Gupta P, Goel R, Pathak S, Srivastava A, Singh SP, Sangwan RS, Asif MH, Trivedi PK. 2013. De novo assembly, functional annotation and comparative analysis of *Withania somnifera* leaf and root transcriptomes to identify putative genes involved in the withanolides biosynthesis. *PLoS One.* 8(5):e62714. doi: [10.1371/journal.pone.0062714](https://doi.org/10.1371/journal.pone.0062714).
- Gupta S, Bohra M, Sharma K, Kachhwaha S, Kothari S, Jain R. 2021. Leaves and roots of micropropagated plants adopt different pathways for withanolide biosynthesis in *Withania coagulans*: A comparative transcriptome study. doi: [10.21203/rs.3.rs-299335/v1](https://doi.org/10.21203/rs.3.rs-299335/v1). [AQ]
- Gupta SK, Jadhav S, Gohil D, Panigrahi GC, Kaushal RK, Gandhi K, Patil A, Chavan P, Gota V. 2022. Safety, toxicity and pharmacokinetic assessment of oral Withaferin-A in mice. *Toxicol Rep.* 9: 1204–1212. doi: [10.1016/j.toxrep.2022.05.012](https://doi.org/10.1016/j.toxrep.2022.05.012).
- Ha JW, Yu JS, Lee BS, Kang DM, Ahn MJ, Kim JK, Kim KH. 2022. Structural characterization of withanolide glycosides from the roots of *Withania somnifera* and their potential biological activities. *Plants (Basel).* 11(6):767. doi: [10.3390/plants11060767](https://doi.org/10.3390/plants11060767).
- Heynink K, Lahtela-Kakkonen M, Van der Veken P, Haegeman G, Vanden Berghe W. 2014. Withaferin A inhibits NF-kappaB activation by targeting cysteine 179 in IKKβ. *Biochem Pharmacol.* 91(4):501–509. doi: [10.1016/j.bcp.2014.08.004](https://doi.org/10.1016/j.bcp.2014.08.004).
- Inagaki K, Mori N, Honda Y, Takaki S, Tsuji K, Chayama K. 2017. A case of drug-induced liver injury with prolonged severe intrahepatic cholestasis induced by Ashwagandha. *Acta hepatologica Japonica* 58: 448–454. doi: [10.2957/kanzo.58.448](https://doi.org/10.2957/kanzo.58.448).
- Jan R, Asaf S, Numan M, Lubna , Kim K-M. 2021. Plant secondary metabolite biosynthesis and transcriptional regulation in response to biotic and abiotic stress conditions. *Agronomy.* 11(5):968. doi: [10.3390/agronomy11050968](https://doi.org/10.3390/agronomy11050968).
- Kakar SS, Ratajczak MZ, Powell KS, Moghadamfalahi M, Miller DM, Batra SK, Singh SK. 2014. Withaferin A alone and in combination with cisplatin suppresses growth and metastasis of ovarian cancer by targeting putative cancer stem cells. *PLoS ONE* 9(9): e107596. doi: [10.1371/journal.pone.0107596](https://doi.org/10.1371/journal.pone.0107596).
- Kaushik MK, Kaul SC, Wadhwa R, Yanagisawa M, Urade Y. 2017. Triethylene glycol, an active component of Ashwagandha (*Withania somnifera*) leaves, is responsible for sleep induction. *PLoS One.* 12(2): e0172508. doi: [10.1371/journal.pone.0172508](https://doi.org/10.1371/journal.pone.0172508).
- Khanna KL, Schwarting AE, Rother A, Bobbit JM. 1961. Occurrence of tropine and pseudotropine in *Withania somnifera*. *Lloydia.* 24: 179–181.
- Kohnen-Johannsen KL, Kayser O. 2019. Tropane Alkaloids: Chemistry, pharmacology, biosynthesis and production. *Molecules.* 24(4):796. doi: [10.3390/molecules24040796](https://doi.org/10.3390/molecules24040796).
- Kumar P, Singh R, Nazmi A, Lakhanpal D, Kataria H, Kaur G. 2014. Glioprotective effects of Ashwagandha leaf extract against lead induced toxicity. *Biomed Res Int.* 2014:182029. doi: [10.1155/2014/182029](https://doi.org/10.1155/2014/182029).
- Kumar P, Banik SP, Goel A, Chakraborty S, Bagchi M, Bagchi D. 2023. Chemical, microbial and safety profiling of a standardized *Withania somnifera* (Ashwagandha) extract and withaferin A, a potent novel phytotherapeutic of the millennium. *Funct Foods Health Dis.* 13(2): 36–51. doi: [10.31989/ffhd.v13i2.1071](https://doi.org/10.31989/ffhd.v13i2.1071).
- Kumar S, Mathew SO, Aharwal RP, Tulli HS, Mohan CD, Sethi G, Ahn KS, Webber K, Sandhu SS, Bishayee A. 2023. Withaferin A: A pleiotropic anticancer agent from the Indian medicinal plant *Withania somnifera* (L.) Dunal. *Pharmaceuticals (Basel).* 16(2):160. doi: [10.3390/ph16020160](https://doi.org/10.3390/ph16020160).
- Kumari M, Gupta RP. 2015. In vitro antibacterial effect of *Withania somnifera* root extract on *Escherichia coli*. *Vet World.* 8(1):57–60. doi: [10.14202/vetworld.2015.57-60](https://doi.org/10.14202/vetworld.2015.57-60).
- Langade D, Kanchi S, Salve J, Debnath K, Ambegaokar D. 2019. Efficacy and safety of Ashwagandha (*Withania somnifera*) root extract in insomnia and anxiety: A double-blind, randomized, placebo-controlled study. *Cureus.* 11(9):e5797. doi: [10.7759/cureus.5797](https://doi.org/10.7759/cureus.5797).
- Lee IC, Choi BY. 2016. Withaferin-A—A natural anticancer agent with pleiotropic mechanisms of action. *Int J Mol Sci.* 17(3):290. doi: [10.3390/ijms17030290](https://doi.org/10.3390/ijms17030290).
- Lin CC, Yang TY, Lu HJ, Wan CK, Hsu SL, Wu CC. 2021. Attenuating role of withaferin A in the proliferation and migration of lung cancer cells via a p53-miR-27a/miR-10b pathway. *Oncol. Lett.* 21(3):232. doi: [10.3892/ol.2021.12493](https://doi.org/10.3892/ol.2021.12493).
- Lopresti AL, Smith SJ, Malvi H, Kodgule R. 2019. An investigation into the stress-relieving and pharmacological actions of an ashwagandha (*Withania somnifera*) extract: A randomized, double-blind, placebo-controlled study. *Medicine (Baltimore).* 98(37): e17186. doi: [10.1097/MD.00000000000017186](https://doi.org/10.1097/MD.00000000000017186).
- Lubarska M, Halaśiński P, Hryhorowicz S, Mahadea DS, Łykowska-Szuber L, Eder P, Dobrowolska A, Krela-Kaźmierczak I. 2023. Liver dangers of herbal products: A case report of Ashwagandha-induced liver injury. *Int J Environ Res Public Health.* 20(5):3921. doi: [10.3390/ijerph20053921](https://doi.org/10.3390/ijerph20053921).
- Mayola E, Gallerne C, Esposti DD, Martel C, Pervaiz S, Larue L, Debuire B, Lemoine A, Brenner C, Lemaire C. 2011. Withaferin A induces apoptosis in human melanoma cells through generation of reactive oxygen species and down-regulation of Bcl-2. *Apoptosis.* 16(10):1014–1027. doi: [10.1007/s10495-011-0625-x](https://doi.org/10.1007/s10495-011-0625-x).
- Mikulska P, Malinowska M, Ignacyk M, Szustowski P, Nowak J, Pesta K, Szeląg M, Szklanny D, Judasz E, Kaczmarek G, Ejiohuo OP,

- Paczowska-Walendowska M, Gościński A, Cielecka-Piontek J. 2023. Ashwagandha (*Withania somnifera*)-current research on the health-promoting activities: A narrative review. *Pharmaceutics*. 15(4): 1057. doi: [10.3390/pharmaceutics15041057](https://doi.org/10.3390/pharmaceutics15041057).
- Ministry of Ayush. 2021. Subject-advisory for refrain from use of Ashwagandha (*Withania somnifera*) leaves. [accessed 2023 June 1]. <https://cdn.ayush.gov.in/wp-content/uploads/2021/10/advisory-on-aswagandha.pdf>.
- Modi SJ, Tiwari A, Ghule C, Pawar S, Saste G, Jagtap S, Singh R, Deshmukh A, Girme A, Hingorani L. 2022. Pharmacokinetic study of withanosides and withanolides from *Withania somnifera* using ultra-high performance liquid chromatography-Tandem mass spectrometry (UHPLC-MS/MS). *Molecules*. 27(5):1476. doi: [10.3390/molecules27051476](https://doi.org/10.3390/molecules27051476).
- Nagella P, Naik PM, Manohar Sh, Hosakatte NM. 2010. Distribution of withanolide A content in various organs of *Withania somnifera* (L.) Dunal. *Intern J Pharma Bio Sci*. 1. ISSN: 0975-6299.
- Ncube B, Van Staden J. 2015. Tilting plant metabolism for improved metabolite biosynthesis and enhanced human benefit. *Molecules*. 20(7):12698-12731. doi: [10.3390/molecules200712698](https://doi.org/10.3390/molecules200712698).
- Nile SH, Nile A, Gansukh E, Baskar V, Kai G. 2019. Subcritical water extraction of withanosides and withanolides from Ashwagandha (*Withania somnifera* L) and their biological activities. *Food Chem Toxicol*. 132:110659. doi: [10.1016/j.fct.2019.110659](https://doi.org/10.1016/j.fct.2019.110659).
- Orrú A, Marchese G, Ruiu S. 2023. Alkaloids in *Withania somnifera* (L.) Dunal root extract contribute to its anti-inflammatory activity. *Pharmacology*. 108(3):301-307. doi: [10.1159/000527656](https://doi.org/10.1159/000527656).
- Ozawa M, Morita M, Hirai G, Tamura S, Kawai M, Tsuchiya A, Oonuma K, Maruoka K, Sodeoka M. 2013. Contribution of cage-shaped structure of physalins to their mode of action in inhibition of NF-κB activation. *ACS Med Chem Lett*. 4(8): 730-735. doi: [10.1021/ml400144e](https://doi.org/10.1021/ml400144e).
- Pandey SS, Singh S, Pandey H, Srivastava M, Ray T, Soni S, Pandey A, Shanker K, Babu CSV, Banerjee S, Gupta MM, Kalra A. 2018. Endophytes of *Withania somnifera* modulate in planta content and the site of withanolide biosynthesis. *Sci Rep*. 8(1):5450. doi: [10.1038/s41598-018-23716-5](https://doi.org/10.1038/s41598-018-23716-5).
- Patel SB, Rao NJ, Hingorani LL. 2016. Safety assessment of *Withania somnifera* extract standardized for withaferin A: Acute and sub-acute toxicity study. *J Ayurveda Integr Med*. 7(1): 30-37. doi: [10.1016/j.jaim.2015.08.001](https://doi.org/10.1016/j.jaim.2015.08.001).
- Pingali U, Pilli R, Fatima N. 2014. Effect of standardized aqueous extract of *Withania somnifera* on tests of cognitive and psychomotor performance in healthy human participants. *Pharmacognosy Res*. 6(1):12-18. doi: [10.4103/0974-8490.122912](https://doi.org/10.4103/0974-8490.122912).
- Priyandoko D, Ishii T, Kaul SC, Wadhwa R. 2011. Ashwagandha leaf derived withanone protects normal human cells against the toxicity of methoxyacetic acid, a major industrial metabolite. *PLoS One*. 6(5): e19552. doi: [10.1371/journal.pone.0019552](https://doi.org/10.1371/journal.pone.0019552).
- Rangaraju S, Lokesh AN, Chenna A. 2019. Improved production of withanolides in adventitious root cultures of *Withania somnifera* by suspension culture method. *Biosci Biotech Res Commun*. 12(1):73-79. doi: [10.21786/bbrc/12.1/10](https://doi.org/10.21786/bbrc/12.1/10).
- Remenapp A, Coyle K, Orange T, Lynch T, Hooper D, Hooper S, Conway K, Hausenblas HA. 2022. Efficacy of *Withania somnifera* supplementation on adult's cognition and mood. *J Ayurveda Integr Med*. 13(2): 100510. doi: [10.1016/j.jaim.2021.08.003](https://doi.org/10.1016/j.jaim.2021.08.003).
- Rodríguez-Concepción M, Forés O, Martínez-García JF, González V, Phillips MA, Ferrer A, Boronat A. 2004. Distinct light-mediated pathways regulate the biosynthesis and exchange of isoprenoid precursors during Arabidopsis seedling development. *Plant Cell*. 16(1):144-156. doi: [10.1105/tpc.016204](https://doi.org/10.1105/tpc.016204).
- Sangwan RS, Chaurasiya ND, Lal P, Misra L, Tuli R, and Sangwan NS (2008), Withanolide A is inherently de novo biosynthesized in roots of the medicinal plant Ashwagandha (*Withania somnifera*). *Physiologia Plantarum*, 133: 278-287. doi: [10.1111/j.1399-3054.2008.01076.x](https://doi.org/10.1111/j.1399-3054.2008.01076.x).
- Saleem S, Muhammad G, Hussain MA, Altaf M, Bukhari SNA. 2020. *Withania somnifera* L.: Insights into the phytochemical profile, therapeutic potential, clinical trials, and future prospective. *Iran J Basic Med Sci*. 23(12):1501-1526. doi: [10.22038/IJBMS.2020.44254](https://doi.org/10.22038/IJBMS.2020.44254).
- Sharma L, Maurya B, Rai SP. 2023. An overview of biotechnological interventions and abiotic elicitors on biomass and withanolide biosynthesis in *Withania somnifera* (L.) Dunal, *Industrial Crops and Products*. 193: 116238 doi: [10.1016/j.indcrop.2023.116238](https://doi.org/10.1016/j.indcrop.2023.116238).
- Siddiqui S, Ahmed N, Goswami M, Chakrabarty A, Chowdhury G. 2021. DNA damage by Withanone as a potential cause of liver toxicity observed for herbal products of *Withania somnifera* (Ashwagandha). *Curr Res Toxicol*. 2: 72-81. doi: [10.1016/j.crttox.2021.02.002](https://doi.org/10.1016/j.crttox.2021.02.002).
- Sikandan A, Shinomiya T, Nagahara Y. 2018. Ashwagandha root extract exerts anti-inflammatory effects in HaCaT cells by inhibiting the MAPK/NF-κB pathways and by regulating cytokines. *Int J Mol Med*. 42(1):425-434. doi: [10.3892/ijmm.2018.3608](https://doi.org/10.3892/ijmm.2018.3608).
- Singh M, Poddar NK, Singh D, Agrawal S. 2020. Foliar application of elicitors enhanced the yield of withanolide contents in *Withania somnifera* (L.) Dunal (variety, Poshita). 3 *Biotech*. 10(4):157. doi: [10.1007/s13205-020-2153-2](https://doi.org/10.1007/s13205-020-2153-2).
- Singh M, Jayant K, Singh D, Bhutani S, Poddar NK, Chaudhary AA, Khan SU, Adnan M, Siddiqui AJ, Hassan MI, Khan FI, Lai D, Khan S. 2022. *Withania somnifera* (L.) Dunal (Ashwagandha) for the possible therapeutics and clinical management of SARS-CoV-2 infection: Plant-based drug discovery and targeted therapy. *Front Cell Infect Microbiol*. 12: 933824. doi: [10.3389/fcimb.2022.933824](https://doi.org/10.3389/fcimb.2022.933824).
- Siriwardane AS, Dharmadasa RM, Samarasinghe K. 2013. Distribution of withaferin A, an anticancer potential agent, in different parts of two varieties of *Withania somnifera* (L.) Dunal. grown in Sri Lanka. *Pak J Biol Sci*. 16(3):141-144. doi: [10.3923/pjbs.2013.141.144](https://doi.org/10.3923/pjbs.2013.141.144).
- Speers AB, Cabey KA, Soumyanath A, Wright KM. 2021. Effects of *Withania somnifera* (Ashwagandha) on stress and the stress-related neuropsychiatric disorders anxiety, depression, and insomnia. *Curr Neuropharmacol*. 19(9): 1468-1495. doi: [10.2174/1570159X19666210712151556](https://doi.org/10.2174/1570159X19666210712151556).
- Srivastava S, Sanchita, Singh R, Srivastava G, Sharma A. 2018. Comparative study of Withanolide biosynthesis-related miRNAs in root and leaf tissues of *Withania somnifera*. *Appl Biochem Biotechnol*. 185(4):1145-1159. doi: [10.1007/s12010-018-2702-x](https://doi.org/10.1007/s12010-018-2702-x).
- Sudeep HV, Gouthamchandra K, Shyamprasad K. 2020. Molecular docking analysis of Withaferin A from *Withania somnifera* with the glucose regulated protein 78 (GRP78) receptor and the SARS-CoV-2 main protease. *Bioinformation*. 16(5):411-417. doi: [10.6026/97320630016411](https://doi.org/10.6026/97320630016411).
- Sultana T, Okla MK, Ahmed M, Akhtar N, Al-Hashimi A, Abdelgawad H, Haq IU. 2021. Withaferin A: From ancient remedy to potential drug candidate. *Molecules*. 26(24):7696. doi: [10.3390/molecules26247696](https://doi.org/10.3390/molecules26247696).
- Tang Q, Ren L, Liu J, Li W, Zheng X, Wang J, Du G. 2020. Withaferin A triggers G2/M arrest and intrinsic apoptosis in glioblastoma cells via ATF4-ATF3-CHOP axis. *Cell Prolif*. 53(1):e12706. doi: [10.1111/cpr.12706](https://doi.org/10.1111/cpr.12706).
- Tandon N, Yadav SS. 2020. Safety and clinical effectiveness of *Withania somnifera* (Linn.) Dunal root in human ailments. *J Ethnopharmacol*. 255: 112768. doi: [10.1016/j.jep.2020.1](https://doi.org/10.1016/j.jep.2020.1).
- Teoh ES. 2015. Secondary metabolites of plants. *Medicinal Orchids of Asia*. 59-73. doi: [10.1007/978-3-319-24274-3_5](https://doi.org/10.1007/978-3-319-24274-3_5).
- Tharakan A, Shukla H, Benny IR, Tharakan M, George L, Koshy S. 2021. Immunomodulatory effect of *Withania somnifera* (Ashwagandha) extract—A randomized, double-blind, placebo controlled trial with an open label extension on healthy participants. *J Clin Med*. 10(16): 3644. doi: [10.3390/jcm10163644](https://doi.org/10.3390/jcm10163644).
- Thorat SA, Kaniyassery A, Poojari P, Rangel M, Tantry S, Kiran KR, Joshi MB, Rai PS, Botha AM, Muthusamy A. 2022. Differential gene expression and withanolides biosynthesis during in vitro and ex vitro growth of *Withania somnifera* (L.) Dunal. *Front Plant Sci*. 13:917770. doi: [10.3389/fpls.2022.917770](https://doi.org/10.3389/fpls.2022.917770).
- Tiwari S, Gupta SK, Pathak AK. 2021. A double-blind, randomized, placebo-controlled trial on the effect of Ashwagandha (*Withania somnifera* dunal.) root extract in improving cardiorespiratory endurance and recovery in healthy athletic adults. *J Ethnopharmacol*. 272:113929. doi: [10.1016/j.jep.2021.113929](https://doi.org/10.1016/j.jep.2021.113929).

- Tóth M, Benedek AE, Longerich T, Seitz H-K. 2023. Ashwagandha-induced acute liver injury: A case report. Clin Case Rep. 11:e7078. doi: [10.1002/ccr3.7078](https://doi.org/10.1002/ccr3.7078).
- Verma N, Gupta SK, Tiwari S, Mishra AK. 2021. Safety of Ashwagandha root extract: A randomized, placebo-controlled, study in healthy volunteers. Complement Ther Med. 57: 102642. doi: [10.1016/j.ctim.2020.102642](https://doi.org/10.1016/j.ctim.2020.102642).
- Widodo N, Shah N, Priyandoko D, Ishii T, Kaul SC, Wadhwa R. 2009. Deceleration of senescence in normal human fibroblasts by withanone extracted from ashwagandha leaves. J Gerontol A Biol Sci Med Sci. 64(10):1031–1038. doi: [10.1093/gerona/glp088](https://doi.org/10.1093/gerona/glp088).
- White PT, Subramanian C, Motiwala HF, Cohen MS. 2016. Natural withanolides in the treatment of chronic diseases. Adv Exp Med Biol. 928: 329–373. doi: [10.1007/978-3-319-41334-1_14](https://doi.org/10.1007/978-3-319-41334-1_14).
- Yang J, Yan W, Li Y, Niu L, Ye H, Chen L. 2019. The natural compound withaferin A covalently binds to Cys239 of β -Tubulin to promote tubulin degradation. Mol Pharmacol. 96(6): 711–719. doi: [10.1124/mol.119.117812](https://doi.org/10.1124/mol.119.117812).
- Zhang H, Cao CM, Gallagher RJ, Timmermann BN. 2014. Antiproliferative withanolides from several solanaceous species. Nat Prod Res. 28(22): 1941–1951. doi: [10.1080/14786419.2014.919286](https://doi.org/10.1080/14786419.2014.919286).
- Zhao L, Chang WC, Xiao Y, Liu HW, Liu P. 2013. Methylerythritol phosphate pathway of isoprenoid biosynthesis. Annu Rev Biochem. 82:497–530. doi: [10.1146/annurev-biochem-052010-100934](https://doi.org/10.1146/annurev-biochem-052010-100934).
- Ziegenfuss TN, Kedia AW, Sandrock JE, Raub BJ, Kerksick CM, Lopez HL. 2018. Effects of an Aqueous extract of *Withania somnifera* on strength training adaptations and recovery: The STAR trial. Nutrients. 10(11): 1807. doi: [10.3390/nu10111807](https://doi.org/10.3390/nu10111807).

A Placebo-Controlled, Double-Blind Clinical Investigation to Evaluate the Efficacy of a Patented *Trigonella foenum-graecum* Seed Extract “Fenfuro®” in Type 2 Diabetics

Debasish Hota, Biswa M. Padhy, Rituparna Maiti, Debasish Bisoi, Jyoti Prakash Sahoo, Binod K. Patro, Pawan Kumar, Apurva Goel, Samudra P. Banik, Sanjoy Chakraborty, Mehul Rungta, Manashi Bagchi & Debasish Bagchi


To cite this article: Debasish Hota, Biswa M. Padhy, Rituparna Maiti, Debasish Bisoi, Jyoti Prakash Sahoo, Binod K. Patro, Pawan Kumar, Apurva Goel, Samudra P. Banik, Sanjoy Chakraborty, Mehul Rungta, Manashi Bagchi & Debasish Bagchi (17 Jul 2023): A Placebo-Controlled, Double-Blind Clinical Investigation to Evaluate the Efficacy of a Patented *Trigonella foenum-graecum* Seed Extract “Fenfuro®” in Type 2 Diabetics, Journal of the American Nutrition Association, DOI: [10.1080/27697061.2023.2233008](https://doi.org/10.1080/27697061.2023.2233008)

To link to this article: <https://doi.org/10.1080/27697061.2023.2233008>



Published online: 17 Jul 2023.



Submit your article to this journal 



Article views: 69




View related articles 



View Crossmark data 



A Placebo-Controlled, Double-Blind Clinical Investigation to Evaluate the Efficacy of a Patented *Trigonella foenum-graecum* Seed Extract “Fenfuro®” in Type 2 Diabetics

Debasish Hota^a , Biswa M. Padhy^a , Rituparna Maiti^a , Debasis Bisoi^b , Jyoti Prakash Sahoo^c , Binod K. Patro^d , Pawan Kumar^e , Apurva Goel^f , Samudra P. Banik^g , Sanjoy Chakraborty^h , Mehul Rungta^e , Manashi Bagchiⁱ  and Debasis Bagchi^j 

^aDepartment of Pharmacology, All India Institute of Medical Sciences (AIIMS), Bhubaneswar, Orissa, India; ^bDepartment of Pharmacology, AIIMS, Bibinagar, Hyderabad, India; ^cDepartment of Pharmacology, SCB Medical College & Hospital, Cuttack, Orissa, India; ^dDepartment of Community and Family Medicine, AIIMS, Bhubaneswar, Orissa, India; ^eR&D Department, Chemical Resources (CHERES), Panchkula, Haryana, India; ^fRegulatory Department, Chemical Resources (CHERES), Panchkula, Haryana, India; ^gDepartment of Microbiology, Maulana Azad College, Kolkata, India; ^hDepartment of Biological Sciences, New York City College of Technology/CUNY, Brooklyn, New York, USA; ⁱDepartment of R&D, Dr. Herbs LLC, Concord, California, USA; ^jDepartment of Biology, College of Arts and Sciences, and Department of Psychology, Gordon F. Derner School of Psychology, Adelphi University, Garden City, New York, USA

ABSTRACT

Background: *Trigonella foenum-graecum* (Fenugreek) is an extensively researched phytotherapeutic for the management of Type 2 diabetes without any associated side effects. The major anti-diabetic bioactive constituents present in the plant are furostanolic saponins, which are more abundantly available in the seed of the plant. However, the bioavailability of these components depends on the method of extraction and hence formulation of the phytotherapeutic constitutes a critical step for its success.

Objective: The present study reports the efficacy of a novel, patented fenugreek seed extract, Fenfuro®, containing significant amount of furostanolic saponins, in an open-labelled, two-armed, single centric study on a group of 204 patients with Type 2 diabetes mellitus over a period of twelve consecutive weeks.

Results: Administration of Fenfuro® in the dosage of 500 mg twice daily along with metformin and/or sulfonylurea-based prescribed antidiabetic drug resulted in a reduction of post-prandial glucose by more than 33% along with significant reduction in fasting glucose, both of which were greater than what resulted for the patient group receiving only Metformin and/or Sulfonylurea therapy. Fenfuro® also resulted in reduction in mean baseline HOMA index from 4.27 to 3.765, indicating restoration of insulin sensitivity which was also supported by a significant decrease in serum insulin levels by >10% as well as slight reduction in the levels of C-peptide. However, in the case of the Metformin and/or Sulfonylurea group, insulin levels were found to increase by more than 14%, which clearly indicated that drug-induced suppression of glucose levels instead of restoration of glucose homeostasis. Administration of the formulation was also found to be free from any adverse side effects as there were no changes in hematological profile, liver function and renal function.

Conclusion: The study demonstrated the promising potential of this novel phytotherapeutic, Fenfuro®, in long-term holistic management of type-2 diabetes.

ARTICLE HISTORY

Received 2 May 2023
Revised 16 June 2023
Accepted 30 June 2023

KEYWORDS

Trigonella foenum-graecum; fenugreek seeds; type 2 diabetes (T2D); clinical study; HbA1c; HOMA-IR; safety

Introduction

Type 2 Diabetes has emerged as one of the most significant alarming diseases in recent times, closely following the footsteps of obesity, its clinical counterpart in metabolic syndrome. It accounts for more than 90% of all cases of diabetes and according to the projection of the International Diabetes Federation, more than 12% of the global population will be living with Type 2 diabetes by the end of 2045 (1). Chronic insulin resistance or insensitivity of insulin to free plasma glucose remains to be the primary cause behind development of Type 2 diabetes. Patients with the disease often suffer from multiple microvascular ailments including

retinopathy, nephropathy, and neuropathy (2). Chronic insulin resistance, often coupled with obesity increases the cardiovascular risk factors and contributes to the development of Metabolic syndrome (MetS) (3).

Type 2 Diabetes is a multifactorial disorder with both genetic as well as environmental/lifestyle factors accounting for abnormal glucose homeostasis associated with the disease. Regulation of glucose metabolism is tightly controlled by a network of Signal transduction pathways which coordinate glycogen synthesis, glycogenolysis, glycolysis and gluconeogenesis for meeting the energy needs of the vital organs of our body (4). However, a breakdown in the regulation of

either of these pathways leads to altered glucose homeostasis. Three key mechanisms have been identified for the development of impaired glucose metabolism and development of insulin resistance: (a) Binding of insulin to specific tyrosine kinase receptors (InsR) initiates the insulin signaling pathway mediated by the activation of phosphoinositide 3-kinase (PI3K) and mitogen-activated protein kinases (MAPKs) respectively which culminates in the upregulation of Glut 4 receptor for mediating glucose uptake. FOXO1, a transcription factor belonging to Forkhead Box O proteins, is responsible for upregulation of the gluconeogenic genes as well as downregulation of glycolysis. The activity of FOXO1 is kept in check by PI3K mediated phosphorylation which prevents its translocation into the nucleus for driving expression of target genes. However, any impairment in the insulin signaling pathway leads to constitutive activation of FOXO1 (4).

The resultant increase in concentration of glucose levels in plasma thus initiates unresponsiveness to insulin (5); (b) Increase in the rate of mitochondrial β -oxidation leads to accumulation of an excess of acetyl CoA which results in feedback inhibition of glycolytic pathway with concomitant increase in concentration of glucose in plasma and loss of insulin sensitivity (6); and (c) Intermediates of fatty acid metabolism may arrest PI3K pathway by Protein Kinase C mediated phosphorylation of serine and threonine residues in Insulin Receptor Substrate (IRS) (7). The disease etiology of Type 2 diabetes is intricately connected with obesity (8). In particular, the accumulation of belly fat is a significant marker toward development of insulin resistance and pre-diabetic hyperglycemia (9). Although the exact molecular connection between increase in free fatty acids and development of insulin resistance remains to be deciphered completely, several reports have indicated that free fatty acids (FFAs) from visceral body fat bring about activation of the inflammatory response which causes dysregulation of the insulin receptor substrate (IRS)/phosphoinositide-3-kinase (PI-3K)/protein kinase B (PKB) axis with concomitant development of insulin resistance (4).

The first line of therapy which medical practitioners frequently advise prediabetic patients is a drug free health regimen including appropriate diet and regular exercise for at least 30 min. Primary non-pharmacological interventions include appropriate diet and exercise (10). Most of the currently available drugs including metformin and sulfonylureas are based on suppressing hepatic gluconeogenesis, boosting insulin secretion, increasing insulin sensitivity, and stimulating glucose uptake (11, 12). However, they suffer from a plethora of side effects including diarrhea and lactic acidosis for metformin and hypothyroidism and obesity in case of the sulfonylureas (13). Under the circumstances, use of phytotherapeutics has shown significant promise for safe and effective management of hyperglycemia and arresting development of insulin resistance (14). Several bioactive polyphenols including resveratrol (15), emodin (16), ellagic acid (17) as well as flavonoid polyphenols such as Epigallocatechin gallate (18), Curcumin (19), Baicalein (20), Naringenin (21), Hesperetin (22), Chrysin (23), Genistein (24), Kaempferol (25), Eriodictyol (26), Apigenin (27), and Quercetin (28)

have shown promising results in management of Type 2 diabetes and many more are still to be explored. In this respect, the anti-diabetic potential of Fenugreek seed extract has been in vogue as a traditional knowledge in Indian Ayurveda and Oriental folklore since time immemorial (29, 30).

The plant is enriched in proteins, vitamins, and micronutrients, and contains several bioactive compounds including steroid saponins and alkaloids such as trigonelline, coumarins, flavonoids, sterols, lecithin, choline and nicotinic acid and polyphenols such as rhaponticin and isovitexin (31). Ranade and Mudgalkar (32) demonstrated that dietary addition of fenugreek seeds was able to significantly reduce post-prandial hyperglycemia (32). In another study, the fenugreek seed powder was also reported to alleviate dyslipidemia, a prime cause of development of cellular insulin resistance (33). The administration of the fenugreek seed powder for a longer period was able to bring down substantially fasting plasma glucose as well as glycated hemoglobin (34). Apart from its promising role in the treatment of diabetes, Fenugreek seed extract has also been found to be valuable phytotherapeutic against cancer, cholesterolemia, oxidative stress and a booster of immune surveillance (35).

Previous studies by our group had also demonstrated the anti-diabetic potential of Fenugreek in a human trial involving more than 154 diabetic subjects (36). The objective of the present clinical study was to investigate the efficacy of a novel formulation of fenugreek seed extract "Fenfuro" in an open-labeled two-armed, single centric model of more than 204 subjects with diabetes for a period of twelve weeks and ascertain its safety.

Materials and methods

Fenfuro[®], a patented *Trigonella foenum-graecum* seed extract

This study investigated a patented *T. foenum-graecum* seed extract (Fenfuro[®], Batch No F0715, Mfg Date July 2015, US Patent 8,217,165B2; European Patents EP 2285821B1 and EP2437763 B1; Indian Patents 285647 and 371174; African Patents AP 3077; and Chinese Patents CN102448479 B [Patent Holder: Chemical Resources (CHERESO), Panchkula, Haryana, India] enriched in 54.1% total furostanolic saponins (detected by HPLC), which utilized a novel water-ethanol extraction process in a GMP-NSF certified manufacturing plant.

Ethical approval

The clinical study design and subject recruitment procedures were conducted following a stringent inclusion and exclusion criteria procedure. The clinical practices and procedures, and methodologies of this randomized double-blind, single-center, two-arm, comparative study were performed in compliance and accordance with International Council for Harmonization (ICH) guidelines for Good Clinical Practices (GCP), including the archiving of essential documents as per International Ethical Standards guaranteed by the Declaration

of Helsinki and its subsequent amendments. Patient confidentiality was strictly maintained throughout the study. Institutional Ethics Committee (IEC) of the All India Institute of Medical Sciences (AIIMS), Bhubaneswar, approved this study protocol (Protocol #T/EM-F/Pharm/14/05 dated May 8, 2015, Ref: IRB Proposal “Clinical Evaluation of Fenugreek Seed Extract, a Nutraceutical, in Patients with Type-2 Diabetes: An Add-On Study” [Protocol # CR001/01/15 (Version-2)]). The study was also duly registered on clinical-trials.gov (NCT02693392).

Subject information and consent

Prior to the recruitment of subjects, the IEC-approved study protocol and the inclusion and exclusion criteria were demonstrated in detail to all study participants and subsequently asked to sign off the IEC-approved consent forms. All recruited subjects read and duly signed the health questionnaire and the Consent Form. Subject confidentiality was strictly enforced. Adverse event monitoring was strictly ascertained.

Study compliance

Both the placebo and treatment capsules (Fenfuro[®]) were distributed to the recruited patients by the site staff during this clinical investigation. Individual data entry was controlled by the study coordinator(s) and endorsed by the Principal Investigator (PI). Moreover, the study associate responsible for distribution of the study capsules was instructed by the PI to sign the investigational product (IP) accountability log.

Allocation concealment

To prevent selection bias in this randomized control trial, allocation concealment was carried out to the study groups from those responsible for the assessment of the patients entering the trial. Adequate measures including sequentially numbered opaque capsules in coded pack of 60 capsules in a sealed aluminum pouches were used for concealing the identity.

Study discontinuation clause

The criteria for the “stopping” of trial or “discontinuation criteria” was only in the case of serious adverse events (as defined in safety assessments clause).

Recruitment of study participants

Following a rigorous IRB-approved inclusion and exclusion criteria (Table 1), all subjects were examined, screened, and critically evaluated for this clinical investigation. After a rigorous screening of 340 subjects, a total of 204 male and female subjects were recruited and evenly divided into placebo and treatment groups. As a double-blind study, the randomization codes were generated by SAS procedure PROC PLAN using block design. The recruited subjects were asked not to alter their daily physical activities. Table 2 exhibits the demographic data of the recruited subjects in the placebo and treatment (Fenfuro[®]) groups.

Subjects were instructed to consume either placebo or treatment (Fenfuro[®]) capsules. Treatment (Fenfuro[®]) group was instructed to consume Fenfuro[®] capsules (2 capsules of 500mg each/day; batch number: FEN0715) over a period of 12 consecutive weeks. All placebo and treatment subjects maintained daily diaries and get it regularly endorsed by the study coordinators and finally countersigned by the principal investigator. Adverse event monitoring was strictly enforced.

Gender and age-wise distribution

In this investigation, male: female ratio placebo group was 67.7: 32.3, while in the treatment (Fenfuro[®]) group the male: female ratio was 68.5: 31.5. Moreover, in Fenfuro[®]-treated group, average age of the study population was 53.03 years, and in an on-going anti-diabetic therapy-treated group, average age of the study population was 52.22 years. Both the groups were evenly distributed age-wise.

Study compliance

Study coordinators meticulously distributed the placebo and treatment (Fenfuro[®]) capsules to the enrolled subjects. At the

Table 1. Inclusion and exclusion criteria.

A Inclusion criteria
1. Either gender and attending diabetic clinical at hospital.
2. Age between 25 and 60 years
3. Type 2 diabetes mellitus of less than 5 years duration
4. On oral hypoglycemic agents (Metformin ± Sulfonylurea)
5. No change in anti-diabetic treatment for the last one month
6. HbA1c >7.5%
7. Fasting plasma glucose not exceeding 180 mg/dL
8. Patients with negative urine sugar
B. Exclusion criteria
1. Diabetes other than type 2 diabetes mellitus
2. Evidence of renal disease (serum creatinine > 1.5 mg/dl)
3. Evidence of liver disease (AST/ALT >3 times of normal)
4. Pregnant and lactating mothers and women intending pregnancy
5. Participation in any other clinical trial with in the last 30 days
6. History of any hemoglobinopathy that may affect the determination of glycosylated Hemoglobin (HbA1c)
7. Treatment with oral anti-diabetic agents (other than metformin or sulfonylurea) during the 12 wk before baseline visit.
8. History of intolerance or hypersensitivity to sulfonylurea or metformin or Fenugreek Seed extract.
9. Any condition which in the opinion of the PI that is significant and can make the patient unsuitable for study or can place it under additional risk, such as intolerance, allergy to fenugreek seeds or its extract.

Table 2. Demographic data of the study population.

Data (mean \pm SD)	Placebo	Fenfuro ^a
Body Weight (Kg)	67.1 \pm 11.3	68.9 \pm 11.5
Height (cm)	159.7 \pm 10.9	181.8 \pm 17.9
BMI (kg/m ²)	26.2 \pm 4.9	26.7 \pm 4.0
SBP (mmHg)	131.7 \pm 17.8	127.2 \pm 16.6
DBP (mmHg)	77.2 \pm 10.8	76.3 \pm 9.2
Pulse rate (/min)	84.2 \pm 12.6	80.4 \pm 5.3

Data are expressed as mean \pm S.D.

beginning of each month, all the subjects were provided one pack of 60 capsules in a sealed aluminum pouch and instructed to consume two capsules each day and maintain a record in the daily diary. The investigational product was instructed to store at room temperature in a cool and dark place protected from direct sunlight. Allocation of the investigational product was done by the site staff only. Distribution of the product was maintained in the IP accountability log provided by the sponsor to the site staff. Each entry was maintained separately with the date/signature of the PI and study coordinators. The study coordinator responsible for the distribution of the study capsules was instructed to sign off the IP accountability log. IP accountability log was available at the time of the audit.

Concomitant medication

All concomitant prescription medications taken during the study by the participants were recorded on the case report forms (CRFs). Reported medications included concomitant prescription medications, over-the-counter medications (OTC) and non-prescription medications.

Assessment of safety

Safety of patients consuming investigational products was assessed whenever the patient visited the clinical study site. All the subjects visited the clinic every 4 wk for their routine physical checkup, returned the unused capsules, if any, and collected their next 4 wk capsules from the study coordinators. At each follow-up visit, safety was assessed by checking physical signs of any adverse drug reaction. At baseline and last follow-up visit, the safety was assessed by laboratory investigations also as described above.

Moreover, serum glutamic oxaloacetic transaminase activity (SGOT), serum glutamic pyruvic transaminase activity (SGPT), serum alkaline phosphatase activity (ALP), serum bilirubin, blood urea nitrogen (BUN) level, serum creatinine level, hemoglobin level, total leukocyte counts (TLC), serum urea, creatinine, cholesterol, LDL-C, HDL-C, and triglyceride levels were critically assessed at the baseline and at the completion of 12 consecutive weeks of supplementation.

Assessments of efficacy

This clinical investigation was conducted on the subjects suffering from type 2 diabetes for not more than 5 years. Moreover, the HbA1c readings in all the recruited subjects were $> 7.5\%$ and the fasting blood glucose ≤ 180 mg/dl. All

the recruited subjects in both the placebo and treatment (Fenfuro^a) groups were on metformin and/or sulfonylurea. Accordingly, the effect of metformin and/or sulfonylurea would be similar in both placebo and treatment (Fenfuro^a) groups.

Assessment of fasting and postprandial blood glucose levels

Fasting and postprandial plasma glucose levels (mg/dL) were assessed at 0, and 12 wk of investigation using kits from authorized distributor of Johnson & Johnson Ltd, Mumbai, India.

Determination of glycosylated hemoglobin (HbA1c) levels

HbA1c levels were assessed at 0, and 12 wk of investigation using kits manufactured by Bio-Rad Laboratories (Irvine, CA, USA).

Assessment of homeostatic model assessment for insulin resistance (HOMA-IR) levels

HOMA-IR values to approximately estimate insulin resistance, were assessed at 0, and 12 wk of investigation and calculated according to the formula: fasting insulin (microU/L) \times fasting glucose (nmol/L)/22.5.

Assessment of c-peptide level (ng/ml)

Fasting and postprandial C-peptide levels were assessed at 0 and 90 days of treatment using the kits manufactured by DiaSorin S.p.A. (Saluggia, Italy).

Assessment of insulin levels

Insulin levels were assessed at 0 and 90 days of treatment using kits manufactured by Elabscience Biotechnology, Wuhan, China.

Monitoring of the adverse events

All recruited study participants were specifically advised to record all types of adverse events in their daily diary during the duration of this investigation. During each of their visits, subjects were critically questioned if they had experienced any uncomfortable situation/problems or difficulties. Taken together, adverse event reporting was strictly enforced.

Statistical analyses

Data was decided to be described as mean \pm standard deviation (S.D.). The baseline characteristics were compared between the two groups using t-test and other statistical parameters. Appropriate parametric and non-parametric tests

were used according to the data. Appropriate statistical tests such as t-test and chi-square test were used to evaluate efficacy and safety of Fenfuro[®] in type 2 diabetic patients.

Results

Influence of Fenfuro[®] on fasting and post-prandial plasma glucose levels

Fenfuro[®] supplementation exhibited no effect on fasting blood glucose level. However, post-prandial plasma glucose levels were significantly improved ($p=0.0001^{**}$) in both placebo and Fenfuro[®] supplemented groups (Table 3).

Fenfuro[®] on C-peptide and plasma insulin levels in the placebo- and fenfuro[®]-treated subjects

No significant changes in c-peptide and insulin levels were observed in both the placebo and Fenfuro[®]-treated subjects following completion of 12 wk of treatment (Table 4).

Efficacy of Fenfuro[®] on glycosylated hemoglobin level (HbA1c) and HOMA-IR levels

Mean HbA1c levels reduced significantly ($p=0.0001^{**}$) in the Fenfuro[®]-treated subjects from baseline levels of 8.127% to 5.16% following completion of 12 wk of treatment. The HbA1c levels also decreased significantly ($p=0.0001^{**}$) in the placebo group (on-going anti-diabetic therapy-treated subjects) from baseline value of 8.122% to 5.653% at the end of 12 consecutive weeks of treatment (Table 5). However, the reduction was more in Fenfuro[®]-supplemented group as compared to the ongoing anti diabetic therapy group. However, the change between the groups was statistically non-significant.

Fenfuro[®] supplementation resulted in normalizing the mean HbA1c levels of the study population. Basically, the HbA1c levels decreased significantly in the study population of both groups on completion of the treatment. Mean HbA1c levels decreased more in Fenfuro[®]-treated group as compared to the placebo group (on-going anti-diabetic therapy group) (Table 5).

HOMA-IR level was reduced in Fenfuro[®]-supplemented subjects, while an increase in the HOMA-IR level was observed in the placebo-group (on-going anti diabetic therapy group) (Table 5). Thus, Fenfuro[®] supplementation improved insulin sensitivity and reduced insulin resistance.

Table 3. Efficacy of Fenfuro[®] on fasting and post-prandial plasma glucose levels in the placebo- and Fenfuro[®]-treated subjects.

Parameters	Groups	Baseline	12-Weeks of Treatment	p value
Fasting Glucose (mg/dl)	Placebo	145.5 ± 29.5	144.2 ± 46.4	0.6308
	Fenfuro [®]	144.1 ± 35.6	139.4 ± 40.7	0.318
Post-Prandial Glucose (mg/dl)	Placebo	239.3 ± 67.1	156.6 ± 120.0**	0.0001**
	Fenfuro [®]	230.5 ± 65.3	153.7 ± 103.8**	0.0001**

Data are expressed as mean ± S.D.

**Significant reduction.

Table 4. Efficacy of Fenfuro[®] on C-peptide and plasma insulin levels in the placebo-and Fenfuro[®]-supplemented subjects.

Parameters	Groups	Baseline	12-Weeks of Treatment	p-value
c-Peptide Level (ng/ml)	Placebo	2.2 ± 1.4	2.3 ± 1.3	0.5459
	Fenfuro [®]	2.1 ± 1.0	1.9 ± 0.7	0.1447
Insulin Level	Placebo	12.8 ± 15.0	14.7 ± 23.6	0.557
	Fenfuro [®]	12.3 ± 10.5	10.9 ± 6.4	0.265

Data are expressed as mean ± S.D.

Table 5. Glycosylated hemoglobin (HbA1c) and HOMA-IR levels in the placebo- and Fenfuro[®]-supplemented subjects.

Parameters	Groups	Baseline	12-Weeks	p-value
Glycosylated Hemoglobin (HbA1c)	Placebo	8.1 ± 1.3	5.7 ± 3.5**	0.0001**
	Fenfuro [®]	8.1 ± 1.8	5.2 ± 3.6**	0.0001**
HOMA-IR	Placebo	4.8 ± 4.9	4.8 ± 6.1	0.903
	Fenfuro [®]	4.3 ± 3.5	3.8 ± 2.5	0.245

Data are expressed as mean ± S.D.

**Significant reduction.

Clinical biochemistry and immuno-hematological parameters

No significant changes in the liver, kidney, and cardiovascular function tests (SGOT, SGPT, ALP, serum bilirubin, blood urea nitrogen and creatinine levels) were observed following completion of 12 wk of supplementation in both placebo and Fenfuro[®] groups (Table 6). No significant change in the immune-hematological parameter including total leukocyte counts was observed at the end of 12 consecutive weeks of supplementation (Table 6). In the differential leukocyte count (%) parameters including neutrophil count, lymphocyte count, monocyte count, basophil count, and eosinophil count, no significant changes were observed (data not shown).

Adverse events

No significant adverse events were reported in this investigation.

Table 6. Effect of placebo and Fenfuro[®] on total blood chemistry and immuno-hematological parameters.

Parameters	Groups	Baseline	12-Weeks of Treatment	p-value
SGOT (AST) U/L	Placebo	25.7 ± 11.8	24.8 ± 12.1	0.582
	Fenfuro [®]	24.5 ± 7.9	24.5 ± 9.1	0.987
SGPT (ALT) (U/L)	Placebo	41.2 ± 17.8	39.8 ± 17.8	0.458
	Fenfuro [®]	37.4 ± 14.4	37.7 ± 16.8	0.863
ALP (U/L)	Placebo	98.5 ± 27.2	96.2 ± 28.7	0.314
	Fenfuro [®]	92.1 ± 27.5	93.4 ± 23.7	0.581
Serum Bilirubin U/L	Placebo	0.6 ± 0.6	0.6 ± 0.2	0.643
	Fenfuro [®]	0.6 ± 0.3	0.6 ± 0.3	0.324
Blood Urea Nitrogen (mg/dl)	Placebo	23.0 ± 5.7	22.5 ± 6.1	0.445
	Fenfuro [®]	21.1 ± 5.9	21.2 ± 6.3	0.911
Creatinine (mg/dl)	Placebo	0.9 ± 0.3	0.9 ± 0.2	0.452
	Fenfuro [®]	0.9 ± 0.2	0.9 ± 0.2	0.091
Hemoglobin (g/dl)	Placebo	12.9 ± 1.6	13.1 ± 1.6	0.163
	Fenfuro [®]	13.0 ± 1.6	13.2 ± 1.8	0.43
Total Leukocyte Count	Placebo	7.9 ± 2.0	8.1 ± 2.2	0.529
	Fenfuro [®]	7.8 ± 2.3	8.0 ± 1.7	0.580

Data are expressed as mean ± S.D.

Discussion

The usefulness of Fenugreek seed extract in controlling hyperglycemia has been reported by several studies and is a well-established phenomenon. However, not many of them have attempted to understand systematically the probable mechanism involved in fenugreek mediated control of blood sugar level. The biological effect of fenugreek is mostly believed to be exerted by its rich content of more than 60% (w/w) furostanolic saponins as demonstrated earlier by our team (37). Gaddam et al. had reported that administration of 5gm of fenugreek powder twice daily before meals resulted in substantial decrease in fasting glucose and postprandial plasma glucose (38). Kiss et al. went one step ahead and found that melanin-concentrating hormone (MCH) played a critical role in mediating the insulin sensitizing effect of Fenugreek (39). Najdi et al. also reported that administration of Fenugreek extract in a dosage of 2gm per day resulted in a significant decrease in blood glucose level (40). Addepalli et al. reported significant reduction of fasting blood glucose as well as HbA1C on continued supplementation with Fenugreek powder for a period of 12 months (41).

As a result of the action of Fenfuro[®], both the fasting as well as the postprandial blood glucose went down, but the effect was more significant in case of the glucose measured after consumption of meal. It is known that postprandial blood glucose bears a more direct relationship with hyperglycemia and its marker HbA1c (42). It also gives a more direct risk indication of cardiovascular complications than fasting glucose (43). A potent clinical marker of chronic hyperglycemia is the covalent attachment of sugars to the amino group side chain of proteins and other cellular macromolecules, commonly known as protein glycation (44). In this respect, the most frequently used and reliable tool is the measurement of extent of glucose attachment to hemoglobin because of persistently elevated serum glucose concentration (45). Supplementation of conventional therapeutic regimen of Metformin-Sulfonylurea with Fenfuro[®] resulted in more significant arrest in glycation of Hemoglobin as compared to Metformin-sulfonylurea alone. Moreover, inclusion of Fenfuro[®] also caused a significant decrease of Homeostatic Model Assessment (HOMA) index as compared with the placebo (anti-diabetic regime) group. HOMA index is a recognized marker for assessment of β cell function and therefore also monitors the production of insulin (46). Unlike the Metformin-Sulfonylurea combination which did not result in any change of HOMA index, administration of Fenfuro[®] resulted in decrease of HOMA index. To assess the pancreatic beta cell function, the C peptide test is often reliably employed since it is produced proportionately along with insulin (47). No significant changes were observed both for C-peptide as well insulin levels in the Fenfuro[®] supplemented patient group. The results together clearly indicated that the incorporation of Fenfuro[®] increased insulin sensitivity and restored glucose homeostasis instead of merely increasing the production of insulin as observed in the Metformin-sulfonylurea placebo group. Similar findings have also been reported by Dalvi et al. where administration of Fenugreek extract resulted in a slight decrease in both C-peptide as well insulin levels after 12 wk (48). As already discussed, restoration of insulin sensitivity mandates proper functioning of

the insulin signaling pathway where phosphoinositide kinases play a significant part by preventing overactivation of FOXO transcription factors and subsequent induction of gluconeogenic pathways. Fenfuro[®] probably acts by preventing buildup of glucose from noncarbohydrate sources *via* gluconeogenesis and also regularizes insulin secretion. A slight decrease in insulin levels in the Fenfuro[®] group also suggests that elicitation of oxidative stress by NADPH oxidase 4 (NOX4) due to enhanced insulin secretion is prevented inside the cellular atmosphere. The above optimal insulin concentration leads to an altered insulin signaling pathway, as a result of which PI3-kinase phosphorylates Rac instead of PIP2. Activated Rac boosts the activity of NOX4, eventually leading to production of ROS (49).

The mechanisms leading to insulin resistance or loss of sensitivity of insulin receptor to glucose are complex and poorly understood. One probable cause is FOXO3 mediated increase in gluconeogenic enzymes which results in overabundance of concentration of glucose in plasma thus resulting in insulin sensitivity. On the other hand, increase in concentration of insulin beyond normal levels also results in malfunction of the IRS pathway and phosphorylation of RAC instead of Akt, which results in elucidation of inflammatory response (Schematic Diagram Figure 1).

The safety of Fenugreek formulation has been demonstrated earlier through Ames' test and toxicity testing (37). However, since the components of insulin signaling pathway has cross-talks with several other significant physiological responses of the body including proper functioning of the cardiovascular system, optimized lipid metabolism and inflammatory response; it was essential to investigate whether the consumption of Fenugreek adversely affected the functioning of the kidney, liver and cardiovascular system. Levels of SGOT, SGPT and ALP as markers of liver function (50) were found to be grossly unaltered both in the placebo as well as in the Fenfuro[®] supplemented group. Consequently, there was also no change in the serum bilirubin levels. Reports on the effect of Fenugreek on liver function till date have been contrasting. While some studies have demonstrated Fenugreek induced necrosis of liver hepatocytes in lactating females (51) high several old as well as new studies had demonstrated the hepatoprotective effect of Fenugreek seed extract against potential liver toxicity (52, 53). Probably, the dosage of consumption is the determining factor in governing protective action or toxicity of the phytotherapeutic (54).

The gross imbalance in glucose homeostasis occurring due to insulin resistance is known to result in elicitation of inflammatory response and concomitant oxidative stress (55). As discussed earlier, an alteration in the insulin signaling pathway may also aggravate this response. Additionally, insulin resistance can also disrupt the normal lipid metabolism leading to elevated levels of plasma triglycerides, suppressed levels of high density lipoproteins and appearance of low density lipoproteins. Therefore, lipids accumulate on the inner linings of blood vessels and bring about cardiovascular complications (55). Hematological parameters including hemoglobin and total leukocyte count were unaltered in the Fenfuro[®] group. Alongside, there was no significant change in serum creatinine and blood urea nitrogen, confirming that the extract did not confer any toxicity on consumption.

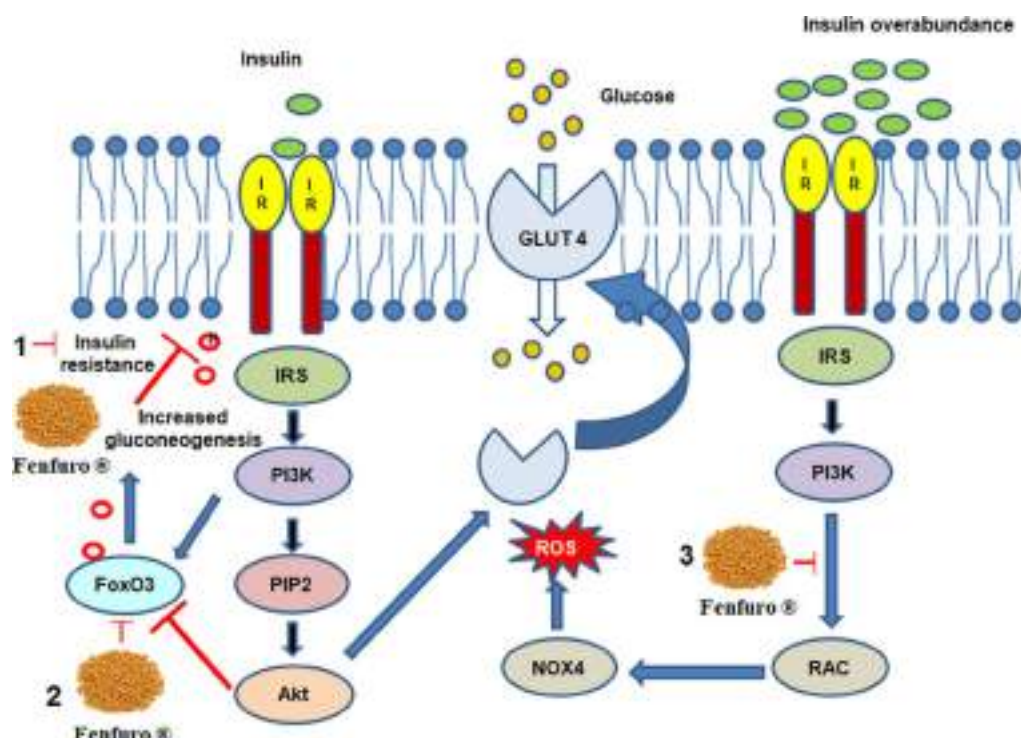


Figure 1. Impairments in insulin signaling pathway and potential targets of Fenfuro®: Normal operation of the insulin signaling pathway causes initiation of a phosphorelay which leads to Akt mediated activation and translocation of GLUT4 receptor in adipocytes for sequestration of glucose from extracellular environment. However, defects in the signaling pathway leads to phosphorylation of the wrong substrate FOXO, this in turn leads to enhanced gluconeogenesis. An abundance of glucose eventually leads to development of chronic insulin resistance. On the other hand, excess insulin also leads to faulty signaling where PI3K phosphorylates RAC instead of PIP2. RAC in turn activates NOX4 for elicitation of ROS and oxidative stress. Fenfuro (Fenugreek seed extract is believed to act at three potential targets in this cascade (1) Preventing FOXO mediated glucose production from non-carbohydrate sources (2) Preventing Akt mediated phosphorylation of FOXO and (3) Preventing activation of NOX4.

Conclusion

Although the exact molecular mechanism of Fenugreek induced lowering of blood glucose remains to be deciphered, it is mostly accepted that the furostanolic saponins along with the alkaloid trigonelline and pectins mediate the hypoglycemic effect of fenugreek extract by boosting the (IRS)-1/PI3K/AKT mediated upregulation of GLUT-4 receptor (56). These bioactive molecules are also thought to exert their

action by mediating gastric emptying. The present studies reinstated the efficacy of Fenugreek seed extract in the form of a novel patented formulation, Fenfuro®, in alleviating the clinical symptoms of Type 2 diabetes and normalizing the insulin response pathway.

There are numerous phytotherapeutics whose anti-diabetic properties are well documents (Table 7) (57–68). However, fenugreek seed not only lowers blood glucose but also is known for lowering inflammatory response, treating

Table 7. Current reports on commonly used nutraceuticals in the management of diabetes other than Fenugreek.





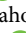



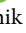




Nutraceutical	Model of study	Mode of action	Reference
Anacardium occidentale (Cashew nuts) bark	Diabetic mice	Anacardic acid in cashew boosts glucose uptake	(57)
Peel, pulp and seed of Lychee fruit	Wistar rats	Reduces blood sugar level, shows synergistic action with Metformin	(58)
Cinnamon powder	<i>In vitro</i> and <i>in silico</i> studies	Suppresses alpha amylase and alpha glucosidase	(59)
Astragalus polysaccharide	T2DM rat	Prevents expression of GLUT 2 and GLUT 4 as well as genes for glycolipid metabolism	(60)
Blueberry anthocyanins	HEPG2 cell line and streptozotocin-induced diabetic mice	Reduces expression of gluconeogenesis enzymes through AMPK signaling pathway	(61)
Aqueous extracts of <i>Allium cepa</i>	Streptozotocin-induced diabetic rat	Acts like Metformin, increases GLP-1	(62)
Carica papaya leaves	Streptozotocin-Induced Type-2 Diabetic Rats	Lowers muscle insulin Resistance through IR/GLUT 4 signaling pathways	(63)
Resveratrol	Elderly male patients with T2DM	Reduces Glucose-6-phosphatase activity	(64)
Moringa leaves hot infusion	Streptozotocin-Induced Type-2 Diabetic Rats	Lowering of blood glucose	(65)
Psidium guajava (Guava leaves)	Streptozotocin-Induced Type-2 Diabetic Rats	Restores glycogen synthase activity and reduced glycogen phosphorylase	(66)
Zingiber officinale (Ginger) aqueous extract	Mice	Increased glucose uptake	(67)
Curcumin	T2DM Rats	Increase in insulin clearance and reduction in serum creatine	(68)

dyslipidemia, and minimizing the factors responsible for onset of Metabolic syndrome and cardiovascular diseases. However, further mechanistic insights can only be warranted after ascertaining the Fenugreek induced changes in the expression profiles of the components of the insulin signaling pathway. Owing to the unprecedented rise in incidences of lifestyle associated disorders coupled with the low cost availability of Fenugreek plants across the globe, it has the potential to become the most sought after next-gen phyto-therapeutic for both prevention and treatment of a plethora of human maladies.

Disclosure statement

No potential conflict of interest was reported by the author(s).

ORCID

Debasish Hota  <http://orcid.org/0000-0002-7339-1773>
 Biswa M. Padhy  <http://orcid.org/0000-0003-3142-8213>
 Rituparna Maiti  <http://orcid.org/0000-0003-4063-9178>
 Debasis Bisoi  <http://orcid.org/0000-0002-6241-9670>
 Jyoti Prakash Sahoo  <http://orcid.org/0000-0002-1721-4836>
 Binod K. Patro  <http://orcid.org/0000-0003-0019-4522>
 Pawan Kumar  <http://orcid.org/0000-0002-2822-8133>
 Apurva Goel  <http://orcid.org/0000-0003-2909-4226>
 Samudra P. Banik  <http://orcid.org/0000-0003-0075-7508>
 Sanjoy Chakraborty  <http://orcid.org/0000-0002-6213-5483>
 Mehul Rungta  <http://orcid.org/0000-0002-4969-0394>
 Manashi Bagchi  <http://orcid.org/0000-0002-1527-6419>
 Debasis Bagchi  <http://orcid.org/0000-0001-9478-6427>

References

- Sun H, Saeedi P, Karuranga S, Pinkepank M, Ogurtsova K, Duncan BB, Stein C, Basit A, Chan JCN, Mbanya JC, et al. IDF Diabetes Atlas: global, regional and country-level diabetes prevalence estimates for 2021 and projections for 2045. *Diabetes Res Clin Pract.* 2022;183:109119. doi:10.1016/j.diabres.2021.109119.
- Freeman AM, Pennings N. Insulin resistance. [Updated 2022 Sep 20]. In: statPearls [Internet]. Treasure Island (FL): statPearls Publishing; 2023. Jan-. Available from: <https://www.ncbi.nlm.nih.gov/books/NBK507839/>
- Roberts CK, Hevener AL, Barnard RJ. Metabolic syndrome and insulin resistance: underlying causes and modification by exercise training. *Compr Physiol.* 2013;3(1):1–58. doi:10.1002/cphy.c110062.
- Bagchi D, Nair S (Eds.). In: Nutritional and therapeutic interventions for diabetes and metabolic syndrome. 2nd Ed. Elsevier/ Academic Press London, UK, 2018. <https://www.elsevier.com/books/nutritional-and-therapeutic-interventions-for-diabetes-and-metabolic-syndrome/bagchi/978-0-12-812019-4>
- Lee S, Dong HH. FoxO integration of insulin signaling with glucose and lipid metabolism. *J Endocrinol.* 2017;233(2):R67–R79. doi:10.1530/JOE-17-0002.
- Gutch M, Kumar S, Razi SM, Gupta KK, Gupta A. Assessment of insulin sensitivity/resistance. *Indian J Endocrinol Metab.* 2015;19(1):160–4. doi:10.4103/2230-8210.146874.
- Khalid M, Alkaabi J, Khan MAB, Adem A. Insulin signal transduction perturbations in insulin resistance. *IJMS.* 2021;22(16):8590. doi:10.3390/ijms22168590.
- Wondmkuon YT. Obesity, insulin resistance, and type 2 diabetes: associations and therapeutic implications. *Diabetes Metab Syndr Obes.* 2020;13:3611–6. doi:10.2147/DMSO.S275898.
- Hsieh CJ, Wang PW, Chen TY. The relationship between regional abdominal fat distribution and both insulin resistance and sub-clinical chronic inflammation in non-diabetic adults. *Diabetol Metab Syndr.* 2014;6(1):49. doi:10.1186/1758-5996-6-49.
- Wang Z, Wang J, Chan P. Treating type 2 diabetes mellitus with traditional chinese and Indian medicinal herbs. *Evid Based Complement Alternat Med.* 2013;2013:343594. doi:10.1155/2013/343594.
- Kastuyama H, Yanai H. Does metformin assist new anti-diabetic drugs to succeed? *J Clin Med Res.* 2019;11(2):151–5. doi:10.14740/jocmr3706.
- Costello RA, Nicolas S, Shivkumar A. Sulfonylureas. [Updated 2023 Mar 7]. In: statPearls [Internet]. Treasure Island (FL): StatPearls Publishing; 2023. Jan-. Available from: <https://www.ncbi.nlm.nih.gov/books/NBK513225/>
- Zhang F, Xiang H, Fan Y, Ganchuluun TA, Kong W, Ouyang Q, Sun J, Cao B, Jiang H, Nie S. The effects of sulfonylureas plus metformin on lipids, blood pressure, and adverse events in type 2 diabetes: a meta-analysis of randomized controlled trials. *Endocrine.* 2013;44(3):648–58. doi:10.1007/s12020-013-9970-6.
- Alam S, Sarker MMR, Sultana TN, Chowdhury MNR, Rashid MA, Chaity NI, Zhao C, Xiao J, Hafez EE, Khan SA, et al. Antidiabetic phytochemicals from medicinal plants: prospective candidates for new drug discovery and development. *Front Endocrinol (Lausanne).* 2022;13:800714. doi:10.3389/fendo.2022.800714.
- Jeyaraman MM, Al-Yousif NSH, Singh Mann A, Dolinsky VW, Rabbani R, Zarychanski R, Abou-Setta AM. Resveratrol for adults with type 2 diabetes mellitus. *Cochrane Database Syst Rev.* 2020;1(1):CD011919. doi:10.1002/14651858.
- Martorell M, Castro N, Victoriano M, Capó X, Tejada S, Vitalini S, Pezzani R, Sureda A. An Update of anthraquinone derivatives emodin, diacerein, and catenarin in diabetes. *Evid Based Complement Alternat Med.* 2021;2021:3313419. doi:10.1155/2021/3313419.
- Amor AJ, Gómez-Guerrero C, Ortega E, Sala-Vila A, Lázaro I. Ellagic acid as a tool to limit the diabetes burden: updated evidence. *Antioxidants (Basel).* 2020;9(12):1226. doi:10.3390/antiox9121226.
- Zhu T, Li M, Zhu M, Liu X, Huang K, Li W, Wang SX, Yin Y, Li P. Epigallocatechin-3-gallate alleviates type 2 diabetes mellitus via β -cell function improvement and insulin resistance reduction. *Iran J Basic Med Sci.* 2022;25(4):483–8. doi:10.22038/IJBMS.2022.58591.13016.
- Pivari F, Mingione A, Brasacchio C, Soldati L. Curcumin and type 2 diabetes mellitus: prevention and treatment. *Nutrients.* 2019;11(8):1837. doi:10.3390/nu11081837.
- Fu Y, Luo J, Jia Z, Zhen W, Zhou K, Gilbert E, Liu D. Baicalein protects against type 2 diabetes via promoting islet β -cell function in obese diabetic mice. *Int J Endocrinol.* 2014;2014:846742. doi:10.1155/2014/846742.
- Li S, Zhang Y, Sun Y, Zhang G, Bai J, Guo J, Su X, Du H, Cao X, Yang J, et al. Naringenin improves insulin sensitivity in gestational diabetes mellitus mice through AMPK. *Nutr Diabetes.* 2019;9(1):28. doi:10.1038/s41387-019-0095-8.
- Yang H, Wang Y, Xu S, Ren J, Tang L, Gong J, Lin Y, Fang H, Su D. Hesperetin, a promising treatment option for diabetes and related complications: a literature review. *J Agric Food Chem.* 2022;70(28):8582–92. doi:10.1021/acs.jafc.2c03257.
- Ramírez-Espinosa JJ, Saldaña-Ríos J, García-Jiménez S, Villalobos-Molina R, Ávila-Villarreal G, Rodríguez-Ocampo AN, Bernal-Fernández G, Estrada-Soto S. Chrysin induces antidiabetic, antidyslipidemic and anti-inflammatory effects in athymic nude diabetic mice. *Molecules.* 2017;23(1):67. doi:10.3390/molecules23010067.
- Zhang N, Zhang W, Guo X, Liu J, Li S, Zhang H, Fan B. Genistein protects against hyperglycemia and fatty liver disease in diet-induced prediabetes mice via activating hepatic insulin signaling pathway. *Front Nutr.* 2022;9:1072044. doi:10.3389/fnut.2022.1072044.

25. Alkhalidy H, Moore W, Wang Y, Luo J, McMillan RP, Zhen W, Zhou K, Liu D. The flavonoid kaempferol ameliorates streptozotocin-induced diabetes by suppressing hepatic glucose production. *Molecules*. 2018;23(9):2338. doi:10.3390/molecules23092338.
26. Al-Ishaq RK, Abotaleb M, Kubatka P, Kajo K, Büsselberg D. Flavonoids and their anti-diabetic effects: cellular mechanisms and effects to improve blood sugar levels. *Biomolecules*. 2019;9(9):430. doi:10.3390/biom9090430.
27. Xu Y, Li X, Wang H. Protective roles of apigenin against cardiometabolic diseases: a systematic review. *Front Nutr*. 2022;9:875826. doi:10.3389/fnut.2022.875826.
28. Ansari P, Choudhury ST, Seidel V, Rahman AB, Aziz MA, Richi AE, Rahman A, Jafrin UH, Hannan JMA, Abdel-Wahab YHA. Therapeutic potential of quercetin in the management of type-2 diabetes mellitus. *Life (Basel)*. 2022;12(8):1146. doi:10.3390/12081146.
29. Modak M, Dixit P, Londhe J, Ghaskadbi S, Devasagayam TP. Indian herbs and herbal drugs used for the treatment of diabetes. *J Clin Biochem Nutr*. 2007;40(3):163–73. doi:10.3164/jcbn.40.163.
30. Medagama AB, Senadhira D. Use of household ingredients as complementary medicines for perceived hypoglycemic benefit among Sri Lankan diabetic patients; a cross-sectional survey. *J Interact Ethnopharmacol*. 2015;4(2):138–42. doi:10.5455/jice.20150202035223.
31. Przeor M. Some common medicinal plants with antidiabetic activity, known and available in Europe (a mini-review). *Pharmaceuticals*. 2022;15(1):65. doi:10.3390/ph15010065.
32. Ranade M, Mudgalkar N. A simple dietary addition of fenugreek seed leads to the reduction in blood glucose levels: a parallel group, randomized single-blind trial. *Ayu*. 2017;38(1–2):24–7. doi:10.4103/ayu.AYU_209_15.
33. Geberemeskel GA, Debebe YG, Nguse NA. Antidiabetic effect of fenugreek seed powder solution (*Trigonella foenum-graecum* L.) on hyperlipidemia in diabetic patients. *J Diabetes Res*. 2019; Sep 52019:8507453. doi:10.1155/2019/8507453.
34. Gupta A, Gupta R, Lal B. Effect of *Trigonella foenum-graecum* (fenugreek) seeds on glycaemic control and insulin resistance in type 2 diabetes mellitus: a double blind placebo controlled study. *J Assoc Physicians India*. 2001;49:1057–61. PMID: 11868855.
35. Wani SA, Kumar P. Fenugreek: a review on its nutraceutical properties and utilization in various food products. *J Saudi Soc Agric Sci*. 2018;17(2):97–106. doi:10.1016/j.jssas.2016.01.007.
36. Verma N, Usman K, Patel N, Jain A, Dhakre S, Swaroop A, Bagchi M, Kumar P, Preuss HG, Bagchi D. A multicenter clinical study to determine the efficacy of a novel fenugreek seed (*Trigonella foenum-graecum*) extract (Fenfurol™) in patients with type 2 diabetes. *Food Nutr Res*. 2016;60:32382. doi:10.3402/fnr.v60.32382.
37. Swaroop A, Bagchi M, Kumar P, Preuss HG, Tiwari K, Marone PA, Bagchi D. Safety, efficacy and toxicological evaluation of a novel, patented anti-diabetic extract of *Trigonella foenum-graecum* seed extract (Fenfurol). *Toxicol Mech Methods*. 2014;24(7):495–503. doi:10.3109/15376516.2014.943443.
38. Gaddam A, Galla C, Thummiseti S, Marikanty RK, Palanisamy UD, Rao PV. Role of Fenugreek in the prevention of type 2 diabetes mellitus in prediabetes. *J Diabetes Metab Disord*. 2015;14:74. doi:10.1186/s40200-015-0208-4.
39. Kiss R, Szabó K, Gesztelyi R, Somodi S, Kovács P, Szabó Z, Németh J, Priks J, Kurucz A, Juhász B, et al. Insulin-sensitizer effects of fenugreek seeds in parallel with changes in 46. Plasma MCH levels in healthy volunteers. *IJMS*. 2018;19(3):771. doi:10.3390/ijms19030771.
40. Najdi RA, Hagraas MM, Kamel FO, Magadmi RM. A randomized controlled clinical trial evaluating the effect of *Trigonella foenum-graecum* (fenugreek) versus glibenclamide in patients with diabetes. *Afr Health Sci*. 2019;19(1):1594–601. doi:10.4314/ahs.v19i1.34.
41. Addepalli SK, Nigam N, Kumar S. Antidiabetic effect and preference of fenugreek with dietary modifications in patients with prediabetes: an interventional parallel randomized study. *J Diabetol*. 2022;13(1):83–94. doi:10.4103/jod.jod_40_21.
42. Haddadinezhad S, Ghazaleh N. Relation of fasting and postprandial and plasma glucose with hemoglobinA1c in diabetics. *Int J Diabetes Dev Ctries*. 2010;30(1):8–10. doi:10.4103/0973-3930.60002.
43. Jiang J, Zhao L, Lin L, Gui M, Alesteng Q, Wu B, Wang S, Pan B, Ling Y, Gao X. Postprandial blood glucose outweighs fasting blood glucose and HbA1c in screening coronary heart disease. *Sci Rep*. 2017; Oct 277(1):14212. doi:10.1038/s41598-017-14152-y.
44. Rabbani N, Thornalley PJ. Protein glycation - biomarkers of metabolic dysfunction and early-stage decline in health in the era of precision medicine. *Redox Biol*. 2021;42:101920. doi:10.1016/j.redox.2021.101920.
45. Sherwani SI, Khan HA, Ekhzaimy A, Masood A, Sakharkar MK. Significance of HbA1c test in diagnosis and prognosis of diabetic patients. *Biomark Insights*. 2016;11:95–104. doi:10.4137/BMI.S38440.
46. Minh HV, Tien HA, Sinh CT, Thang DC, Chen CH, Tay JC, Siddique S, Wang TD, Sogunuru GB, Chia YC, et al. Assessment of preferred methods to measure insulin resistance in Asian patients with hypertension. *J Clin Hypertens (Greenwich)*. 2021;23(3):529–37. doi:10.1111/jch.14155.
47. Leighton E, Sainsbury CA, Jones GC. A practical review of C-peptide testing in diabetes. *Diabetes Ther*. 2017;8(3):475–87. doi:10.1007/s13300-017-0265-4.
48. Dalvi SM, Patwardhan MS, Yeram N, Patil VW, Patwardhan SY. Evaluation of biochemical markers in type 2 diabetes mellitus with adjunct therapy of fenugreek seed aqueous extract. *J Med Plants Stud*. 2019;7(1):109–13. <https://www.plantsjournal.com/archives/2019/vol7issue1/PartB/7-1-16-596.pdf>
49. Campa CC, Ciruolo E, Ghigo A, Germena G, Hirsch E. Crossroads of PI3K and Rac pathways. *Small GTPases*. 2015;6(2):71–80. doi:10.4161/21541248.2014.989789.
50. Lala V, Zubair M, Minter DA. Liver function tests. [Updated 2022 Oct 5]. In: StatPearls [Internet]. Treasure Island (FL): StatPearls Publishing; 2023. Jan-. Available from: <https://www.ncbi.nlm.nih.gov/books/NBK482489/>.
51. Partiula B, Dougherty R. The dangers of herbal supplements: a case of acute liver injury from fenugreek: 2273. *Am J Gastroenterol*. 2017; 2006; Fenugreek. [Updated 2022 Aug 15]. Available from: 112: s 1247–S1248. *Drugs and Lactation Database (LactMed®)* [Internet]. Bethesda (MD): national Institute of Child Health and Human Development <https://www.ncbi.nlm.nih.gov/books/NBK501779/>. doi:10.14309/00000434-201710001-02274.
52. Haeri MR, Izaddoost M, Ardekani MR, Nobar MR, White KN. The effect of fenugreek 4-hydroxyisoleucine on liver function biomarkers and glucose in diabetic and fructose-fed rats. *Phytother Res*. 2009;23(1):61–4. doi: 10.1002/ptr.2557. doi:10.1016/j.jssas.2016.01.007.
53. Fatima SN, Masood J. Fenugreek seeds attenuate thioacetamide induced liver damage. *Pak J Pharm Sci*. 2021;34(3):933–42. PMID: 34602416.
54. Alam SS, Mazumder AK, Akhter R, Md Jahangir S. (2019) Study of Sub-Acute Toxicity Profile of Fenugreek (*Trigonella foenum-graecum*) Seeds in Kidney Tissues of Albino Rat: A Randomized Control Trial. *Chatt Maa Shi Hosp Med Coll J*. 2019;18(1):36–43. doi:10.3329/cmshmcj.v18i1.42131.
55. Ormazabal V, Nair S, Elfeky O, Aguayo C, Salomon C, Zuñiga FA. Association between insulin resistance and the development of cardiovascular disease. *Cardiovasc Diabetol*. 2018;17(1):122. doi:10.1186/s12933-018-0762-4.
56. Xu J, Wang S, Feng T, Chen Y, Yang G. Hypoglycemic and hypolipidemic effects of total saponins from *Stauntonia chinensis* in diabetic db/db mice. *J Cell Mol Med*. 2018;22(12):6026–38. doi:10.1111/jcmm.13876.
57. Encarnação S, De Mello-Sampayo C, Carrapiço B, São Braz B, Jordão AP, Peleteiro C, Catarino L, Silva IBMD, Gouveia LF, Lima BS, et al. *Anacardium occidentale* Bark as an antidiabetic agent. *Plants (Basel)*. 2022;11(19):2637. doi:10.3390/plants11192637.
58. Contreras-Castro AI, Oidor-Chan VH, Bustamante-Camilo P, Pelayo-Zaldívar C, Díaz de León-Sánchez F, Mendoza-Espinoza

- JA. Chemical characterization and evaluation of the antihyperglycemic effect of Lychee (*Litchi chinensis* Sonn.) cv. Brewster. *J Med Food*. 2022;25(1):61–9. doi:10.1089/jmf.2021.0098.
59. Bahtiasyah AA, Hidayati L, Wijayanti N, Nuringtyas TR. Antidiabetic activity of cinnamon and agarwood combination. *Indones Biomed J*. 2023;15(2):132–40. doi:10.18585/inabj.v15i2.2132.
 60. Luo MJ, Wang Y, Chen SY, Yang ZM. Astragalus polysaccharides alleviate type 2 diabetic rats by reversing the expressions of sweet taste receptors and genes related to glycolipid metabolism in liver. *Front Pharmacol*. 2022;13:916603. doi:10.3389/fphar.2022.916603.
 61. Herrera-Balandrano DD, Chai Z, Hutabarat RP, Beta T, Feng J, Ma K, Li D, Huang W. Hypoglycemic and hypolipidemic effects of blueberry anthocyanins by AMPK activation: in vitro and in vivo studies. *Redox Biol*. 2021;46:102100. doi:10.1016/j.redox.2021.102100.
 62. Ighodaro OM, Adeosun AM, Ujomu TS, Durosinlorun OO, Okosa CC. Combination therapy of *Allium cepa* L. and *Cucumis sativa* L. extracts in streptozotocin-induced diabetic rat model. *Futur J Pharm Sci*. 2021;7(1):227. doi:10.1186/s43094-021-00371-8.
 63. Roy JR, Janaki CS, Jayaraman S, Periyasamy V, Balaji T, Vijayamalathi M, Veeraraghavan VP. Carica papaya reduces muscle insulin resistance via IR/GLUT4 mediated signaling mechanisms in high fat diet and streptozotocin-induced type-2 diabetic rats. *Antioxidants (Basel)*. 2022;11(10):2081. doi:10.3390/antiox11102081.
 64. Ma N, Zhang Y. Effects of resveratrol therapy on glucose metabolism, insulin resistance, inflammation, and renal function in the elderly patients with type 2 diabetes mellitus: A randomized controlled clinical trial protocol. *Medicine (Baltimore)*. 2022;101(32):e30049. doi:10.1097/MD.00000000000030049.
 65. Toma A. Antidiabetic activity of hot tea infusion of leaves of moringa stenopetala in streptozotocin-induced diabetic rats. *J Exp Pharmacol*. 2022;14:309–16. doi:10.2147/JEP.S371354.
 66. Tella T, Masola B, Mukaratirwa S. Anti-diabetic potential of Psidium guajava leaf in streptozotocin induced diabetic rats. *Phytomedicine Plus*. 2022;2(2):100254. doi:10.1016/j.phyp-lu.2022.100254.
 67. Pakan P, Lidia K, Riwu M. Investigation of ginger (*Zingiber officinale*) aqueous extract as an anti-diabetic in vitro. *IOP Conf Ser: Earth Environ Sci*. 2021;913(1):012108. doi:10.1088/1755-1315/913/1/012108.
 68. Machado DI, de Oliveira Silva E, Ventura S, Vattimo MFF. The effect of curcumin on renal ischemia/reperfusion injury in diabetic rats. *Nutrients*. 2022;14(14):2798. Erratum in: *Nutrients*. 2022 Nov 15;14(22): PMID: 35889755; PMCID: PMC9323852. doi:10.3390/nu14142798.



Beneficial Effects of a Novel Fenugreek Seed Extract (*Trigonella foenum-graecum*, Furocyst®) in Women with Polycystic Ovary Syndrome (PCOS): A Follow-up Compliance Clinical Investigation

Pushplata Sankhwar, S. P. Jaiswar, Sonali Yadav, Vandana Awasthi, Apurva Goel, Pawan Kumar, Samudra P. Banik, Manashi Bagchi & Debasis Bagchi

To cite this article: Pushplata Sankhwar, S. P. Jaiswar, Sonali Yadav, Vandana Awasthi, Apurva Goel, Pawan Kumar, Samudra P. Banik, Manashi Bagchi & Debasis Bagchi (2023) Beneficial Effects of a Novel Fenugreek Seed Extract (*Trigonella foenum-graecum*, Furocyst®) in Women with Polycystic Ovary Syndrome (PCOS): A Follow-up Compliance Clinical Investigation, Journal of the American Nutrition Association, 42:7, 691-699, DOI: [10.1080/27697061.2022.2145526](https://doi.org/10.1080/27697061.2022.2145526)

To link to this article: <https://doi.org/10.1080/27697061.2022.2145526>



Published online: 28 Nov 2022.



Submit your article to this journal



Article views: 196









View related articles



View Crossmark data



Beneficial Effects of a Novel Fenugreek Seed Extract (*Trigonella foenum-graecum*, Furocyst®) in Women with Polycystic Ovary Syndrome (PCOS): A Follow-up Compliance Clinical Investigation

Pushplata Sankhwar^a , S. P. Jaiswar^a, Sonali Yadav^a, Vandana Awasthi^a, Apurva Goel^b , Pawan Kumar^c , Samudra P. Banik^d , Manashi Bagchi^e  and Debasis Bagchi^{f,g} 

^aDepartment of Obstetrics & Gynecology, King George's Medical University, Lucknow, India; ^bRegulatory Department, Chemical Resources (CHERES), Panchkula, India; ^cResearch and Development Department, Chemical Resources (CHERES), Panchkula, India; ^dDepartment of Microbiology, Maulana Azad College, Kolkata, India; ^eResearch & Development Department, Dr. Herbs LLC, Concord, California, USA; ^fDepartment of Biology, Adelphi University, Garden City, New York, USA; ^gDepartment of Pharmaceutical Sciences, Texas Southern University, Houston, Texas, USA

ABSTRACT

Introduction: Polycystic Ovary Syndrome (PCOS) is an endocrine disorder which accounts for infertility around the world. The disease is characterized by elevated secretion of androgens in the women which results in enlargement of ovaries with accumulation of fluid filled cysts, irregular menstrual cycles, and hirsutism. This study reports the efficacy of a patented, standardized *Trigonella foenum-graecum* extract (Furocyst®) as an effective phytotherapeutic for effective management of PCOS.

Objective: This randomized one-arm study assessed the efficacy of Furocyst® in 107 female volunteers over a period of 12 consecutive weeks.

Method: Following approvals of the Institutional Ethical Committee and clinicaltrials.gov, 107 female volunteers (age: 18–45 years) were recruited. Subjects consumed Furocyst® capsules (1,000 mg/day p.o.) over a period of 12 consecutive weeks. Physical (Sonographic scan, Hirsutism Score, Menstrual cycle, Body Weight, BMI, Height, Waist Circumference and Blood Pressure) and biochemical parameters (LH/FSH ratio, TSH, Prolactin, Fasting insulin, Fasting Glucose, triglyceride, cholesterol, HOMA Index, free and total testosterone, 2-hour GTT, DHEAS) were assessed at the beginning of the study as well as at intervals of 4 weeks till 12 weeks to determine the efficacy of Furocyst® on PCOS induced damage on reproductive and endocrine system.

Results: Furocyst® treatment induced >40% reduction of mean cyst sizes in both ovaries with corresponding reduction of in ovarian volumes. LH:FSH ratio was also significantly improved with corresponding reduction in total testosterone and prolactin levels. As a result of improvement in endocrine function, menstrual cycle became regular in the subjects. Furocyst® also reduced the severity of other associated ailments such as insulin resistance, dyslipidemia, and improved liver function significantly.

Conclusions: This study reinstated the efficacy of Furocyst® as a safe phytotherapeutic to reverse the effects of PCOS inflicted damage on the female reproductive system without any adverse events.

ARTICLE HISTORY

Received 28 September 2022

Accepted 4 November 2022

KEYWORDS

PCOS; Hyperandrogenism; *Trigonella foenum-graecum* seed extract; Furocyst®; phytotherapeutics; insulin resistance

Introduction

Polycystic Ovary Syndrome (PCOS) has emerged as the single most significant threat to the reproductive health of women globally. The prevalence of the disease has increased steeply since its first proper clinical description and diagnosis (1). According to a recent estimate, approximately 1 in 10 women has PCOS over the world. PCOS is a complex multifactorial disease caused chiefly by the dysbiosis of the female hypothalamic–pituitary–ovarian (HPO) axis (2, 3) resulting in gross imbalance in reproductive hormones like LH, FSH, estrogen and testosterone (4). The significant rise in testosterone levels resulting in hyperandrogenism is

responsible for several reproductive abnormalities like chronic ovulatory dysfunction, menstrual irregularity, reduced fertility as well as post pregnancy complications such as gestational diabetes mellitus (GDM) and pregnancy-induced hypertension (PIH) (5). Observable clinical features of the disease include hirsutism, pelvic pain, acne and appearance of dark patches on the skin. Apart from reproductive maladies, onset of PCOS also leads to many metabolic disorders including insulin resistance, obesity and cardiovascular disease (CVD) (6, 7). Elevated testosterone levels together with concomitant drop in FSH arrest further development of the follicles (8). These

prematurely terminated follicles develop into fluid-filled cysts, the signature pathophysiology of PCOS (6).

Owing to its multifactorial nature as well as complex etiology, development of a tangible therapy has not been possible. The intended medicines have been shown to bring down or cure only a specific symptom or ailment associated with PCOS instead of treating it from the root cause. The most popular therapies in this regard have been antiandrogenic drugs (9), insulin sensitizers (10), artificial ovulation inducers (11), and oral contraceptives (12). Metformin has been found to be very promising with regards to its use both as an insulin sensitizing agent as well as an ovulation inducer (13). Drugs such as rosiglitazone and pioglitazone have also yielded encouraging results against hirsutism and insulin resistance. However, a single medication which can address all the issues together has eluded both researchers as well as clinicians till date. Therefore, it is very much apparent that a treatment regimen of PCOS will be based on its management rather than its cure or prevention (9).

The use of phytotherapeutics for treatment of chronic, complex and multifactorial ailments has been in vogue for many centuries in oriental countries including India. Frequently, ethnomedicines have yielded encouraging results in treatments of female reproductive problems like irregular menstrual periods, menstrual cramping, uterine fibroids and infertility (14). These have been also successful in some respect in alleviating the symptoms and disorders in PCOS (15, 16). The active constituents in these plant combinatorial therapies have been found to exert their action mainly through interaction with the α/β estrogen receptors (17, 18), induction of vasoconstriction (19), regulation of blood sugar and reduction of serum levels of triglycerides and LDL-cholesterols (14).

Fenugreek (*Trigonella foenum-graecum*) seeds have been a century-old effective home-remedy for treating gynecological problems of women. It is most popular as a flavor enhancer in culinary delicacies in oriental countries of south-east and alongside has many therapeutic benefits also. Fenugreek seeds are fortified with multiple protective components such as choline, inositol, biotin, multivitamins, fiber and iron. They have established roles in stimulating insulin to bring down hyperglycemia, improving testosterone and estrogen levels to rejuvenate reproductive health, alleviate hypercholesterolemia, cure hepatotoxicity, nullify oxidative stress and restore overall body homeostasis (20). Many studies have reported the benefits of Fenugreek seeds in management of hormonal disorders resulting in post and peri-menopausal problems (21). Their potential in alleviating PCOS related complications had also been documented by several earlier studies (22). Previous reports in our laboratory have shown that a fenugreek seed extract, enriched in 40% furostanolic saponins can effectively rectify the altered LH:FSH ratio and regularize menstrual periods in women belonging to reproductive age (23). In the present investigation, an open labeled, single armed, single-centric, and non-comparative study was carried out on the effect of consumption of Furocyst[®], a Fenugreek seed extract formulation, on premenopausal women affected with PCOS.

Materials and methods

A novel, patented Trigonella foenum-graecum seed extract

Furocyst[®] [Chemical Resources (CHERESO), Panchkula, India][US and European Patents# US 8,754,205 B2; US 8,217,165 B2; EP 2285821 B1], a water-ethanol extracted *Trigonella foenum-graecum* (family Leguminosae) seed extract fortified in 45% furostanolic saponins [26-O-beta-D-glucopyranosyl-22-hydroxyfurost-5-ene-3-beta,26-diol-3-O-beta-diglucorhamnoside (CAS#: 84625-40-1), manufactured in an NSF-GMP certified manufacturing facility, was used in this study. Furocyst[®] was stored at room temperature in a cool and dark place and protected from sunlight.

Ethical and regulatory approvals

Study design, subject recruitment and assessment following the rigorous inclusion and exclusion criteria, study compliance, protocols, procedures, and methodologies of this open labeled, one-arm, single-center, and non-comparative study were conducted in compliance with the International Council for Harmonization (ICH) guidelines for Good Clinical Practices as per the procedures and protocols of international standards guaranteed by the Declaration of Helsinki and amendments implemented later. The study protocol (CR-PCOS/1-15) was duly approved by the Institutional Ethics Committee (IEC) (Registration No. ECR/262/Inst/UP/2013) located at King George's Medical University, Lucknow, UP, (Protocol #6107/Ethics/R.Cell-15 dated May 7, 2015; Ref: IRB Proposal "To Study the Efficacy and Safety of Standardized Fenugreek Seed Extract in Polycystic Ovary Syndrome patients (PCOS) (Ref. Code 71st ECM 11-A/P9). Prior to the recruitment, the IEC-approved study protocol including inclusion and exclusion criteria and IEC-approved study protocol were explained to all study participants, and all subjects duly signed the informed consent forms. The study was also registered in the Central Drugs Standard Control Organization (CDSCO) DCGI approval of Ethics Committee (ECR/421/George's/Inst/UP/2013/Re-Registration-2016). Finally, the protocol entitled "To study the efficacy and safety of Furocyst in polycystic ovary syndrome (PCOS) patients" was enrolled in the clinical study registration NCT02703064 (<https://clinicaltrials.gov/ct2/show/study/NCT02703064?term=Furocyst&cond=PCOS&rank=1>) All enrolled subjects read and duly signed the health questionnaire. Subject confidentiality was strictly enforced. Adverse event monitoring was strictly ascertained.

Protocols and procedures

Analytical kits for serum aspartate transaminase (AST)/serum glutamic oxaloacetic transaminase (SGOT), serum alanine transaminase (ALT)/serum glutamate-pyruvate transaminase (SGPT), serum alkaline phosphatase activity (ALP), serum urea, serum glucose, serum insulin, serum triglyceride (TG), high density lipoproteins (HDL), luteinizing hormone (LH), follicular stimulating hormone (FSH), thyroid stimulating

hormone (TSH) and prolactin levels were purchased from Siemens USA (Authorized representative Schenker India Pvt Ltd, Gurgaon, Haryana, India). Hemoglobin levels (Hb), total leukocyte count (TLC) and differential leukocyte count (DLC) were assessed using electronic impedance in a Beckman Coulter Counter (Beckman Coulter India Pvt Ltd, New Delhi, India). Ultrasound was conducted in a GE LOGIQ P5 ultrasound system provided by Wipro GE Healthcare Pvt Ltd (Bangalore, India). Dia Sources' ELISA kit (catalog#CAN-FTE-260), purchased from Krishgen Biosystems, Mumbai, India, was used to measure free testosterone, while and total testosterone was measured using an automated bidirectionally interfaced Chemiluminescent Immunoassay (CLIA) from Siemens Health Care Pvt Ltd, Mumbai, India. Dehydroepiandrosterone sulfate (DHEA-S) was measured using the Cobas Electrochemiluminescence Immunoassay (ECLIA) (catalog# 03000087122) kit purchased from Roche Diagnostics India Pvt Ltd, Mumbai, India. Hemoglobin level was evaluated using a Sysmex fully automated bidirectional analyzer (SYSMEX XN-1000) purchased from Transasia Bio Medicals Ltd, Mumbai, India, and fasting blood glucose (FBS) levels were assessed using photometry technology (Agappe Diagnostics Ltd, Mumbai, India).

Recruitment of subjects

All enrolled subjects were physically examined and critically screened for this clinical investigation according to the inclusion and exclusion criteria (Table 1). Enrolled subjects were instructed not to alter their routine physical activities and plans. Following rigorous screening, a total of 107 female subjects (age: 18-45 Y; average age of the study population: 25.94 ± 5.78 Y; pulse rate: 74.10 ± 4.06) were recruited. Furocyst (2 capsules of 500mg each/day; batch numbers: FUR0517, FUR0117, FUR0415, FUR0416, and FUR0816) was consumed by all the subjects over a period of 12 consecutive

weeks to determine its efficacy in reducing ovarian volume and the number of ovarian cysts. All Subjects maintained daily diaries, which were regularly endorsed by the study coordinators and endorsed by the principal investigator. Adverse event monitoring was strictly enforced.

Study compliance

Furocyst® capsules were meticulously distributed by the project coordinators. All subjects were provided one pack of 60 capsules in a sealed aluminum pouches at the beginning of each month and directed to consume two capsules every day. The records of individual entry were maintained separately with the date/signature of the subject, endorsed by the study coordinators(s) and principal investigator and thus IP accountability log was maintained.

Assessment of safety

Serum aspartate transaminase (AST)/serum glutamic oxaloacetic transaminase (SGOT), serum alanine transaminase (ALT)/serum glutamate-pyruvate transaminase (SGPT), serum alkaline phosphatase activity (ALP), serum urea, hemoglobin, differential leukocyte counts (DLC), creatinine, cholesterol, HDL-C, and triglyceride levels were meticulously checked at the baseline and at the completion of 12 weeks of treatment.

Clinical assessment of Furocyst® in female subjects

Physical, biochemical, and hematological parameters were assessed at baseline, 4-, 8-, and 12-weeks post-treatment (Table 2). Time-dependent efficacy of Furocyst was determined on the number of cysts (both on right and left ovaries) and on the reduction in ovarian volume (both on right and left ovaries) at baseline, 4-, 8-, and 12-weeks post-treatment. Hirsutism score, menstrual cycle, luteinizing hormone (LH), follicle stimulating hormone (FSH), LH/FSH

Table 1. Inclusion and Exclusion Criteria

Inclusion criteria

- Diagnosed with PCOS by Rotterdam criteria (22)
- Premenopausal women (age: 18–45 years) and BMI ($<42 \text{ kg/m}^2$)
- Adequate hepatic, renal, cardiac, and hematological functions
- Willingness to participate in the study and follow the norms
- Provide informed consent in writing for the study
- Regularly visit the hospital clinic, as and when required, for follow up
- Stable body weight for the last two months (permissible change $<3 \text{ kg}$)
- Physicians' approval for selected patients

Exclusion criteria

- Male subjects
- Postmenopausal women subjects
- Women with hysterectomy
- Women suffering from hyperprolactinemia
- Women suffering from congenital adrenal hyperplasia
- Subjects suffering from Cushing's syndrome
- Acute or chronic medical illness including hepatic, cardiac or renal insufficiency, COPD, or gastrointestinal disorders
- Uncontrolled hypertensive subjects
- Diabetics on drugs
- Use of oral contraceptives or HRT for last three months.
- Patients diagnosed with androgen secreting tumors
- Patients with thyroid dysfunction (T3, T4 level is higher than that in normal women of reproductive age)
- Pregnant or lactating mothers.
- Smoking or drug addicts or with psychiatric illness
- Subjects with hypogonadotropic and hypogonadism (central origin of ovarian dysfunction)

Table 2. Clinical Assessment of Furocyst

Time point	Parameters assessed
Baseline (Visit 1)	Sonographic scan, Hirsutism Score, Menstrual cycle, Body Weight, BMI, Height, Blood Pressure, Waist Circumference, LH, FSH, LH/FSH ratio, TSH, Prolactin, Fasting Insulin, Fasting Glucose, HOMA index, Free and Total Testosterone, 2-hour GTT, DHEAS
4-Week Post-Treatment (Visit 2)	LH, FSH, LH/FSH ratio, Hirsutism Score, Menstrual cycle, Body Weight, BMI, Height, Blood Pressure
8-Week Post-Treatment (Visit 3)	LH, FSH, LH/FSH ratio, Hirsutism Score, Menstrual cycle, Body Weight, BMI, Height, Blood Pressure
12-Week Post-Treatment (Visit 4)	Sonographic scan, Hirsutism Score, Menstrual cycle, Body Weight, BMI, Height, Blood Pressure, Waist circumference, LH, FSH, LH/FSH ratio, TSH, Prolactin, Fasting insulin, Fasting Glucose, HOMA Index, Free and Total Testosterone, 2-hour GTT, DHEAS

Table 3. Effects of Furocyst[®] on Body Weight, and BMI

Parameters	Baseline	Week 4	Week 8	Week 12
Body weight (kg)	57.69 ± 12.12	57.34 ± 11.94	56.86 ± 12.05	56.47 ± 11.58
BMI (kg/m ²)	24.58 ± 5.35	24.53 ± 5.30 (<i>p</i> = 0.253)	24.44 ± 5.42* (<i>p</i> = 0.047)	24.16 ± 5.29* (<i>p</i> = 0.017)
Waist circumference (cm)	54.74 ± 28.85	–	–	54.46 ± 28.65* (<i>p</i> = 0.003)

Data are expressed as mean ± S.D. *n* = 107. *Significant reduction.

ratio, thyroid stimulating hormone (TSH), and prolactin levels were assessed. Dehydroepiandrosterone sulfate (DHEAS), fasting insulin, fasting glucose, HOMA index, free and total testosterone levels were also assessed.

Adverse events monitoring

All adverse events were meticulously recorded by the study participants, who recorded their daily activities in the diaries. These diaries were regularly verified by the study coordinators and endorsed by the principal investigator. Subjects were instructed to record all their daily activities including adverse events, i.e., headache, diarrhea, running nose, or temperature in their diaries. In case of emergency, all subjects were instructed to contact the principal investigator immediately.

Statistical methods

Data was indicated as mean ± standard deviation (SD). All the baseline parameters were compared between the two groups using t-test and other statistical parameters. Appropriate parametric and non-parametric test were used according to the data. Appropriate statistical tests such as t-test and chi-square test were conducted to evaluate the safety and efficacy of Furocyst in PCOS patients. Hirsutism score was analyzed using Wilcoxon signed rank test.

Results

Time-dependent effects of furocyst[®] on body weight, body mass index (BMI) and waist circumference in pre-menopausal women

Influence of Furocyst[®] treatment was investigated on time-dependent changes in body weights and BMI at baseline, 4-, 8- and 12-weeks of treatment (Table 3). A time-dependent non-significant reduction in body weight was observed, while BMI was significantly reduced at both 8- and 12-weeks post-treatment. At the completion of

12 weeks of supplementation, the waist circumference was significantly reduced.

Effect of furocyst[®] on mean cyst size, ovary volume and hirsutism levels in pre-menopausal women

Effect of Furocyst[®] were investigated on the number of cysts on the ovary, ovary volume and hirsutism levels at baseline, and week 12 of treatment. Significant reduction in the mean cyst size on the right and left ovary (Table 4), ovary volume (Table 5), and hirsutism levels were observed.

The mean cyst size in the right ovaries decreased by 41.57% from 6.35 mm to 3.71 mm on completion of the treatment (*p*-value 0.0001*), while the mean cyst size in the left ovaries decreased by 44.92% from 6.50 mm to 3.58 mm on completion of the treatment (*p*-value 0.0001*). The mean right ovary volume decreased by 29.32% from 12.72 cc to 8.99 cc at the completion of the study (*p*-value 0.0001*), while

Table 4. Effects Furocyst[®] on Mean Cyst Size (mm) on the Left and Right Ovary

Mean cyst size (mm)	Furocyst [®]
Right (Baseline)	6.35 ± 2.22
Right (Visit 4)	3.71 ± 1.07*
<i>p</i> -Value	0.0001↓
Left (Baseline)	6.50 ± 2.21
Left (Visit 4)	3.58 ± 1.29*
<i>p</i> -Value	0.0001↓

Data are expressed as mean ± S.D. *n* = 107. *Significant reduction.

Table 5. Effect of Furocyst[®] on Ovary Volume

Ovary volume (cm ³)	Furocyst [®]
Right (Baseline)	12.72 ± 3.84
Right (Visit 4)	8.99 ± 3.56*
<i>p</i> -Value	0.0001↓
Left (Baseline)	12.36 ± 21.80
Left (Visit 4)	9.42 ± 3.29*
<i>p</i> -Value	0.0001↓

Data are expressed as mean ± S.D. *n* = 107. *Significant reduction.

Hirsutism score was significantly reduced after 8 weeks of treatment (*p* = 0.038*) and 12-weeks of treatment (*p* = 0.002*).

Table 6. Effect of Furocyst® on Menstrual Cycle in Study Volunteers

Status	Menstrual cycle							
	Baseline (Visit 1)		Visit 2		Visit 3		Visit 4	
	Frequency	Percent (%)	Frequency	Percent (%)	Frequency	Percent (%)	Frequency	Percent (%)
Delayed	66	75.9	45	52.9	26	33.3	9	12.3
Irregular	20	23.0	16	18.8	10	12.8	6	8.2
Regular	1	1.1	24	28.2	42	53.8	58	79.5

Data are expressed as % (percentage); $n = 107$.

Table 7. Effect on Furocyst® on Luteinizing Hormone (LH) and Follicle Stimulating Hormone (FSH)

Parameters	Furocyst® mean + SD
LH (mIU/ml)	
Baseline	10.91 + 7.16
Visit 2 (Week 4)	8.62 + 6.15** ($p = 0.001$)
Visit 3 (Week 8)	7.94 + 5.51** ($p = 0.002$)
Visit 4 (Week 12)	6.23 + 2.67** ($p = 0.0001$)
FSH (mIU/ml)	
Baseline	7.30 + 6.83
Visit 2 (Week 4)	7.34 + 6.61 ($p = 0.918$)
Visit 3 (Week 8)	7.21 + 6.61 ($p = 0.075$)
Visit 4 (Week 12)	7.42 + 1.74** ($p = 0.0001$)
LH/FSH ratio	
Baseline	1.73 + 1.16
Visit 2 (Week 4)	1.28 + 0.67** ($p = 0.001$)
Visit 3 (Week 8)	1.18 + 0.88** ($p = 0.0001$)
Visit 4 (Week 12)	0.90 + 0.49** ($p = 0.0001$)

Data are expressed in mean \pm S.D. $n = 107$. **Significant reduction.

the left ovary volume decreased by 23.78% from 12.36 cc to 9.42 cc on completion of the treatment (p -value 0.0001*). Overall, the right and left ovary volume reduced by 96.7% and 90% of the enrolled subjects, respectively.

Interestingly, 15 subjects got pregnant during the study, while complete dissolution of cysts was observed in 8 enrolled subjects. More than 65% of patients exhibited reduction in cyst size in both left and right ovaries.

Influence of furocyst® on menstrual cycle in pre-menopausal women

Table 6 demonstrates the effects of Furocyst® on the improvement and regularization of menstrual cycle. Following are the categorized improvements observed

Menstrual cycle: At the baseline (visit 1), the menstrual cycle was observed to be delayed in 75.9% of the study population which was decreased to 52.9% of the study population following treatment with Furocyst® over a period of 4 weeks (Visit 2). On Visit 3, the delayed menstrual cycle reduced to 33.3% of the study population, which was further decreased to only 12.3% of the study population after 12 weeks (Visit 4) of Furocyst® treatment.

Irregular menstrual cycle: At the baseline (visit 1), irregular menstrual cycle was observed in 23% of the study population which was reduced to 18.8% of the study population following treatment with Furocyst® over a period of 4 weeks (Visit 2). On Visit 3, 12.8% of the enrolled subjects had irregular menstrual cycle which was further reduced to 8.2% of the study population at the completion of the study.

Regular menstrual cycle: At the baseline (visit 1), menstrual cycle was regular in only 1.1% of the enrolled subjects. Following 4 weeks (visit 2) of Furocyst® supplementation, the regularity in menstrual cycle was improved in 28.2% of the study population. At the completion of 8 weeks of treatment (visit 3), the enrolled subjects with regular menstrual cycle was increased to 53.8%, while the number was further increased to 79.5% of the study population at the completion of 12 weeks of treatment (visit 4).

Effect of furocyst® on luteinizing hormone (LH) and follicle stimulating hormone (FSH)

Time-dependent reductions in LH and FSH levels were observed in the Furocyst®-treated subjects as compared to the baseline. Furocyst® treatment significantly reduced the LH levels at 4-, 8- and 12-weeks of treatment. Overall, LH levels were decreased up to 42.89% in these subjects at the completion of 12 weeks of treatment. On the contrary, FSH level significantly increased at the completion of 12 weeks of treatment. Time-dependent significant gradual reduction in LH/FSH ratio was observed at the completion of week 4-, week 8-, and week 12 of treatment. The LH/FSH ratio decreased up to 47.97% in the study population as the completion of the treatment (**Table 7**).

Effect on furocyst® on serum thyroid stimulating hormone (TSH), prolactin hormone, fasting insulin, and dihydroepiandrosterone sulfate (DHEAS) levels

Non-significant change in mean TSH level was observed in the Furocyst®-treated subjects. At the end of 12 weeks of treatment, the mean prolactin level significantly reduced by 21.64% ($p = 0.0001^{**}$), while the fasting insulin level significantly reduced by 45.12% ($p = 0.0001^{**}$) at the completion of 12-weeks of treatment. Mean DHEAS level of the study population was 164.56 μ g/dl at the initiation of the study, which was significantly reduced from 164.56 μ g/dl to 157.97 μ g/dl ($p = 0.006$) at the completion of 12 weeks of Furocyst® treatment (**Table 8**).

Effect of furocyst® on fasting glucose, HOMA index, glucose tolerance test (GTT), free and total testosterone

Following completion of 12 weeks of treatment, non-significant changes in fasting glucose, free testosterone and bound testosterone levels were observed. Although reductions in all these three parameters were observed

Table 8. Effect of Furocyst® on Thyroid Stimulating Hormone (TSH), Prolactin and Fasting Insulin.

Parameters	Furocyst® mean + SD
TSH (μIU/ml)	
Baseline	2.79 + 1.00
Visit 4 (week 12)	2.71 + 1.12 (<i>p</i> = 0.529)
Prolactin (ng/ml)	
Baseline	13.40 + 5.89
Visit 4 (week 12)	10.50 + 5.10* (<i>p</i> = 0.0001)
Fasting insulin (μU/ml)	
Baseline	14.98 + 15.02
Visit 4 (week 12)	8.22 + 6.42* (<i>p</i> = 0.0001)
DHEAS (μg/dl)	
Baseline	164.56 + 59.73
Visit 4 (week 12)	157.97 + 60.47* (<i>p</i> = 0.006)

Data are expressed in mean ± S.D. *n* = 107. *Significant reduction.

Table 9. Effects of Furocyst® on Fasting Glucose, HOMA Index, Free and Total Testosterone

Parameters	Furocyst®
Fasting glucose (mg/dl)	
Baseline	89.20 + 12.32
Visit 4 (week 12)	86.62 + 8.87 (<i>p</i> = 0.085)
HOMA index	
Baseline	3.33 + 3.64
Visit 4 (week 12)	1.78 + 1.45* (<i>p</i> = 0.0001)
Free testosterone (pg/ml)	
Baseline	2.60 + 1.51
Visit 4 (week 12)	2.11 + 1.17 (<i>p</i> = 0.051)
Total testosterone (pg/ml)	
Baseline	299.53 + 236.47
Visit 4 (week 12)	251.40 + 245.09 (<i>p</i> = 0.09)

Data are expressed in mean ± S.D. *n* = 107. *Significant reduction.

(Table 9). Furocyst® exhibited a significant reduction (46.54%) in the HOMA index as compared to baseline (Table 9), and the decrease was observed in 75.6% of the study population at the completion of 12 weeks of treatment. Following 12-weeks of Furocyst® treatment, non-significant change in the GTT levels were observed in the enrolled subjects (data not shown). Table 9 exhibits that although considerable reductions were observed in both free- and bound testosterone levels, but these were non-significant reductions.

Effect of furocyst® on serum SGOT/AST, SGPT/ALT, ALP, urea, creatinine and triglyceride levels at the initiation and completion of the investigation

No significant changes were observed in the serum SGOT/AST, urea and triglyceride levels were observed in the study participants at the completion of 12 weeks of treatment as compared to the baseline (Table 10). Significant reductions in the serum SGPT/ALT, ALP, and creatinine levels were observed at the completion of the clinical trial (Table 10), however, the values remained within the normal range.

Table 10. SGOT, SGPT, ALP, Urea, and Creatinine Levels at the Initiation and Completion of 12 Weeks of Treatment

Parameters	Furocyst®
SGOT/AST (U/L)	
Baseline	29.92 + 11.10
Visit 4 (Week 12)	28.74 + 7.99 (<i>p</i> = 0.127)
SGPT/ALT (U/L)	
Baseline	32.60 + 21.28
Visit 4 (Week 12)	28.10 + 12.82* (<i>p</i> = 0.007)
ALP (U/L)	
Baseline	93.31 + 24.91
Visit 4 (Week 12)	88.32 + 22.14* (<i>p</i> = 0.016)
Urea (mg/dl)	
Baseline	15.44 + 6.11
Visit 4 (Week 12)	14.54 + 6.19 (<i>p</i> = 0.064)
Creatinine (mg/dl)	
Baseline	0.71 + 0.16
Visit 4 (Week 12)	0.66 + 0.14* (<i>p</i> = 0.032)

Data are expressed in mean ± S.D. *n* = 107. *Significant reduction.

Effect of furocyst® on cholesterol, HDL, triglyceride, hemoglobin, and total leukocyte count (TLC) and differential leukocyte count (DLC) at the initiation and completion of the study

No significant changes were observed in the cholesterol, triglyceride and hemoglobin (Hb) levels were observed in the Furocyst® group at the completion of the clinical trial (Table 11). Significant increases in the HDL levels were observed, while the mean total leukocyte count (TLC) level significantly reduced (Table 11).

There was non-significant change in the differential leukocyte count (DLC) including neutrophils, lymphocytes, monocytes, eosinophils, and basophils count of the study population at the completion of 12-weeks of treatment (data not shown).

Discussion

The etiology of PCOS has remained to be complex and poorly understood due to simultaneous involvement of a plethora of signaling pathways as revealed by Genome Wide Association Studies (24). Therefore, it has not been possible to associate any single factor for development of this syndrome. The efficacy of Fenugreek seed extract in alleviating the symptoms of PCOS had been demonstrated earlier both by our group as well as others (22, 23). The present clinical investigation was kept open labeled and single-armed to understand categorically the reversal of physiological changes inflicted by PCOS on consumption of Furocyst®, an optimized Fenugreek seed extract formulation enriched with the three principal components galactomannan, 4-OH isoleucine, and steroidal saponin along with other vital nutrients (25).

The two most significant clinical features for identification of PCOS according to Rotterdam criterion (26) are formation of fluid filled cysts and enlargement of at least one of the ovaries beyond 10 ml. However, absence of cyst

Table 11. Effect of Furocyst® on Cholesterol, HDL, Triglyceride, Hemoglobin, and Total Leukocyte Count (TLC) and Differential Leukocyte Count (DLC) at the Initiation and Completion of the Study.

Parameters	Furocyst®
Cholesterol (mg/dl)	
Baseline	164.28 ± 29.37
Visit 4 (week 12)	165.19 ± 26.44 ($p=0.700$)
HDL (mg/dl)	
Baseline	43.58 ± 10.33
Visit 4 (week 12)	45.27 ± 8.09* ($p=0.03^*$)
Triglyceride (mg/dl)	
Baseline	113.11 ± 59.55
Visit 4 (Week 12)	107.30 ± 41.33 ($p=0.303$)
Hemoglobin (Hb) (g/dl)	
Baseline	13.08 ± 1.57
Visit 4 (week 12)	13.25 ± 1.10 ($p=0.162$)
TLC ($\times 10^3 \mu\text{l}$)	
Baseline	6.69 ± 1.87
Visit 4 (week 12)	6.16 ± 1.49** ($p=0.002$)

Data are expressed in mean \pm S.D. $n=107$, **Significant reduction.

does in no way imply absence of PCOS. The cyst sizes were reduced significantly together with corresponding decrease in the volumes of both ovaries. This clearly indicated that Furocyst® was able to alleviate PCOS inflicted damage in the reproductive anatomy. PCOS is by and large a gross endocrine disorder believed to originate from hypothalamic insensitivity to progesterone. This results in uncontrolled secretion of androgen hormones in the ovary including testosterone, dihydrotestosterone, dehydroepiandrosterone and DHEA-sulfate. Due to elevated levels of insulin under PCOS, production of Sex Hormone Binding Globulin (SHBG) decreases in the body, which also contributes substantially to the rise in free testosterone (27). PCOS leads to gross imbalance in the gonadotrophin axis which is reflected in severe alteration in the levels of most of the reproductive hormones. Heightened gonadotropin secretion leads to reduced follicle development. Parallely, there is a significant drop in the levels of Follicle Stimulating Hormone (FSH), responsible for production of estradiol, regulation of the menstrual cycle and growth of eggs in ovaries (27). Estrogens maintain a low level of gonadotropin throughout the cycle by effecting a negative feedback-loop on hypothalamic gonadotropin-releasing hormone, Luteinizing hormone (LH) and FSH secretion. FSH induced LH surge occurs as a normal physiological response in a healthy pituitary-hypothalamus system which promotes initial maturation of the follicles (28). However, in PCOS, the regulation over LH surge is lost leading to significant rise in its levels which further augments the level of testosterone in the body. As a result of altered LH and FSH levels, the healthy ratio of LH:FSH is jeopardized (4). Prolactin is another key marker for assessment of endocrine function during pregnancy. It is necessary for enlargement of the mammary gland and breastfeeding after birth; however elevated levels of prolactin before or during pregnancy can adversely affect fertility or normal delivery of the baby (29). Furocyst® was also able to bring down successfully the levels of prolactin over the 12 weeks

of study period. Concomitant with the normalization of hormone levels, regularity in the menstrual cycle was also restored.

Onset of PCOS is almost always associated with insulin resistance. Although the symptoms of insulin resistance start to appear much later after those of PCOS, recent evidence has indicated that insulin resistance plays a major role in the development of the latter (30). Besides maintaining glucose homeostasis, insulin also facilitates fatty acid uptake and inhibits lipolysis in adipose tissue. This excess accumulation of abdominal fat is one of the hallmark features of PCOS and insulin resistance aggravates this condition. Enhanced insulin secretion, on the other hand, brings about heightened release of androgen which again promotes PCOS. Since PCOS affects many cellular signaling pathways simultaneously, it is imperative that its onset will also disrupt the body's lipid metabolism. In fact, PCOS is also associated with dyslipidemia and cholesterolemia with rise in levels of low-density lipoproteins (LDL) and triglycerides (31). This also explains why PCOS can often lead to development of Cardiovascular Diseases (CVD). Consumption of Furocyst® over a period of 4 weeks onwards was able to significantly decrease levels of both fasting insulins, fasting glucose as well as triglyceride. Insulin resistance was assessed with homeostasis model of assessment (HOMA) index, a widely accepted clinical marker where an index value of 2.5 is considered to be an indicator of insulin resistance in adults (32). As a result of Furocyst® consumption, HOMA index dropped by close to 60 percent well within normal levels indicating the alleviation of insulin resistance.

Another serious concern which occurs co-laterally with dyslipidemia and development of insulin resistance in PCOS is alcohol independent damage to liver function referred to as Nonalcoholic Fatty Liver Disease (NAFLD) (33). Early detection of liver function by virtue of analysis of marker enzymes such as Alkaline Phosphatase Test (ALP), Serum Glutamate Pyruvate Transaminase (SGPT), Serum Glutamate Oxaloacetate Transferase (SGOT) as well as by virtue of certain excreted metabolites including urea and creatinine. Furocyst® significantly brought down the levels of all of these clinical markers thus substantiating its role in treatment of PCOS.

In women of reproductive age, leukocytosis is an early predictor for onset of PCOS along with chronic low grade inflammatory response (34). Fenugreek seed is effective in restoring the overall homeostasis of the body including negotiation of free radicals and minimization of oxidative stress (35). A furostanolic saponin termed protodioscin has been implicated to be the major phytonutrient responsible for the huge but largely unexplored potential of fenugreek seed extract (36). Consumption of Furocyst® for twelve weeks slightly improved blood Hemoglobin and also brought down the total leukocyte count indicating that it was able to curb the effects of PCOS associated inflammatory response in the body. Cumulatively, this novel formulation of Fenugreek seed extract seemed to be a promising new natural therapeutic for management of PCOS and overall rejuvenation of the body.

Conclusion

Despite unprecedented advancement in medical research with the inception of new tools like CRISPR, Artificial Intelligence, Immunotherapy and Telehealth, both prognosis as well as establishment of a proper therapeutic regimen for PCOS has remained to be a challenging feat both for scientists as well as medical practitioners. This has been inflicted chiefly by the involvement of multiple components as well as their complex crosstalk in determining the etiology of the disease. In this regard, there has been a continual interest toward exploration and development of natural compounds which could be effectively employed for treatment of PCOS and subsequently arrest the onset of other associated ailments including diabetes, obesity and cardiovascular disorders. Fenugreek seeds enriched in multiple nutrients along with alkaloids, flavonoids, amino acids, saponins, steroidal saponins and fibers have been used as effective remedies against a plethora of diseases as well as for overall rejuvenation of health and vitality. The present studies reinstated our earlier observations in a randomized open ended single armed model and paved the way for further elucidation of the molecular mechanisms of the individual active components of Furocyst[®] which can synergistically be developed as a wonder drug for treatment of PCOS.

Disclosure statement

No potential conflict of interest was reported by the author(s).

ORCID

Pushplata Sankhwar  <http://orcid.org/0000-0001-7194-623X>
 Apurva Goel  <http://orcid.org/0000-0003-2909-4226>
 Pawan Kumar  <http://orcid.org/0000-0002-2822-8133>
 Samudra P. Banik  <http://orcid.org/0000-0003-0075-7508>
 Manashi Bagchi  <http://orcid.org/0000-0002-1527-6419>
 Debasis Bagchi  <http://orcid.org/0000-0001-9478-6427>

References

- Stein IF, Leventhal ML. Amenorrhea associated with bilateral polycystic ovaries. *Am J Obstet Gynecol*. 1935;29(2):181–91. doi:10.1016/S0002-9378(15)30642-6
- Witchel SF, Roumimper H, Oberfield S. Polycystic ovary syndrome in adolescents. *Endocrinol Metab Clin North Am*. 2016;45(2):329–44. doi:10.1016/j.ecl.2016.01.004
- Witchel SF, Oberfield SE, Peña AS. Polycystic ovary syndrome: pathophysiology, presentation, and treatment with emphasis on adolescent girls. *J Endocr Soc*. 2019;3(8):1545–73. doi:10.1210/je.2019-00078
- Saadia Z. Follicle stimulating hormone (LH: FSH) ratio in polycystic ovary syndrome (PCOS) – obese vs. non-obese women. *Med Arch*. 2020;74(4):289–93. doi:10.5455/medarch.2020.74.289-293
- Kamalanathan S, Sahoo JP, Sathyapalan T. Pregnancy in polycystic ovary syndrome. *Indian J Endocrinol Metab*. 2013;17(1):37–43. doi:10.4103/2230-8210.107830
- El Hayek S, Bitar L, Hamdar LH, Mirza FG, Daoud G. Polycystic Ovarian Syndrome: An Updated Overview. *Front Physiol*. 2016;7:124. doi:10.3389/fphys.2016.00124
- Deswal R, Narwal V, Dang A, Pundir CS. The prevalence of polycystic ovary syndrome: a brief systematic review. *J Hum Reprod Sci*. 2020;13(4):261–71. Epub 2020 Dec 28. doi:10.4103/jhrs.JHRS_95_18
- Liu T, Cui YQ, Zhao H, Liu HB, Zhao SD, Gao Y, Mu XL, Gao F, Chen ZJ. High levels of testosterone inhibit ovarian follicle development by repressing the FSH signaling pathway. *J Huazhong Univ Sci Technolog Med Sci*. 2015;35(5):723–9. doi:10.1007/s11596-015-1497-z
- Badawy A, Elnashar A. Treatment options for polycystic ovary syndrome. *Int J Womens Health*. 2011;3:25–35. doi:10.2147/IJWH.S11304
- Pasquali R, Gambineri A. Insulin sensitizers in polycystic ovary syndrome. *Front Horm Res*. 2013;40:83–102. doi:10.1159/000341837
- Huang S, Du X, Wang R, Li R, Wang H, Luo L, O'Leary S, Qiao J, Mol BWJ. Ovulation induction and intrauterine insemination in infertile women with polycystic ovary syndrome: a comparison of drugs. *Eur J Obstet Gynecol Reprod Biol*. 2018;231:117–21. doi:10.1016/j.ejogrb.2018.08.002
- Vrbíková J, Cibula D. Combined oral contraceptives in the treatment of polycystic ovary syndrome. *Hum Reprod Update*. 2005;11(3):277–91. doi:10.1093/humupd/dmi005
- Johnson NP. Metformin use in women with polycystic ovary syndrome. *Ann Transl Med*. 2014;2(6):56. doi:10.3978/j.issn.2305-5839.2014.04.15
- Akbaribazm M, Goodarzi N, Rahimi M. Female infertility and herbal medicine: an overview of the new findings. *Food Sci Nutr*. 2021;9(10):5869–82. doi:10.1002/fsn3.2523
- Arentz S, Abbott JA, Smith CA, Bensoussan A. Herbal medicine for the management of polycystic ovary syndrome (PCOS) and associated oligo/amenorrhoea and hyperandrogenism; a review of the laboratory evidence for effects with corroborative clinical findings. *BMC Complement Altern Med*. 2014;14:511. doi:10.1186/1472-6882-14-511
- Azin F, Khazali H. Phytotherapy of polycystic ovary syndrome: a review. *Int J Reprod Biomed*. 2022;20(1):13–20. doi:10.18502/ijrm.v20i1.10404
- Ye H, Shaw IC. Dietary isoflavone-induced, estrogen receptor- β -mediated proliferation of Caco-2 cells is modulated by gallic acid. *Food Chem Toxicol*. 2020;145:111743. doi:10.1016/j.fct.2020.111743
- Akbaribazm M, Khazaei MR, Khazaei M. Phytochemicals and antioxidant activity of alcoholic/hydroalcoholic extract of *Trifolium pratense*. *Chin Herb Med*. 2020;12(3):326–35. doi:10.1016/j.chmed.2020.02.002
- Cheng G, Wilczek B, Warner M, Gustafsson JA, Landgren BM. Isoflavone treatment for acute menopausal symptoms. *Menopause*. 2007;14(3 Pt 1):468–73. doi:10.1097/GME.0b013e31802cc7d0
- Syed QA, Rashid Z, Ahmad MH, Shukat R, Ishaq A, Muhammad N, Ur Rahman HU. Nutritional and therapeutic properties of fenugreek (*Trigonella foenum-graecum*): a review. *Int J Food Prop*. 2020;23(1):1777–91. doi:10.1080/10942912.2020.1825482
- Khanna A, John F, Das S, Thomas J, Rao J, Maliakel B, Im K. Efficacy of a novel extract of fenugreek seeds in alleviating vasomotor symptoms and depression in perimenopausal women: a randomized, double-blinded, placebo-controlled study. *J Food Biochem*. 2020;44(12):e13507. doi:10.1111/jfbc.13507
- Bashtian MH, Emami SA, Mousavifar N, Esmaily HA, Mahmoudi M, Poor AHM. Evaluation of Fenugreek (*Trigonella foenum-graecum* L.), Effects Seeds Extract on Insulin Resistance in Women with Polycystic Ovarian Syndrome. *Iran J Pharm Res*. 2013;12(2):481. PMID: 24250624 PMCID: PMC3813238–475.
- Swaroop A, Jaipuria AS, Gupta SK, Bagchi M, Kumar P, Preuss HG, Bagchi D. Efficacy of a novel fenugreek seed extract (*Trigonella foenum-graecum*, Furocyst) in polycystic ovary syndrome (PCOS). *Int J Med Sci*. 2015;12(10):825–31. doi:10.7150/ijms.13024
- Shim U, Kim HN, Lee H, Oh JY, Sung YA, Kim HL. Pathway analysis based on a genome-wide association study of polycystic ovary syndrome. *PLoS One*. 2015;10(8):e0136609. doi:10.1371/journal.pone.0136609

25. Goyal S, Gupta N, Chatterjee S. Investigating Therapeutic Potential of *Trigonella foenum-graecum* L. as Our Defense Mechanism against Several Human Diseases. *J Toxicol*. 2016;2016:1250387. doi:[10.1155/2016/1250387](https://doi.org/10.1155/2016/1250387)
26. Smet ME, McLennan A. Rotterdam criteria, the end. *Australas J Ultrasound Med*. 2018;21(2):59–60. doi:[10.1002/ajum.12096](https://doi.org/10.1002/ajum.12096)
27. Johansson J, Stener-Victorin E. Polycystic ovary syndrome: effect and mechanisms of acupuncture for ovulation induction. *Evid Based Complement Alternat Med*. 2013;2013:762615. doi:[10.1155/2013/762615](https://doi.org/10.1155/2013/762615)
28. Weiss G, Skurnick JH, Goldsmith LT, Santoro NF, Park SJ. Menopause and hypothalamic-pituitary sensitivity to estrogen. *JAMA*. 2004;292(24):2991–6. doi:[10.1001/jama.292.24.2991](https://doi.org/10.1001/jama.292.24.2991)
29. Al-Chalabi M, Bass AN, Alsalman I. Physiology prolactin. Treasure Island (FL): StatPearls Publishing; 2022 Jan [accessed 2021 Jul 29]. <https://www.ncbi.nlm.nih.gov/books/NBK507829/>
30. Unluhizarci K, Karaca Z, Kelestimur F. Role of insulin and insulin resistance in androgen excess disorders. *World J Diabetes*. 2021 May 15;12(5):616–29. doi:[10.4239/wjd.v12.i5.616](https://doi.org/10.4239/wjd.v12.i5.616)
31. Kim JJ, Choi YM. Dyslipidemia in women with polycystic ovary syndrome. *Obstet Gynecol Sci*. 2013;56(3):137–42. doi:[10.5468/ogs.2013.56.3.137](https://doi.org/10.5468/ogs.2013.56.3.137)
32. Singh Y, Garg MK, Tandon N, Marwaha RK. A study of insulin resistance by HOMA-IR and its cut-off value to identify metabolic syndrome in urban Indian adolescents. *J Clin Res Pediatr Endocrinol*. 2013;5(4):245–51. doi:[10.4274/Jcrpe.1127](https://doi.org/10.4274/Jcrpe.1127)
33. Vassilatou E. Nonalcoholic fatty liver disease and polycystic ovary syndrome. *World J Gastroenterol*. 2014 Jul 14;20(26):8351–63. doi:[10.3748/wjg.v20.i26.8351](https://doi.org/10.3748/wjg.v20.i26.8351)
34. Almaeen AH, Alduraywish AA, Nabi M, Shah NN, Shaik R, Tantry BA. Quantitative changes in white blood cells: correlation with the hallmarks of polycystic ovary syndrome. *Medicina (Kaunas)*. 2022;58(4):535. doi:[10.3390/medicina58040535](https://doi.org/10.3390/medicina58040535)
35. Mukthamba P, Srinivasan K. Dietary fenugreek (*Trigonella foenum-graecum*) seeds and garlic (*Allium sativum*) alleviates oxidative stress in experimental myocardial infarction. *Food Sci Hum Wellness*. 2017;6(2):77–87. doi:[10.1016/j.fshw.2017.04.001](https://doi.org/10.1016/j.fshw.2017.04.001)
36. Maheshwari A, Verma N, Swaroop A, Bagchi M, Preuss HG, Tiwari K, Bagchi D. Efficacy of Furosap™, a novel *Trigonella foenum-graecum* seed extract, in enhancing testosterone level and improving sperm profile in male volunteers. *Int J Med Sci*. 2017;14(1):58–66. doi:[10.7150/ijms.17256](https://doi.org/10.7150/ijms.17256)



Chemical, microbial and safety profiling of a standardized *Withania somnifera* (Ashwagandha) extract and Withaferin A, a potent novel phytotherapeutic of the millennium

Pawan Kumar¹, Samudra P. Banik², Apurva Goel³, Sanjoy Chakraborty⁴, Manashi Bagchi⁵, and Debasis Bagchi^{6,7}

¹Research and Development Department, Chemical Resources (CHERES), Panchkula, Haryana, India; ²Department of Microbiology, Maulana Azad College, Kolkata, India; ³Regulatory Department, Chemical Resources (CHERES), Panchkula, India; ⁴Department of Biological Sciences, New York City College of Technology/CUNY, Brooklyn, NY, USA; ⁵Research & Development Department, Dr. Herbs LLC, Concord, CA, USA; ⁶Department of Biology, Adelphi University, Garden City, NY, USA; ⁷Department of Pharmaceutical Science, Texas Southern University, Houston, TX, USA

***Corresponding author:** Debasis Bagchi, PhD, Professor, Department of Biology, Adelphi University, Garden City, NY 11530, USA

Submission Date: January 26th, 2023; **Acceptance Date:** February 17th, 2022; **Publication Date:** February 23rd, 2023

Please cite this article as: Kumar P., Banik S. P., Goel A., Chakraborty S., Bagchi M. Bagchi D. Chemical, microbial and safety profiling of a standardized *Withania somnifera* (Ashwagandha) extract and Withaferin A, a potent novel phytotherapeutic of the millennium. *Functional Foods in Health and Disease* 2023; 13(2): 36-51. DOI:

<https://www.doi.org/10.31989/ffhd.v13i2.1071>

ABSTRACT

Background: *Withania somnifera* (L.) Dunal, popularly known as Ashwagandha, is an ethnomedicinal plant with multiple pharmacotherapeutic applications. The diverse medicinal properties of the plant are largely due to the presence of withanolides, a group of C28 ergostane based steroidal lactones, with several sites of unsaturation and oxygenation. Withaferin A, a major withanolide present in Ashwagandha plant accounts for its emerging new roles to treat cancer, arthritis, inflammatory responses, immunomodulatory properties, and neuronal disorders. The root and leaf extracts are specifically important constituent materials for the development of phytotherapeutics, mostly intended for oral consumption. Several studies have been carried out to delineate the toxic manifestations of the extract for human consumption.

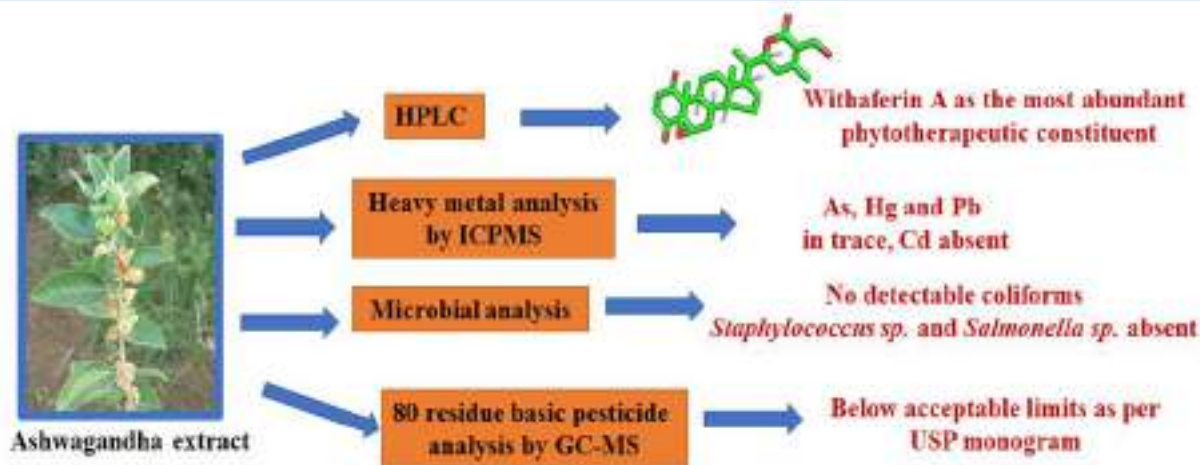
Objective: Establish the broad-spectrum safety of W-ferinAmax ashwagandha (WFA).

Study: This investigation demonstrated a novel, standardized W-ferinAmax ashwagandha (WFA) extraction technology from the whole herb of *Withania somnifera*, conducted HPLC analysis to identify the constituents, detected the heavy metals, microbiological contaminants, pesticides contaminants, and safety profile.

Results: A novel extraction technology was employed to obtain WFA from the whole plant of *Withania somnifera*. HPLC analysis revealed that WFA contains a total of 15.4% Withanolides. In particular, Withaferin A, Withanoside IV, and Withanolide A contents were 6.469%, 1.022%, and 0.073%, respectively. The extract contained only 0.403 ppm of heavy metals out of which traces of arsenic, mercury and lead were detected, and cadmium was absent. USP recommended 80 residue basic pesticide screening indicated that the extraction was safe for human consumption. It was also found to be free from pathogenic microbes as assessed by the absence of *E. coli* and other coliforms, *Salmonella* and *Staphylococcus* species.

Conclusion: The data generated cumulatively indicated that WFA is safe for further downstream processing and for human consumption.

Keywords: Ashwagandha, Withaferin A, phytotherapeutics, material safety; heavy metals; pesticides



©FFC 2023. This is an Open Access article distributed under the terms of the Creative Commons Attribution 4.0 License (<http://creativecommons.org/licenses/by/4.0>)

INTRODUCTION

The use of *Withania somnifera* (also called Ashwagandha or Indian winter cherry) as an herbal medicine for the treatment of multiple ailments related to regulation of blood sugar, cardiac health, reduction of inflammation and pain, management of stress and improvement of cognitive function have been reported since ancient times especially in Indian subcontinent and southeast

Asia [1-3]. The plant contains class of steroidal lactone metabolites known as withanolides, a C28 steroidal backbone with structural variations arising from differential oxidation at various sites [4-6]. Its main constituent, Withaferin A is implicated in plant defence against pathogens as well as protective drought or low temperature. Chemically, it is 5,6:22,26-diepoxyergosta-2,24-diene-1,26-dione substituted by hydroxy groups at

positions 4 and 27. Withaferin A has emerged as an effective therapeutic application and acts as an anti-cancer agent by promoting cellular apoptosis through a variety of mechanisms [7]. It is believed to be a potent inhibitor of angiogenesis [8]. Simultaneously, it also possesses strong immunomodulatory as well as cardio-protective activity [9,10]. Furthermore, it is being considered as a novel candidate for drug developments to treat neuronal disorders due to its ability to cross Blood-Brain Barrier [11]. Most of the immune-modulatory and anti-cancer activity of the compound is based on its inhibitory effect on NF- κ B mediated signalling pathway [12]. It also acts as an inhibitor of myocardial ischemia by upregulating AMP-Activated Protein Kinase-Dependent B-Cell Lymphoma2 signalling [10].

Many studies have been conducted earlier to assess the safety of Ashwagandha as a therapeutic for oral consumption and all of them have demonstrated that the plant is free from any toxic side effects in all practical dosages used thus far in various formulations. However, there have been some studies which have indicated that uncontrolled and high doses may cause bowel irritability, diarrhoea, and vomiting. Few reports are available on human trials, which indicated that *W. somnifera* may exhibit neurosedative effects and at times can also bring about acute respiratory distress causing a sharp fall in blood pressure and cardiac arrhythmia [13-16].

We developed W-ferinAmax ashwagandha (WFA), a methanol-water extract from the whole herb of *Withania somnifera* (Ashwagandha), in our laboratories and the total Withanolide content was found to 15.4%. HPLC analysis was conducted to detect total Withanolides, Withanoside IV, Withaferin A and Withanolide A. The bioaccumulation of heavy metals was also assessed using Shimadzu inductively coupled plasma mass spectrometry ICMPS-2030.

According to the guidelines issued by US Pharmacopeia (USP), any material of botanical origin meant for human consumption must be either completely free or contain trace pesticides within the specified and recommended tolerable limits. Accordingly, detection of 80-compound basic pesticide screening with GC/MS-MS was carried out, using a comprehensive quantitative analysis following the AOAC Official Method 2007. Residual solvents were analyzed as per ICH/Food Industry guidelines.

MATERIALS AND METHODS

Extraction and manufacturing of W-ferinAmax ashwagandha (WFA) from the whole Ashwagandha (*Withania somnifera*) herb: The phytochemical authentication and verification of the *Withania somnifera* (L.) Dunal whole herbs was performed by the in-house herbalist/botanist with authentic herbarium samples. Furthermore, to revalidate, phytochemical profiling was done using an HPLC. *Withania somnifera* whole herbs were freshly harvested and dried under shade at 30°C to minimize the loss/degradation of the active constituents. Moisture content at this stage was found to be about 9% as analysed according to guidelines of USP 43. Thereafter, it was extracted using methanol: water in an NSF-GMP certified facility. Thereafter, the solvent was evaporated by fractional distillation and the extract was defatted with hexane. at a solvent to sample ratio of 1:10. Samples were stirred for 12 h and the hexane was removed by filtering, then replaced every 12 h for a total time of 48 h. Finally, it was concentrated, ground, and sieved to obtain a homogenous powder containing the active constituents. This was stored in a desiccated chamber until further analysis. Figure 1 demonstrates the flow chart of the manufacturing procedure.

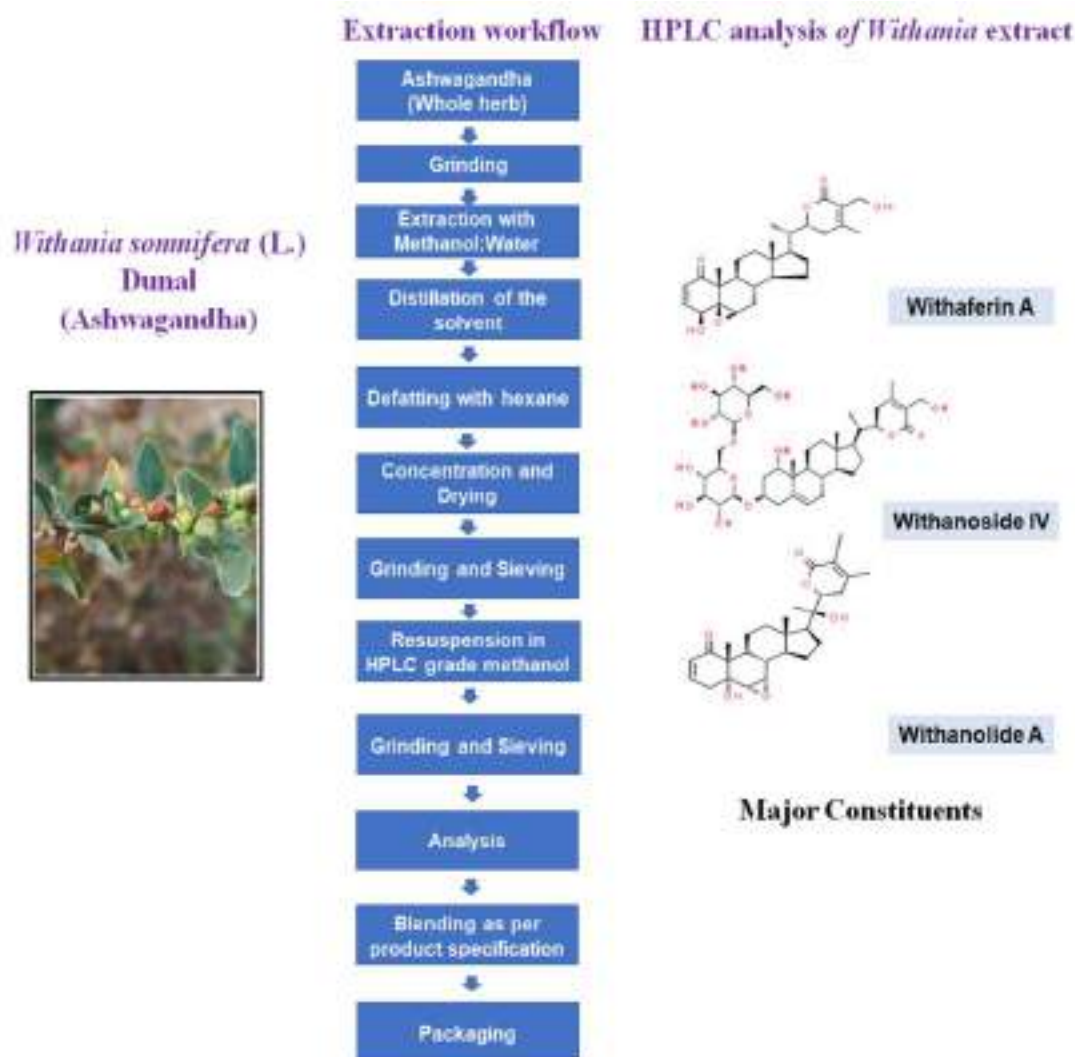


Figure 1: Major phytherapeutic constituents of *Withania somnifera* (L.) Dunal (Ashwagandha). An extract from the whole herb was prepared as indicated in the flow chart before analysis by HPLC.

Analysis of W-ferinAmax ashwagandha (WFA) by HPLC:

The recommended methodology of USP (USP 43, Ashwagandha/Dietary supplements) was used for the analysis of WFA by HPLC. The HPLC system (Shimadzu, LC-2010CHT /LC-2030 C) was equipped with a quaternary pump and vacuum degasser, temperature control column compartment, autosampler, and UV detector. Briefly, about 100 mg of WFA was dissolved in about 7 ml of HPLC grade methanol, heated gently in a water bath for 20 minutes, cooled and diluted with methanol. The HPLC was equipped with a reverse-phase L1 C18 HPLC column (4.6 mm x 25 cm, end capped; 5 µm packing L1) (Phenomenex Luna, Torrance, California, USA) at a flow

rate of 1.5 ml/min and the column temperature was maintained at 27°C. The mobile phase consisted of Solution 1: Potassium dihydrogen phosphate (0.14 g) was dissolved in 990 ml of HPLC grade water, 0.5 ml of phosphoric acid was added, mixed well, and diluted with HPLC grade water to 1000 ml. The solution was filtered through a 0.45 µm membrane filter and degassed in a sonicator for 3 minutes; Solution 2: filtered and degassed HPLC grade acetonitrile solvent. The pumps were programmed to run a gradient of 95% Solution 1, 5% Solution 2 to 5% Solution 1, 95% Solution 2 over a period of 40 minutes (Table 1).

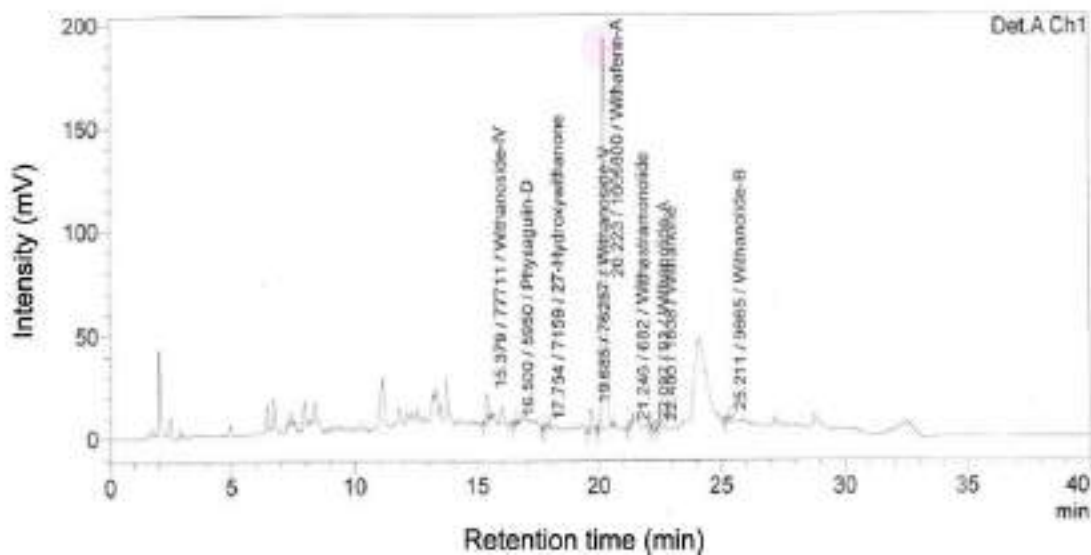


Figure 2: HPLC Chromatogram of W-ferinAmax ashwagandha, a powdered herb extract from *Withania somnifera* (L.) Dunal (Ashwagandha) showing Withaferin A as the major component (pink shaded) along with other withanolides, withanosides, withanones, withastramonolide and physagulin D.

Table 1. Chromatographic parameters

Mobile Phase	Solution 1: Potassium dihydrogen phosphate; Solution 2: Acetonitrile			
Column	Reverse-phase L1 C18 HPLC column (4.6 mm x 25 cm)			
Wavelength	227 nm			
Flow rate (ml/min)	1.5 ml/minute			
Gradient	Time (Min)	Flow (ml/min)	Mobile phase Solution A (%)	Mobile phase Solution B (%)
	0.0	1.5	95	5
	18.0	1.5	55	45
	25.0	1.5	20	80
	28.0	1.5	20	80
	30.0	1.5	95	5
	40.0	1.5	95	5
Injection Volume	20 µl			
Run Time	40 minutes			
Column Temperature	27°C			
Sample Temperature	Ambient			

Sample Solution: 100 mg of accurately weighed WFA was dissolved in 7 ml of HPLC grade methanol, heated gently in a water bath for 20 minutes, cooled and diluted with

methanol. A 20 µl of aliquot of the sample was injected through a HPLC column (as described above) at a flow rate of 1.5 ml/min with a column temperature of 27°C in

a gradient of the two solutions (see gradient program as above) over a period of 40 minutes, using a UV detector at 227 nm.

Preparation of Standard Solutions: Stock solutions of all marker constituents were prepared at a concentration of 1.0 mg/mL in methanol. The calibration curves were prepared using solutions of different concentrations ranging from 10 to 550 µg/mL. Composite standard solution containing 0.1 mg/ml of USP Withanolide A RS and 0.1 mg/ml of USP Withanoside IV RS in HPLC grade methanol along with pure standard (1000 ppm) of Withaferin A (99.99% purity) and Withanolide A (99%) were also run parallelly under the same set of conditions.

The percentage of withanolide aglycones was calculated as:

- $= Ru/Rs \times Cs \times (V/W) \times 100$
- Where Ru = sum of the peak areas of Withaferin A, 12-deoxywithastramonolide, Withanolide A, Withanone and Withanolide B from sample solution
- Rs = peak area of Withanolide A from standard solution
- Cs = Concentration of USP Withanolide A RS in standard solution (mg/ml)
- V = Volume of the sample solution in ml
- W = Weight of the Ashwagandha extract (in mg)

The percentage of withanolide glycosides in the Solution was calculated as:

- $= Ru/Rs \times Cs \times (V/W) \times 100$
- Ru = sum of the peak areas of withanoside IV, withanoside V, and withanoside VI from Sample solution
- Rs = peak area of withanoside IV from Standard solution

- Cs = concentration of USP Withanoside IV RS in Standard solution (mg/mL)
- V = volume of the Sample solution (mL)
- W = Weight of the Ashwagandha extract (in mg)
- Add the percentages of withanolide aglycones and withanolide glycosides.

Methodology Validation: USP 43 Validation of Compendial Procedures was followed, and as outlined in the ICH guidelines, HPLC method was validated in terms of precision, accuracy, and linearity. All the assay method and procedure were repeated and evaluated in triplicate. The limit of detection (LOD) and limit of quantification (LOQ) were ascertained by injecting serial dilutions of solutions of the ISRN Analytical Chemistry 3-4 standards with known concentrations. The LOD and LOQ were calculated based on the signal-to-noise ratio of more than 3-4 times for LOD and 10-12 times for LOQ, respectively.

Heavy metal analysis of W-ferinAmax ashwagandha (WFA) using Shimadzu inductively-coupled-plasma-mass spectrometry (ICPMS): Analysis of heavy metals was carried out using a Shimadzu ICPMS-2030 inductively coupled plasma mass spectrometer (Shimadzu Scientific Instruments, Inc., Columbia, MD, USA) coupled with an auto sampler AS-10. Certified individual reference standards from Sigma Aldrich 1000 ppm were employed for making the stock solution and calibration. The parameters used are shown in Table 2. Approximately 1-2 gm of homogenized WFA was completely digested under pressure with 6 mL of nitric acid (HNO₃) and 1 mL of perchloric acid (HClO₄). After subsequent cooling, they were filtered using a 0.45 µm filter (Whatman Millipore, Clifton, NJ, USA) and adjusted to 50 mL with 1% HNO₃. Lead (Pb), cadmium (Cd), arsenic (As), and mercury (Hg) were detected in the final solution.

Table 2. Instrument parameters for Shimadzu ICPMS 2030

Instrument	Shimadzu ICPMS 2030
Acquisition type	Quantitative
Quantitation method	Calibration curve method
Replicates	3
Profile integration time	Mid
Sweeps/Replicate	10
Solvent rinse (Low and High)	45 Sec
Sample rinse (Low and High)	45 Sec
Rotation speed (Low)	20 RPM
Rotation speed (High)	60 RPM
Integration mode	Auto

Basic pesticide screening in *W-ferinAmax ashwagandha* (WFA) using an Agilent 7000D Triple Quadrupole GC/MS

System: Pesticide detection was carried out according to USP guidelines using an Agilent 7000D Triple Quadrupole GC/MS System (Agilent Technologies, Santa Clara, California, USA). This method is applicable to the multi-residue analysis of 80 pesticides in various foods and dietary supplements. Briefly, about 100 ml of 10% (w/v) WFA in acetone was prepared and allowed to stand for 20 minutes. To it, 1 ml of toluene solution containing 1.8 mg of carbophenothion was added and mixed thoroughly. The solution was subsequently filtered and washed twice with acetone. It was then dried using a rotary evaporator set below 40°C until complete evaporation of the solvent was attained. The evaporation was repeated after dissolving the residue in minimal volume of toluene, filtered, and finally diluted in toluene to 10.0 ml. For detection of Organochlorine, Organophosphorus, and Pyrethroid Insecticide, a size-exclusion chromatography using a 7.8- mm × 30-cm stainless steel column with 5-mm packing L21 was used along with toluene as the mobile phase at a flow rate of about 1

mL/min. The column was calibrated using test solutions of the pesticides prior to analyses. An alkali flame-ionisation detector was used, and hydrogen was used as the carrier gas. The temperature of the injection port temperature was maintained at 250°C and that of the detector was maintained at 275°C. The column temperature was programmed in the following way: 80°C for the first minute and then increased to 150°C at a rate of 30°C/min, maintained at 150°C for 3 min, then increased to 280°C at a rate of 4°C/min and maintained at this temperature for 1 min. Carbophenothion was used as the internal standard. A measured aliquot of the sample was injected subsequently and the chromatograms were recorded. The content of each pesticide was determined from the peak areas of each pesticide. Typical limit of quantification (LOQ) estimated during the method validation are at or below 0.01 mg/kg for the majority of the analytes.

Analysis of the microbial load in *W-ferinAmax ashwagandha* (WFA): Presence of microflora in WFA was ascertained according to USP guidelines for safety ana-

lyses of samples of botanical origin. A 10% (w/v) WFA solution was prepared in sterile potassium phosphate buffer (pH 7.2). Then the sample was diluted suitably with the same buffer and passed through membrane filters for transferring the microbes of the sample to the membrane. In order to obtain the Total Aerobic Microbial Count (TAMC) and the number of CFUs per gram or millilitre of the product, the membrane filter was placed aseptically to the surface of a Soybean-Casein Digest Agar (in three replicates) and incubated at 37°C for 48-72 hrs. Total combined yeasts and moulds count (TYMC) was also obtained in a similar manner using Sabouraud Dextrose Agar. In order to ascertain the anaerobic flora, the pour plate method was used. 1 ml volume (3 replicates for each dilution) was taken for each dilution over which molten Soybean-Casein Digest agar was poured and incubated at 37°C for 48-72 hrs. In order to detect coliforms, the same membrane filtration test was performed using filter pads saturated with lauryl sulphate Tryptose broth, a selective media used for detection of coliforms. Subsequently, the filter pads were transferred into the base of petri-dishes with a sterilised pad dispenser and incubated at 37°C for 24 hrs for enumeration of total coliforms. For specific detection of fecal coliforms (*E. coli*), the incubation temperature was set at 44.5°C. Lysine-Mannitol-Glycerol agar was used for detection of *Salmonella sp.* [17] whereas Tryptic Soy broth Agar was used to detect *Staphylococcus sp.* using the same technique [18].

Statistical analysis: The results are expressed as mean \pm S.D. All the data were analyzed using one-way analysis of

variance followed by Tukey's post-hoc test. A value of $p < 0.05$ was considered statistically significant.

RESULTS

W-ferinAmax ashwagandha (WFA), a standardized *Withania somnifera* extract: The standardized W-ferinAmax ashwagandha (WFA), extracted from the whole Ashwagandha (*Withania somnifera*) herb, appeared as a brown-colored powder with a bulk density ranging between 0.5 to 0.75 gm/ml. It was subsequently dried and subjected to HPLC analysis for estimation of the major chemical constituents. Loss in mass after drying was not more than 6 percent, while the particle size (minimum 95% passes through 40 mesh), residual solvents (not more than 3000 ppm methanol and 290 ppm n-hexane) and elemental impurities (not more than 10 ppm) conforms to USP 43.

Determination of Total Withanolides, Withanositide IV, Withaferin A, and Withanolide A content in W-ferinAmax ashwagandha (WFA): The content of different withanolides in WFA was detected by HPLC analysis (Figure 2). Three significant peaks corresponding to Withanositide IV, Withaferin A and Withanolide A were identified according to their retention times (Fig 2). It was found that total Withanolide content in WFA was 15.4%, while the concentration of Withaferin A was 6.469%. Also, the Withanositide IV and Withanolide A contents were found to be 1.022% and 0.073%, respectively (Table 3).

Table 3. Key constituents in W-ferinAmax ashwagandha (WFA) as determined by HPLC

Constituents	Amount (%)
Total Withanolides	15.4%
Withanositide IV	1.022%
Withaferin A	6.469%
Withanolide A	0.073%

Assessment of *W-ferinAmax ashwagandha (WFA)* for heavy metal and pesticide screening: Leaching of heavy metals in the soil has increased unprecedentedly over the last few decades both due to natural as well as anthropogenic reasons. Consequently, their bioaccumulation in the plant body has also gone up to levels which are deemed unfit for subsequent human consumption. Even higher has been the threat posed by uncontrolled application of pesticides for which often there is little or no mitigation. Pesticides not only persist in the environment for longer times, but they are also biotransformed to other potentially more toxic forms [19] thus making them more difficult to contain. In order to carry out a quantitative investigation regarding the safety of Ashwagandha extracts with regards to heavy metals and commonly used pesticides as per guidelines of USP, their contents were determined in the Ashwagandha extract.

Arsenic, mercury and lead were detected in trace limits within permissible levels (Table 4) but no cadmium was found in WFA. Ingestion of heavy metals has been associated with numerous adverse effects. It is well acclaimed that long term exposure to Arsenic increases the risk of many diseases including skin cancer, hyperpigmentation and diabetes [20]. Mercury is a potent neurotoxin, and its commonest form methyl mercury is associated with impaired senses, muscle weakness and lack of coordinated muscle movement

[21]. Prolonged exposure to Pb blocks heme synthesis and hence leads to severe anaemia, additionally lead poisoning also leads to neurological disorders like dementia [22]. The Environmental Protection Agency (EPA) has set the pesticide limits in Withaferin A as mentioned in the Code of Federal Regulations (40 CFR Part 180) or the Federal Register (FR). In case of pesticides where EPA approved tolerance level has not been indicated, the limit is calculated by the formula: Limits (mg/kg) = AME/100B where A is the acceptable daily intake (ADI), as published by FAO-WHO, in mg/kg of body weight; M is body weight, in kg (60 kg); and B is the daily dose of the article, in kg and E is the extraction factor of the preparation method, determined experimentally. The 80-compound basic pesticide screen carried out by GC analyses as recommended by USP guidelines, Environmental Protection Agency, showed that the pesticide traces found in the preparation were within the acceptable limit for most of the compounds screened except for Coumaphos, Demeton-S and Disulfoton (Table 5). All three of these are popularly used organo-thiophosphate pesticides with acute neurotoxicity. They are strong inhibitors of acetyl-choline esterase [23] activity leading to severe loss of neuronal coordination and death in extreme cases [24]. The gross absence of pesticides above significant detection limits indicated that the extract was safe to be developed as a potent Withaferin A enriched phytotherapeutic.

Table 4. Heavy metal analysis in *W-ferinAmax ashwagandha (WFA)*

Heavy metal	Results
Arsenic	0.1159 ppm
Cadmium	Not detected
Mercury	0.2020 ppm
Lead	0.0851 ppm
Total Heavy Metals	0.4030 ppm

As per USP 43 guidelines, the allowable limits for each of the above is not more than 10 ppm.

Table 5: Basic pesticide screen in Ashwagandha root extract

Name	Amount in mg/kg (Limit in mg/kg)	Name	Amount in mg/kg (Limit in mg/kg)
Aldrin	<0.010 (0.05)	Hexachlorocyclohexane, alpha- (alpha-BHC) HCH, beta- beta-BHC) HCH, delta- (delta- BHC)	<0.010 (0.3)
Bromopropylate	<0.010 (3)		
Cadusafos	<0.010		
Carbophenothion	<0.010 (0.8)	Heptachlor, Heptachlor exoepoxide	<0.010 (0.05)
Chlordane (cis+trans)	<0.010 (0.05)	Hexachlorobenzene	<0.010 (0.1)
Chlorfenvinphos (E- and Z-isomers)	<0.010 (0.5)	Lindan (gamma-HCH, gamma-BHC)	<0.010 (0.6)
Chlorpyrifos-ethyl	0.068 (0.2)	Malathion	<0.010 (1)
Chlorpyrifos-methyl	<0.010 (0.1)	Methacrifos	<0.010 (0.05)
Coumaphos	<0.010 (0.00025)	Mevinphos (E- and Z-isomers)	<0.010 (0.1 mg/cubic metre)
Cyfluthrin (sum of isomers)	<0.010 (0.1)	Methidathion	<0.010 (0.2)
Cyhalothrin, lambda-	<0.010 (0.1)	Methoxychlor	<0.010 (0.05)
Cypermethrin (sum of isomers)	0.11 (1)	Mirex	<0.010 (0.01)
(Chlorthal-dimethyl, DCPA)	<0.010 (0.01)	Oxadiazon	<0.010
dichlorodiphenyldichloroethane, p, p'-	<0.05 (1)	Parathion-methyl, Parathion	<0.010 (0.2)
Dichlorodiphenyldichloroethylene, DDT, o, p'- DDT, p,p'-		Pentachloranisole	<0.010 (0.01)
		Pendimethalin	<0.05 (0.1)
Deltamethrin (0.5 mg/kg)	<0.010	Pentachloroaniline	<0.010
Demeton-S	<0.010 (0.0003)	Pentachlorobenzene	<0.01(0.012)
Diazinon	<0.010 (0.5)	Permethrin (sum of isomers)	<0.010 (1)
Dichlofenthion	<0.010	Pentachlorothioanisole	<0.010
Dichlorvos	<0.010 (1)	Piperonyl butoxide	<0.010 (3)
Dicloran (DCNA)	<0.010	Phorate	<0.010
Dieldrin	<0.010 (0.005)	Phosalone	<0.010 (0.1)
Disulfoton	<0.010	Pirimiphos-ethyl	<0.010 (0.05)

Endosulfan I (alpha-isomer), Endosulfan II (beta-isomer), Endosulfan sulfate	<0.010 (3)	Procymidone	<0.010 (0.1)
		Pirimiphos-methyl	<0.010 (4)
		Propetamphos	<0.010
Endrin	<0.010 (0.05)	Profenofos	<0.010 (0.1)
EPN	<0.010 (0.5)	Propargite	<0.05
Ethion	<0.010 (2)	Propyzamide (Pronamide)	<0.010
Ethoprophos (Ethoprop)	<0.010 (0.035)	Prothiofos	<0.010 (0.05)
Fenchlorphos (Ronnel)	<0.010 (0.1)	Quinalphos	0.42 (0.05)
Fenitrothion	<0.010 (0.5)	Quintozene (Pentachloronitrobenzene)	<0.010 (1)
Fenpropathrin	<0.010 (0.03)	Tecnazene	<0.010 (0.05)
Fensulfothion	<0.010 (0.05)	Tetradifon	<0.010 (0.3)
Fenthion	<0.010 (0.05)	Vinclozolin	<0.010 (0.4)
Fenvalerate/Esfenvalerate (sum of isomer)	<0.010 (1.5)	Fluvalinate, tau- (sum of isomers)	<0.010 (0.5)
Fipronil	<0.0050	Fonofos	<0.010 (0.05)

The acceptable limits are as per USP monogram (Chapter 561) and InChem guideline.

Analysis of Microbial Load in W-ferinAmax ashwagandha (WFA):

Herbal extracts are often contaminated by microbial growth which comes from adjoining rhizospheres of the plant. Although presence of microbes symbiotically boosts production of a number of secondary metabolites of commercial importance [25], in many cases they are also responsible for spoilage of downstream production processes with a subsequent hefty production cost. Therefore, it is a mandate for industries to have a prior assessment of microbial load in the raw materials. According to the recommendations of USP 43 for materials of botanical origin, total bacterial count should be within 10^4 CFU/gm, and the total combined mold and yeasts count should be within 10^3 CFU/g. In addition, the sample should be free from all kinds of coliforms including faecal coliforms which are the APHA certified indicator organism, Staphylococci which are also potential indicators for the presence of pathogens (National Research Council (US) Sub-

committee on Microbiological Criteria) as well as Salmonella, the potent human pathogens [26].

Safety of Withaferin A and W-ferinAmax ashwagandha (WFA):

Several scientists around the world have assessed the safety and toxicological profile of the Ashwagandha extract and its constituents. Sharma et al. [27] have demonstrated that oral administration of aqueous Ashwagandha extract (100 mg/kg/day) to rats over a period of eight consecutive months didn't exhibit any toxicity. Prabu et al. [28] have also demonstrated that oral administration of methanolic extract of Ashwagandha (2,000 mg/kg/day) over a period of 28 consecutive days induce no toxicity.

Singh et al. [29] have reported the oral acute LD₅₀ of Withania somnifera to be 1750 mg/kg body weight in albino mice. Sharada et al. [30] have determined the acute toxicity in Swiss Albino mice and sub-acute toxicity in Wistar rats. No deaths were reported following administration of a single intraperitoneal administration of

1100 mg/kg body weight within 24 hr. The oral LD₅₀ was reported to be 1260 mg/kg body weight. Oral administration of 100 mg *Withania somnifera* extract/kg body weight/day over a period of 30 consecutive days didn't cause any mortality or significant changes in peripheral blood constituents or other parameters [30]. In another independent settings, Gupta et al. [31] conducted extensive toxicological evaluation including both acute and sub-acute toxicity of oral Withaferin A in mice. These researchers reported that withaferin A exhibited no toxicity or death up to 2000 mg/kg body weight in the acute toxicity study. The sub-acute toxicity study was conducted in mice following oral administration of 10-, 70-, and 500 mg/kg body weight/day of Withaferin A over a period of 28 consecutive days. Extensive toxicological analyses including mortality rate, serum chemistry, physiological, and hematological assessment exhibited no signs of toxicity at all the dose levels used in this study. The authors reported that Withaferin A is extremely safe even at high doses and the No Observed Adverse Effect Level (NOAEL) of Withaferin A to be a minimum of 500 mg/kg body weight [31].

Withaferin A is the one of the most potent chemical constituents' responsible for a major part of *Ashwagandha*'s therapeutic potential. It is believed to evolve as a promising anti-cancer drug in near future owing to the versatile structural modifications which can be performed on its side chain leading to significant enhancement of its pharmacological activity [32]. Several researchers have demonstrated that both Withaferin A and Withanolide D exhibit anti-tumor efficacy [33-35]. Vaishnavi et al. (2012) have demonstrated that Withaferin A exhibited cytotoxic activities in both normal and cancer cells [36].

Analysis of standardized W-ferinAmax *ashwagandha* (WFA) exhibited that the total Withanolide content is 15.4%, out of which Withaferin A, Withanoside

A and Withanolide A contents are 6.469%, 1.02% and 0.073%, respectively (Table 3). Recommended daily dose of WFA is 500 mg/day, which contains approximately 15% of total Withanolide. Thus, our recommended daily dose of WFA is quite safe for human consumption and possess a huge span of margin of safety.

Discussion: The medicinal plant *Ashwagandha*, scientifically known as *Withania somnifera* Dunal (family Solanaceae) and commonly known as Indian ginseng or Winter cherry, is a stout herb that reaches a height of 170 cm and carries yellow flowers and berry-like red fruit. Indigenous and Ayurvedic medicine have recognized *Ashwagandha* for more than 3000 years [1-6]. The old elementary foundational scripts in Ayurveda, *Caraka (Charaka)* and *Sushruta Samhitas* describe *Ashwagandha* as a medicinal plant exhibiting the enhancement of multiple vital physiological functions including (a) muscle and physical strength, (b) vitality and vigour, (c) nourishing, (d) spermatogenic, (e) sexual and repro-ductive performance [2-4].

Ashwagandha is a reservoir of biologically active alkaloids (isopelletierine, anaferine, cuscohygrine, anahygrine, etc.), steroidal lactones (withanolides including Withaferin A, Withanoside IV, Withanolide A, and others), flavonoids, phenolic acids, alkaloids, saponins, tannins, saponins and volatile oils conferring a host of therapeutic potential [1,2]. These novel phytonutrients have exhibited an array of health benefits including immune enhancing, adoptogenic, anti-aging, anti-diabetic, anti-arthritis, anti-anxiety, hepato-protective and cardioprotective activities, simultaneously offering protection against various neuro-degenerative diseases, impotency, amnesia, and several other ailments [1-4]. However, breast-feeding, and pregnant women, and people with autoimmune diseases with rheumatoid arthritis, type 1 diabetes, and lupus, and Hashimoto's

thyroid should avoid Ashwagandha for their daily consumption [1-3,7-10,37].

It has also been recently demonstrated by independent research groups that Withaferin A can effectively bind to the Spike protein of SARS-COV-2 thus effectively sequestering it from binding to ACE-2 protein [32, 37, 38]. In the process, it also does not downregulate cellular ACE-2 expression, thus also being compatible with diabetic patients. Gupta et al. reported that Withaferin A, being the major constituent in *Withania somnifera*, also exhibits multiple therapeutic benefits including immune enhancing, vitality, and vigour, hepato-, cardio- and neuroprotective properties [32-34, 38,39]. As discussed earlier, Ashwagandha and its constituents has multiple health benefits.

Maharia et al. (2010) had earlier reported the toxic manifestation induced following bioaccumulation of heavy metals by Ashwagandha root [40]. Accordingly, the accumulation of toxic heavy metals including arsenic (As), cadmium (Cd), mercury (Hg), and lead (Pb) was critically investigated using an ICPMS. Our investigational analysis clearly demonstrated that the total heavy metal load in the extract is way less than permissible limit of 10 ppm, as specified in the USP 43.

Pesticides accumulate in plants through indiscriminate use in agricultural fields, so much that they are sometimes also significantly bioabsorbed by non-crop plants. Therefore, despite their indispensability for commercial production of food-crops and aesthetic plants, pesticides continue to pose a serious threat to human health because of their non-perishability in the ecosystem and bioconversion to other more toxic forms. The major chemical groups of pesticides include the organochlorines (DDT, Endrin, Chlordane etc.), Organophosphates (Trichlorfon, glyphosate etc.), Carbamates (Carbaryl, Carbofuran etc.) and Pyrethroids (Permethrin, chrysanthemic acid) [41]. Coumaphos is not a popular and widely used pesticide, however it is frequently used

in apicultures to confer protection against ectoparasites of bees. Based on recent evaluation of pesticide traces in veterinary products, the revised Maximum Residue Limit of Coumaphos has been fixed at 0.1 ppm in honey [42] which is much higher than ADL of 0.00025 ppm as set by ESDA. Therefore, the toxicity associated with the consumption of traces of Coumaphos with the *Withania* extract powder will be negligible, considering the fact that the extract will not be consumed be further processed to develop therapeutic formulations.

The extract was also found to be grossly free from any residual solvents. In parallel, we conducted extensive microbiological testing to determine the total bacterial and fungal counts, total coliform and *Escherichia coli* (*E. coli*), *Salmonella sp.*, and *Staphylococcus aureus* (*S. aureus*). The results showed that the total bacterial count is less than 10^4 cfu/g and the total fungal count is less than 10^3 cfu/g, while *E. coli*, *Salmonella*, *S. aureus*, and *Coliform* were altogether absent in the sample.

Safety and toxicity analyses are now mandated for any nutraceutical product development. Owing to its growing interest and importance in the phyto-pharmaceutical sector, many upcoming therapeutics are believed to be based on purified Withaferin A instead of incorporating the wholesome Ashwagandha extract. Therefore, the present studies carried out on safety assessment of standardized ashwagandha extract have been meant to provide important insights for designing further downstream purification of Withaferin A.

CONCLUSION

Taken together, *Withania somnifera* plant derived and standardized W-ferinAmax ashwagandha (WFA) contains a total of 15.4% Withanolides as demonstrated by HPLC. Specifically, Withaferin A, Withanoside IV, and Withanoline A contents in WFA were 6.469%, 1.022%, and 0.073%, respectively. Furthermore, WFA contains only 0.403 ppm of heavy metals out of which traces of arsenic,

mercury and lead were detected, and cadmium was absent, which complies with USP 43 guidelines. Microbiological screening exhibited the absence of *E. coli*, *Salmonella*, *S. aureus* and *Coliform* in WFA, while it complies with the total bacterial and fungal counts. Furthermore, USP 43 recommended 80 residue basic pesticide screening was conducted, which complies with as per USP 43 guidelines. No Observed Adverse Effect Level (NOAEL) for Withaferin A was reported to be a minimum of 500 mg/kg body weight. These studies demonstrated that a daily recommended dose of 500 mg W-ferinAmax ashwagandha (WFA), containing a total of approximately 15% of total Withanolide, is safe for further downstream processing into therapeutics or health supplements for human consumption.

Abbreviations: ACE-2, angiotensin converting enzyme 2; ADI, acceptable daily intake; AOAC, Association of Official Analytical Chemists; APHA, American Public Health Association; CFU, colony forming unit; FR, Federal Register; GC-MS – gas chromatography-mass spectrometry; EPA, environmental protection agency; HPLC, high performance liquid chromatography; LOD – limit of detection; LOQ – limit of quantification; NOAEL - no

observed adverse effect level (NOAEL); ppm: parts per million; SARS-COV-2, Severe Acute Respiratory Syndrome Coronavirus 2; TAMC, total aerobic microbial count; TYMC, total combined yeasts and moulds count; USP, United States Pharmacopeia; WFA, W-ferinAmax ashwagandha

Competing interests: PK and AG are employees of Chemical Resources (CHERESO), the study sponsor. DB, SPB, SC, and MB are independent consultants who drafted the manuscript. All authors critically reviewed and approved the manuscript. All authors have declared that they have no other conflict of interest.

Author's contributions: All authors contributed equally and approved the version of the manuscript to be submitted.

Acknowledgements: We would like to express thank to Ms. Kamaljit Kaur, Deputy General Manager, Corporate Affairs, Chemical Resources (CHERESO), India.

Funding: This study was funded by Chemical Resources (CHERESO), Panchkula, Haryana, India.

REFERENCES

1. Dar NJ, Hamid A. & Ahmad, M. Pharmacologic overview of *Withania somnifera*, the Indian Ginseng. *Cell Mol Life Sci.* 2015; 72: 4445–4460 (2015). DOI: <https://doi.org/10.1007/s00018-015-2012-1>.
2. Paul S, Chakraborty S, Anand U, Dey S, Nandy S, Ghorai M, Saha SC, Patil MT, Kandimalla R, Proćków J, Dey A. *Withania somnifera* (L.) Dunal (Ashwagandha): A comprehensive review on ethnopharmacology, pharmacotherapeutics, biomedical and toxicological aspects. *Biomed Pharmacother.* 2021 Nov; 143: 112175. DOI: <https://doi.org/10.1016/j.biopha.2021.112175>.
3. Mandlik Ingawale DS, Namdeo AG. Pharmacological evaluation of Ashwagandha highlighting its healthcare claims, safety, and toxicity aspects. *J Diet Suppl.* 2021; 18(2): 183-226. DOI: <https://doi.org/10.1080/19390211.2020.1741484>.
4. White PT, Subramanian C, Motiwala HF, Cohen MS. Natural Withanolides in the Treatment of Chronic Diseases. *Adv Exp Med Biol.* 2016; 928: 329-373. DOI: https://doi.org/10.1007/978-3-319-41334-1_14.
5. Choudhary D, Bhattacharyya S, Bose S. Efficacy and Safety of Ashwagandha (*Withania somnifera* (L.) Dunal) Root Extract in Improving Memory and Cognitive Functions. *J Diet Suppl.* 2017; 14(6): 599-612. DOI: <https://doi.org/10.1080/19390211.2017.1284970>.
6. Kulkarni SK, Dhir A. *Withania somnifera*: an Indian ginseng. *Prog Neuropsychopharmacol Biol Psychiatry.* 2008; 32(5): 1093-1105. DOI: <https://doi.org/10.1016/j.pnpb.2007.09.011>.

7. Lee IC, Choi BY. Withaferin-A--A Natural Anticancer Agent with Pleiotropic Mechanisms of Action. *Int J Mol Sci.* 2016; 17(3): 290. DOI: <https://doi.org/10.3390/ijms17030290>.
8. Mohan R, Hammers HJ, Bargagna-Mohan P, Zhan XH, Herbstritt CJ, Ruiz A, Zhang L, Hanson AD, Conner BP, Rougas J, Pribluda VS. Withaferin A is a potent inhibitor of angiogenesis. *Angiogenesis* 2004; 7(2): 115-122. DOI: <https://doi.org/10.1007/s10456-004-1026-3>.
9. Tharakan A, Shukla H, Benny IR, Tharakan M, George L, Koshy S. Immunomodulatory effect of Withania somnifera (Ashwagandha) extract - A randomized, double-blind, placebo-controlled trial with an open label extension on healthy participants. *J Clin Med.* 2021; 10(16): 3644. DOI: <https://doi.org/10.3390/jcm10163644>.
10. Guo R, Gan L, Lau WB, Yan Z, Xie D, Gao E, Christopher TA, Lopez BL, Ma X, Wang Y. Withaferin A prevents myocardial ischemia/reperfusion injury by upregulating AMP-activated protein kinase-dependent B-Cell lymphoma 2 signalling. *Circ J.* 2019; 83(8): 1726-1736. DOI: <https://doi.org/10.1253/circj.CJ-18-1391>.
11. Ram N, Peak SL, Perez AR, Jinwal UK. Implications of Withaferin A in neurological disorders. *Neural Regen Res.* 2021; 16(2): 304-305. DOI: <https://doi.org/10.4103/1673-5374.290894>.
12. Heyninck K, Lahtela-Kakkonen M, Van der Veken P, Haegeman G, Vanden Berghe W. Withaferin A inhibits NF-kappaB activation by targeting cysteine 179 in IKKβ. *Biochem Pharmacol.* 2014; 91(4): 501-509. DOI: <https://doi.org/10.1016/j.bcp.2014.08.004>.
13. Singh N, Bhalla M, de Jager P, Gilca M. An overview on ashwagandha: a Rasayana (rejuvenator) of Ayurveda. *Afr J Tradit Complement Altern Med.* 2011; 8(5 Suppl): 208-213. DOI: <https://doi.org/10.4314/ajtcam.v8i5S.9>.
14. Joshi VK, Joshi A. Rational use of Ashwagandha in Ayurveda (Traditional Indian Medicine) for health and healing. *J Ethnopharmacol.* 2021; 276: 114101. DOI: <https://doi.org/10.1016/j.jep.2021.114101>.
15. Gopukumar K, Thanawala S, Somepalli V, Rao TSS, Thamatham VB, Chauhan S. Efficacy and safety of Ashwagandha root extract on cognitive functions in healthy, stressed adults: A randomized, double-blind, placebo-controlled study. *Evid Based Complement Alternat Med.* 2021; 2021: 8254344. DOI: <https://doi.org/10.1155/2021/8254344>.
16. Speers AB, Cabey KA, Soumyanath A, Wright KM. Effects of Withania somnifera (Ashwagandha) on stress and the stress-related neuropsychiatric disorders anxiety, depression, and insomnia. *Curr Neuropharmacol.* 2021; 19(9): 1468-1495. DOI: <http://dx.doi.org/10.2174/1570159X19666210712151556>.
17. Missiakas DM, Schneewind O. Growth and laboratory maintenance of Staphylococcus aureus. *Curr Protoc Microbiol.* 2013 Feb; Chapter 9: Unit 9C.1. DOI: <https://doi.org/10.1002/9780471729259.mc09c01s28>.
18. Cox JM. Lysine-mannitol-glycerol agar, a medium for the isolation of Salmonella spp., including S. typhi and atypical strains. *Appl Environ Microbiol.* 1993; 59(8): 2602-2606. DOI: <https://doi.org/10.1128/aem.59.8.2602-2606.1993>.
19. Lushchak VI, Matviishyn TM, Husak VV, Storey JM, Storey KB. Pesticide toxicity: a mechanistic approach. *EXCLI J.* 2018; 17: 1101-1136. DOI: <http://dx.doi.org/10.17179/excli2018-1710>.
20. Khan MI, Ahmad MF, Ahmad I, Ashfaq F, Wahab S, Alsayegh AA, Kumar S, Hakeem KR. Arsenic exposure through dietary intake and associated health hazards in the middle east. *Nutrients.* 2022; 14(10): 2136. DOI: <https://doi.org/10.3390/nu14102136>.
21. Bernhoft RA. Mercury toxicity and treatment: a review of the literature. *J Environ Public Health.* 2012; 2012: 460508. DOI: <https://doi.org/10.1155/2012/460508>.
22. Wani AL, Ara A, Usmani JA. Lead toxicity: a review. *Interdiscip Toxicol.* 2015; 8(2): 55-64. DOI: <https://doi.org/10.1515/intox-2015-0009>.
23. Williamson SM, Moffat C, Gomersall MA, Saranzewa N, Connolly CN, Wright GA. Exposure to acetylcholinesterase inhibitors alters the physiology and motor function of honeybees. *Front Physiol.* 2013; 4: 13. DOI: <https://doi.org/10.3389/fphys.2013.00013>.
24. Gill KD, Flora G, Pachauri V, Flora SJS. Neurotoxicity of organophosphates and carbamates. In *Anticholinesterase pesticides* (eds T. Satoh and R.C. Gupta). 2011. DOI: <https://doi.org/10.1002/9780470640500.ch18>.
25. Ludwig-Müller J. Plants and endophytes: equal partners in secondary metabolite production? *Biotechnol Lett.* 2015; 37(7): 1325-1334. DOI: <https://doi.org/10.1007/s10529-015-1814-4>.
26. Wang X, Zhu S, Zhao JH, Bao HX, Liu H, Ding TM, Liu GR, Li YG, Johnston RN, Cao FL, Tang L, Liu SL. Genetic boundaries delineate the potential human pathogen Salmonella bongori into discrete lineages: divergence and speciation. *BMC Genomics.* 2019; 20(1): 930. DOI: <https://doi.org/10.1186/s12864-019-6259-z>.

27. Sharma S, Dahanukar S, Karandikar SM. Effects of long-term administration of the roots of Ashwagandha (*Withania somnifera*) and Shatavari (*Asparagus racemosus*) in rats. *Indian Drugs*. 1986; 23: 133–139.
28. Prabu PC, Panchapakesan S, Raj CD. Acute and sub-acute oral toxicity assessment of the hydroalcoholic extract of *Withania somnifera* roots in Wistar rats. *Phytother Res*. 2013; 27(8): 1169–1178. DOI: <https://doi.org/10.1002/ptr.4854>.
29. Singh N, Bhalla M, de Jager P, Gilca M. An overview on ashwagandha: a Rasayana (rejuvenator) of Ayurveda. *Afr J Tradit Complement Altern Med*. 2011; 8(5 Suppl): 208–213. DOI: <https://doi.org/10.4314/ajtcam.v8i5S.9>.
30. Sharada AC, Emerson Solomon F, Uma Devi P. (1993) Toxicity of *Withania Somnifera* root extract in rats and mice. *Intern J Pharmacogn*. 1993; 31(3): 205–212. DOI: <https://doi.org/10.3109/13880209309082943>.
31. Gupta SK, Jadhav S, Gohil D, Panigrahi G.C., Kaushal R.K., Gandhi K, Patil A, Chavan P, Gota V. Safety, toxicity, and pharmacokinetic assessment of oral Withaferin-A in mice. *Toxicology Rep*. 2022; 9: 1204–1212. DOI: <https://doi.org/10.1016/j.toxrep.2022.05.012>.
32. Straughn AR, Kakar SS. Withaferin A: a potential therapeutic agent against COVID-19 infection. *J Ovarian Res*. 2020; 13(1): 79. DOI: <https://doi.org/10.1186/s13048-020-00684-x>.
33. Vanden Berghe W, Sabbe L, Kaileh M, Haegeman G, Heynink K. Molecular insight in the multifunctional activities of Withaferin A. *Biochem Pharmacol*. 2012; 84(10): 1282–1291. DOI: <https://doi.org/10.1016/j.bcp.2012.08.027>.
34. Vyas AR, Singh SV. Molecular targets and mechanisms of cancer prevention and treatment by Withaferin A, a naturally occurring steroidal lactone. *AAPS J*. 2014, 16, 1–10. DOI: <https://doi.org/10.1208/s12248-013-9531-1>.
35. Mondal S, Mandal C, Sangwan R, Chandra S, Mandal C. Withanolide D induces apoptosis in leukemia by targeting the activation of neutral sphingomyelinase-ceramide cascade mediated by synergistic activation of c-Jun N-terminal kinase and p38 mitogen-activated protein kinase. *Mol Cancer*. 2010; 9: 239. DOI: <https://doi.org/10.1186/1476-4598-9-239>.
36. Vaishnavi K, Saxena N, Shah N, Singh R, Manjunath K, Uthayakumar M, Kanaujia SP, Kaul SC, Sekar K, Wadhwa R. Differential activities of the two closely related withanolides, Withaferin A and Withanone: bioinformatics and experimental evidences. *PLoS One*. 2012; 7(9): e44419. DOI: <https://doi.org/10.1371/journal.pone.0044419>.
37. Soumya NP, Mini S, Sivan S, Mondal S. Bioactive compounds in functional foods and their role as therapeutics. *Bioactive Compounds in Health and Disease* 2021; 4(3): 24–39. DOI: <https://doi.org/10.31989/bchd.v4i3.786>.
38. Teibo JO, Ayinde KS, Olaoba OT, Adelusi TI, Teibo TKA, Bamikunle MV, Jimoh YA, Alghamdi S, Abdulaziz O, Rauf A, El-Saber Batiha G. Functional foods' bioactive components and their chemo-prevention mechanism in cervical, breast, and liver cancers: A systematic review. *Functional Foods in Health and Disease* 2021; 11(11): 559–585. DOI: <https://www.doi.org/10.31989/ffhd.v11i11.818>
39. Atteeq M. Evaluating anticancer properties of Withaferin A - a potent phytochemical. *Front Pharmacol*. 2022; 13: 975320. DOI: <https://doi.org/10.3389/fphar.2022.975320>.
40. Maharia RS, Dutta RK, Acharya R, Reddy AV. Heavy metal bioaccumulation in selected medicinal plants collected from Khetri copper mines and comparison with those collected from fertile soil in Haridwar, India. *J Environ Sci Health B*. 2010; 45(2): 174–181. DOI: <https://doi.org/10.1080/03601230903472249>.
41. Kaur R, Kaur R, Rani S, Malik AK, Kabir A, Furton KG. Application of fabric phase sorptive extraction with gas chromatography and mass spectrometry for the determination of organophosphorus pesticides in selected vegetable samples. *J Sep Sci*. 2019; 42(4): 862–870. DOI: <https://doi.org/10.1002/jssc.201800854>.
42. EFSA (European Food Safety Authority), 2016. Reasoned opinion on the setting of maximum residue levels for amitraz, coumaphos, flumequine, oxytetracycline, permethrin and streptomycin in certain products of animal origin. *EFSA Journal* 2016; 14(8):4570, 39 pp. DOI: <https://doi.org/10.2903/j.efsa.2016.4570>.

A comparative account of antibacterial efficacy of *Madhuca longifolia* (J Konig) J.F. Macbr and *Butea monosperma* (Lam) Taub flower extracts

Avishek Ghosh

Department of Microbiology, Maulana Azad College (Kolkata), India.

(Corresponding author: Avishek Ghosh*)

(Received: 21 March 2023; Revised: 25 April 2023; Accepted: 14 May 2023; Published: 20 June 2023)

(Published by Research Trend)

ABSTRACT: Plants and its various parts have been used with medicinal effects from the ancient times. Numerous parts of plants including leaves, flowers, barks, roots, obviously fruits and total plant body may be considered as source of variety of medicinal values. The phytochemicals, precisely the secondary metabolites have potent antimicrobial activities. Here, in this particular study, the antibacterial effect of flower extracts of *Madhuca longifolia* and *Butea monosperma* against enteric pathogens like *Shigella flexneri*, *Salmonella enterica* Typhimurium, *Pseudomonas aeruginosa* and *Escherichia coli* (control) was tested. Flowers of above mentioned plants were collected and extracted with methanol and methanolic extracts were made into powder form. The preservation of flowers in their original state as far as possible was a challenging task in this study since loss of original quality could influence actual effect of the phytochemicals on the target bacteria. These powdered extracts were used to treat enteric pathogens to study different growth and pathogenicity related properties. Inhibition of growth and other pathogenic potentials by the use of these extracts were evident in case of the above mentioned well-known enteric pathogens from this particular study. The obtained result indicated that, *Madhuca longifolia* flower extract was more potent compared to *Butea monosperma* flower extract in antibacterial activity.

Keywords: Phytochemicals, Ethnomedicine, Biofilm, Minimal Inhibitory Concentration, Minimal Bactericidal Concentration.

INTRODUCTION

Medicinal plants may be defined as a group of plants those possess some special properties qualifying them as article of drugs and therapeutic agents and are used for medicinal purposes (Chopra & Doiphode 2002). Plants and plant products have been considered to have medicinal roles and used to heal many diseases from ancient times. There is evidence of use of Hollyhock by Neanderthals dating back to 60000 years ago in present day Iraq (Cowan, 1999). These plants are still used in ethnomedicines (Cowan, 1999). Indian traditional herbal and ethnomedicinal practices date back to approximately 5000 years ago since Charaka and Sushruta Samhita refer to the use of 341 and 395 herbal medicines (Dev, 1999). Egyptian history ("Ebers Papyrus") also reports the use of plants or plant products as medicine from 1500 BCE (Borchardt, 2002).

The use of medicinal properties of plants has seen quite a lot of financial investments and that will continue since the health beneficial effects of herbals have started gathering attention newly (Hoareau & Dasilva, 1999). According to the observation by UNESCO, the use of traditional medicinal plants in developing countries has been carried out as on normative basis (Goncalves, n.d.). Also UNESCO reports indicated about the choice of these traditional medicinal plants for preparation of various herbal chemotherapeutic

agents with better acceptance probability over the conventional antibiotics (Kenya, 1998). Combinatorial therapy consisting of antibiotics and phytochemicals can overcome the antibiotic-resistance in certain cases as combination of epigallocatechin gallate (EGCG) with tetracycline resulted in synergistic effect where EGCG inhibited bacterial efflux pump and consequently, the effect of tetracycline could become more pronounced (Khameneh *et al.*, 2019).

Plants have the ability to synthesise numerous aromatic substances which are phenolics or their derivatives (GEISSMAN, 1963). These compounds are principally secondary metabolites and naturally serve as plant defence mechanisms against microbes, insects and herbivores (Cowan, 1999). Antimicrobial plants products can be broadly divided into several categories: phenolics and polyphenols (simple phenol & phenolic acids; quinones; flavones, flavonoids & flavonols; tannins), terpenoids and essential oils, alkaloids, lectins & polypeptides and other minor compounds (Cowan, 1999). The medicinal usages of *Ocimum tenuiflorum* (Tulsi), *Azadirachta indica* (Neem), *Curcuma longa* (Turmeric), *Rauvolfia serpentina* (Sarpagandha) etc. are very common in practice. Earlier studies have shown that the fresh fruit extracts (both aqueous and alcoholic) from *Malus domestica*, *Punica granatum*, *Psidium guajava*, and *Citrus sinensis* possess antibacterial and antifungal activities tested against Gram positive bacteria like *Bacillus subtilis* & *Staphylococcus aureus*;

Gram negative bacteria like *Escherichia coli* & *Pseudomonas aeruginosa* and fungus *Candida albicans* (Malaviya & Mishra 2011).

Butea monosperma or 'Flame of Forest' is a member of family Fabaceae and colloquially known as Palash, dhak, Bastard Teak etc. This tree is common throughout India, Myanmar, Sri Lanka. Almost every part of the tree are being utilised for several thousand years owing to the medicinal value and many other purposes (DAVE *et al.*, 2019; Kapoor, 2018). Indian Ayurvedic texts refer to Palash as a medicinal plant since its leaves, stem, flowers, seeds and roots have been widely used as traditional ethnomedicine (DAVE *et al.*, 2019). Palash has proven to be astringent, anti-diarrhoeal, anti-dysenteric and anti-helminthic in nature. The phyto-components of flower extract like butein, butrin, isobutrin and isocoreospin have been shown to possess anti-inflammatory including antioxidant properties of rutin. These phyto-extracts were also shown to have anti-diabetic and hepato-protective characteristics (DAVE *et al.*, 2019).

Madhuca longifolia is commonly known as butter tree, colloquially called Mahuya belongs to the family Sapotaceae and widely distributed across various regions of India in arable and plaeotropic lands. It is a large, shady, deciduous tree. Main phyto-chemical composition of Mahuya includes tannins, saponins, β -amyrin, β -amyrin acetate, β -amyrincinate, β -amyrindecinate, betullic acid, ursolic acid, stigma sterol, β carotene and quercetin (Reddy *et al.*, n.d.). The distilled liquor from flowers brings the fame for the tree and widely used to prepare household vinegar. The distilled juice of flowers is considered as tonic with nutritional value. Mahuya preparations are used to remove intestinal worms, treating respiratory infections and other ailments in Indian folk medicine (Yadav *et al.*, 2011b, 2011a). Phyto-components like madhucic acid (pentacyclic triterpenoid), madhusa zone (untypical isoflavone) and glycosides present in Mahuya flower extract were shown to have medicinal beneficial effects like antioxidant and anti-diabetic properties (Ramadan *et al.*, 2016).

Considering the different health beneficial and medicinal properties of *Butea monosperma* and *Madhuca longifolia*, in this current work, the direct effect of these plants' flower extracts on the common enteric pathogens was explored in details by studying the growth inhibition pattern, effect on generation time, inhibition of biofilm formation of the enteric pathogenic bacteria like *Shigella flexneri*, *Salmonella enterica* Typhimurium and *Pseudomonas aeruginosa* taking *E. coli* K12 as the control type.

MATERIALS AND METHODS

A. Preparation of flower extracts

Butea monosperma and *Madhuca longifolia* fresh flowers were collected from Betla, Jharkhand, India. 300g of each type of flower was shade dried thoroughly for 6-7 days. The dried materials were crushed properly and soaked in 300ml methanol for 3 days to dissolve the constituents completely. After that, the extracts were filtered twice and concentrated up to 30% using

rotary evaporator. These concentrated extracts were further made into powdered form by freeze drying. For experimental purposes, these extracts were dissolved in dimethyl sulphoxide (DMSO) to prepare 1mg/ml stock solution and this was diluted in DMSO accordingly.

B. Antibacterial assays

Antibacterial assays including effect on bacterial generation time, minimal inhibitory concentration (MIC), minimal bactericidal concentration (MBC), inhibition of bacterial growth by agar diffusion and anti-biofilm formation activity assay were performed following usual procedures. The test bacterial types *Shigella flexneri*, *Salmonella enteric* Typhimurium, *Pseudomonas aeruginosa* and *Escherichia coli* K12 were procured from Division of Bacteriology, National Institute of Cholera & Enteric Diseases, Kolkata. The common antibiotics like Kanamycin & Tetracycline were used to compare the antibacterial efficiencies of these extracts.

Bacterial growth curve assay for generation time calculation

Growth curve and generation time of each of these test bacterial types was determined in presence of 0.25mg/ml of each extract in Nutrient broth. Extracts dissolved in DMSO were filter sterilised before adding to the broth. Untreated Nutrient broth was used as control. Variation in generation time was calculated by comparing the bacterial growth in presence or absence of the extracts.

C. MIC & MBC assay

MIC for each of the bacterial types was determined by growing the bacterial types in presence of a range of 2.5 μ g-500 μ g extracts. Similarly, MIC of these test bacterial types against the antibiotics was also performed with the same range of concentrations. For determination of MBC, bacterial samples from the corresponding MIC set and next two higher concentrations were plated on Nutrient agar plates to obtain bacterial colonies. MBC values were determined by observing CFU on the nutrient agar plates.

D. Antibacterial sensitivity assay

This was determined by agar diffusion assays. Briefly, the log phase cultures of each of the bacterial types were plated with nutrient agar medium by pour-plate technique. After solidification of the media, wells were made on agar surface and in those wells various concentrations of the extracts were applied. Solvent DMSO was used as the control here.

E. Calculation of sensitivity index (SI)

SI = Diameter of Inhibition zone of the extracts / Diameter of Inhibition zone of the standard

F. Calculation of relative % inhibition (RPI)

RPI = 100 (X-Y)/(Z-Y)

X- Total area of inhibition of test extract

Y- Total area of inhibition of solvent

Z- Total area of inhibition of standard

G. Biofilm formation assay

Biofilm formation will be estimated by following the protocol described by George A. O'Toole (O'Toole,

2011). Briefly, test bacterial types were cultured in Luria Bertani broth supplemented with 0.25mg/ml of each extract and incubated o/n at 35°C in static condition. Then after discarding the spent medium cells were washed with sterile distilled water twice. Adherent cells were stained with 0.1% crystal violet solution for 10-15 mins, extra stain was washed twice and dried for a few hours. Remaining crystal violet was solubilised by 30% AcOH and absorbance was measured at 550nm against AcOH blank. Bacteria cultured in un-supplemented Luria Bertani broth were treated as control in this case.

H. Phytochemical assay

Qualitative tests for the presence of alkaloids, tannins, flavonoids, glycosides were carried out following standard methods (Harborne, 1984).

I. Statistical analysis

Data collected in the study are expressed as the mean \pm standard error of mean (S.E.M.) and statistical analysis was carried out by using one-way analysis of variance (ANOVA) method. P value of less than 0.05 was considered to be statistically significant. All groups were compared with Dimethyl sulfoxide treated control group.

RESULTS AND DISCUSSION

A. Phytochemical profiling of the plant extracts

Table 1: Phytochemical constituent analysis of *B. Monosperma* & *M. longifolia* flower extracts.

Parameters	Test	Result	
		<i>B. monosperma</i>	<i>M. longifolia</i>
Alkaloids	Wagner's Test	++	+++
Tannins	Lead acetate Test	++	++
Flavonoids	Aluminium chloride Test	++	+
Glycosides	Borntranger Test	-	-

+ indicates presence or positive reaction, ++ and +++ indicates presence in higher degree, - indicates absence or negative reaction

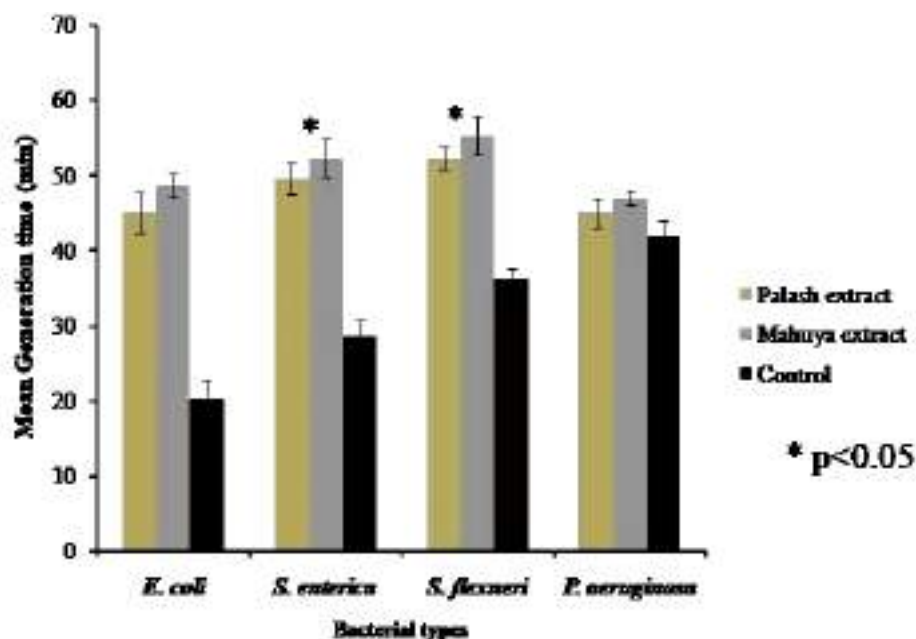


Fig. 1. Effect of mahuya and plash extracts on the mean generation time of *E. coli*, *S. enterica*, *S. flexneri* and *P. aeruginosa*.

Qualitative studies for various phytochemicals present in the flower extracts of palash and mahuya showed the presence of alkaloids, flavonoids and tannins which is represented in Table 1.

B. Variation in bacterial generation time

Calculation of generation time of test bacterial types in presence of the extracts has shown significant change for *E. coli* K12, *S. Enteric* & *S. flexneri* but not for *P. aeruginosa*. The mean generation time has increased from 20 min to 48 min respectively for palash and mahuya extracts. Similar results were obtained in cases of *S. flexneri* where mean generation has changed from 36 min to 49 min and 52 min respectively for palash and mahuya extracts. For *S. enterica* mean generation time also increased from 28 min to 49 min and 52 min for palash and mahuya extracts respectively. In case of *S. enterica* another interesting observation was the extension of lag phase which was changed from 2hrs to 3.5hrs & 3.8hrs for palash and mahuya extracts. Growth of *P. aeruginosa* in presence of both palash and mahuya extracts resulted in increase in generation time but that was not very significant since it only changed from 42 min to 47 min and 47 min respectively for palash and mahuya extracts. The changes in the generation time resulted here is represented in Fig. 1 where mean results from three independent experiments have been shown.

C. Determination of MIC and MBC

For determination of MIC, 10ml of NB with or without the palash and mahuya extracts was inoculated with 0.1ml of each of the bacterial types. The final concentrations of the plant extracts used here were 2.5, 5, 10, 25, 50, 100, 150, 200, 250, 300, 400 & 500 µg/ml. The MIC value of the common antibiotics kanamycin and tetracycline against these test bacterial types were also determined for comparison using the same range of antibiotic concentrations. The results indicated that, mahuya extract has proven to be more efficient in inhibiting the bacterial growth compared to palash extract and antibiotics used here. The MIC for mahuya in case of pathogens like *S. enterica*, *S. flexneri* was 50-100µg/ml & 100-150µg/ml and for *P. aeruginosa* it was 150-200µg/ml, whereas MIC for kanamycin against these bacteria were 25-50 µg/ml and for tetracycline it was 10-25 µg/ml for *S. enterica* and *S. flexneri* and 50-100 µg/ml for *P. aeruginosa*. The MIC values for palsh extract was also smaller than antibiotics but was comparatively higher than the MIC values of mahuya extract. The results showing the different values are summarized in Table 2.

MBC was assayed by growing the test bacterial types with the plant extracts concentrations just higher than the MIC value and then counting the CFU after plating each set on nutrient agar plate. The concentration of the plant extract where no growth was observed on the nutrient agar plate was considered as the corresponding MBC. The resulted MBC values for *S. enterica*, *S. flexneri* and *P. aeruginosa* were found to be 100; 125; 225µg/ml for palash extract and 100; 150; 180µg/ml for mahuya extract respectively. The detailed results for MBC values are represented in Table 3.

D. Antibacterial sensitivity assay by agar diffusion

Antibacterial sensitivity assay by agar diffusion has also resulted in significant efficiency of palash and mahuya extract to inhibit the growth of the test bacterial types. The zones of bacterial growth inhibition induced by plant extracts were maximum in case of *E. coli* K12 which was the reference strain and the inhibition zones

in cases of *S. flexneri* and *S. enterica* were found to be slightly lesser than that of in case of *E. coli* K12 but the values were significant to consider the inhibition efficiency of palash and mahuya extracts by in comparison to the antibiotics as shown in Table 4 in terms of activity indices. The growth of *P. aeruginosa* was also inhibited by the plant extracts but the effect of both of the plant extracts on *P. aeruginosa* was less compared to the other test bacterial pathogen studied here. Control sets were prepared by using the solvent DMSO. Antibacterial sensitivity is also demonstrated by calculating the relative percentage inhibition (RPI) (Table 4) considering the solvent effect and by comparing with the inhibition induced by equal amount of the standard antibiotic kanamycin and this is depicted in Table 4. Here also the relative highest inhibition was shown in case of the reference bacteria *E. coli* and mahuya extract could show greater relative inhibition than palash extract as the pathogens *S. enterica* and *S. flexneri* were inhibited by 68.5% & 79.7% and 46.05% & 58.2% by palash and mahuya extracts respectively. *P. aeruginosa* growth inhibition was observed to be least amongst the pathogens since it could be inhibited by only 41.36% and 52.28% by palash and mahuya extracts respectively (Fig. 2).

E. Biofilm formation assay

Biofilm formation is considered as a crucial step for pathogenesis of enteric and other pathogens. Successful biofilm formation by pathogens eases the infection and subsequent growth and multiplication of pathogens inside the host. In this current study, it was observed that, the flower extracts possessed anti-biofilm forming activity too against *S. enterica*, *S. flexneri* and *P. aeruginosa* and also *E. coli* K12. The biofilm formation could be inhibited almost 50% in case of *S. enterica*, *S. flexneri* & *E. coli* K12. For *P. aeruginosa*, biofilm formation was inhibited but only up to 35% suggesting that palash and mahuya extracts have anti-biofilm effect on all of these test bacterial types but slightly less effective against *P. aeruginosa*.

Table 2: Details of MIC values of *B. monosperma* & *M. longifolia* flower extracts against *E. coli*, *S. enterica*, *S. flexneri* & *P. aeruginosa*.

Bacteria	MIC value (µg/ml)			
	Palash Extract	Mahuya Extract	Kanamycin	Tetracycline
<i>E. coli</i>	25-50	25-50	2.5-5	5-10
<i>S. enterica</i>	50-100	50-100	25-50	10-25
<i>S. flexneri</i>	50-100	100-150	25-50	10-25
<i>P. aeruginosa</i>	150-200	100-150	25-50	50-100

Table 3: MBC values of *B. monosperma* & *M. longifolia* flower extracts against against *E. coli*, *S. enterica*, *S. flexneri* & *P. aeruginosa*.

Bacteria	MBC value (µg/ml)	
	Palash Extract	Mahuya Extract
<i>E. coli</i>	50	50
<i>S. enterica</i>	100	100
<i>S. flexneri</i>	125	150
<i>P. aeruginosa</i>	225	180

Table 4: Activity Indices of *B. monosperma* & *M. longifolia* extracts on the test bacteria *E. coli*, *S. enterica*, *S. flexneri* & *P. aeruginosa*.

Bacteria	Mean diameter of inhibition zone (mm)			AI (Palash Ext)	AI (Mahuya Ext)
	Palash extract	Mahuya extract	Kanamycin		
<i>E. coli</i>	29±0.8	32±0.4	33±0.5	0.87	0.97
<i>S. enterica</i>	26±0.6	28±0.5	31.3±0.6	0.83	0.89
<i>S. flexneri</i>	18±0.6	18.5±0.7	29.5±0.3	0.61	0.63
<i>P. aeruginosa</i>	17±0.3	19±0.2	23±0.5	0.74	0.82

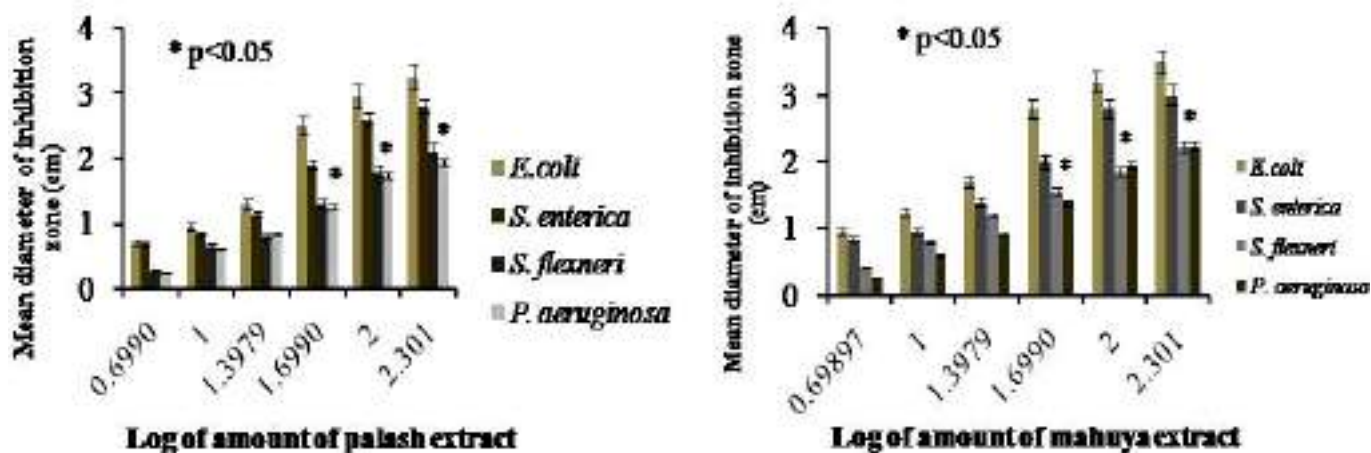


Fig. 2. Antibacterial sensitivity assay of palash and mahuya extracts against *E. coli*, *S. enterica*, *S. flexneri* and *P. aeruginosa* by agar diffusion method.

The anti-biofilm formation activity of palash and mahuya extracts has been summarized in Fig. 3. Another aspect of biofilm formation, the swarming motility was also studied in case of *P. aeruginosa*, since swarming motility of *P. aeruginosa* is considered as an important factor in its biofilm formation and subsequent pathogenesis.

It was evident from the above results that, the flower extracts of palash and mahuya have shown significant levels of antibacterial effects. The antibacterial effect was highest in case of the laboratory strain *E. coli* K12 since the other bacterial types *S. flexneri*, *S. enterica* and *P. aeruginosa* are known for their pathogenic potential. These pathogenic bacteria evolve with many strategies to sustain in the host system and combat the hosts' responses during their pathogenesis.

Here in this particular study, palash and mahuya flower extracts could inhibit the growth and multiplication process of the above mentioned enteric pathogens which is evident from the increase in mean generation time i.e. almost doubling the generation time for *S. flexneri* and *S. enterica* suggesting that the extracts have some bio-active components which can inhibit the pathogen multiplication notably. The growth of *P. aeruginosa* was not inhibited as much as the other two pathogens used in this study- this may suggest the uniqueness of *P. aeruginosa* in withstanding the inhibitory effect exerted by the flower extracts.

The study of MIC and MBC values is also suggestive of the fact that, these extracts were almost equally effective. The notable observation was that these extracts were effective at microgram levels. Here also the interaction of these extracts with *P. aeruginosa* shown that, the MIC value was relatively higher than other two pathogenic bacterial types. Similar results were also obtained for standard antibiotics against *P. aeruginosa*. Effect of mahuya leaf extract was studied by earlier research also showed the inhibitory properties on bacteria like *E. coli* and *Staphylococcus aureus* but these were laboratory strains not the pathogenic ones. It showed that the effective minimal concentration of leaf extract was 0.35mg (Swarnalatha, n.d.) but here in this study palash and mahuya flower extracts proved to be even more efficient since the MIC value observed was in the range of 100µg/ml for the test bacterial samples. Bacterial growth inhibition study by agar diffusion method has also indicated that, these extracts could significantly reduce the growth of pathogens *S. enterica* and *S. flexneri* but growth inhibition observed in case of *P. aeruginosa* was slightly lesser than other two pathogens. Activity indices at 100µg/ml level against *S. enterica* was 0.83 for palash extract and 0.89 for mahuya extract implying that pathogen growth was reduced notably by these extracts.

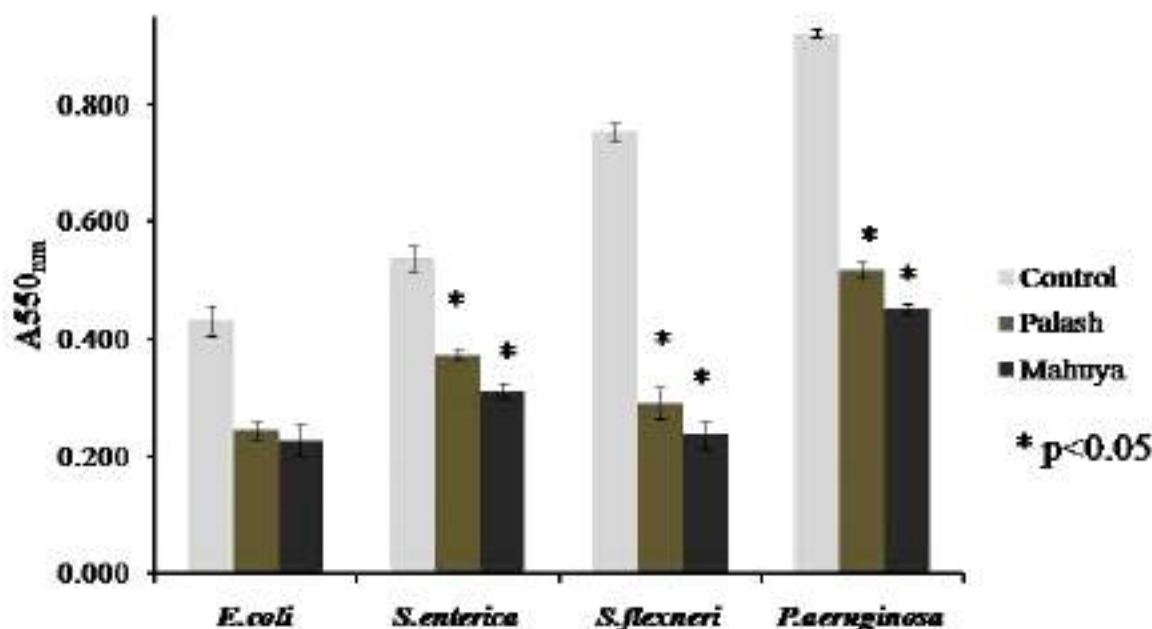


Fig. 3. Inhibition of Biofilm formation by palash and mahuya extracts on *E. coli*, *S. enterica*, *S. flexneri* and *P. aeruginosa*.

This was also further strengthened by relative percentage inhibition (RPI) where *S. enterica* and *S. flexneri* were shown to be inhibited by 68.5% & 79.7% and 46% & 58.2% by palash and mahuya extracts respectively. Other studies have shown that, extracts of various parts of palash plant have inhibitory effect against the common bacteria like *Bacillus subtilis*, *Staphylococcus aureus* and *Bacillus cereus* (Dave *et al.*, 2019).

Inhibition of biofilm formation has been the most crucial aspect of this study since the biofilms developed by the pathogens is a key step in rooting themselves in the host system. Successful biofilm development actually changes the pathogenic bacterial behaviour in the way that they start to behave as a community not as the single cell and this change in bacterial behaviour helps them to combat many drugs and multiple host responses. If a compound can inhibit this biofilm formation and development, the potential of the pathogen in manifesting the disease becomes significantly lesser. In this context, the present study adds the role of palash and more importantly mahuya extract which have crucially decreased the biofilm development by *S. flexneri*, *S. enterica* and *P. aeruginosa*.

CONCLUSION

The present day scenario of growing multiple drug resistance amongst various bacterial pathogens places a challenging task to treat most of the bacterial diseases. To overcome this problem, the trend of using complementary and alternative medicines is expanding in many developing countries in recent years. In this aspect, the ethnomedicinal values of these plants may be revisited following their usage from ancient times. This particular study throws light on the usage of flower extracts of *B. monosperma* and *M. longifolia* against the important enteric pathogens and most significantly against the pathogen *P. aeruginosa*. The

findings from this study will be helpful in strengthening the research on alternative medicines which demands the further detailed profiling of these types of bio-active compounds in combating various diseases in future.

FUTURE SCOPE

The uses of chemotherapeutic drugs have become the choice of modern day medical treatments but it is also well established that, consumption of these drugs cause moderate to severe side effects. The bio-active products of herbal and plant origin, known from ancient times, do not have such severe side effects. From this point of view, it may be taken into account that, the flower extracts discussed in this study can be considered as effective alternatives in present scenario. The combinatorial usage of these extracts along with suitable chemotherapeutic drugs may also attract research interest in future. Also, there may be further researches required to specify the particular molecular pathways by which these extracts show antimicrobial activities and also dose and form of the extract to be used for medial trials with animals as well as humans. These studies may show the pathway of a greener approach in treating various microbial enteric diseases in future.

Author's Contribution. The total study was conceived, designed, conducted and written by AG.

Acknowledgement. The author is earnestly thankful to Prof. Sankar Narayan Sinha, Department of Botany, University of Kalyani, West Bengal for his expert inputs and support during the study. Author sincerely acknowledges The Principal, Maulana Azad College and Head of the Microbiology Department, Maulana Azad College for allowing the above study to be conducted.

Conflict of Interest. None.

REFERENCES

- Borchardt, J. K. (2002). The Beginnings of Drug Therapy: Ancient Mesopotamian Medicine. *Drug News & 15(6): 284-290(2023)*

- Perspectives*, 15(3), 187–192.
- Chopra, A., & Doiphode, V. V. (2002). Ayurvedic medicine. Core concept, therapeutic principles, and current relevance. *The Medical Clinics of North America*, 86(1), 75–89, vii.
- Cowan, M. M. (1999). Plant Products as Antimicrobial Agents. *Clinical microbiology reviews* (Vol. 12, Issue 4).
- Dave, K. M., Darji, P. P., & Gandhi, F. R. (2019). Antimicrobial Activity and Phytochemical Study of Plant Parts of *Butea monosperma*. *Journal of Drug Delivery and Therapeutics*, 9(4-A), 344–348.
- Dev, S. (1999). Ancient-modern concordance in Ayurvedic plants: some examples. *Environmental Health Perspectives*, 107(10), 783–789.
- Geissman, T. A. (1963). *Flavonoid Compounds, Tannins, Lignins and Related Compounds* (pp. 213–250).
- Goncalves, M. P. (n.d.). *A Cultural decade: reflections on the World Decade for Cultural Development, 1988-1997; Studies and reports of the Unit of Cultural Research and Management; Vol. 5; 1998*.
- Harborne, J. B. (1984). *Phytochemical Methods*. Springer Netherlands. <https://doi.org/10.1007/978-94-009-5570-7>
- Hoareau, L., & Dasilva, E. J. (1999). Medicinal plants: a re-emerging health aid. In *EJB Electronic Journal of Biotechnology* (Vol. 2, Issue 2).
- Kapoor, L. D. (2018). *CRC Handbook of Ayurvedic Medicinal Plants*. CRC Press.
- Kenya. (1998). REGIONAL AFRICA Promotion of Ethnobotany and the Sustainable Use of Plant Resources in Africa United Nations Educational, Scientific and Cultural Organization Norway Funds-in-Trust Royal Ministry of Foreign Affairs.
- Khameneh, B., Iranshahy, M., Soheili, V., & Fazly Bazzaz, B. S. (2019). Review on plant antimicrobials: a mechanistic viewpoint. *Antimicrobial Resistance & Infection Control*, 8(1), 118.
- Malaviya, A., & Mishra, N. (2011). Antimicrobial activity of tropical fruits. *Biological Forum—An International Journal*, 3(1), 4.
- O’Toole, G. A. (2011). Microtiter Dish Biofilm Formation Assay. *Journal of Visualized Experiments*, 47.
- Ramadan, M. F., Mohdaly, A. A. A., Assiri, A. M. A., Tadros, M., & Niemeyer, B. (2016). Functional characteristics, nutritional value and industrial applications of *Madhuca longifolia* seeds: an overview. In *Journal of Food Science and Technology* (Vol. 53, Issue 5, pp. 2149–2157). Springer India.
- Reddy, S. K., Sai, D., Sarma, K., Siva, A., Reddy, K., Akhil, M., & Siva Sankar, C. H. (n.d.). 2013, 3(1) phytochemical and antimicrobial activity of whole plant of *Madhuca indica*.
- Swarnalatha, S. P. M. (n.d.). *Invitro Antimicrobial Activity of Madhuca Longifolia Leaf Extract*.
- Yadav, S., Suneja, P., Hussain, Z., Abraham, Z., & Mishra, S. K. (2011a). Genetic variability and divergence studies in seed and oil parameters of mahua (*Madhuca longifolia* Koenig) J.F. Macbride accessions. *Biomass and Bioenergy*, 35(5), 1773–1778.
- Yadav, S., Suneja, P., Hussain, Z., Abraham, Z., & Mishra, S. K. (2011b). Prospects and potential of *Madhuca longifolia* (Koenig) J.F. Macbride for nutritional and industrial purpose. *Biomass and Bioenergy*, 35(4), 1539–1544.

How to cite this article: Avishek Ghosh (2023). A comparative account of antibacterial efficacy of *Madhuca longifolia* (J Konig) J.F. Macbr and *Butea monosperma* (Lam) Taub flower extracts. *Biological Forum – An International Journal*, 15(6): 284-290.

RESEARCH ARTICLE

OPEN ACCESS

An Account of Hygienic Practices and Street Food Safety Around the Medical Colleges of Kolkata, India

Avishek Ghosh 

Department of Microbiology, Maulana Azad College, Kolkata, West Bengal, India.

Abstract

The safety of street food is an important aspect in the field of nutrition security. A cross sectional study was conducted among street food vendors around the medical colleges of Kolkata selected by simple random sampling. Data were collected by interviewing the selected food vendors with the predesigned schedule and observation. Microbiological analyses of food samples selected randomly from seventy five vendors were carried out. Food vendors unwilling or abstaining from the interview could not be selected in this current study. None of the food vendors used head cap or apron or hand gloves during preparation or selling of foods. Only 25.33% of food vendors covered the foods after preparation. Most of the vendors were cleaning their serving utensils in stagnant water of bucket. The continuous re-use of same stagnant water for washing non-disposable utensils led to deposition of food materials on them and this increased the chance of chemical and microbial contamination as well as enhanced the food borne intoxication. Half of the food samples were contaminated with the organisms causing Food Borne Diseases. Significant relationship was found between various hygienic practices and presence of probable food borne pathogenic bacteria. Approximately 81% of the food vendors did not have clean nails and nor did they use gloves for food service resulting in increased chances of microbial contamination in the foods. Also, the amount of food vendors using the leftover food of previous day was 44% meaning a significant decrease in food quality due to mixing of leftover foods. So, the hygienic practices of the food vendors around the medical colleges of Kolkata were very poor and foods served were contaminated.

Keywords: Street Foods, Street Food Vendors, Food Safety, Hygienic Practices, Food Borne Diseases

*Correspondence: ovghsh_1085@hotmail.com

Citation: Ghosh A. An Account of Hygienic Practices and Street Food Safety Around the Medical Colleges of Kolkata, India. *J Pure Appl Microbiol.* 2023;17(4):2502-2513. doi: 10.22207/JPAM.17.4.48

© The Author(s) 2023. **Open Access.** This article is distributed under the terms of the [Creative Commons Attribution 4.0 International License](https://creativecommons.org/licenses/by/4.0/) which permits unrestricted use, sharing, distribution, and reproduction in any medium, provided you give appropriate credit to the original author(s) and the source, provide a link to the Creative Commons license, and indicate if changes were made.

INTRODUCTION

The Food and Agriculture Organization of United Nations (FAO) defines Street foods as ready-to-eat foods and beverages prepared and/or sold by vendors and hawkers, especially in streets and other public places. Street food retailing is wide spread in urban areas of developing countries.¹ It provides cost effective source of nourishment especially for the low-income workers of the urban poor populations.^{2,3} According to a 2007 study from the FAO, 2.5 billion people eat street food every day all over the world. Since it is obvious that proper hygienic quality of street vended foods is questionable, these may lead to food borne diseases which remain a major public health concern globally especially in case of diarrheal diseases. So, the safety of street foods is the most important aspect in the field of nutrition security. Ensuring food safety has been recognized as an important component in protecting the health of the people.⁴

According to National Policy for Urban Street Vendor/Hawker, in India, street food vendors constitute approximately 2% of the population of a metropolis.⁵ Street foods are conceived as major public health concern since there is lack of infrastructure in assessing and monitoring large number of street food vendors due to their mobility, miscellany and transitory nature.^{6,7}

The eating habits of a considerable number of people in Kolkata have changed like many metropolises due to increase in city's labour force and other mandatory aspects. Street foods area adopted chiefly because they are inexpensive, the taste is acceptable and they are conveniently available wherever people are gathered purposefully (schools, marketplaces, railway stations and office centers'). In Sealdah area, Kolkata, 1 to 2 % of the consumers spent between Rs. 1,500 to Rs.2,000 per month on street foods. On an average, regular consumers spent Rs. 750 on street foods per month.

Most of the studies done on street foods in India and abroad had indicated that these foods were not meeting the recommended microbiological standards and were contaminated with various pathogens viz. *E. coli*, *Vibrio cholerae*, *Salmonellae*, *Listeria* sp., etc. bringing mortality

worldwide.⁸ The microbiological status of the food has been reported to be dependent on several factors like quality of raw material; handling and processing of food, microorganisms those survive the preservation and storage treatment, post process contamination.⁹ The recent cases of food poisoning in Kottayam district of the state of Kerala and very recent street food poisoning incident in Koderma district of Jharkhand emphasize the poor knowledge of food safety, hygiene and microbiological quality of the foods served. Also, the food poisoning case in a religious gathering in Maharastra may be considered as an example of lack of concept of proper food hygiene amongst common people.¹⁰ There is a gross lack of awareness of epidemiological significance of street foods and no concept of food hygiene and safety measures along with very little public awareness about the safety of foods vended in streets. Earlier epidemiological studies suggest that, this poor knowledge about street food safety and host-pathogen relationship could lead to cases of food poisoning. There had been incidences of food poisoning outbreaks from street foods in Shangdong province (China) where 691 outbreaks were recorded along with 49 deaths during the span of 1983 to 1992.¹¹ Besides direct health consequences, these food borne illnesses can reduce the productivity and economic output, and also impose substantial stress on health care system.^{12,13} Identification of precise sources of microbial contamination is crucial when devising strategies to reduce further outbreaks.

MATERIALS AND METHODS

A cross sectional study was conducted among the street food vendors around the medical colleges of Kolkata who sold ready to eat foods especially in the street or market or any public place.

The duration of the study was two months from January 2020 to February 2020, since this period of the year becomes dry with lesser amount of moisture in the environment and chances of microbial contamination gets decreased. The aim of the study was to check the hygienic condition especially in the microbiological context at the time where chances of contaminations become lower due to environmental factors.

Taking prevalence (p) = 23; as indicated in an earlier similar study conducted in Kenya by Muhonja and Kimathi¹⁴ and absolute error as 10%, the sample size was determined by using the formula $n = (1.96)^2 pq / L^2$ and it was 68. [Prevalence (p) = 23%, $q = (100 - p) = 77\%$; L = estimate of precision, here taken as 10%.] By considering the non-response cases as 10% of the total sample; the revised sample size was 75.

There are seven medical colleges in Kolkata. The total number of food vendors around (within 50 metres radius) all medical colleges were listed and 75 food vendors were selected by simple random sampling.

There were two parts of this study- first; assessing the hygienic practices of the street food vendors and the microbiological analyses of selected food samples to check the food safety. Assessment of hygienic practices was done among 75 randomly selected food vendors and food samples for microbiological analysis were collected from 30% of food vendors selected by simple random sampling as similarity of food vending operations and poor hygienic conditions along with concept of food safety were observed amongst various food vendors examined. The gross activity of mesophilic bacteria usually stays low during the winter season in January and February at Kolkata. The study aimed to determine the microbiological standard of street foods even in that weather condition when chances bacterial contamination usually keeps low.

Data collection

Data collection was done in two ways- direct observation and interview with predesigned, pretested schedule. Confidentiality of the responses was assured. The data were collected specially on demography, sources of water, display of food items, types of serving plates, mode of washing plates, management of left-overs and personal hygiene.

Food sample collection procedure

Food Sample collection for bacterial analysis was performed during the month of January and February, 2020. The average outside temperature during that period was 26°C. The

microbiological studies were conducted during the end of February and beginning of March, 2020. Generally, the food samples were taken at the time of lunch. The foods of interest were purchased from the street vendors as it is for self-consumption. After the collection food samples were carried to the laboratory in pre-sterilized, labeled containers. The collected food samples were brought to the laboratory as soon as possible and kept in refrigerator but not for more than 36 hours.

Microbiological analyses

For microbiological analyses detection of *E.coli*, *Staphylococcus sp.*, *Shigella sp.* and *Enterobacter sp.* were emphasised since these are well known for water and food borne contaminations.¹⁵ Briefly, food samples were weighed at first and then pH of the foods were measured. Each sample was thoroughly mixed with calculated volume of sterile distilled water. Serial dilutions of samples were prepared for further analysis. After serial dilution, the diluted samples were transferred to the Nutrient Agar plates, and incubated at 37°C for overnight. After incubation the numbers of colonies were counted on the plates. The isolated colonies of microorganisms were transferred to fresh Nutrient agar plate for maintenance and further characterisation. For the identification of bacteria, the isolated colonies were morphologically characterized, e.g. colonial growth and pigmentation. The bacterial isolates were primarily characterized by Gram staining procedure using compound light microscope with oil-immersion objective. The different media used for this microbiological analysis were EMBagar, MacConkey agar. In biochemical characterization, Catalase test, IMViC test, Starch hydrolysis, Carbohydrate fermentation (lactose, sucrose, dextrose) was also performed. Presence of Lactic acid bacteria in curd related foods were analysed by using MRS medium in an aerobic condition.

Statistical analyses

Correlation between presence of food borne pathogens and various hygienic factors were assessed by logistic regression analysis using 'R'.

RESULTS AND DISCUSSION

Out of the 75 street food vendors interviewed, 89.33% were male and 10.67% were female. Majority of the food vendors (56.00%)

belonged to 40-60 years' age group followed by 41.33% in the age group of 20-30 years.

36% of the study population was selling puri/paratha/muri/ghoogni/daal/alurdam. 12% vendors sold sugar cane juice/lassi. 16% of

Table 1. Overall hygienic practices of the food vendors (n=75)

Attributes		Frequency	Percentage
Nature of foods	Hot	11	14.67
	Cold	13	17.33
	Both	51	68.00
Types of plates for servings foods	Disposable	23	30.67
	Non-disposable	38	50.67
	Both	14	18.67
Process of cleaning of serving plates (n=52)	By dropping in same buckets	48	92.31
	Under running water	4	7.69
Presentation of food items	Exposed	26	34.67
	Covered	19	25.33
	Both	30	40.00
Management of left-overs	No left over	32	42.67
	Used on next days	33	44.00
	Eat at home	9	12.00
	Thrown away	1	1.33
Fly Nuisance	Yes	35	46.67
	No	40	53.33
Cleaning of hands	With cloths	51	68.00
	With water	21	28.00
	With soaps	3	4.00
Water source for cooking	Tap water	73	97.33
	No water (sold ready-to-eat foods)	2	--

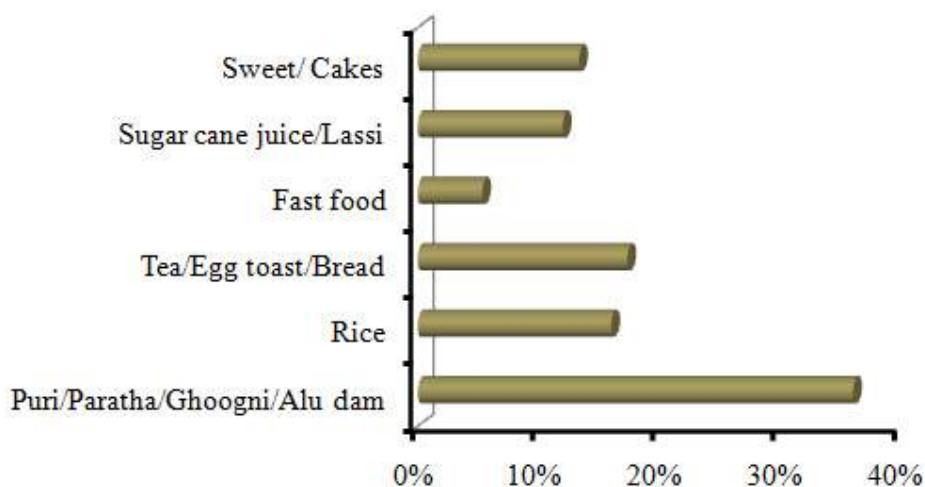


Figure 1. Diversity of food items sold by street food vendors

them sold Rice, 17.33% sold tea, biscuits, bread/eggtoast, and 5.33% sold fast-foods and remaining were selling other things like sweets, cake, etc. (Figure 1).

All the food vendors used tap water for drinking. 73 vendors out of 75 were using tap water for cooking and remaining two were not using water for cooking because they sold ready-to-eat packaged food (Table 1). Tap water was used for was hing plates by 100% of the food vendors who were not using disposable plates.

Most of the food vendors (88%) carried water by drums from the water sources to their business premises. 8% used bottles and 4% bucket for this purpose. Muindeand Kuria's study found water was ferried from homes of the street food vendors because no potable water was available at their areas of operation.¹⁶ They reported that 86%

food vendors in their survey were using tap water. This mainly depends upon the socio economic status of the vendor as well as the family. This also concurred with the study conducted by Bryan *et al.* and Abdalla *et.al.*^{8,17} Water may be a source of *E. coli*, *Campylobacter sp.* and previous studies have indicated the scarcity of potable water at many regions of Asia, Africa, South America to be used by street food vendors for various purposes.¹⁸ Indian studies have also shown the presence of low potability of water with respect to microbiological standards used for drinking and dish washing^{19,20} at street food vending stalls which is similar for most of the cases observed in this study too.

96% of the vendors were selling food on road. Twelve out of seventy five, sold food near open drains and seven vendors sold food near garbage. So, there was a high chance of

Table 2. Relation between hygienic practices and presence of food borne pathogens

Attributes	R ² value
Vendors used clean clothes	1.27#
Mode of hand cleaning (soap/only water/only a cloth)	2.069**
Vendors used left-over foods on next day	1.761**
Fly nuisance present in the food	2.954**

**indicates p<0.05 & # indicates p>0.05

Table 3. Average total bacterial count in various food items

FoodItems	Average ln CFU/ml or ln CFU/g ± SD
Ghooghny	15.570 ±0.75
Bread	17.296 ±0.87
Egg Toast	15.229 ±0.56
Rosogolla	11.775 ±0.65
Sugar Cane Juice	17.182 ±0.84
Chhatu Sarbat	16.639 ±1.05
Lassi	9.210 ±0.43
Fruit Juice	16.643 ±1.03

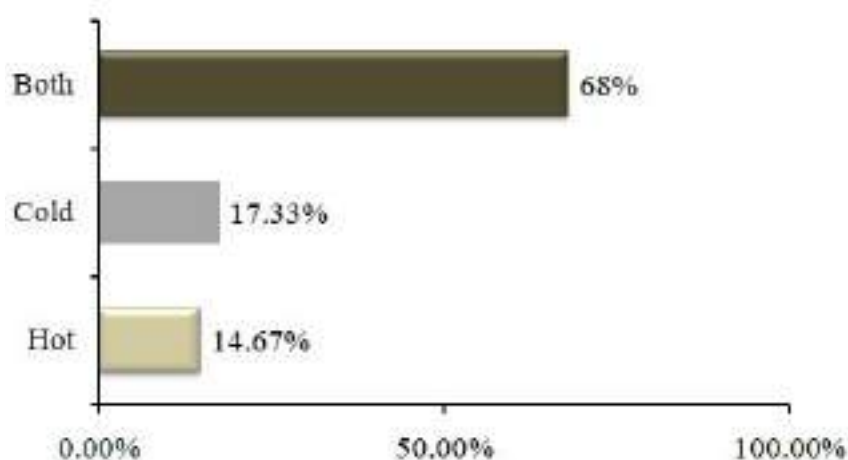


Figure 2. Distribution of food vendors according to type of food items

contamination of food with dust, vehicle exhausts, pathogenic microorganisms *etc.* So it was evident that, usually food vending conditions for several vendors were unsuitable and this type of scenario was reported earlier also relating to food borne diseases.^{19,21} It was observed in this study that, in many cases the same vending place is utilized by several vendors sequentially promoting chances of cross-contaminations.

14.67% of vendors served hot foods and 17.33% served cold foods (Figure 2). Selling of hot foods may decrease the chances of microbial contamination but heating and cooling down a food item in repeated cycles may also decrease the quality of food considerably.²² The cold or ambient temperature foods may have great chance of microbial contamination along with other types of contaminations. Inadequate reheating of stored foods during the busy periods with high

demands and obviously to save fuel as observed in this case, may also become a cause for bacterial development in the food. Similar observations contributing to increase in microbial load in such street foods were reported earlier too.²³

Among vendors using non-disposable (Figure 3) plates 92.31% were cleaning their serving utensils in stagnant water of bucket (Figure 4); (Table 1). Comfort O. Chukuezi found that the 47.62% of the vendors washed their utensils with dirty water which was recycled.²⁴ Properly cleaned utensils and cooking as well as food vending equipments are required for maintenance of food safety. The status of utensils observed in this study was not satisfactory with respect to sanitary and hygienic standards as poorly cleaned utensils in stagnant water may contain residual food items and can facilitate microbial growth as well as generation of bacterial exotoxins and needless to

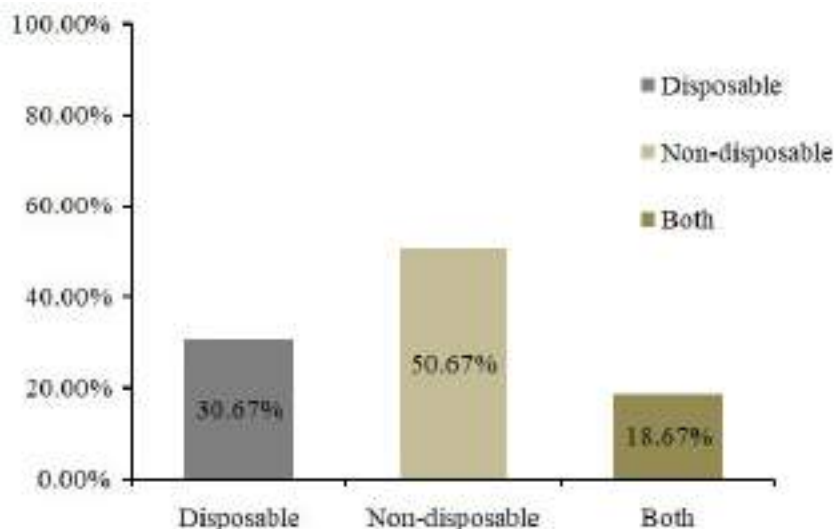


Figure 3. Street food vendors according to use of different types of plates for serving foods (n=75)

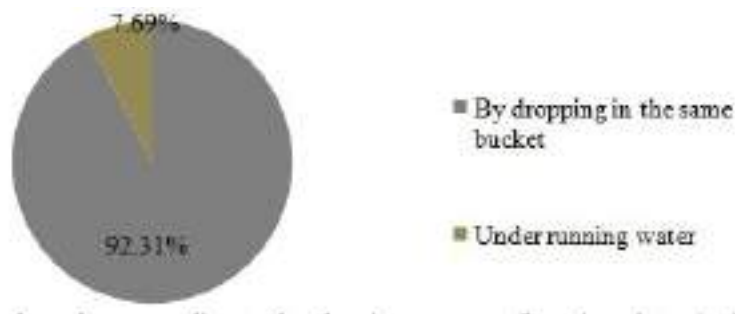


Figure 4. Street food vendors according to the process of cleaning serving plates (n=52)

say cross-contamination similar to some previous studies.¹¹

For the protection of foods from microorganism, dust, flies it is desirable to keep the foods covered. 34.67% of the food vendors kept food open and 25.33% covered the foods (Figure 5). 40% of the vendors kept some foods open and some covered (Table 1).

42.67% of the food vendors usually had no leftovers. A good percentage (44%) of vendors kept the left-overs for the next day use, 1.33% threw away the left-overs and 12% took the leftovers at home. As a very high percentage of food vendors served their leftover in next day, the freshness of foods was not there and quality was compromised. Comfort O. Chukuezi also found same kind of results where 42.86% had leftovers for serving the next day with poor storage facilities. The reason behind this may be due to poor socio-economic status and to reduce the cost they used the leftovers on the next day.

This concurred with the study of Muinde & Kuria which revealed that 35% of the vendors had left-over.¹⁶ Out of those, 32.1% reported consuming them and the rest stored them for the following day's sale. Consumption of left-over food on next day may impose the chances of contamination and degradation of food quality as a whole but these points were not seemed to be considered by the food vendors. Storage of unsold foods for next day or next round of business was obvious amongst the street food vendors here but usually storage conditions were improper leading to high microbial growth of diverse types. This practice of storing left-over foods was also identified in previous studies and significant microbial load was reported in Pakistan.²⁵⁻²⁷ The hot and humid weather of Kolkata city almost round the year also supports this type of microbial development on the left-over foods. A study based on Chandigarh reported about the marked increase of microbial load on storage for 16-24 hrs and principal bacterial

Table 4. Selected bacterial types in food samples tested

No.	Food Items	Avg. pH	Probable bacterial types			
			<i>E. coli</i>	<i>Staphylococcus</i> <i>sp.</i>	<i>Shigella</i> <i>sp.</i>	<i>Enterobacter</i> <i>sp.</i>
1.	Ghooghny	5.22	+	+	-	+
2.	Bread	5.20	+	+	+	-
3.	Egg Toast	6.30	-	-	+	+
4.	Rosogolla	5.40	-	-	-	+
5.	Sugar Cane Juice	3.90	-	+	-	+
6.	Chatu Sarbat	5.80	-	-	+	-
7.	Lassi	4.35	-	+	+	-
8.	Fruit Juice	3.20	-	-	-	+

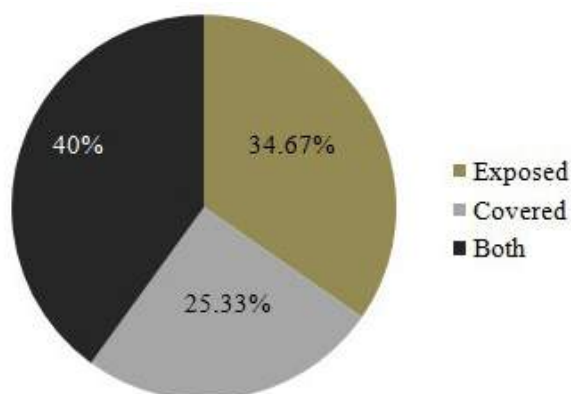


Figure 5. Street food vendors according to the presentation of food items (n=75)

types identified were *Salmonellae*, *Shigellae*, *Pseudomonas* etc. as enteric pathogens.¹¹ A recent study carried out in Lucknow, UP also speculated about the chances of contamination by faecal food

borne pathogens due to the filthy conditions of street food vending both in the personal as well as community hygiene aspects and regarded the street food mostly as unhygienic.²⁸

Table 5. Relation between food vending strategy with potential hazard and probable microbiological threats

Attributes	Potential Hazard	Probable microbiological threat
Water and raw materials used (Principally tap water was used and washing of non-disposable plates insame water for several times)	Inappropriate waste disposal Vegetables and raw food materials	Transmission of enteric pathogens like faecal <i>E.coli</i> , <i>Salmonella enterica</i> , <i>Shigellasp</i> , faecal <i>Streptococci</i> , <i>Vibrio cholerae</i> etc.
Utensils & other equipments	Chemical contamination and severe Environmental pollution	Probability of passage of spore formers like <i>Bacillus</i> , <i>Clostridium</i> , food borne <i>Listeriae</i> etc. Leaching of chemicals from the utensils due to repeated cycles of heating and serving foods without considering the quality of the utensils. Most importantly, damage to the environment due to improper disposal of non-degradable plastic and other polymeric food plates.
Food storage & reheating	Improper storage condition of foods and reheating	This may lead to growth and multiplication of food borne intoxicants like <i>Clostridium botulinum</i> and <i>Staphylococcus aureus</i> which can lay the potent and moderately heat stable bacterial toxins in the foods.
Personal Hygiene (Mostly dirty clothes and aprons used)	Bacterial & parasitic hazards	Unclean nails and unhygienic & dirty cloths may lead to contamination by <i>Staphylococci</i> , <i>Entamoeba</i> and helminths
Food vending location (Near garbage and open sewages)	Indecent food handling	Dirty and unhygienic locations as near to garbage or open sewage passage may lead to cross-contamination involving microbes facilitating faecal-oral routes and also vector-borne diseases due to fly nuisance.

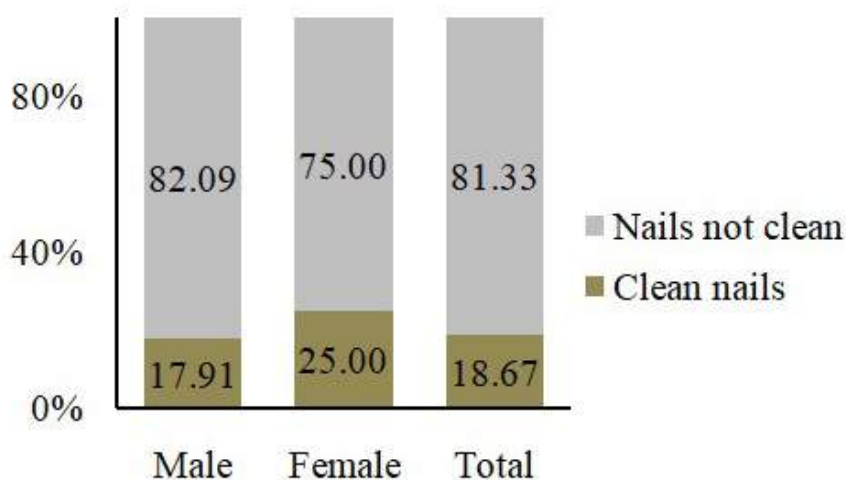


Figure 6. Personal hygiene of food vendors according to cleanliness of nails

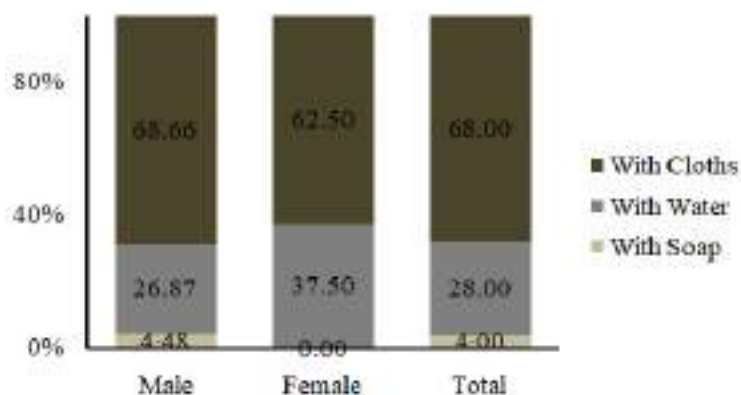


Figure 7. Distribution of food vendors according to hand washing hygiene

Personal hygiene is an important aspect to everybody and it is very essential for food vendors because poor personal hygiene increase the contamination greatly. In this study, none of the food vendors used head cap or apron or hand gloves during preparation or selling of foods indicating lack of proper personal hygiene. Previous studies have shown that, use of aprons, gloves or head cap during serving the food items was practiced by only small proportion of the food vendors and this practice of not following the use of gloves or head cap or aprons led to less safety of street,²⁴ since they found that 42.86% did not use aprons; 47.62% handled food with bare hands and 52.38% wore no hair covering while 61.90% handled money while serving food. Hygienic practices of street food vending of densely populated cities were also found to be similar as demonstrated in a previous study in China where low financial condition of the vendors was identified as a potential cause of ill hygiene of street foods.²⁹

Only 20% of food vendors wore clean clothes and remaining (80%) wore unclean clothes. 82.09% of the male food vendors wore clean clothes. On the other hands 62.50% of female food vendors wore clean clothes. Wearing of metallic jewellerys during food handling may not be considered as hygienic since food materials may get deposited on the jewellerys and stick to those leading to increased chance of microbial contaminations and biochemical reactions occurring on the metallic jewellerys due to

microbial growth can lead to chemical poisoning and this was also observed previously.²⁴

The nails of the maximum number of food vendors were not clean and they were handling the food without gloves. 82.09% of the males and 75% of females and in total 81.33% of food vendors did not have clean nail. 17.91% of males and 25% of females and in total 18.67% of the vendors possessed cleannails (Figure 6). Handling of foods in unsanitary ways such as using dirty hands, unclean nails, use of old and dirty aprons, gloves are considered as sources of contaminations as reported in a few studies.¹⁸

It is necessary aspect of personal hygiene to wash the hands properly before handling the food items to minimise the possibility of contamination of foods. But as shown in the study found that most of the food vendors cleaning hands with filthy clothes and very few of them washed their hands by soap before preparation of foods (Figure 7). The female street food vendors were found to be little bit more hygienic as compared to male food vendors. The personal hygiene and properly maintained food vending stalls in relation to street food safety was a concern as depicted in South Africa too where almost 76% of the street food vendors had very little knowledge about food safety and consequently led to poor sanitary quality of street foods.³⁰

46.67% of the food vendors had fly nuisance (Table 1) and this might come out to be a serious problem in terms of hygienic quality of the foods. Since flies may bring about serious

concerns in the hygienic condition of the food by contaminating the foods with many dirty materials like sewage and faecal matters. This also increases the chance of contaminating the food materials with probable food borne pathogens. In this study, it was observed that fly nuisance had significant relation with the presence of probable food borne pathogens (Table 2).

The bacterial load in sugar cane juice, fruit juice, chhatu-sarbat was relatively higher as they were not served as a hot food and compared to the other food items; the water content of these foods is high too. The bacterial load of Rosogolla was less which might be due to presence of sugar into it where sugar acted as a natural preservative.

Total bacterial count in rosogolla (solid food category) and lassi (liquid food items) were small compared to the other food items. The total bacterial count in the food items assayed is depicted in the Table 3.

Half of the food samples were contaminated with organisms which may cause food borne diseases. *Shigella* sp., *Staphylococcus* sp., *E.coli*, were present in lassi, chhatu-sarbat, sugar cane juice, rosogolla, egg toast, bread and ghooghny of those 24 food samples (Table 4) which may cause serious food poisoning. Coli forms were found in 8.33% of the food samples. The presence of *E.coli* in food is chiefly an indicator of faecal contamination, concluding that those food samples might be faecally contaminated. Previous studies have also reported about the presence of *E.coli* in almost half of the samples assayed. The total bacterial load depicted here is a serious problem from the consumer point of view, since the numbers of users of these foods are very high, complicating the problems more. FSSAI also do not give any such concrete guideline about the permissive microbial load in respect of these types of foods.³¹

The correlation between presence of food borne pathogens and various hygienic practices was studied. In this aspect, it was observed that, except the clothes worn by the food vendors, other hygienic attributes played significant roles in inducing probable food borne pathogens in the foods. Hygienic factors like mode of hand cleaning (soap/only water/only a piece of cloth), leftover foods and presence of flies in the foods

contributed significantly in introducing food borne pathogens (Table 2).

The current study illustrates general practices of street food vendors around medical college and hospitals of Kolkata city. Since street foods are basically served with bare hands and the hands as well as fingers, nails are the most common ways to spread contaminations from other parts of the body like nose, lips, mouth, legs and faeces too, the hygienic quality is of utmost importance which is also in accordance with the data published by WHO.³¹ Here we have observed that, hygienic condition of the hands is very poor amongst most of the studied street food vendors which increased the chance of contamination by organisms like *E. coli*, *Listeriae*, *Salmonellae* etc.^{31,32} Also, the supply of clean water for washing hands and utensils maintaining the proper hygienic standard according to microbial and other aspects is not available at all the places in the city enhancing the chance of contracting microbial contaminants.⁸

Selection of food vending sites as the places around busy medical colleges is also impactful as major hospitals are associated with medical colleges and people are bound to avail the facilities available at medical colleges and associated hospitals as per medical emergency.

Analysis of hazards and probable microbial threats

Since several attributes of street food vendors like type and quality of water, utensils used, locations of the vending stalls, serving hot/cold/reheated foods were thoroughly studied, a potential hazard and probable microbiological threat analysis is predicted (Table 5) following the review work by S. Rane.¹¹

CONCLUSION

The hygienic practices of the food vendors around the medical colleges of Kolkata were very poor. Majority of the vendors did not maintain proper personal hygiene. Foods were not safe as half of the food samples were contaminated with the bacteria, both fecal and non-fecal, that can cause food borne diseases. This might be due to lack of proper knowledge regarding food hygiene.

Another thing that has to be considered in respect of street food vending in Kolkata city is that the financial condition of the food vendors is usually poor and they look for the profit as high as possible with their least possible investment.

Therefore, education of the food vendors about personal hygiene becomes necessary and trainings should therefore, be arranged for the street food vendors on various aspects of personal hygiene. The state may think about conducting such workshops, training programmes involving NSS from different educational institutions. The FSSAI should also think to frame some baseline about the permissive microbial load in these foods readily sold in the streets.

Future scope

This type of studies on larger scale may be undertaken in future by the people in National Service Scheme from many educational institutions. This would help gather the knowledge of food safety, personal hygiene for food handling and spread the concept of nutrition security with respect to potable standard of foods amongst the street food vendors of developing countries contributing to nation development. Also FSSAI may impose guidelines to increase the hygienic quality of street foods depending on the results of this type of further studies.

ACKNOWLEDGMENTS

The author is grateful to Sri Malay Mitra, AIHH&PH, Kolkata for helping in the collection of data. The author sincerely acknowledges The Principal & Head of Microbiology Department, Maulana Azad College Kolkata for allowing to conduct the study by using the laboratory facility. The author is also grateful to the Department of Higher Education, Govt. of West Bengal for the financial resources.

FUNDING

None.

DATA AVAILABILITY

All datasets generated or analyzed during this study are included in the manuscript.

ETHICS STATEMENT

Not applicable.

REFERENCES

- Solomons NW, Gross R. Urban Nutrition in Developing Countries. *Nutr Rev.* 1995;53(4):90-95.doi: 10.1111/j.1753-4887.1995.tb01526.x
- Kaferstein F, Abdussalam M. Food Safety in the 21st Century, 77; 1999. Accessed September 21, 2023. <https://www.ncbi.nlm.nih.gov/pmc/articles/PMC2557642/pdf/10327714.pdf>
- Freese E, Romero-Abal ME, Solomons NW, Gross R. The microbiological safety of typical Guatemalan foods from street vendors, low-income homes and hotels. *Int J Food Sci Nutr.* 1998;49(1):27-38.doi: 10.3109/09637489809086401
- The Prevention of Food Adulteration Act & Rules, Govt. of India(as on 1.10.2004).; 2004. Accessed September 21, 2023. <https://fssai.gov.in/upload/uploadfiles/files/pfa-acts-and-rules.pdf>
- Bhowmik SK. Street Vendors in Asia/ : A Review Growth of Street Vending. *Econ Polit Wkly.* 2005;2256-2264.
- Ghosh M, Wahi S, Kumar M, Ganguli A. Prevalence of enterotoxigenic *Staphylococcus aureus* and *Shigella spp.* in some raw street vended Indian foods. *Int J Environ Health Res.* 2007;17(2):151-156.doi: 10.1080/09603120701219204
- De Sousa CP. The Impact of Food Manufacturing Practices on Food borne Diseases. *Braz arch Bioltechnol.* 2008;51(4):815-823.doi: 10.1590/S1516-89132008000400020
- Bryan FL, Michanie SC, Alvarez P, Paniagua A. Critical Control Points of Street-Vended Foods in the Dominican Republic. *J Food Prot.* 1988;51(5):373-383. doi: 10.4315/0362-028X-51.5.373
- Jones RN. Microbiological Conclusions. *Drugs.* 1991;42(Suppl 3):22-24.doi: 10.2165/00003495-199100423-00006
- Bajaj S, Dudeja P. Food poisoning outbreak in a religious mass gathering. *Med J Armed Forces India.* 2019;75(3):339-343.doi: 10.1016/j.mjafi.2018.12.015
- Rane S. Street Vended Food in Developing World. *Hazard Analyses.* 2011;51(1):100-106.doi: 10.1007/s12088-011-0154-x
- Mosupye FM, von Holy A. Microbiological hazard identification and exposure assessment of street food vending in Johannesburg, South Africa. *Int J Food Microbiol.* 2000;61(2-3):137-145.doi: 10.1016/S0168-1605(00)00264-6
- Martins JH. Socio-economic and hygiene features of street food vending in Gauteng. *South African J Clin Nutr.* 2006;19(1):18-25.doi: 10.1080/16070658.2006.11734085
- Muhonja F, Kimathi GK. Faith Muhonja, George KobiaKimathi. Assessment of Hygienic and Food Handling Practices among Street Food Vendors in Nakuru Town in Kenya. *Sci J Public Heal.* 2014;2(6):554-559. doi:10.11648/j.sjph.20140206.19
- Lacey RW. Food-borne bacterial infections. *Parasitology.* 1993;107(S1):S75-S93.doi: 10.1017/S0031182000075521
- Muinde OK, Kuria E. Hygienic and Sanitary Practices of Vendors of Street Foods in Nairobi, Kenya. *African J Food Agric Nutr Dev.* 2005;5(8):01-14.doi: 10.18697/

- ajfand.8.1060
17. Abdalla MA, Suliman SE, Bakhiet AO. Food safety knowledge and practices of mobile food vendor in Atbara city(nahereIneel state student). *African J Biotechnol.* 2009;8(24):696-6971.
18. Dawson RJ, Canet C. International activities in street foods. *Food Control.* 1991;2(3):135-139.doi: 10.1016/0956-7135(91)90081-7
19. Nicolas B, Abdoul BR, Aly S, Amadou OTC, Jules IA, Alfred TS. Hygienic status assessment of dish washing waters, utensils, hands and pieces of money from street food processing sites in Ouagadougou (Burkina Faso). *African J Biotechnol.* 2006;5(11):1107-1112. <http://www.academicjournals.org/AJB>
20. Bhat RV, Waghay K. Profile of street foods sold in Asian countries. *World Rev Nutr Diet.* 2000;86:53-99. doi: 10.1159/000059731
21. Bryan FL, Bartleson CA, Christopherson N. Hazard Analyses, in Reference to Bacillus cereus , of Boiled and Fried Rice in Cantonese-Style Restaurants 1. *J Food Prot.* 1981;44(7):500-512.doi: 10.4315/0362-028X-44.7.500
22. Yadav BS, Sharma A, Yadav RB. Studies on effect of multiple heating/cooling cycles on the resistant starch formation in cereals, legumes and tubers. *Int J Food Sci Nutr.* 2009;60(supL 4):258-272.doi: 10.1080/09637480902970975
23. Omemu AM, Aderoju ST. Food safety knowledge and practices of street food vendors in the city of Abeokuta, Nigeria. *Food Control.* 2008;19(4):396-402. doi: 10.1016/j.foodcont.2007.04.021
24. Okoroha C. Assessing the Food Safety and Hyienic Practices of Street Food Vendors in south Western Nigeria. *ISEE Conf Abstr.* 2016;2016(1):50-57.doi: 10.1289/isee.2016.4596
25. El-Sherbeeney MR, Saddik MF, Bryan FL. Microbiological profiles of foods served by street vendors in Egypt. *Int J Food Microbiol.* 1985;2(6):355-364.doi: 10.1016/0168-1605(85)90026-1
26. Bryan FL, Teufel P, Riaz S, Roohi S, Qadar F, Malik ZUR. Hazards and Critical Control Points of Street-Vending Operations in a Mountain Resort Town in Pakistan. *J Food Prot.* 1992;55(9):701-707.doi: 10.4315/0362-028X-55.9.701
27. Bryan FL, Teufel P, Riaz S, Roohi S, Qadar F, Malik ZUR. Hazards and Critical Control Points of Street-Vended Chat, a Regionally Popular Food in Pakistan. *J Food Prot.* 1992;55(9):708-713.doi: 10.4315/0362-028X-55.9.708
28. Verma R, Patel M, Shikha D, Mishra S. Assessment of food safety aspects and socioeconomic status among street food vendors in Lucknow city. *J Agric Food Res.* 2023;11:100469.doi: 10.1016/j.jafr.2022.100469
29. Ma L, Chen H, Yan H, Wu L, Zhang W. Food safety knowledge, attitudes, and behavior of street food vendors and consumers in Handan, a third tier city in China. *BMC Public Health.* 2019;19(1):1128.doi: 10.1186/s12889-019-7475-9
30. Nkosi NV, Tabit FT. The food safety knowledge of street food vendors and the sanitary conditions of their street food vending environment in the Zululand District, South Africa. *Heliyon.* 2021;7(7):e07640.doi: 10.1016/j.heliyon.2021.e07640
31. WHO. Health Surveillance and Management Procedures for Food-Handling Personnel.; 1989. Accessed September 17, 2023. <https://iris.who.int/handle/10665/39610>
32. Pether JV, Gilbert RJ. The survival of salmonellas on finger-tips and transfer of the organisms to foods. *J Hyg (Lond).* 1971;69(4):673-681.doi: 10.1017/S002217240002194X